The Effect Of Forward Sweep On A Wing/Body Junction

Arnott, Alistair Duncan

The Effect Of Forward Sweep On A Wing/Body Junction ~~Flow~~

Alistair Duncan Arnott

Thesis submitted for the degree of Doctor of Philosophy

1996

Department of Aeronautical Engineering

Queen Mary and Westfield College

University of London

Abstract

A study has been carried out of the aerodynamic interference flow arising at the junction of a swept-forward wing, which is cambered, but without taper or twist and a flat plate on which a fully-developed, turbulent boundary layer approaches the junction. Initial CFD predictions of the pressures over the wing were carried out by the author at BAe, Hatfield. Flow visualisation tests and surface pressure measurements over the wind tunnel model were conducted at wing incidences from -3° to +9°. With the wing at 0° incidence, a single-tube yawmeter was used to explore the flow field around the leading-edge of the junction and an X-wire anemometer to examine the mean velocity and turbulence fields in the streamwise corners and at the trailing edge. The Reynolds number of the tests, based on the streamwise chord and free stream velocity of 30 m/s, was 1.03×10^6.

At low incidence, a very weak separation occurred in the plate boundary layer, a very short distance upstream of the junction. However the oncoming stream converges into the junction, appearing to confine any vortical motion at the leading edge to within a very thin layer below the closest point of measurement to the plate. Rudimentary vortical flow developed slightly downstream of the leading edge, but dissipated further downstream. Although weak vortices were measured in the trailing-edge, cross-plane, these were attributed to corner separations just upstream. The turbulence activity in the streamwise corners was found to be surprisingly low, especially in the compression side of the junction. Estimates of skin-friction showed that it was lower over the majority of the trailing-edge cross-plane than in the plate boundary layer upstream of the junction. At higher incidence, flow visualisation showed that the junction region had severe stall characteristics, with 3-dimensional recirculation regions forming.

Acknowledgements

This project was funded wholly by the former Research Department of the sadly now defunct British Aerospace, Hatfield, Civil Aircraft Factory, under contract HY-110706. Their support: financial, intellectual and the provision of facilities, is greatly appreciated.

I owe a great deal of thanks to my supervisor, Dr Leonard Bernstein, for not only having the faith to give me the job in the first place, but also for his invaluable advice and encouragement during the years and his patient reading of the various texts that have culminated in this thesis. In addition, Dr David Petty, although not officially a supervisor, deserves a big thankyou for his additional advice, support and help in the laboratory.

Very grateful thanks (and quite a few pints) go to the technicians involved with the project, in particular Ian Bater, Ken Taplin, Roger Montague and Danny Neighbour. Their skill, friendliness and help made the lab work so much easier and more bearable.

I would like to thank my friends and colleagues for their friendship, help, fondness of sport, curry & beer and generally reminding me that I was allowed to switch off after 5pm. There's no way I could do everybody justice - sorry! However, for very different but gratefully remembered reasons, I would like to thank in particular: Diana, Andy Clarke, Ade, Marion, Sheila, Pete & Sue, Paul & Theresa, Andy Sowdon, Geoff, Maria, Fawaz, Shen Shen, Nick, Andy Denny, Kathy, Anthony, Richard, Louise, Mike,and John. Rather more bizzarely, thanks to the RAF for letting me go, otherwise I wouldn't have had the chance to do this!

However, by far and away the biggest thank you of the lot must go to my parents and brother for their monumental support, affection and everything else they have done to make life easier for me whilst doing this.

Contents

List of Figures and Plates

Figures

Figure 20 Exaggerated view of the leading edge of figure 10.

Figure 21 Viscous predictions obtained from **FELMA**, of pressure distribution over the aerofoil section, at:

(a) $\alpha = +3°$, (b) $\alpha = +6°$ & (c) $\alpha = +9°$.

Figure 22 Inviscid predictions obtained from **SPARV** of chordwise pressure distribution at stations along the span of the wing of aspect ratio 4, with a reflection plate at the wing tip, at:

(a) $\alpha = +1°$ & (b) $\alpha = +3°$

Spanwise interval *Y/c* between stations = 0.2.

(continued...

Figure 22 Inviscid predictions obtained from **SPARV** of chordwise pressure distribution at stations along the span of the wing of aspect ratio 4, with a reflection plate at the wing tip, at:

(c) $\alpha = +5°$ & (d) $\alpha = +7°$

Spanwise interval *Y/c* between stations = 0.2.

...concluded)

Figure 23 Inviscid predictions obtained from **SPARV** of chordwise pressure distribution at stations along the span of the wing of AR = 8, with a reflection plate at the wing tip, at $\alpha = +3°$. Spanwise interval *Y/c* between stations = 0.2.

Figure 24 Inviscid predictions obtained from **SPARV** of chordwise pressure distribution at stations along the span of the wing of aspect ratio 4, with a free wing tip, at $\alpha = +7°$. Spanwise interval *Y/c* between stations = 0.2.

Figure 25 Locations around the aerofoil section at which pressure tubes were inlaid.

Figure 26 Locations of pressure tappings in the plate.

Figure 27 3-D view of the wing and plate showing the *left-handed* axis system.

Figure 28 Oblique view of the wing mounted in the wind tunnel.

Figure 29 The roof-mounted traversing gear.

Figure 43 Semi-logarithmic plot of the velocity profile at (X,Z)/mm = (-500,-120), compared with the log-law: $\frac{\overline{U}}{u_\tau} = 5.75 \log\left(\frac{u_\tau (Y - Y_o)}{\nu}\right) + 5.5$.

Figure 44(a) Pressure distributions on the wing, at various non-dimensional spanwise distances Y/c from the junction, at α = -3°.

Figure 44(b) Pressure distributions on the wing, at various non-dimensional spanwise distances Y/c from the junction, at α = 0°.

Figure 44(c) Pressure distributions on the wing, at various non-dimensional spanwise distances Y/c from the junction, at α = +3°.

Figure 44(d) Pressure distributions on the wing, at various non-dimensional spanwise distances Y/c from the junction, at α = +6°.

Figure 44(e) Pressure distributions on the wing, at various non-dimensional spanwise distances Y/c from the junction, at α = +9°.

Figure 45(a) Surface Cp contours on the plate, around the leading edge of the junction, at α = -3°.

Figure 45(b) Surface Cp contours on the plate, around the leading edge of the junction, at α = 0°.

Figure 45(c) Surface Cp contours on the plate, around the leading edge of the junction, at α = +3°.

Figure 45(d) Surface Cp contours on the plate, around the leading edge of the junction, at α = +6°.

Figure 45(e) Surface Cp contours on the plate, around the leading edge of the junction, at α = +9°.

Figure 46 Spanwise distribution of normal-force coefficient at α = -3°, 0°, +3°, +6° & +9°.

Figure 47 Spanwise distribution of lift-force coefficient at α = -3°, 0°, +3°, +6° & +9°

.

Figure 54 Cross-flow velocity vectors in the junction at $\alpha = 0°$, in planes normal to the tangents to the wing profile on both sides of the junction at $X = 10$ mm:

(a) Plane D — $\beta_S = -72.8°$ & (b) Plane I — $\beta_S = 62.8°$.

Figure 55 Cross-flow velocity vectors in the junction at $\alpha = 0°$, in planes normal to the tangents to the wing profile on both sides of the junction at $X = 40$ mm:

(a) Plane E — $\beta_S = -81.3°$ & (b) Plane J — $\beta_S = 77.9°$.

Figure 56 Profiles of static pressure coefficient through the plate boundary layer, in the leading-edge region at $\alpha = 0°$, in planes normal to the tangent to the local wing profile around the leading edge.

(continued...

Figure 56 Profiles of static pressure coefficient through the plate boundary layer, in the leading-edge region at $\alpha = 0°$, in planes normal to the tangent to the local wing profile around the leading edge.

...concluded)

Figure 57 Profiles of velocity vector Q/U_∞ through the plate boundary layer, in the leading-edge region at $\alpha = 0°$, in planes normal to the tangent to the local wing profile around the leading edge.

(continued...

Figure 57 Profiles of velocity vector Q/U_∞ through the plate boundary layer, in the leading-edge region at $\alpha = 0°$, in planes normal to the tangent to the local wing profile around the leading edge.

...concluded)

Figure 58 Profiles of $(\overline{U}, \overline{V}, \overline{W})/U_\infty$ through the plate boundary layer in Plane K, normal to the tangent to the wing lower-surface profile at $X = 300$ mm, at various distances from the junction. Wing incidence $\alpha = 0°$.

(continued...

Figure 58 Profiles of $(\overline{U}, \overline{V}, \overline{W})/U_\infty$ through the plate boundary layer in Plane *K*, normal to the tangent to the wing lower-surface profile at X = 300 mm, at various distances from the junction. Wing incidence $\alpha = 0°$.

...concluded)

Figure 59 Profiles of $(\overline{U}, \overline{V}, \overline{W})/U_\infty$ through the plate boundary layer in Plane *L*, normal to the tangent to the wing upper-surface profile at X = 300 mm, at various distances from the junction. Wing incidence $\alpha = 0°$.

(continued...

Figure 59 Profiles of $(\overline{U}, \overline{V}, \overline{W})/U_\infty$ through the plate boundary layer in Plane *L*, normal to the tangent to the wing upper-surface profile at X = 300 mm, at various distances from the junction. Wing incidence $\alpha = 0°$.

...concluded)

Figure 60 Profiles of $(\overline{u^2}, \overline{v^2}, \overline{w^2})/U_\infty^2$ through the plate boundary layer in plane *K*, normal to the tangent to the wing lower-surface profile at X = 300 mm, at various distances from the junction. Wing incidence = 0°.

(continued...

Figure 60 Profiles of $(\overline{u^2}, \overline{v^2}, \overline{w^2})/U_\infty^2$ through the plate boundary layer in plane *K*, normal to the tangent to the wing lower-surface profile at X = 300 mm, at various distances from the junction. Wing incidence = 0°.

...concluded)

Figure 61 Profiles of $(\overline{u^2}, \overline{v^2}, \overline{w^2})/U_\infty^2$ through the plate boundary layer in plane *L*, normal to the tangent to the wing upper-surface profile at X = 300 mm, at various distances from the junction. Wing incidence = 0°.

(continued...

Figure 61 Profiles of $(\overline{u^2}, \overline{v^2}, \overline{w^2})/U_\infty^2$ through the plate boundary layer in plane *L*, normal to the tangent to the wing upper-surface profile at X = 300 mm, at various distances from the junction. Wing incidence = 0°.

...concluded)

Figure 67 Contours of $(\overline{u^2},\overline{v^2},\overline{w^2})/U_\infty^2$ in the junction at α = 0° (viewed from downstream), in planes normal to the tangent to the wing profile on both sides of the junction at X = 300 mm:

(a) $\overline{u^2}/U_\infty^2$, (b) $\overline{v^2}/U_\infty^2$ & (c) $\overline{w^2}/U_\infty^2$.

Figure 68 Surface maps of $(\overline{u^2},\overline{v^2},\overline{w^2})/U_\infty^2$ in the junction at α = 0°, in planes normal to the tangent to the wing profile on both sides of the junction at X = 300 mm:

(a) $\overline{u^2}/U_\infty^2$, (b) $\overline{v^2}/U_\infty^2$ & (c) $\overline{w^2}/U_\infty^2$.

Figure 69 Contours of $(\overline{uv},\overline{uw},\overline{vw})/U_\infty^2$ in the junction at α = 0° (viewed from downstream), in planes normal to the tangent to the wing profile on both sides of the junction at X = 300 mm:

(a) $\overline{uv}/U_\infty^2$, (b) $\overline{uw}/U_\infty^2$ & (c) $\overline{vw}/U_\infty^2$.

Figure 70 Surface maps of $(\overline{uv},\overline{uw},\overline{vw})/U_\infty^2$ in the junction at α = 0°, in planes normal to the tangent to the wing profile on both sides of the junction at X = 300 mm:

(a) $\overline{uv}/U_\infty^2$, (b) $\overline{uw}/U_\infty^2$ & (c) $\overline{vw}/U_\infty^2$.

Figure 71 Profiles of $(\overline{U},\overline{V},\overline{W})/U_\infty$ through the plate boundary layer at α = 0° in plane *TE* (X = 500 mm), at various distances normal to the chord line in the -Z direction.

(continued...

Figure 71 Profiles of $(\overline{U},\overline{V},\overline{W})/U_\infty$ through the plate boundary layer at α = 0°, in plane *TE* (X = 500 mm), at various distances normal to the chord line in the -Z direction.

...concluded)

Figure 72 Profiles of $(\overline{U},\overline{V},\overline{W})/U_\infty$ through the plate boundary layer at α = 0°, in plane *TE* (X = 500 mm), at various distances normal to the chord line in the +Z direction.

(continued...

Figure 72 Profiles of $(\overline{U}, \overline{V}, \overline{W})/U_\infty$ through the plate boundary layer at α = 0°, in plane *TE* (X = 500 mm), at various distances normal to the chord line in the $+Z$ direction.

...concluded)

Figure 73 Semi-logarithmic plots of the measured $\overline{U}$ -velocity profiles, compared with the log-law:

$$\frac{\overline{U}}{u_\tau} = 5.75 \log\left(\frac{u_\tau (Y - Y_o)}{\nu}\right) + 5.5,$$

at stations in plane *TE* (X = 500 mm), in the $-Z$ direction.

Figure 74 Semi-logarithmic plots of the measured $\overline{U}$ -velocity profiles, compared with the log-law:

$$\frac{\overline{U}}{u_\tau} = 5.75 \log\left(\frac{u_\tau (Y - Y_o)}{\nu}\right) + 5.5,$$

at stations in plane *TE* (X = 500 mm), in the $+Z$ direction.

Figure 75 Distribution of boundary-layer shape parameter H, in plane *TE* (X = 500 mm).

Figure 76 Distribution of skin-friction coefficient on the plate, in plane *TE* (X = 500 mm).

Figure 77 Profiles of $(\overline{u^2}, \overline{v^2}, \overline{w^2})/U_\infty^2$ through the plate boundary layer at α = 0°, in plane *TE* (X = 500 mm), at various distances normal to the chord line in the $-Z$ direction.

(continued...

Figure 77 Profiles of $(\overline{u^2}, \overline{v^2}, \overline{w^2})/U_\infty^2$ through the plate boundary layer at α = 0°, in plane *TE* (X = 500 mm), at various distances normal to the chord line in the $-Z$ direction.

...concluded)

Figure 78 Profiles of $(\overline{u^2}, \overline{v^2}, \overline{w^2})/U_\infty^2$ through the plate boundary layer at α = 0°, in plane *TE* (X = 500 mm), at various distances normal to the chord line in the $+Z$ direction.

(continued...

Figure 78 Profiles of $(\overline{u^2},\overline{v^2},\overline{w^2})/U_\infty^2$ through the plate boundary layer at α = 0°, in plane *TE* (X = 500 mm), at various distances normal to the chord line in the +Z direction.

...concluded)

Figure 79 Profiles of $(\overline{uv},\overline{uw},\overline{vw})/U_\infty^2$ through the plate boundary layer at α = 0°, in plane *TE* (X = 500 mm), at various distances normal to the chord line in the -Z direction.

(continued...

Figure 79 Profiles of $(\overline{uv},\overline{uw},\overline{vw})/U_\infty^2$ through the plate boundary layer at α = 0°, in plane *TE* (X = 500 mm), at various distances normal to the chord line in the -Z direction.

...concluded)

Figure 80 Profiles of $(\overline{uv},\overline{uw},\overline{vw})/U_\infty^2$ through the plate boundary layer at α = 0°, in plane *TE* (X = 500 mm), at various distances normal to the chord line in the +Z direction.

(continued...

Figure 80 Profiles of $(\overline{uv},\overline{uw},\overline{vw})/U_\infty^2$ through the plate boundary layer at α = 0°, in plane *TE* (X = 500 mm), at various distances normal to the chord line in the +Z direction.

...concluded)

Figure 81 Contours of $\overline{U}/U_\infty$ in the junction at α = 0° (viewed from downstream), in plane *TE* (X = 500 mm).

Figure 82 Surface map of $\overline{U}/U_\infty$ in the junction at α = 0°, in plane *TE* (X = 500 mm).

Figure 83 Cross-flow velocity vectors in the junction at α = 0° (viewed from downstream), in plane *TE* (X = 500 mm).

Figure 84 Contours of $(\overline{u^2},\overline{v^2},\overline{w^2})/U_\infty^2$ in the junction at α = 0° (viewed from downstream), in plane *TE* (X = 500 mm):

(a) $\overline{u^2}/U_\infty^2$, (b) $\overline{v^2}/U_\infty^2$ & (c) $\overline{w^2}/U_\infty^2$.

Figure 85 Surface maps of $(\overline{u^2},\overline{v^2},\overline{w^2})/U_\infty^2$ in the junction at α = 0°, in plane *TE* (*X* = 500 mm):

(a) $\overline{u^2}/U_\infty^2$, (b) $\overline{v^2}/U_\infty^2$ & (c) $\overline{w^2}/U_\infty^2$.

Figure 86 Contours of $(\overline{uv},\overline{uw},\overline{vw})/U_\infty^2$ in the junction at α = 0° (viewed from downstream), in plane *TE* (*X* = 500 mm):

(a) $\overline{uv}/U_\infty^2$, (b) $\overline{uw}/U_\infty^2$ & (c) $\overline{vw}/U_\infty^2$.

Figure 87 Surface maps of $(\overline{uv},\overline{uw},\overline{vw})/U_\infty^2$ in the junction at α = 0 in plane *TE* (*X* = 500 mm):

(a) $\overline{uv}/U_\infty^2$, (b) $\overline{uw}/U_\infty^2$ & (c) $\overline{vw}/U_\infty^2$.

Plates

Plate 1 Orientation of cotton tufts at zero wind speed, on:

(a) wing lower surface and -*Z* side of the plate &

(b) wing upper surface and +*Z* side of the plate.

Plate 2(a) Surface oil-flow patterns on the plate and lower surface of the wing at α = -3°, free stream from left to right.

Plate 2(b) Surface oil-flow patterns on the plate and upper surface of the wing at α = -3°, free stream from right to left.

Plate 2(c) Surface oil-flow patterns around the leading edge of the junction at α = -3°, viewed from the +Z side of the junction, free stream from right to left.

Plate 2(d) Surface oil-flow patterns in the trailing edge region at α = -3°, viewed from the +Z side of the junction, free stream from right to left.

Plate 2(e) Tuft behaviour at α = -3° on:

(i) wing lower surface and -*Z* side of the plate &

(ii) wing upper surface and +*Z* side of the plate.

Plate 3(a) Surface oil-flow patterns on the plate and lower surface of the wing at α = 0°, free stream from left to right.

Plate 3(b) Surface oil-flow patterns on the plate and upper surface of the wing at $\alpha = 0°$, free stream from right to left.

Plate 3(c) Surface oil-flow patterns around the leading edge of the junction at $\alpha = 0°$, viewed from the -Z side of the junction, free stream from left to right.

Plate 3(d) Surface oil-flow patterns in the trailing edge region at $\alpha = 0°$, viewed from the +Z side of the junction, free stream from right to left.

Plate 3(e) Tuft behaviour at $\alpha = 0°$ on:

(i) wing lower surface and -*Z* side of the plate &

(ii) wing upper surface and +*Z* side of the plate.

Plate 4(a) Surface oil-flow patterns on the plate and lower surface of the wing at $\alpha = +3°$, free stream from left to right.

Plate 4(b) Surface oil-flow patterns on the plate and upper surface of the wing at $\alpha = +3°$, free stream from right to left.

Plate 4(c) Surface oil-flow patterns around the leading edge of the junction at $\alpha = +3°$, viewed from the -Z side of the junction, free stream from left to right.

Plate 4(d) Surface oil-flow patterns around the leading edge of the junction at $\alpha = +3°$, viewed from the +Z side of the junction, free stream from right to left.

Plate 4(e) Tuft behaviour at $\alpha = +3°$ on:

(i) wing lower surface and -*Z* side of the plate &

(ii) wing upper surface and +*Z* side of the plate.

Plate 5(a) Surface oil-flow patterns on the plate and lower surface of the wing at $\alpha = +6°$, free stream from left to right.

Plate 5(b) Surface oil-flow patterns on the plate and upper surface of the wing at $\alpha = +6°$, free stream from right to left.

Plate 5(c) Surface oil-flow patterns around the leading edge of the junction at $\alpha = +6°$, viewed from the Z side of the junction, free stream from left to right.

Plate 5(d) Surface oil-flow patterns around the leading edge of the junction at $\alpha = +6°$, viewed from the +Z side of the junction, free stream from right to left.

Plate 5(e) Surface oil-flow patterns in the trailing-edge region of the junction, at $\alpha = +6°$, viewed from the +Z side of the junction, free stream from right to left.

Plate 5(f) Tuft behaviour at $\alpha = +6°$ on:

(i) wing lower surface and -*Z* side of the plate &

(ii) wing upper surface and +*Z* side of the plate.

Plate 6 Tuft behaviour on the upper surface of the wing and +Z side of the plate at $\alpha = +7°$.

Plate 7 Tuft behaviour on the upper surface of the wing and +Z side of the plate at $\alpha = +8°$.

Plate 8(a) Surface oil-flow patterns on the plate and lower surface of the wing at $\alpha = +9°$, free stream from left to right.

Plate 8(b) Surface oil-flow patterns on the plate and upper surface of the wing at $\alpha = +9°$, free stream from right to left.

Plate 8(c) Surface oil-flow patterns around the leading edge of the junction at $\alpha = +9°$, viewed from the -Z side of the junction, free stream from left to right.

Plate 8(d) Surface oil-flow patterns around the leading edge of the junction at $\alpha = +9°$, viewed from the +Z side of the junction, free stream from right to left.

Plate 8(e) Surface oil-flow patterns on the plate in the trailing-edge region, at $\alpha = +9°$, viewed from the +Z side of the junction, free stream from right to left.

Plate 8(f) Tuft behaviour at $\alpha = +9°$ on:

(i) wing lower surface and -*Z* side of the plate &

(ii) wing upper surface and +*Z* side of the plate.

List of Tables

Nomenclature

Arabic symbols

a_1	Constant in Bradshaw's (1971) turbulence model (see section 2.6).
a	Distance along the semi-major axis of an ellipse
A	Calibration constant for a hot wire.
AR	Aspect ratio of the wing.
b	Distance along the semi-minor axis of an ellipse
B	Calibration constant for a hot wire.
c	Length of wing chord in the streamwise direction.
C	Calibration constant for a hot wire.
C_a	Sectional force coefficient in the directional along the aerofoil chord line, $axial\ force/0.5\rho U^2 c$.
C_d	Sectional drag force coefficient, $drag/0.5\rho U^2 c$.
C_l	Sectional lift force coefficient, $lift/0.5\rho U^2 c$.
$C_{l_{max}}$	Maximum sectional lift coefficient.
C_n	Sectional force coefficient normal to the aerofoil chord line, $normal\ force/0.5\rho U^2 c$.
C_p	Pressure coefficient.
D	Cylinder diameter.
E	Instantaneous output voltage of a hot wire (Section 5.7).
H	Boundary layer shape parameter (Section 6.6.5).
G, H	Functions relating to flow pitch and yaw angle when using the yawmeter, see section 4.6.3.
k_{ij}	Set of calibration constants for the yawmeter.
K	Plane normal to section profile in which X-wire measurements were taken.
L	Plane normal to section profile in which X-wire measurements were taken.
p	Pressure.
$p_{1,2,3,4\ \&\ 5}$	Pressure measured by yawmeter at the rotational and translational positions of the tubes.

p_{sc}	Static pressure measured at the walls of the settling chamber, upstream of the contraction.
p_{tap}	Static pressure measured at a pressure tapping in the wing or plate.
p_{ws}, , p_{∞}	Static pressure measured at the walls of the working section.
$\overline{q^2}$	Mean square of the turbulence intensity, $= \left(\overline{u^2} + \overline{v^2} + \overline{w^2}\right)$
q_{eff}	Effective cooling velocity of flow over a hot wire.
Q	Resultant mean-velocity vector, $Q = \sqrt{U^2 + V^2 + W^2}$.
$Ox_p y_p z_p$	Local, *left-handed*, axes system for X-wire probe at 0°, 90° rotational positions, see figure 39(a).
$O\,x'_p y'_p z'_p$	Local, *left-handed*, axes system for X-wire probe at 45°, 135° rotational positions, see figure 39(b).
O*XYZ*	Wind tunnel, *left-handed*, cartesian coordinate frame with origin at leading edge of junction, see figure 27.
R	Radius of curvature of leading edge.
Re	Reynolds number.
S, T	Functions relating to flow speed and static pressure when using the yawmeter, see section 4.6.3.
T	Wing maximum thickness.
u, v, w	Velocity fluctuations in the *left-handed* O*XYZ*, wind tunnel axes system in figure 27.
$\boldsymbol{u}$	Velocity correlation matrix for the fluctuations in velocity in the O*XYZ* axes frame.
u_p, v_p, w_p	Velocity fluctuations in the $Ox_p y_p z_p$ axes system for the X-wire probe, at the 0°-, 90°-rotations in figure 39(a).
$\boldsymbol{u}_p$	Velocity correlation matrix for the fluctuations in velocity in the $Ox_p y_p z_p$ axes frame.
u'_p, v'_p, w'_p	Velocity fluctuations in the $O\,x'_p y'_p z'_p$ axes system for the X-wire probe, at the 45°-, 135°-rotations in figure 39(b).
$\boldsymbol{u}'_p$	Velocity correlation matrix for the fluctuations in velocity in the $O\,x'_p y'_p z'_p$ axes frame.

u_p^*	Second matrix in the $Ox_py_pz_p$ axes frame, produced by transforming u'_p from $O\,x'_py'_pz'_p$ axes into $Ox_py_pz_p$ axes.
$u_p^\dagger$	Third velocity correlation matrix in the $Ox_py_pz_p$ axes frame obtained by averaging equivalent terms in u_p & u_p^*.
u_ψ	Transform of $u_p^\dagger$ through the probe yaw angle.
u_θ	Transform of u_ψ through the probe pitch angle, is equivalent to u in wind-tunnel axes system O*XYZ*.
$\overline{U}$, $\overline{V}$, $\overline{W}$	Mean velocity components in the *left-handed* O*XYZ*, wind tunnel axes system in figure 27.
$\boldsymbol{U}$	Matrix of mean velocity components $\overline{U}$, $\overline{V}$, $\overline{W}$.
$\overline{U_p}$, $\overline{V_p}$, $\overline{W_p}$	Steady velocity components in the $Ox_py_pz_p$ axes system for the X-wire probe, at the 0°-, 90°-rotations in figure 39(a).
$\boldsymbol{U_p}$	Matrix of mean velocity components $\overline{U_p}$, $\overline{V_p}$, $\overline{W_p}$.
$\overline{U'_p}$, $\overline{V'_p}$, $\overline{W'_p}$	Mean velocity components in the $O\,x'_py'_pz'_p$ axes system for the X-wire probe, at the 45°-, 135°-rotations in figure 39(a).
$\boldsymbol{U'_p}$	Matrix of mean velocity components $\overline{U'_p}$, $\overline{V'_p}$, $\overline{W'_p}$.
U_∞	Undisturbed freestream velocity.
x	Distance along chord line of section profile from the leading edge.
x_3	Distance normal to the tangent to the local section profile.
X	Distance in the streamwise direction, from origin of *left-handed* O*XYZ* axes system, see figure 27.
	Distance along semi-major axis of an ellipse.
Y	Distance normal to the plate, from origin of *left-handed* O*XYZ* axes system, see figure 27.
Z	Distance normal to the O*XY* plane, from origin of *left-handed* O*XYZ* axes system, see figure 27.
	Distance along semi-minor axis of an ellipse.

Greek symbols

α	Incidence of wing.
α_g	Angle of resultant of 2 shear stresses, see Section 2.6.
α_τ	Angle of resultant of 2 mean-velocity gradient vectors, see Section 2.6.
β_p	Separation parameter proposed by Visbal (1991), see Section 2.6.
β	Angle of rotation of the rotary table on the roof mounted traversing gear, see Section 4.6.3.
β_s	Angle between the normal to the local slope of the section profile and the chord line; positive angles indicate $+Z$ side of the junction, negative angles indicate $-Z$ side of the junction.
δ^*	Boundary layer displacement thickness.
γ_b	Fraction of time for which strong reverse (upstream) flows are present in a horseshoe-vortex separation region, see Section 2.3.
μ_τ	Friction velocity at the wall in a boundary layer.
ν	Kinematic viscosity of a fluid.
ν_t	Eddy viscosity in a boundary layer.
θ	Pitch angle of flow relative to plate surface, positive away from plate.
	Momentum thickness in a boundary layer.
ρ	Density of air.
τ_w	Shear stress at a wall surface.
ψ	Eulerian flow yaw angle, positive in the $+Z$ direction.

Superscripts

$\overline{}$	Mean value.

Chapter 1

Introduction

The efficiency of an aircraft is undoubtedly dependant upon its drag. Drag dictates an aircraft's cruising speed and the amount of fuel burned during flight, thereby contributing towards its operating costs. Continual refinements in major component design and improvements in surface finishes have produced large improvements in performance. However, aside from "laminar flow control", further gains must come from the reduction of "secondary drag".

1.1 - Interference drag and the generation of horseshoe vortices

The junctions between aircraft components are areas where secondary drag can arise, this contribution to the total drag of the aircraft being termed "interference drag". Interference drag is defined as the change in drag force that occurs when 2 components are joined, over and above the sum of the drag of the 2 components taken in isolation. In the junction region, the viscous layers over the components interfere with each other and locally, the boundary layer thickness changes and 3-dimensional separations and vortical flows arise. From this it would seem that the interference always has a detrimental effect on the performance of the aircraft. However Hoerner (1965), in his review, noted that some studies had found the interference drag to be negative, *i.e* an improvement. Briefly, it transpires that the interference drag for any particular junction is influenced by its geometry and conditions in the flow upstream, but a fuller account of the characteristics of junction flows is presented in Chapter 2. The fact that the interference may be either beneficial or detrimental to the performance of an aeroplane, renders the investigation of the junction region of great interest to designers.

On aircraft, the major junction between components in the airstream is that between a half-wing and the fuselage. Although small, a positive value for the interference drag for this junction can represent a considerable amount of additional fuel burnt over the operating

life of an aircraft. Therefore, aircraft designers are increasingly interested in investigating such flows in order to improve aircraft performance. An idealisation of a wing/body junction is the corner between 2 flat plates intersecting at a right angle, a notable example of research into this type of junction being presented by Gersten (1959). However in that case, the resulting secondary flow is driven entirely by Reynolds stress gradients in the flow. For an obstacle mounted on a body on which a boundary layer has developed, a much more powerful mechanism is at work around the leading-edge of the junction: the approaching boundary layer is skewed by the presence of the obstacle and separates in the adverse pressure gradient in that region. Between the separation line and the leading edge of the junction, a strong vortical flow is formed, which wraps around the leading-edge and passes downstream as in figure 1. It is this mechanism that is most relevant to the study of wing/fuselage interference drag. The shape of the vortical flow has given rise to the generic name "horseshoe-" or "collar-" vortex.

Horseshoe vortices are not only a problem for the aircraft designer. They arise around the bases of bridge piers and oil-rig jackets where these are driven into the river or sea bed and produce scouring of the bed around the leg. Horseshoe vortices also arise around the junctions between ship and submarine hulls with their keels and sails respectively, the propulsion systems of such vessels often being situated in the wake of such junctions. It can thus be seen that secondary flows and horseshoe vortices specifically, are also of great interest to civil engineers and naval architects.

As will be shown in Chapter 2, over the last 15 years this type of flow has been thoroughly investigated for junctions formed by mounting cylinders of circular or aerofoil section, or wings, normal to a plate. The majority of these studies have been largely concerned with the flow structure around the leading edge of the junction and not the interference drag itself. This has led to the *wing* frequently being idealised as a cylindrical body of bullet-, or teardrop-shaped cross section. By comparison however, the effect of sweep on the junction flow has received scant attention. Given that an enormous number of aircraft flying today incorporate wings that have swept-back leading edges, this may seem surprising, although it can be argued that researchers are wise to concentrate on firstly understanding the flow around a relatively simple junction geometry. Some results have

been presented briefly by Hoerner (1965) regarding interference drag for strut/plate junctions, with the strut swept both forward and aft. Also Jupp (1980) investigated the effect on the drag of the Airbus A310, of careful filleting of the root of the swept-back main wing. However details of the structure of the flowfield around a swept-back wing/body junction have appeared only recently (Bernstein & Hamid, 1993, 95 & 96). In addition, no results have been presented, up to now, regarding the structure of a flowfield around a swept-forward wing/body junction. This therefore provided the *raison d'être* for the investigation which is the subject of this thesis.

1.2 - The case for swept-forward wings on aircraft

Wing sweep has been used for many years to reduce the wave drag of aircraft flying at supersonic, or high subsonic, Mach numbers. Although virtually all swept-wing aircraft have been designed using sweep back the concept of forward sweep is not new. Indeed in 1944, the flight trials of the world's first jet bomber, the Junkers Ju-287 shown in figure 2, were accomplished, the design of which incorporated a swept-forward main wing (Holzbauer, 1950). However it was not until 1964 that a swept-forward wing aircraft went into production with the HFB 320 Hansa Jet shown in figure 3 (Wocke & Davies, 1964). Both these aircraft used moderate amounts of sweep, -25° and -15° respectively.

Sweeping the wings forward brings several advantages over backward sweep. Due to longitudinal stability considerations, in a conventional wing/tailplane configuration, a swept-back wing joins the fuselage forward of the aircraft centre of gravity. As this is where the fuselage cross-sectional area is greatest, the area rule for transonic/supersonic flight dictates that the fuselage must be waisted in this region to achieve a smooth distribution of cross-sectional area along the length of the aircraft, producing the "Coke-bottle" shape typified by the Blackburn Buccaneer. This brings obvious disadvantages where passenger cabins, fuel tanks or stores bays are concerned. Swept-forward wing configurations have usually been designed with a canard foreplane. This positions the wing root much further along the fuselage, aft of the centre of gravity of the aircraft. In this case, application of the area rule means that the largest amount of fuselage waisting is incorporated much nearer the tail of the aircraft where the fuselage has begun to taper

anyway, aft of passenger cabins etc. as shown in figure 4. Thus, using a swept-forward wing, the useful fuselage volume near its centre of gravity is potentially larger than using a swept-back wing. This brings the benefit that large loads may be carried nearer the centre of gravity of the aircraft.

Uhuad, Weeks & Large (1983) have also described potential reductions in drag using a swept-forward wing instead of a swept-back wing, these reductions arising in one of 2 ways. The first is shown in figure 5(a). Comparing swept-forward and swept-back wings in transonic flow, if the leading-edge sweep angles, taper and aspect ratios, shock locations and wing areas are equal, the sweep angle of the shock on the upper-surface of the swept-forward wing is greater than that of the swept-back wing. This results in less wave drag for the swept-forward wing. Alternatively, as in figure 5(b), if both wings have equal wing area, aspect & taper ratios and are designed for equal aerodynamic conditions, with the locations and sweep angles of the transonic-shock being equal, the resulting sweep angle of the leading-edge is less for the swept-forward wing, hence its profile drag will be less than that of the swept-back wing. Redecker & Wichmann (1991) also concluded that the smaller sweep angle of the leading edge renders forward sweep more suitable than aft sweep for natural laminar flow wings, due to the reduced crossflows and increased stability of the attachment line. These are of course ideal situations as the wing tip and root regions will considerably modify the streamline patterns. However extensive wind tunnel tests by Nangia (1984) have confirmed that an aircraft configuration using a swept-forward main wing plus canard foreplanes produces appreciable improvements in lift/drag over an equivalent swept-back wing plus tailplane arrangement, in addition to the expected improvements in the handling characteristics at high lift.

The spanwise loading distribution for a swept-forward wing means that its centre of pressure is located nearer the root than for an equivalent swept-back wing. Thus, as incidence increases, a swept-forward wing will begin to stall in the root regions first, the stalled region spreading outboard to the tips as incidence is increased further. Consequently, outboard ailerons remain effective over a much greater incidence range. In addition, if equivalent swept-forward and swept-back wings are operating at equal lift, the wing-root bending moment for the swept-forward wing is less because of the inboard

centre of pressure. Thus the wing structure may be made lighter, or if the aspect ratio is allowed to increase until both bending moments are equal, the induced drag of the swept-forward wing is less. However the tendency to early separation in the root region of a swept-forward wing means that the design of the root may well be something of a compromise between the maintenance of attached flow and minimum interference drag, as noted by Uhuad, Weeks & Large (1983).

To alleviate the increase in loading from tip to root, the trailing edge may be cranked so that the taper ratio inboard of the crank is substantially greater than that outboard. This produces a longer chord length at the root than would otherwise be obtained and hence reduces the loading intensity there. In addition a useful effect from using a lifting canard arrangement is that, depending on how closely the lifting surfaces are coupled, the downwash from the canard reduces the effective incidence of the wing root and hence shifts the region of maximum loading outboard, an effect compounded by the tip vortex from the canard if it passes over the wing upper surface.

However, one major obstacle has prevented the widespread use of forward sweep, namely structural divergence, as reviewed by Weissharr (1980). The torsional axis of a swept-forward wing of conventional box structure usually lies aft of the aerodynamic centre. Increments of lift, due to a gust for example, act at the aerodynamic centre and would therefore produce an increase of sectional incidence, as shown in figure 6, causing a further lift increase. The torsional stiffness is a fixed structural property while the aerodynamic loads are proportional to the dynamic pressure. If the aircraft speed is increased beyond a critical value (the divergence speed), structural failure will occur. It is this factor that has limited the amount of sweep to the moderate angles seen on the Ju-287 and Hansa Jet. The Hansa jet even incorporated wing-tip fuel tanks, the centres of gravity of which were positioned forwards of the elastic axis of the wing such that they provided a restoring moment against the nose-up twisting action of the wing.

To achieve the required stiffness for large wing-sweep angles at high speed however, the weight of a metal swept-forward wing becomes prohibitive. Fortunately, it was discovered that the directional properties of carbon-fibre composites could be used to

control twist, enabling the design of swept-forward wings that resist the twisting-up action of the leading edge and delayed divergence until much higher speeds. The real benefit is that using carbon composites, the weight of a swept-forward wing is less than a metal one of identical stiffness. It is this development in materials technology that makes swept-forward winged aircraft a feasible option open to a designer.

The Grumman X-29 shown in figure 7, built to investigate the integration of a wide variety of new technologies, was designed with a wing with a leading-edge sweep angle of -30°. The wing box covers were made from laminated carbon fibre sheets which provided the necessary stiffness. The main wing is situated well aft on the fuselage, pitch control being provided by a closely-coupled canard foreplane. The interaction between the canard and the main wing, in particular the effects of the downwash from the foreplane as mentioned earlier, have been studied by Griffin & Jonas (1983). This showed that the spanwise flow into the root was greatly reduced over the inboard section of the wing as a result of the canard downwash. The X-29 has been extensively flight tested, proving that successful design of a swept-forward, composite-winged aircraft is possible and many articles have been written in aviation magazines regarding its unusual aerodynamics and performance (see Spacht *et al,* 1986, for example).

Wind tunnel tests of swept-forward winged models have confirmed the theoretical benefits of forward sweep, but have also highlighted areas for further investigation, in particular the root region. As swept-forward wings are now a practical option for the aircraft designer, it seems appropriate to investigate the aerodynamic interference effects in the junction between a forward-swept wing with a body. Herein are presented what are believed to be the first published data pertaining to the structure of the flow around a swept-forward wing/body junction.

Chapter 2 contains a review of previous research, both theoretical and experimental, into wing/body junction and analogous flows. The theoretical/computational problem is formidable for such flows at flight Reynolds numbers. In practical situations, the fuselage boundary layer approaching the leading edge of the junction is already a fully-developed, turbulent one. Even with the most powerful computing resources available today, direct

solution of the governing Navier-Stokes equations is impossible for such a case. A more realistic approach, using some kind of turbulence modelling, is hindered by the lack of a suitable model for the turbulence characteristics in such a complex, 3-dimensional situation. Instead the computational predictions described in Chapter 3, during the design of the wind tunnel model for the investigation, are based on somewhat more primitive approaches. There the potential-flow solutions are coupled to boundary-layer calculations. As a result, the horseshoe vortex could not be predicted by these codes and the calculations were actually performed to predict the pressure distribution over likely wing designs.

Almost all the investigations of wing/fuselage interference flows have idealised the fuselage by replacing it with a flat plate, upon which a turbulent boundary layer has been allowed to develop fully. This idealisation has been made in this investigation too, Chapter 4 describing the experimental set-up for the measurements, involving flow visualisation. surface-pressures and flowfield traverses with a yawmeter and X-wire anemometer. The experimental procedures involved in making these measurements and the data reduction associated with them are described in Chapter 5. The results are presented and discussed in Chapter 6, with the conclusions from the investigation and suggestions for future work following in Chapter 7.

Chapter 2

Review of Previous Research

2.1 - Introduction

This chapter is concerned with reviewing the efforts of previous researchers into junction flows and the strong secondary motions therein. A considerable amount of research has been undertaken into the problem of horseshoe-vortex flows, although most of the investigations performed have, for simplicity, been around configurations using circular cylinders, or symmetrical wings at nonlifting incidences. Only a few have involved junctions at lifting incidences and knowledge of the effects of sweep on junction flows is even more limited. The review will first discuss some of the relatively simple flows around cylinder/flat-plate junctions, then go on to examine the performance of more realistic wing/fuselage junctions.

It will be seen that the nature of such flows is influenced by conditions in the approaching boundary layer, by Reynolds number and by the leading-edge shape of the obstacle. Because of shortfalls in computer processing power and memory, the early research into junction flows has been almost exclusively experimental. Also, experimental data regarding the turbulence structure around wing/body junctions have only been available in sufficient quantities for the validation of computational calculations of junction flows since the mid-1980's. Indeed, one of the aims of the current investigation is the accumulation of such data for this purpose. The vast improvements in the areas of computer power, memory and data available for validation have enabled computer simulations to grow in importance and some of the simulations performed to date are discussed later in the chapter.

2.2 - The general nature of junction flows

Using simple geometries, *e.g.* circular cylinders mounted on flat plates, there have been several investigations into the nature of junction interference flows. Some of the earliest work was performed by Johnston (1960) and Schwind (1962). Johnston described the nature of the flow field around a cylinder/plane intersection with its 3-dimensional stagnation point and horseshoe vortex formation, a classic photograph of the flow in the plane of symmetry of such a junction being reproduced by Thwaites (1960). Although the experiments were conducted in laminar flow, similar flow patterns occur when a turbulent boundary layer separates around an obstacle.

Schwind also conducted experiments into horseshoe vortices produced by a 60° wedge mounted on a plate in laminar flow. He categorised his observations into 5 types of flow regime: at the lowest wind speeds, boundary layer separation was evident upstream of the wedge, but no discernible vortices were present, which seemed to contradict both Johnston and Thwaites. At such low speeds however, any vortical motion may have been so weak as to be undetectable by Schwind's experiments.. As the velocity was increased, he observed that a vortex system similar to that in figure 8(a) became visible. With a further increase in velocity, the number of vortices increased to 4, the system beginning to oscillate as the velocity was increased still further. However the values of freestream velocity which marked the change from one regime to another were ill-defined, the flow regimes being able to alternate between states at some velocities. This behaviour was confirmed by Baker (1979) who conducted a detailed investigation into the number, position and motion of laminar separation vortices around cylinders. He discovered that the number of vortices could increase from 2 to 4 to 6 (see figure 8), eventually producing an unstable vortex system.

In addition, Baker (1980) investigated turbulent horseshoe vortices around the bases of circular cylinders of various diameters. The heights of all the cylinders were identical, except for the cylinder of largest diameter which was built in sections so that its height could be varied. From surface oil-flow studies he concluded that a 4-vortex system existed upstream of the cylinders, although smoke flow visualisation failed to confirm any

fine detail because of turbulence. Surface pressure measurements were made in the plane of symmetry, for both laminar and turbulent investigations. All the pressure distributions showed a levelling out of (or dip in) pressure coefficient at positions which were shown by surface oil-flow visualisation to correspond to the centre of the primary oncoming-flow vortex in each case. Keeping the cylinder diameter constant, these positions did not appear to change with the Reynolds number based on the freestream. However, the primary separation points and vortex centres were found to move slightly closer to the cylinder as the thickness of the oncoming boundary layer was decreased.

In addition, the values of pressure coefficient at the leading edge of the cylinder increased as the thickness of the oncoming boundary layer was decreased. Finally, flow visualisation experiments were carried out around the base of the cylinder of largest diameter, to examine the effect of cylinder height on the separated region. Baker (1980) discovered that for a length/diameter ratio > 1.5, the position of separation of the floor boundary layer was virtually independent of the cylinder height. Thus, the size of the separated region is dependant on the cylinder diameter when the cylinder is tall and on the cylinder height when the cylinder is short.

More detailed investigations into turbulent flow around cylinder/flat plate junctions have been carried out by Eckerle & Langston (1987), who found only one separation line on the plate; the patterns associated with the formation of multiple vortices and separation/reattachment lines obtained by Baker were not evident. Flow field measurements in the separated region with a 5-hole yawmeter indicated that a vortex system was not formed in the plane of symmetry, rather the main vortex "developed... ...as the separated flow moved around the cylinder". This differed from an investigation using similar methods by Pierce, Kim & Harsh (1987), who measured a vortex in the plane of symmetry upstream of a teardrop-shaped cylinder, although it should be remembered that a 5-hole yawmeter has a rather large measuring volume for accurate use in such a highly-sheared flow. Eckerle & Langston (1987) also measured wall static pressures in the corner, in the plane of symmetry, which were virtually identical to the freestream stagnation pressure, whereas in the experiments of Pierce *et al* (1987) amongst others, the surface pressures measured in the corner were much less than freestream stagnation. This

posed the question of what conditions influenced the formation of either type of separation?

Eckerle & Awad (1991) developed a parameter based on the Reynolds number Re_D, cylinder diameter D and the displacement thickness δ^* of the oncoming boundary layer, to correlate the findings above with freestream conditions and blockage produced by the boundary layer. Analysing data obtained previously by other researchers, they discovered that for the investigations where freestream-stagnation pressures were measured on the cylinder/wall surface in the plane of symmetry, values of this parameter $\left(\mathrm{Re}_D\right)^{1/3} (D/\delta^*)$ were greater than 1040. However for the experiments where the surface pressures measured in the junction were less than stagnation, $\left(\mathrm{Re}_D\right)^{1/3} (D/\delta^*) < 673$.

This implied the existence of a critical value of $\left(\mathrm{Re}_D\right)^{1/3} (D/\delta^*)$, less than 1040 but greater than 673. To extend this correlation to vortex formation they conducted experiments at several velocities using *L*aser *D*oppler *A*nemometry (*LDA*) around a circular cylinder mounted on a flat plate, a turbulent boundary layer being allowed to develop on the plate. Over the range of test wind speeds, the junction flow was found to change. For $\left(\mathrm{Re}_D\right)^{1/3} (D/\delta^*) = 960$ a fully-formed vortex existed, however at $\left(\mathrm{Re}_D\right)^{1/3} (D/\delta^*) = 1150$ only the rudiments of a vortex system were measured and for $\left(\mathrm{Re}_D\right)^{1/3} (D/\delta^*) > 1360$ a fully-developed vortex was undetectable. This agreed approximately with the findings regarding the pressures in the corner and also the flowfield results of Eckerle & Langston (1987) and Pierce *et al* (1987), leading Eckerle & Awad to suggest that the critical value of $\left(\mathrm{Re}_D\right)^{1/3} (D/\delta^*)$ was approximately 1000.

Their interpretation of this phenomena was that at freestream velocities above a certain value, the reversed flow had sufficient momentum to overcome viscous forces in the separation region, allowing it to move upstream before turning to flow around the cylinder. At low velocities however, the momentum could be dissipated by viscous forces allowing a vortex to form. In addition, Eckerle & Awad make a claim, based on the boundary-layer shape parameter, that the 4-vortex model due to Baker was interpreted

from smoke-flow visualisation in a transitional boundary layer, not a fully-developed turbulent one.

Agui & Andreopoulos (1992) conducted detailed experiments into cylinder/endwall junction flows using high-frequency pressure transducers to provide information on the meandering nature of the turbulent horseshoe vortex system. Again the pressure distribution on the floor in the plane of symmetry showed a dip corresponding to the position of the horseshoe vortex inferred from oil-flow visualisation. In addition the probability density function (*p.d.f.*) of pressure fluctuations in the plane of symmetry was found to be bimodal at the position of the vortex, which indicated periodic or intermittent flow behaviour. They postulated that this behaviour was influenced by vortex shedding from the cylinder and/or the boundary layer separating unsteadily from the floor.

Agui & Andreopoulos (1992) also investigated the instantaneous nature of the vortex system in the plane of symmetry using laser-sheet flow-visualisation. The topological methods of Hunt, Abell, Peterka & Woo (1978), for example, could be applied to instantaneous *snapshots* obtained from such a visualisation method to try to determine the evolution of the vortex system with time. One vortex, termed the primary vortex, was always present in the images, its spatial unsteadiness being confirmed with the amplitude of motion being of the order of one boundary layer thickness. This motion seemed to be linked to the arrival of large-scale turbulent structures in the approaching plate boundary layer at the junction and the role of these structures in the dynamics of the junction flowfield was deemed worthy of further investigation. The primary vortex induced upflow from the wall, intermittently forming other vortices in the separated region upstream of the primary vortex, which either rotated in the opposite sense to the primary vortex, or were *mushroom-shaped*. However these secondary vortices evolved extremely quickly, rendering detection by time-averaging methods impossible.

2.3 - Wing/body junction flows

From the above studies it can be seen that various flow structures have been discovered or postulated around geometries which are relatively simple compared to a lifting wing/body

junction. Only a small amount of research seems to have been carried out before the 1980's on actual wing/body, or wing/strut, interference. Hawthorne (1954) performed some experiments using water flow around struts of elliptical and bicuspid profiles mounted in sand and found that the sand was scoured away from around the junctions, being deposited further downstream. At 0° incidence the depth and area of scour around the bicuspid strut were considerably less than around the elliptical strut, there also being marked differences in the positions of the maximum depths of scour around the struts. The blunt leading-edge geometry of the elliptical profile appears to have given rise to a strong horseshoe vortex, the strong shearing actions within producing the greatest depth of scour at the leading edge. Conversely the separation around the much more slender nose of the bicuspid profile appears to have been weak, the scouring at the nose being only one tenth as deep as for the elliptic strut and occupying a much smaller area. The deepest scouring for the bicuspid profile was actually found at the location of the maximum thickness (*i.e.* at the mid-chord) due to the increase in shear stress near the sand bed as the flow accelerated up to the maximum thickness. However even here, the depth of scour was still considerably less than anywhere around the base of the elliptic strut.

A review of interference drag was presented by Hoerner (1965) based largely on studies, made prior to and during World War 2, of the intersections of struts with walls. He reported that the evidence regarding the effects of wall boundary-layer thickness on interference drag was conflicting. One investigation found that the interference drag for struts of approximately 10% thickness/chord ratio decreased as the boundary layer thickness was increased up to 8% of the strut chord. The data presented even suggested that the interference drag could be negative for strut thickness/chord ratios below 8%. Conversely, another investigation found that the interference drag increased as the thickness of the boundary layer was increased up to 3% of the strut chord, this latter investigation using a strut of 33% thickness/chord ratio. The results on which the review was based were probably the first evidence that the interference drag was strongly dependant on the junction geometry, particularly the slenderness ratio of the wing, although Hoerner did not make any connection. The review also reported that the position where a wing joined a fuselage was found to have a large effect on the interference drag of the junction. However no mention was made concerning the presence

of horseshoe vortices and their effects. The drag forces for a wide variety of tail configurations were reviewed too, the interference drag being found to increase markedly with the number of corners present.

Barber (1978) measured profiles of total pressure across the wakes of junctions produced by NACA 65-series struts mounted on a flat-plate, the turbulent boundary layer thickness being 12% of the strut chord. When compared to traverses in an undisturbed boundary layer he calculated that there was only a small additional loss of total pressure due to the intersection. In addition, the intersection losses for the configurations were hardly affected by incidence. It was concluded that the boundary layer produced a strong horseshoe vortex which brought high-momentum flow into the streamwise corners, thus delaying separation in those regions almost until the trailing edge, even at incidence. He repeated the measurements in a so-called *thin* (as opposed to $0.12c$ thick) boundary layer formed by mounting the struts so that their leading edges were almost coincident with the leading edge of the plate. The pressure losses in the wake of the junction increased over those measured in the thicker boundary layer and were influenced to a greater degree by incidence. From these results Barber concluded that the thickness of the approaching boundary layer is an important factor in junction flows.

The work reviewed so far gives qualitative and general global information on the effects of the horseshoe vortex system on the flowfield around the junction. However, although the problem of the horseshoe vortex had been identified, quantitative information concerning the structure of the vortex (especially turbulence data) was sparse until the work of Shabaka and Bradshaw (1981). Using a crossed hot-wire probe, they investigated the flow structure in the streamwise corners of an idealised wing/fuselage junction at several distances downstream from the leading edge. The "wing" was mounted perpendicularly to a flat plate and comprised a parallel-sided body, with a semi-elliptic nose of 6:1 slenderness ratio. They found that the skew-induced secondary flow (horseshoe vortex) dominated over the stress-induced secondary flows even at the trailing edge. In addition, the boundary layer on the plate was found to thin underneath the core of the vortex, the distance of which from the corner changed only slightly with distance downstream from the leading edge.

The experiments of Hawthorne prompted Mehta (1984) to investigate the effect of nose shape on a wing/flat-plate junction, similar to that investigated by Shabaka & Bradshaw. The "wing" comprised one of 3 interchangeable leading-edge sections, attached to an afterbody with parallel sides as shown in figure 9. The leading edges were generated using the equation $\left(\frac{X}{a}\right)^n + \left(\frac{Z}{b}\right)^n = 1$, with different values of exponent n to produce (in order of increasing bluntness): a wedge-elliptic section (n = 1.5), an elliptic section (n = 2) and a super-elliptic section (n = 3). Using the super-elliptic nose, marked kinks in the mean-velocity contours in the streamwise corner were evident, showing that high momentum fluid had been brought into the corner. These kinks were less severe for the elliptic section and even smaller for the wedge-elliptic section, showing that fluid from the free stream did not penetrate into the corner to the same degree. The secondary flows in the corners (figure 9) and concentrations of vorticity were also greatest for the super-elliptic leading edge and weakest for the wedge-elliptic leading edge. Mehta therefore concluded that the size and strength of the horseshoe vortex increased with nose bluntness and, as such vortices could persist to a considerable distance downstream, the only practical way of controlling the strength of the horseshoe separation was to adjust the leading-edge shape.

Kubendran, McMahon & Hubbartt (1984) investigated a junction of similar geometry to that of Shabaka & Bradshaw, the slenderness ratio of the semi-elliptic nose being 1.5:1. Taking measurements with static-pressure and hot-wire probes in a single cross-stream plane downstream of the leading edge, they found similar results: *i.e.* high-momentum fluid was transported down towards the plate, between the vortex core and the corner, low-momentum fluid outboard of the vortex core being transported upwards. By appealing to the law-of-the-wall, they extrapolated measured profiles of mean velocity to the plate and "wing" surfaces. Using these extrapolations, they calculated the momentum deficit in the junction. Additionally the momentum deficits for the "wing" and plate in isolation from each other were calculated by assuming that the boundary layer profiles well away from the junction were identical to the undisturbed 2-dimensional boundary layers on the components when separated. Comparing the deficit in the junction with the sum of the deficits for the separated components, they found that the interference

produced a small (but unexpectedly favourable) effect, *i.e.* the momentum deficit for the junction was smaller than for the components in isolation. They referred to this difference in the momentum deficit as being the interference drag of the junction, although strictly this latter quantity includes the difference in the pressure drag term too. In addition as their "wing" did not taper towards its trailing edge, the adverse pressure gradient found in a complete wing/body junction was absent. To estimate the interference drag correctly, their investigation should have incorporated surveys across the wake of the junction using a static pressure probe in addition to a hot wire. Therefore, strictly, their investigation merely measured the momentum force in the streamwise corner.

It had been indicated by Briley & McDonald (1982) that, in order to enable the numerical modelling of junction flows, the flow characteristics in both the horseshoe vortex and the streamwise corners should be considered in conjunction. They also emphasised that experimental data from the leading edge region were needed in order to provide the necessary initial conditions for the computational codes. Therefore, Kubendran, McMahon & Hubbartt (1986) continued their investigation around the junction used in their 1984 investigation, concentrating their measurements in planes near to the leading edge of the junction. In the plane of symmetry, mean velocity measurements showed that the reversed flow was confined to a region very close to the surface of the plate. Downstream of the leading edge, the horseshoe vortex grew to be stronger than that investigated by Shabaka and Bradshaw and lay further from the corner. They concluded that this was due to the difference in bluntness of the leading edges of the 2 models, which agreed with the findings of both Mehta and Hawthorne.

Due to the parallel-sided afterbodies in the investigations of Shabaka & Bradshaw, Mehta and Kubendran *et al*, the adverse pressure gradients found in real wing/fuselage junctions were absent from their investigations. Therefore Devenport & Simpson (1986) used a wing with a 1.5:1 elliptic nose and NACA 0020-section tail in their study of a turbulent junction flow. The wing was mounted normal to a flat plate, the wing incidence being 0°, with the axes origin at the leading edge. The X-axis followed the streamwise direction, the Y-axis lay normal to the plate along the wing leading edge and the Z-axis was normal to the XY plane, completing a right-handed coordinate system. Oil-flow visualisation

revealed similar patterns to those obtained by Baker (1980) and Sepri (1973) and an example of Devenport & Simpson's results is reproduced in figure 10. Unusually, rather than accumulating on the separation line A at X/T = -0.47, the paint built up on a line B at X/T = -0.28, which was originally thought to be a second separation line. However, closer examination revealed that the streaks of paint passed through the line B. They thus interpreted line B as depicting a change in the shear stress at the plate surface as the reversed flow from the leading edge region flowed upstream towards the separation point, the flow between the leading edge and line B being of higher shear than that between line B and the separation point. Although hot-wire traverses through the boundary layer were performed, traverses on the plane of symmetry were only made upstream of the separation point because of the flow reversal present between the separation point and leading edge.

Inside the separation region Devenport & Simpson (1986) made traverses to one side of the plane of symmetry, between the separation point and maximum thickness of the wing. In this region, profiles of mean velocity and Reynolds stresses indicated that line B indeed marked a boundary between high-velocity fluid close to the corner and low-velocity fluid between line B and the separation line. The time-averaged Reynolds stresses in the vicinity of line B were up to an order of magnitude greater than those found in a fully-developed, flat-plate boundary layer. Thus, on the plane of symmetry, Devenport & Simpson inferred that a twin vortex system was present, as in figure 8(a).

Methods used to acquire flowfield data such as pitot tubes and hot wires have the disadvantage that the probe is inserted into the flow, thereby disturbing it. The need for accurate measurements to validate CFD codes led to the use of *LDA* systems which, although having measuring volumes marginally larger than crossed-wire probes, do not produce any flow disturbance. Abid & Schmitt (1986) used *LDA* to investigate the leading-edge junction region of a straight wing having a semi-circular leading-edge and simply-streamlined afterbody. Oil-flow visualisation revealed a line of pigment on the plate inside the separation region, similar to the results of Devenport & Simpson. However this was interpreted as a second separation line, as measurements in the plane of symmetry revealed concentrations of extremely low magnitudes of mean velocity in 2 separate locations in the separated region. These positions also corresponded to

concentrations of high turbulence kinetic energy. These findings thus led Abid & Schmitt to conclude that a 4-vortex system was present as in figure 8(b).

It can be seen that some debate exists over the numbers and exact structure of turbulent horseshoe-vortices, quite different flow structures being interpreted from similar surface-flow visualisation patterns around similar junction configurations. Since measurements in the leading-edge regions of junction flows were needed to resolve the instantaneous structure of such flows, Devenport & Simpson (1987) continued their investigation using *LDA* to examine in detail the flow in the plane of symmetry upstream of the leading edge. They confirmed their earlier impression of a 2-vortex system, which was corroborated later by Pierce & Shin (1992). In addition, histograms of probability-density functions of the components of mean velocity and shear stress in the plane of symmetry were found to be bimodal in the vortex region. These implied that the instantaneous turbulence structure was coherent and oscillated in the plane of symmetry.

The production and advection terms of the turbulence kinetic energy equation were calculated from the velocities and Reynolds stresses, a strong concentration of positive production of turbulence energy being found approximately coincident with the region of bimodal flow. This suggested that the production of turbulence energy was due to the fluctuations of the vortex. However the advection term did not display any strong association with the region of bimodal instability, instead being concentrated in 4 regions around the centre of the time-mean vortex. The oscillations of the vortex are probably due to the fact that, as some of the flow upstream from the leading edge is entrained by the vortex, the position of the vortex is expected to be influenced by the extent of this backflow. This in turn depends on the momentum of the backflow compared with that of the near-wall flow in the streamwise direction. Thus, as both flows fluctuate with time, the position of the vortex can be expected to vary with these fluctuations.

In the favourable pressure gradient that exists in the region between the leading edge and maximum thickness of the wing, the vortex is accelerated and turned from lying in the cross-stream direction to lie in the streamwise direction. As part of their continuing study, Devenport & Simpson (1988) used *LDA* to take flow measurements in planes

approximately normal to the local direction of the flow as it wrapped around the leading edge, these planes being shown in figure 11 . They found that the vortex appeared to move slightly away from the wing and the intensities of the Reynolds stresses and turbulence-kinetic energy reduced as the section contour was followed.

In addition, bimodal histograms were found for all 3 components of mean velocity in the region of the vortex. These were consistent with the turning of the vortex around the nose to follow the junction contour, suggesting that the coherent structures persist around the side of the wing. However, the flow between the vortex and the corner did not seem to be influenced by the region of bimodal instability. Instead the strong, favourable pressure gradient, in conjunction with the action of the vortex bringing high-momentum, low-turbulence fluid from the freestream into the corner, was thought to stabilise the flow in this region producing almost uniform mean-velocity components and much reduced turbulence production close to the corner.

Devenport & Simpson (1989) presented further velocity measurements in the region between the leading edge and maximum thickness, observing the deflection of the mean velocity vectors around the leading edge. Profiles of mean velocity outside the separation region were found to be characteristic of a turbulent boundary layer. Inside the separation region however, the influence of the vortex caused increased velocities close to the plate surface, over and above the values expected from the pressure field alone. This had the effect of flattening the velocity profiles. Between the line-of-low-shear and the corner the profiles had been modified so much that the mean velocity decreased then increased again with distance normal to the plate. In addition, values of $\sqrt{\left(\overline{u^2} / U_\infty^2\right)}$ close to the wing were found to be up to 50% lower than at the same height above the plate at line B in figure 10. The maximum value of $\sqrt{\left(\overline{u^2} / U_\infty^2\right)}$ close to the wing was no greater than 8% and bimodal histograms were not obtained in this region. These observations led to the proposal that the flow on the flat plate in this region was "laminarescent" due to the action of the vortex.

In addition, an array of 29 hot-wire probes set into the plate, between planes 3 & 4 in figure 11 to measure the skin friction in this region. This array is shown in the accompanying sketch, taken from Devenport & Simpson (1989). The array was aligned approximately normal to the local mean flow direction, the span of the array being sufficient to include the flow both inside and outside the separation region. Although the wires were sampled almost simultaneously, the readings from adjacent wires did not correlate particularly well with each other. However, when the distributions of skin friction from successive samples were compared to each other, the peaks and troughs in the distributions were found to lie in almost identical places, thereby suggesting streamwise turbulence structures, *i.e.*: the "footprint" of the horseshoe vortex. Additionally, the slight meandering of the pattern suggested that fluctuations in the position of the vortex in the plane of symmetry were convected downstream as the vortex was twisted to lie in the streamwise direction.

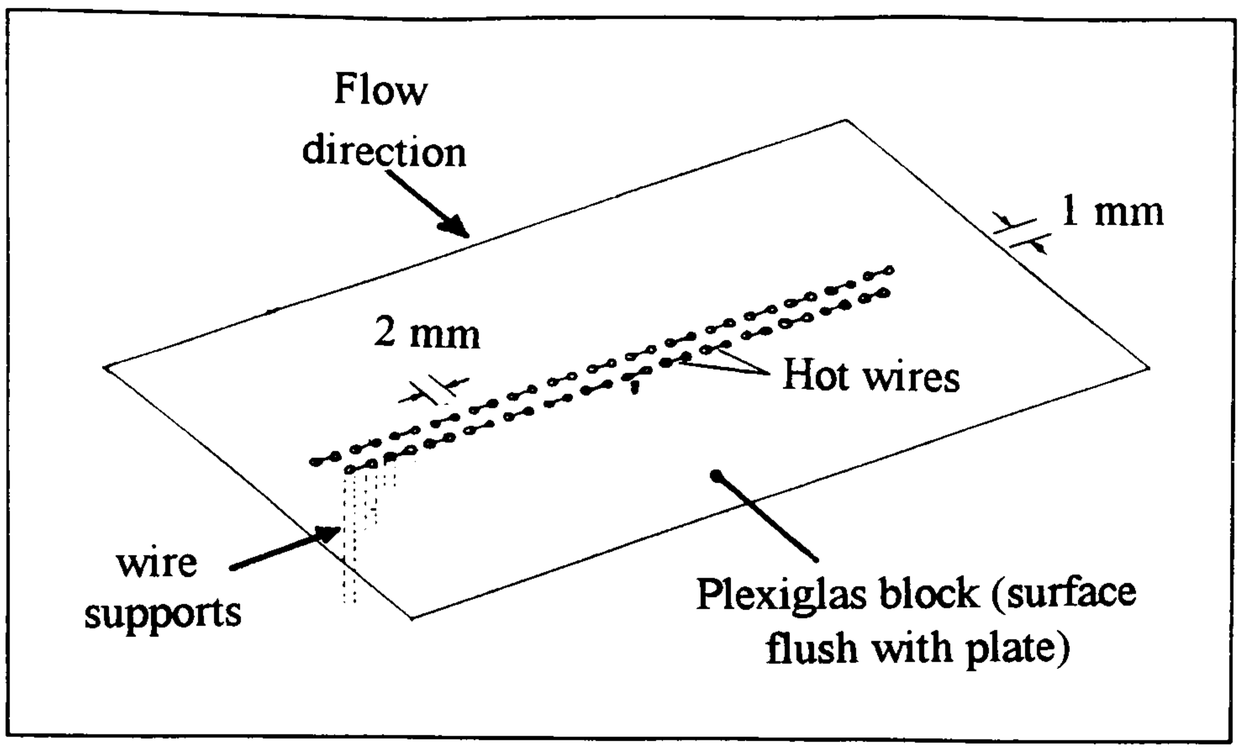

Devenport & Simpson (1990) carried out further analysis of the bimodal probability-density functions of velocity, between the separation point and leading edge, in the plane of symmetry. They observed that maxima in profiles of $\overline{u^2}/U_\infty^2$, $\overline{v^2}/U_\infty^2$ & $\overline{uv}/U_\infty^2$ through the boundary layer at various locations, occurred close to the locations where the peaks of the bimodal probability-density functions were furthest apart. In addition, in the bimodal distributions of streamwise velocity U one peak was centred near zero velocity, whilst the second peak was centred at a negative velocity. They concluded the velocity variation with time was bistable and switched between 2 states, which may explain why Abid & Schmitt obtained double-peaked graphs of velocity and turbulence energy. These states were termed the "zero-flow mode" and "backflow mode".

By devising an approximate method to separate the bimodal histograms into "zero- and backflow" modes, they made estimates of (a) the velocity vectors in the separation region

for both modes and (b) the fraction of time γ_b that the backflow mode was present. For the zero-flow mode, a tightly-wound vortex was evident at $X/T \approx -0.15$, but the streamwise velocity component U was virtually zero between $-0.2 \leq X/T \leq -0.35$. When the "backflow mode" was present, a single vortex was present between $0 \leq X/T \leq -0.35$, producing highly negative values of U and high shear stresses close to the floor over that length. Contours of γ_b showed that the 2 modes were extreme states and for most of the time, the flow in the separation region was actually in a state of transition from one mode to the other. They therefore proposed that the oscillation of the vortex could be pictured at its various stages, by using combinations of velocity vectors in the "zero- and backflow" modes.

The fluctuations between the velocity states may also explain the existence of line B in figure 10, using the following hypothesis. When the "zero-flow mode" is present, paint is forced to move upstream by the influence of the vortex at $X/T \approx -0.15$. As the paint passes further upstream, the level of shear decreases and eventually the paint comes to rest in the region between $-0.2 \leq X/T \leq -0.35$. When the "backflow mode" is present, the vortex occupies most of the separation region. Thus it influences a larger region than the small vortex in the "zero-flow mode" and causes the paint to move from the line of accumulation, in addition to streaks that run through the region where paint had accumulated. As the flow fluctuates between the 2 modes, the paint on the line of accumulation is not swept away completely. Hence, over time, a balance will occur between the movement and accumulation of paint, this balance being line B.

Using the junction of Devenport & Simpson (1986-90), Devenport *et al* (1990) extended the investigation to examine the effects on the junction flow of halving the thickness of the plate boundary layer. This reduction produced only a small reduction (≈4%) in the stand-off distance of the separation point from the leading edge, consistent with the findings of Baker (1980). In addition, with the thin boundary layer the levels of Reynolds normal stress $\overline{u^2}/U_\infty^2$ measured across the wake, 2 chord lengths downstream of the trailing edge, were only slightly higher than in the thick boundary layer. Although this is a long distance downstream of the trailing edge, by which point much of the turbulence could have

decayed, Devenport *et al* (1990) concluded that although the thickness of the oncoming boundary layer does affect the horseshoe vortex, it is of minor importance in its effect on the levels of turbulence in junction flows.

It would seem reasonable to expect that the adverse pressure gradient downstream of the maximum thickness of a wing/body junction would influence the horseshoe vortex as it passed downstream. Devenport & Simpson (1992) therefore made further investigations into the flowfield of their junction, making measurements in planes normal to the chord line at $0.75c$ & $1.07c$ downstream of the leading edge, the results being compared to earlier results obtained between the leading edge and maximum thickness. The vortex centre had already been shown to move gradually further from the wing and reduce in intensity between the leading edge and maximum thickness. These characteristics were found to continue downstream of the maximum thickness, the space between the vortex and wing remaining filled with low-turbulence fluid entrained from the freestream. In addition downstream of the maximum thickness, the line of low shear moved away from the wing and merged with the separation line, the bimodal unsteadiness becoming dissipated, eventually disappearing altogether by $0.75c$.

The investigations of Devenport & Simpson (1986-90) have formed the most comprehensive study of a wing/body junction to date. The considerable quantity of data and variety of flow features led them to compare the results with the predictions of the turbulence models of various *CFD* codes in order to validate them for junction flows. Their findings (Devenport & Simpson, 1992) will be discussed in Section 2.6 where some of the theoretical methods used to predict junction flows are examined.

The unsteadiness of the junction vortices produces not only fluctuations in velocity, but also large fluctuations in pressure which, like the velocity fluctuations, are non-periodic. This prompted Ölçmen & Simpson (1994) to investigate the characteristics of such variations upstream of junctions formed by symmetric wing/strut sections with a flat plate. Six sectional shapes were used in the investigation: Sand-1850, NACA-0015 & -0012 aerofoils, a teardrop-shaped section, the wing used by Devenport & Simpson (1986-90) and a similar wing with a parallel-sided centre portion. The flat plate formed part of a

false floor in the tunnel through which the sections passed, a pair of microphones being mounted flush with the top surface of the plate, in the plane of symmetry upstream of the junction. The coordinate system was that used by Devenport & Simpson (1986-90 & 92) throughout their investigation (shown partly in figure 11) with X in the streamwise direction, Y normal to the plate and Z normal to the XY plane forming a right-handed axis system.

Surface oil-flow visualisation tests performed to reveal the behaviour of the limiting streamlines in each junction showed that features which were qualitatively identical to figure 10 were present in all, *i.e.* a separation line upstream of the wing, the scour pattern of a horseshoe vortex and a line of accumulation of paint between the separation line and the leading edge which eventually merged with the separation line. Of the 6 patterns obtained, the most unsteady wake was produced by the teardrop aerofoil.

Histograms of the root-mean-square of the pressure fluctuations upstream of the leading edge were obtained also for all 6 configurations. For a particular junction, the value of the fluctuations at the leading edge was found to be several times greater than that measured upstream of the separation region. With increasing distance upstream from the leading edge, the fluctuations increase from the leading-edge value to peak in the vicinity of the line of low shear observed in the oil-flow visualisation tests, then decrease gradually to the almost constant value found in the boundary layer upstream of the separation region. Calculations of the flatness and skewness of the histograms of pressure fluctuation obtained showed that the majority of the histograms were not Gaussian. The Sand-1850 and NACA-0012 junctions did not exhibit bimodal histograms of pressure fluctuations, these being obtained, however, for the other 4 junctions. The junction using the teardrop-shaped section produced the largest range over which the bimodal histograms occurred, whereas for the NACA-0015 junction a bimodal histogram was found at only one location upstream of the leading edge.

It is therefore evident that these fluctuations and the associated forces generated on the body surfaces are also linked to the geometry of the leading-edge. By assuming that, over a long period of time, the vortex is confined within a certain portion of the separation

region, Ölçmen & Simpson (1994) defined a control volume adjacent to the junction surfaces. From this they derived an empirical relationship linking the pressure fluctuation, the U-& V-momentum-flow rates and the body geometry. This relation showed that the pressure fluctuation was linked logarithmically to the V-momentum rate and to the 0.4 power of the U-momentum rate.

2.4 - The flow around lifting and/or swept wing-body junctions

Most of the studies of the behaviour of the flowfield around wing/body junctions have been with the "wing" mounted normal to the body and at 0° incidence to the airstream. By comparison the more complex and realistic flow around the junction between a lifting and/or swept wing and body has received little attention.

Hawthorne (1954) performed more sand scouring experiments to investigate the effects of incidence and found that for small incidences, the depth of scouring around the junctions increased for both profiles, the contour patterns either side of the chord lines of the profiles becoming asymmetric, with the scouring on the compression sides of the junctions being slightly deeper than on the suction sides. The deepest scour around the bicuspid profile still occurred at the mid-chord and was still less deep than around the nose of the elliptical one, although the difference between them was not as marked as at 0° incidence. In addition Hoerner's (1965) review presented some experimental results regarding the interference drag of lifting junctions, showing that the interference drag increased as approximately the square of the lift coefficient.

Early attempts at obtaining flowfield data in the corners were made by Sepri (1973) who investigated the flow at several incidences around the junction of an unswept NACA-0012 section wing and flat-plate. From flow visualisation studies he concluded that a 4-vortex system existed which influenced the flow in the streamwise corners and wake in addition to the leading-edge region. Also a 5-tube yawmeter was used to measure cross-flow velocities, discovering that the vorticity levels on the suction side of the junction were stronger than that on the compression side and that they did not become equal to each other downstream of the junction. Additionally, as the plate was approached from

outboard, the wake of the wing could be followed along a straight line through the boundary layer to the plate. These observations were also presented by Barber (1978) for his experiments using the NACA-65 series struts mounted in a 12%*c* thick boundary layer. The findings implied that the Kutta-Joukowski condition could be applied to the wing both inside and outside the plate boundary layer.

Devenport *et al* (1990) reported on the turbulent wake structure for a lifting junction also. Using the same junction as used in their investigation into the effects of boundary layer thickness, surface pressure and oil-flow visualisation measurements were made at $\alpha = 0°$, +6° & 12°. Although the streak patterns and pressure contours retained the same features at incidence as they did at 0°, the separation point and line of low shear moved further upstream on the plate and the width of the separated region at the trailing edge also increased with incidence. Measurements were also made across the wake, of streamwise mean velocity component $\overline{U}$ and non-dimensionalised Reynolds stress component $\overline{u^2} / U_\infty^2$ at $\alpha = 0°$ & +6°, using a rake of hot wires which was positioned normal to the floor. The qualitative effect of incidence was to deflect the wing-wake and vortex legs, by different amounts, so that the vortex on the suction side lay slightly further from the wake than at 0°, whereas the vortex on the compression side was closer to the wake than at 0°. The turbulence levels in the vortex cores at +6° also differed from their values at 0°, being increased in the vortex on the suction side but decreased in the vortex on the other side of the junction.

Wood & Westphal (1992) postulated that an additional contribution to the secondary flow in a wing/fuselage junction may arise from vorticity shed by the wing. To test this theory they took measurements, at several incidences, around the junction between a straight wing of NACA-0012 section and a flat-plate. The sectional-lift coefficient of the wing was found to decrease only slightly from the mid-span to the junction, implying that vorticity shed from the wing contributed only a tiny amount to the trailing vorticity in the horseshoe vortex, the legs of which were found to dominate the flow downstream of the junction. Flowfield measurements, in planes normal to the freestream direction, showed that the interaction between the wing wake and plate boundary layer was confined to a narrow region between the legs of the vortex. Confirming the findings of Devenport *et al*

(1990), at incidence this region was deflected progressively towards the compression side of the junction with distance downstream. Measurements across the wake confirmed that the turbulence and vorticity levels on the suction side of the junction were higher than on the other side, distributed over a greater area, the vorticity in both legs diffusing with increasing distance downstream.

With only a few investigations conducted so far into the effect of wing incidence on horseshoe vortices, knowledge of the flowfields around lifting junction configurations remains somewhat less than for symmetric wings at zero incidence. Wing sweep would be expected to complicate the flowfield further and it should come as no surprise that the number of investigations concerning a junction involving a lifting, swept wing is even fewer. It would appear from Hoerner's (1965) review that some investigations were performed into the effects of inclining a junction during World War 2. They indicated that as a strut was swept forwards or rearwards the interference drag reduced, a discovery which was attributed to wing crossflow. If the wing were inclined to produce dihedral or anhedral, the interference drag increased due to a more severe separation in the tighter corner. In addition, Jupp (1980) makes reference to reducing the interference drag of the swept-back wing/fuselage junction on the Airbus A310. However he did not divulge any information regarding the structure of the flowfield around the junction.

It appears that the first flowfield data from an investigation into a lifting, swept-wing junction have been reported by Bernstein & Hamid (1993 & 95). They used a NACA-0015 section wing, mounted on a flat plate to give a sweep angle of 20° and 0° dihedral, it being expected that sweepback would provide some natural relief to the flowfield and reduce the severity of the separation of the approaching boundary layer compared to a straight junction of the same profile. However, oil-flow visualisation tests with the wing at a range of incidences showed little difference from junctions using unswept wings at incidence studied, for example, by Sepri (1973).

With the wing at 0° incidence, surface pressure measurements on the plate clearly showed a pressure rise up to the wing leading edge. At incidence, the shape of the isobars on the compression-surface side of the plate was clearly affected by the leg of the horseshoe

vortex, whilst the effects on the suction-side were masked because the isobars lay almost parallel to the vortex leg. On the wing itself, at small incidences the sectional lift coefficient showed little variation between the junction and the mid-span. However for $\alpha \geq +6$, clear reductions in lift coefficient close to the junction became evident. The pressure drag of the wing in the mid-span region also showed little variation with spanwise distance at near zero incidences. However, much closer to the junction, the sectional pressure drag showed a progressive and marked increase as the distance from the junction reduced. As the wing incidence was increased, so did the pressure drag across the whole span, but even allowing for this the rise in pressure drag near the junction began progressively further from it and reached higher values there.

Indications of vortical structures and high levels of turbulence were found around the leading edge which indicated that sweepback had produced only marginal relief for the boundary layer. As incidence was increased, the levels of turbulence on the 2 sides of the junction followed the same traits found by Devenport *et al* (1990) and Wood & Westphal (1992). Confirmation of the tiny amount of relief afforded by the angle of sweep was obtained from velocity surveys across the wake. In addition to the mean-velocity defect due to the wing wake, additional defects could be seen either side of the wing wake due to the vortex cores and peaks measured in profiles of turbulence quantities across the wake correlated to the vortex-induced mean-velocity defects. This investigation showed that even a swept-back junction should benefit from some extra form of flow control.

The results presented by Bernstein & Hamid (1993 & 95) remain thus far the only published experimental data into a swept-back wing/body junction. As mentioned in Chapter 1 however, no investigations of the flowfield around a swept-forward wing/body junction have been reported.

2.5 - Controlling horseshoe vortices

Apart from the work of Kubendran, McMahon & Hubbartt (1984), estimations of the actual interference drag of wing/fuselage junctions from measurements, appear to be non-existent. As Kubendran, McMahon & Hubbartt found that the interference drag for their

junction was negative there would seem little point in trying to eliminate it. However it should be pointed out that the absence of streamlining on the afterbody removed the adverse pressure gradient found in a more realistic wing/fuselage junction. This would certainly have an adverse effect on the total and possibly the interference drag too.

Whatever the sign of the interference drag of a junction, considerable non-uniformity of the flow and energy dissipation downstream of the leading edge still exist due to the vortex. Reducing these characteristics would be of real benefit to aircraft designers and naval architects. The engines of business jets are often mounted on the fuselage aft of the main wing and the possibility, when the aircraft is at incidence, that a leg of the horseshoe vortex may enter the intake should be taken into consideration. In the design of ships and submarines, reducing the strength of the horseshoe vortex around the keel or sail would produce a decrease in the level of cavitation and associated acoustic noise generated by the junction and would probably increase the efficiency of the propulsion system. This latter benefit concerning efficiency may also be useful in the design of turbomachinery cascades where the wake from one blade impinges onto the leading-edge of a downstream blade. For civil- and offshore-engineering applications, reductions in the strength of horseshoe vortices would reduce the scouring of the bed around the bases of bridge piers and piles of oil/gas production platforms.

Various ways of reducing the strengths of the secondary flows in the wing/fuselage corner have been examined. One of the earliest attempts was performed by Gough (1928) on a high-wing cabin monoplane for which the leading edges of the wings joined the cabin roof, level with the top of the front windscreen. He used simple, quarter-circle fillets of differing radii in the streamwise corners to blend the wing into the fuselage and indeed found the drag and propulsive efficiency to improve slightly as a result. However no modifications were made to extend the leading edge upstream. The use of fillets and fairings on strut/strut intersections has been reviewed by Hoerner (1965). He states that improvements using only a radiused fairing are limited, the optimum radius being between 4% & 8% of the chord. For an appreciable reduction in interference drag the fairing needs to extend beyond the trailing-edges of the struts, although this is more strictly applicable to strut intersections in a freestream than controlling horseshoe vortices.

Bearing in mind previous research which had indicated that the junction flowfield is primarily influenced by the leading edge shape, Scheiman & Kubendran (1985) investigated a junction formed from a sharp-nosed wing mounted normal to a flat plate. One surface of the wing was flat, forming a rectangular corner in the streamwise direction: the other surface was a circular arc, producing firstly a favourable then an adverse pressure gradient. Although some secondary flow was evident, it was considered insufficient to result from the actions of a horseshoe vortex. At first this would appear strange as the vorticity in the approaching plate boundary layer would be expected to become skewed around the leading edge of the junction. However with such a sharp leading edge in this junction, the type of severe separation found in junctions using wings with blunter leading edges appears to have been negated. In the rectangular corner the secondary flows were attributed to Reynolds stress gradients, whereas on the curved side of the junction, the secondary flow was attributed to the lateral curvature of the flowfield. It is likely that a very weak separation has occurred at the leading edge, with the vorticity in the boundary layer being unable to roll up into a discrete vortex. However a sharp leading edge is impractical from the point of view of leading-edge separation at non-zero incidences and would also complicate the manufacture of the wing.

A more practical approach seemed to be to increase locally the slenderness ratio of the wing over the part of the span immersed in the fuselage boundary layer, by extending the wing section forwards from its maximum thickness gradually as the root was approached. This type of modification (see figure 12 for example) could be incorporated as a leading-edge fillet simply added to the main wing design. The fillets shown in figure 12 were used by Kubendran & Harvey (1985) to evaluate their effect on the junction pressure drag about a NACA-0012 wing, at various incidences, mounted in a turbulent boundary layer on a flat-plate. Comparisons of the total pressure deficit across the wake with and without the fillets, revealed that the fillets had a beneficial effect on the pressure drag, although the improvements lessened at incidence as the simple extensions began to act as slender delta wings. They also discovered that the benefits could increase then decrease as the fillet size was increased, thereby indicating that a junction fillet would need careful optimisation.

Kubendran, Bar-Sever & Harvey (1988) subsequently used fillets B & C in figure 12 for smoke-flow visualisation and surface-pressure measurements, in a laminar boundary layer, around the same junction as Kubendran & Harvey (1985). A smoke wire stretched across the boundary layer at various heights above the plate provided visualisation of the streamlines and photographs were taken of their behaviour. Without the fillets, the flow separation upstream of the leading edge and the horseshoe-vortex formation were clearly visible. The severity of the separation was found to increase at incidence, the influence of the junction being visible above the height of the boundary layer. With the addition of the fillets at $\alpha = 0°$, the boundary layer separation took place at the leading edge of the fillet and reductions in the extent of the separated region were apparent. The greatest improvements were observed for the longer of the 2 fillets, for which results were also presented of its performance at 4° incidence and compared to the unfilleted case. At this incidence the fillet eliminated flow separation upstream of the leading edge, the fillet appearing to shed tiny vortices from its sides into the compression-side corner. The tests showed that fillets with a length:height ratio greater than 1 were the most effective in reducing the separation, confirming that a high slenderness ratio (small nose radius) reduces the strength of the horseshoe separation.

Maughmer *et al* (1989) examined the integration of the wing and fuselage on a sailplane model to investigate if improvements in performance could be made on an already refined aircraft configuration by fairing the leading edge of the wing root, upstream of the maximum thickness. Three fairings of differing nose bluntness were used with the linear and parabolic planform shapes shown in figure 13, to test 6 integration geometries. Although the fairings were small compared to the wing area, they produced surprisingly large changes in drag force, some being detrimental. The bluntest of the parabolic fairings actually produced an increase in drag of up to 15% over almost the whole drag polar of the model. However, for the slimmest fairing, the parabolic planform achieved equal performance to that of the wing alone and the linear planform actually produced a 3-5% decrease in drag over much of the drag polar for the model.

Since it had been shown that radius fillets in the streamwise corners reduced the secondary flows there, it was thought that extending the fillets around the leading edge would be

beneficial too. However, an investigation by Devenport *et al* (1990), around the junction shown in figure 14, revealed otherwise. The fillet was a simple, quarter-circle arc to blend the wing into the plate. Hot-wire measurements across the wake of the filleted junction showed that the boundary layer in the vicinity of the vortex legs was thicker and the vortex centres appeared further from the wake than without the fillet. As part of their programme of research into wing/body junctions, Bernstein & Hamid (1993) also examined the leading-edge region for such a fillet, on a junction formed from a semi-circular nose with a parallel-sided afterbody, mounted on a flat plate. Their results showed a similar picture to Devenport *et al*, the fillet merely displaced the separation point and horseshoe vortex system further upstream and did not appear to reduce its strength.

An investigation into the performance of an empirically designed fillet, as opposed to simple linear extensions forwards from the maximum thickness, is mentioned by Jupp (1980) in his paper on the interference aspects of the Airbus A310 wing. A leading-edge fillet had been used on the wing of the earlier A300 airliner, although the design of that fillet did not receive as much attention since the potential savings in cruise drag for the A300 were smaller than the A310. The thicker wing root and larger leading-edge radius of the A310 made possible greater savings in cruise drag if the horseshoe vortex could be reduced in strength. The advances in computational methods made since the A300 programme, released more time in the wind-tunnel testing programme for the evaluation of refinements to the A310 wing design, including an investigation of suitable fillet geometries. No details of the experimental investigation were released, but Jupp mentioned that fillets were moulded, by eye, using plasticene on a model of the junction. Oil-flow visualisation tests were conducted around the fillet shapes, those which produced the most promising streakline patterns having robust copies made of them. These copies were subjected to further, more extensive, testing. Jupp reported that the shape chosen for production appeared to suppress the vortex, the streamlines dividing smoothly along the fillet. The reduction in cruise drag of the A310 obtained by addition of the junction fillet was compared with the equivalent reduction obtained by the addition of a fillet to the A300. That for the A310 was 1⅓% more than that for the A300.

The only other reported investigation into the performance of an empirically-designed leading-edge fillet for a swept wing was conducted by Bernstein & Hamid (1993 & 96) as part of their research into the swept-back junction mentioned earlier. The fillet extended forward from the leading edge of a NACA 0015-section wing, swept at 20°, as shown in figure 15. The fillet shape is complex, drooped at its leading edge and is similar to that fitted to the wing glove of an Airbus A320. The addition of the fillet altered the junction flow significantly, the abrupt upstream separation, as in figure 10, being replaced by a gradual one, vorticity being shed from a line meeting the leading-edge apex of the fillet (figure 16). This line represents the dividing streamline, vortex sheets rolling up on either side of the fillet. The impression was gained that this junction vortex was somewhat weaker than without the fillet. With the wing at incidence, the relief offered by the fillet was reduced and a weak separation took place on either side of the fillet.

The surface pressure measurements showed that the fillet reduced the pressure rise in the leading-edge corner and also the peak suction pressure coefficient at incidence. Consequently, the pressure gradient aft of the peak suction was reduced. These effects indicate that the vortex formation is less abrupt than for the unfilleted case. The effect of the fillet on the spanwise distribution of lift was to produce an even more marked reduction in lift as the junction was approached, but its effect on the pressure drag was inconclusive. The fillet also effected a gradual skewing of the oncoming velocity profiles. Well upstream of the fillet, the velocity profiles were skewed slightly more than for the unfilleted case, but near the fillet the skew angle was considerably reduced, and at the junction itself, flow reversal was eliminated. The velocity profiles across the wake revealed a velocity defect associated with the junction flow either side of the aerofoil in addition to that of the normal wake; these velocity defects were less for the filleted case and the vortices lay closer to the junction.

The fillet reduced the levels of non-dimensionalised turbulence intensity $\overline{q^2}/U_\infty^2$ in the vicinity of the leading edge, in some cases at $\alpha = 0$ to about $1/6^{th}$ of the value without the fillet. The fillet displaced the concentrations of turbulence away from the plate and thickened the turbulent region there however. At and downstream of, the trailing edge, the fillet reduced the intensities of the Reynolds stresses and also the skin friction on the

plate. It was therefore concluded that careful design of the fillet to offer relief to the oncoming flow could be beneficial.

It is clear that the horseshoe vortices can be modified and improvements to junction flowfields made by extending that part of the wing which lies in the boundary layer, forward from the maximum thickness. The fact that such modifications are localised means that suitable fillet shapes can be incorporated into designs far more easily than complex modifications to the whole of the wing root region, the design of which often has other influencing factors such as the interaction of the transonic shock waves on the wing with the fuselage. Importantly, it also means that such local modifications can be retrofitted to existing wing planforms.

Recently a unique method of controlling a junction flowfield has been reported by LaFleur & Langston (1993). The technique is termed "iceformation" and has been developed as a contour design method (*e.g.* LaFleur, 1988) that alters the form of the separation region. It uses a water flow past a surface which is cooled such that ice forms naturally on it, the formed shape being a function of the local heat transfer and shear stress. The growing ice modifies the flowfield, which in turn influences the ice shape via increased or reduced shear stresses at the boundary, eventually reaching a stable situation. The process had been studied previously over flat plates and was also used to achieve improvements in diffuser design, but this is the first example of it being applied to a junction flowfield.

Their investigation involved a cylinder/flat-plate junction which was immersed in a laminar boundary layer flow. Preliminary experiments at Reynolds numbers of 737, 1480 & 1843 were each performed with 3 different combinations of water/flat-plate temperature ratios, giving a set of 9 experimental conditions. The ice shapes all displayed a symmetric, wedge-shaped build up of ice leading up to the junction, which then suddenly fell away to reveal a system of valleys and ridges wrapping around the cylinder where the ice had been scoured away by a horseshoe vortex system. The contour shapes obtained were processed to yield the experimental conditions that would form an optimum junction contour as regards the drag performance. The experiment was then performed at the new set of flow

parameters and castings were taken of the ice contours formed, these being recast to give 2 replicas of the shape formed.

Each pair of replicas and a pair of cylinders were then mounted on a flat plate, forming a junction on each side. The plate was then aligned vertically in a wind tunnel, attached to a force balance, for comparisons of the drag coefficients between (a) the optimum, ice-formed junction; (b) the plain cylinder/plate junction and (c) the cylinder/plate junction with a wedge, identical to the ice-formed wedge but without the scour patterns, added to the leading edge so that the projected frontal area was equal to that for (a). The drag coefficient C_D for each junction was based on the total frontal area of the particular junction.

Lafleur & Langston reported that the C_D of junction (a) was significantly lower than that of junction (b), although this is meaningless as the results are presented, due to the difference in the projected frontal areas of the 2 junctions. However, a C_D comparison may be made between (a) and (c) as the projected frontal areas are identical. Although the notation in their comparisons is confusing it would appear that, taking the strut, plate, junction and whole cylinder into account, the value of C_D measured for the ice-formed junction, above a Reynolds number of 0.6×10^6, was 10% lower on average than for the cylinder/plate junction with the artificial wedge. By subtracting the drag of the strut, the drag reduction for the plate/cylinder/iceform shape was estimated as 18% of the drag of the plate/cylinder/wedge shape. However a more useful comparison would have been between the actual drag force (/*N*) between the plain cylinder/plate junction and the ice-formed junction at identical wind speeds. They proposed that the iceform shape provides a pocket for the vortices, reducing their influence over the remainder of the junction and favourably altering the pressure gradients and shear stresses in the junction.

All the methods of controlling the horseshoe vortex have used a local modification of the wing geometry to reduce the strength of the secondary flows. Such flows must still exist however, even if weak, since the spanwise vorticity still present in the approaching boundary layer must stretch around the junction to pass downstream. To remove the

secondary flows caused by the horseshoe separation, the boundary layer vorticity must be removed, *e.g.* by suction through the wall surface.

Suction had been used previously in a wing/body junction by Goldsmith (1961) to maintain a laminar flowfield in the junction. However, in Goldsmith's paper, the horseshoe vortex itself was not afforded any mention. This prompted Philips, Cimbala & Treaster (1992) to investigate the effectiveness of suction through the body in eliminating it. They made flowfield measurements around an idealised straight wing mounted on a flat plate, with a rectangular, porous section in the plate just upstream of the leading edge. With no suction applied, strong secondary flows and vorticity concentrations in the streamwise corners were revealed as expected. However with a low suction-flow rate applied through the porous section, the horseshoe vortex could no longer be identified. As the suction was increased, small concentrations of vorticity began to appear, produced by interaction between the edge of the suction region and the boundary layer over the rest of the plate. They did not describe what effect suction had on the interference drag of the junction. However the use of suction seems to be a realistic way of eliminating the horseshoe vortex and since the suction rate can be altered to suit different flow conditions, it could be implemented in practical configurations.

The research discussed thus far has shown that the horseshoe vortex in a wing/fuselage junction can be weakened significantly or even eliminated. It should be borne in mind however, that the addition of a fillet to modify the geometry of the leading edge of the junction increases the wetted area subject to skin friction and changes the pressure drag of the junction. The fillet design would therefore need to be one which produced the best compromise between decreased interference drag and probable increases of other forms of drag.

If suction through porous surfaces in the junction were to be used, the optimum suction rates to eliminate the horseshoe vortex under all flight regimes would also need investigation. There are also other considerations designers must take into account if using suction, *e.g.* the cost of the system, blockage of the porous screen by insects, the power for the suction pump: is an extra motor needed, or will power be taken from the

main propulsion engines? The extra weight of the system will also need to be taken into account and airline companies will be concerned with the extra complexity of servicing. With these factors it seems that, until the implementation of suction control is forced by fuel prices for example, designers will continue to use passive devices, *i.e.* optimised filleting at the wing root.

To carry out optimisation of such modifications experimentally could be extremely time consuming and costly in terms of wind tunnel testing. Although processor time on a supercomputer is expensive also, it is becoming steadily cheaper and the use of *CFD* codes to model junction flows is becoming more attractive. Codes which have been previously validated against existing experimental data for the complex flow around a wing/body junction could be used to assess possible future junction designs, the most promising of which could then be tested experimentally. In addition to discussing some of the theoretical methods used by early researchers to postulate the structure of junction flows, the next section also discusses some of the computational predictions which have been performed and evaluates their performance.

2.6 - Analytical and computational methods for solving junction flows

Given the complex nature of junction flows, it is hardly surprising that theoretical work concerning such flows has been extremely limited until recently. Hawthorne (1954) performed a small-perturbation analysis of the flow around surface-mounted obstacles, but did not make any predictions concerning vortical motion, merely observing that the vorticity in the streamwise direction increased rapidly in regions where skewing of low-speed flow occurred, *i.e.* upstream of obstructions in the boundary layer. However the theory was invalid for the large disturbances produced by round-nosed obstacles.

Kinematical studies have since become tools used to infer the 3-dimensional flow pattern from oil/dye flow-visualisation patterns. In the past the dye streaks from such patterns were treated as representing the limiting streamlines in the flow, these lines originating from the front attachment point on a body. Maskell (1955) demonstrated how the limiting streamlines described a 3-D skeletal structure of the viscous flow and described that

separation could occur in one of 2 ways: a "bubble" separation where singularities define the separation and attachment points and a pocket of recirculatory flow is present, or a "free-shear layer" separation, where the separation streamline is aligned, in general, obliquely to the external flow. The limiting streamlines were held to join the separation streamline tangentially, the merged streamlines then leaving the body as a surface of separation. In this latter case the separation streamline was not terminated by singularities as in the case of the "bubble" separation. This concept was not accepted by all since later research, *e.g.* by Legendre (1956), was unable to accommodate the very complicated behaviour of the limiting streamlines which Maskell's idea called for.

Lighthill (1963) abandoned the use of limiting streamlines to describe the flowfield and instead, worked with the skin-friction forces on the surface. These form a continuous vector field over the body and are defined even in the vicinity of separation lines, which are themselves skin-friction lines. Lighthill showed, in contrast, that limiting streamlines are defined everywhere on a surface except near separation lines where they leave the surface rapidly. Thus it was moved that there was no basis for inferring the behaviour of limiting streamlines near separation lines, from surface oil-flow patterns. Lighthill's ideas have formed what has been termed the topological approach to the inferral of an external flowfield from a surface oil-flow pattern, where flow separation occurs only along a line connecting 2 critical points on a surface. These points are labelled saddles, nodes or foci and the connecting lines are skin friction lines upon which other lines have coalesced as the surface-shear stress approaches zero. These critical features are then developed to describe the flowfield above the surface.

However, the description of flow separations using the concepts in Maskell's (1955) paper has still been pursued by some researchers, especially Wang (1972 & 74) in his calculations of the flow over a prolate spheroid at various incidences. This approach has become termed the phenomenological approach. The "bubble" and "free-shear" types of separation noted by Maskell are termed "closed" and "open" separations by Wang. It is generally agreed that a "closed" separation is equivalent to the topological viewpoint. However the absence of the need for flow singularities on the body surface where an open separation is inferred, leads some researchers to suggest that the phenomenological

approach is not rigorous enough. Délery (1992) disputes the concept of open separation by claiming that "a separation is always closed... ...by definition, separation implies the existence of a separator that closes, or isolates, one domain in the flowfield". Tobak & Peake (1982) argued that "closed" and "open" separations should be renamed global and local respectively. The topological approach appears less prone to misinterpretation of the patterns and as such has been the most widely accepted of the two, other examples of the use of this technique being given by Dallmann (1983) and Chapman (1986).

Using topological concepts it has been shown by Hunt *et al* (1978) that constraints exist on the number of nodes minus the number of saddle points. These constraints are useful as a test of whether the inferred flow is kinematically possible. Hunt *et al* (1978), amongst others, analysed flows over cuboids and cylinders mounted in a surface boundary layer and have shown that the rules governing the skin-friction line behaviour on a surface could be extended to the 3-D flowfield itself. They were able to postulate the existence of multiple horseshoe-vortex systems around the leading edges and complex systems of nodal and saddle points in the flowfield and on the obstacle surfaces. It should be remembered however, that their experiments from which the patterns were inferred were conducted at low Reynolds numbers and other patterns may exist at higher Reynolds numbers. Certainly as the object's incidence relative to the freestream is varied, the topological pattern can be expected to change considerably. It is inadvisable to predict the flow around a new configuration solely from kinematical considerations; rather they should be used to complement experimental data and numerical calculations. Knowledge of the surface patterns associated with known flowfields can then be used to build up a picture of the flow from the surface patterns on a more complex shape.

An early simulation of a cylinder/flat-plate junction mounted in a laminar boundary layer was carried out by Kaul, Kwak & Wagner (1985). They used a circular cylinder of length:diameter ratio of 10:1, mounted in a 2-dimensional channel so that the ends of the cylinder were in contact with opposite walls of the channel, the nominal Reynolds number of the test being 10^3 based on the cylinder diameter. A twin-vortex system was formed upstream of the cylinder, like that found by Baker in figure 8(a) and as the Reynolds

number of the simulation was decreased, the saddle point of separation was found to move upstream, further away from the cylinder.

A similar junction flow was computed by Visbal (1991) at Reynolds numbers ranging from 5×10^2 to 5×10^3. His coordinate system defined X in the freestream direction, Z normal to the plate and Y normal to the XZ plane, forming a right-handed coordinate system. At the lowest Reynolds numbers, a twin-vortex system was found, the topology being shown in figure 17. However a comparison with the 2-vortex system due to Baker (1979) in figure 8(a), reveals differences between the 2 topologies. Whereas Baker inferred the saddle point on the floor upstream of the junction to be a separation point, Visbal computed it to be an attachment point instead. Visbal's computations also corroborated a photograph taken by Kawahashi & Hosoi (1989) using laser-speckle velocimetry. Whether this new topology or the classical one was formed seemed governed by the value of what Visbal termed a separation parameter, defined as $\beta_p = \left(\partial\omega_y/\partial x\right)\Big/\left(\partial\omega_x/\partial y\right)$ where ω_x & ω_y are the vorticity components in the X & Y directions respectively.

The classical twin-vortex topology was computed when $\beta_p > 1$ and the new topology when $\beta_p < 1$. At higher Reynolds numbers (approximately 1.5×10^3), a 4-vortex system was computed, changing to a 6-vortex one as the Reynolds number was increased to 2.6×10^3. The separation parameter β_p was also found to affect the multiple-vortex systems as it did the twin-vortex system, the multiple system eventually becoming unstable and cyclic at a Reynolds number of approximately 5×10^3. Code parameters such as time step and grid spacing were changed in order to investigate whether or not such unsteadiness was a physical phenomenon, or was merely induced by the code itself. Qualitative features of the unsteadiness were unaltered however, leading Visbal to conclude that the code was capable of modelling the instability found in experimental investigations of laminar horseshoe vortices.

Other computational investigations around obstacle/flat-plate junctions have been performed, including a few at supersonic Mach numbers (Hung, 1991 and Lakshmanan & Tiwari, 1993), but turbulent simulations of actual wing/body junctions seem to be confined

to the investigations of Sung & Lin (1988) and Devenport & Simpson (1992). Sung & Lin performed their simulation around a junction between a flat plate and a NACA-0020 section wing where the nose section was replaced by 1.5:1 semi-ellipse. The code used incorporated the turbulence model of Baldwin & Lomax (1978) and was run for a Mach number of 0.1 giving a Reynolds number of 5.5×10^5. The configuration was identical to that of an experimental investigation by Dickinson (1986) and data from his experiments were used to validate the results. The code was then used to predict the effectiveness of leading- and trailing-edge fillets in weakening the horseshoe vortex.

These fillets are shown in figure 18 and were simple extensions forward and aft from the maximum thickness of the wing. The results of the simulations confirmed those of Kubendran, Bar-Sever and Harvey (1988) that a leading-edge fillet is most effective in diffusing the horseshoe vortex system when its length is greater than its height. The trailing-edge fillets were also effective in diffusing streamwise vortices created in the trailing edge corners, although Sung and Lin were unable to conclude which of the trailing edge fillets performed best.

The *CFD* simulations of Devenport & Simpson (1992) mentioned earlier in Section 2.3, tried 6 different turbulence models. Although some of the models were designed for predicting flows around simpler configurations, it is obviously important to know what the limits of a particular model are. The junction configuration for the computational predictions was identical to that defined earlier for their experimental study (Devenport & Simpson, 1986-90 & 92), with the shear stress components and velocity gradients in the (X, Z) directions being defined by $(-\overline{uv}, -\overline{vw})$ and $(\partial U/\partial Y, \partial W/\partial Y)$ respectively. Comparing the results against their experimental data obtained from the planes shown in figure 11, they assessed the performance of these models in predicting the magnitude of the relative shear force $\sqrt{\left(\overline{uv}\right)^2+\left(\overline{vw}\right)^2}\Big/U_\infty^2$ and evaluated the suitability of the closure assumptions of the models.

Three of the turbulence models were based on the concept of a prescribed eddy-viscosity ν_t to predict the magnitude of $\sqrt{\left(\overline{uv}\right)^2+\left(\overline{vw}\right)^2}\Big/U_\infty^2$ from the measured mean-velocity

distributions, namely: (a) a simple model which defines ν_t in terms of height above the plate and the mixing length; (b) the Cebeci-Smith (1974) model and (c) the Johnson-King model. The latter 2 models are variations on the simple model, but use a smoothing function between the inner- and outer-portions of the boundary layer. The Johnson-King model was originally designed for 2-D boundary layers in an adverse pressure gradient, being adapted for 3-D flows by Abid (1988).

The other 3 models evaluated were the k-ε model, an algebraic-stress model and the model due to Bradshaw (1971) which relates the turbulence kinetic energy and shear-stress magnitude by a simple proportionality constant a_1. Instead of predicting $\sqrt{\left(\overline{uv}\right)^2+\left(\overline{vw}\right)^2}\Big/U_\infty^2$ from the velocity distributions, these 3 models were given the measured turbulence kinetic energy distribution from which to predict values of the resultant shear force. Apart from the algebraic-stress model, the methods imply or assume a fixed relationship between the angles of the resultant shear-force and mean-velocity gradient vectors, these angles being defined by:

$$\alpha_\tau = \tan^{-1}\left(\frac{-\overline{vw}}{-\overline{uv}}\right) \quad \text{and} \quad \alpha_g = \tan^{-1}\left(\frac{\partial W/\partial Y}{\partial U/\partial Y}\right), \qquad \text{,... ... ...(2.1).}$$

Usually these 2 angles are assumed to be equal, implying that the eddy viscosities in the streamwise and crossflow directions are also equal. However the algebraic-stress model is theoretically capable of predicting any lead or lag between these vectors.

Due to space limitations in their paper, Devenport & Simpson (1992) presented comparisons of their computations for only one corner plane, *i.e.* plane 8 in figure 5. Here experimental contours of the resultant shear force found in the plane were compared with the predictions from all 6 models. Of the prescribed eddy-viscosity models, the Cebeci-Smith model appeared most suited to predicting the contours of $\sqrt{\left(\overline{uv}\right)^2+\left(\overline{vw}\right)^2}\Big/U_\infty^2$ although the differences between measured and predicted values were larger in other planes. There were large discrepancies between the prediction of the simple mixing-length

model and experiment, especially near the plate surface and the Johnson-King model underpredicted significantly the shear-stress magnitude for most of the plane.

Considering the k-ε, algebraic-stress and Bradshaw models, noting that they were given the turbulence kinetic energy distribution from which to predict the resultant shear force, it was surprising that these methods were found to perform hardly better than the prescribed eddy-viscosity models. The contours produced by the k-ε model did not resemble the experimental contours, the predicted contours of $\sqrt{\left(\overline{uv}\right)^2+\left(\overline{vw}\right)^2}\Big/U_\infty^2$ were much flatter and the maximum value was stronger and lay closer to the plate than for experiment. Bradshaw's model (using his recommended value for a_1) also overpredicted the shear-stress magnitude over much of the plane, but the prediction was found to improve by optimising the value of a_1. Of the 3 non-prescribed eddy-viscosity models, the algebraic-stress model was considered to predict most realistically, the contours of $\sqrt{\left(\overline{uv}\right)^2+\left(\overline{vw}\right)^2}\Big/U_\infty^2$ for the corner plane shown.

Devenport & Simpson (1992) concluded that the Cebeci-Smith and algebraic-stress models were the most suited of those tested for predicting horseshoe-vortex type flows. None of the models however showed any strong correlation between the predicted and measured angles between the resultant shear force and the mean-velocity gradients, showing that the relationship between α_τ and α_g did not follow any simple pattern. Therefore they also concluded that new methods which accurately model the full, shear-stress transport equations, in particular the pressure-strain term, were needed in order that these angles could be predicted accurately.

2.7 - Summary

The research so far, both experimental and computational, has shown that vortex systems in laminar flow can involve 2, 4 or 6 vortices, the number increasing with the Reynolds number of the flow. It has also been shown that they become unsteady in position with a further increase in Reynolds number. In turbulent flow, the horseshoe vortex displays a more complex behaviour which is not yet fully understood and causes some difference of

opinion among researchers, especially with respect to their number. The vortex system has been shown to be easily affected by the arrival of turbulence structures from upstream of the junction and is unstable with respect to position.

It has been shown that the strongest junction vortices in both laminar and turbulent flow are produced by bluff obstructions of large nose-radius/low-slenderness ratio. It appears that the relevant parameters are the Reynolds number, and the ratio δ^*/R of boundary-layer displacement thickness to radius of curvature of the leading edge of the projection. The strengths of the secondary flows can be reduced by using a sharpened leading edge, although this would lead to early leading-edge separation if the configuration were placed at incidence. Wing sweepback offers only a small amount of relief to the pressure rise as the junction is approached and hence the horseshoe vortex is not altered significantly.

It has also been shown that carefully-designed fairings between wings and fuselages offer a convenient method of reducing the secondary flows in the streamwise corners and the interference drag, though for optimum results the fairing needs to extend both forward and aft of the wing. The "fillets" need to extend forward in such a way that they gradually increase the nose slenderness ratio as the wing root is approached from outboard. It also seems advantageous that some leading-edge droop should be incorporated in the fillet to offer relief to the oncoming flow when the wing is at its "design" incidence. The trailing-edge fillet may simply be an extension aft of the local chord from the maximum thickness similar to those used by Sung & Lin (1988). These aft extensions increase the slenderness ratio of the root even further and reduce the severity of the adverse pressure gradients in the streamwise corners as the trailing edge is approached. Thus the separations that arise in such corners without filleting are reduced or eliminated. However, it should be borne in mind that these additions increase the wetted area and any beneficial reduction in interference pressure-drag may be compensated by the increase in skin friction drag. The only way of eliminating the horseshoe vortex is to remove the wall boundary layer just upstream of the junction and an experiment using controlled suction through the wall has been shown to be extremely effective to this end.

Among the theoretical methods used for the calculation of junction flows, potential-flow theory is unable to predict either the spanwise vorticity field approaching the obstruction or the consequent horseshoe vortex. The direct numerical simulation of such flows at realistic values of Reynolds number is currently impossible due to insufficient computer power and memory. To attempt computational solutions of junction flows, the only feasible starting point at present is the Reynolds-averaged Navier-Stokes equations, provided a suitable turbulence model is available. For complex, anisotropic turbulence, such models will need to be based on experimental data. However, the aforementioned lack of computer memory and until recently, accurate experimental data in sufficient quantities to validate the codes, have been considerable obstacles towards the development of computer codes to solve the problem of junction flows. Although more and more flowfield data are becoming available from investigations into straight-winged and swept-back wing junctions, experimental data from a swept-forward wing/body junction have been, up to now, unavailable.

It might be expected that forward sweep would have some effect on the horseshoe vortex, since the pressure field for a swept-forward wing will influence conditions in the body boundary layer as it approaches the junction. The characteristics of this pressure field were an important consideration in the choice of a suitable profile shape for the model wing used in this investigation. Therefore computational simulations were carried out to predict the flow over the intended wing profile. Although the codes used did not incorporate turbulence models and therefore were incapable of predicting the structure of the vortex, they still gave valuable predictions of the pressure fields over the wing itself. The details of these simulations are given in the next chapter.

Chapter 3

Computational Simulations and Model Design

3.1 - Introduction

At the commencement of the project, the choice of aerofoil section for the wind tunnel model had not been made. At that time a research programme was underway at the project sponsors, the former research department at British Aerospace, Hatfield, into the aerodynamic design of a swept-forward wing (code number *HH10*) for a business jet. Thus, it was thought pertinent to use a section from the *HH10* wing for the wind tunnel model rather than a NACA 4-digit profile for example. The *HH10* wing incorporated both twist and taper, the section profile changing considerably from root to tip. The leading edge was straight, the trailing edge incorporating a crank thus increasing the forward-sweep angle of the trailing edge at the root. The variation in section along the span meant that the choice of a suitable section for the wind tunnel model required some consideration and so facilities were made available at BAe, Hatfield for the author to conduct *CFD* simulations to investigate the flow over proposed wind tunnel models. The calculations were performed, using the 2- and 3-dimensional codes ***FELMA*** and ***SPARV*** respectively, for a freestream velocity of 30 m/s and Reynolds number of 1.0×10^6 based on the streamwise chord. Both codes are described briefly in section 3.2.

After consultations at BAe, Hatfield, the section profile used for the 2-*D* investigation was taken from *section-7*, midway between the root and the trailing-edge crank of the *HH10* wing and scaled to give a streamwise chord of length c = 500 mm. The section outline is shown in figure 19 along with the chord and camber lines. The camber line is complex, it being heavily loaded towards the rear of the section, in addition to having negative camber close to the leading edge (see figure 20). This shape resulted from the design of the *HH10* wing by the *inverse method*, in which the required flow conditions around specific sections along the span were used to define the shape of the wing.

For the 3-D calculations, there were conflicting considerations. To simulate the real wing, the model wing should have taper and twist, although for ease of manufacture, an untapered, untwisted wing was desired. It was felt that since the section used in the 2-D investigation was not the actual root section of the *HH10* wing and the *fuselage* was being simulated by a flat plate, it was unnecessary to complicate the model wing shape with taper, twist or a change in profile along its span. Therefore the section in figure 19 formed the streamwise-section profile along the semi-span of the model wing, which was limited to 1 m by the height of the wind tunnel to be used. The sweep angle was chosen, after consultation with BAe, at -28°. Due to the low aspect ratio of the model wing (AR = 4), it was considered possible that flow structures from the tip region might interfere with and modify the flow around the root junction. Thus it was necessary to investigate whether a region of quasi 2-D flow existed in the mid-span region of the model wing, separating the tip and root regions and the ***SPARV*** code was used to investigate the characteristics of the flow over the intended model shape, checking its suitability for the wind-tunnel model.

3.2 - The computational codes

3.2.1 - *FELMA*

FELMA, or ***F***inite-***EL***ement ***M***ethod for ***A***erofoils, is a 2-D code developed at BAe, Hatfield, see King & Williams (1988), for calculating the compressible potential flow around multi-element aerofoils, with viscous/inviscid interactions capable of modelling flow separation and predicting $C_{l_{max}}$. The code works by discretising the transonic potential-flow equations on a H-type computational grid using the method of finite elements. The resulting set of non-linear difference equations is solved using line relaxation sweeps in alternating directions as the smoothing procedure within a multi-grid solution algorithm which facilitates rapid convergence. The laminar boundary layer is modelled using a compressible version of a model by Thwaites (1960). Transition from laminar to turbulent flow can be incorporated in one of 3 ways, assuming:

a) natural transition of the attached boundary layer as predicted by Granville's (1953) criterion,

b) if laminar separation occurs before natural transition then a laminar separation bubble is modelled by Horton's (1967) semi-empirical method, or

c) the point of transition can be specified in the steering code.

The lag-entrainment method due to Green *et al* (1972) is used over the turbulent portion of the boundary layer. The coupling between the boundary layer and the inviscid flow can be performed in a variety of ways within **FELMA**: direct coupling, semi-inverse coupling or quasi-simultaneous coupling, depending on flow conditions.

3.2.2 - *SPARV*

SPARV, or ***S***ource ***P***atch ***A***nd ***R***ing ***V***ortex, is a 3-D code developed by BAe, Brough from a thesis by Petrie (1979) to analyse complex aircraft/store configurations. It is a panel method which defines a series of N quadrilaterals, which in general are non-planar, on a surface. On each panel, usually at the centroid, a control point and a unit normal outward from the surface are specified. Sources, or combinations of a source and doublet, of constant, but initially unknown strengths are placed at the control points. The sources are responsible for thickness effects and the doublet distribution is responsible for both incidence and camber effects, since a constant-strength doublet panel is equivalent to a ring vortex around the perimeter of the panel.

By placing the source and doublet distributions on the surface instead of internally, the problems of having to determine a control surface and the appearance of a trailing vortex sheet from the trailing edge are avoided. By splitting the total number N of panels into $N/2$ on each of the upper and lower surfaces and defining corresponding singularities on the 2 surfaces to be equal, the boundary-condition equation splits into 2 simultaneous equations with the singularity strengths as the unknowns. The boundary condition of zero flow along the unit normal to the surface is applied and the equations are solved iteratively to give the source and doublet distributions. The vorticity at a point can then be calculated from the doublet distribution and the velocity and pressure coefficient at that point can then be calculated.

The basic code as described above performs inviscid calculations. For viscous calculations, ***SPARV*** has been coupled with the boundary-layer method *BLCROS3D* developed at BAe, Brough. This method uses Lighthill's transpiration approach to replace the zero flow condition normal to the surface by a transpiration velocity derived from the rate of change of the displacement surface. The code however does not incorporate a turbulence model and therefore could not be used to predict the horseshoe vortex around the swept-forward junction.

3.3 - *FELMA* calculations

The aim of the calculations using ***FELMA*** was to predict the 2-D pressure distribution over the aerofoil section. Viscous calculations were performed at $\alpha = +3°$, 6° & 9°, the results being shown in figure 21. At $\alpha = +3°$ the pressure distribution at the leading edge is twin peaked, the first peak being the standard, leading-edge suction peak. The cause of the second peak is revealed in the exaggerated view of the leading edge in figure 20. Here, in addition to the initially negative camber, the slope of the camber line can be seen to change at $x = 25$ mm ($x/c = 0.05$), exactly where the second peak is situated. Additionally, the shape of the camber line also produces a third peak in the pressure distribution at $x/c \approx 0.6$, this peak being at the crest of the camber line.

As the incidence was increased, the leading-edge suction began to dominate and absorb the small peak at $x/c = 0.05$. Additionally, at $\alpha = +6°$ & 9°, the pressure distributions over the upper surface show evidence of flow separation just upstream of the trailing edge.

3.4 - Initial *SPARV* calculations

Predictions of the pressure distribution over the whole wing were attempted using ***SPARV***. Inviscid simulations were carried out at $\alpha = +1°$, 3°, 5° & 7°, reflection plates being used at the wing root and tip, simulating the intended experimental arrangement of the wing spanning the tunnel from floor to roof. The reflection plates have the effect of creating a swept-forward junction at the tunnel floor and a swept-back junction at the tunnel roof. Thus the terms root and tip are not strictly correct, but have been retained for

ease of description, *root* referring to the swept-forward junction, *tip* referring to the swept-back junction. The chordwise pressure distributions obtained at sections along the span are shown in figures 22(a) to (d), the spanwise interval between each sectional pressure distribution being $\Delta Y/c = 0.2$, Y being measured in the spanwise direction from the *root*, normal to the plate.

3.4.1 - *SPARV* calculations at $\alpha = +1°$

At $\alpha = +1°$, figure 22(a), the sectional pressure distributions in the *tip* region are dominated by the rear-loading of the camber line, the leading edge suction peak being almost non-existent. As the *root* is approached from the *tip*, the suction peak at $x/c \approx 0.6$ increases to a maximum value between $Y/c = 0.4$ & 0.2, then decreases slightly towards $Y/c = 0$. The leading-edge suction also increases as the *root* is approached, reaching a maximum at the *root* section. Due to the shape of the section, a broad suction peak can also be seen in the pressure distribution on the lower surface. The strength of this peak diminishes as the *root* is approached from the *tip*. Thus, as expected, the aerodynamic loading increases from the *tip* to the *root*.

3.4.2 - *SPARV* calculations at $\alpha = +3°$

At $\alpha = +3°$, figure 22(b), the trends in the sectional pressure distributions at $\alpha = +1°$ continue. In addition, the leading-edge suction is more pronounced along the whole span. Although the suction peak at $x/c \approx 0.6$ still dominates the chordwise pressure distribution in the *tip* region, the trend in the value of the leading-edge suction peak from the *tip* to the *root* means that the leading-edge suction dominates over the rear suction peak at the *root*. An interesting feature is the change in the suction peak at the leading-edge from a single peak at the *tip*, to a twin peak at the *root*. The twin-peak is caused by a combination of (a) the flow rounding the leading edge and (b) the change in slope of the camberline at $x/c = 0.05$. Further outboard, because of the reduction in leading-edge loading, it would seem that the effective sectional incidence is reduced. The suction peak at the leading edge is reduced in strength, but the suction peak at $x/c = 0.05$ remains. Retrospectively, it

also seems that the apparent leading-edge suction peaks at $\alpha = +1°$ are actually due to the change in slope of the camberline at $x/c = 0.05$.

3.4.3 - *SPARV* calculations at $\alpha = +5°$ & $7°$

As incidence was increased further to $\alpha = +5°$ & $7°$, figures 22(c) & (d) respectively, the suction at the leading-edge increased. At both incidences, in the *root*, the increased leading-edge suction absorbs the suction peak at $x/c = 0.05$. Further outboard however, the double suction peak is still evident, in the mid span at $\alpha = +5°$ and slightly further outboard at about $Y/c = 1.6$, at $\alpha = +7°$. The trends noted at lesser incidences in the upper-surface suction peak at $x/c = 0.6$ and lower-surface pressure coefficient, continue at $\alpha = +5°$ & $7°$.

3.4.4 - Summary of initial *SPARV* calculations

In brief, at all incidences tested, the pressure distributions show expected increases in loading as the *root* is approached from the *tip*. Also, as incidence is increased, the strength of the suction peak at the leading edge increases across the span. Figures 22(a) to (d) all show regions of little change in pressure distribution around the mid-span. This suggests that a wing of semi-span 1 m and chord 500 mm might be sufficient to ensure that flow from the wing *tip* was not interfering with the *root* junction flow. To test this further, additional calculations were performed.

3.5 - Additional *SPARV* calculations

The additional ***SPARV*** calculations were designed to examine what influence, if any, the wing *tip* exerted over the flow at the *root*. Two sets of calculations were performed using: (a) an aspect ratio of 8 and (b) an aspect ratio of 4, without the reflection plate forming the swept-back junction; hence a true root and tip exist for this latter configuration.

3.5.1 - *SPARV* calculations for the wing of aspect ratio 8

The aspect ratio was increased to 8 by using a wing of semi-span 2 m, all other conditions being retained. This was to examine the effect on the pressure distribution at the *root*, of moving the *tip* further from it. Figure 23 shows the inviscid pressure distributions for this configuration at $\alpha = +3°$, obtained at stations spaced at intervals $\Delta Y/c = 0.4$ along the span. The results are almost identical to those calculated for an aspect ratio of 4 (figure 22(b)); at each station, there is a slightly greater difference between the pressure distributions over the upper and lower surface at aspect ratio 8 signifying an increase in aerodynamic loading. Also the pressure recovery at the trailing-edge *tip* of the wing of aspect ratio 8 is slightly greater. These slight differences were expected as a result of the increased aspect ratio. Inviscid results were obtained only at $\alpha = +3°$, simulations performed later at $\alpha = +1°$, 5° & 7° and attempts at viscous simulations all failed due to a lack of disc space for the output files.

3.5.2 - *SPARV* calculations for the wing with a free tip

The second set of control calculations used the wing of aspect ratio 4, but removed the reflection plate at the swept-back junction to create a free tip. ***SPARV*** calculations around this configuration were attempted at $\alpha = +1°$, 3°, 5° & 7°. However inviscid results only were obtained at $\alpha = +1°$ & 7°, the simulations at $\alpha = +3°$ & 5° failing due to lack of disc space. The results obtained for the free tip at $\alpha = +1°$ appeared virtually identical to those for the case with the reflection plate at the *tip* in figure 22(a), any differences being too small to be noticed visually.

The results obtained with the free tip at $\alpha = +7°$ are shown in figure 24 for comparison with the reflection plate case, figure 22(d). The sectional pressure distributions between the *root* and $Y/c = 1.4$ also appear virtually identical. However between $1.6 \leq Y/c \leq 2.0$ there are differences over the upper surface at the trailing edge. In figure 22(d), the pressure distribution in this region, aft of $x/c = 0.6$, shows a gradual pressure rise towards the trailing edge. In figure 24, the corresponding pressure distribution shows only a small pressure rise until approximately $x/c = 0.95$, after which it rises rapidly. This reduction in

adverse pressure gradient over a considerable part of the rear of the free tip is probably due to the action of a tip vortex re-energising the flow in that region, thereby increasing the suction over the upper surface. A possible reason for no differences between the 2 cases being apparent at $\alpha = +1°$ is that the induced tip vortex is of insufficient strength at this incidence to affect the pressure distribution noticeably. The fact that no differences were evident in the *root* region indicated further that a wing model of aspect ratio 4 would be suitable.

3.6 - Summary of computational predictions

Attempts to obtain viscous output data from all the ***SPARV*** simulations described above were made using variations to the steering code but with no success; the disc space problem described above severely hindered these attempts. The control calculations showed that an increase in aspect ratio, or a free wing tip, had virtually no effect on the inviscid flow around the *root*. Therefore, in the absence of viscous data, it was concluded that a model of semi-span 1 m and chord 500 mm would be suitable for testing in the wind tunnel. The model manufacture and data acquisition equipment used in the experimental investigation are described in the next chapter.

Chapter 4

Model Manufacture and Experimental Arrangement

This chapter is concerned with the model manufacture and the experimental apparatus. In order to investigate the mean flow behaviour and turbulence quantities in the junction, surface-flow visualisation and pressure measurements were made, in addition to yawmeter and crossed-wire anemometry measurements in the external flow field. The equipment used and the experimental arrangements for such measurements are described below.

4.1 - The wind tunnel

The wind tunnel used was the Queen Mary & Westfield College (QMW) No.1 tunnel. This is a return-circuit tunnel of contraction ratio 7.2:1, capable of airspeeds up to 45 m/s, with a freestream turbulence level of approximately 1.2%. A single 25 kW-motor drives a 7-bladed propeller rated at a maximum of 1000 rev/min. This motor is situated in the tunnel, in a streamlined nacelle, immediately downstream of the first diffuser and its housing is separated from the diffuser by a 50-mm gap filled with rubber to minimise transmission of motor/fan vibration to the working section.

At its entrance, the test section is 1.22 m in width, 1.0 m in height and 2.45 m in length, fillets being used to minimise secondary flows in the streamwise corners. Opposite walls are parallel throughout the working section, but the corner fillets diverge slightly to allow for boundary-layer growth along the walls of the tunnel. Illumination is provided by fluorescent lights mounted in the corner fillets between the roof and side walls. In the roof of the working section is a rectangular opening, 1.93 m in length by 0.3 m in width, to enable measuring probes to be positioned using a traversing gear mounted on the roof. The opening can be closed using wooden slats of various widths.

Speed control is via the main dc-motor, with a small dc-motor coupled to it for fine adjustments. Pressure tappings fitted in the walls of the settling chamber and at the

entrance to the working section, are connected to a Betz manometer enabling the reference dynamic pressure to be read. The resolution of the manometer is 0.1 mm H_2O, enabling the free-stream velocity U_∞ to be set with an accuracy of approximately 0.1% at 30 m/s. To enable the tunnel to run continuously for long periods, 4 cooling motors are used to prevent the fan motor overheating. As a result, the air temperature inside the tunnel is kept reasonably constant.

4.2 - Model design

The computational-flow calculations in Chapter 3 showed that a wing/body junction, using a half wing of the constant section shown in figure 19, of streamwise chord c = 500 mm, semi-span 1 m and forward-sweep angle of 28° was suitable for the experimental investigation. The body would be represented by a flat plate, forming a false floor in the working section, the wing passing through the plate creating a swept-forward junction at the root.

The wing

The wing was manufactured from *Tancast-8* rigid-polyurethane foam, in which 2 steel bars were embedded parallel to the leading edge to provide extra stiffness. The foam was used because of its excellent stability in varying conditions of temperature and humidity. Thirty-nine grooves were cut parallel to the leading edge at the positions shown in figure 25 and listed at Appendix A. These positions were chosen with the aid of the computed pressure distributions over the wing and include grooves along the leading and trailing edges. Copper tubes, 2.4 mm in diameter, were cemented in the grooves, the wing surface being then sealed with *Isopon* body filler and hand finished to shape. To prevent blockage of the pressure tubing by the flow visualisation dye, the pressure tappings were left undrilled until flow visualisation was complete. Twenty-two chordwise rows of holes, each 0.5 mm in diameter, were then drilled into the tubes at the distances from the plate listed at Appendix B. The rows were concentrated near the root to improve the resolution of the measurements in that region.

Early oil-flow visualisation tests revealed that laminar separation of the wing boundary layers, with turbulent reattachment further downstream, occurred at the moderate Reynolds number of the tests. Therefore the boundary layers on both surfaces were made artificially turbulent by a transition strip. Commonly, a strip of adhesive-backed sandpaper or small-diameter wire is used for this purpose. However these 2 methods are thought to be rather crude, as they force transition by 2-dimensional separation bubbles immediately up- and down-stream of the strip, with associated thickening of the boundary layer.

A more refined method is to use distributed roughness such as *ballotine* (glass micro-balls) attached in a random pattern in a narrow strip. The balls produce isolated projections into the boundary layer growing on the wing. A tiny separation region exists around each ball, producing turbulent flow downstream of it. Each turbulent region grows in a wedge-shaped fashion, similar to the growth of a natural turbulent spot as described by Schlichting (1979), the wedges coalescing at approximately the rear of the strip, producing turbulent flow over the remainder of the wing. The ballotine needs to be applied in a random pattern as described by Arnott & Jones (1994) to achieve the described effect. If the distribution is too dense, the strip performs like a wire; too sparse and the wedges will not coalesce rapidly enough.

With the wing *in situ*, extremely thin layers of water-soluble glue, 5 mm wide, were applied to both surfaces of the wing and the ballotine were blown sparingly onto the glue, any regions where the ballotine had been applied insufficiently or extravagantly being amended. In the absence of flight test data, with the wing at 0° incidence, the strips were placed at $x/c = 0.07$ following a recommendation from BAe, Hatfield. The minimum diameter of ballotine needed to effect transition was calculated from data given by Braslow, Hicks & Harris (1966) and Rae & Pope (1984). The ballotine were sieved to obtain balls of a narrow diameter range, the lower end of the range was chosen to be only slightly greater than the minimum needed to produce a turbulent wedge, as balls which were smaller in diameter than required would be useless.

The *body*

The *body* of the junction was idealised as a flat plate of length and width equal to the working section of the tunnel. Made from *melamine*-faced chipboard and supported on 4 battens, the plate provided a false floor in the working section 100 mm above the tunnel floor. The leading edge of the plate is elliptic in section and incorporates a 5° nose-down droop. The plate boundary layer was tripped 25 mm from its leading edge and 1350 mm ahead of the wing by a sandpaper strip placed across the width of the plate. It was ensured that the floor was flat and parallel to the floor of the working section with the aid of a spirit level, metal shims being inserted between the battens and the floor of the working section where necessary to ensure a level surface.

The plate incorporated a turntable made from *melamine*-faced plyboard. This turntable was mounted on height-adjustable castors to facilitate changes of model incidence and to ensure that a flush join existed between the turntable and plate. The small, unavoidable clearance gap was covered with adhesive tape once the desired incidence had been set. The turntable was also fitted with pressure tappings around the leading edge after flow visualisation had been completed; their positions are shown in figure 26.

4.3 - Installation of the wing

The wing was installed vertically in the tunnel by passing it through a close-fitting slot in the plate turntable and bolting it to a second turntable in the tunnel floor. Any small gaps that remained between the wing and plate turntable were filled with plasticene. The rotation axes of the 2 turntables were coincident and the plate turntable was fixed to the tunnel floor turntable so that the junction incidence could be altered using a hand-cranked mechanism outside the tunnel, with a resolution of $\pm 0.1°$. The coordinate system used was the *left-handed* Cartesian one shown in figure 27, with the origin at the leading edge of the junction. As the wing was installed vertically, upper surface in the text refers to the wing surface on the $+Z$ side of the junction, lower surface refers to the surface on the $-Z$ side as defined in figure 27.

At the roof, the wing was supported by a backrigger to a metal cross-beam in the tunnel roof so that the wing could rotate about the turntable axis. The furthest upstream of the roof slats was secured to the tunnel roof and holes were drilled in the slat, on a radius from the axis of rotation of the turntables, at intervals of 1° from -10° to +10° (see figure 28). The tip of the wing could be thus fixed at incidence, preventing any aerodynamic twisting of the model, by passing a bolt through this slat into the backrigger. To prevent the formation of a second junction by the wing tip and tunnel roof, a gap of approximately 5 mm was left between the wing tip and roof. The leading edge of the wing tip lay about 400 mm downstream of the entrance to the working section.

4.4 - The roof-mounted traversing gear

The roof-mounted traversing gear is shown in figure 29 and was used to position the probe accurately in the tunnel. It consists of a combination of *Unislides* (marked A, B, C & D) arranged to give movement in 3 axes. In addition, it was fitted with a rotary table E, which enabled probe movement in yaw. *Unislides* B and C were coupled by a toothed belt M to ensure that the lead screws J and K were driven together. The range of movement available is 0.8 m longitudinally, 0.3 m vertically and 0.45 m transversely, each with a resolution of 0.05 mm. The rotary table has an unrestricted range of movement in either direction with a resolution of 0.1°. All movements of the *Unislides* and rotary table were effected by stepper motors marked F. To increase the range of movement in the longitudinal direction, the traversing gear was mounted on 2 parallel bars running the length of the working section.

A vertical stem *G* was mounted on the axis of the rotary table, projecting down into the tunnel through the roof opening. Attached to this stem was a horizontal sting of square cross-section which incorporated a saddle slide. The faces of the sting were ground flat and parallel ensuring a tight fit between it and the saddle, thus maintaining the probe in the vertical plane as the slide position was changed during the experiments.

4.5 - Data acquisition equipment

Control over data acquisition was through an 80286-based PC fitted with an IEEE-488 interface card. This was linked to a *Hewlett-Packard* 3455A digital voltmeter and *Digiplan* stepping-motor drive. The control unit for the stepping motors was fitted with 2 IEEE-488 cards, each having 3 output channels in order to drive the pressure switches and probe traversing gear via d.c. synchronous stepper motors. Probe positioning, pressure switch rotation and data collection were thus controlled through the IEEE interface via programs written in *Microsoft QuickBASIC 4.5*.

4.6 - Experimental arrangements

The following 4 sub-sections describe the experimental arrangements for the flow visualisation, surface pressure, yawmeter and crossed-wire investigations.

4.6.1 - Surface-flow visualisation experiments

For flow visualisation experiments, the wing, plate, and interior walls of the tunnel were painted matt black. The surfaces of the wing and plate were gently sanded with fine waterproof, abrasive paper and rubbed with silicone polish to seal the surface against the paraffin used in the oil/dye experiments. In addition, the fluorescent white lights in the roof of the tunnel were replaced by fluorescent UV lights.

Two types of test were conducted, one using the surface oil/fluorescent-dye technique, the other using tufts of 'dayglo' cotton thread. The oil-flow technique was used to provide information on the position and behaviour of the limiting streamlines in the junction and

involves applying a thin layer of paint, composed of oil and a fluorescent dye, to the surface. The technique works on the principle that shear stresses in the boundary layer force the oil to move in the local stream direction, leaving streaks of dye on the surface. Once the oil has evaporated off the surface, the streak patterns produced can be photographed. Maltby (1962) has shown that if the oil film is very thin, the directions of the streaks are an extremely good approximation to the skin-friction vector just above the

surface and the general 3-dimensional flow structure above the surface may be inferred from the pattern. Where the shear stress is quite high, e.g. under a vortex, the oil/dye layer is thinned or scoured away allowing the surface underneath to show through. Where the shear stress is low, e.g. near separation or a stagnation point, then the paint accumulates leaving a highlighted region.

There is a danger where surface oil-flow visualisation is used on vertical surfaces that in regions of low momentum the oil streaks tend to be influenced also by gravity, giving a slightly false indication of the streamline behaviour. The tufts therefore were employed to help in interpreting the surface-oil flow patterns. The behaviour of the tufts confirmed regions of separated and/or reversed flow and whether the streaks of dye were due to the influence of the flow field or gravity. For the tuft tests, a grid was marked out on the plate, parallel to the X and Z axes, at intervals of 25 mm ($0.05c$). Where the grid met the wing, it was continued onto the wing surfaces parallel with the leading edge and streamwise chord. The tufts were attached to the node points in the grid with a tiny spot of water-soluble glue at each node.

A 35-mm single-lens reflex camera, fitted with a 35-70 mm zoom lens was used to photograph both the streak patterns and tuft behaviour on Kodak T-Max 400 film. White light was prevented from reaching the patterns, the only illumination coming from the UV fluorescent lights in the tunnel roof. The UV light excited the dye molecules causing them to fluoresce, emitting white light. Attaching a UV-blocking filter to the front of the lens prevented ambient UV light from reaching the film, but allowed the visible light emitted to pass through, thereby raising the contrast in the recorded image. To achieve the maximum depth-of-field in the recorded images of the oil-flow patterns the lens aperture was set to *f*/22, the exposure times ranging from 15 to 30 seconds. For the tuft tests an exposure time of 2 seconds was suitable, the lens aperture being widened to *f*/4. However, because of the low level of visible light emitted, the film had to be push-rated to ISO 1600 for both sets of tests. This artificial increase in film speed was then compensated for during the film development stage.

4.6.2 - Surface pressure measurements

For the surface pressure measurements, the *Digiplan* motor-drive was used to drive two motorised, 32-port, pressure switches. The pressure tubes from the wing and plate were grouped into bundles and could be connected to the pressure switches via male/female couplings so that each group could be measured in turn. The nozzles on the male halves of the couplings had their rubber O-rings replaced and vacuum grease applied to the new rings to improve the pressure seal across the face of the couplings. In addition, the tunnel reference pressures were connected to each switch. The output from either switch was passed to a pressure transducer, with a range of ±200 mm H_2O, that had been calibrated against a Betz manometer with a resolution of 0.1 mm H_2O. The calibration slope of the transducer was found to be linear to within 0.1%. The output voltage was displayed on the voltmeter and sampled by the PC, a diagram of the apparatus being shown in figure 30.

4.6.3 - Yawmeter investigation

A single-tube yawmeter was used to measure the mean velocities around the nose of the junction. The yawmeter, or "Chu-tube" as it is known at QMW, is shown in figure 31 and works on the same principle as the 5-hole Conrad-type, but only uses 2, closely-fitting, concentric tubes. The inner tube is of 0.635 mm internal diameter and its tip is scarfed at 45° to its longitudinal axis, about which the tube can be rotated by 4 successive 90° rotations to provide information on the mean flow direction. The outer tube is of 1.09 mm internal diameter and 1.56 mm external diameter and is cut normal to its axis. It can be slid forwards just to cover the tip of the inner tube in order to measure total pressure, graphite grease being used as an airseal between the 2 tubes.

A complete cycle of measurements at a point in the flow involves the readings from the inner tube at each of its 4 rotation positions and the reading of total pressure with the outer tube slid forward. The notation used during a cycle of rotations and translations of the single-tube yawmeter is shown in figure 32 and compared to that used with a Conrad-type yawmeter. The principles of operation of the single-tube yawmeter are described fully by Chu *et al* (1987), but a brief description is presented here.

The angles of the local velocity vector at the probe tip relative to the axis of the yawmeter are defined in figure 33, β being the angle of rotation of the turntable E of the traversing gear and θ being the pitch angle of the probe. However when the yawmeter is pitched, any rotation β is about an axis perpendicular to the freestream direction rather than the probe stem in figure 31. The Eulerian yaw angle ψ relative to the probe axis is therefore related to β & θ by the following relationship:

$$\tan\psi = \tan\beta \sec\theta \qquad \ldots\ldots\ldots (4.1).$$

Since the pressure registered by a tube of the yawmeter is a scalar function of the angle that the flow makes with the tube, using the notations shown in figures 32 & 33 we may write:

$$p_i = p_\infty + f_i(\psi,\theta)\,\tfrac{1}{2}\rho Q^2 \qquad i = 1,\ldots,5 \qquad \ldots\ldots\ldots (4.2),$$

where p_i is the pressure registered by the yawmeter at the 5 positions shown in figure 32, p_∞ is the static pressure at the measuring station, $Q^2 = U^2 + V^2 + W^2$ and $f_i(\psi,\theta)$ is a function of both yaw angle ψ and pitch angle θ. Again, using the notation in figures 32 & 33, four functions can be defined:

$$G(\psi,\theta) = \frac{p_3 - p_1}{p_5 - \tfrac{1}{2}(p_3 + p_1)} \quad \text{and} \quad H(\psi,\theta) = \frac{p_4 - p_2}{p_5 - \tfrac{1}{2}(p_4 + p_2)} \qquad \ldots\ldots\ldots (4.3),$$

$$S(\psi,\theta) = \frac{p_5 - p_\infty}{\tfrac{1}{2}\rho Q^2} \quad \text{and} \quad T(\psi,\theta) = \frac{p_5 - \tfrac{1}{4}(p_1 + p_2 + p_3 + p_4)}{\tfrac{1}{2}\rho Q^2} \qquad \ldots\ldots\ldots (4.4).$$

After calibration, measured values of p_1 to p_5 in an unknown flowfield yield G and H and hence ψ and θ. Once the flow angles are known, $T(\psi, \theta)$ can be determined, from which the local flow speed Q follows. The function $S(\psi, \theta)$, together with Q and p_5, then yields the local static pressure p_∞.

The pressures measured by the yawmeter were passed, in addition to the tunnel reference pressures, to a pressure switch. The pressure-switch output was fed to the pressure transducer, from which the output to the voltmeter was sampled in a similar way to the surface pressures. A diagram of the equipment is presented in figure 34.

4.6.4 - Crossed-wire anemometer investigation

A DANTEC type-55P61 crossed-wire (X-wire) probe was used to measure flow velocities and Reynolds stresses in transverse planes around the junction. The probe consists of 2 wires lying in parallel planes separated by a small distance, typically 1 mm, the wires also being arranged at an angle of 90° to each other. The wires were made from platinum-plated tungsten and were of overall length 3 mm and active sensing length and diameter 1.25 mm and 5 μm respectively. This gives a measuring volume slightly less than 1 mm^3.

The probe and holder were supported in the working section in the same way as the yawmeter, the signals from both wires being transmitted via 5-m coaxial cables to a Thermal Systems Inc (*TSI*) series-1050, dual-input, constant-temperature, linearised anemometer. The output from each wire was fed to a *TSI* model 1015C correlator and in addition, an oscilloscope was connected across the anemometer outputs. The correlator output could be switched to pass either the steady-flow or turbulent-fluctuation signal from each wire, in addition to the sum and difference of the fluctuations, to the digital voltmeter. The voltmeter could be programmed to display either type of signal, these being sampled by the PC in turn. A diagram of the experimental arrangement is shown in figure 35.

Chapter 5

Experimental Procedure

5.1 - Introduction

This chapter is concerned with the acquisition of flow data in the junction. The types of measurements made were as follows:

a) flow visualisation,
b) surface pressure measurements,
c) yawmeter measurements around the nose of the junction, &
d) X-wire measurements in the junction corners and trailing-edge cross-plane.

All the experiments were performed at a free stream velocity of 30 m/s and Reynolds number of 1.03×10^6 based on the streamwise chord. The flow visualisation and surface pressure measurements were performed at α = -3°, 0°, +3°, 6° & 9°; the yawmeter and X-wire measurements were made at α = 0° only. For the surface pressure, yawmeter and X-wire measurements, the tunnel was left running for approximately 1½ hours each morning to warm up before any measurements were taken, in order to minimise errors due to ambient temperature drift.

The surface oil-flow experiments revealed that at non-zero incidences, extremely short separation bubbles occurred just aft of the leading edge of the wing. These were due to laminar separation, with subsequent transition to turbulence in the free shear layer and turbulent reattachment. The locations of the bubbles downstream from the leading edge changed with incidence and therefore the positions of the transition strips were changed too in order to fix transition at these positions. At each incidence the transition strips were applied at the distances downstream of the leading edge listed at Appendix C. For each change of position of the transition strips, the minimum diameter of ballotine needed to effect transition also changed, the new values being calculated as in Chapter 4. The

techniques used for all of the above experiments, in addition to probe calibrations and data reduction, are given below.

5.2 - Flow visualisation

Surface oil-flow tests

For the oil-flow tests, a fluorescent paint was made from *Saturn-yellow* powder, paraffin, liquid paraffin and oleic acid in the proportions detailed in Arnott & Jones (1994). The paint was stirred thoroughly and applied using a small foam sponge. This gave a more even coverage than a brush and also avoided the problem of confusing brush marks with streaklines formed by the flow. Any dribbles that occurred due to over-application were soaked up before sealing the tunnel. When applied correctly, the paint was thick enough to allow the tunnel to be sealed before the paint had begun to run under gravitational influence. Immediately after the tunnel hatch was closed, an assistant accelerated the tunnel rapidly to 30 m/s and the flow of the oil was viewed through glass windows in the tunnel walls. Sketches were made of the pattern as it developed and the tunnel was left running until the pattern had dried.

Photography of the streak patterns was carried out inside the tunnel, the camera being tripod mounted and a remote release being used to avoid camera shake. Exposure control was manual, the minimum aperture of the lens being used to obtain maximum depth of field in the picture. Once photography was complete, the pattern was gently rubbed off with a soft cloth and the incidence changed for the next run.

Tuft flow visualisation

The tuft motion was photographed from outside the tunnel using blackout curtains draped over and behind the camera to prevent white light from entering the working section. The positions of the tufts and their orientations with the tunnel off was photographed for comparison with their behaviour during the tests. With the tunnel running, the behaviour of the tufts was photographed from both sides of the junction at the incidences listed above, the tunnel being shut down briefly for each change in incidence, then restarted. Because of the changes in flow behaviour shown by the oil/dye experiments on the $+Z$ side

of the junction, between α = +6° & 9°, additional photographs of the tuft behaviour on that side of the junction were taken in 0.5° steps to observe the growth of a separation region.

5.3 - Voltmeter sampling procedure

The surface pressure, yawmeter and X-wire measurements all involved sampling the readings displayed on the voltmeter and recording a time-averaged result. After each movement of the pressure switches, yawmeter or X-wire, a period of 3 seconds was allowed for the voltmeter reading to settle, before sampling began. The sampling routine took a number n of readings and calculated their average. It then took one more reading and compared the average of (n+1) readings with that of n readings. If the difference between the 2 averages was less than a value specified in the acquisition program, then the average of (n+1) readings was accepted; if not then a further 5 readings were taken and comparison made between (n+5) and (n+6) samples. This process was repeated until the difference fell inside the specified value, set at 5×10^{-5} V, which corresponded to about 1% of the smallest mean voltage measured. Obviously for the majority of readings, this error will be an even smaller percentage.

5.4 - Measurement of surface pressure

At each incidence, the tunnel reference pressures and pressure distributions over the wing and plate were measured, although due to the arrangement of pressure tappings on the wing, it was necessary to measure the wing pressures using a slightly different procedure from that for the plate pressures. However both procedures involved sampling the pressures connected to each port on the pressure switches in rotation, the switches being operated separately. The tunnel reference pressures were connected such that they were measured once every complete rotation of either switch. Also, with each change of incidence, the chordwise positions of the roughness strips on the wing were changed to the positions listed at Appendix C. The surface pressures measured on both the wing and plate were expressed in coefficient form by the equation:

$$C_p = \frac{(p_{tap} - p_{ws})}{(p_{sc} - p_{ws})} \times 0.981 \qquad \ldots\ldots\ldots (5.1).$$

where p_{tap} is the pressure measured at an individual tapping on the model, p_{ws} is the pressure measured on the walls of the working section and p_{sc} is the pressure measured on the walls of the settling chamber. The coefficient 0.981, is a constant based on the contraction ratio of the tunnel. The root-mean square error in C_p due to the resolution of the transducer, was estimated to be $\Delta C_p = \pm 0.003$ (Pentz & Shott, 1988).

5.4.1 - Surface pressures on the wing

The surface pressures over the wing were measured in chordwise rows. Initially, the row furthest from the junction on the upper and lower surfaces of the wing, i.e. at $Y/c = 0.71$, was left uncovered. All other rows of pressure tappings were taped over with narrow strips of *transferseal* (a thin adhesive tape). The pressure tubes from the wing and the tunnel reference pressures were sampled and the pressure switches rotated back to their starting positions. The tunnel was shut down and the next row of tappings on each side of the wing was uncovered. Strips of *transferseal* were placed over the rows of tappings measured previously and the tunnel restarted. Approximately 20 minutes was left before the newly-uncovered rows were measured. This process was repeated at each spanwise station of pressure tappings, enabling the sectional pressure distribution over the wing to be measured as the junction was approached from the mid-span. After the measurements of wing-surface pressure were complete at a particular wing incidence, the pressures on the plate were measured before changing incidence.

5.4.2 - Surface pressures on the plate

Four bundles of tubes from the pressure tappings in the plate and the tunnel reference pressures, were connected to the pressure switches, the tubes on each switch then being sampled in rotation. The tubes were also connected to a multi-tube manometer during sampling as a visual check for pressure leaks. The sampling process meant that the surface pressures on the plate had to be measured in batches, the acquisition program being

paused whilst the next 4 bundles of tubes were connected in their place until all the plate tappings had been sampled. The tunnel was shut down and the wing incidence changed.

5.5 - Coordinate systems used for flowfield measurements

To attempt to follow the path of the horsehoe vortex as it wrapped around the leading edge and passed downstream, flowfield measurements with both yawmeter and X-wire probes were to be made in planes normal to the wing/plate intersection at the junction. For this, in addition to the left-handed coordinate system (X, Y, Z), a second coordinate system was used. This is composed of 4 components defined thus: at various distances X along the chord line from the leading edge, the tangents to the wing profile on both upper and lower surfaces were calculated, normals to these tangents then being drawn on the plate. The angle between each normal and the OX-axis reversed was termed β_s, the distance along each normal from the corner of the junction being labelled x_3. The distance x_3 was always taken as a positive number, the angle β_s denoting which side of the chord line the plane is. The fourth element of this system is Y, the vertical height above the plate. Thus the coordinate system is described by (X, β_s, x_3, Y) and oblique views of the system on both sides of the junction are shown in figure 36, in addition to the (X, Y, Z) system used for measurements with the X-wire at the trailing edge.

5.6 - Using the single-tube yawmeter

5.6.1 - Calibration of the yawmeter

Calibration of the yawmeter was carried out in the empty wind tunnel, at a freestream velocity of 30 m/s. Initially, it was necessary to align the yawmeter with the freestream. In order to do this, the averages of 200 readings of each of p_1 to p_4 were recorded and the ratios p_1/p_3 and p_2/p_4 compared. If these lay within 0.5% of 1.0 then the probe was taken as being aligned with the flow and calibration could begin. Otherwise, small corrections were made to the yawmeter setting angles and the procedure repeated.

The calibration was performed over the pitch-angle range $+25° \geq \theta \geq -25°$, at intervals of 5°. At each pitch angle, the rotary table was yawed through the range $+30° \geq \beta \geq -30°$, at intervals of 4°, thus producing a grid of 11×16 calibration points. The pitch angles of the yawmeter were set using a vernier protractor with a resolution of 5′ of arc, the rotation in yaw being controlled through the PC. During the calibration it was essential that the tip of the yawmeter remained at the same point in the flow. Therefore, after each change in pitch angle, the tip of the yawmeter was repositioned under the axis of rotation of the rotary table by means of the movable saddle on the horizontal slide in figure 22. In addition the traversing gear was used to restore the tip of the yawmeter to the same height above the plate. For this purpose a vernier height gauge, with a resolution of 0.02 mm, was used to measure the elevation of the centre of the probe tip above the false floor. The required correction was then input through the PC. The yawmeter was then realigned with the free stream before yawing the rotary table to $\beta = +30°$ and continuing the calibration at the new value of θ.

At each point in the grid, the pressures p_1 to p_5 were recorded and the functions $G(\psi, \theta)$, $H(\psi, \theta)$, $S(\psi, \theta)$ & $T(\psi, \theta)$ calculated. These were then surface-fitted by the method of least squares to a Chebyshev polynomial:

$$F(\psi,\theta) = \sum_{i=0}^{m}\sum_{j=0}^{n} k_{ij}\, \psi^i \theta^j \qquad \ldots\ldots\ldots (5.2),$$

where $F(\psi, \theta)$ denotes a function whose mean square deviation from the measured data is minimised at all points of the calibration and k_{ij} gives the calibration constants which fit the observed data most closely. A sixth order polynomial, *i.e.* $m = n = 6$ was found to be satisfactory. The maximum deviations of the fit from the measured data, over the whole grid of points, were 0.75° in pitch and 0.45° in yaw.

5.6.2 - Flowfield measurements with the yawmeter

At distances along the chord line of $X = 0.5$, 1, 2.5, 10 & 40 mm from the leading edge of the junction, lines were marked out on the plate normal (± 0.5°) to the tangents to the

local profile of the upper and lower surfaces of the wing as shown in figure 37. For ease of reference, the normal planes are referred to in the text by the letters *A* to *J*, planes *A* to *E* being on the -*Z* side of the junction and planes *F* to *J* being on the +*Z* side. The labelling of each normal, along with its angle β_s between it and the O*X*-axis reversed, is shown in figure 37. The relationships between each plane, its distance from the leading edge and angle β_s are also detailed at Appendix *D*. Along each normal points were marked out at distances x_3, from the local wing surface as shown in figure 37. Traverses with the yawmeter were made at these points, in the *Y*-direction normal to the plate. It should be noted that because the traverses are normal to the plate and the wing is swept forward, the position of the probe relative to the leading edge of the wing changes during a traverse — it effectively moves a distance *Y*tan28° downstream.

It was necessary to pitch the yawmeter at an angle of -3° so that measurements could be made near the plate. However, with the probe tip under the axis of the rotary table, the tip of the yawmeter could not be positioned close to the corner of the junction, the wing thickness and sweep angle producing an overhang which obstructed the vertical stem attached to the traversing gear. Since it was necessary to maintain the tip of the yawmeter on the axis of the table only during calibration, the yawmeter was moved as far forwards on the horizontal sting as possible.

It was expected that the profiles of the flow angles through the boundary layer would show significant changes through the range of values of x_3 at which traverses were made. As this 3-D flowfield was unknown, the first traverse in each plane was performed at the station furthest from the junction at x_3 = 80 mm. At this distance from the corner it was expected that the yaw and pitch angles were likely to be close to the freestream direction and exhibit the least change over the traverse. The next traverse was made at x_3 = 60 mm and so on until all the traverses in a plane had been completed. This procedure enabled any trends in the profiles, as the junction was approached, to be followed and an allowance for this made in the next traverse by yawing the probe by a suitable amount before it commenced. Thus any changes to the probe setting angle during a traverse were greatly minimised.

A full traverse was from $2 \leq Y/\text{mm} \leq 40$, although complete traverses could not be obtained close to the corner, as the probe came into contact with the wing at higher values of Y. The probe tip was set at $Y = 2$ mm above the floor with the aid of the vernier height gauge. To ensure that body weight did not distort the configuration during this process, care was taken that only the false floor was lain upon and not the turntable itself above which the probe height was being set, the turntable being supported independantly from the false floor. The air was then accelerated to 30 m/s. Aerodynamic drag on the probe support meant that the probe tip was displaced downstream slightly, off the measuring station. To compensate for this, the probe tip was brought back above the measuring station, whilst the air was moving at 30 m/s, with the aid of a roof-mounted telescope. This was always carried out, whilst the probe was at $Y = 2$ mm to minimise any parallax error, before the start of each traverse.

At each point in a traverse, the tunnel reference pressures were recorded, then the yawmeter pressures p_1 to p_5. The values G & H were calculated from equation (4.3) to check that the flow pitch and yaw angles relative to the probe were inside the calibration grid. If not, then the probe setting angles were changed and the process repeated. If so, the probe settings, pressures p_1 to p_5 and free stream velocity were written to a data file. As far as possible the relative pitch and yaw angles were kept within ±20°. However near the leading-edge corner, it was necessary to use the whole calibration grid as the pitch angles of the flow became large. The probe was moved in the $+Y$ direction to the next point in the traverse and the process of pressure measurement repeated for the remainder of the traverse.

On completion of the traverse, the probe was moved back down to $Y = 2$ mm by reversing the stepper motor for the number of steps moved during the traverse and positioned over the next station on the floor to commence another traverse. This was repeated for the traverses performed during a day, the number of which varied. To use the height gauge to reset the probe to $Y = 2$ mm after each traverse would have involved continual starting and stopping of the tunnel. Instead, since the false floor and turntable had been levelled, the plate and the translations of the probe in the XZ plane were taken as being parallel. The

height gauge was used at the end of each day's experiments to confirm the height of the yawmeter. Any errors were found to be negligible.

5.6.3 - Data reduction of the yawmeter measurements

Using the pressures p_1 to p_5 and the calibration coefficients for G, H, S & T, the flow angles, velocity magnitude and static pressure were calculated at each point in the traverses. The values of G and H calculated from equation (4.3) were inserted into equation (5.2) to give 2 equations in θ and ψ relative to the yawmeter, which were solved by Newton-Raphson iteration. Using these angles the functions T and S were calculated which, after insertion into equation (4.3), yielded Q and p_∞ respectively. The velocity vectors were then transformed into the wind tunnel coordinate frame and the static pressures and velocity vectors were non-dimensionalised using equation (5.1) and free stream velocity respectively.

As G, H, S & T are derived from the pressures p_1 to p_5, in addition to the uncertainties in the flow pitch and yaw angles from the calibration, the resolution of the pressure transducer will have some bearing on the results. However the uncertainties in p_1 to p_5 will have been "built-in" to the calibration itself, although to what extent it is uncertain. Numerical experiments on the raw results, including the uncertainties in p_1 to p_5 in the calculation of G & H, yielded differences in their values which were approximately equal to the maximum residuals from the polynomial surface fit. These new values were put through the analysis program which yielded the flow pitch and yaw angles, indicating that the additional, most-probable *rms* errors in the flow angles were ±0.3° in pitch and ±0.4° in yaw. At a few values of x_3 however, near the plate at Y = 2 mm, the peak errors in the flow angles were as much as ±1.5°. At those particular stations the numerators and denominators in the calculations of G & H were approximately equal, thus the effect of incorporating the errors in pressure was greater than at other stations.

How these errors relate to the deviations from the calibration fit is uncertain. Further numerical experiments were performed to examine the knock-on effect on the values of local static pressure and velocity. For these calculations, the ±1.5° error in flow angles

noted above was added to the largest deviations from the calibration for G & H. These new flow angles were put through the analysis program for S & T, along with the incorporation of the uncertainties in p_1 to p_5 to give a conservative estimate for the errors in the values of local static pressure and velocity. These gave errors in the local static pressure coefficient and mean velocity of up to $\Delta C_p = \pm 0.04$ and $\Delta Q = \pm 0.02 U_\infty$ respectively.

5.7 - Using the X-wire anemometer

Before an X-wire probe was used, it was examined under a *Shadomaster* microscope to ensure that the wires were straight and intact. If a wire were kinked or bow-shaped, the probe was sent away for repair, since the wire would not then be at the 45°-angle required by the data reduction theory. The response equations were derived using the assumptions outlined by Mojola (1972) although, instead of Mojola's constant power law, the calibration law due to Siddall and Davies (1972) was used,

$$E^2 = \mathrm{A} + \mathrm{B}\sqrt{q_{eff}} + \mathrm{C}q_{eff} \qquad \ldots\ldots\ldots (5.3),$$

where E is the output voltage, q_{eff} is the effective cooling velocity and A, B & C are constants corresponding to a least-squares curve fit to the calibration data over the whole speed range. The response equations used to process the results into the mean-flow velocity components and Reynolds stresses were those derived by Johnston (1986).

Taking voltage measurements with the wires aligned firstly in vertical planes, the 0° position in figure 38(a), then rotated through 90° (figure 38(c)), gives rise to the local cartesian coordinate system shown in figure 39(a), with Ox_p being aligned with the probe axis, Oy_p in the "plane" containing the wires and Oz_p normal to the $Ox_p y_p$ plane. In this frame the mean velocities and 5 of the 6 correlations for the velocity fluctuations relative to the probe axes can be calculated, the missing component being $\overline{v_p w_p}$ (where the overbar denotes time-mean average). The term velocity correlation is used here, as strictly the term Reynolds stress involves multiplying by $-\rho$, where ρ is the density of the fluid

(Schlicting, 1979). However to transform these quantities into wind tunnel, or *body-fixed* axes, all the components of the velocity-correlation matrix/Reynolds stress tensor are needed. If additional voltage measurements are taken with the probe rotated to 45° and 135° positions, as in figures 38(b) & (d) respectively, then this gives rise to a second, cartesian frame at 45° to the frame aligned with the 0°-, 90°-probe positions (see figure 39(b)). In the 45°, 135°-frame, the axis Ox'_p is along the probe axis and is identical to Ox_p; Oy'_p is aligned with the "plane" containing the wires and Oz'_p is normal to the $Ox'_p\, y'_p$ plane. Here the missing component from the velocity-correlation matrix is $\overline{v'_p w'_p}$. The matrix components in either of the frames can be transformed through the angle of rotation of the probe about its axis so that they are expressed in terms of the measured components in the other, as detailed at Appendix D. This allows the missing $\overline{v_p w_p}$ or $\overline{v'_p w'_p}$ component in the respective axis frames to be calculated to complete either tensor, though with some duplication of terms. This redundancy is described later.

5.7.1- Calibration of the X-wire probe

Calibration of the X-wire anemometer was carried out in the free stream of the working section, well upstream of the model, at the start of each day's measurements. The probe was fixed with its axis parallel to the free stream and the wires aligned in vertical planes (the 0°-position in figure 38). Calibration was carried out over the approximate wind speed range 15 to 33 m/s. At each set wind speed, the steady components of the output voltage from both wires were recorded, the time-averaging procedure described in Section 5.3 being used. The probe was rotated through 90° about its axis, the time-mean voltages for both wires recorded again and the probe rotated back to the 0° position. The air speed was then increased to the next value and the procedure repeated. At the end of each calibration run, curves of the form of equation (5.3) were fitted for each wire, at both rotational positions, by the method of least squares. The calibration constants for each wire at both rotational positions were thus obtained and written to file. Typical values of A, B & C for the 2 wires at the 0°- & 90°-positions are given below:

Table 1 - Example values of the calibration constants for the X-wire probe

	Wire 1 at 0°	Wire 2 at 0°	Wire 1 at 90°	Wire 2 at 90°
A	3.8012	3.7675	3.6392	3.7327
B	2.9466	2.8739	3.0392	2.8703
C	-0.1815	-0.1826	-0.1926	-0.1817

The calibration constants for wires 1 & 2 at the 0°- & 90°-rotations were also used for wires 1 & 2 at the 45°- & 135°-rotations respectively.

5.7.2 - Measurements in the plate boundary layer upstream of the junction

In order that data from this investigation may be compared with future CFD simulations around the junction, for the purpose of code validation, it is important that the conditions in the approaching "fuselage" boundary layer are known. To this end, a traverse normal to the surface of the plate was made with the X-wire anemometer, upstream of the junction and to the side of the centreline, at (X, Z)/mm = (-500, -120). This traverse also gave a check of the data acquisition and analysis programs as the results were compared with reference data for 2-dimensional, turbulent boundary layers. The plate boundary layer at X = -500 mm was expected to be 2-dimensional. Therefore the probe was aligned parallel with the centreline of the tunnel and pitched down at -3° so that measurements could be taken close to the floor, measurements being taken between $3 \leq Y/\text{mm} \leq 40$. The height of the X-wire above the turntable was set in the same way as for the yawmeter, the crossing point of the wires being used as the reference point for the height of the probe. The traverse was performed using the probe at its 0°, 90° rotations only.

With the X-wire probe set at Y = 3 mm and the wires aligned in the 0° position, the steady and fluctuating components for each wire, along with both the sum and difference of the fluctuations, were sampled using the time-averaging procedure detailed in Section 5.3. The probe was then rotated to the 90°-position and the data sampling repeated. Once sampling at this height had been completed, the probe was then moved up to the next measuring station. The raw data were analysed using the calibration for that day and the

wire-response equations, with a program which calculated the mean velocities U, V & W and 5 of the 6 correlations for the fluctuating components of velocity.

Using the notation in figure 39(a), 2 values each of $\overline{U_p}$ and $\overline{u_p^2}$, respectively the mean, steady velocity and mean-square fluctuation along the axis of the probe, were obtained from the measurements at each probe position. To smooth out any differences, the pairs of values were averaged, these averages being substituted for $\overline{U_p}$ and $\overline{u_p^2}$ in the mean-velocity matrix and velocity-correlation matrix respectively. As slight differences between the 2 values of each component were present, the root-mean-squares (*rms*) of the deviations from the averages were calculated at each station. This was also done for later measurements of $\overline{U_p}$ & $\overline{u_p^2}$ in the streamwise corners and at the trailing edge. The *rms* deviations from the local values of $\overline{U_p}$ & $\overline{u_p^2}$ were approximately ±1% & ±6% respectively.

5.7.3 - Mean velocity and turbulence measurements in the streamwise corners and at the trailing edge

Measurements with the X-wire probe were carried out at the positions on the plate shown in figure 40. At X = 300 mm, these are defined by the coordinates (β_s, x_3, Y) as for the yawmeter measurements. The normal on the -Z side of the junction was labelled plane K, that on the +Z side labelled plane L. At the trailing edge, X = 500 mm, stations were marked out parallel with the Z-axis. Again, at each station, measurements were made in vertical traverses from Y = 3 mm to Y = 40 mm, the coordinate system (X, Y, Z) being used to describe the probe position. The reader is referred to the oblique view of the two coordinate systems in figure 36.

The analysis of the turbulence quantities assumed that the probe was aligned with the local flow direction, which changed during a traverse. However, the probe pitch angle was fixed at -3° so that measurements could be taken close to the floor. Thus, only the probe yaw angle could be changed during a traverse. It was therefore necessary to investigate the changes in flow yaw angle with increasing height Y above the plate. Traverses to

discover these changes were carried out with the X-wire probe aligned with the OX-axis, the yaw angles obtained after data reduction were used to align the probe with the local flow direction during the actual measurements of mean flow velocities and turbulence quantities.

Measurements of mean flow and turbulence quantities were made with the probe kept pitched down at -3°. To ensure that the probe tip remained over the same point on the plate whilst it was being yawed, the probe tip was brought under the axis of the rotary table. Starting at Y = 3 mm, the probe was aligned in yaw with the local flow. With the wires at the 0° position, the steady and fluctuating voltage components for each wire and both the sum and difference of the fluctuating components were measured as described before. The same readings were taken with the probe rotated through 45°, 90° & 135° about its axis. The probe was then rotated back to the 0° position and the data acquisition process repeated at all other points in a traverse, the yaw angle of the probe being changed so that it remained aligned with the local flow direction. This was repeated for each traverse station, a typical traverse of this sort taking approximately 70 minutes. Up to 3 traverses per day were performed immediately after calibration, the remainder of the day being used for analysis of the day's results. Frequent cleaning of the wires helped to minimise drift due to surface contamination.

5.7.4 - Reduction of X-wire data in the streamwise corners and at the trailing edge

Analysis of the data obtained at each point was carried out with a program which was an extension of that for the analysis of the boundary layer upstream of the model.

Mean velocities

It is convenient here to set out the matrices of mean velocities that exist for the 2 axes frames. With reference to figure 39, these are defined as follows:

$$\text{for the 0°-, 90°- axes frame, } \boldsymbol{U}_{\mathbf{p}} = \begin{bmatrix} \overline{U_p} \\ \overline{V_p} \\ \overline{W_p} \end{bmatrix}$$

and for the 45°-, 135°- axes frame, $\boldsymbol{U}'_{\mathrm{p}} = \begin{bmatrix} \overline{U'_{\mathrm{p}}} \\ \overline{V'_{\mathrm{p}}} \\ \overline{W'_{\mathrm{p}}} \end{bmatrix}$ ..... (5.4)

As for the measurements in the approaching boundary layer, 2 values of $\overline{U_{\mathrm{p}}}$ were obtained for the 0°-, 90°-axes frame. Additionally, 2 values of $\overline{U'_{\mathrm{p}}}$ were obtained for the 45°-, 135° -axes frame. As $\overline{U_{\mathrm{p}}}$ & $\overline{U'_{\mathrm{p}}}$ represent the same quantity, *i.e.* the mean velocity along the axis of the probe, the 4 values were averaged together, with an rms deviation from the local averages of ±0.2 m/s (1%). The mean-velocity $\overline{V'_{p}}$ was transformed into the 0°, 90°-frame and averaged with $\overline{V_{p}}$, the rms deviation from which was ±0.4 m/s. Likewise, $\overline{W'_{\mathrm{p}}}$ was transformed and averaged with $\overline{W_{\mathrm{p}}}$, the rms deviations from which was ±0.2 m/s.

Actual values are quoted for the cross-flows instead of percentages, as the probe was deliberately aligned to make $\overline{W_{\mathrm{p}}}$ small. As such, at some stations, the deviations from the averages are similar to the actual values of the velocity components. Therefore to quote a percentage difference would give misleadingly large values.

The resulting mean-velocity vectors, were transformed through the probe setting angles to give $\overline{U}$, $\overline{V}$ & $\overline{W}$ as described at Appendix E. The deviations from the velocity averages mentioned above are not strictly the errors in $\overline{U}$, $\overline{V}$ & $\overline{W}$ as the uncertainties in the setting angles due to the resolution of the rotary table/vernier protractor, although small, will have some bearing through the transformations. Therefore to obtain final estimates for the errors in the mean velocities, sample calculations to account for this were performed. These indicated that the rms errors in $\overline{U}$, $\overline{V}$ & $\overline{W}$ were:

Table 2 - Rms errors in the mean velocities obtained from the X-wire probe

Rms error in $\overline{U}$	Rms error in $\overline{V}$	Rms error in $\overline{W}$
±0.33 m/s ($0.01U_{\infty}$)	±0.35 m/s ($0.012U_{\infty}$)	±0.25 m/s ($0.008U_{\infty}$)

The error in the measurement of the freestream velocity U_∞ is ±0.03 m/s ($0.1\%U_\infty$) and may be neglected in comparison with the errors in $\overline{U}$, $\overline{V}$ & $\overline{W}$.

Mean flow angles

The mean flow angles θ and ψ relative to wind-tunnel axes, at the X-wire measurement stations, are calculated from $\overline{U}$, $\overline{V}$ & $\overline{W}$: $\theta = \tan^{-1}\left(\overline{V}/\overline{U}\right)$ and $\psi = \tan^{-1}\left(\overline{W}/\overline{U}\right)$. As such the errors in θ and ψ can be obtained from the errors in Table 2. The rms error in θ is estimated at ±0.8°, with a maximum of approximately ±1.5°. For ψ, the rms error is ±0.6°, with a maximum of ±1°.

Correlations of the velocity fluctuations

For each axes frame, a matrix of velocity correlations exists and they are defined thus:

$$\text{for the 0°-, 90°-axes frame, } \boldsymbol{u_p} = \begin{bmatrix} \overline{u_p^2} & \overline{u_p v_p} & \overline{u_p w_p} \\ \overline{v_p u_p} & \overline{v_p^2} & \overline{v_p w_p} \\ \overline{w_p u_p} & \overline{w_p v_p} & \overline{w_p^2} \end{bmatrix}$$

$$\text{and for the 45°-, 135°-axes frame, } \boldsymbol{u'_p} = \begin{bmatrix} \overline{u_p'^2} & \overline{u_p' v_p'} & \overline{u_p' w_p'} \\ \overline{v_p' u_p'} & \overline{v_p'^2} & \overline{v_p' w_p'} \\ \overline{w_p' u_p'} & \overline{w_p' v_p'} & \overline{w_p'^2} \end{bmatrix} \quad \ldots\ldots\ldots (5.5).$$

The analysis program calculated the missing component $\overline{v_p' w_p'} = \overline{w_p' v_p'}$ in $\boldsymbol{u'_p}$, from the known components in $\boldsymbol{u_p}$, as shown at Appendix E. This allowed $\boldsymbol{u'_p}$ to be completed, the matrix being transformed through 45° to give a complete second matrix in the 0°, 90°-frame, labelled $\boldsymbol{u_p}^*$. As the incomplete matrix $\boldsymbol{u_p}$ already existed in the 0°, 90°-frame, this transformation duplicated most of the terms in $\boldsymbol{u_p}$. Similar to the mean velocity components, the duplicated terms were averaged, however $\overline{v_p w_p}$ was simply set equal to $\overline{v_p w_p}^*$. This created a complete third matrix $\boldsymbol{u_p}^\dagger$ in the 0°, 90°-frame, containing the averaged values as shown at Appendix E. The rms deviations of individual components in $\boldsymbol{u_p}$ and $\boldsymbol{u_p}^*$ from their corresponding local averages were as follows:

Table 3 - Rms deviations from the averages of components in u_p and u_p^*

Rms deviation from average of $\overline{u_p^2}$ & $\overline{u_p^2}^*$	Rms deviation from average of $\overline{v_p^2}$ & $\overline{v_p^2}^*$	Rms deviation from average of $\overline{w_p^2}$ & $\overline{w_p^2}^*$	Rms deviation from average of $\overline{u_p v_p}$ & $\overline{u_p v_p}^*$	Rms deviation from average of $\overline{u_p w_p}$ & $\overline{u_p w_p}^*$
± 0.3 m^2/s^2	± 0.15 m^2/s^2	± 0.15 m^2/s^2	± 0.3 m^2/s^2	± 0.2 m^2/s^2

Where $\overline{v_p w_p}$ is concerned an estimate of the uncertainty may be made from the uncertainties in $\overline{v_p^2}$ and $\overline{w_p^2}$, through the relationship used to calculate $\overline{v_p' w_p'}$:

$$\overline{v_p' w_p'} = 0.5\left(\overline{w_p^2} - \overline{v_p^2}\right) \qquad \ldots\ldots\ldots (5.6).$$

If the rms deviations in $\overline{v_p^2}$ and $\overline{w_p^2}$, are each ± 0.15 m^2/s^2 then these combine[1] to produce an rms deviation in $\overline{v_p' w_p'}$ and hence $\overline{v_p w_p}$ of ± 0.11 m^2/s^2.

Again it seems more appropriate to use dimensional deviations, not percentages, as the velocity correlations tend to zero far from the plate and the fractional errors become extremely large. Perhaps a better way of putting these deviations into context with the results would be to non-dimensionalise them by U_∞^2, the square of the freestream velocity.

Thus using the probe at 4 rotational positions enabled a complete velocity-correlation matrix relative to the probe to be calculated. This matrix $u_p^\dagger$ was transformed through the probe setting angles to give the velocity correlations $\overline{u^2}$, $\overline{v^2}$, $\overline{w^2}$, $\overline{uv}$, $\overline{uw}$ & $\overline{vw}$ referred to wind tunnel axes. As the velocity-correlation matrices u_p and u_p^* were in the same frame, it is possible to gauge the uncertainties in the velocity correlations from the differences between equivalent components. Non-dimensionalising by the square of the

[1] $\Delta \overline{v_p' w_p'} = \sqrt{\left(0.5\,\Delta \overline{v_p^2}\right)^2 + \left(0.5\,\Delta \overline{w_p^2}\right)^2}$, from Pentz & Shott (1988).

freestream velocity, the rms uncertainties in the velocity correlations are estimated at:

Table 4 - Rms uncertainties in the correlations of the velocity fluctuations relative to the wind-tunnel axes system

Uncertainty in $\overline{u^2}/U_\infty^2$	Uncertainty in $\overline{v^2}/U_\infty^2$	Uncertainty in $\overline{w^2}/U_\infty^2$	Uncertainty in $\overline{uv}/U_\infty^2$	Uncertainty in $\overline{uw}/U_\infty^2$	Uncertainty in $\overline{vw}/U_\infty^2$
±0.0003	±0.0002	±0.0002	±0.0003	±0.0002	±0.0001

The analysis was performed for each point in a traverse and complete descriptions of the matrix and tensor transformations are given at Appendix E.

5.8 - Presentation of results

The photographs from the flow visualisation tests, data from the measurements of surface pressures and flowfield measurements with the yawmeter and X-wire are discussed in the next chapter.

Chapter 6

Results and Discussion

It is convenient to discuss the surface flow visualisations, surface pressure measurements, yawmeter and X-wire measurements separately, examining the data for each incidence in turn.

6.1 - Conditions in the plate boundary layer upstream of the junction

The results obtained from the traverse through the plate boundary layer, upstream of the junction, at (X, Z)/mm = (-500, -120) are presented in figures 41(a) to (d). The variation of $\overline{U}$, $\overline{V}$ & $\overline{W}$ through the boundary layer is shown in figure 41(a). The thickness of the boundary layer at this distance upstream can be seen to be approximately 16 mm. The values of the cross-stream velocities $\overline{V}$ & $\overline{W}$ stay almost constant with height Y above the plate and are at most, 2% of the velocity $\overline{U}$ in the freestream direction. The pitch and yaw angles of the flow have been calculated from $\overline{V}$ & $\overline{W}$ for each value of Y and are shown in figure 41(b). The pitch angle θ stays approximately constant through the boundary layer at +1°, the yaw angle ψ varies very slightly with Y from approximately -1° at Y = 3 mm, to near zero for Y > 20 mm. It is possible that, even this far upstream, the junction may still have a slight effect on the yaw angle through the boundary layer. However, since the accuracy obtainable with a X-wire anemometer is of the order of 1°, they are felt to be small enough to be acceptable.

Here, as $\overline{V}$ & $\overline{W}$ are small compared to U, it is probable that the velocity profile for U will be of the form of the well-established "law-of-the-wall":

$$\frac{\overline{U}}{u_\tau} = 5.75 \log\left(\frac{u_\tau Y}{\nu}\right) + 5.5 \qquad \ldots\ldots\ldots (6.1).$$

This would allow the skin-friction coefficient C_f on the plate, to be estimated using a Clauser plot (Clauser, 1956). Indeed plotting measured values of $\overline{U}/U_\infty$ against $\log\left(\frac{U_\infty Y}{\nu}\right)$ at this station in figure 42, it seems possible to fit a straight line through the experimental points nearest $\left(\frac{U_\infty Y}{\nu}\right) = 10000$ with little deviation to either side. Multiplying both sides of equation (6.1) by u_τ/U_∞, where u_τ is the friction velocity ($u_\tau = \sqrt{\tau_w/\rho}$), we get:

$$\frac{\overline{U}}{U_\infty} = 5.75\,\frac{u_\tau}{U_\infty}\log\left(\frac{U_\infty Y}{\nu}\right) + 5.5\,\frac{u_\tau}{U_\infty} - 5.75\,\frac{u_\tau}{U_\infty}\log\left(\frac{U_\infty}{u_\tau}\right) \quad \ldots\ldots\ldots (6.2).$$

Thus a family of curves of $\overline{U}/U_\infty$ can be plotted against $\log\left(\frac{U_\infty Y}{\nu}\right)$ for various values of u_τ/U_∞, enabling a straight line to be fitted to the measured data over the inner-region of the boundary layer as explained by Young (1989).

However as can be seen from figure 42, a suitable value of u_τ could not be found such that the data on the straight line region could be fitted by equation (6.2). This lead to doubt over the initial position of the probe relative to the plate. As explained in Chapter 5, any small displacement downstream of a probe tip, off the stations marked on the plate at the working speed, was corrected for with the help of a roof-mounted telescope. However if there had been any small change in height Y of the probe tip also, this could not be discerned due to the restricted optical access into the working section. In order to fit the measured profile for $\overline{U}$ to the log-law, a small correction Y_o to the probe height was introduced (Bernstein & Hamid, 1995 & 96), such that:

$$\frac{\overline{U}}{u_\tau} = 5.75\log\left(\frac{u_\tau\left(Y - Y_o\right)}{\nu}\right) + 5.5 \quad \ldots\ldots\ldots (6.3).$$

The value of Y_o was found by a iteration for a least-squares fit to the measured data over the approximate range, $30 \leq \left(\frac{u_\tau (Y - Y_o)}{\nu}\right) \leq 350$. This range of validity shifts according to effects of any external pressure gradients and different researchers quote slightly different values, however the values here are accepted by many, *e.g.* Young (1989) and White (1991). As Y_o was changed, so did u_τ, therefore Y_o was chosen to minimise the sum of the squares of the differences between the straight-line fit and the measured data over the range above. This fit to the measured profile is shown in figure 43, the value of Y_o being 1.31 mm. However the fit only encompasses 3 data points. Including a fourth point took the fit considerably outside the above range and reduced its quality, although the value of u_τ obtained by regression analysis was found to be rather insensitive to the value of Y_o.

Using the correction Y_o = 1.31 mm, the boundary layer displacement thickness δ^*, momentum thickness θ and shape parameter H were calculated to be: δ^* = 2.66 mm, θ = 1.44 mm & H = 1.85. The value of the coefficient of skin friction at this station upstream was calculated from:

$$C_f = \frac{\tau_w}{\frac{1}{2}\rho U_\infty^2} = \frac{2u_\tau^2}{U_\infty^2} \qquad \ldots\ldots\ldots (6.4)$$

and was found to be $C_f = 0.0027$.

The time-averaged turbulence quantities are shown in figure 41(c) & (d). Figure 41(c) confirms the rms turbulence level $\sqrt{\overline{q^2}} = \sqrt{\overline{u^2} + \overline{v^2} + \overline{w^2}}$ in the freestream at $1.2\%U_\infty$ and the profiles of $\overline{u^2}, \overline{v^2}$ & $\overline{w^2}$ across a boundary layer were compared with figure 21.15 in Tritton (1988), based on data obtained by Klebanoff (1955). A good agreement was found between both sets of data, showing that a 2-D turbulent boundary layer exists upstream of the junction. The variations in the velocity correlations $\overline{uv}$ & $\overline{uw}$, non-dimensionalised by U_∞^2, are shown in figure 41(d) (the $\overline{vw}$ component is absent from

figure 41(d) as explained in Section 5.72). Again the values are comparable with those obtained by previous researchers. The profile for $\overline{vw}$ will be similar to that for $\overline{uw}$.

The profile for $\overline{uv}$ in figure 41(d) affords a useful "second opinion" on the value of the skin-friction coefficient C_f obtained from the Clauser plot in figure 43. Dividing C_f by 2 gives $u_\tau^2/U_\infty^2 = 0.00135$. Bearing in mind that very close to the wall, the turbulence stresses reduce whilst laminar shear increases to keep their sum constant, this value of u_τ^2/U_∞^2 is a plausible extrapolation to the wall of the non-dimensionalised Reynolds shear stress – $\overline{uv}/U_\infty^2$.

6.2 - Flow visualisation results

Plate 1 shows the orientation of the tufts on both sides of the junction at zero wind speed. The spacing between the attachment points of the tufts on the plate is 25 mm in the X- and Z-directions and on the wing, 25 mm along the chord line and along parallels to the leading edge. At each incidence, the behaviour of the tufts at the working speed of 30 m/s was compared with plate 1.

6.2.1 - Wing incidence = -3°

The oil-flow patterns on the lower and upper surfaces of the wing are shown in plates 2(a) and (b) respectively. The lower surface of the wing exhibits spanwise flow into the junction over the rear half of the chord. This appears to flow onto the plate near the trailing edge, however no other unusual flow behaviour is evident. The paint streaks over the upper surface start to turn into the junction at about $x/c = 0.7$ (aft of the crest of the upper surface). At $x/c = 0.9$ (line **A**), the streaklines have turned more or less parallel to the trailing edge to flow into the junction, leaving virtually no streaking of the paint between line **A** and the trailing edge. As the pattern developed, the paint was seen to collect along line **A**, indicating a line of low shear stress, then run off under the influence of gravity. It is likely that in the adverse pressure gradient that exists there the flow separates from the upper surface at line **A**.

However it is also possible that as the flow loses momentum as it approaches line **A**. gravity has influenced the path of the streaklines. Also, an adverse pressure gradient exists over the rear of the lower surface and it was suspected that the streaklines there had also been influenced by gravity. Therefore plates 2(a) & (b) were compared with the tuft behaviour at 30 m/s (plate 2(e)) and with the wind off (plate 1). On the lower surface, slight differences exist between the tuft orientations at speed and the gradients of the paint streaks. However on the upper surface, the tufts between the leading edge and $x/c = 0.85$ lie aligned with the free stream and only those tufts aft of $x/c = 0.85$ indicate spanwise flow into the junction. From these comparisons, it may be concluded that gravity has influenced the flow of paint on both surfaces, more so on the upper than the lower. However the tufts have shown that the spanwise flow on the upper surface between about $x/c = 0.85/0.9$ and the trailing edge is genuine, albeit of low shear.

Plate 2(c) shows a close-up of the flow around the leading edge. On the plate, a saddle point can be seen at point **B**, although no accumulation of pigment appears to have built up around it or the associated limiting streakline around the leading edge. The separation region between **B** and the corner is unexpectedly small, the stand-off distance of the saddle point being approximately 25 mm ($0.05c$). In addition the alternate light and dark, crescent-shaped regions around the leading edge, indicative of the strong shearing motions produced by a horseshoe-vortex system, are unexpectedly absent. Streaks of paint can be seen in the separation region downstream of the saddle point. However due to the small size of the separation region, it is difficult to resolve any pattern between the saddle point and leading edge. The oil streaks on the plate between the corner of the junction and the separation line become indistinguishable from those outside the separated region at approximately $X/c = 0.1$. The tufts on the plate did not show any oscillatory motion near the leading edge of the junction, merely indicating instead the skewing of the plate boundary layer.

In plate 2(b) & (d), the streaklines on the plate can be seen to curve in to meet the streamwise corner between $X/c = 0.6$ & 0.7, slightly upstream of point **C**. The pattern in this region is quite dark, indicating that the shear stresses in the corner flow there are strong. This is likely to be caused by the high suction pressures produced at the crest of

the upper-surface wing profile accelerating the plate boundary layer and skewing it into the corner. Immediately downstream of this region however, the slope of the junction contour becomes negative, producing an adverse pressure gradient towards the trailing edge. The level of shear in the corner undoubtedly reduces as the trailing edge is approached from $X/c = 0.7$ and a line of paint can be seen emanating from the corner at point **C** in plate 2(d). At first sight this would obviously seem like a separation line, indicating that a small pocket of separated flow exists at the trailing-edge. However. interpretation of the pattern is complicated by the paint running off the wing down line **A** meeting the junction at point **C**. This paint has produced streaks on the plate, from the junction, which confuse any underlying pattern. It is believed however, that the flow does separate from the corner between point **C** and the trailing edge, although the exact path of the line of separation seems to be mixed with, or even overwritten by the streaks from paint that has run off the wing. Supporting evidence for this separation is given by the mottled pattern at **D** in plate 2(d) and the oscillatory behaviour of 2 tufts on the upper surface in plate 2(e(ii)), one row up from the plate at $x/c = 0.9$ & 0.95. The 2 streaklines on the plate diverging from the trailing edge in plate 2(d) show the imprint of the wake on the plate.

6.2.2 - Wing incidence = 0°

Plate 3(a) shows the junction viewed from the $-Z$ side at $\alpha = 0°$. Spanwise flow over the rear of the lower surface is still evident, although it is less marked than that at $\alpha = -3°$. The pattern on the $+Z$ side of the junction in plate 3(b) also displays similarities to that at $\alpha = -3°$, although the line **E** of low shear on the wing has moved forwards slightly to $x/c \approx 0.85$. Comparison of the streak photographs with the tuft photographs in plates 3(e(i) & (ii)) however shows that, as at $\alpha = -3°$, the flow of paint over both surfaces of the wing has been affected by gravity. The streaks on the upper surface turn to flow parallel to the trailing edge upstream of line **E**, whereas the tufts in plate 3(e(ii)) show that the upstream boundary of the spanwise flow is coincidental with line **E**.

Plate 3(c) shows a close up of the leading edge of the junction, revealing that the flow approaches the wing at an angle from the $-Z$ side of the junction because of the camber of

the wing. The distance between the saddle point **F** and the junction has reduced to 20 mm, although the root loading has undoubtedly increased. Detail in the separation region is still indistinct and there is no indication of the horseshoe vortex but a flow structure similar to that at $\alpha = -3°$ probably exists.

Moving from the leading edge into the $+Z$ (suction) side of the junction in plate 3(b), the streaklines on the plate curve in towards the corner of the junction, meeting the wing at approximately $X/c = 0.6$. A close up of the trailing edge region in plate 3(d) shows that further downstream towards the trailing edge however, the flow appears to separate from the streamwise corner at point **G**, at about $X/c = 0.80$. Slightly downstream of **G**, paint from line **E** runs off the wing into the junction and joins the separation line from **G**. In the trailing-edge corner, at point **H**, no distinct pattern can be discerned and the paint streaks on the plate downstream of **H** meander slightly, indicating that the boundary between the wake and flow from the $+Z$ side of the junction is unsteady. Also in plate 3(d), a narrow, dark stripe can be seen on the plate at the boundary between the wing wake and the flow in the $-Z$ side of the junction, indicating high shear along the boundary. The tufts closest to the trailing-edge corner show more movement at $\alpha = 0°$ than at $\alpha = -3°$, indicating that the separation from this region is slightly more severe at $\alpha = 0°$.

6.2.3 - Wing incidence = +3°

At $\alpha = +3°$, some of the trends noticed from $\alpha = -3°$ to 0° incidence are continued, most noticeably the forward movement of the line of low shear on the upper surface of the wing. In addition the degree of spanwise flow over the lower surface in plate 4(a) has reduced from that at $\alpha = 0°$, though there is still a difference between the gradient of the streaks and the tuft orientations in plate 4(e(i)). On the upper surface of the wing (plate 4(b)) the line of low shear **I** has moved upstream to $x/c \approx 0.8$. As the tufts in plate 4(e(ii)) indicate spanwise flow between line **I** and the trailing edge, it is believed that similarly to $\alpha = -3°$ & 0°, the spanwise flow is of insufficient shear to produce streaks. In the trailing-edge corner at **J**, the mottled pattern produced by the sponge has been blurred. This is most probably due to separation of the flow from the corner and plate 4(e(ii)) confirms this, the separation region appearing to have grown in size from at $\alpha = 0°$.

The close up of the flow around the -Z side of the leading edge in plate 4(c) shows that the saddle point **K** on the plate lies about 30 mm from the corner, further from the junction than that at 0°. The limiting streaklines can only just be made out as they wrap around the leading edge and still no pattern exists that indicates the presence of a vortex or other coherent, high-shear flow structure above the plate.

The flow around the +Z side of the leading edge is shown in plate 4(d). There is an accumulation of dye (region **L**) in the corner immediately downstream of the leading edge. This is held to be a small separation region, formed just downstream of the peak suction, as a result of the increase in root loading from $\alpha = 0°$ to +3°. This feature appears to be the origin of a region of high shear on the wing, marked at **M**, just above the corner and some of the tufts in this region do show a small degree of oscillation.

6.2.4 - Wing incidence = +6°

At $\alpha = +6°$, the changes in flow characteristics from $\alpha = 0°$ to +3° become even more marked. For instance, the spanwise flow on the lower surface has almost disappeared, see plate 5(a). On the upper surface of the wing, the line **N** of low shear has moved upstream to $x/c \approx 0.75$, the paint collecting along this line and running into the junction (plate 5(b)). Again, comparing plate 5(b) with the tuft behaviour in plate 5(f) the paths of the streaklines have been affected by gravity, although the effect seems to be much less than at smaller incidences. Also in plate 5(b), as the flow sweeps around the leading edge onto the +Z side of the junction, an unusual feature can be seen at **O** immediately downstream of the leading edge. Regions of high-shear marked **P** and **Q** are revealed on the plate and wing respectively, short distances from the streamwise corner, by dark swathes in the downstream direction. Further downstream on the +Z side of the junction, the flow appears to have separated from the corner at $x/c = 0.62$.

Plate 5(c) shows a close-up of the dividing flow around the leading-edge viewed from the -Z side of the junction. The saddle point **S** stands off the junction by about 40 mm, although again the limiting streamlines which wrap around the leading edge are not marked by any accumulation of pigment. A dark region can be seen at **T**, 15 mm from the

junction, between the saddle point and the junction. The nature of the streaks suggests that at $\alpha = +6°$, a horseshoe vortex system has been formed around the leading edge and it would seem reasonable to infer that the system is similar to that in figure 2(a). In addition, in plate 5(f(i)), the tufts in the region of high shear **T** and the inferred vortex system as it passes downstream, show oscillatory motion. This shows that the flow around the leading edge is unsteady.

A close-up of the flow around the $+Z$ side of the leading edge is shown in plate 5(d). The pattern at the previously-mentioned feature at point **O** has a rather confused, marbled appearance and it is not readily apparent from the photograph what flow structure is present. However immediately downstream of **O**, there appears to be a separated region in the streamwise corner, extending downstream for about $0.15c$. In plate 5(f(ii)), the path of the horseshoe vortex as it wraps around the leading edge can be traced from the oscillations of the tufts on the plate. In addition the tufts nearest the corner, 25 mm downstream of the leading edge, are oscillating whilst pointing upstream. This is at the same point as **O** in plate 5(d), which is therefore believed to be a small pocket of reversed flow. The tufts immediately downstream of the reversed-flow region are oscillating quite violently, confirming that a small region of separated flow exists downstream of **O**.

Region **P** indicates that a vortex is formed above the $+Z$ side of the plate as the flow wraps around the leading edge, the vortex approximately following the junction contour as it passes downstream, until it reaches the corner separation **R** and is deflected in the $+Z$ direction. The region **Q** of high shear originates from the boundary between the pocket of reversed flow and the attached wing flow and continues in the streamwise direction for about $0.25c$. The high-shear region **Q** can be seen in the tuft photographs as oscillations of the 2 rows of wing tufts nearest the junction.

The flow at the trailing-edge corner on the $+Z$ side of the junction is shown in close up in plate 5(e). The corner separation at point **R** can be seen in more detail, the separation line extending both up the wing and onto the plate. Just downstream of point **R**, the paint from the line **N** of low shear runs into the corner and it can be seen that the corner separation modifies the locus of line **N** near the plate. The separation region at the

trailing-edge corner is slightly larger than that at $\alpha = +3°$, the paint pattern in that region being similar to that near the leading edge at **O**. The separation at the trailing-edge corner considerably modifies the paths of the streaklines on the plate, deflecting them in the $+Z$ direction. The extent of the spanwise flow on the upper surface is confirmed at $0.25c$ forwards from the trailing edge. However as the junction is approached from the mid-span, the spanwise flow breaks down as a result of the corner separation at the trailing edge. Plate 5(f(ii)) shows that the tufts in this region oscillate wildly, the size of the separation region being estimated as occupying a parallelogram-shaped region approximately $0.25c$ along the chord by $0.2c$ along the span.

6.2.5 - Wing incidence = +6.5° to +8.5°

Photographs were taken of the tuft behaviour on the $+Z$ side of the junction only, as incidence was increased in steps of 0.5° between +6° and +9°. The intention was to determine the incidence at which the separation region just downstream of the leading edge corner at +6° had grown to cover the whole chord length. This occurred at approximately $\alpha = +7°$; it can be seen from plate 6 that all the wing tufts in the first 2 rows up from the corner are vibrating. The pocket of reversed flow in the corner just downstream of the leading edge has grown slightly in the downstream direction, extending to $X/c = 0.2$. In addition, the majority of wing tufts in the 2 rows, 75 & 100 mm from the corner follow the free stream direction, but show some vibration.

Plate 7 shows the $+Z$ side of the junction at $\alpha = +8°$. At the nose of the junction, only the tufts nearest to the corner are oscillating, all others along the leading edge and at $X/c = 0$ *on the plate* are well behaved. However, as the distance along the chord is increased, the area affected by the flow separation has grown dramatically to occupy a much greater area than at $\alpha = +7°$. The extent of the reversed-flow region in the corner, just downstream of the nose has increased. This reversed flow appears to form part of a recirculation region on the wing, the centre of which is situated in the second row of wing tufts outboard from the corner, at about $x/c = 0.15$. Far outboard ($Y >= 200$ mm), spanwise flow on the wing can be seen between $x/c \approx 0.7$ and the trailing edge. However as the spanwise flow approaches the junction, it breaks down when it meets the separated region.

6.2.6 - Wing incidence = +9°

The oil-flow over the lower surface and -Z side of the junction is shown in plate 8(a). The saddle point on the plate can be seen at point **U** and there is an impression of a horseshoe vortex system wrapping around the leading edge between **U** and the nose of the junction. The tuft behaviour near the leading edge in plate 8(f(i)) indicates that the plate boundary layer has separated at **U** and confirms that the flow around the nose of the junction is unsteady.

The oil-flow pattern over the +Z side of the junction is shown in plate 8(b). At this incidence, the separation around the wing root occupies a considerable part of the wing upper surface and plate. Far from the junction the flow over the upper surface is well behaved until it meets the line **V** of low shear at $x/c = 0.7$, the flow aft of this line being into the junction until it meets the corner separation at **W**. However in the corner, from the leading edge to $x/c = 0.7$, the +Z side of the junction is dominated by reversed flow and the paint streaks at **X** are contrary to the freestream direction. Between the streamwise and reversed flows, a large region of low momentum flow can be seen at **Y** in plate 8(b), where the pattern is extremely disorderly. Where the outboard boundary of **Y** meets the line of low shear **V**, some paint accumulates in the low-momentum flow and forms droplets which are affected by gravity. Also in this region however, the spanwise flow down the wing can be seen to turn towards the leading edge and join the reversed flow in the corner to mark the inboard boundary of **Y**. The flow along the lower boundary of **Y** divides at the leading-edge, some of the flow moving down to meet the plate, the rest moving up the leading-edge to join the attached wing flow. Therefore, region **Y** appears to be the eye in a recirculatory flow on the upper surface of the wing. The regions of attached and reversed flow and the location of the eye are confirmed in the tuft photograph in plate 8(f(ii)).

The saddle point **U** and separation region can be seen in greater detail in plate 8(c). Again the limiting streamline between the oncoming boundary layer and the separation region is rather indistinct. In Arnott *et al* (1993) the regions at **Z** were originally thought to lie under a vortex, as part of a 4-vortex system similar to figure 2(b). However on closer

inspection, they appear to originate from the saddle point **U**. Also, the paint streaks in **Z** do not seem to suggest vortical motion above them. These features throw into doubt the inference of a 4-vortex system. Between **U** and the corner there are alternate light and dark regions. The light region **AA** indicates a low-shear region, the dark region **BB** indicates high shear. In addition, the paint streaks in **BB** do suggest the existence of a vortex above the region. Thus, it now seems most probable that a 2-vortex system exists, as in figure 2(a). Between **BB** and the corner there is another light region; this is probably the imprint of an attachment line similar to A_o in figure 8(a). To satisfy kinematical considerations, a tiny counter-rotating vortex is inferred to exist right in the corner. This is formed from flow down the leading-edge separating in the junction, forming the counter-rotating vortex.

The leading edge is viewed in close-up from the $+Z$ side of the junction in plate 8(d). The accumulation of paint in the leading-edge corner can be seen in greater detail here at **CC**. From **CC** a line of paint can be seen to stretch downstream marked at **EE**. The flow separates from the leading edge along this line, which marks the boundary between the flow in the streamwise direction and the reversed flow in the $+Z$ corner. Although the paint streaks on the plate between **EE** and the corner are faint, they confirm the reversed flow. The reversed flow stagnates at **CC** producing the accumulation of paint. In addition, the tuft behaviour in plate 8(f(ii)) approximately confirms the path of line **EE**. In addition, a region of high shear can be seen to develop at **DD**. This grows in the downstream direction, angled away from the junction by the separation with distance downstream.

In plate 8(e), it can be seen that the separation region stretches considerably further in the $+Z$ direction than at $\alpha = +6°$. The dividing line **EE** between forward and reversed flow can still be seen as the trailing edge is approached from upstream. However aft of the trailing edge, no coherent flow structure can be identified, apart from some weak streamwise flow near **DD** at the bottom edge of plate 8(e). Thus, at $\alpha = +9°$, it can be seen that the flow separation in the junction region is quite severe, producing some very undesirable flow features.

6.2.7 - Summary of flow visualisation results

In summary, the flow visualisation tests confirm the *root-stall* phenomenon, characteristic of swept-forward wings, in contrast to the *tip-stall* behaviour of swept-back wings. They also indicate that at zero or low-incidence, the disturbance to the plate boundary layer is low and the apparent separation upstream of the nose is extremely weak.

6.3 - Surface pressure distributions on the wing and plate

The pressures measured on the surface of the wing and plate have been expressed as coefficients C_p, using the tunnel reference pressures as explained in Section 5.4. The pressure coefficients on the wing are plotted in figures 44(a) to (e) as $-C_p$ against chordwise position x/c, at various non-dimensionalised distances Y/c along the span from the junction. The pressure coefficients on the plate are plotted in figures 45(a) to (e) as surface isobars around the leading edge. The contour levels were interpolated linearly from values of C_p measured at the tappings, the positions at which isobars intercepted the junction being determined with help from the wing pressure measurements.

6.3.1 - Wing incidence = -3°

The variation in chordwise pressure distribution along the span at $\alpha = -3°$ is shown in figure 44(a). At the leading edge, the suction peak occurs on the lower surface, *i.e.* negative lift; compression exists over the upper surface. At the spanwise stations furthest from the junction, the pressure distributions indicate that a region of 2-D flow exists over the wing there. However as Y/c decreases further, the suction at the leading edge increases, approximately doubling in magnitude. Aft of this peak however the pressure gradient over the lower surface is adverse. Conversely the pressure gradient over the upper surface is favourable between $0 \leq x/c \leq 0.6$, then adverse aft of this until $x/c \approx 0.9$. From this point up to the trailing edge the pressure gradient levels off somewhat, indeed for $Y/c \leq 0.018$ it is almost zero (*i.e.* constant pressure). This is indicative of a weak flow separation. This, coupled with the position of line **A** in plate 2(b), further suggests that the flow over the upper surface separates at $x/c \approx 0.9$.

The surface isobars on the plate in the leading edge region are shown in figure 45(a). The suction and compression regions on the plate as the oncoming boundary layer meets the junction are obvious. The isobars approaching the leading edge correlate well with the path of the dividing streamline in plates 2(a) to (c), although they do not give any indication that a horseshoe vortex is present at the leading edge. Likewise, neither do the isobars on the -Z (suction) side of the junction downstream of the nose (at $X \approx 40$ mm). There they show that the plate static pressure is lowest right in the corner. If a horseshoe vortex were present, one would expect a pressure minimum at a short distance from the corner, which followed approximately the junction contour.

Such a phenomenon, occurs on the +Z (pressure) side for $X > 40$ mm. Here the isobars show that a weak pressure minimum occurs along a line which follows approximately the junction contour about 15 mm from the corner. This is consistent with the effects of a vortex above the plate and also with the results of Bernstein & Hamid (1995). However it should be remembered that the flow visualisation results for this investigation did not give any indication of a horseshoe vortex.

6.3.2 - Wing incidence = 0°

The chordwise distributions of pressure coefficient at $\alpha = 0°$ are shown in figure 44(b)[2]. At all stations, the suction over the upper surface is greater than over the lower. Away from the junction, the sectional pressure distribution corresponds to the camberline shape. A weak suction peak exists at $x/c \approx 0.05$ produced by the change in slope of the camberline at that point (see figure 20). This peak increases in strength as the junction is approached. Aft of this, the pressure gradient is adverse until $x/c \approx 0.2$, where it becomes favourable once more up to the suction "peak"[3] or local pressure minimum produced by the rear loading at $x/c = 0.6$. This feature is dependant on Y/c too, it being seen that it reduces in strength as the junction is approached. The pressure gradient immediately aft

---

[2] The tappings at $x/c = 0.07$ lay underneath the transition strip producing spikes in the graphs and therefore are omitted.

[3] At $\alpha = 0°$ and higher incidences, the term peak to describe the shape of the pressure distribution on the wing upper surface at $x/c = 0.6$ is not really suitable, as it is more of a levelling off, or plateau, in the pressure gradient.

of $x/c = 0.6$ is adverse, but levels out again for approximately $x/c \geq 0.9$. Again this region of constant pressure coefficient coincides with the region of spanwise flow parallel to the trailing edge, providing confirmation that the flow separates from the upper surface at line **E** in plates 3(b) & (d).

On the plate, figure 45(b), the pressure rise as the leading edge is approached is evident. It is uncertain however, whether or not the flow stagnates in the corner. The isobars again correlate with the oil-flow pattern in plate 3(c), but do not have any particular distinguishing features.

6.3.3 - Wing incidence = +3°

The measured chordwise pressure distributions at $\alpha = +3°$, at various distances along the span, are shown in figure 44(c). At $Y/c \approx 0.353$ the suction peak at the leading edge is extremely sharp, with the indication of a weak, secondary pressure minimum at $x/c = 0.05$. The pressure gradient becomes virtually zero between $x/c = 0.2$ & 0.6, aft of which the pressure gradient is adverse once more, until about $x/c > 0.85$ where the pressure levels out at roughly atmospheric. This last feature confirms that the flow has separated from the upper surface at line **I** in plates 4(b) & (d).

The possibility that the sudden decrease in suction between $0 \leq x/c \leq 0.05$ was due to a pressure leak was checked for and discounted. Therefore, in the midspan, the sudden drop in suction immediately aft of the leading edge and kink are genuine features. The leading-edge peak is due to incidence, that at $x/c = 0.05$ is produced by the slope of the camberline as explained previously. As the junction is approached, the leading-edge suction peak increases in strength and broadens to absorb the secondary peak. From this it would not be unreasonable to assume that the sectional loading increases from tip to root. However, as at $\alpha = 0°$, the suction over the rear of the section reduces as the junction is approached. As will be seen later this offsets the increase in lift at the leading edge.

It is logical to compare the measured pressure distributions at $\alpha = +3°$ with the computational predictions from the CFD codes. The results from **FELMA** in figure 21(a) match the experimental distributions most closely at $Y/c = 0.353$ and slightly further outboard. Some differences are evident, most notably the experimental suction peak at the leading-edge being stronger and sharper than predicted; also the pressure recovery at the trailing edge found experimentally is less than predicted. However the kink in the pressure distribution over the upper surface at $x/c = 0.05$ and values of pressure coefficient over the rest of the chord are well predicted at such distances from the junction.

Comparison of the experimental pressure distributions with those predicted in figure 22(b) using **SPARV** is slightly less easy than for **FELMA**, since the spanwise positions Y/c at which experiments were made do not coincide with those of the predicted distributions. In addition, the actual values of the predicted data are not available to the author for plotting on the same graph as the experimental measurements. Nevertheless, approximate comparisons can be made by interpolating linearly between the predicted pressure distributions. Although both sets of distributions show the same qualitative behaviour over the approximately range $0.35 \geq Y/c \geq 0$, *e.g.* the suction at the leading edge increases as the junction is approached, there are major quantitative differences. Over the spanwise distances at which measurements were made, it appears that **SPARV** underestimates the suction at the leading edge by approximately 50%. Whereas in the experimental distributions the suction peak at the leading edge dominates, in the majority of the predicted distributions, the dominant suction peak is at $x/c = 0.05$ due to the camberline. It is not until very close to the junction that the predicted peak at the leading edge becomes noticeable. An additional difference between prediction and experiment is evident at the trailing edge: as the **SPARV** calculations were inviscid, the flow separation and associated levelling out of the pressure distribution aft of $x/c \approx 0.85$ were not predicted. However, the predicted values of the local pressure minimum at $x/c \approx 0.6$ are very similar to the measured values and the decrease in the strength of the rear peak as the junction is approached from the midspan is also predicted rather well.

In figure 45(c), the pressure rise on the $-Z$ side of the plate as the junction is approached can be clearly seen, in addition to the suction on the $+Z$ side. The isobars are consistent

with the paths of the streaklines in plate 4(c). The isobars at (X, Z)/mm ≈ (20, 20) have kinks in them, showing that some structure is bringing slightly higher pressure fluid into the corner. Another look at plate 4(d) suggests that there is some correlation between the kinks and the pigment accumulation marked at **L**. In fact the kink in the C_p = -1.0 isobar is situated at the upstream edge of **L**. The downstream edge of **L** is situated at $X \approx 35$ mm, which correlates with a very slight kink in the C_p = -0.8 isobar. The likely explanation for **L** is that it is the imprint on the plate of a small pocket of separated flow immediately downstream of the leading edge.

6.3.4 - Wing incidence = +6°

At α = +6° the changes in the sectional distributions become even more marked as shown in figure 44(d). For all the spanwise stations measured, the levelling-off in the pressure gradient over the upper surface occurs aft of x/c = 0.75. This ties in with the position of line **N** in plate 5(b). However there are also major changes in the sectional distributions with distance from the junction. As the root is approached, the suction peak at the leading edge increases progressively, until $Y/c \approx 0.053$ where its shape too begins to alter. Additionally, as Y/c decreases to 0, again the pressure reached at x/c = 0.6 increases progressively.

The shape of the pressure distributions for $Y/c \leq 0.053$, gives the impression of a pressure leak across those tappings. This was checked for however and again, disproved. Thus it would appear that some flow feature in the streamwise corner acts to reduce the suction over the upper surface, near the junction, just downstream of the leading edge. The oil-flow patterns and tuft behaviour in plates 5(b) & (d) show that the reversed-flow region at **O** lies between the leading edge and x/c = 0.07. Although **O** is spatially very small, the effect of the reversed-flow on the pressure distribution over the upper surface is felt up to $Y/c \approx 0.053$. Consequently the leading-edge suction is reduced and the wing root is partially stalled.

On the +Z side of the plate, see figure 45(d), the location of the peak suction region is coincident with the upstream edge of region **O** in plate 5(d). On the -Z side of the plate, it

is almost certain that the flow stagnates near $X/c = 0.013$ due to the pressure coefficient at $Y/c = 0.002$ in this region being extremely close to $C_p = +1$. There are also kinks in the $C_p = +0.3$ & $+0.4$ isobars at (X, Z)/mm $\approx$ (-25, -20), which correlate with the position of the saddle point **S** in plate 5(c).

6.3.5 - Incidence = +9°

The chordwise pressure distributions at $\alpha = +9°$ are shown in figure 44(e). Furthest from the plate, a strong suction peak exists at the leading edge. Aft of this, the local minimum in pressure can just be discerned, but at $x/c \approx 0.4$ here, not 0.6. The reason for this can be seen in the flow visualisation photographs in plates 8(b) & (f(ii)). The area encompassed by the recirculation/separation region on the upper surface can be seen to grow outboard from the root with distance downstream from the leading edge. This far along the span the flow over the upper surface is only attached between the leading edge and $x/c = 0.4$, hence the maximum there.

Moving slightly inboard, although the strong suction peak at the leading edge remains, it is not as prominent. In addition the separation region occupies a greater fraction of the chord, affecting the pressure distribution over the upper surface accordingly. Even further inboard, at $Y/c = 0.106$, the suction peak at the leading edge of the upper surface seems at first sight to have disappeared. On closer inspection, the pattern of the pressure coefficients near the leading edge indicates that a small peak, too sharp to be resolved due to the spacing between the pressure tappings, may exist between $x/c = 0.0$ & 0.012. The behaviour of the tuft at the leading edge, two rows outboard from the junction, indicates that the flow is attached at the leading edge and supports the suggestion that at $Y/c = 0.106$, a sharp suction peak exists very near the leading edge.

For $Y/c \leq 0.071$ the recirculation/separation region affects the whole chord to the effect that the suction peak at the leading edge has disappeared completely, the pressure distributions having almost identical appearances. Over the upper surface, the pressure distributions between $0 \leq x/c \leq 0.24$ are flat-topped, aft of which the pressure increases gradually to meet the lower-surface pressure distribution at the trailing edge. The

pressure differential between upper and lower surfaces becomes slightly less as Y/c reduces. The pressures on the lower surface at $x/c \approx 0.013$ are close to stagnation; interestingly for the row of tappings closest to the junction ($Y/c = 0.002$), the pressure actually reaches stagnation at $x/c = 0.013$. Although it is unlikely that the free stream will actually reach stagnation at the leading edge over the main part of the wing, it seems reasonable that this will occur right in the junction.

Figure 45(e) shows the isobars on the plate at $\alpha = +9°$. The kinks in the $C_p = +0.4$ & 0.5 isobars correlate well with the position of region **BB** in plate 8(c). The kinks are consistent with the existence of a vortex above the plate, reducing the static pressure on the surface of the plate immediately below the vortex. Therefore region **BB** is believed to be the "footprint" of a horseshoe vortex. The level of shear stress under the path of the vortex indicated in the flow visualisation photographs decreases with distance downstream, probably because it moves away from the plate surface with X/c and/or dissipates slightly. On the $+Z$ side of the junction, the isobars on the plate are closely spaced very close to the streamwise corner, but form a plateau further away as shown by the $C_p = -1.1$ & 1.2 isobars. Comparing figure 45(e) with plate 8(d) reveals that the area enclosed by $C_p = -1.2$ is coincident with region **CC** in plate 8(d).

6.4 - Variation of lift and drag along the wing span

The pressure distributions at each distance Y/c from the junction have been integrated around the chord to give the local force coefficients C_n (figure 46) and C_a due to pressure, normal to and along the chord line respectively, using:

$$C_n = \oint C_p \, d(x/c) = 2\oint C_p \sqrt{x/c} \, d\left(\sqrt{x/c}\right) \qquad \ldots\ldots\ldots (6.5)$$

$$\text{and } C_a = \oint C_p \, d(z/c) \qquad \ldots\ldots\ldots (6.6).$$

The evaluation of the integrals directly is prone to errors, as the minimum and maximum values of C_p will occur most often between a pair of pressure tappings. The first form of the integral for C_n is very sensitive to this; the second form of equation (6.5) avoids this

since the variation of the integrand $C_p\sqrt{x/c}$ with $\sqrt{x/c}$ is relatively gentle (Bernstein, 1991). Where the integral for C_a is concerned, the most significant source of error here arises in another way which is explained shortly. The sectional lift and pressure drag coefficients are then obtained from:

$$\begin{bmatrix} C_l \\ C_d \end{bmatrix} = \begin{bmatrix} \cos\alpha & -\sin\alpha \\ \sin\alpha & \cos\alpha \end{bmatrix} \begin{bmatrix} C_n \\ C_a \end{bmatrix} \quad \ldots\ldots\ldots (6.7).$$

The uncertainty in individual values of C_p produces errors in the lift and drag coefficients and as the integrals in equations (6.1) & (6.2) were evaluated trapezoidally, additional errors of uncertain magnitude are introduced. It is unlikely that the error in C_p of 0.003 will add to all the values on the pressure side and subtract from all the values on the suction side of the wing. This would create an error in C_l of as much as $\Delta C_l = \pm 0.006$, however the more likely rms error is ± 0.003. The errors in C_d are slightly more difficult to estimate. The integral involves the difference in area between loops which arise when C_p is plotted against z/c. When these areas are of similar size, the percentage change in C_a and therefore C_d, due to errors in C_p, can be large. However sample calculations using $\Delta C_p = \pm 0.003$ give an error of $\Delta C_d = \pm 0.002$. The variations in the lift and pressure-drag of the wing, as the junction is approached from the mid-span, are shown in figures 47 & 48 respectively for all 5 incidences.

6.4.1 - Sectional lift distribution along the wing span

Figure 47 shows that at the 3 lowest incidences tested (α = -3°, 0° & +3°), the sectional lift remains approximately constant across the span. At α = -3°, the wing is operating below its zero-lift angle. For these incidences the increase in suction at the leading edge of the lower surface as Y/c decreased, was expected to produce a corresponding increase in downforce in the spanwise distribution of C_l. As the root is approached from outboard, the positive pressure on the upper surface near the leading edge and over the rear of the lower surface, reduce and increase respectively by small amounts. Although $\Delta C_p(x/c)$ is

only weakly dependant on Y/c, it seems that these changes are enough to offset the increase in nose-down suction at the leading edge.

The spanwise lift distributions at $\alpha = +6°$ and $+9°$, show the effect of the onset and growth of the stalled region in the root. For $\alpha = +6°$ the value of C_l shows a very slight increase as Y/c decreases from 0.71 to approximately 0.1. Closer to the plate, the local lift coefficient levels off, then reduces into the junction. This reduction in lift is such that C_l in the junction is only 90% of the value in the mid span. At $\alpha = +9°$, the changes in pressure distribution over the upper surface, shown in figure 44(e), as Y/c is decreased have a more marked effect on the spanwise lift distribution in figure 47. In the mid span, there is very little change in C_l, the calculated values all being within 2% of each other. However between $Y/c = 0.265$ & 0.002, the local lift coefficient reduces steadily such that at $Y/c = 0.002$, C_l is approximately 75% of its value in the mid span.

6.4.2 - Sectional pressure-drag distribution along the wing span

The sectional pressure-drag distributions are shown in figure 48. At $\alpha = -3°$, the pressure drag away from the junction is positive, which does not seem unreasonable. However a very striking feature is that for $\alpha = 0°$ the pressure drag away from the junction has reduced to approximately zero and at $\alpha = +3°$, it is negative, *i.e.* a thrust force. As the wing incidence was increased to $+6°$, the pressure drag away from the junction returned to approximately zero and at $+9°$, at similar spanwise positions, the drag is large and positive. Even more striking is the fact that, apart from at $+9°$, the interaction between wing and plate is favourable, *i.e.* the local pressure-drag coefficient diminishes as the junction is approached. This contrasts with the results of Bernstein & Hamid (1995), who found that the interaction between a swept-back wing and plate had an unfavourable effect on the pressure drag. Importantly here, the range of incidence for which the pressure drag away from the junction is negative includes values typical of flight, the corresponding lift coefficients being in the range 0.1 to 0.5.

Away from the junction, resolving the surface pressure forces in the chordwise direction, a much greater proportion of the model profile experiences a thrust force than for say, a NACA 4-digit section, due to the sectional shape. Thus the rearward force produced by suction aft of the maximum thickness is offset to a greater extent (Arnott, Bernstein & Petty, 1996). At $\alpha = -3°$, this axial force is still rearwards and combined with the force normal to the chord line, resolved through the angle of incidence, the drag force is still positive. At $\alpha = 0°$ & $+3°$ however, away from the junction, the increased suction at the leading edge is large enough for C_a to be a thrust force coefficient and overcome the rearward component produced by resolving C_n through the angle of incidence; therefore C_d is negative. Away from the junction at $\alpha = +6°$, although C_a has become more negative, C_n has also increased and the larger angle of incidence means when the forces are resolved, the contributions are of similar magnitude and the drag force is again approximately zero. For $\alpha = +9°$, $C_n\sin\alpha + C_a\cos\alpha > 0$ even though C_a is negative and the pressure drag is correspondingly positive.

The favourable interaction between wing and plate for $-3° \leq \alpha \leq 6°$ arises due to the suction at the leading edge increasing and that over the rear of the upper surface decreasing as the junction is approached. Thus the corresponding thrust and rearward components of C_a increase and decrease respectively and the pressure drag reduces steadily as the junction is approached, although there is some scatter in the integral near the plate for $\alpha = +3°$. For $\alpha = +6°$, the pressure drag also reduces as the junction is approached, until $Y/c \approx 0.05$, where although there is some scatter in the pressure-drag distribution, it appears to level out. This coincides with a loss in lift shown in figure 47, believed to be caused by a small region of separated flow as mentioned in Section 6.3.4. At $\alpha = +9°$, as the junction is approached, the loss in suction at the leading edge produced by the stalled region in the root comes into effect and the pressure drag increases accordingly.

6.5 - Yawmeter measurements at 0° incidence

Measurements with the single-tube yawmeter were made around the leading edge in traverses normal to the plate surface, at stations lying on normals to the intersection of the

wing profile with it, as shown in figure 37. The data are presented here in figures 49, 50, 56 & 57 as profiles of the flow yaw angles, pitch angles, static-pressure coefficient and velocity magnitude respectively through the boundary layer, the flow angles being defined in the wind-tunnel coordinate frame O*XYZ*. Each figure comprises 10 graphs (a) to (j), each showing profiles of a particular quantity in a plane normal to the tangent to the wing-profile at the junction (NB it should be remembered the probe tip effectively moves downstream a distance $Y\tan 28°$ relative to the leading edge as the height Y of the probe above the floor is increased). A sketch of the location of the planes around the nose of the junction is also included in the top-right corner of each figure. In addition the flow angles and velocity vectors have been resolved into the planes *A* to *J* to show the cross flows in these planes, these being presented in figures 51 to 55.

6.5.1 - Variations in flow yaw angle ψ around the nose of the junction

Figure 49 presents the variations in yaw angle through the boundary layer for all 10 measurement planes around the leading edge shown in figure 37.

Examining firstly the -*Z* side of the junction: planes *A* & *B*, shown in figures 49(a) & (b) respectively, are close to the dividing streakline and saddle point **F** in plate 3(c). Interestingly, plane *A* is actually on the side of the dividing streakline which passes around the leading edge into the +*Z* corner of the junction, hence for $x_3 \geq 40$ mm the yaw angles are all positive. Closer to the corner, due to the sweep angle, the leading edge of the wing influences the flow angle far above the plate, but obviously as *Y* reduces, the leading edge is further aft and the skewing of the boundary layer then dominates as for the other profiles in this plane. Traverses closer to the corner than $x_3 = 20$ mm in this plane yielded flow pitch angles which were outside the range of the yawmeter calibration and are therefore not shown. In plane *B* the profiles are broadly similar to those in plane *A*, as the direction of approach of the plate boundary layer in that region is also influenced by the wing camber. In this plane measurements could be made very close to the corner and the profiles at x_3/mm = 10 & 5 show that right in the corner, just above the plate surface, the flow is skewed in the -ψ direction.

These trends are prevalent in plane C, shown in figure 49(c), for which again all the measuring stations are upstream of the leading edge. However in the remaining planes in this side of the junction, D & E shown in figures 49(d) & (e) respectively, the form of the profiles has changed again. In these 2 planes, each profile shows that the yaw angle remains approximately constant over its top 3 quarters, but close to the plate the profiles curve showing that ψ becomes gradually more negative as the plate is neared. Also moving from $60 \geq x_3/\text{mm} \geq 5$, successive profiles are shifted in the $-\psi$ direction due to the influence of the wing contour. Interestingly though, in planes D & E, even allowing for the accuracy of the yawmeter, the largest yaw angles were not measured in the profiles closest to the corner, but slightly further away.

The profiles in the $+Z$ side of the junction, shown figures 49(f) to (j), are roughly mirror images of their corresponding profiles in figures 49(a) to (e).

It is interesting that in planes D, E, I & J, that the yaw angles are largest at a short distance from the corner. The presence of a horseshoe vortex, situated a short distance from both plate and wing surfaces, would accentuate the skewing of the flow in its vicinity, producing this phenomenon. However before any conclusions are reached, it is sensible to examine the flow pitch angles.

6.5.2 - Variations in flow pitch angle θ around the nose of the junction

Figure 50 presents the variations in pitch angle through the boundary layer for all 10 measurement planes around the leading edge shown in figure 37.

Again starting in the -Z side of the junction with plane A in figure 50(a), the flow furthest from the junction shows a small pitch-down angle, which remains almost constant with decreasing height Y through the boundary layer. This is slightly surprising as the flow must turn parallel with the plate surface at some value of Y, but it appears that such events are confined to within a tiny distance above the plate surface. As the corner is neared, the profiles retain broadly this shape, but show a shift towards slightly larger pitch-down

angles, apart from the profile closest to the corner. Here the variation of pitch angle with height Y is much greater and is not monotonic, although it remains quite smooth.

Moving further downstream, the profiles furthest from the corner in planes B & C are similar to corresponding ones in plane A. Closest to the corner, the approximate form of the profile at x_3 = 20 mm in plane A is repeated, but the changes in pitch angle and reversals in the trends of the profiles are considerably exaggerated.

In the next plane downstream, plane D shown in figure 50(d), again the pitch angles in the profiles furthest from the corner remain virtually constant at very small, negative values. Nearer the corner in plane D the profiles are of the form of those in planes B & C, however the magnitude of θ, and changes in it as Y varies, are significantly reduced from the values shown by their counterparts in planes B & C. These reductions are continued in plane E, shown in figure 50(e), where the pitch angles are approximately zero over most of the profiles, although the 2 profiles closest to the junction do show a very small increase in pitch-down angle close to the plate.

In the $+Z$ side of the junction the profiles of θ in planes F to J, shown in figures 50(f) to (j) respectively, are this time, almost exact copies of their counterparts in the $-Z$ side of the junction, as opposed to the profiles of ψ which were loosely mirror images of each other in the 2 sides of the junction. Again none of the profiles show any coherent upflow from the plate.

Overall the profiles of ψ & θ in figure 49 & 50 respectively are notable for their smoothness in depicting the changes in flow angle through the boundary layer. However far more interesting is the fact that although some of the yaw angle profiles change sign over their length, hinting at possible vortical motion, the pitch angles are either zero or negative; they do not show any upflow which would provide further evidence of a horseshoe vortex. Although it is difficult to separate the flow field associated with a horseshoe vortex from that due to the sweep of the wing, this downflow toward the plate and the yaw angle profiles correspond to an appropriately signed vortex in the separation region. However some doubt is thrown as one would additionally expect that the pitch

angles for at least one of the profiles, be positive over a small range of Y. Admittedly these profiles are not the best method of interpreting whether or not a vortex exists. Therefore to gain a different perspective, the mean-velocity vector has been transformed through the flow angles to give vector plots of the cross-flow velocities in the planes A to J.

6.5.3 - Cross-flow velocities around the nose of the junction

Figures 51 to 55 show these cross-flow velocities, each figure showing a pair of planes, on opposite sides of the junction, at X/mm = 0.5, 1, 2.5, 10 & 40 respectively (*i.e.* figure 51 shows planes A & F, figure 52 shows B & G etc.). Each plane is viewed from its downstream side, with the tails of the arrows marking the measurement points. An arrow representing the freestream scale is drawn at the top of each of the vector maps. As the in-plane velocities became smaller with distance downstream, it was necessary to magnify the scale of the arrows accordingly and the reader's attention is drawn to the changes in the length of the arrow for the freestream velocity.

Figure 51 show the cross-flow velocities in planes A & F at $X = 0.5$ mm. These particular planes are almost aligned with the free stream direction so for most of the region shown the $\overline{U}$-component will dominate the picture. However, using this figure in conjunction with the oil-streak photographs in plate 3(c) there is no sign of any upflow associated with boundary layer separation from the plate nor can vortical structures be detected. All the previous research for unswept- and swept-back-wing/plate junctions leads to the expectation of a horseshoe vortex around this junction also. If a discrete vortex has formed in the separation region as it starts to turn around the nose, the reversed flow associated with it seems to be confined to the region defined approximately by $x_3 < 10$ mm and $Y < 2$ mm in these planes.

Moving downstream, to planes B & G at $X = 1$ mm, the reduction in the influence of the freestream velocity can be seen as β_s becomes larger. Here the limited traverses at $x_3 = 5$ mm in both planes clearly show marked pitch-down angles in the corner. However there is no direct evidence of outflow near the plate surface, or upflow in the vicinity of the separation line as it wraps around the nose, though it may occur for $Y < 3$ mm. In fact

there is little firm evidence of vortical flow to be found until X = 10 mm, where figure 54 shows clear evidence of a compressed vortical structure in planes D & I. There are clear indications of an outflow from the corner for (x_3, Y) ≤ (20, 2) mm in both planes at this distance downstream. Further downstream in planes E & J at X = 40 mm, figure 55 shows that the vortical motion has grown in size but is quite weak, the largest out-flow velocity being approximately 15% of the freestream velocity. Curiously, although flow into the wing, down into the floor and outflow along the floor have been detected, no upflow to complete the vortex can be seen.

6.5.4 - Variations in static-pressure around the nose of the junction

The local, static pressures through the boundary layer around the nose of the junction are shown in coefficient form in figure 56. Again starting in the -Z side of the junction, at plane A in figure 56(a), the profiles show that at constant Y the static pressure increases as x_3 decreases. Furthest from the junction the profiles show only a small amount of variation with Y through the boundary layer. Nearer the corner though, the traverses show small reductions in pressure as Y decreases, followed either by an increase again or become virtually constant close to the plate. In the presence of a vortex one would expect the pressure in its proximity to reduce, as hinted at by the 2 profiles just described, but here the flow is accelerating around the leading edge and it is difficult to attribute the phenomenon to a particular reason.

Moving downstream to plane B in figure 56(b), the potential field of the wing is able to affect all the profiles, producing smooth increases in pressure as Y reduces; for some profiles these increases are considerable. This behaviour is repeated in plane C, shown in figure 56(c), although there the changes over the length of the profiles are not quite as great. In plane D, shown in figure 56(d), these increases in static pressure with decreasing Y have become extremely small, so that even close above the plate, the static pressure is just greater than that in the free stream. As for planes A, B & C, the highest pressures were measured right in the corner. Interestingly however in the most downstream plane, this trend is reversed. In plane E in figure 56(e), the profiles have returned to being virtually straight lines, showing that for a particular measurement station, the static

pressure normal to the plate is effectively constant. However as x_3 reduces the pressure normal to the wing profile decreases from a positive to a negative value. This matches the behaviour of the surface pressures on the wing and plate in figures 44(b) & 45(b) respectively.

In the $+Z$ side of the junction the profiles of static pressure in the planes nearest the leading edge show considerable variation both with height Y and distance x_3 normal to the corner. In the most upstream plane F, shown in figure 56(f), the acceleration of the freestream flow around the leading edge is confirmed at the higher values of x_3 & Y. The profiles far from the junction show little change in C_p far above the plate, but close to it, the static pressures increase smoothly towards freestream. The profiles closest to the corner show slightly different behaviour from this, but overall show a small increase in pressure over their length.

In the next plane downstream, plane G in figure 56(g), the profiles are very similar to those in plane B, the corresponding plane in the $-Z$ side of the junction. These trends continue in planes H & I, in figures 56(h) & 56(i) respectively, although the profiles become progressively more bunched together and shifted towards lower pressures with distance downstream. In the final plane in this side of the junction, plane J in figure 56(j) the profiles far from the corner again follow the trends in planes G to I. However as x_3 reduces, the change in pressure over the length of the profile gradually reduces until for the profile closest to the corner, it is almost zero. From plane F to plane J, other important changes in the pattern of the profiles take place too. Whereas in planes F to H, the highest pressures are found right in the corner, in plane I this point has moved away from the corner. By plane J the highest pressures are found at the measurement stations furthest from the junction, whereas the lowest pressures are found closest to the corner. However the pressure field is complicated by the 3-dimensional potential field associated with the wing sweep angle. For this reason the profiles are difficult to interpret.

In the $-Z$ side of the junction the pressures on the plate in figure 45(b) are all plausible extrapolations of the pressure profiles in figures 54(a) to (e) to the plate surface. In the $+Z$ side of the junction, the profiles in planes F to H and most of those in plane I, may be

extrapolated to the values on the plate with a fair degree of confidence too. For the profiles in plane *I* near the corner and those in plane *J*, whilst the extrapolation of the profiles to the plate values is not impossible, it is rather more implausible.

It seems clear that for this 3-dimensional case, the usual boundary layer assumption that the pressure gradient normal to the plate is negligible is not justified. In both sides of the junction, the measurements show that in the most downstream measurement planes, there is some mechanism bringing high-momentum fluid into the corner.

6.5.5 - Variations in the local velocity *Q* around the nose of the junction

The variation in the local mean-velocity vector Q around the nose of the junction, non-dimensionalised by the freestream velocity U_∞, is shown in figure 57. Most of the profiles look like ordinary turbulent boundary layer profiles and compare well with the U-velocity profile upstream of the junction, shown in figure 41(a), with slight differences due to the wing camber and the fact that the plate boundary layer thickens from X = -500 mm to the leading edge of the junction.

There are however some profiles which clearly do not follow this form: firstly that at x_3 = 20 mm in plane *A*, where the local velocity is about 80% of the freestream. As Y reduces, the velocity decreases, then increases, before decreasing again below Y = 20 mm. This dip in the profile coincides with a peak in the profile of static pressure coefficients for this range in figure 56(a). The other profiles which do not follow the form of the freestream profile are those at x_3/mm = 5 & 10 in planes *E* & *J*. Here the profiles show that as x_3 reduces, the velocity defect through the boundary layer gets smaller. This effect coincides with the occurrence of the lowest pressures in those planes, which phenomena may be explained partly by the facts that: (a) planes *E* & *J* are downstream of the high pressure region at the leading edge, the flow accelerating as it follows the junction contour away from the leading edge and (b) the spanwise flow on the wing brings high velocity fluid from the freestream into the junction. The question remains however about the influence of the rudimentary vortex in planes *D*, *E*, *I* & *J*.

Summarising the flow around the leading edge, it would seem that the boundary layer on the plate does separate slightly upstream of the junction. At low incidence, the oil-flow photographs indicate that the separation is very weak and interestingly, very close to the separation point, the upflow associated with separation or a vortex upstream of the junction is absent. It would appear that a discrete horseshoe vortex has not been formed, however as the plate boundary layer is skewed around the leading edge, there must be streamwise vorticity somewhere in the junction. Therefore to explain the absence of a vortex, either the vorticity is so diffuse that it has not been detected, which seems unlikely, or the pressure field of the wing and flow into the junction appear to confine the vorticity into an extremely thin layer which cannot be resolved with this instrument and at this scale.

As the separation region sweeps around the leading edge into the streamwise corners, the spanwise flow down the leading edge must turn tangential to the plate. Thus the rudiments of an extremely weak vortex form in the corners at a short distance downstream of the leading edge. The profiles of flow angle, static pressure and velocity magnitude themselves are quite smooth, even those inside the separation region, indicating that the single-tube yawmeter is a reliable instrument when used carefully. However further investigations are required to separate the influence of the forward-sweep angle from the effects of the wing-section profile. The *HH10* section is extremely sharp-nosed and for further investigations, it would seem sensible to use a leading-edge profile which would be expected to produce a larger separation region. As the separation scales on the bluntness of the obstacle, then experiments using *e.g.* circular cylinders set at various angles of forward sweep to a flat plate should enable the effects of sweep to be isolated.

6.6 - X-wire anemometer results at 0° incidence

Mean velocity and Reynolds stress data were obtained with the X-wire probe at the stations shown in figure 40, in planes *K* & *L* normal to the wing junction profile at $X = 300$ mm and plane *TE* normal to the chord line at the trailing edge ($X = 500$ mm). In order to bring out the main features of the flow, the results are presented in figures 58 to 87 in several different ways:

a) profiles of the mean-velocity components,

b) profiles of the turbulence velocity-fluctuation correlations ("Reynolds stresses"),

c) contour and surface maps of the longitudinal mean-velocity component U/U_∞,

d) vector plots of the mean cross-flow velocities &

e) contour and surface maps of the turbulence velocity correlations.

The results in the planes *K* & *L*, normal to the tangent to the wing profile at $X = 300$ mm are presented first. All data are referred to the wind-tunnel axis frame O*XYZ*, except for the cross-flow velocities in figure 62.

6.6.1 - The mean-velocity field at *X*/*c* = 0.6

Figures 58 & 59 show the profiles of the non-dimensionalised, mean velocities $(\overline{U}, \overline{V}, \overline{W})/U_\infty$ through the boundary layer, in planes *K* & *L*, at $X = 300$ mm. As for the measurements around the leading edge, the results in each plane are presented as a series of graphs at various distances x_3 from the corner.

On both sides of the junction, the profiles furthest from the corners in figures 58 & 59 are similar to those upstream of the junction in figure 41, with a few differences, notably, that the boundary layer has thickened to about 30 mm. Also for most profiles, the $\overline{U}$ velocity above this height becomes constant at something other than the freestream value due to the potential field around the wing. As in figure 41, $\overline{V} \approx 0$ m/s, however $\overline{W}$ in figures 58(a) to (d) has increased slightly and is positive in plane *K*, but negative in plane *L*.

Moving closer to the corner, the $\overline{U}$-velocity profiles in both planes exhibit noticeable changes, showing that relatively high velocity flow exists in the corners. In the region $10 \leq x_3/\text{mm} \leq 25$, the gradient $\partial\overline{U}/\partial Y$ is small in the outer parts of the profiles. The closest profiles to the corner, at $x_3 = 5$ mm, show further changes: the profiles become "S-shaped" as *Y* reduces, showing a jet-like character. The $\overline{V}$ profile remains close to zero throughout the range of x_3, but the $\overline{W}$ profiles show some interesting changes near the plate surface as x_3 reduces.

Clearly the mean-velocities on the $+Z$ (suction) side of the junction show some interesting flow behaviour, which contrasts with the lack of features in the $-Z$ side and one wonders how this relates to the turbulence activity in the 2 sides of the junction. Thus it now seems appropriate to examine the turbulence velocity correlations: effectively the Reynolds stresses divided by $-\rho$.

6.6.2 - The turbulence velocity-correlation ("Reynolds stress") field at $X/c = 0.6$

The turbulence quantities $\overline{u^2}$, $\overline{v^2}$, $\overline{w^2}$, $\overline{uv}$, $\overline{uw}$ & $\overline{vw}$ in planes K & L at $X = 300$ mm, are shown in figures 60 to 63 inclusive as profiles (non-dimensionalised by U_∞^2) through the boundary layer.

Far from the corners on both sides of the junction, the profiles of $\overline{u^2}$, $\overline{v^2}$ & $\overline{w^2}$ in figures 60 & 61 are similar to those well upstream of the junction. Closer to the corners, in both planes K & L, $\overline{v^2}(Y) \approx \overline{w^2}(Y)$, except at $x_3 = 5$ mm in plane L. However it is the $\overline{u^2}$ profile that shows the most interesting phenomenon between $60 \geq x_3/\text{mm} \geq 5$, indeed for some values of x_3, $\overline{u^2}$ is approximately constant over a small range of Y inside the boundary layer itself.

The profiles at $x_3 = 5$ mm in plane L, shown in figure 61(h) are noteworthy. As Y reduces, just below the nominal edge of the boundary layer, large and abrupt increases in $\overline{u^2}$, $\overline{v^2}$ & $\overline{w^2}$ are apparent. Interestingly the $\overline{u^2}$ & $\overline{w^2}$ profiles peak at the same height above the plate before reducing back to values similar to those found nearest the plate in the other traverses. However $\overline{v^2}$ remains approximately constant over a considerable portion of the boundary layer thickness before again reducing in value near the plate.

Far from the corners, the profiles of $\overline{uv}$ in planes K & L (figures 62 & 63) are likewise similar to those upstream of the junction in figure 41(d). Those of $\overline{uw}$ are slightly different though, both to the upstream profile and each other; $\overline{vw}$ remains approximately zero as expected. Moving closer to the corners the trends in the profiles in the 2 planes are quite different and it is more convenient to describe first one plane then the other.

In plane K, as x_3 reduces very little change in the profiles occurs until fairly close to the corner. There $\overline{uv}$ tends to zero, except very close to the plate surface. The $\overline{uw}$ & $\overline{vw}$ profiles in plane K remain either very small, or scattered about zero, except very close to the corner where $\overline{uw}$ shows an increase as Y reduces. In plane L, the $\overline{uv}$ & $\overline{uw}$ profiles contrast sharply with those in plane K, varying considerably with both Y & x_3 over the plane. However the most notable differences between planes K & L are the large peaks in all 3 "shear stresses" shown by the profiles $x_3 = 5$ mm.

To examine how well the notable features in the velocity data correlate with regions of high or low turbulence activity, the data in both planes are summarised below as contour, surface and vector maps.

6.6.3 - Summary of the flow at $X/c = 0.6$

The measurements of $\overline{U}$ in the 2 planes at $X = 300$ mm have been plotted as contour and surface maps (still in the OXYZ frame) in figures 64 & 65. Additionally the $\overline{V}$ & $\overline{W}$ velocities have been transformed through the appropriate angles so that they could be plotted in figure 66 as vectors of the in-plane velocities for K & L; the tail of each vector marks the measurement point. The turbulence quantities $\overline{u^2}$, $\overline{v^2}$, $\overline{w^2}$ are summarised as contour and surface maps in figures 67 and 68 respectively. The quantities $\overline{uv}$, $\overline{uw}$ & $\overline{vw}$ are presented likewise in figures 69 & 70.

In the -Z side of the junction (plane K), the contours of $\overline{U}$, $\overline{u^2}$, $\overline{v^2}$, $\overline{w^2}$ & $\overline{uv}$ far from the corner are parallel to the plate. Close to the corner, the contours dip towards the plate. These features are all consistent with fluid of higher freestream momentum and lower turbulence activity being brought into the corner. However, apart from the expected increase in $\overline{uw}$ close to the wing surface, the lack of activity in $\overline{uw}$ & $\overline{vw}$ on the whole in plane K is extremely surprising. For such a flowfield, one would expect concentrations of these quantities to be present a short distance from the corner, due to the presence of a horseshoe vortex. Additionally the cross-flow velocities in plane K are very weak compared to U_∞, but show that there is slight displacement flow away from the wing

surface (the majority of these velocities are approximately double the error in the mean velocities). They do not show any indication of a streamwise vortex however.

In the $+Z$ side of the junction (plane L), the thickening of the boundary layer on the plate at x_3 = 40 mm is believed to be the continuation downstream of the separation line from around the nose, although this far downstream the term separation line is probably not strictly justified. A more appropriate term might be shear layer between the separation region and plate flow outboard of this. The data have been compared to the oil-flow pattern in plate 3(b), but due to the extremely weak separation, the pattern is too indistinct at this chordwise distance to confirm the supposition. The best estimate that can be made from plate 3(b), is that the separation line lies at very approximately x_3/mm = 30 to 40 from the corner; due to the camera angle, there is a foreshortening effect on the distances on the plate, normal to the wing surface. The cross-flow velocities are relatively weak over much of the plane and do not show any firm evidence of a vortex. It appears that the rudimentary vortex shown in figure 55(b) has dissipated with distance dowstream.

Just inboard of the shear layer on the plate, $\overline{U}$ is extremely high. This coincides with concentrations of $\overline{u^2}$, $\overline{v^2}$, $\overline{w^2}$, $\overline{uv}$ & $\overline{vw}$, that for $\overline{uw}$ being very slightly inboard of the others. As high velocity fluid is directed into the junction at the leading edge by the pressure field of the wing, it must mix to some extent with the shear layer from the separated plate boundary layer as it is skewed around the nose. This is the probable explanation of the concentrations of high $\overline{U}$, "normal stresses" & $\overline{uv}$ at x_3 = 30 mm. The weak concentration of $\overline{vw}$ at x_3 = 30 mm is believed to arise from the skewing of the separation region around the leading edge. The fluctuations which produce $\overline{uv}$ at the leading edge are also skewed such that small components, parallel to the YZ plane, arise. The concentration of $\overline{uw}$ on the plate and its location, is more difficult to explain. It coincides with a local displacement of the $\overline{U}/U_\infty$ = 1.0 contour away from the plate in figure 64(b), upflow from the plate in figure 66(b) and a region where the contours of $\overline{u^2}$, $\overline{v^2}$, $\overline{w^2}$ are tentative since the data show scatter either side of the contour intervals. The phenomena are believed to be linked, but what causes them is uncertain, although it may

arise in the flow very close to the leading edge corner. Additional measurements, further upstream, are needed to establish the origin of the $\overline{uw}$ concentration and upflow.

However there are no reservations about the consistency of the results between $15 \geq x_3/\text{mm} \geq 10$ in plane L. There high streamwise velocities coincide with considerable reductions in the cross-flow velocities and turbulence activity, as a result of the freestream flow being directed into the junction. Nor is there any doubt about the rapid and large increases of turbulence in plane L very close to wing, coincident with a local thickening of the viscous region on the wing and relatively large cross-flow velocities away from the plate surface.

Again though, there is no indication of a coherent vortex in this plane. The rudimentary vortical motion shown in the plane J near the leading edge appears to have been dissipated, which confirms that the junction separation is weak and that a fully-developed horseshoe vortex has not been formed.

Direct comparisons with the flow in straight- or swept-back-wing/body junctions are not possible due to several reasons, the main one being the profile of the *HH10* wing. A considerable amount of turbulence data is presented by Bernstein & Hamid (1993) around a NACA-0012 swept-back wing. However the data were measured nearer the nose, or aft of the trailing edge, of their junction and at different values of wing lift coefficients than the measurements in the current investigation. A very coarse comparison with the results of Bernstein & Hamid (1993) however, indicates that the non-dimensionalised turbulence intensity $\overline{q^2}/U_\infty^2$ at $X/c \approx 0.15$ in their junction, is in general higher than at $X/c \approx 0.3$ the *HH10* junction. However it should be remembered that the turbulence levels will decrease with distance downstream and this comparison is only tentative.

6.6.4 - The mean-velocity field in the trailing-edge cross-plane

The non-dimensionalised, mean velocities $(\overline{U}, \overline{V}, \overline{W})/U_\infty$ at $X = 500$ mm (trailing edge) are shown in profile form in figures 71 & 72. The format of the figures is similar to those

for the mean velocities in planes K & L, but here each graph is at a distance Z normal to the chord line.

At the trailing edge, apart from the fact that the boundary layer thickness has approximately doubled, the profiles of $\overline{U}$ & $\overline{V}$ furthest from the chordline on both sides of the junction resemble their respective profiles upstream of the junction in figure 41. The profiles of $\overline{W}$ far from the chord line are dissimilar however, both to the upstream profile and each other. On the -Z side, the $\overline{W}$ is approximately zero far above the plate surface, but becomes progressively more negative nearer the plate. On the +Z side, $\overline{W}$ remains at a constant, negative value over the length of the traverse.

As the stations move closer to the chord line, whereas the $\overline{U}$, $\overline{V}$ & $\overline{W}$ profiles in the -Z side of the trailing edge in figure 71 remain very similar to each other until quite close to the chord line, the $\overline{U}$ & $\overline{V}$ profiles in the +Z side of the trailing edge show marked changes with Z. The $\overline{U}$ profiles on both sides show a considerable change of form, showing an "S"-shaped, wall-jet-like profile near the plate surface. Very near the chord line, the $\overline{U}$ velocities *close to the plate surface* are higher overall in the -Z side than in the +Z side, the latter velocities obviously being affected by the strong adverse pressure gradient that exists between $300 \leq X/\text{mm} \leq 500$ on the upper surface of the wing and the flow separation from the upper surface. At $Z = 0$ mm the wall-jet-like profile has disappeared and is replaced with a $\overline{U}$ profile that reflects the position of the probe within the wake of the wing[4].

The $\overline{V}$ profiles do not show much change as Z reduces, except near the chord line, where they indicate spanwise flow down the trailing edge, into the junction. However the profiles of $\overline{W}$ show different traits on the 2 sides of the trailing-edge cross-plane. As $|Z|$ reduces, the profiles in the -Z side tend to a form similar to the $\overline{U}$ profiles, whereas those in the +Z side become crudely, mirror images of the $\overline{U}$ profile at each station, but over a

---

[4] One should recall that as Y increases, the probe becomes further from the trailing edge due to the sweep angle of the wing.

smaller range of velocities. Importantly the trends shown in figures 71 & 72 are extremely smooth, *i.e.* very little scatter. The variation in $\overline{W}$ suggests that vortices exist in the trailing-edge cross-plane and again, contours and vector plots to examine the flow structure more easily are presented later.

6.6.5 - Estimates of skin-friction coefficient in the trailing-edge cross-plane

To estimate C_f, the $\overline{U}$-velocity profiles in plane *TE* were plotted using "law-of-the-wall" coordinates (eqn 6.1). A correction Y_o had to be employed here also to bring the experimental points and the log-law together. These profiles of $\overline{U}/u_\tau$ are shown in figures 73 & 74, for $Z < 0$ mm and $Z > 0$ mm respectively. For each profile an attempt was made to fit a straight line through at least 5 points over the range $30 \leq \left(\frac{u_\tau (Y - Y_o)}{\nu}\right) \leq 350$; however this was often not possible[5]. The values of the offsets Y_o used are presented below in table 5:

Table 5 - Values of offsets Y_o at stations in plane *TE* to fit the $\overline{U}$ velocity profile to the law-of-the -wall

Z/mm	-60	-40	-30	-25	-20	-15	-10	-5
Y_o/mm	0.927	0.94	0.03	0.72	1.36	1.58	1.4	0.49
Z/mm	+60	+40	+30	+25	+20	+15	+10	+5
Y_o/mm	1.58	1.79	2.32	2.15	2.43	2.3	2.0	0.368

The profiles furthest from the chord line are similar to each other. As $|Z|$ reduces, the profiles show considerable changes: in the $-Z$ side of the junction, the profiles move closer to the straight line, such that at Z = -15 mm the profile almost lies on the straight line. Closer to the chord line, at Z/mm = -10 & -5, the profiles are inside the wing boundary

---

[5] A 5-point fit was obtained to the profiles at Z/mm = +10, 15 & 20 only. A 4-point fit was obtained to the other profiles, except those at Z/mm = -30 & -5, where straight-line fits over the valid range were obtained to the first 3-points only.

layer/wake and the effect on the profiles is marked, as the upper portion of the profiles depart below the straight line. It is interesting that log-law fits can still be made over a portion of these 2 profiles as the viscous region is no longer a flat-plate boundary-layer flow. However straight-line portions of the velocity profiles were also found in such cases by Bernstein & Hamid(1995) and Kubendran, McMahon & Hubbartt (1984).

On the $+Z$ side of the chord line (figure 74), as Z reduces the profiles develop local peaks and troughs which eventually cross back and forth across the straight line fit. These features can be traced back to the contours of $\overline{U}/U_\infty$. The quality of the straight line fit to the profiles using 4 points at $Z = 25$ mm and even 5 points at Z/mm = 20 & 15 is poor. At these stations the corrections Y_o needed to bring the measured profiles to meet the straight line were as large as the perpendicular distance between the wire support prongs. This places the probe in contact with, or even below the plate surface, which seems ridiculous as a gap was always seen between the probe and the plate at the start of each traverse.

Calculations of the boundary-layer shape parameter H across plane TE (figure 75) show that at Z/mm = 15 & 20, the shape parameter is negative. Whilst this fits in with the velocity profile for a wall-jet, referring to the viscous region there as a boundary layer is not strictly valid. As such, the log-law fit cannot be applied to the profiles at these values of Z with any confidence. Cross-checking these profiles with the flow-visualisation pictures, the flow separation on the upper surface, just upstream of the trailing edge, shown in plate 3(d), leaves a "footprint" on the plate surface. At $X = 500$ mm this footprint lies at approximately $15 \leq Z/\text{mm} \leq 20$ and thus the velocity profiles are immersed in this shear layer which is, for practical purposes, vertical. At Z/mm = 10 & 5, the fits to the data are much better and H is positive again. However the correction to the probe height at 10 mm is still just too large to be possible ($Y_o = 2$ mm); plate 3(d) shows this station is still rather close to the shear layer. At $Z = 5$ mm, the value of Y_o is much more plausible; again it is strange to find straight-line region this close to the chord at the trailing edge, as here the probe is inside the wing wake.

The corresponding values of skin-friction coefficient C_f are shown in figure 76. Remarkably, the value of C_f far from the chord line is approximately 25% less than that

500 mm upstream of the junction and varies smoothly with Z. As the chord line is approached, the skin-friction in the -Z side of the chord line increases to reach values similar to that in the undisturbed plate boundary layer at $Z \approx 15$ mm, then decreases rapidly very close to the chord line. In the +Z side, at first sight C_f remains approximately constant, before reducing considerably in value close to the chord line. All values need to be treated with caution however. At Z/mm = 15 & 20 the values of C_f should not be regarded with any confidence since H is negative there. At Z/mm = 10 & 25, whilst H is positive, the validities of the values of Y_o are questionable and another method of measuring skin friction would probably serve better, such as the array of hot wires parallel with the plate surface used by Devenport & Simpson (1989).

On the -Z side of the chord line, the qualitative behaviour of the skin-friction distribution matches the findings of Bernstein & Hamid (1995) and Kubendran, McMahon & Hubbartt (1984). Also, on the +Z side *e.g.* Z = 5 mm, the very low values of skin friction are qualitatively similar to the findings of previous researchers obtained in the same way, as here the station is inside the wake region.

6.6.6- The turbulence velocity-correlation ("Reynolds stress") field in the trailing-edge cross-plane

The turbulence quantities $\overline{u^2}$, $\overline{v^2}$, $\overline{w^2}$, $\overline{uv}$, $\overline{uw}$ & $\overline{vw}$ in plane TE at X = 500 mm, are presented in figures 77 to 80 as profiles (non-dimensionalised by U_∞^2) through the boundary layer.

Far from the chord line in both sides of the wing, the "normal stress" profiles resemble those in the undisturbed boundary layer, upstream of the junction. As $|Z|$ reduces, the profiles in the +Z side begin to change almost straight away, whereas those in the -Z side do not show appreciable changes until very close to the chord line. However, the form of the changes is similar on both sides of the chord line. Additional peaks appear near the tops of the profiles, which then develop to dominate very close to the chord line. On the chord line itself in figure 80(i), these peaks have all but disappeared, the profiles following a slightly meandering pattern.

The profiles of $\overline{uv}$, $\overline{uw}$ & $\overline{vw}$ furthest from the junction are also very similar to those for an equilibrium boundary layer. As $|Z|$ decreases, these similarities largely continue in the -Z side of the junction until quite close to the chord line. As was found for $\overline{u^2}$, $\overline{v^2}$ & $\overline{w^2}$, this contrasts with the +Z side where large changes in the profiles are evident, some of which become double-peaked. From +30 ≥ Z/mm ≥ +10, besides the large changes in magnitude, the $\overline{uv}$ & $\overline{uw}$ profiles also change sign and back again, the peak values being measured at Z = + 15 mm. The $\overline{vw}$ profiles in the +Z side however show scatter either side of zero, occasionally reaching small peaks, but these are rare occurrences. Overall the profiles again showed slightly more scatter than obtained from the yawmeter and the X-wire measurements at X = 300 mm, but nothing grossly outside the estimated accuracy of the measurements.

6.6.7 - Summary of the flow in the trailing-edge cross-plane

The longitudinal mean velocities, the cross-flow velocities and the first-order correlations of the velocity fluctuations in plane *TE* are presented in figure 81 to 87. The longitudinal velocities and velocity correlations are plotted as contour and surface maps, the cross-flow velocities as vector plots.

The dip in the contours of $\overline{U}$ towards the plate between -20 ≥ Z/mm ≥ -15 coincides with dips in the contours of $\overline{u^2}$, $\overline{v^2}$, $\overline{w^2}$ & $\overline{uv}$. These local reductions also lie just nearer the chord line than what appears to be the centre of rotation of a weak vortex lying just above the plate at Z = -20 mm in figure 83. This vortex is believed to originate in the adverse pressure gradient in the streamwise corner, downstream of plane *K*. It appears to bring lower-turbulence fluid from outside the viscous region, towards the plate inboard of its centre. However nearer the chord line, the fluid that is brought into the junction meets the spanwise flow down the trailing edge and the flow from the +Z side of the junction. Hence the cross-flow velocities at Z = -5 mm in figure 83 suddenly diminish between 25 ≥ Y/mm ≥ 10, coincident with concentrations of all 6 turbulence quantities which correlate well with each other, both in shape and location. These dominate the turbulence activity on this side of the chord line, reaching levels much higher than found in an equilibrium boundary

layer. However the lack of turbulence activity elsewhere on this side of the wing is remarkable.

On the $+Z$ side of plane *TE*, the ridge-shaped concentrations of $\overline{u^2}$, $\overline{v^2}$ & $\overline{w^2}$, from $(Z, Y)/\text{mm} \approx (5, 5)$ to $(35, 35)$, all coincide closely with concentrations of $\overline{uv}$, $\overline{uw}$ & $\overline{vw}$. Most interestingly, whilst the concentrations of $\overline{uw}$ & $\overline{vw}$ are negative all along those ridges, $\overline{uv}$ changes sign partway along. These stress concentrations all lie where the contours of $\overline{U}/U_\infty$ show a local thickening of the wing wake in the $+Z$ direction at $Y \approx 25$ mm in figure 81. The concentrations are also slightly below and to the right of the circulatory flow centred at $(Z, Y)/\text{mm} \approx (15, 30)$ in figure 83. The high levels of turbulence shown by the contours there would appear to be a result of mixing as the cross flow in towards the chord line from $Z \geq 30$ mm meets the circulatory flow.

Very close to the plate at $(Z, Y)/\text{mm} \approx (35, 10)$, concentrations of $\overline{u^2}$, $\overline{v^2}$ & $\overline{w^2}$, higher than in an equilibrium boundary layer, are coincident with a region of high $-\overline{uv}$. The contours of $\overline{vw}$ also hint of a slight increase in levels of that component there. In between these concentrations near the plate surface and the ridges of high $\overline{u^2}$, $\overline{v^2}$ & $\overline{w^2}$ from $(Z, Y)/\text{mm} \approx (5, 5)$ to $(35, 35)$, are valley-like regions where $\overline{u^2}$, $\overline{v^2}$ & $\overline{w^2}$ are similar to those in an equilibrium boundary layer. These regions coincide with the influx of higher U-velocity fluid, high cross-flow velocities and very low (or even zero) values of $\overline{uv}$, $\overline{uw}$ & $\overline{vw}$.

At $X/c = 1.0$, conclusive comparisons of the turbulence levels at the trailing edge, due to the horseshoe separation, with swept-back- or straight-wing/body junctions are not possible. Not even tentative conclusions can be made, partly, due to the reasons mentioned in Section 6.6.3 and also because of the separation along the trailing edge of the wing, which complicates the picture in the trailing-edge cross-plane. The results themselves however indicate that the interference drag may be quite low. Therefore further investigations need to be performed to quantify the flow in this junction with those, using the same wing profile but mounted (a) straight and (b) swept back, on the plate.

Chapter 7

Conclusions and Suggestions for Further Work

7.1 - General conclusions

- Measurements have been made of the pressure, velocity and turbulence fields in the junction region between a swept-forward wing and a flat plate on which a fully-developed, turbulent boundary layer had grown. These measurement are thought to be unique.

7.2 - Specific conclusions

- Separation of the plate boundary layer, as it was skewed around the leading edge, occurred so close to the junction that it was difficult to resolve the flow close to the leading edge.

- No firm evidence was found for the existence of a horseshoe vortex, such as found in the junctions between unswept- or swept-back-wings with flat plates. It is believed that any such evidence is confined to a very thin region outside the range of measurement.

- Surface pressures measured on the wing, integrated to give the local lift and pressure-drag coefficients, showed that at low incidence, the expected increase in loading near the root did not occur and the effect of the interference on the pressure drag was beneficial. At high incidences, the junction displayed severe root-stall characteristics.

- At $\alpha = 0°$, high-momentum, low-turbulence fluid is brought into the streamwise corners of the junction, aft of the mid-chord and at the trailing edge. Weak rotational flow is evident at the trailing edge, but is believed to arise from flow separations in the streamwise corners just upstream of the trailing edge.

- The turbulence behaviour is in qualitative agreement with the findings of previous researchers, the levels of the "Reynolds stresses" being higher in the suction side of the junction than in the compression side. In some parts of the measurement planes, the levels of turbulence are considerably less than would be found in an equilibrium boundary layer.

- The junction appears to have had a beneficial effect on the skin friction on the plate, except for 2 localised areas. One is very close to the junction on the compression side, where C_f is similar to that upstream of the junction. The other region is close to the junction on the suction side, where the estimations are inconclusive.

- Although the skin friction on the wing was not measured, the data indicate that at values of C_L typical of flight, this section and sweep angle could have a beneficial effect on the interference aerodynamics at the junction, reducing the secondary flow and thereby perhaps, the drag.

7.3 - Recommendations for further work

- The complicated geometry of the model gives rise to some difficulties in interpreting the results. Further experiments need to be carried out to separate the effects of forward sweep, nose curvature and camber.

- A good starting point for this would be to use a body with a bluff, *e.g.* semi-circular leading edge. An additional simplification would be to remove the adverse pressure gradient found over the rear of an aerofoil by using a parallel-sided afterbody.

- A technique which may help elucidate the structure of the flow approaching the leading edge, is Particle Image Velocimetry. This technique allows an instaneous "snapshot" of a plane under investigation to be acquired and analysed for velocity and vorticity information.

Bibliography

Abid R (1988) Extension of the Johnson-King turbulence model to the 3 *D* flows. AIAA paper 88-0223.

Abid R & Schmitt R (1986) Experimental study of a turbulent horseshoe vortex using a 3-component laser velocimeter. AIAA paper 86-1069. AIAA/ASME 4th Fluid Dynamics, Plasma Dynamics and Lasers Conference, Georgia.

Agui JH & Andreopoulos J (1992) Experimental investigation of a 3-dimensional boundary layer flow in the vicinity of an upright, wall-mounted cylinder. ASME Journal of Fluids Engineering, **114**, pp 566-576.

Arnott AD, Bernstein L & Petty DG (1993) The aerodynamic interaction between a swept-forward wing and a plate. QMW ER-1016 (commercial-in-confidence), Dept of Aero Eng, Queen Mary & Westfield College, University of London.

Arnott AD, Bernstein L & Petty DG (1996) A note on the pressure drag of a foward-swept-wing plate/junction. The Aeronautical Journal, **100**, pp 281-284.

Arnott AD & Jones MA (1994) Notes on surface-flow visualisation using oil/dye mixtures and tufts, and forced transition due to surface roughness. QMW EP-1096, Dept of Aero Eng, Queen Mary & Westfield College, University of London.

Baker CJ (1979) The laminar horseshoe vortex. Journal of Fluid Mechanics, **95**, pp 347-367.

Baker CJ (1980) The turbulent horseshoe vortex. Journal of Wind Engineering and Industrial Aerodynamics, **6**, pp 9-23.

Baldwin BS & Lomax H (1978) Thin-layer approximation and algebraic model for separated turbulent flows. AIAA paper 78-257.

Barber TJ (1978) An investigation of strut/wall interaction losses. Journal of Aircraft, **15**, pp 676-681.

Bernstein L (1991) Private communication.

Bernstein L & Hamid S (1993) An experimental investigation of wing/body junction flows with and without a fillet. QMW EP-1095, Dept of Aero Eng, Queen Mary & Westfield College, University of London.

Bernstein L & Hamid S (1995) On the effect of a swept-wing/plate junction flow on the lift and drag. The Aeronautical Journal, **99**, pp 293-305.

Bernstein L & Hamid S (1996) On the effect of a strake-like junction fillet on the lift and drag of a wing. The Aeronautical Journal, **100**, pp 39-52.

Bradshaw P (1971) Calculation of 3-dimensional turbulent boundary layers. Journal of Fluid Mechanics, **46**, pp 417-445.

Braslow AL Hicks RM & Harris RV (1966) Use of grit-type boundary layer transition strips on wind tunnel models. NASA TN D-3579.

Burns BRA (1985) Forward sweep: the pros and cons. Interavia, 1/1985, pp 39-41.

Cebeci T & Smith AMO (1974) *Analysis of turbulent boundary layers*. Published by The Academic Press.

Chapman GT (1986) Topological classification of flow separation on 3-dimensional bodies. AIAA paper 86-0485. AIAA 24th Aerospace Sciences Meeting, Reno, Nevada.

Chu J, Rios-Chiquete E, Sarohia S & Bernstein L (1987) The "Chu-Tube"; a velocimeter for use in highly-sheared, 3-dimensional, steady flows. The Aeronautical Journal, **91**, pp 142-149.

Clauser FH (1956) The turbulent boundary layer. Advances in Applied Mechanics, **4**, pp1-51. Edited by Dryden HL & Von Karman Th. Published by The Academic Press.

Dallmann U (1983) Topological structures of 3-dimensional vortex flow separation. AIAA paper 83-1735. AIAA 16th Fluid and Plasma Dynamics Conference, Danvers, Massachusetts.

Délery JM (1992) Physics of vortical flows. Journal of Aircraft, **29**, pp 856-876.

Devenport WJ Agarwal NK, Dewitz MB, Simpson RL & Poddar K (1990) Effects of a fillet on the flow past a wing/body junction. AIAA Journal, **28**, pp 2017-2024.

Devenport WJ & Simpson RL (1986) Some time-dependant features of turbulent appendage-body juncture flows. 16th Symposium of Naval Hydrodynamics, Berkeley, California.

Devenport WJ & Simpson RL (1987) Turbulence structure near the nose of a wing/body junction. AIAA paper 87-1310. AIAA 19th Fluid Dynamics, Plasma Dynamics and Lasers Conference, Honolulu.

Devenport WJ & Simpson RL (1988) LDV measurements in the flow past a wing/body junction. 4th International Symposium on Applications of Laser Anemometry to Fluid Mechanics, Lisbon.

Devenport WJ & Simpson RL (1989) Time-dependant structure in wing/body junction flows. Turbulent Shear Flows, **6**, Springer Verlag, Berlin, pp 232-248.

Devenport WJ & Simpson RL (1990) Time-dependant and time-averaged turbulence structure near the nose of a wing/body junction. Journal of Fluid Mechanics, **210**, pp 23-55.

Devenport WJ & Simpson RL (1992) Flow past a wing/body junction — experimental evaluation of turbulence models. AIAA Journal, **30**, pp 873-881.

Dickinson SC (1986) An experimental investigation of an appendage/flat-plate juncture flow. Report no 86/052, David Taylor Naval Ship R&D Centre, Bethesda, Maryland.

Dryden HL (1953) Review of published data on the effect of surface roughness on transition from laminar to turbulent flow. Journal of the Aeronautical Sciences, **20**, pp 477-482.

Eckerle WA & Awad JK (1991) The effect of freestream velocity on the 3-dimensional, separated-flow region in front of a cylinder. Journal of Fluids Engineering, **113**, pp 37-44.

Gersten K (1959) Corner interference effects. AGARD Report no. 299.

Goldsmith J (1961) Laminar flow at the juncture of 2 aeroplane components. In *Boundary Layer and Flow Control*, vol 2, edited by Lachmann GV, pp 1000-1006. Published by Pergamon Press.

Gough ML (1928) The effects of fillets between wings and fuselages on the drag and propulsive efficiency of an airplane. NACA TN-299.

Granville PS (1953) The calculation of viscous drag of bodies of revolution. Report no. 849, David Taylor Model Basin, Bethesda, Maryland.

Green JE, Weeks DJ & Brooman JWF (1972) Prediction of turbulent boundary layers and wakes in compressible flow by a lag-entrainment method. RAE TR-72231.

Griffin KE & Jonas FM (1983) Wake characteristics and interactions of the canard/wing lifting-surface combination of the X-29 technology demonstrator. AIAA paper 83-1835. AIAA Applied Aerodynamics Conference, Danvers Massachusetts.

Hawthorne WR (1954) The secondary flow about struts and aerofoils. Journal of the Aeronautical Sciences, **21**, pp 588-608 & 648.

Hoerner SF (1965) *Fluid dynamic drag*. Published by author, pp 8-1—8-20.

Holzbauer S (1965) Swept-forward wings. Interavia, **5**, pp 380-382.

Horton HP (1967) A semi-empirical theory for the growth and bursting of laminar separation bubbles. ARC CP-1073.

Hung C-M (1991) Computation of Navier-Stokes equations for 3-dimensional flow separation. AIAA Journal, **29**, pp 1659-1667.

Hunt JCR, Abell CJ, Peterka JA & Woo H (1978) Kinematical studies of the flows around free or surface-mounted obstacles; applying topology to flow visualisation. Journal of Fluid Mechanics, **86**, pp 179-200.

Ishmael SD & Wierzbanowski TJ (1986) X-29 initial flight test results. Aerospace, pp 9-14.

Johnston JP (1960) The turbulent boundary layer at a plane of symmetry in a 3-dimensional flow. Journal of Basic Engineering, **82**, pp 622-627.

Johnston LJ (1986) Two-dimensional turbulent boundary layer/wake mixing. PhD thesis, University of London.

Jupp JA (1980) Interference aspects of the A310 high-speed wing configuration. In Subsonic/transonic Configuration Aerodynamics, AGARD CP-285, pp 11.1-11.16.

Kaul UK, Kwak D & Wagner D (1985) A computational study of saddle point separation and horseshoe vortex system. AIAA paper 85-0182. AIAA 23rd Aerospace Sciences Meeting, Reno Nevada.

Kawahashi M & Hosoi K (1989) Beam-sweep laser speckle velocimetry. Experiments in Fluids, **8**, pp 109-111.

King DA & Williams BR (1988) Developments in computational methods for high-lift aerodynamics. The Aeronautical Journal, **92**, pp 265-288.

Kubendran LR, Bar-Sever A & Harvey WD (1988) Flow control in a wing/fuselage type juncture. AIAA paper 88-0614. AIAA 26th Aerospace Sciences Meeting, Reno Nevada.

Kubendran LR & Harvey WD (1985) Juncture flow control using leading-edge fillets. AIAA paper 85-4097. AIAA 3rd Applied Aerodynamics Conference, Colarado Springs, Colorado.

Kubendran LR, McMahon H & Hubbartt JE (1984) Interference drag in a simulated wing/fuselage type juncture. NASA CR-3811.

Kubendran LR, McMahon H & Hubbartt JE (1986) Turbulent flow around a wing/fuselage type juncture. AIAA Journal, **24**, pp 1447-1452.

Kuethe AM & Chow C-Y (1986) *Foundations of aerodynamics (bases of aerodynamic design)*, 4th edition. Published by Wiley.

LaFleur RS (1988) Exploration of the iceformation method applied to a diffuser. ASME Journal of Fluids Engineering, **110**, pp 244-250.

LaFleur RS & Langston LS (1993) Drag reduction of a cylinder/endwall junction using the iceformation method. ASME Journal of Fluids Engineering, **115**, pp 26-32.

Lakshmanan B & Tiwari SN (1993) Study of supersonic intersection flowfield at modified wing-body junctions. AIAA Journal, **31**, pp 877-883.

Legendre R (1956) Séparation de l'écoulement laminaire tridimensionnel. La Recherche Aéronautique, **54**, pp 3-8.

Lighthill MJ (1963) Attachment and separation in 3-dimensional separated flows. In *Laminar Boundary Layers*, edited by Rosenhead L II, pp 72-82. Published by Oxford University Press.

Maltby RL (1962) Flow visualisation in wind tunnels using indicators. AGARDograph 70, pp 1-74.

Martinuzzi R & Tropea C (1993) The flow around surface-mounted prismatic obstacles placed in fully-developed channel flow. ASME Journal of Fluids Engineering, **115**, pp 85-92.

Maskell EC (1955) Flow separation in 3 dimensions. RAE Aero. report 2565.

Maughmer M, Hallman D, Ruszkowski R, Chappel G & Waitz I (1989) Experimental investigation of wing/fuselage integration geometries. Journal of Aircraft, **26**, pp 705-711.

Mehta RD (1984) Effect of wing nose shape on the flow in a wing/body junction. The Aeronautical Journal, **88**, pp 456-460.

Merzkirch W (1987) *Flow visualisation*, 2nd edition. Published by The Academic Press.

Mojola OO (1972) Turbulent boundary layer along a streamwise corner. PhD Thesis, University of London.

Nangia RK (1984) Subsonic investigations on configurations with forward- and aft-swept wings. ICAS paper 84-2.6.2, 14th International Council of the Aeronautical Sciences Congress, Toulouse.

Ölçmen SM & Simpson RL (1994) Influence of wing shapes on surface pressure fluctuations at wing-body junctions. AIAA Journal, **32**, pp 6-15.

Özcan O & Ölçmen SM (1988) Measurements of turbulent flow behind a wing/body junction. AIAA Journal **26**, pp 494-496.

Pentz M & Shott M (1988) *Handling experimental data*. Edited by F Aprahamian. Published by The Open University Press.

Petrie JAH (1979) Development of an efficient and versatile program for aerodynamic problems. PhD Thesis, Leeds University.

Philips DB, Cimbala JM & Treaster AL (1992) Suppression of the wing/body junction vortex by body surface suction. Journal of Aircraft, **29**, pp 118-122.

Pierce FJ & Shin J (1992) The development of a turbulent junction vortex system. ASME Journal of Fluids Engineering, **114**, pp 559-565.

Rae WH & Pope A (1984) *Low-speed wind tunnel testing*, 2nd edition. Published by Wiley.

Redecker G & Wichmann G (1991) Forward sweep – a favourable concept for a laminar flow wing. Journal of Aircraft, **28**, pp 97-103.

Scheiman J & Kubendran LR (1985) Juncture flow measurements using laser velocimetry. AIAA paper 85-1612. AIAA/ASME 18th Fluid Dynamics, Plasma Dynamics and Lasers Conference, Cincinatti, Ohio.

Schlichting H (1979) *Boundary-layer Theory*, 7th edition. Published by McGraw-Hill.

Schwind R (1962) The 3-dimensional boundary layer near a strut. Gas Turbine Laboratory Report, MIT, USA.

Sepri P (1973) An investigation of the flow in the region of the junction of a wing and a flat plate normal to the span. QMC ER-1002, Department of Aeronautical Engineering, Queen Mary College, University of London.

Shabaka IMMA & Bradshaw P (1981) Turbulent flow measurements in an idealised wing/body junction. AIAA Journal, **19**, pp 131-132.

Siddall RG & Davies TW (1972) An improved response equation for hot-wire anemometry. International Journal of Heat and Mass Transfer. **15**, pp 367-368.

Spacht G, *et al* (1986) Unusual aerodynamics of X-29. Aerospace America, February 1986, pp34-38.

Sung C-H & Lin C-W (1988) Numerical investigation on the effect of fairing on the vortex flows around airfoil/flat plate junctures. AIAA paper 88-0615.

Tennekes H & Lumley JL (1972) *A first course in turbulence*. Published by The Massachusetts Institute of Technology Press.

Thwaites B (1960) *Incompressible aerodynamics*, (editor). Published by The Oxford University Press.

Tobak M & Peake DJ (1979) Topology of 2-dimensional and 3-dimensional separated flows. AIAA paper 79-1480. AIAA 12th Fluid Dynamics and Plasma Dynamics Conference, Williamsburg, Virginia.

Tobak M & Peake DJ (1982) Topology of 3-dimensional separated flows. Annual Review of Fluid Mechanics, **14**, pp 61-85.

Tritton DJ (1988) *Physical Fluid Dynamics*, 2nd edition. Published by The Oxford University Press.

Uhuad GC, Weeks TM & Large R (1983) Wind tunnel investigation of the transonic aerodynamic characteristics of swept-forward wings. Journal of Aircraft, **20**, pp 195-202.

Visbal MR (1991) Structure of laminar juncture flows. AIAA Journal, **29**, pp 1273-1282.

Wang KC (1972) Separation patterns of boundary layer over an inclined body of revolution. AIAA Journal, **10**, pp 1044-1050.

Wang KC (1974) Boundary layer over a blunt body at high incidence with an open-type of separation. Proceedings of the Royal Society of London, Series A, **340**, pp 33-55.

Warwick G (1984) Forward sweep technology. Flight International, June 1984, pp 1563-1567.

Weissharr TA (1980) Divergence of forward-swept composite wings. Journal of Aircraft, **17**, pp 442-448.

White FM (1991) *Viscous fluid flow*, 2nd edition. Published by McGraw-Hill International.

Wocke H & Davies LW (1964) Swept-forward wings for the HFB 320 Hansajet. Aircraft Engineering, **36**, pp 248-251.

Wood DH & Westphal RV (1992) Measurements of the flow around a lifting wing/body junction. AIAA Journal, **30**, pp 6-12.

Young AD (1989) *Boundary layers*. Published by BSP Professional Books.

Appendix A

Positions of Pressure Tubes Around the Streamwise Wing Section

Chordwise position of tube			
Upper surface		Lower surface	
x/*c*	*x*/mm	*x*/*c*	*x*/mm
0.00	0.0	0.00	0.00
0.012	6.0	0.013	6.5
0.03	15.0	0.03	15.0
0.05	25.0	0.05	25.0
0.07	35.0	0.07	35.0
0.09	45.0	0.12	60.0
0.12	60.0	0.20	100.0
0.15	75.0	0.30	150.0
0.18	90.0	0.40	200.0
0.24	120.0	0.50	250.0
0.30	150.0	0.60	300.0
0.40	200.0	0.70	350.0
0.50	250.0	0.80	400.0
0.55	275.0	0.88	440.0
0.60	300.0	0.92	460.0
0.65	325.0	0.96	480.0
0.70	350.0	1.00	500.0
0.75	375.0		
0.80	400.0		
0.85	425.0		
0.90	450.0		
0.94	470.0		
0.98	490.0		
1.00	500.0		

Appendix B

Heights of the Rows of Pressure Tappings on the Wing

Height above plate			
Y/mm	*Y*/*c*	*Y*/mm	*Y*/*c*
0.88	0.002	48.57	0.970
4.42	0.009	52.98	0.106
8.83	0.018	61.81	0.124
13.25	0.027	70.64	0.141
17.66	0.035	88.29	0.177
22.08	0.044	110.37	0.221
26.49	0.053	132.45	0.265
30.91	0.062	176.59	0.353
35.32	0.071	220.74	0.441
39.74	0.08	264.88	0.529
44.15	0.088	353.18	0.706

Appendix C

Positions of Roughness Strips on the Leading Edge of the Wing

	Position of strip, %*x*/*c*	
Angle of incidence	Upper surface	Lower surface
-3°	7.0	2.5
0°	7.0	7.0
+3°	2.5	7.0
+6°	1.0	7.0
+9°	0.5	7.0

Appendix D

The positions of the planes normal to the local wing-profile tangents in figures 30 & 31, in relation to the leading edge the chord line of the wing

Normal plane	Side of junction that the plane is situated.	Distance *X*/mm downstream of the leading edge at which the normal to the wing profile was drawn.	Angle β_s between the normal to the wing-profile tangent and the O*X* line reversed.
A	-*Z*	0.5	-13.6°
B		1.0	-35.8°
C		2.5	-54°
D		10.0	-72.8°
E		40.0	-81.3°
F	+*Z*	0.5	+15.9°
G		1.0	+44.2°
H		2.5	+53.4°
I		10.0	+62.8°
J		40.0	+77.9°
K	-*Z*	300.0	-96.1°
L	+*Z*	300.0	+92.4°

Appendix E

Velocity Transformations for the X-wire Anemometer

This appendix describes the matrix transformations necessary to resolve the X-wire readings in one axis frame through a 45° angle, into a second axis frame. This leads to the calculation of all 6 components of a matrix incorporating the correlations between the fluctuating velocity components, from which the Reynolds stress tensor can be calculated.

Axes systems

Two *left-handed* cartesian axes systems were defined, the initial system being $Ox_p y_p z_p$ and the new system being $Ox'_p y'_p z'_p$, where the subscript p refers to the X-wire probe axes. These systems are sketched below, along their respective unit vectors (i, j, k) and (i', j', k'):

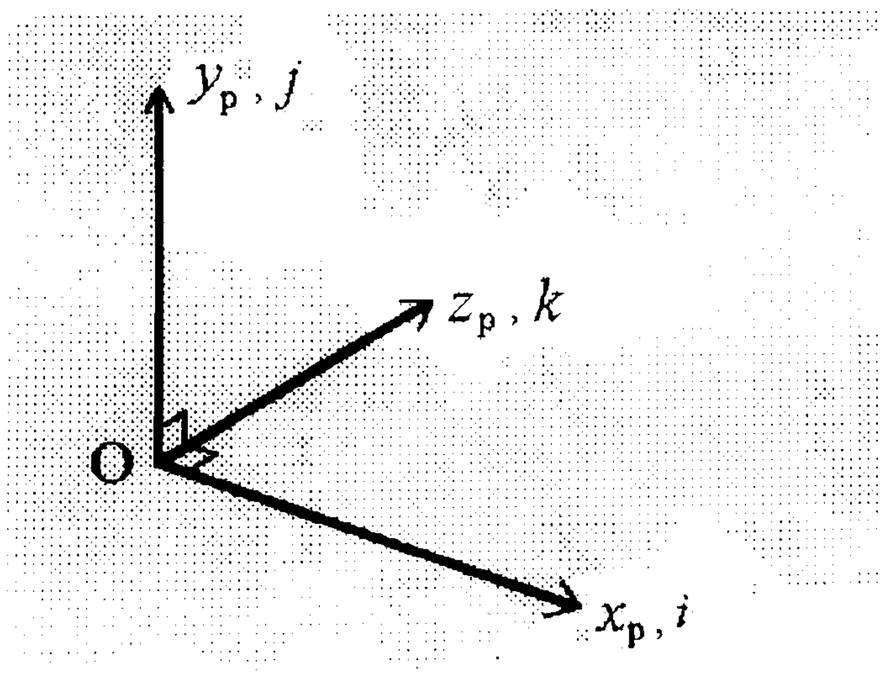

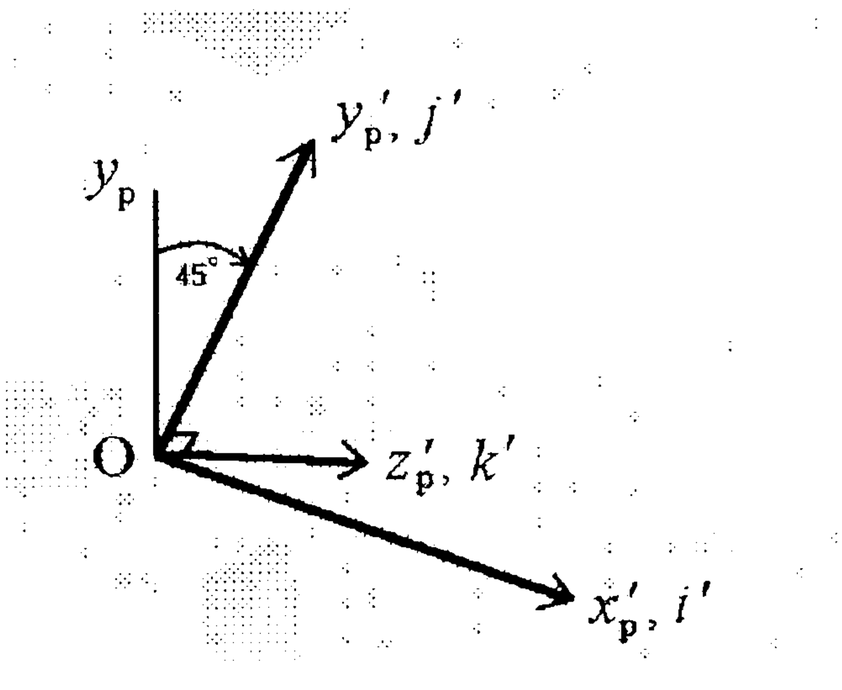

The new system was produced by an anti-clockwise rotation about Ox_p, for a positive rotation in a *left-handed* system. The axes Ox_p & Ox'_p are coaxial, the angles between Oy_p & Oy'_p and Oz_p & Oz'_p being 45° each. The 2 axes systems are thus related.

Fluctuating velocity correlations

The relationship to transform the matrix of correlations of the velocity fluctuations $\boldsymbol{u}_p$ in the initial $Ox_p y_p z_p$ system into its equivalent $\boldsymbol{u}'_p$ in the $Ox'_p y'_p z'_p$ system is:

$$\boldsymbol{u}'_p = [T'] \boldsymbol{u}_p [T] \qquad \ldots\ldots\ldots \text{A1,}$$

where $[T]$ is the matrix of direction cosines and $[T']$ is its transpose. This relationship expands to:

$$\begin{bmatrix} \overline{u'^2_p} & \overline{u'_p v'_p} & \overline{u'_p w'_p} \\ \overline{v'_p u'_p} & \overline{v'^2_p} & \overline{v'_p w'_p} \\ \overline{w'_p u'_p} & \overline{w'_p v'_p} & \overline{w'^2_p} \end{bmatrix} = \begin{bmatrix} l_{11'} & l_{21'} & l_{31'} \\ l_{12'} & l_{22'} & l_{32'} \\ l_{13'} & l_{23'} & l_{33'} \end{bmatrix} \begin{bmatrix} \overline{u^2_p} & \overline{u_p v_p} & \overline{u_p w_p} \\ \overline{v_p u_p} & \overline{v^2_p} & \overline{v_p w_p} \\ \overline{w_p u_p} & \overline{w_p v_p} & \overline{w^2_p} \end{bmatrix} \begin{bmatrix} l_{11'} & l_{12'} & l_{13'} \\ l_{21'} & l_{22'} & l_{23'} \\ l_{31'} & l_{32'} & l_{33'} \end{bmatrix} \qquad \ldots\ldots\ldots \text{A2,}$$

where $l_{11'} = i.i'$ is the cosine of the angle between the Ox_p axis and the Ox'_p axis,

$l_{12'} = i.j'$ is the cosine of the angle between the Ox_p axis and the Oy'_p axis,

$l_{13'} = i.k'$ is the cosine of the angle between the Ox_p axis and the Oz'_p axis,

$l_{21'} = j.i'$ is the cosine of the angle between the Oy_p axis and the Ox'_p axis,

etc..

For a rotation of 45° about the Ox/Ox' axis, the direction cosines become:

$l_{11'} = \cos 0° = 1$	$l_{12'} = \cos 90° = 0$	$l_{13'} = \cos 90° = 0$
$l_{21'} = \cos 90° = 0$	$l_{22'} = \cos 45° = 1/\sqrt{2}$	$l_{23'} = \cos 135° = -1/\sqrt{2}$
$l_{33'} = \cos 90° = 0$	$l_{33'} = \cos 45° = 1/\sqrt{2}$	$l_{33'} = \cos 45° = 1/\sqrt{2}$

The transformation thus becomes:

$$\begin{bmatrix} \overline{u_p'^2} & \overline{u_p' v_p'} & \overline{u_p' w_p'} \\ \overline{v_p' u_p'} & \overline{v_p'^2} & \overline{v_p' w_p'} \\ \overline{w_p' u_p'} & \overline{w_p' v_p'} & \overline{w_p'^2} \end{bmatrix} = \begin{bmatrix} 1 & 0 & 0 \\ 0 & 1/\sqrt{2} & 1/\sqrt{2} \\ 0 & -1/\sqrt{2} & 1/\sqrt{2} \end{bmatrix} \begin{bmatrix} \overline{u_p^2} & \overline{u_p v_p} & \overline{u_p w_p} \\ \overline{v_p u_p} & \overline{v_p^2} & \overline{v_p w_p} \\ \overline{w_p u_p} & \overline{w_p v_p} & \overline{w_p^2} \end{bmatrix} \begin{bmatrix} 1 & 0 & 0 \\ 0 & 1/\sqrt{2} & -1/\sqrt{2} \\ 0 & 1/\sqrt{2} & 1/\sqrt{2} \end{bmatrix} \quad \ldots\ldots\ldots \text{A3}$$

and by multiplying out, gives:

$\overline{u_p'^2} = \overline{u_p^2}$	$\overline{v_p'^2} = \dfrac{\overline{v_p^2} + 2\overline{v_p w_p} + \overline{w_p^2}}{2}$	$\overline{w_p'^2} = \dfrac{\overline{v_p^2} - 2\overline{v_p w_p} + \overline{w_p^2}}{2}$
$\overline{u_p' v_p'} = \overline{v_p' u_p'} = \dfrac{\overline{u_p v_p} + \overline{u_p w_p}}{\sqrt{2}}$	$\overline{u_p' w_p'} = \overline{w_p' u_p'} = \dfrac{\overline{u_p w_p} - \overline{u_p v_p}}{\sqrt{2}}$	$\overline{v_p' w_p'} = \overline{w_p' v_p'} = \dfrac{\overline{w_p^2} - \overline{v_p^2}}{2}$

Using this transformation, it can be seen that the unknown quantity $\overline{v_p' w_p'}$ in $\boldsymbol{u_p'}$ may be calculated from known quantities in $\boldsymbol{u_p}$. For each measurement station $\overline{v_p' w_p'}$ was calculated to complete the matrix $\boldsymbol{u_p'}$. This matrix was then transformed through 45° into the frame in the system $Ox_p y_p z_p$, using the following transformation, to give a second matrix in $Ox_p y_p z_p$, labelled $\boldsymbol{u_p^*}$:

$$\boldsymbol{u_p^*} = \left[T'\right] \boldsymbol{u_p'} \left[T\right] \quad \ldots\ldots\ldots \text{A4},$$

ie:
$$\begin{bmatrix} \overline{u_p^2}^* & \overline{u_p v_p}^* & \overline{u_p w_p}^* \\ \overline{v_p u_p}^* & \overline{v_p^2}^* & \overline{v_p w_p}^* \\ \overline{w_p u_p}^* & \overline{w_p v_p}^* & \overline{w_p^2}^* \end{bmatrix} = \begin{bmatrix} 1 & 0 & 0 \\ 0 & 1/\sqrt{2} & -1/\sqrt{2} \\ 0 & 1/\sqrt{2} & 1/\sqrt{2} \end{bmatrix} \begin{bmatrix} \overline{u_p'^2} & \overline{u_p' v_p'} & \overline{u_p' w_p'} \\ \overline{v_p' u_p'} & \overline{v_p'^2} & \overline{v_p' w_p'} \\ \overline{w_p' u_p'} & \overline{w_p' v_p'} & \overline{w_p'^2} \end{bmatrix} \begin{bmatrix} 1 & 0 & 0 \\ 0 & 1/\sqrt{2} & 1/\sqrt{2} \\ 0 & -1/\sqrt{2} & 1/\sqrt{2} \end{bmatrix}.$$

The term $\overline{v_p w_p}^*$ in $\boldsymbol{u_p^*}$ was used for the unknown term $\overline{v_p w_p}$ in $\boldsymbol{u_p}$. However this transformation also gave a second set of values for the velocity correlation components that were already known in the frame $Ox_p y_p z_p$. To smooth out any slight differences between the components $\overline{u_p^2}$, $\overline{v_p^2}$, $\overline{w_p^2}$, $\overline{u_p v_p}$ & $\overline{u_p w_p}$ in $\boldsymbol{u_p}$ and their corresponding terms in $\boldsymbol{u_p^*}$, the 2 sets of terms were averaged. Thus a complete matrix of the

correlations between the velocity fluctuations relative to the probe was obtained in the frame $Ox_1x_2x_3$. This new matrix is referred to as $u_p^{\dagger}$, where:

$$u_p^{\dagger} = \begin{bmatrix} \overline{u_p^2}^{\dagger} & \overline{u_p v_p}^{\dagger} & \overline{u_p w_p}^{\dagger} \\ \overline{v_p u_p}^{\dagger} & \overline{v_p^2}^{\dagger} & \overline{v_p w_p}^{\dagger} \\ \overline{w_p u_p}^{\dagger} & \overline{w_p v_p}^{\dagger} & \overline{w_p^2}^{\dagger} \end{bmatrix} \quad \ldots\ldots\ldots \text{A5.}$$

where:

$\overline{u_p^2}^{\dagger} = \dfrac{\overline{u_p^2} + \overline{u_p^2}^{*}}{2}$	$\overline{u_p v_p}^{\dagger} = \overline{v_p u_p}^{\dagger} = \dfrac{\overline{u_p v_p} + \overline{u_p v_p}^{*}}{2}$
$\overline{v_p^2}^{\dagger} = \dfrac{\overline{v_p^2} + \overline{v_p^2}^{*}}{2}$	$\overline{u_p w_p}^{\dagger} = \overline{w_p u_p}^{\dagger} = \dfrac{\overline{u_p w_p} + \overline{u_p w_p}^{*}}{2}$
$\overline{w_p^2}^{\dagger} = \dfrac{\overline{w_p^2} + \overline{w_p^2}^{*}}{2}$	$\overline{v_p w_p}^{\dagger} = \overline{w_p v_p}^{\dagger} = \overline{v_p w_p}^{*}$

The matrix $u_p^{\dagger}$ is a complete velocity-correlation matrix in the axes system $Ox_p y_p z_p$ relative to the X-wire probe. This matrix was transformed into the cartesian wind-tunnel axes system simply by performing another 2 transformations through the probe setting angles. The transformation through the probe yaw angle was as follows:

$$u_\psi = \begin{bmatrix} \cos\psi & 0 & -\sin\psi \\ 0 & 1 & 0 \\ \sin\psi & 0 & \cos\psi \end{bmatrix} \begin{bmatrix} \overline{u_p^2}^{\dagger} & \overline{u_p v_p}^{\dagger} & \overline{u_p w_p}^{\dagger} \\ \overline{v_p u_p}^{\dagger} & \overline{v_p^2}^{\dagger} & \overline{v_p w_p}^{\dagger} \\ \overline{w_p u_p}^{\dagger} & \overline{w_p v_p}^{\dagger} & \overline{w_p^2}^{\dagger} \end{bmatrix} \begin{bmatrix} \cos\psi & 0 & \sin\psi \\ 0 & 1 & 0 \\ -\sin\psi & 0 & \cos\psi \end{bmatrix} \quad \ldots\ldots\ldots \text{A6,}$$

where the matrix u_ψ signifies the velocity correlations after the transformation through the probe yaw angle. This matrix was then transformed through the probe pitch angle by the following relationship:

$$\boldsymbol{u}_\theta = \begin{bmatrix} \cos\theta & -\sin\theta & 0 \\ \sin\theta & \cos\theta & 0 \\ 0 & 0 & 1 \end{bmatrix} \boldsymbol{u}_\psi \begin{bmatrix} \cos\theta & \sin\theta & 0 \\ -\sin\theta & \cos\theta & 0 \\ 0 & 0 & 1 \end{bmatrix} \qquad \ldots\ldots\ldots \text{A7.}$$

The matrix $\boldsymbol{u}_\theta$ is actually in the wind tunnel axes system and thus represents the complete velocity correlation matrix $\boldsymbol{u}_{\mathbf{wt}}$ in the wind tunnel axes O*XYZ*, i.e.:

$$\boldsymbol{u}_{\mathbf{wt}} = \boldsymbol{u}_\theta = \begin{bmatrix} \overline{u^2} & \overline{uv} & \overline{uw} \\ \overline{vu} & \overline{v^2} & \overline{vw} \\ \overline{wu} & \overline{wv} & \overline{w^2} \end{bmatrix} \qquad \ldots\ldots\ldots \text{A8.}$$

From this matrix the Reynolds stresses in wind-tunnel axes can be calculated by mutiplying each component by -ρ, where ρ is the density of the fluid.

Mean velocities

In addition, there existed 2 column matrices for the mean-velocity vectors in the 2 systems of probe axes. The vector $\boldsymbol{U}_{\mathbf{p}}$ represented the mean-velocity components $\overline{U}$, $\overline{V}$ & $\overline{W}$ in the frame $\mathrm{O}x_{\mathrm{p}}y_{\mathrm{p}}z_{\mathrm{p}}$ and $\boldsymbol{U}'_{\mathbf{p}}$ represented the mean-velocity components $\overline{U'}$, $\overline{V'}$ & $\overline{W'}$ in the frame $\mathrm{O}x'_{\mathrm{p}}y'_{\mathrm{p}}z'_{\mathrm{p}}$. In order to use both sets of measurements a similar process of transformations was performed to those described for the velocity correlation matrix. The matrix $\boldsymbol{U}'_{\mathbf{p}}$ was transformed into the frame $\mathrm{O}x_{\mathrm{p}}y_{\mathrm{p}}z_{\mathrm{p}}$ by premultiplying by the matrix of direction cosines $[T]$ for the 45°-rotation, giving a second set of velocity components in the frame O*xyz* which was termed $\boldsymbol{U}^*_{\mathbf{p}}$:

$$\boldsymbol{U}^*_{\mathbf{p}} = [T]\ \boldsymbol{U}'_{\mathbf{p}} \qquad \ldots\ldots\ldots \text{A9,}$$

$$i.e.: \begin{bmatrix} \overline{U_{\mathrm{p}}} \\ \overline{V_{\mathrm{p}}} \\ \overline{W_{\mathrm{p}}} \end{bmatrix}^* = \begin{bmatrix} 1 & 0 & 0 \\ 0 & 1/\sqrt{2} & -1/\sqrt{2} \\ 0 & 1/\sqrt{2} & 1/\sqrt{2} \end{bmatrix} \begin{bmatrix} \overline{U'_{\mathrm{p}}} \\ \overline{V'_{\mathrm{p}}} \\ \overline{W'_{\mathrm{p}}} \end{bmatrix}$$

The mean-velocity components in $\boldsymbol{U}_{\mathbf{p}}^{*}$ were then averaged with the components in $\boldsymbol{U}_{\mathbf{p}}$ to produce a second matrix $\boldsymbol{U}_{\mathrm{p}}{}^{\dagger}$ of the mean-velocities in the probe axes system $\mathrm{O}x_{\mathrm{p}}y_{\mathrm{p}}z_{\mathrm{p}}$:

$$\boldsymbol{U}_{\mathrm{p}}{}^{\dagger} = \begin{bmatrix} \overline{U_{\mathrm{p}}}^{\dagger} \\ \overline{V_{\mathrm{p}}}^{\dagger} \\ \overline{W_{\mathrm{p}}}^{\dagger} \end{bmatrix} = \frac{\boldsymbol{U}_{\mathbf{p}} + \boldsymbol{U}_{\mathbf{p}}{}^{*}}{2} \qquad \ldots\ldots\ldots \text{A10.}$$

where:

$\overline{U_{\mathrm{p}}}^{\dagger} = \dfrac{\overline{U_{\mathrm{p}}} + \overline{U_{\mathrm{p}}}^{*}}{2}$	$\overline{V_{\mathrm{p}}}^{\dagger} = \dfrac{\overline{V_{\mathrm{p}}} + \overline{V_{\mathrm{p}}}^{*}}{2}$	$\overline{W_{\mathrm{p}}}^{\dagger} = \dfrac{\overline{W_{\mathrm{p}}} + \overline{W_{\mathrm{p}}}^{*}}{2}$

This mean-velocity matrix underwent 2 further transformations, similar to the velocity correlation matrix, to transform the data into the wind-tunnel axes system shown in figure 21. The data for each measurement station were transformed through the probe angles to give a column matrix in the wind tunnel axes $\boldsymbol{U}_{\mathbf{wt}}$ as follows:

$$\boldsymbol{U}_{\mathbf{wt}} = \begin{bmatrix} \overline{U} \\ \overline{V} \\ \overline{W} \end{bmatrix} = \left[T_{\theta}\right] \left[T_{\psi}\right] \begin{bmatrix} \overline{U_{\mathrm{p}}}^{\dagger} \\ \overline{V_{\mathrm{p}}}^{\dagger} \\ \overline{W_{\mathrm{p}}}^{\dagger} \end{bmatrix} \qquad \ldots\ldots\ldots \text{A11.}$$

$$i.e. \begin{bmatrix} \overline{U} \\ \overline{V} \\ \overline{W} \end{bmatrix} = \begin{bmatrix} \cos\theta & -\sin\theta & 0 \\ \sin\theta & \cos\theta & 0 \\ 0 & 0 & 1 \end{bmatrix} \begin{bmatrix} \cos\psi & 0 & -\sin\psi \\ 0 & 1 & 0 \\ \sin\psi & 0 & \cos\psi \end{bmatrix} \begin{bmatrix} \overline{U_{\mathrm{p}}}^{\dagger} \\ \overline{V_{\mathrm{p}}}^{\dagger} \\ \overline{W_{\mathrm{p}}}^{\dagger} \end{bmatrix} \qquad \ldots\ldots\ldots \text{A12.}$$

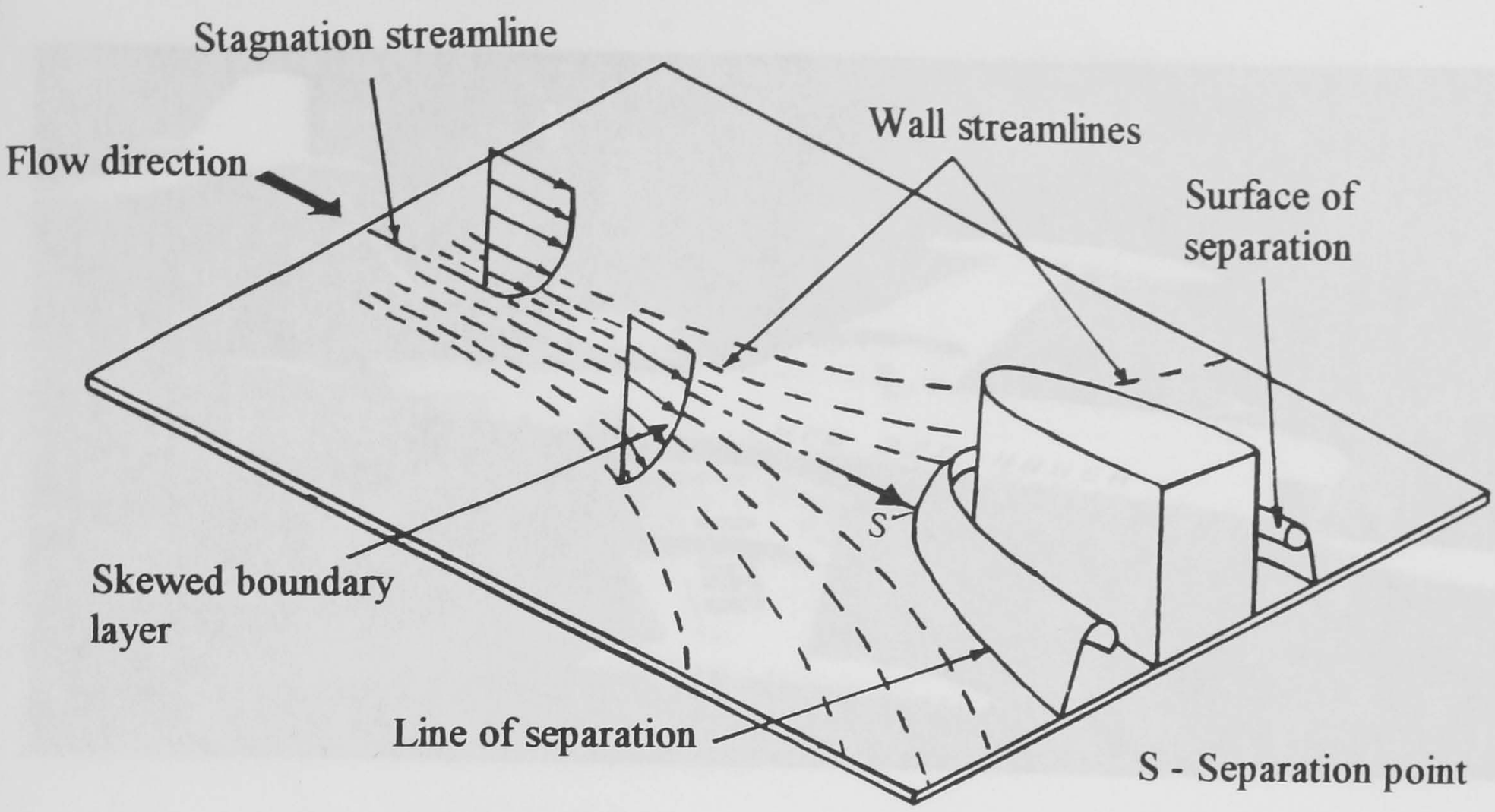

Figure 1 Schematic of the flow around a wing/body junction.

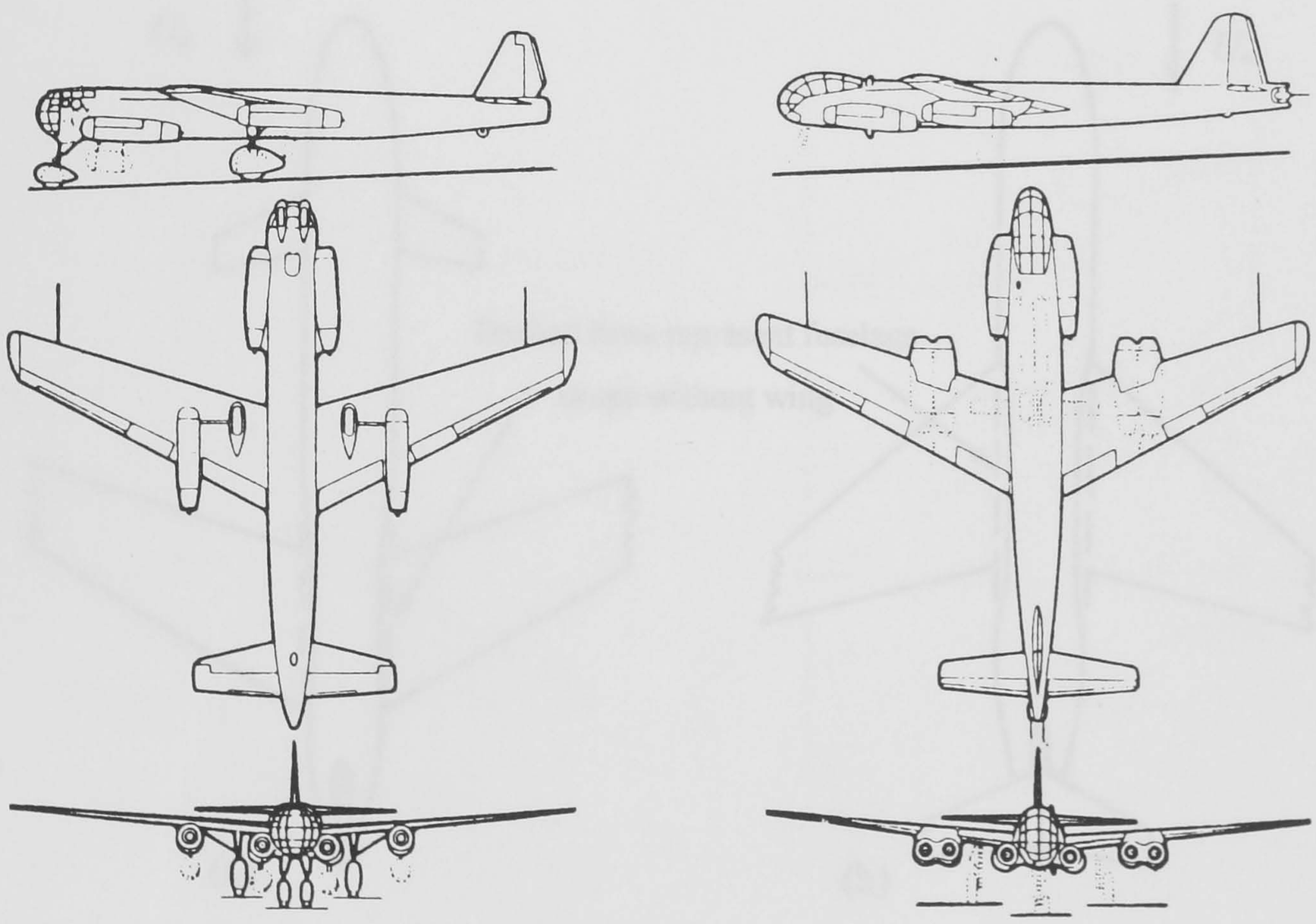

Figure 2 The Junkers Ju-287 jet bomber: the world's first aircraft fitted with a swept-forward wing. The 3-view on the left is of the prototype aircraft which flew in 1944. That on the right is of the intended production version, progress on which was halted due to the events of World War 2.

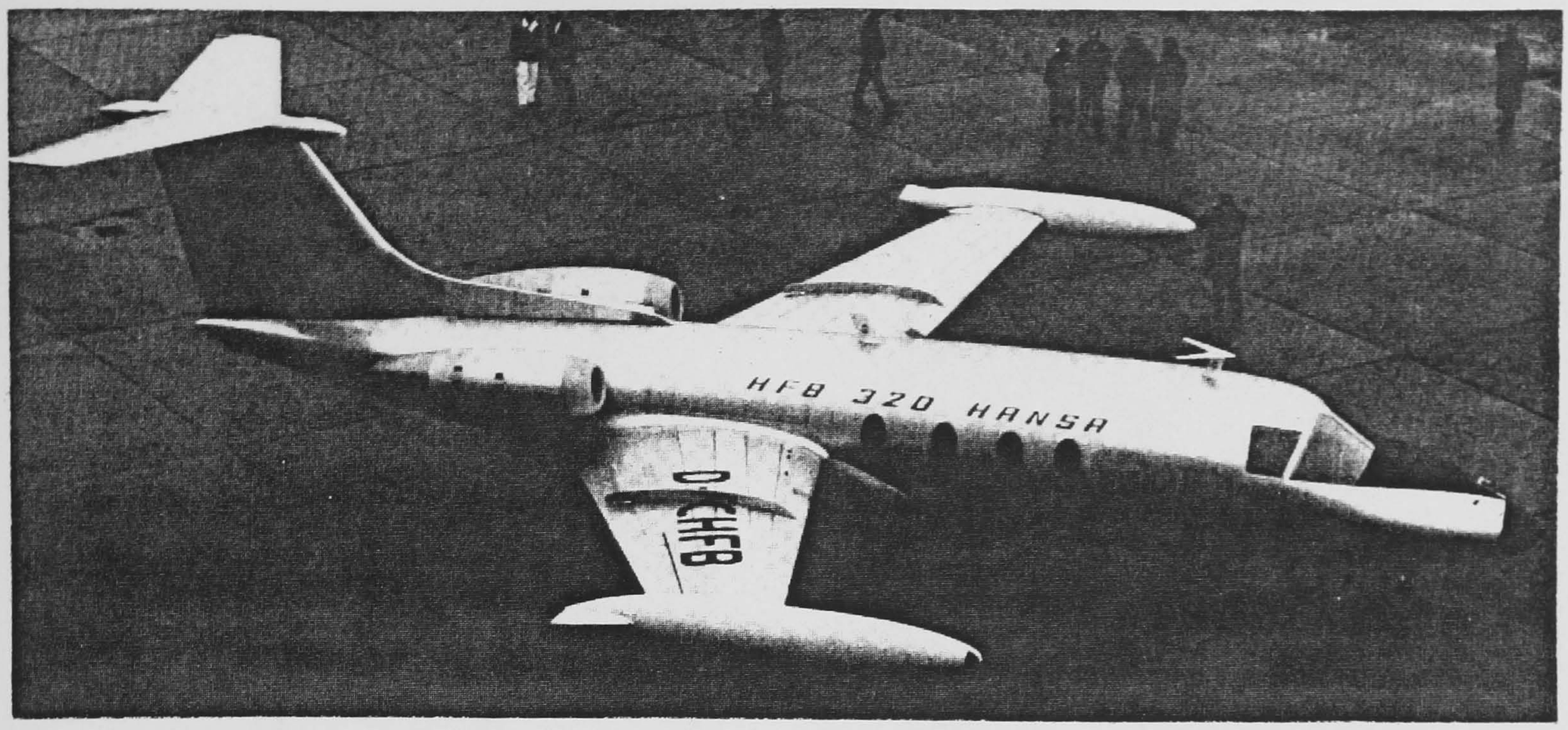

Figure 3 The HFB 320 Hansa Jet. The world's first passenger aircraft fitted with a swept-forward wing (Wocke & Davies, 1964).

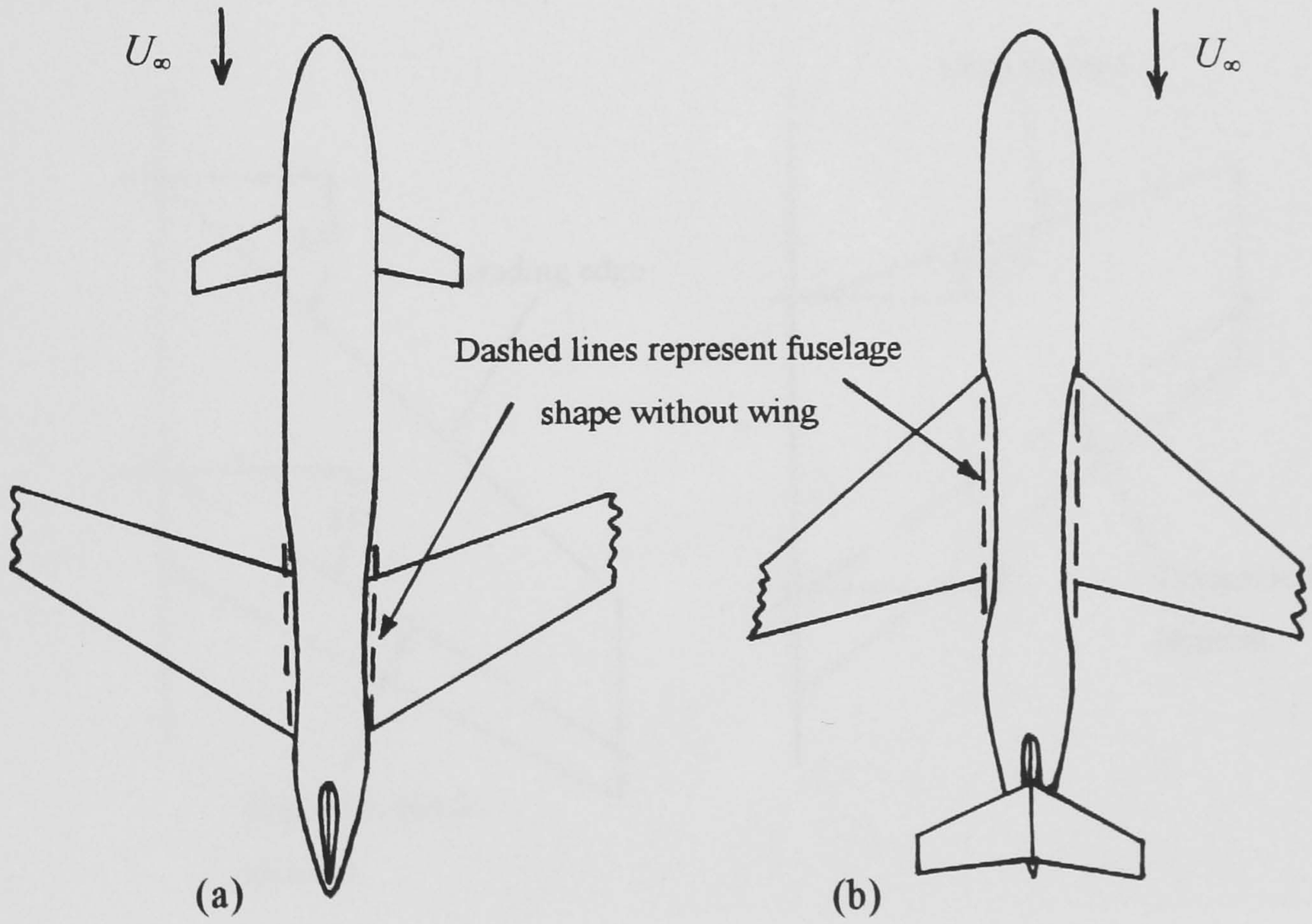

Figure 4 Comparison of area-ruled fuselage shapes for:
(a) a canard/swept-forward wing configuration &
(b) a conventional swept-back wing configuration.

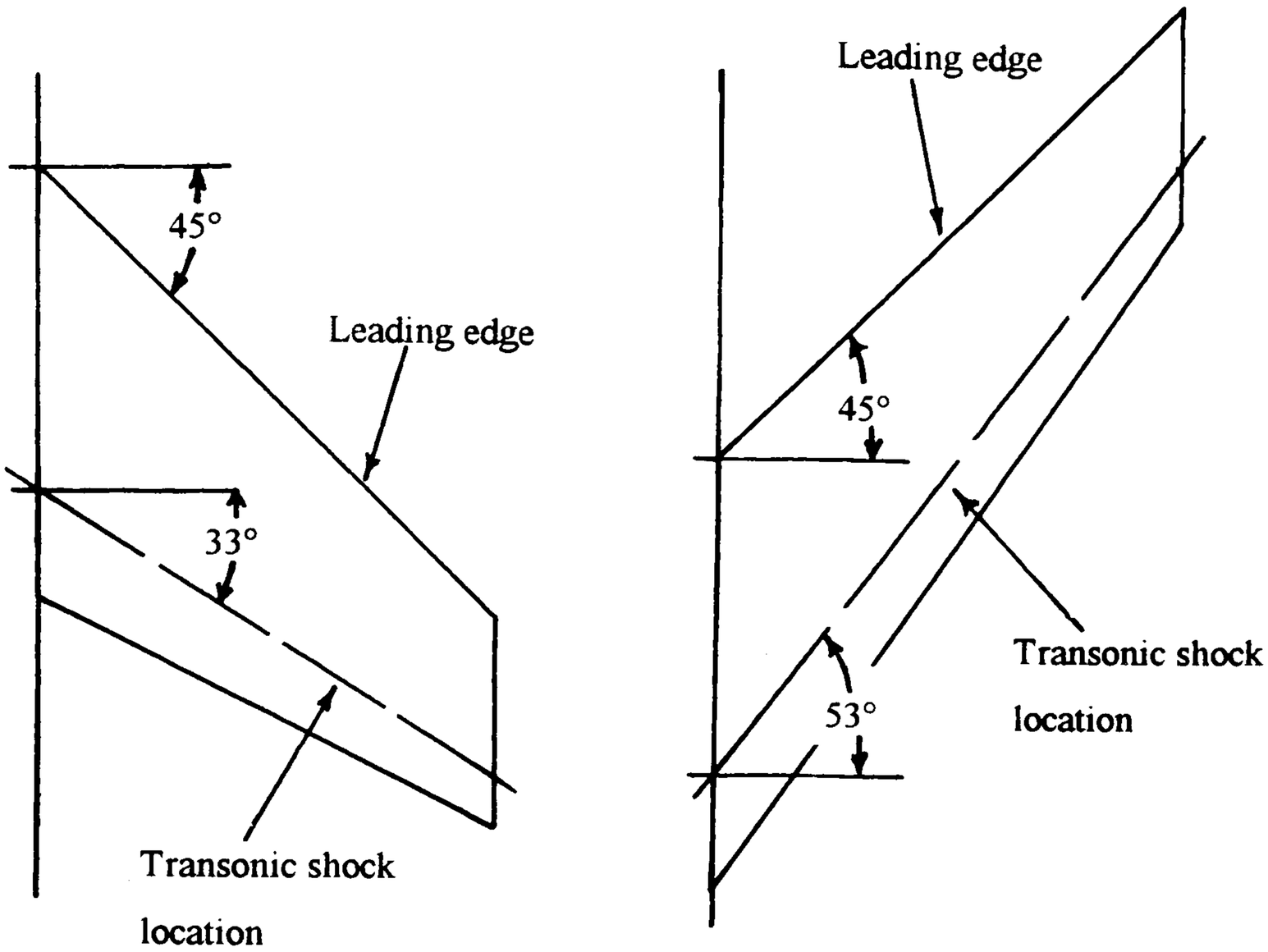

Figure 5(a) Diagram showing the idealised advantage in wave drag gained using a swept-forward wing. The 2 wings are equivalent, having equal leading-edge sweep angles, root chords, taper ratios and spans. The resulting transonic shock wave is more highly swept on the swept-forward wing than on the swept-back wing.

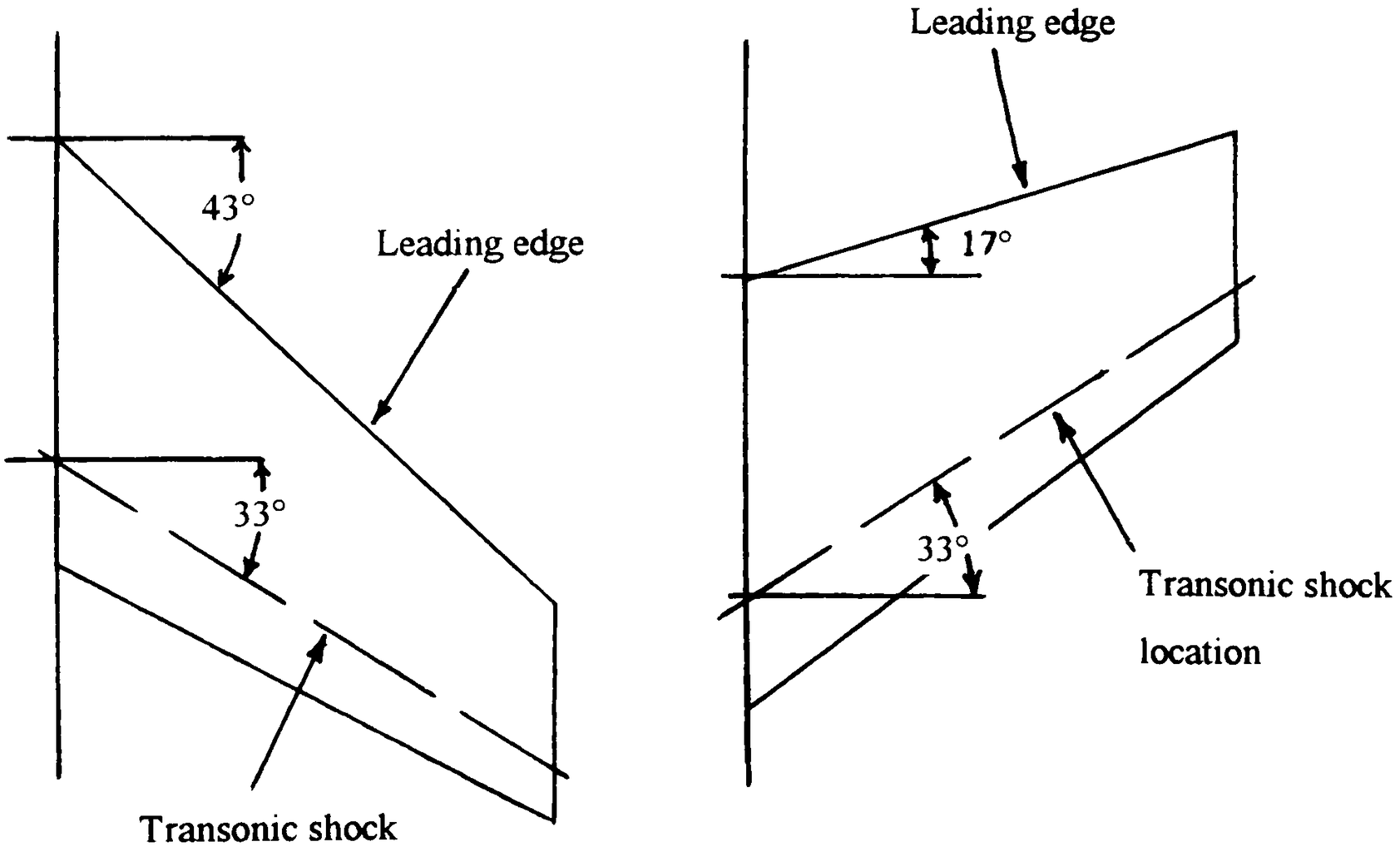

Figure 5(b) Diagram showing the idealised advantage in profile drag gained using a swept-forward wing. The 2 wings are equivalent, having equal transonic-shock sweep angles, root chords, taper ratios and spans. The resulting sweep angle of the leading edge is less for the swept-forward wing than for the swept-back wing.

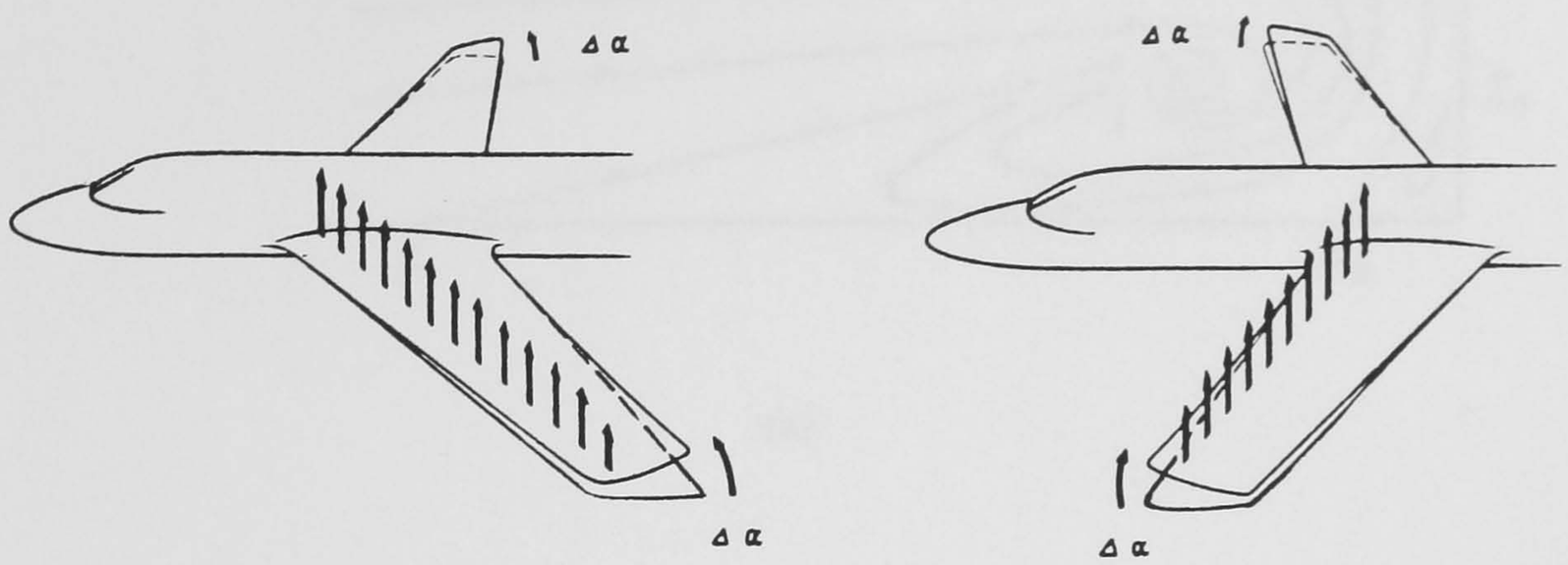

(a) (b)

Figure 6 The elastic deformation of swept-back and swept-forward wings due to gust loads (Wocke & Davies, 1964).

Figure 7 The Grumman X-29 technology demonstrator.

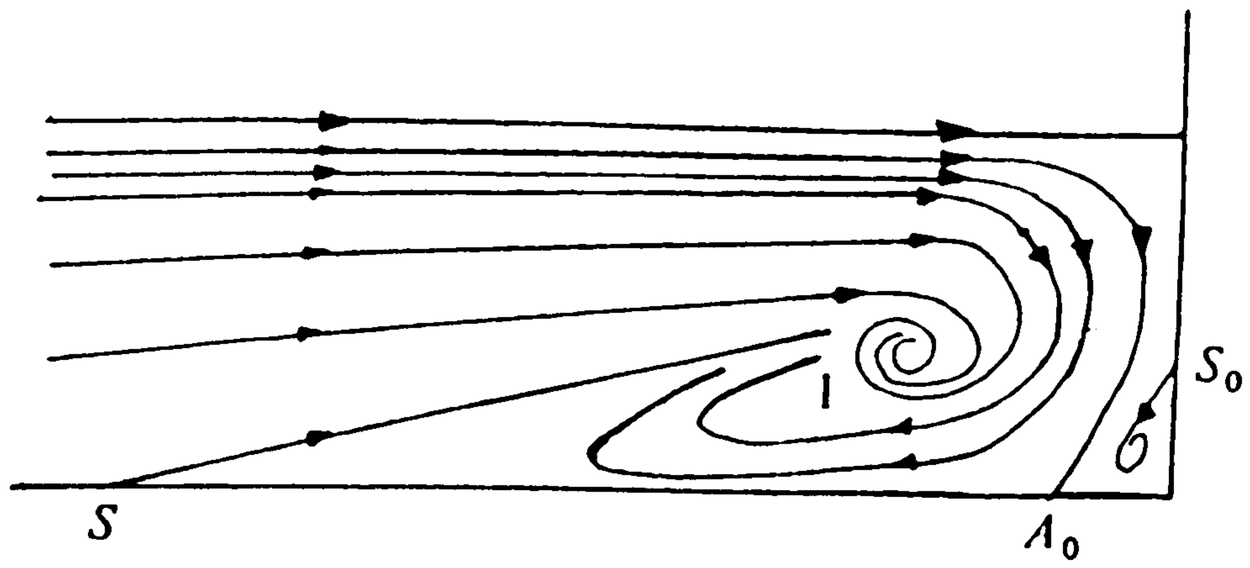

(a)

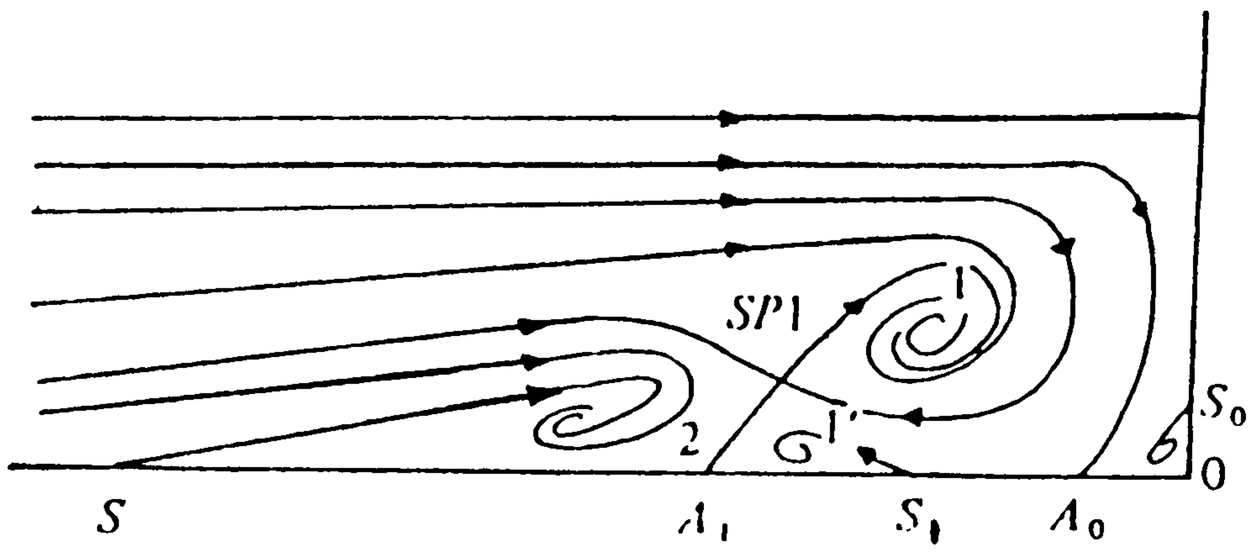

(b)

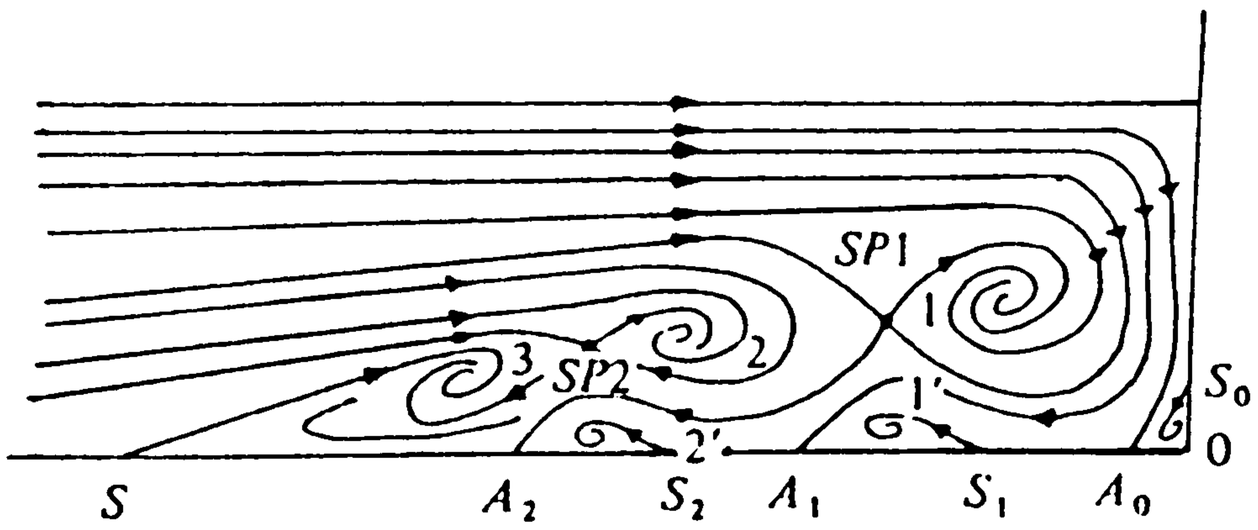

(c)

Legend :

A =	Attachment point
S =	Separation point
SP =	Saddle point in flow
1, 2, 3 =	Oncoming flow vortices
0, 1', 2' =	Counter-rotating vortices

Figure 8 Examples of topologies of:
(a) 2-vortex, (b) 4-vortex and (c) 6-vortex separations upstream of an obstacle, along its centreline (after Baker, 1979).

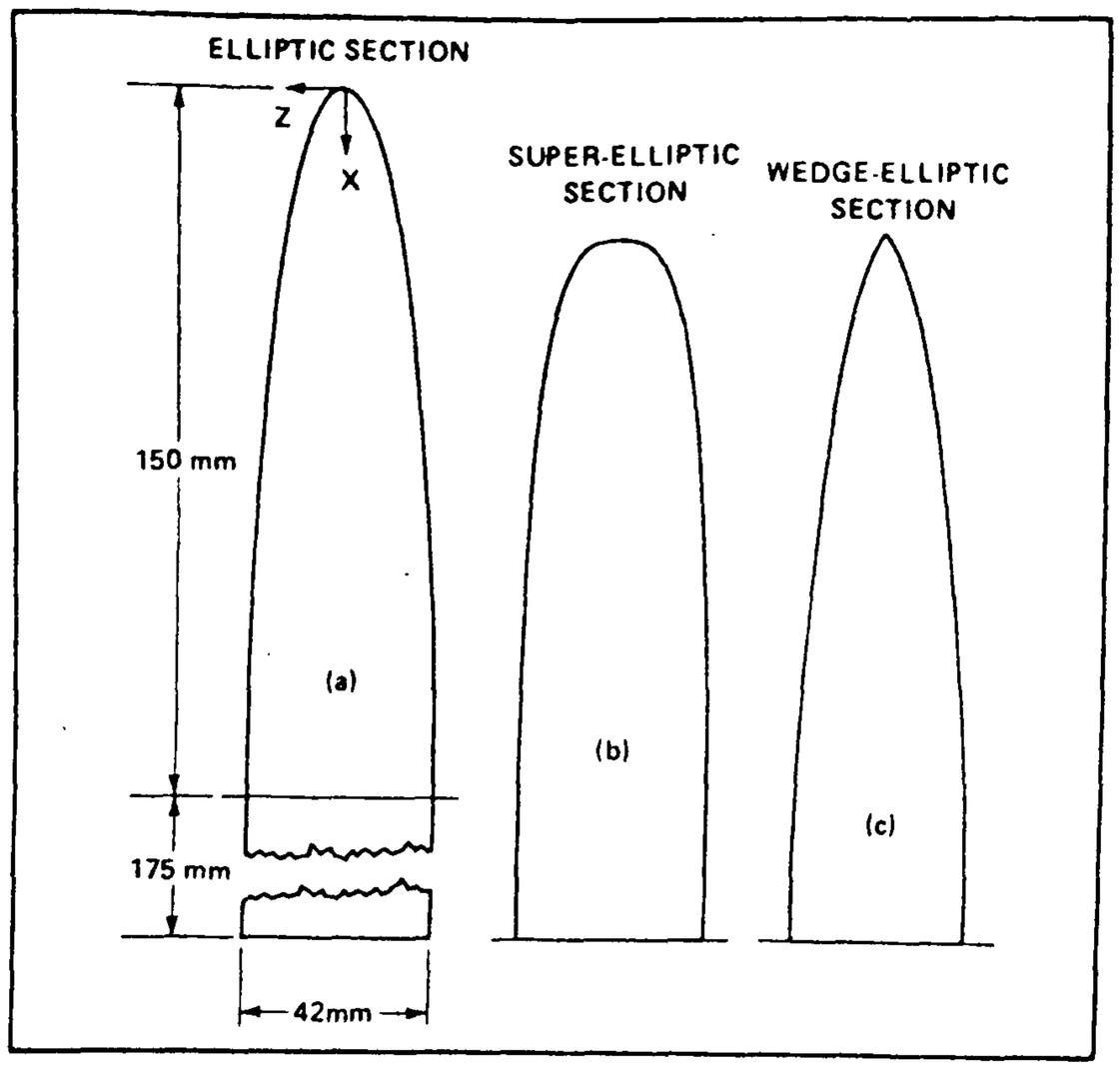

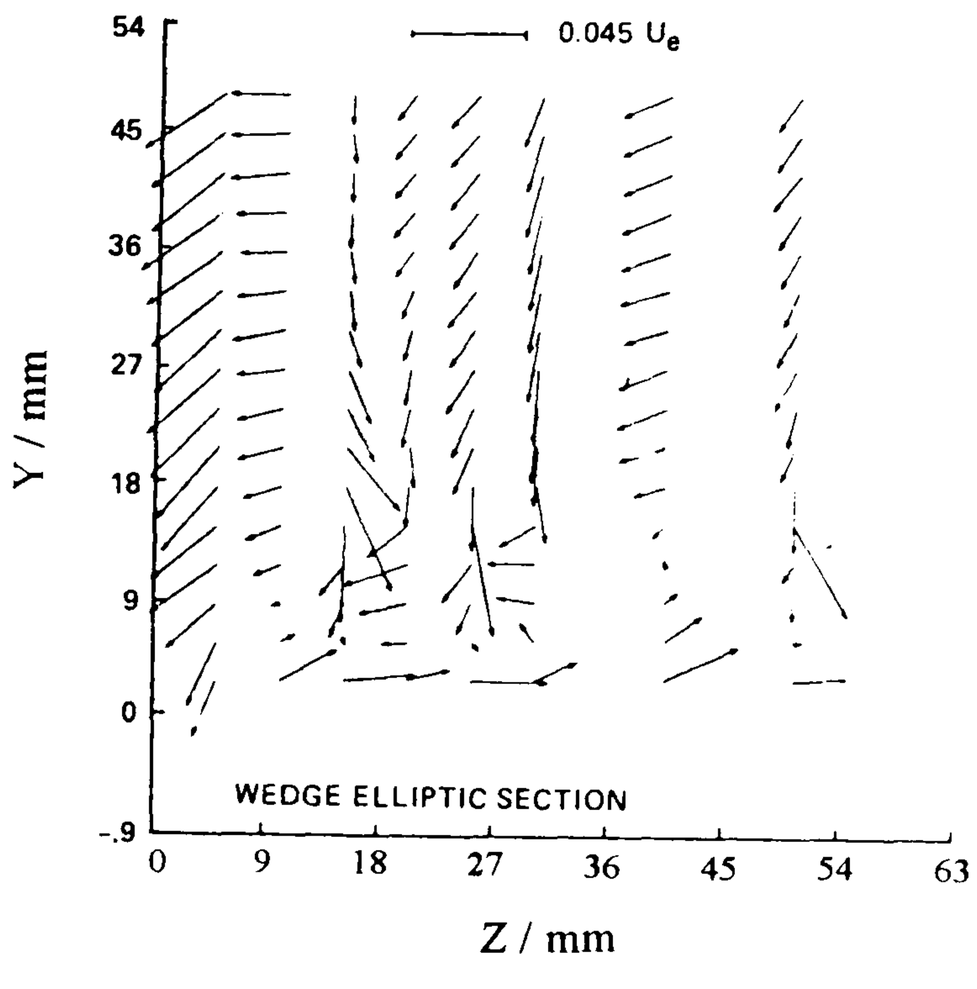

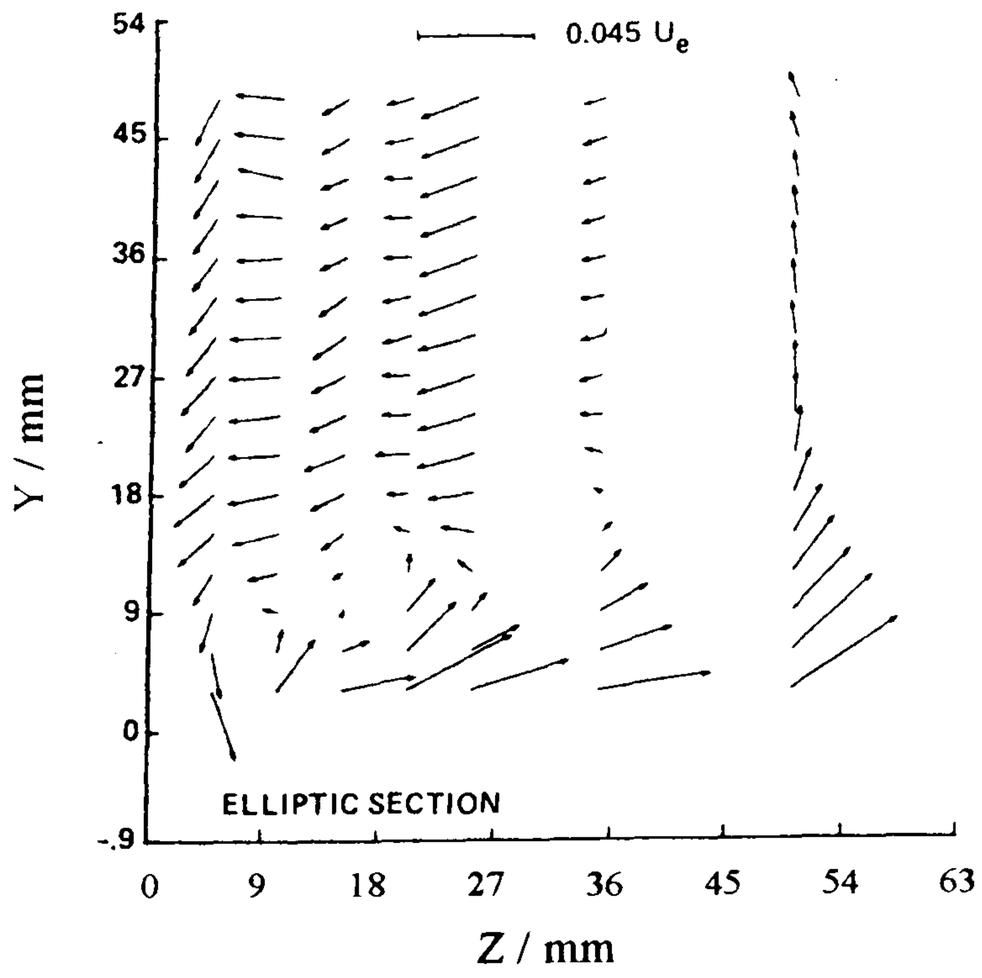

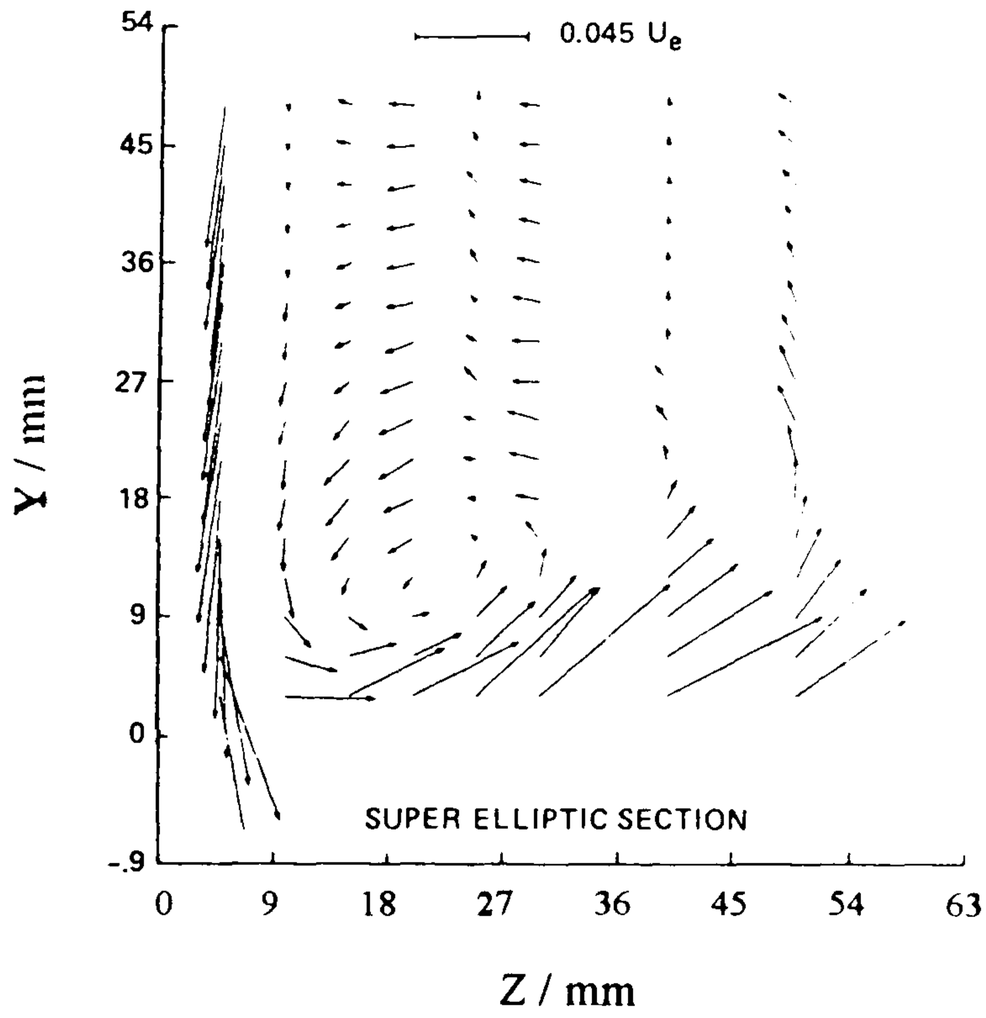

Figure 9 Plan views of the leading-edge shapes used by Mehta (1984) and secondary-flow vectors obtained for each leading edge shape, in a plane normal to the freestream direction, 175 mm (0.54c) downstream of the leading edge of the junction.

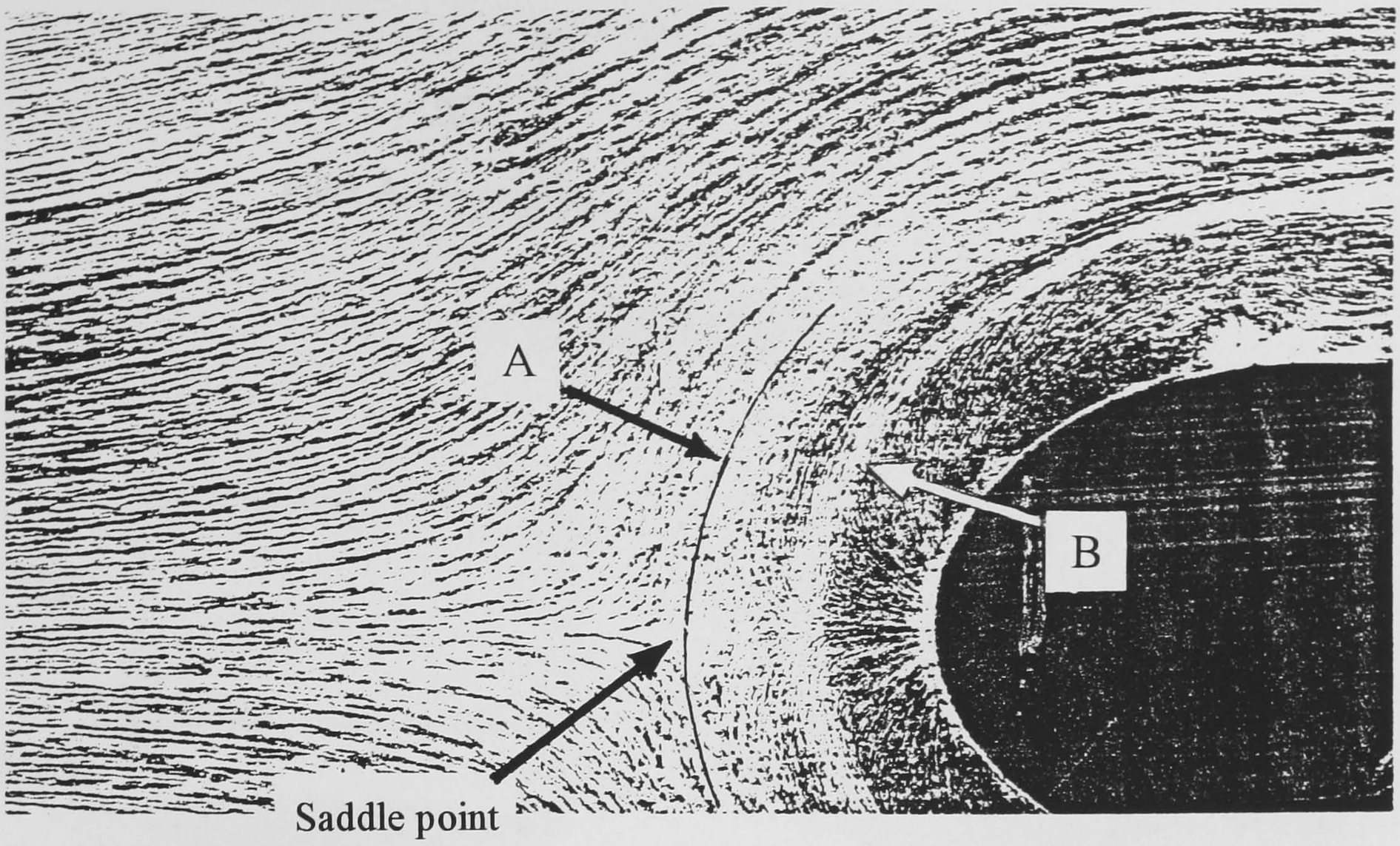

Figure 10 Surface oil-flow pattern obtained by Devenport and Simpson (1986).

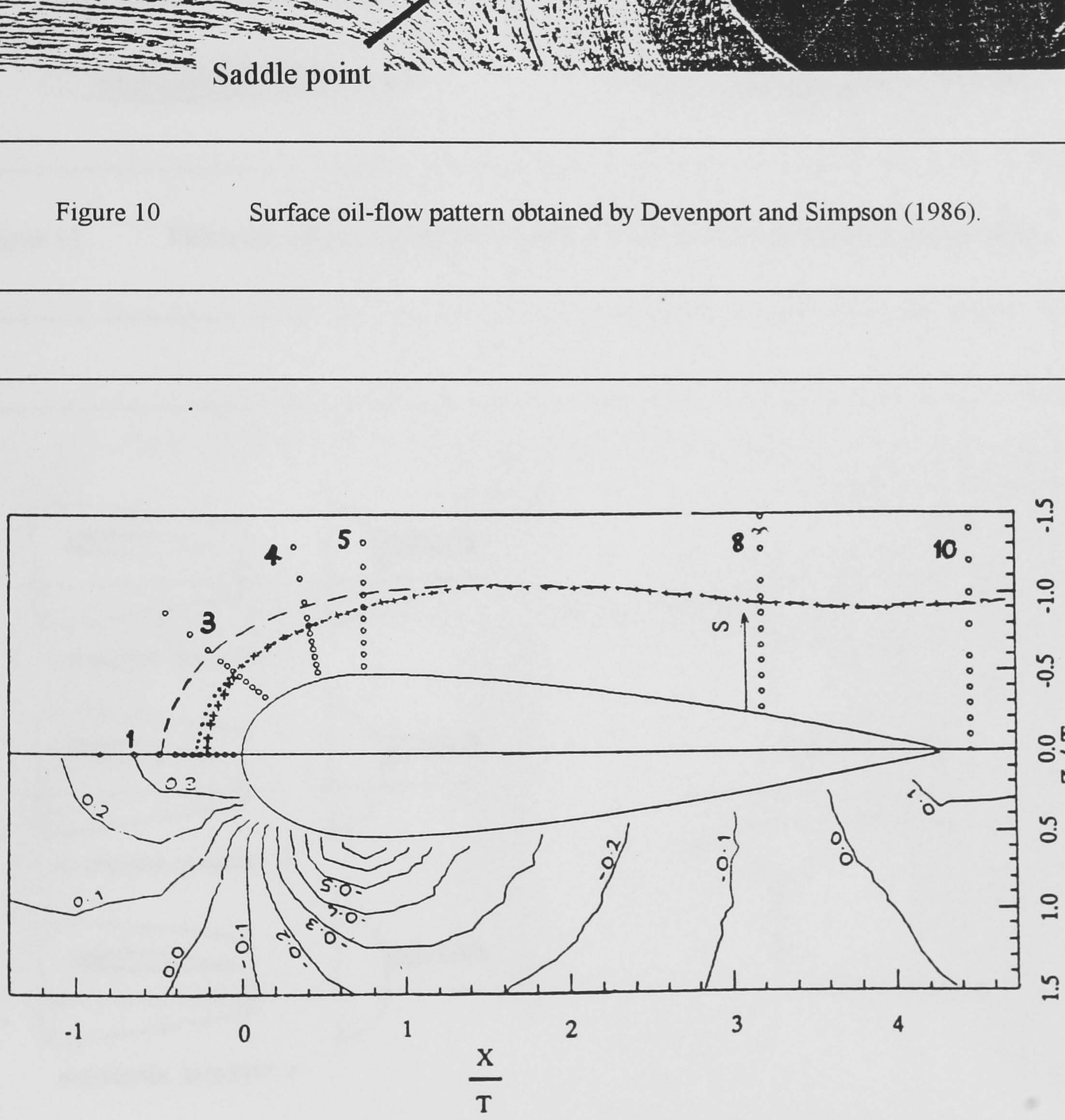

Figure 11 Contours of surface pressure coefficient on the plate and planes for LDA measurements of Devenport & Simpson (1986-90 & 92). Symbols: ○ locations of LDA profiles through boundary layer; – – line of separation; • • locus of line *B* in figure 3 and + + locus of peak turbulence kinetic energy in the vortex.

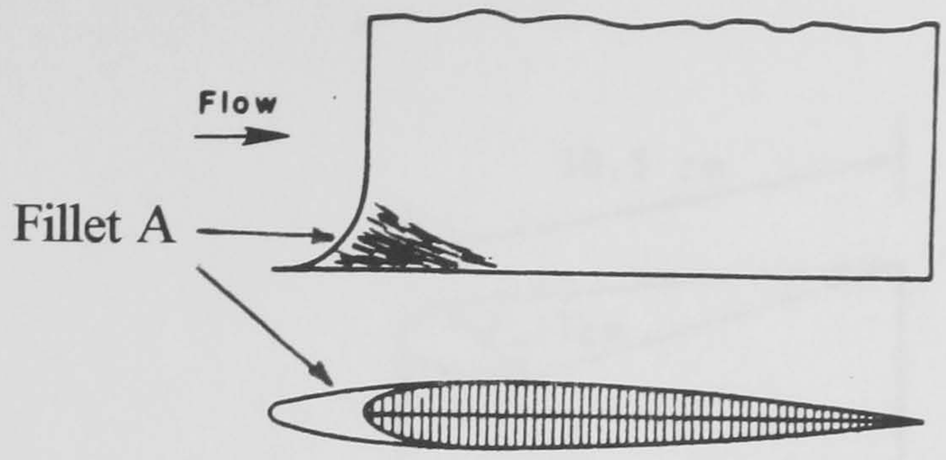

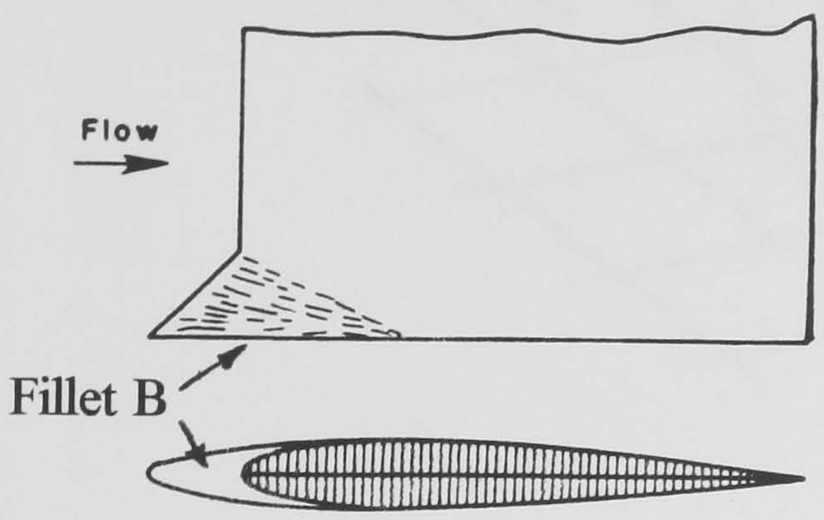

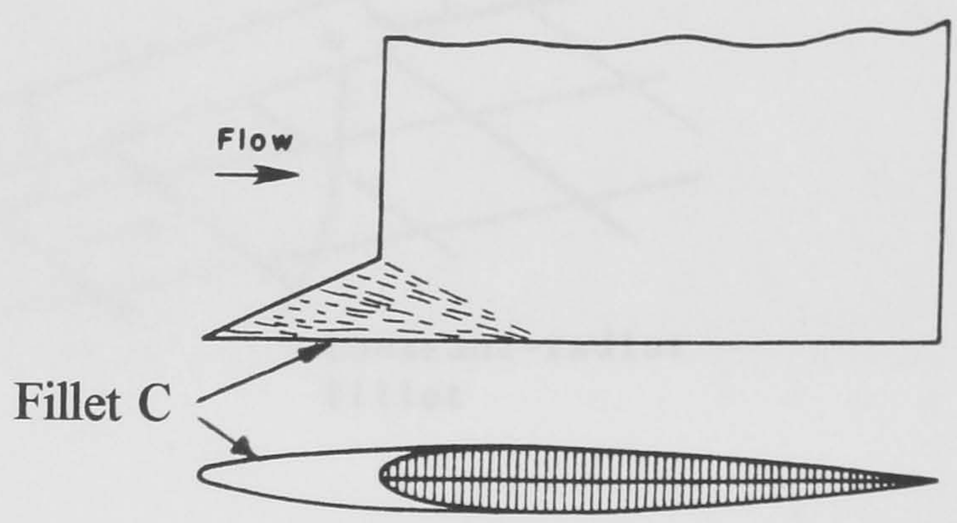

Figure 12 Fillets as used by Kubendran & Harvey (1988), in both laminar and turbulent flow.

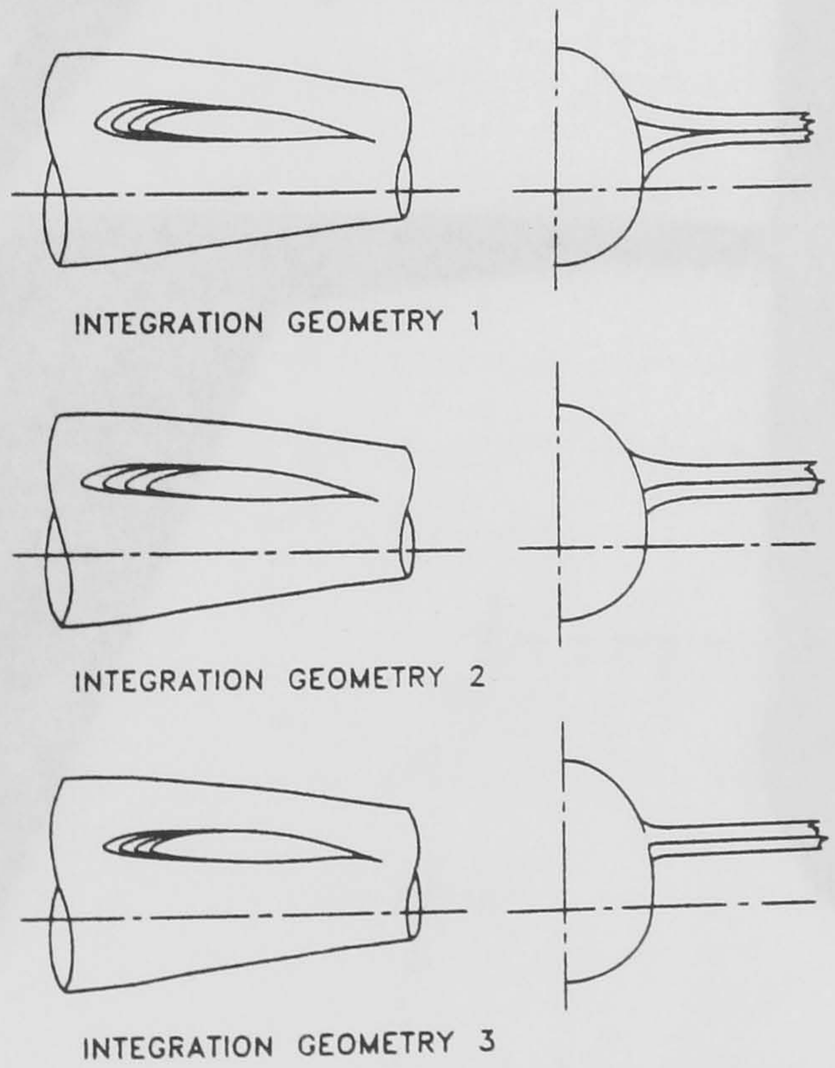

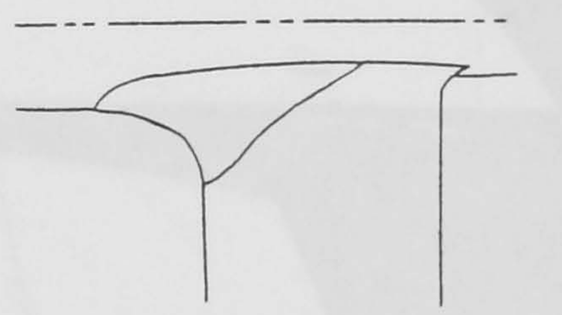
PARABOLIC PLANFORM - A

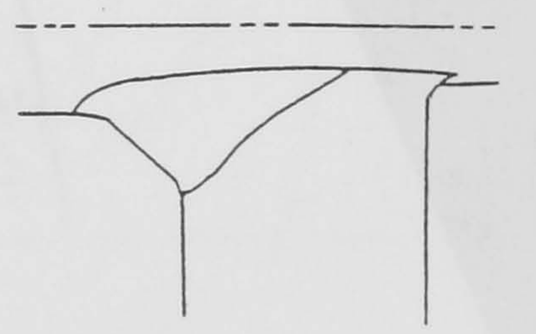
LINEAR PLANFORM - B

Figure 13 Profiles of fillets used by Maughmer *et al* (1989) on a sailplane model, each of the 3 integration geometries being combined with the 2 planform shapes to give 6 fillet geometries.

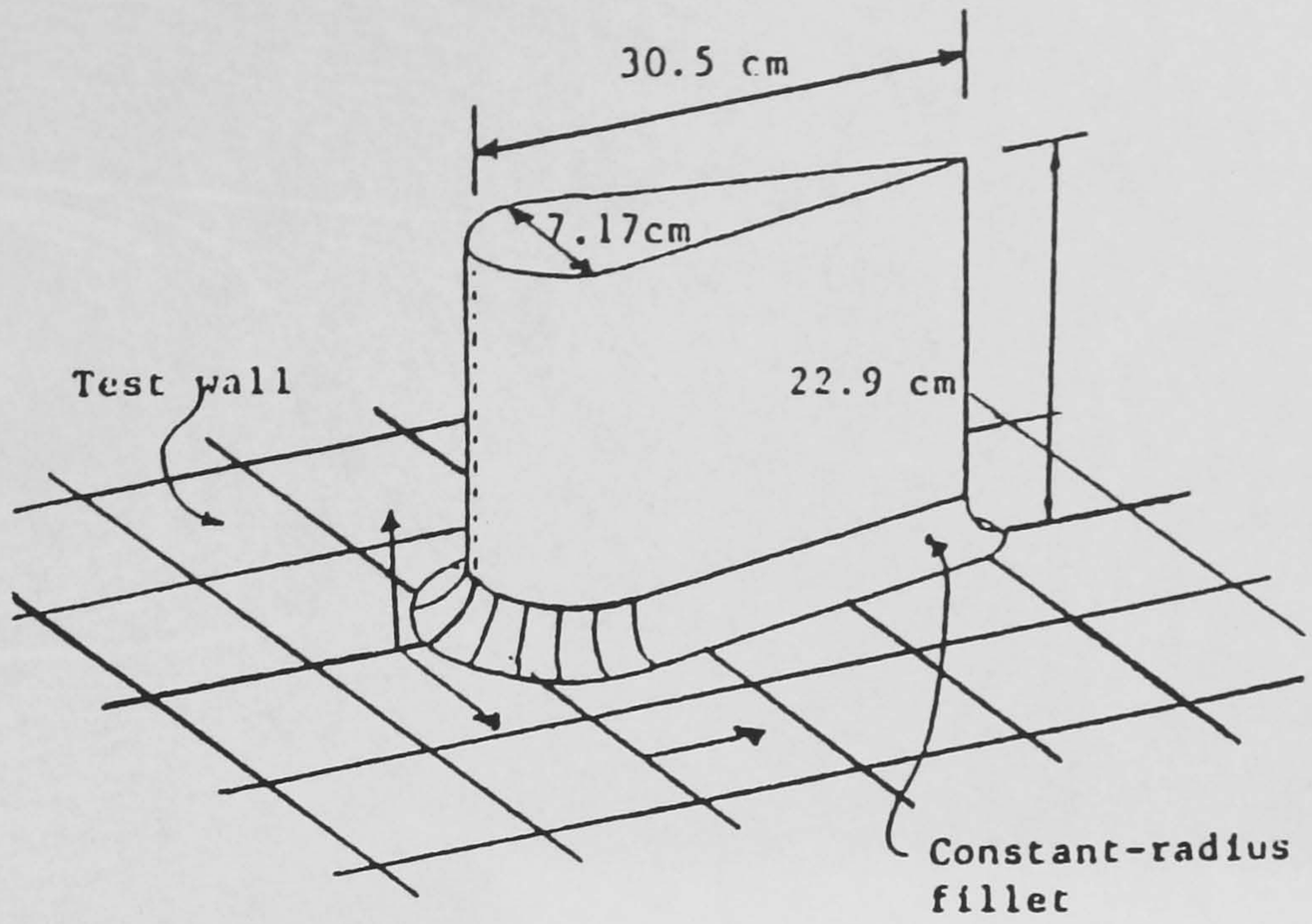

Figure 14 Quarter-circle fillet as used by Devenport *et al* (1990).

Figure 15 Fillet as used by Bernstein & Hamid (1993 & 96) on a swept-back NACA-0015 wing/flat-plate junction.

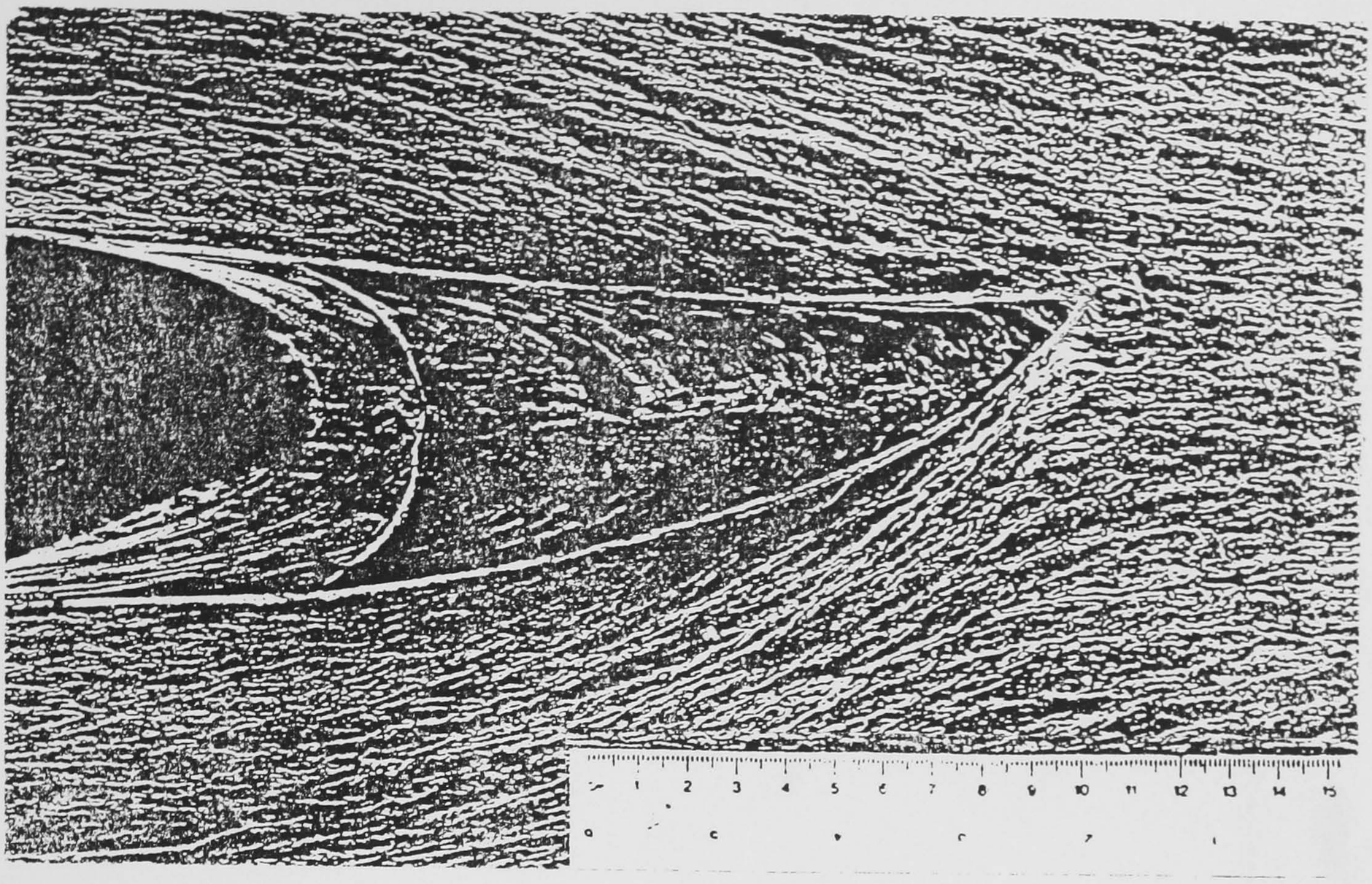

Figure 16 Surface oil-flow visualisation around the fillet used by Bernstein & Hamid (1993 & 96) at $\alpha = 0°$, (flow from right to left).

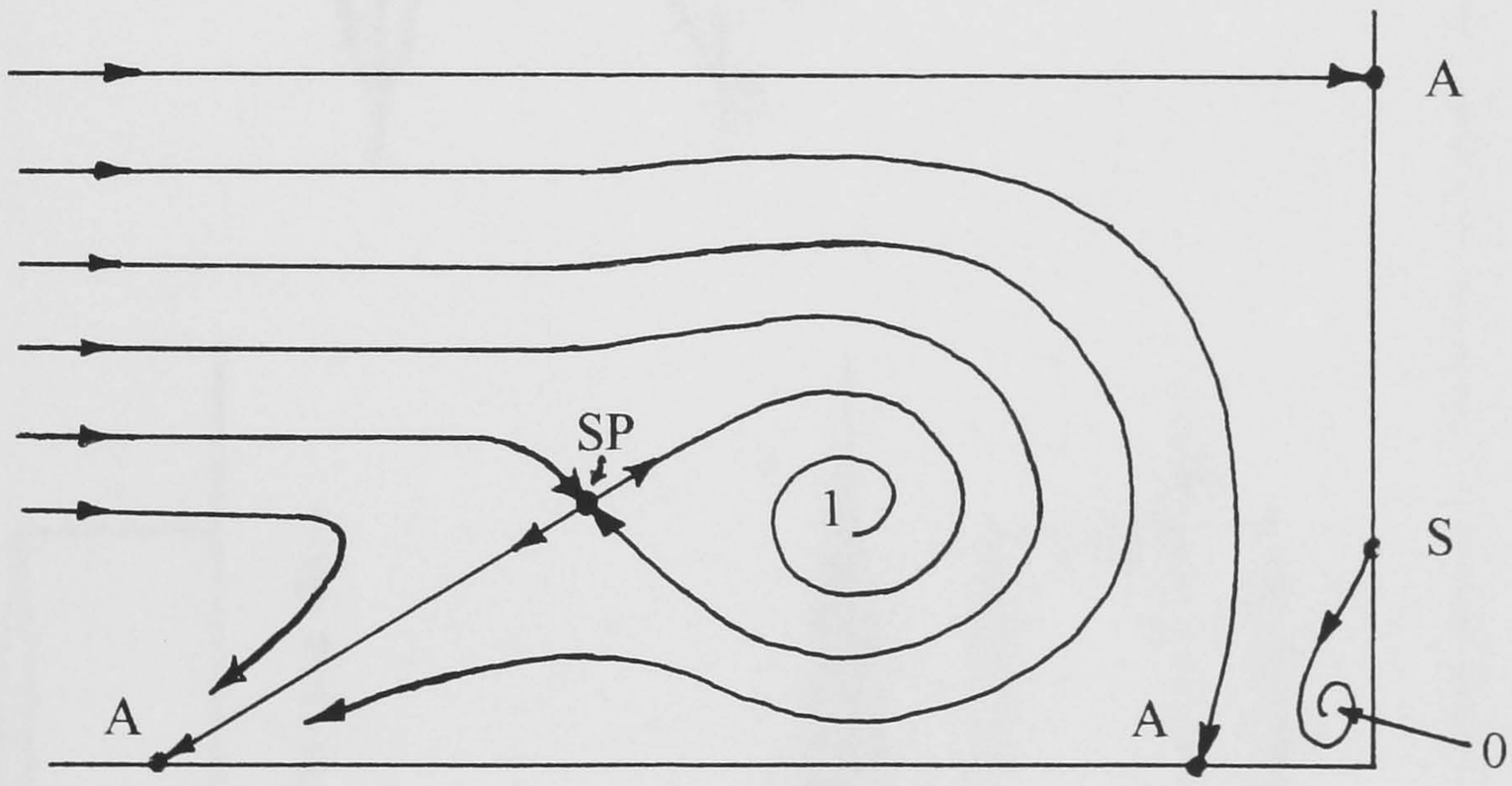

Legend:

A =	Attachment point
S =	Separation point
SP =	Saddle point in flow
1 =	Oncoming flow vortex
0 =	Counter-rotating vortex

Figure 17 Topology of a 2-vortex separation upstream of a cylinder, obtained from numerical simulation by Visbal (1991) and experiments by Kawahashi & Hosoi (1989).

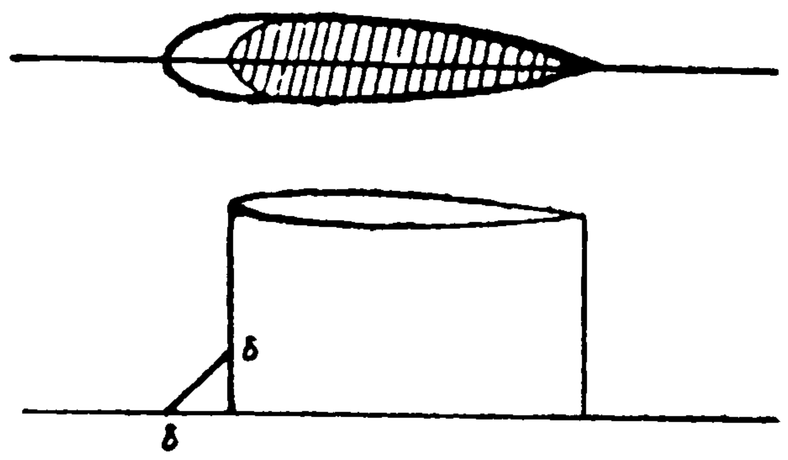

(a) Fairing No.1

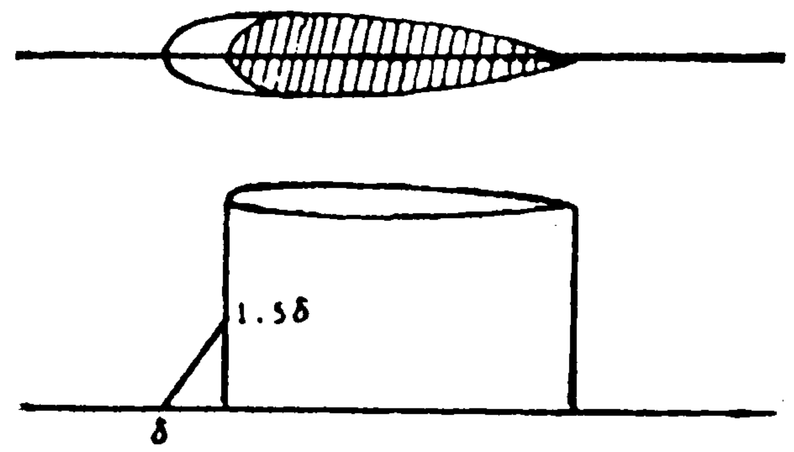

(b) Fairing No.2

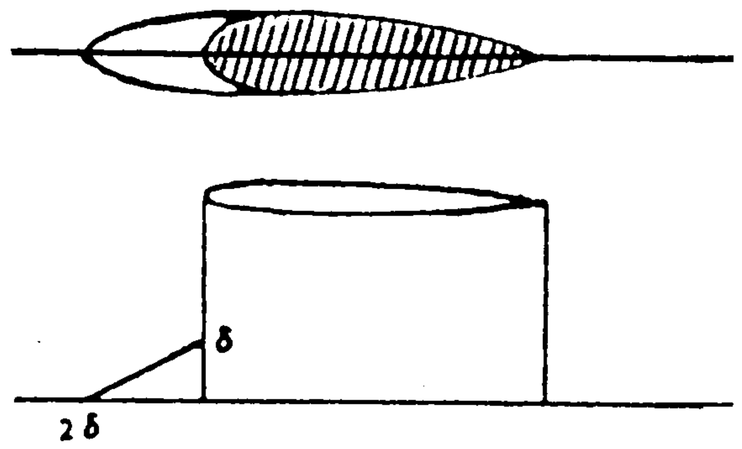

(c) Fairing No.3

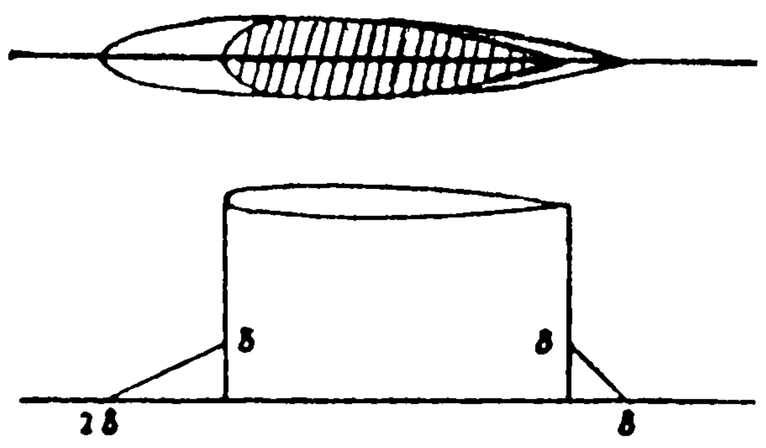

(d) Fairing No.4

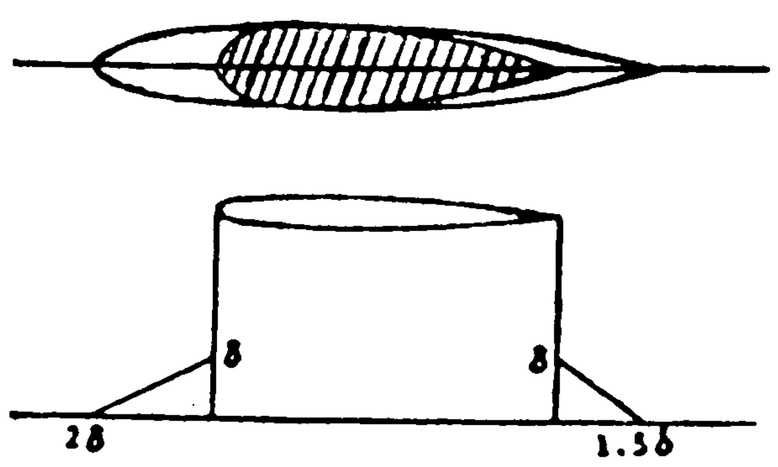

(e) Fairing No.5

Figure 18 Examples of fillets used by Sung & Lin (1988).

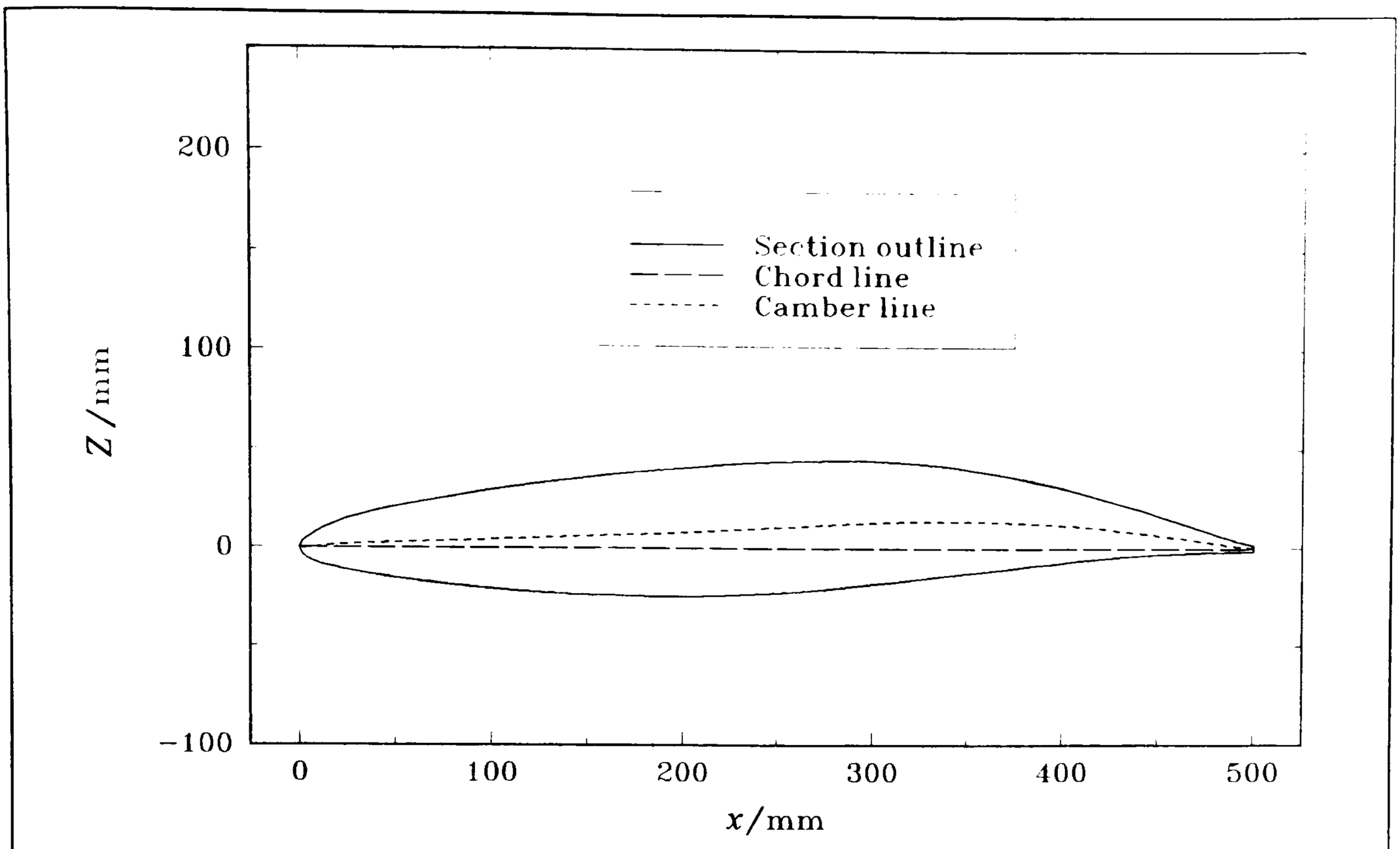

Figure 19 Aerofoil section taken from the British Aerospace *HH10* swept-forward wing.

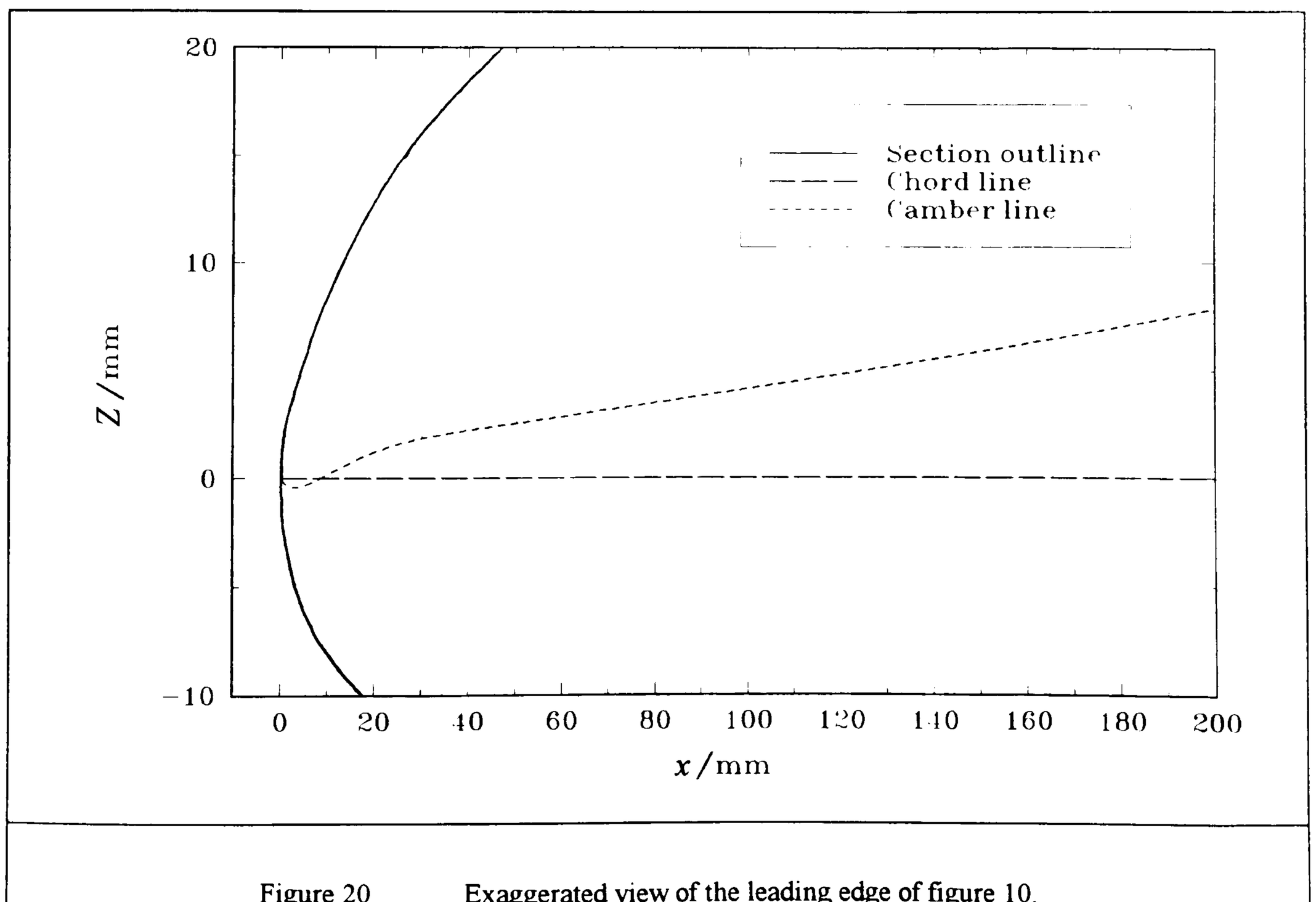

Figure 20 Exaggerated view of the leading edge of figure 10.

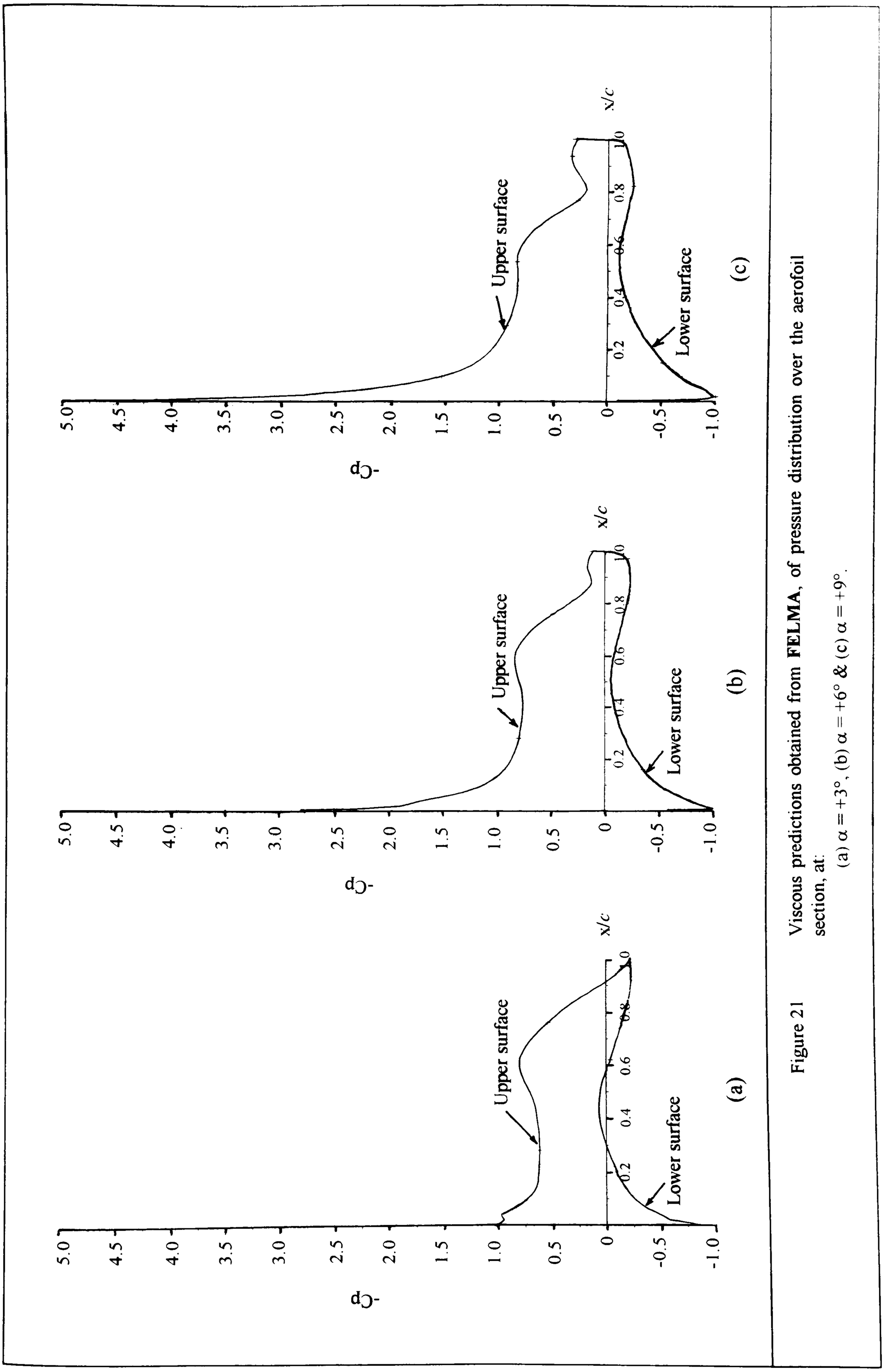

Figure 21 Viscous predictions obtained from **FELMA**, of pressure distribution over the aerofoil section, at:
(a) $\alpha = +3°$, (b) $\alpha = +6°$ & (c) $\alpha = +9°$.

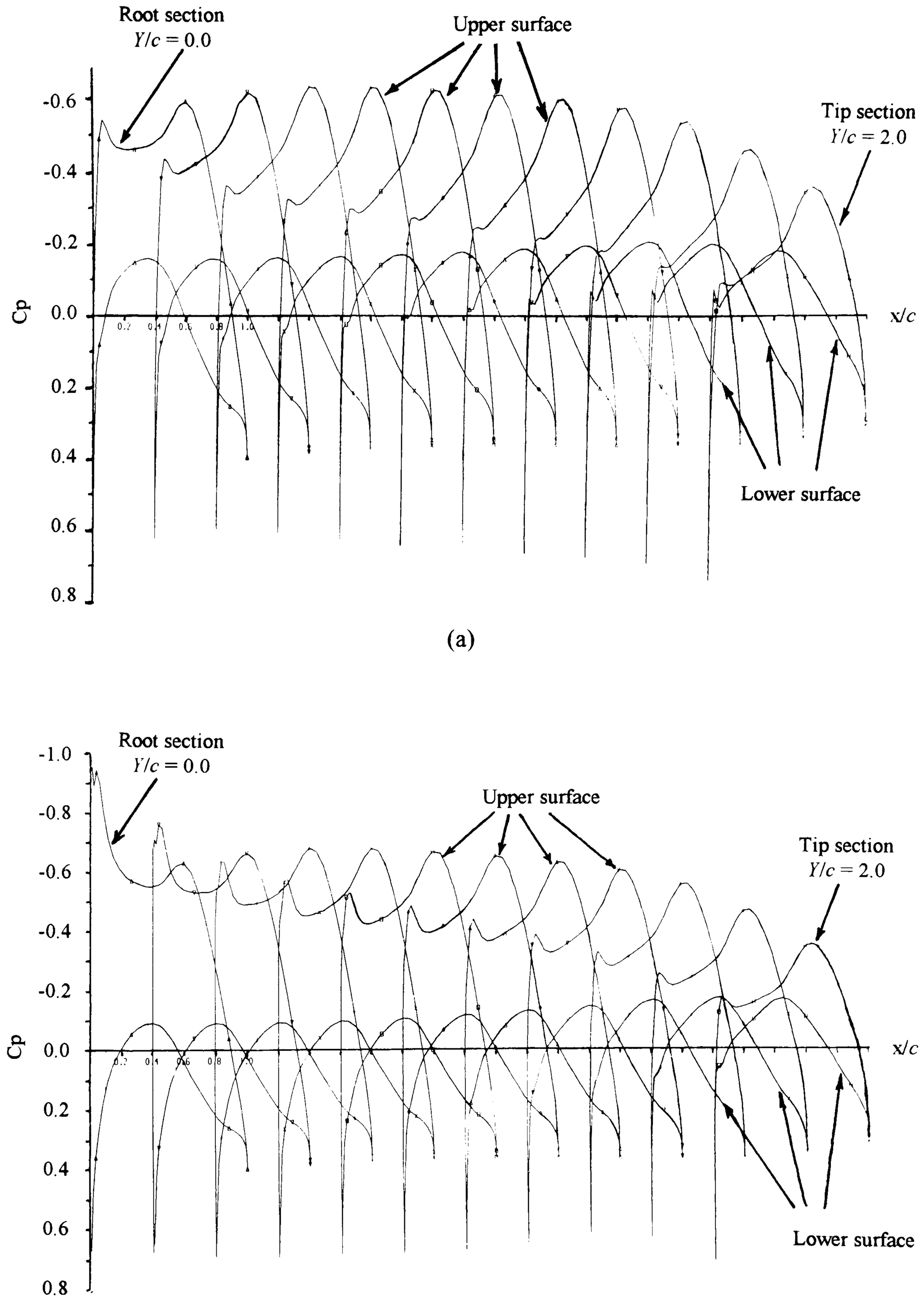

Figure 22 Inviscid predictions obtained from **SPARV** of chordwise pressure distribution at stations along the span of the wing of aspect ratio 4, with a reflection plate at the wing tip, at:
(a) $\alpha = +1°$ & (b) $\alpha = +3°$
Spanwise interval Y/c between stations = 0.2. (continued...

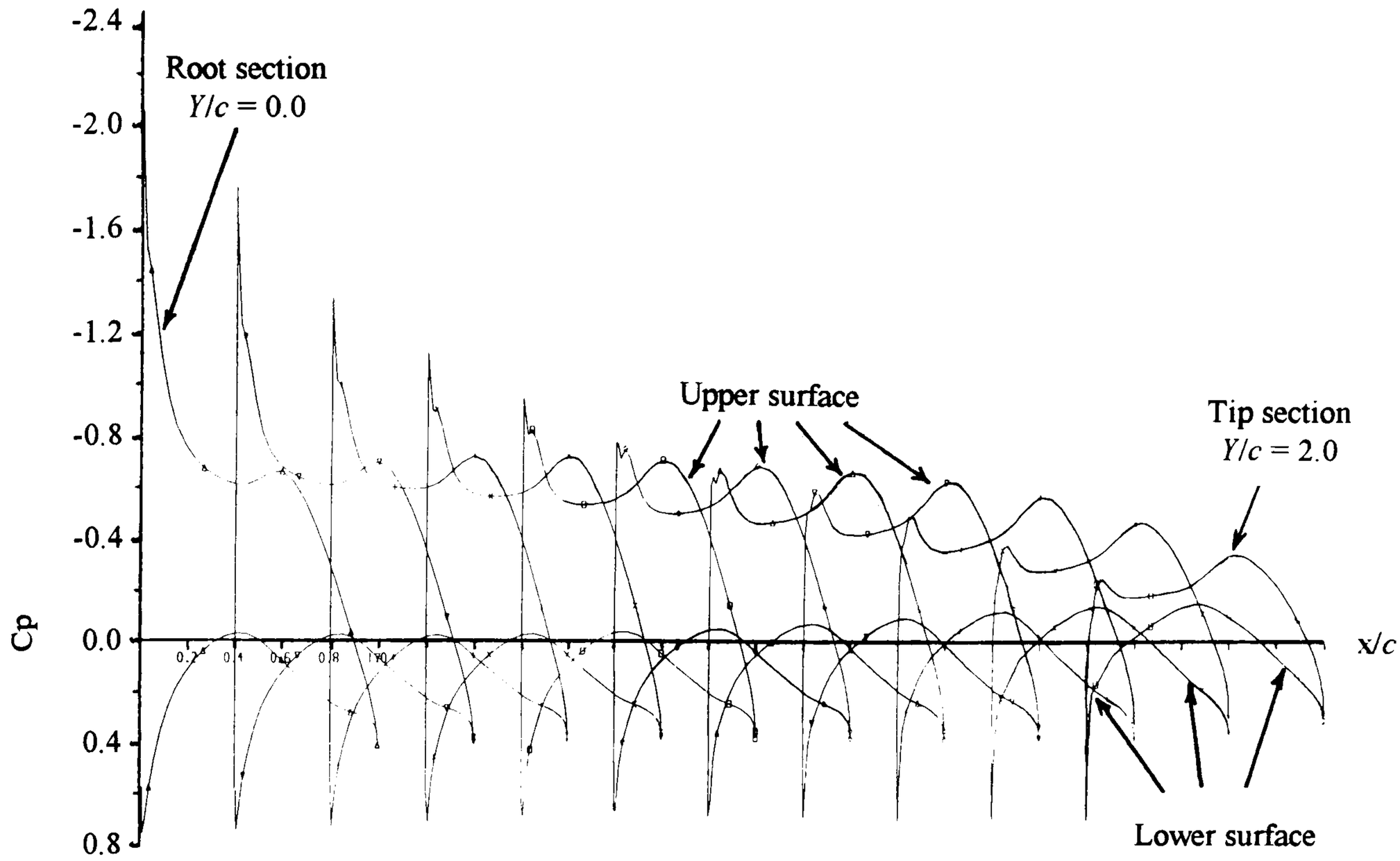

(c)

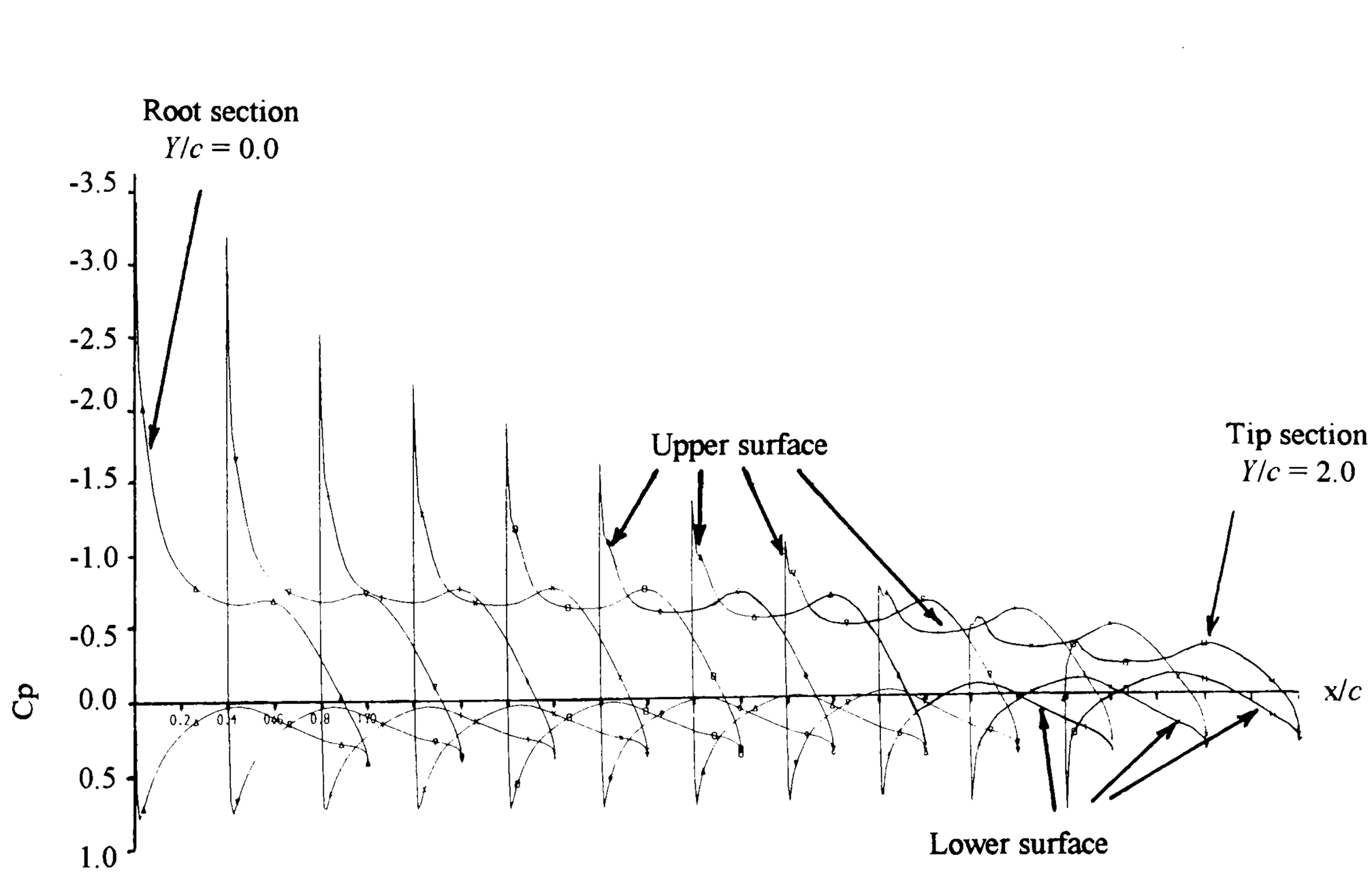

(d)

Figure 22 Inviscid predictions obtained from **SPARV** of chordwise pressure distribution at stations along the span of the wing of aspect ratio 4, with a reflection plate at the wing tip, at:
(c) $\alpha = +5°$ & (d) $\alpha = +7°$
Spanwise interval Y/c between stations = 0.2. ...concluded)

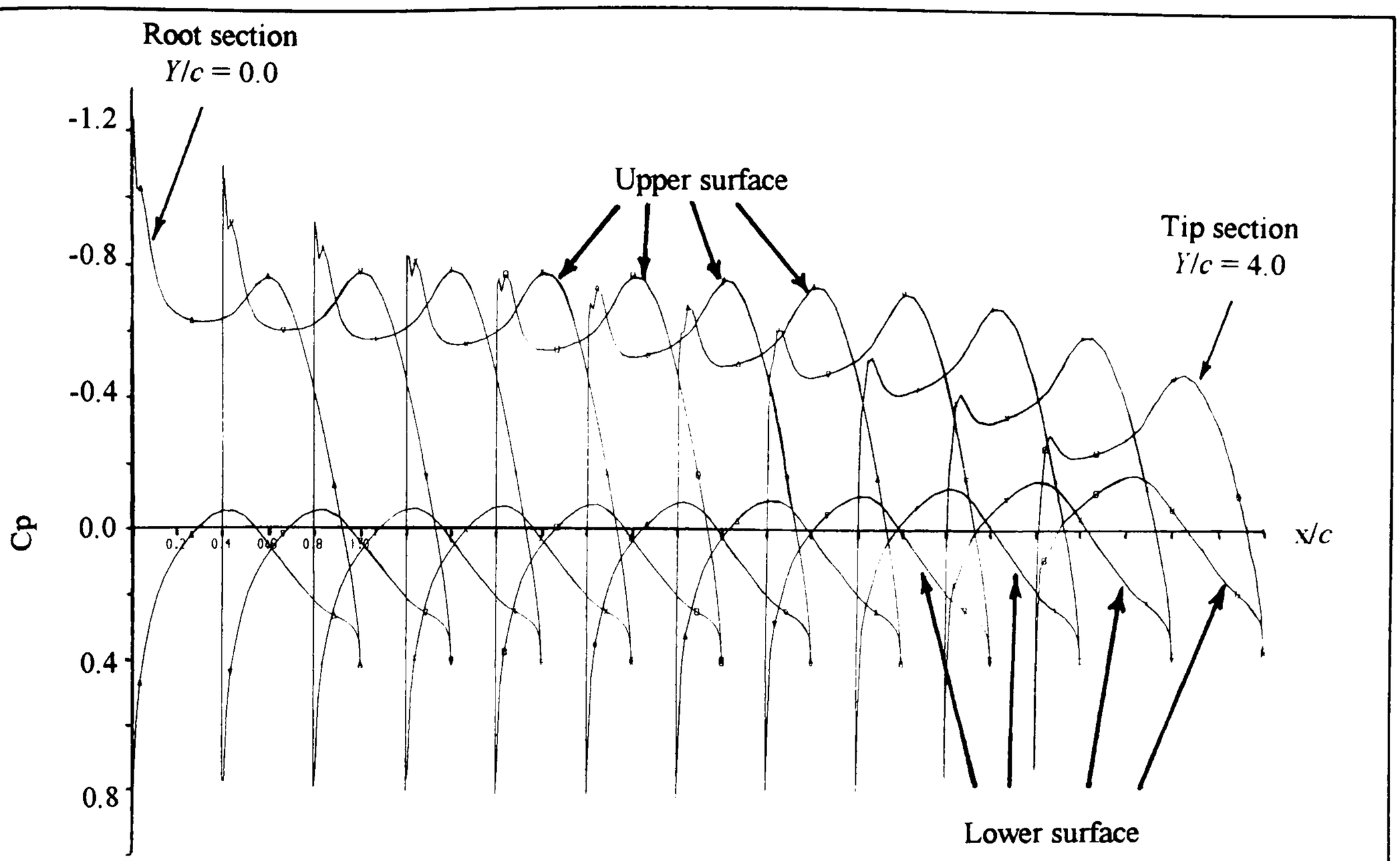

Figure 23 Inviscid predictions obtained from **SPARV** of chordwise pressure distribution at stations along the span of the wing of aspect ratio 8, with a reflection plate at the wing tip, at $\alpha = +3°$. Spanwise interval Y/c between stations = 0.4.

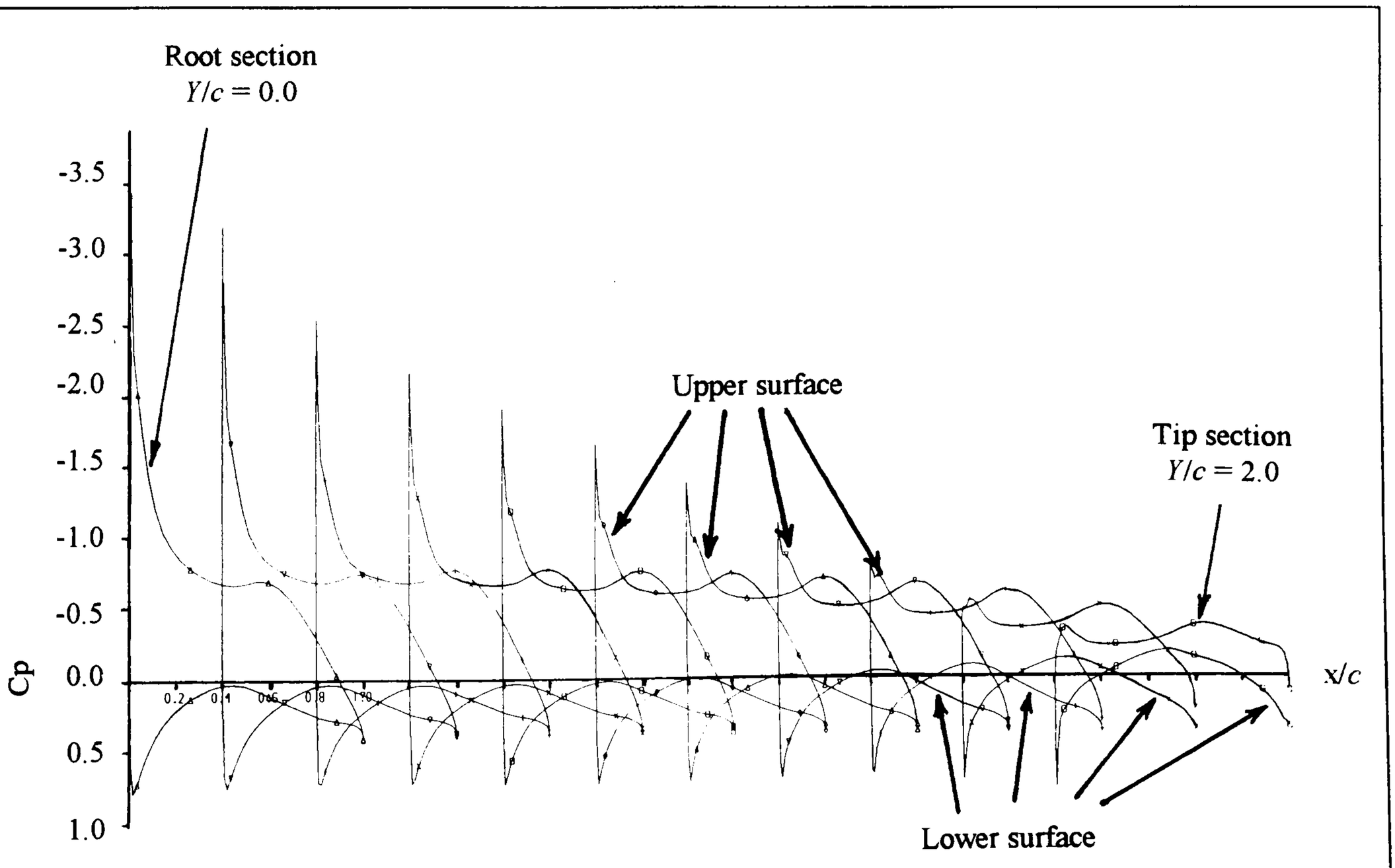

Figure 24 Inviscid predictions obtained from **SPARV** of chordwise pressure distribution at stations along the span of the wing of aspect ratio 4, with a free wing tip, at $\alpha = +7°$. Spanwise interval Y/c between stations = 0.2.

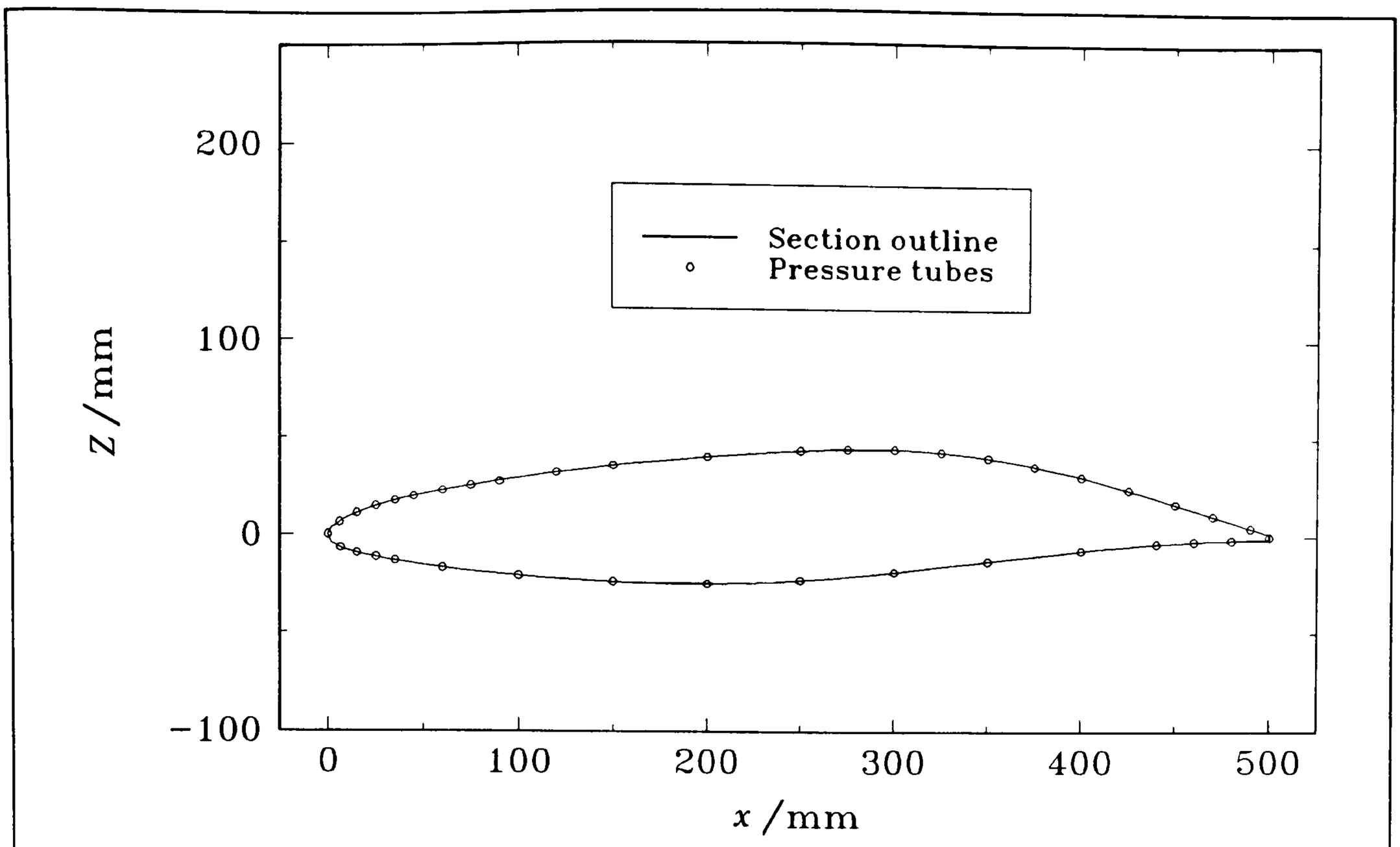

Figure 25 Locations around the aerofoil section at which pressure tubes were inlaid.

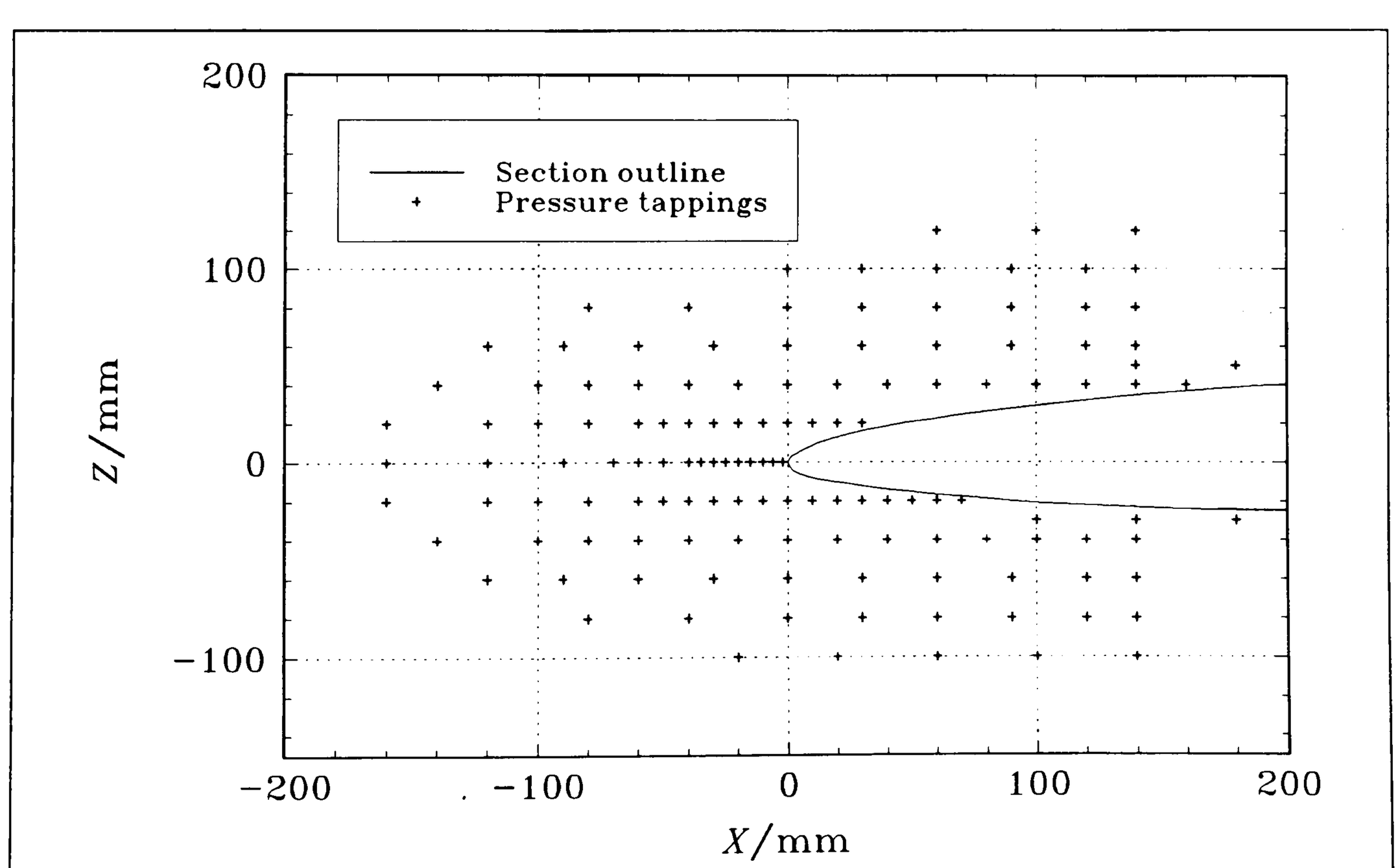

Figure 26 Locations of pressure tappings in the plate.

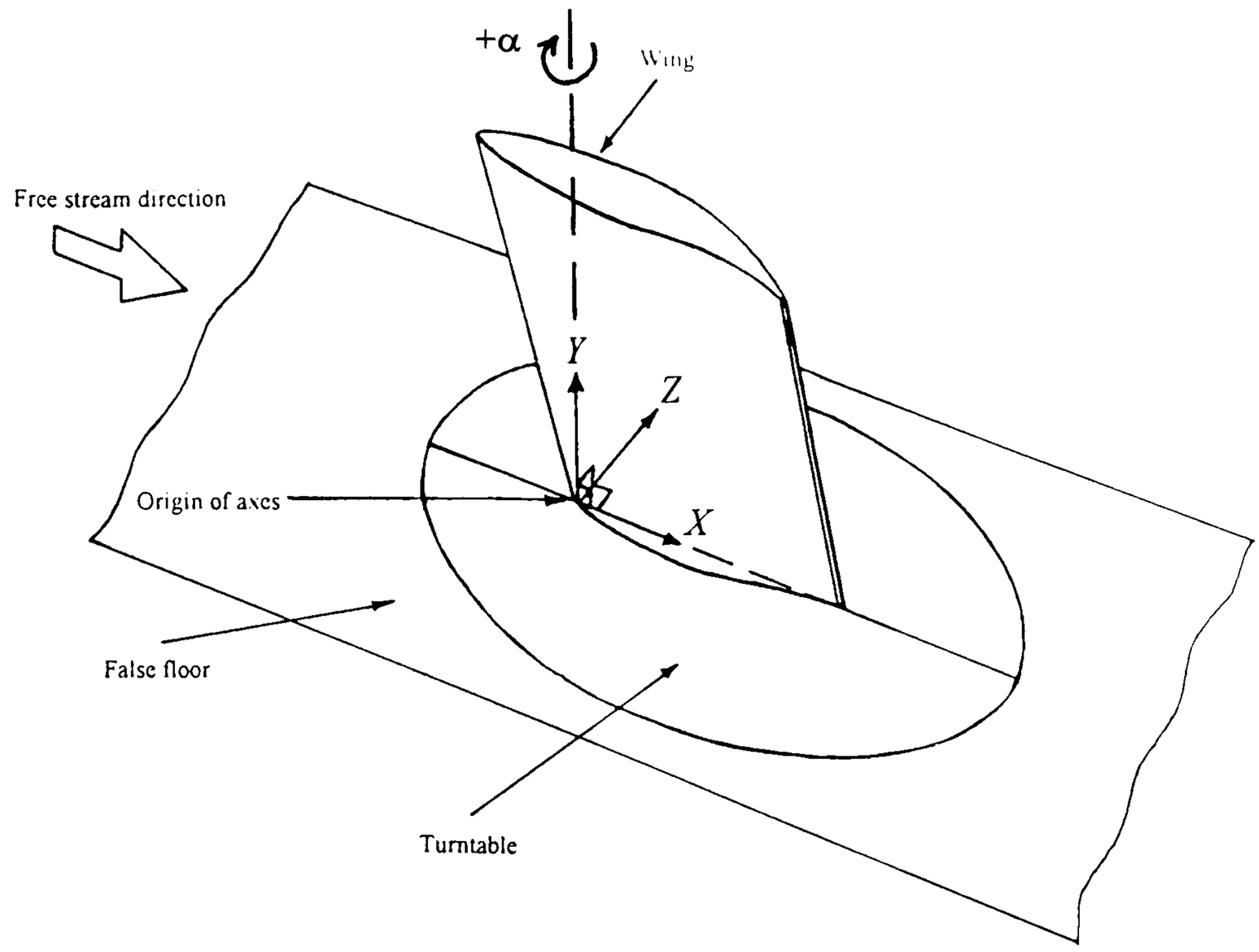

Figure 27 3-D view of the wing and plate showing the *left-handed* axis system.

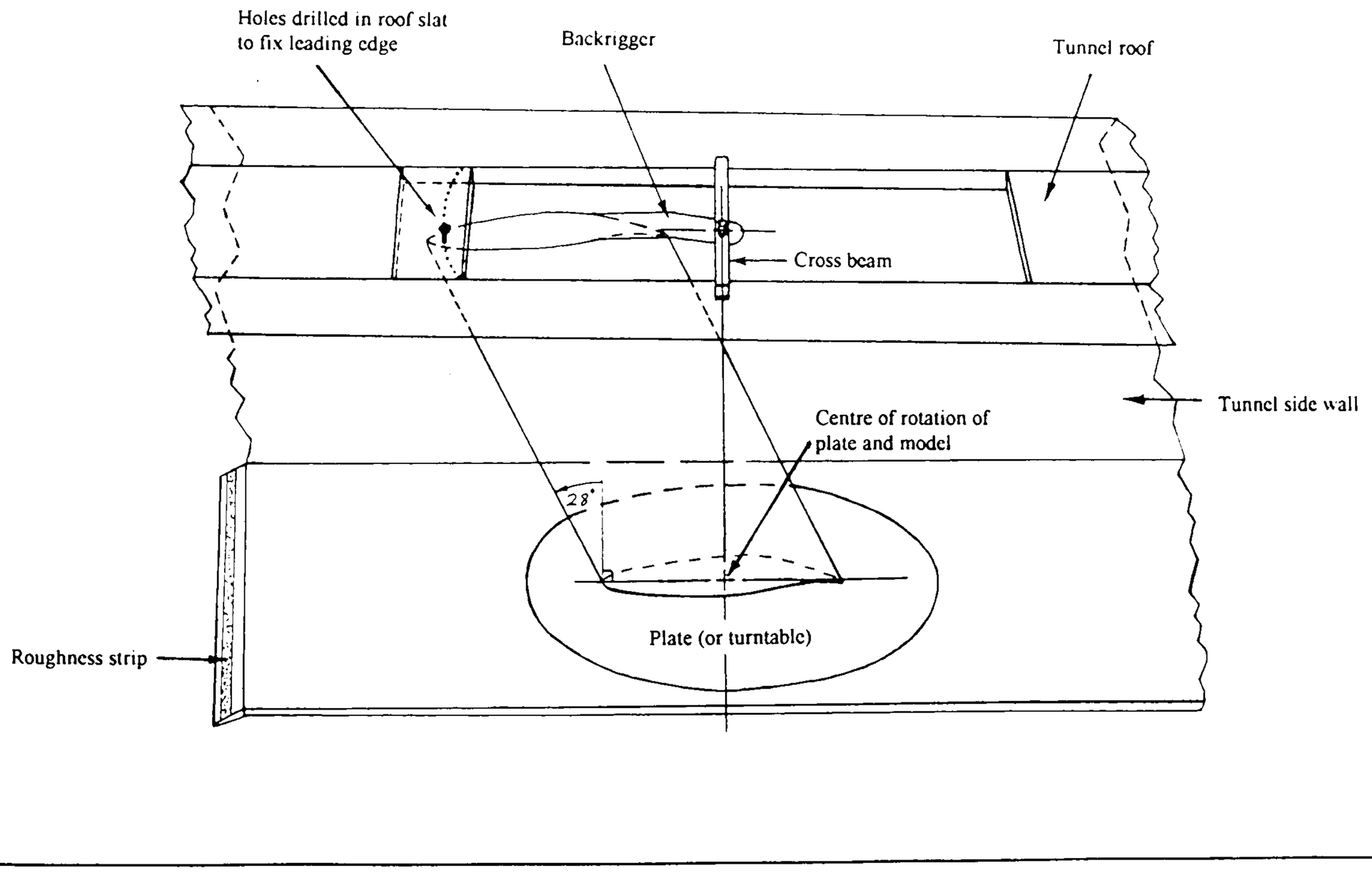

Figure 28 Oblique view of the wing mounted in the wind tunnel.

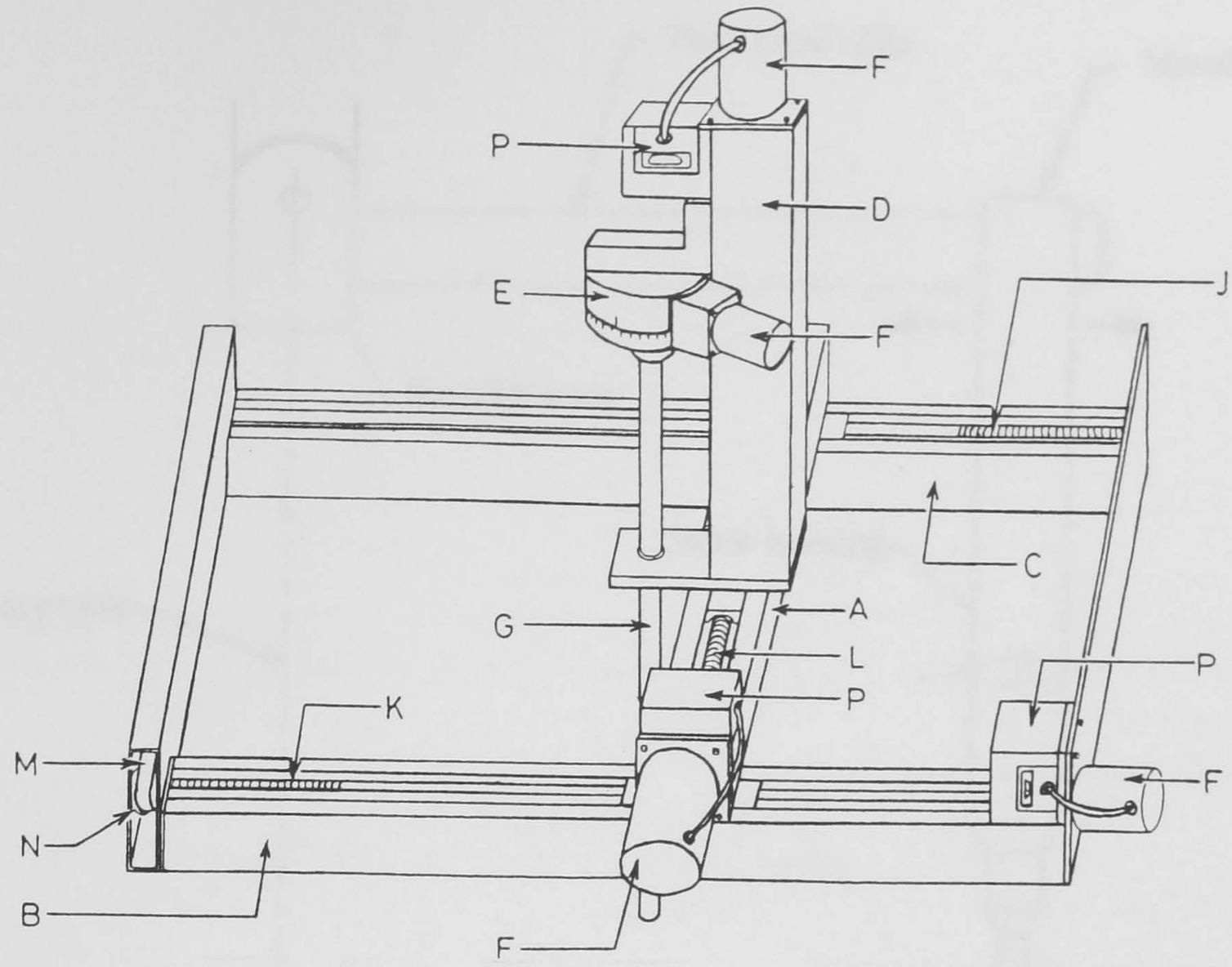

Figure 29 The roof-mounted traversing gear.

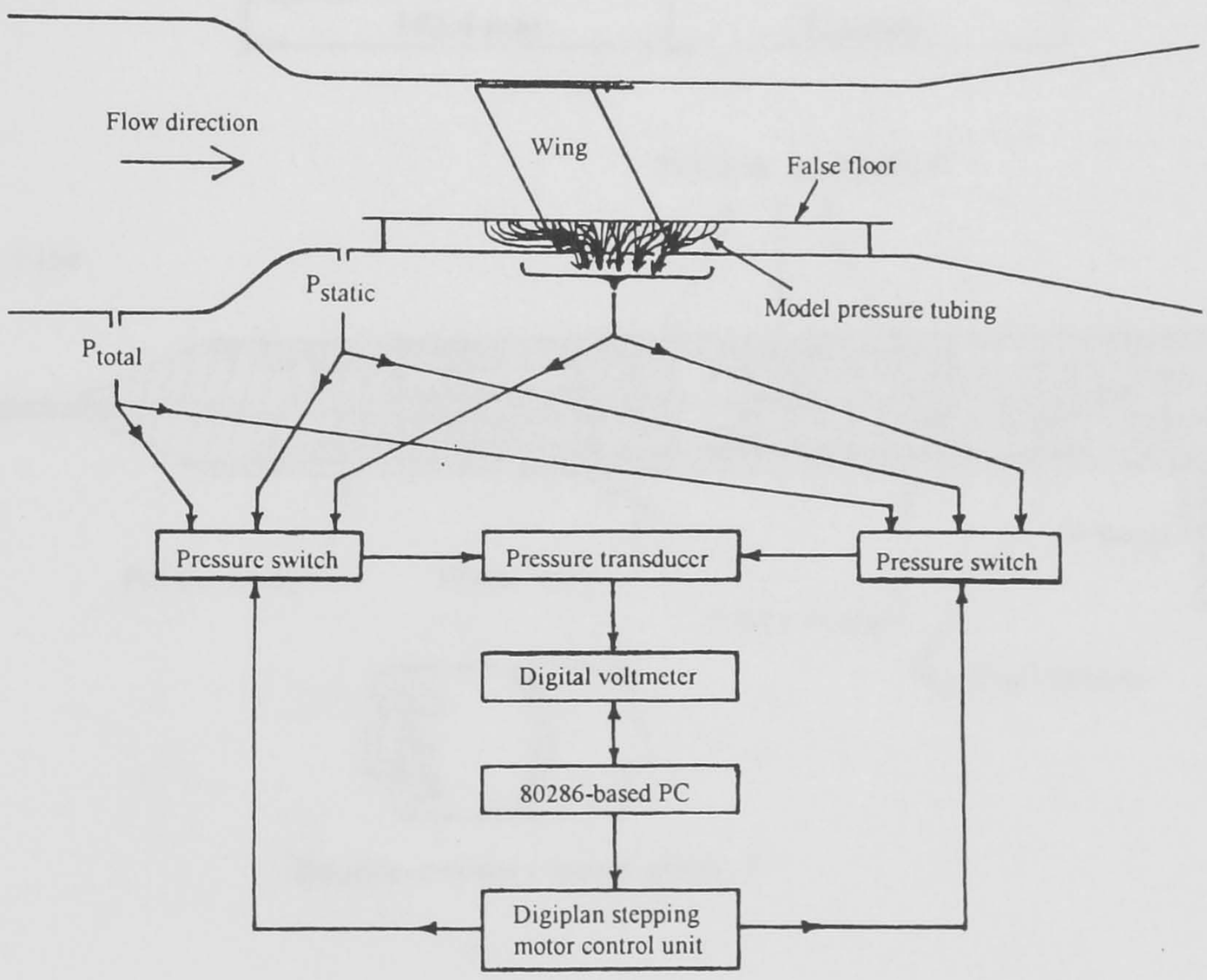

Figure 30 Experimental apparatus for the surface pressure measurements.

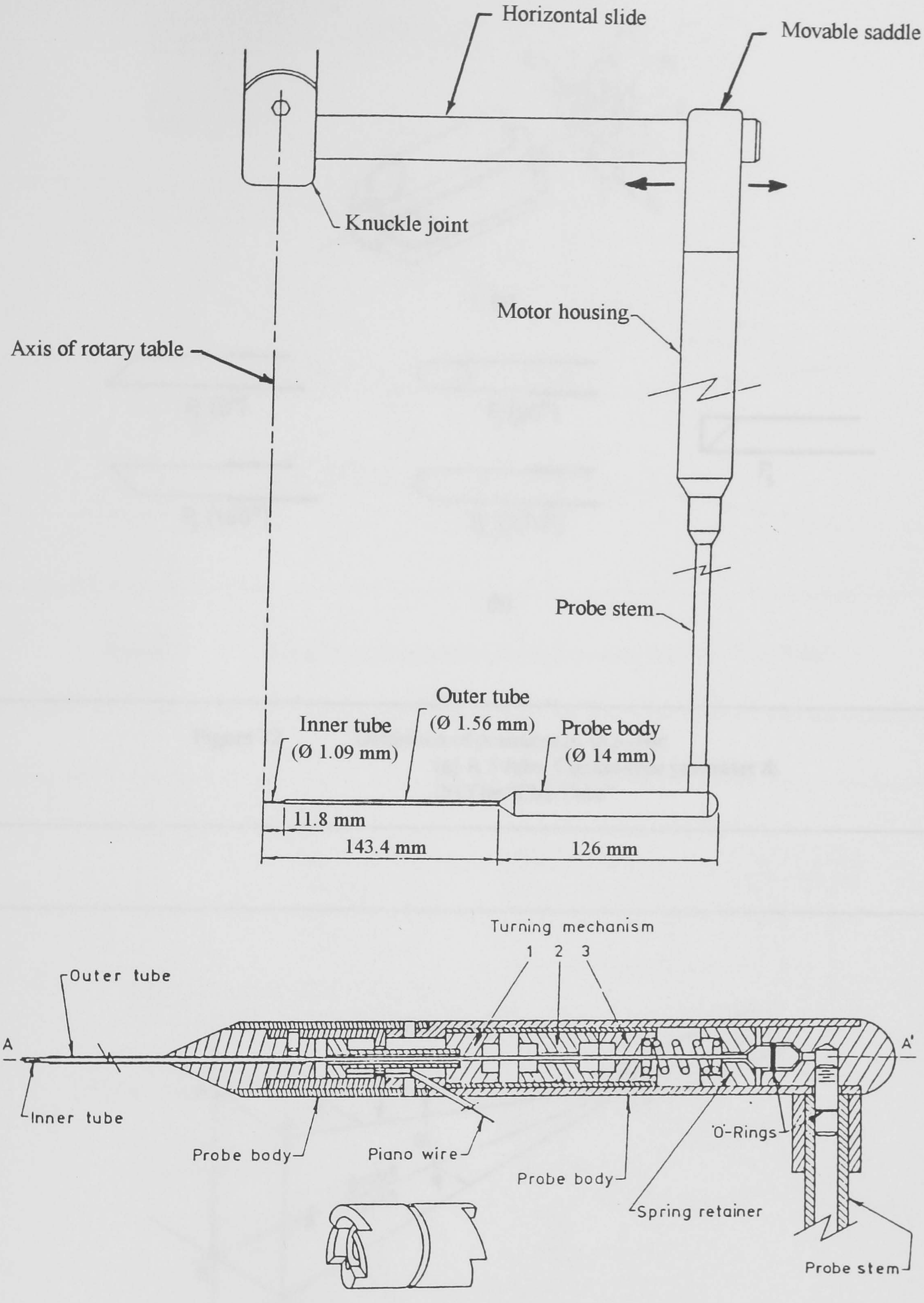

Figure 31 The "Chu-Tube": a single-tube yawmeter.

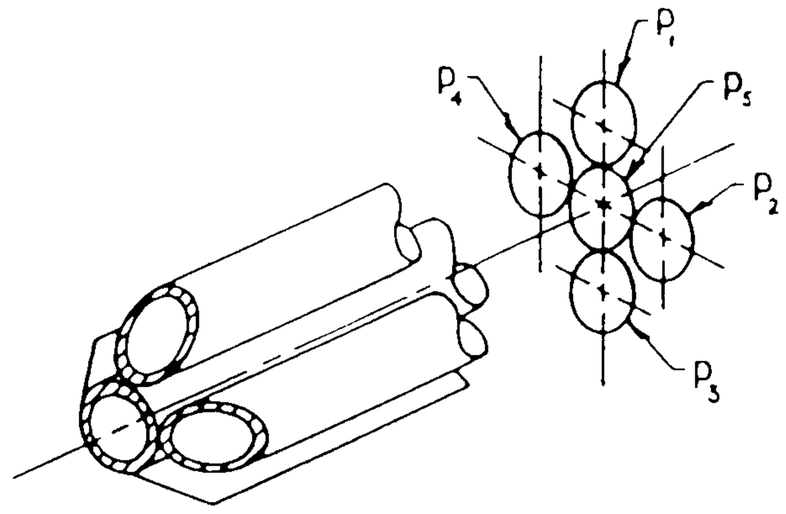

(a)

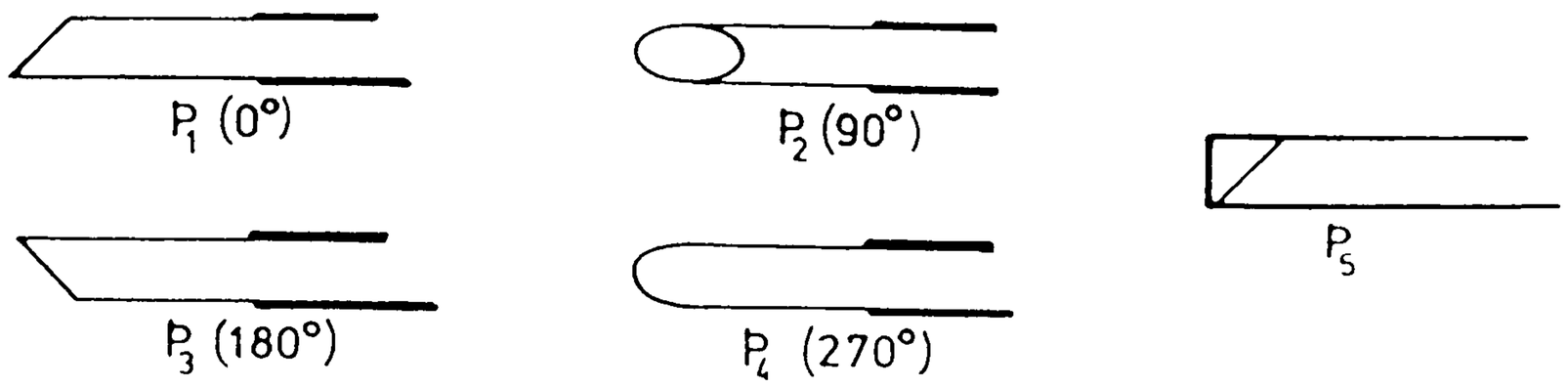

(b)

Figure 32 Definition of pressures p_1 to p_5 for:
(a) A 5-tube, Conrad-type yawmeter &
(b) The "Chu-Tube".

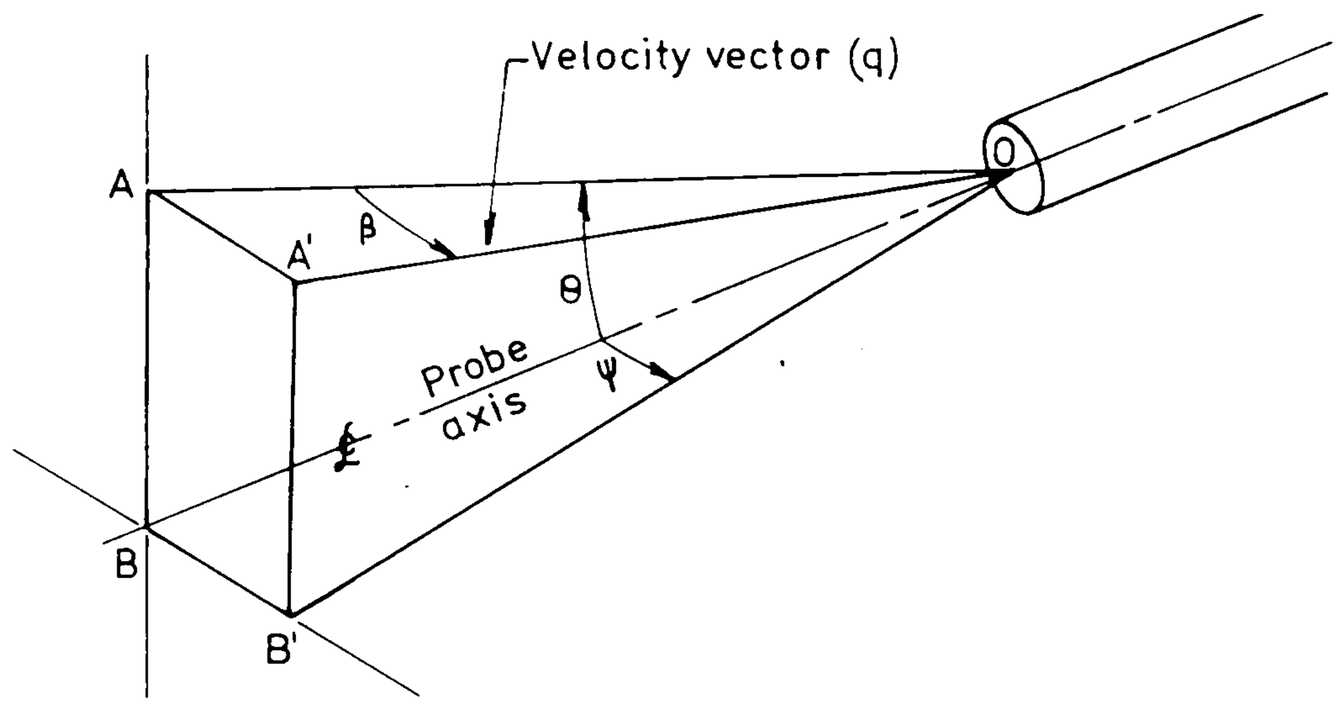

Figure 33 Definition of the yaw and pitch angles in relation to the "Chu-Tube".

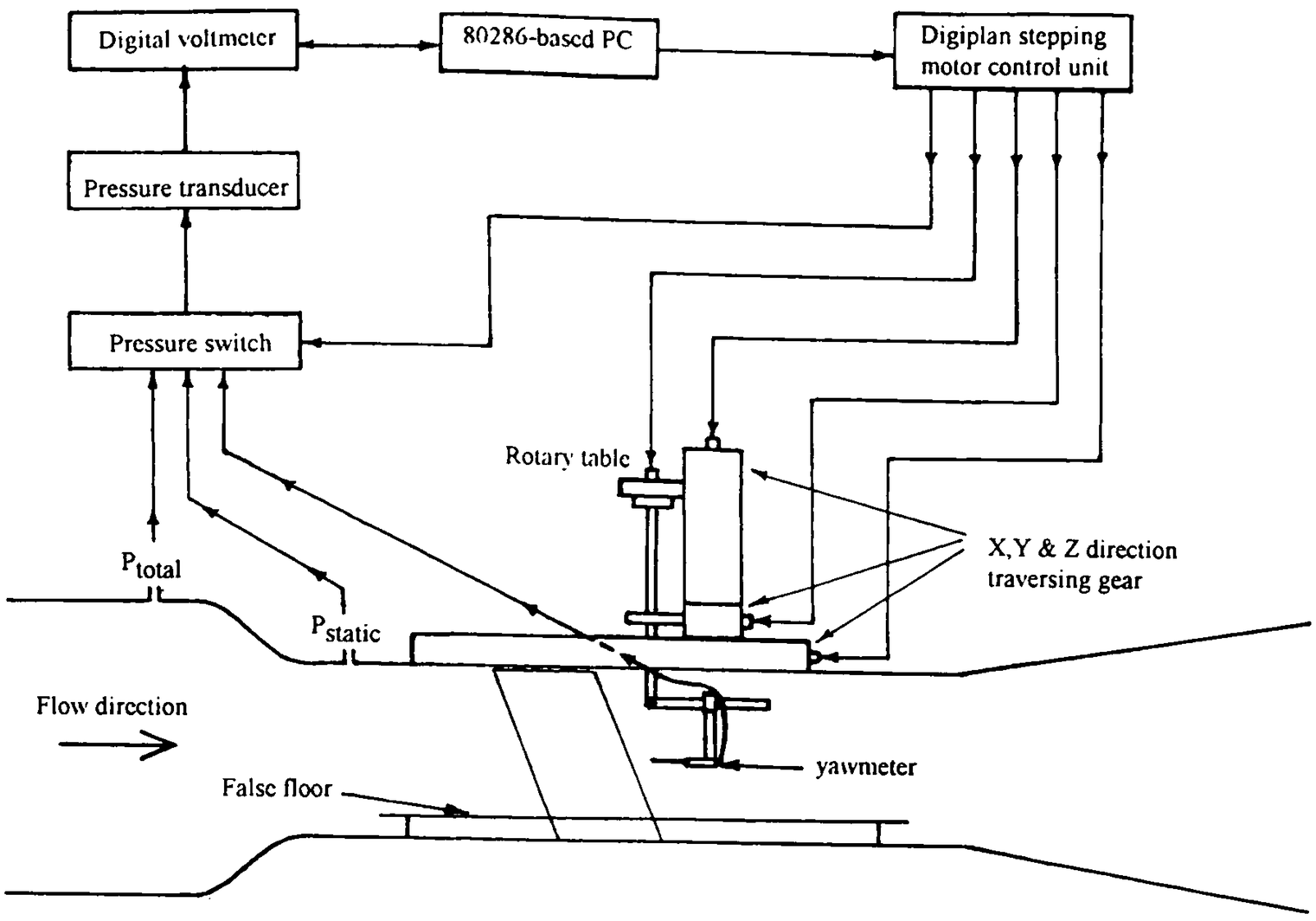

Figure 34 Experimental apparatus for measurements with the "Chu-Tube".

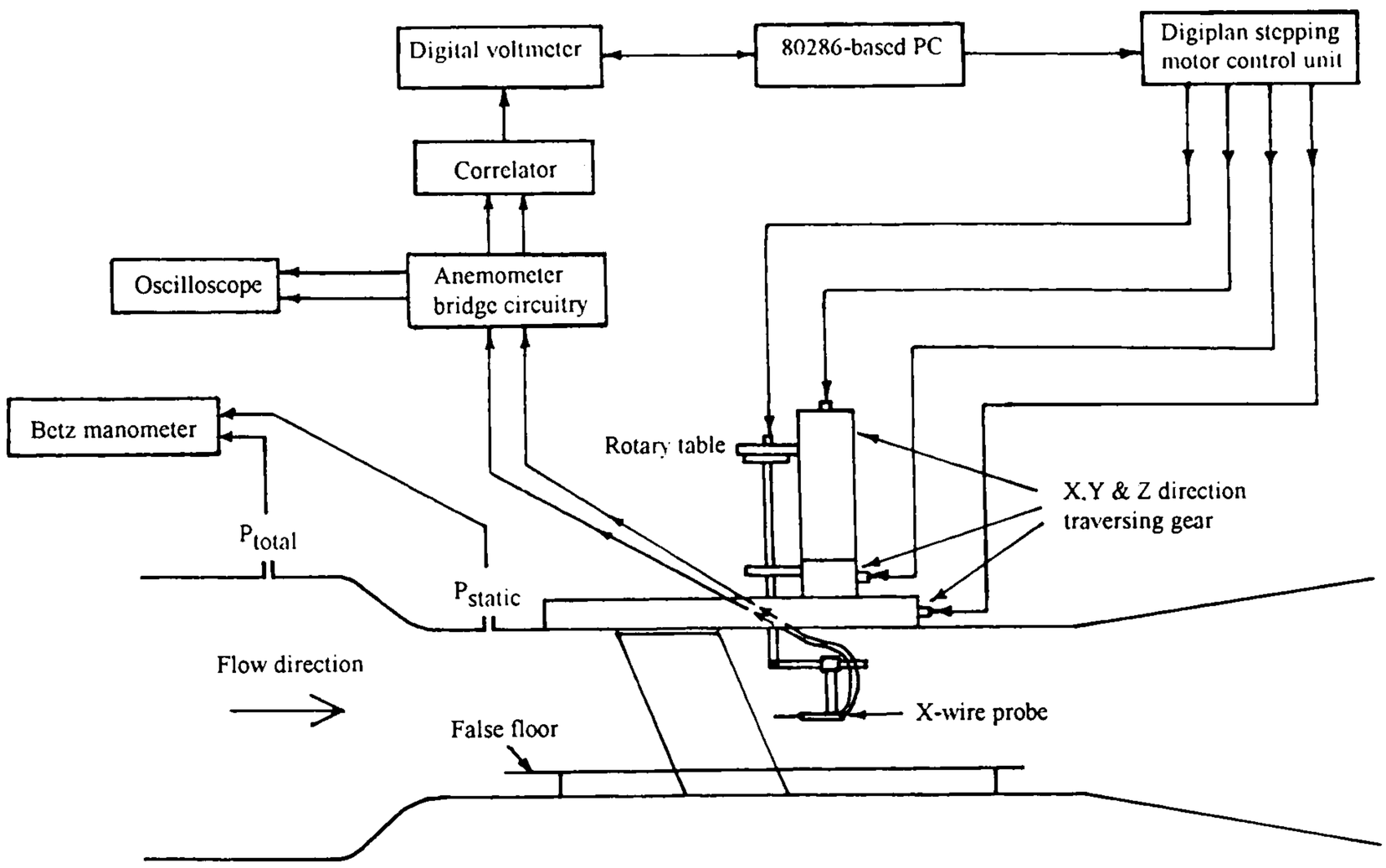

Figure 35 Experimental apparatus for measurements with the X-wire probe.

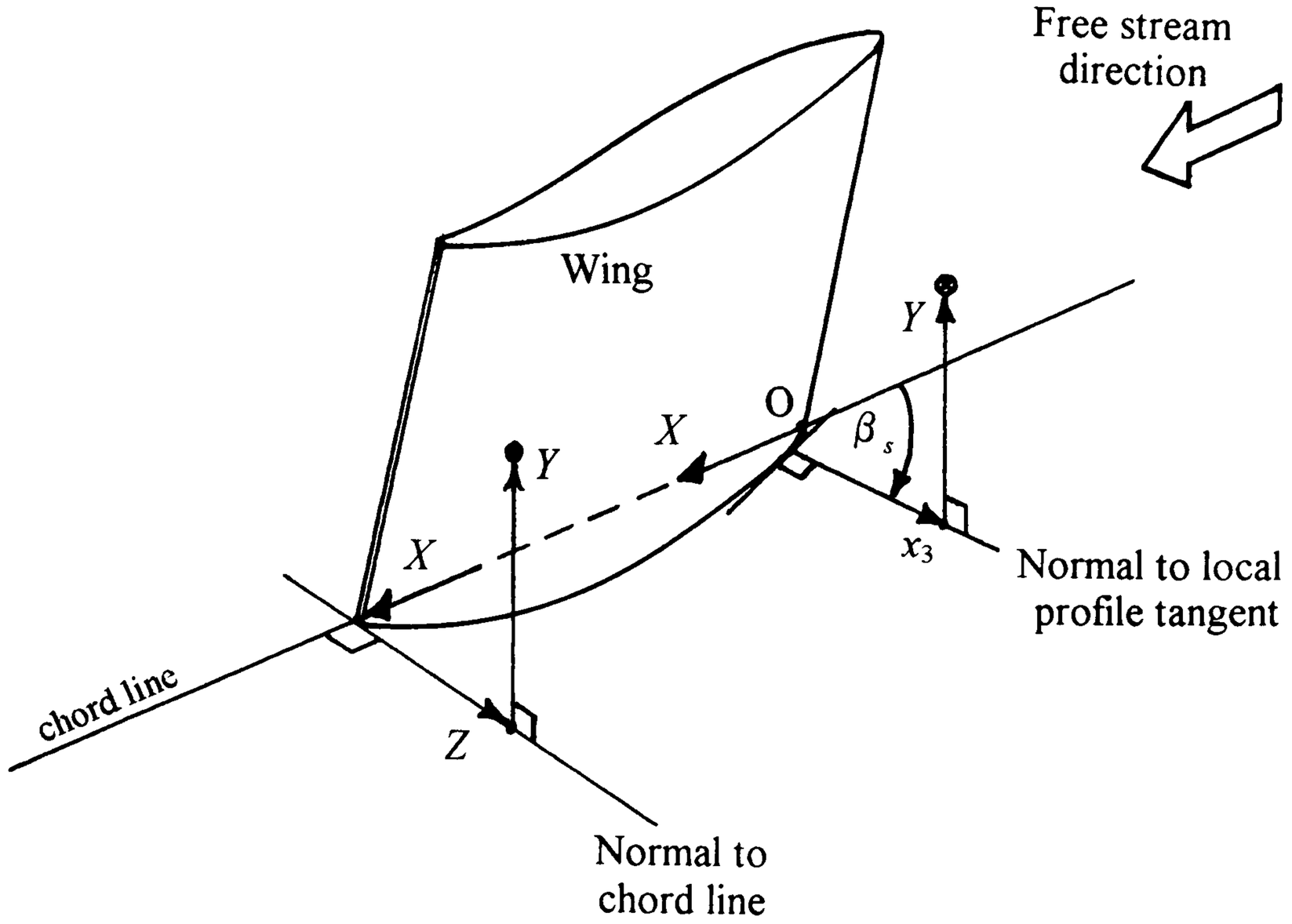

(a)

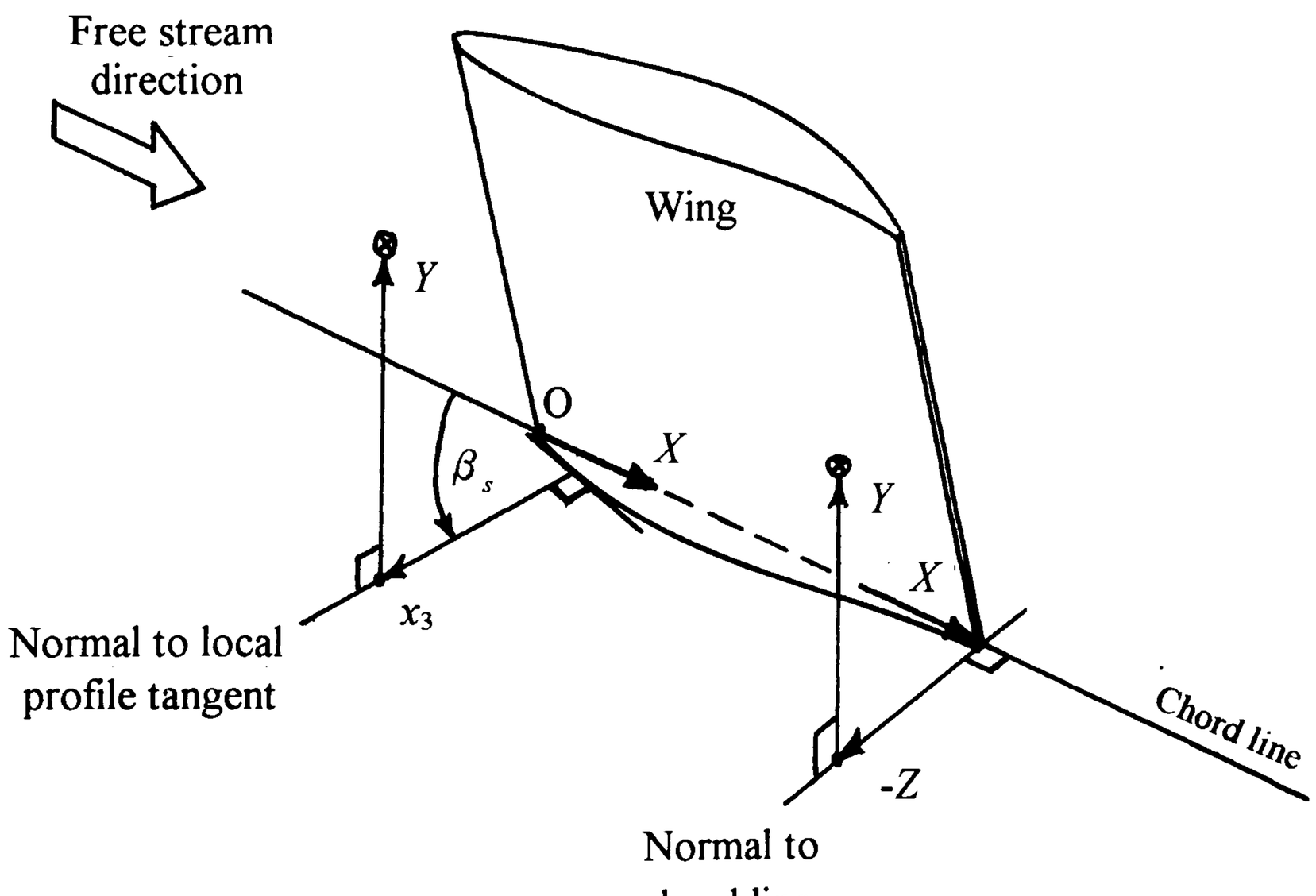

(b)

Figure 36 Oblique views of coordinate systems (X, β_S, x_3 Y) and (X, Y, Z) from:
(a) +Z side of the junction &
(b) -Z side of the junction.

Planes are normal to the tangent to the local profile of the wing surface.

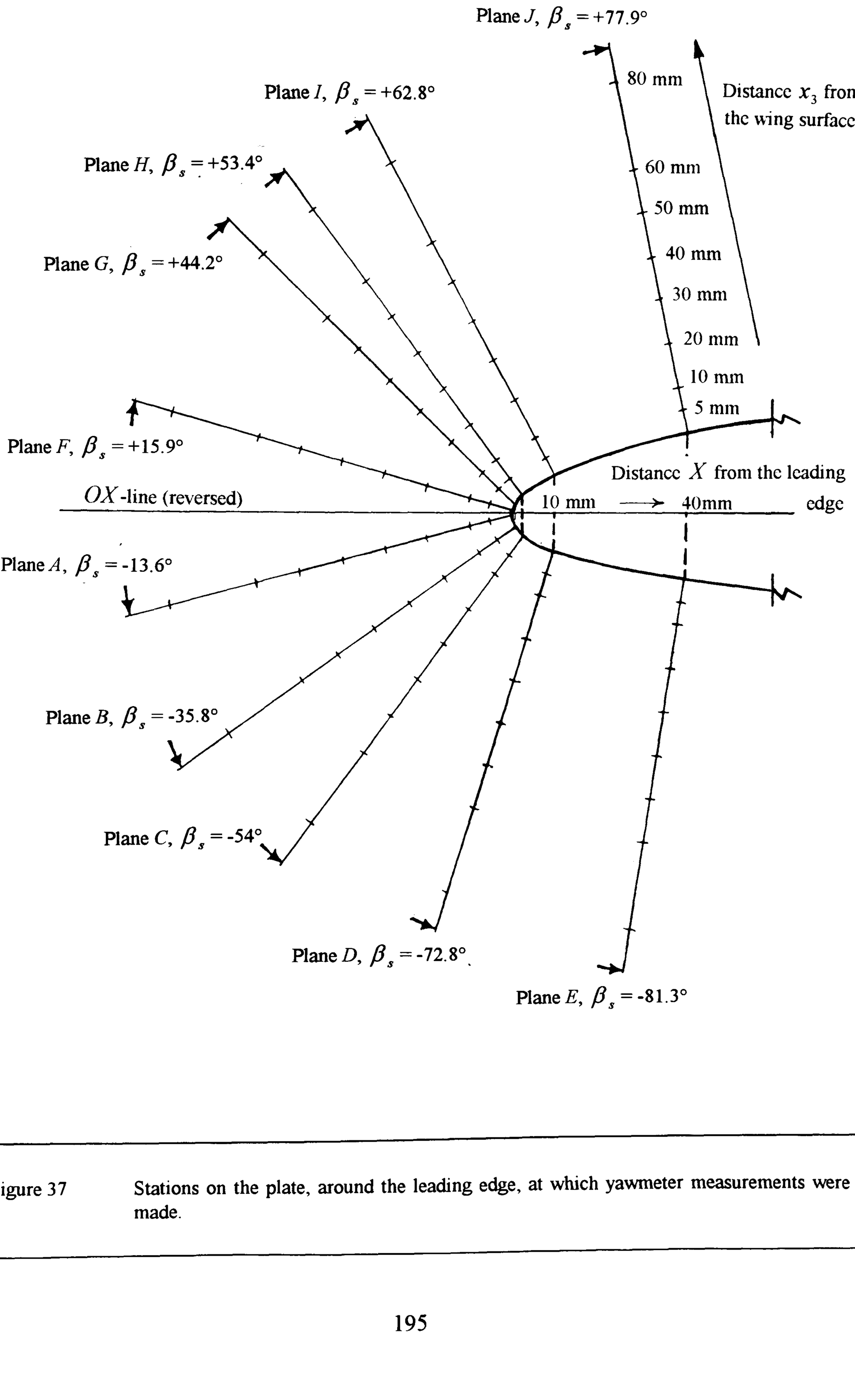

Figure 37 Stations on the plate, around the leading edge, at which yawmeter measurements were made.

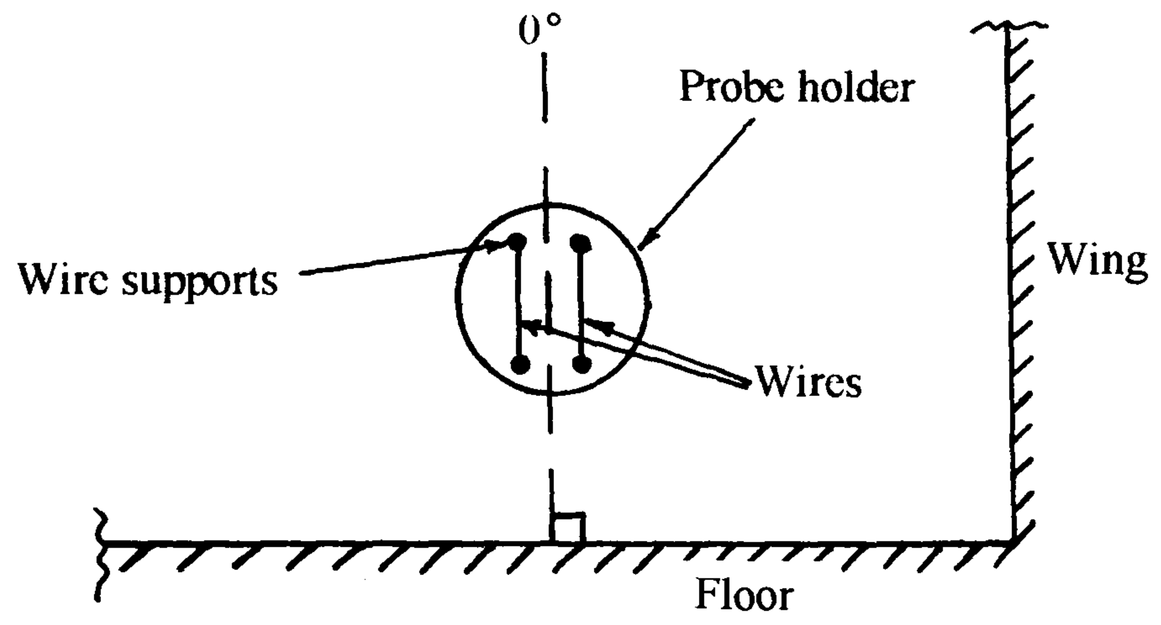

(a)

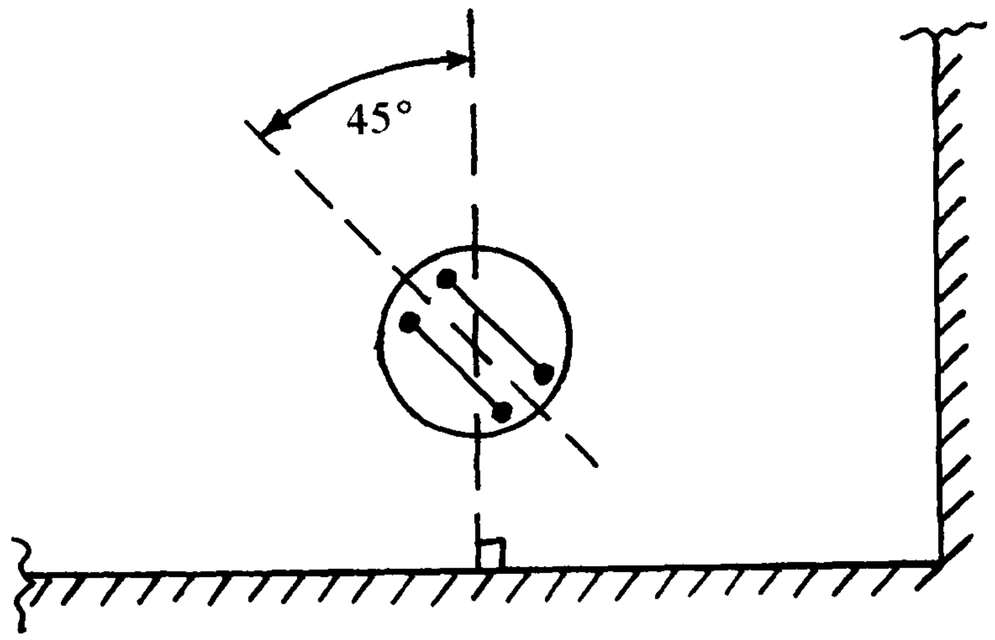

(b)

(c)

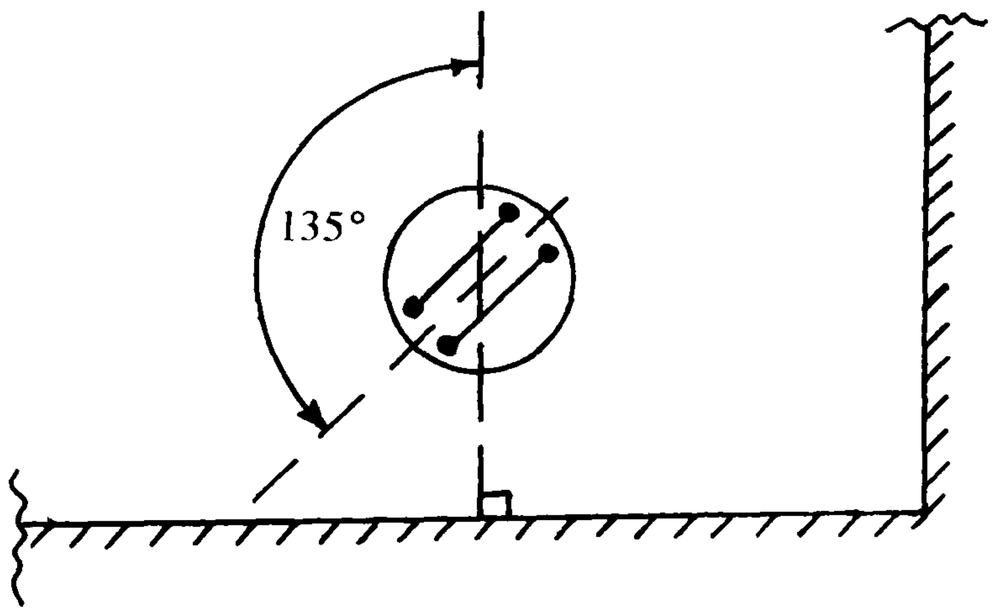

(d)

Figure 38 The X-wire probe at its 4 rotations, viewed from upstream (not to scale): (a) 0°-, (b) 45°-, (c) 90°- & (d) 135°-positions.

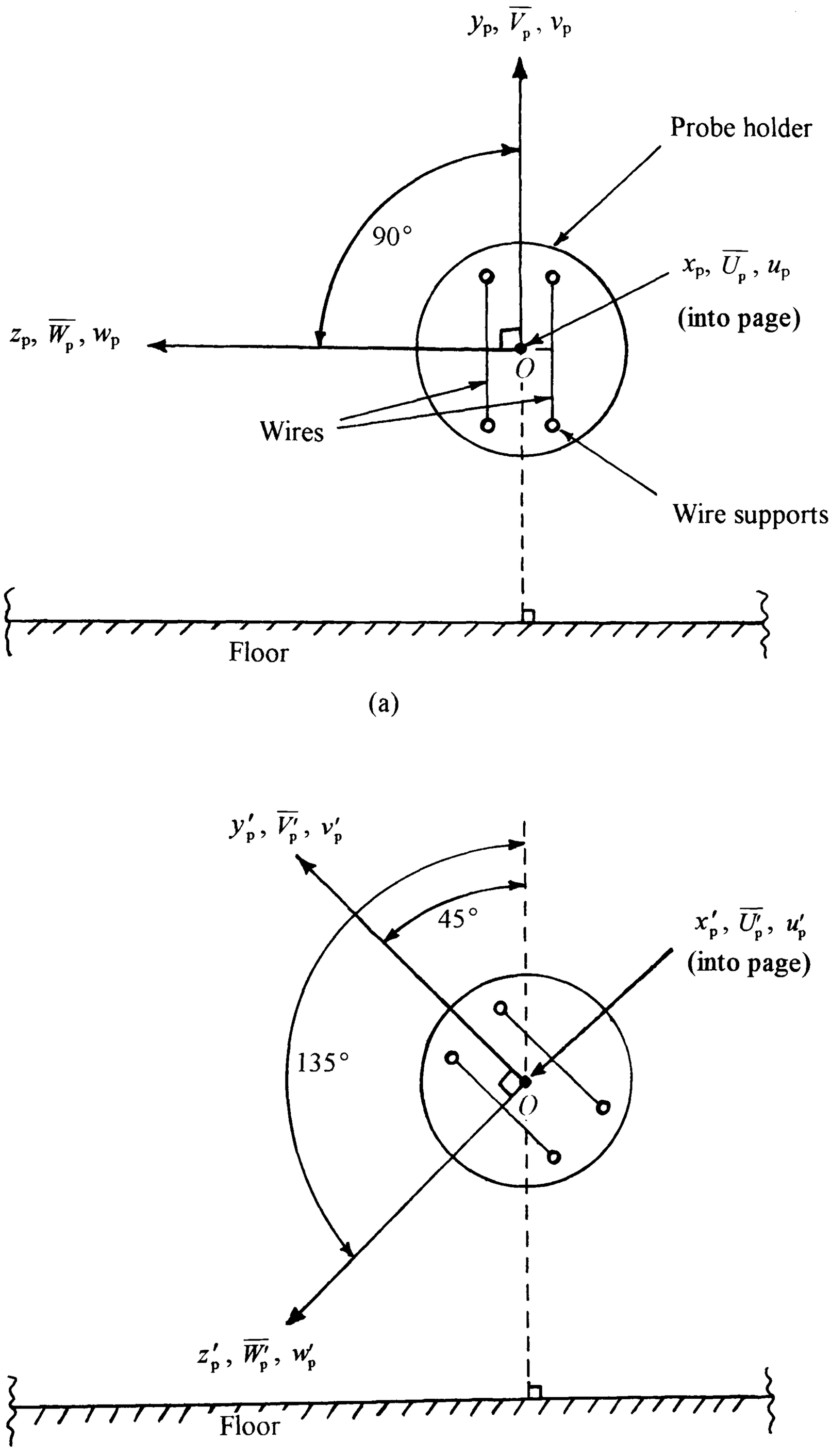

Figure 39 Definition of the local axis system for the X-wire probe, viewed from upstream.

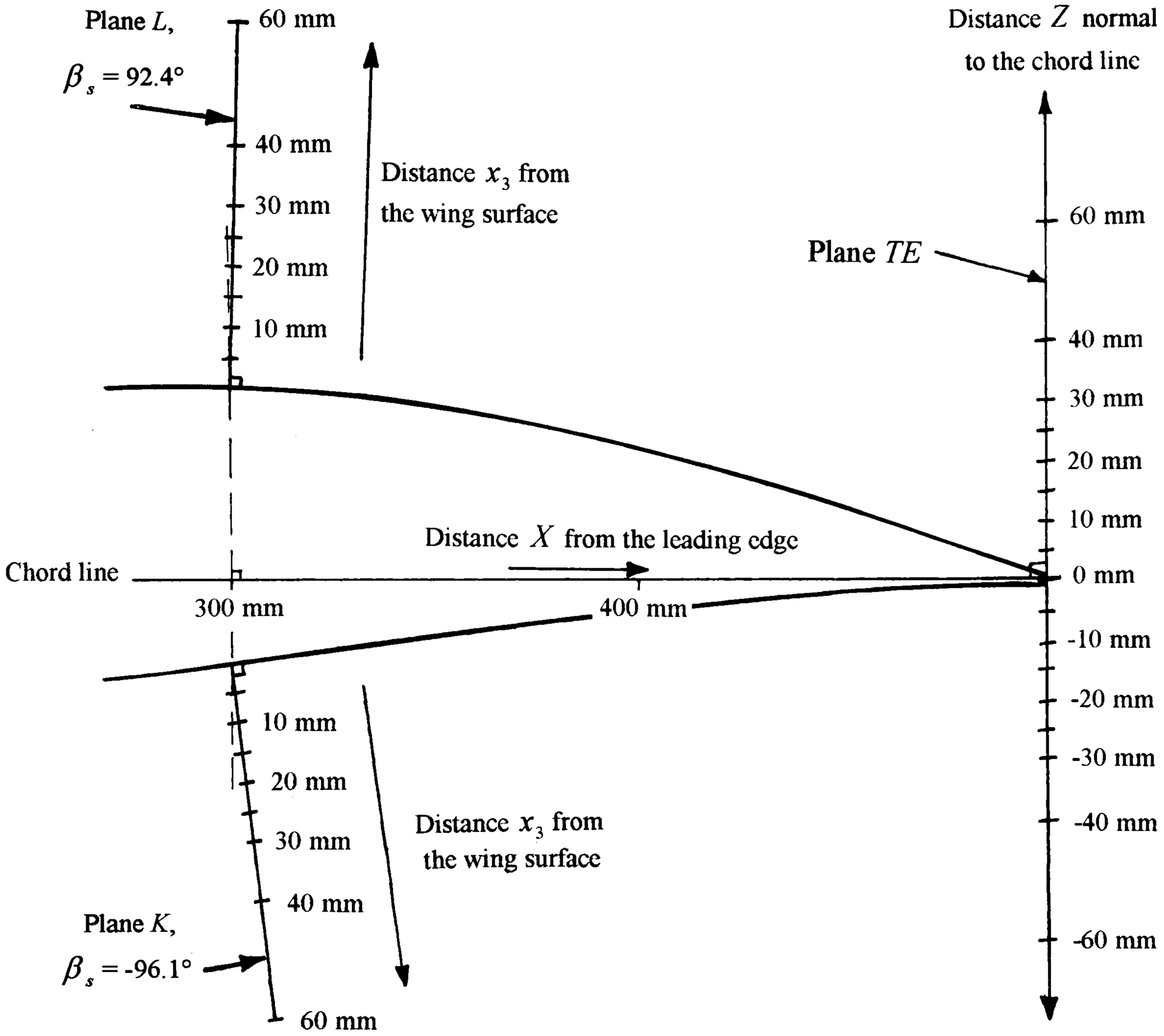

Planes are normal to the tangent to the local profile of the wing surface.

Figure 40 Stations on the plate at which X-wire measurements were made, in planes normal to the tangents to the wing profile at $X = 300$ mm ($0.6c$) and in the cross-stream plane at the trailing edge, $X = 500$ mm ($1.0c$).

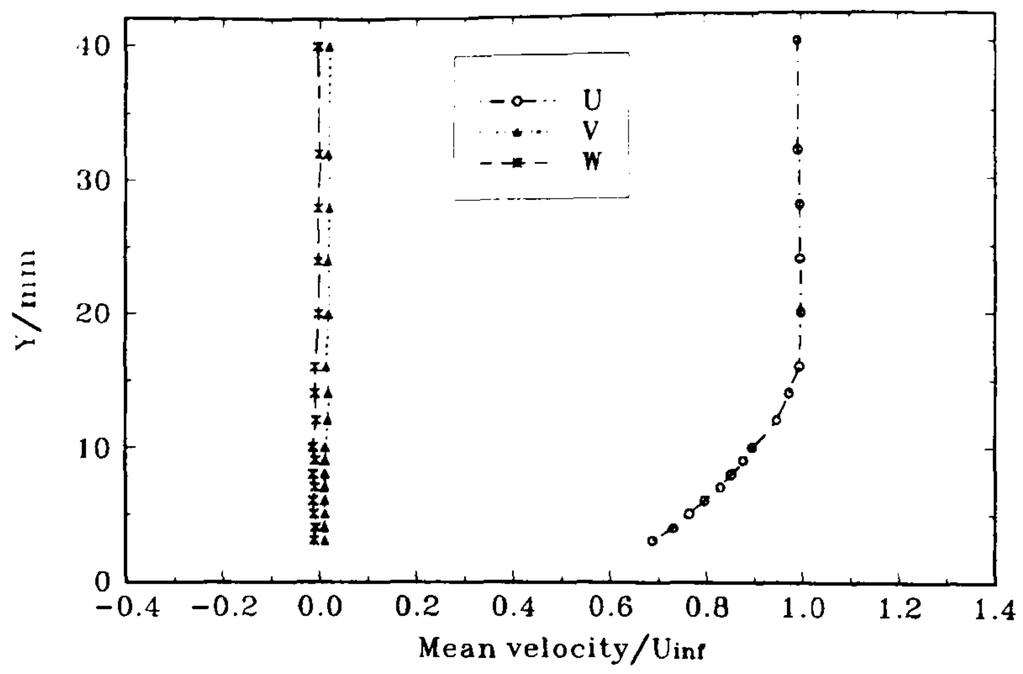

Figure 41 Upstream conditions in the plate boundary layer at (X,Z)/mm = (-500,-120):
(a) Mean velocities $(\overline{U}, \overline{V}, \overline{W})/U_\infty$, (b) Flow pitch and yaw angles (θ, ψ),
(c) Turbulence quantities $(\overline{u^2}, \overline{v^2}, \overline{w^2})/U_\infty^2$ & (d) Turbulence quantities $(\overline{uv}, \overline{uw})/U_\infty^2$

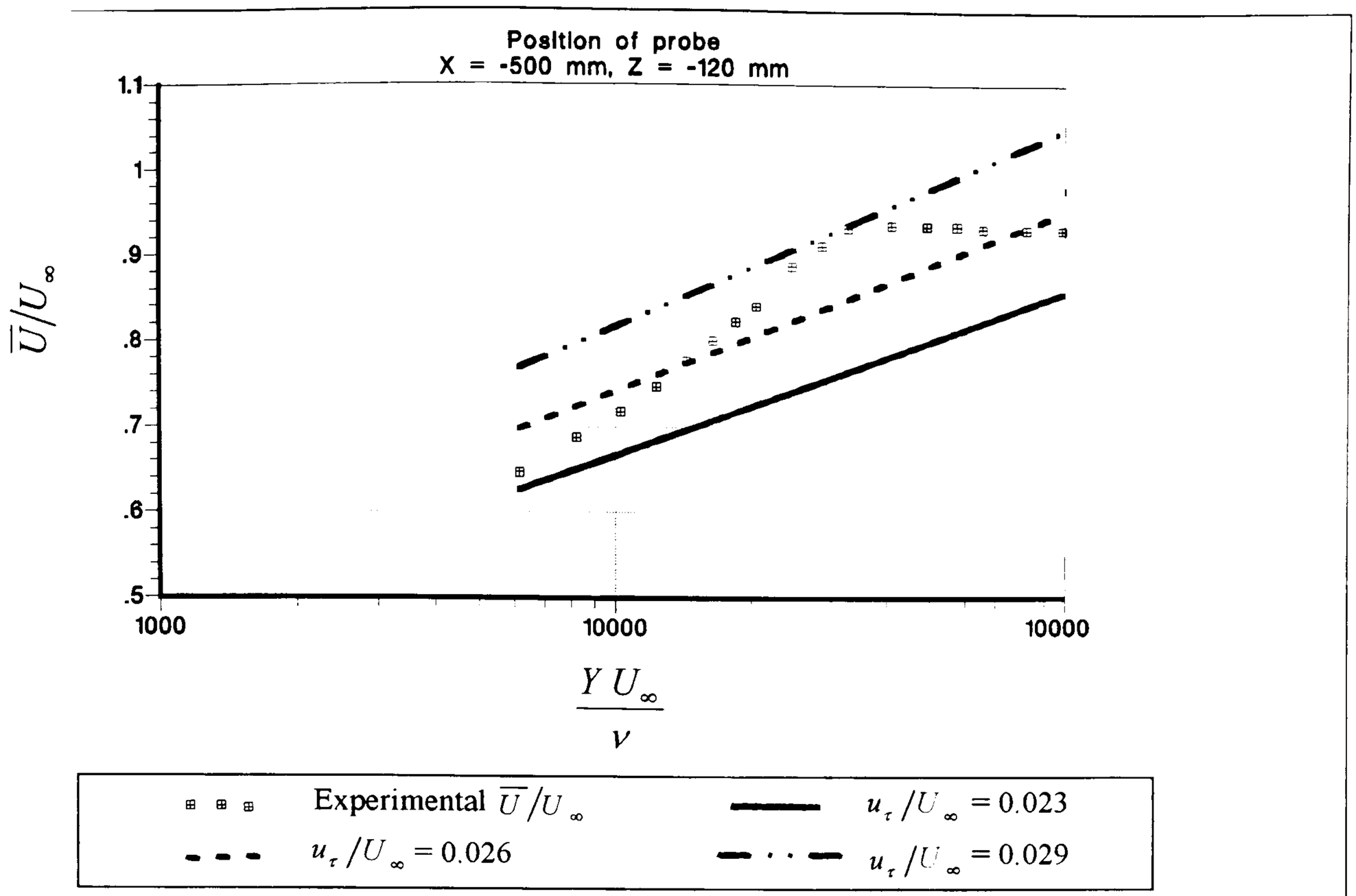

Figure 42 Semi-logarithmic plot of the $\overline{U}/U_\infty$ profile at $(X,Z)/\text{mm} = (-500,-120)$. The straight lines correspond to calculated values of $\overline{U}/U_\infty$ from equation (6.2) using the quoted values of u_τ/U_∞.

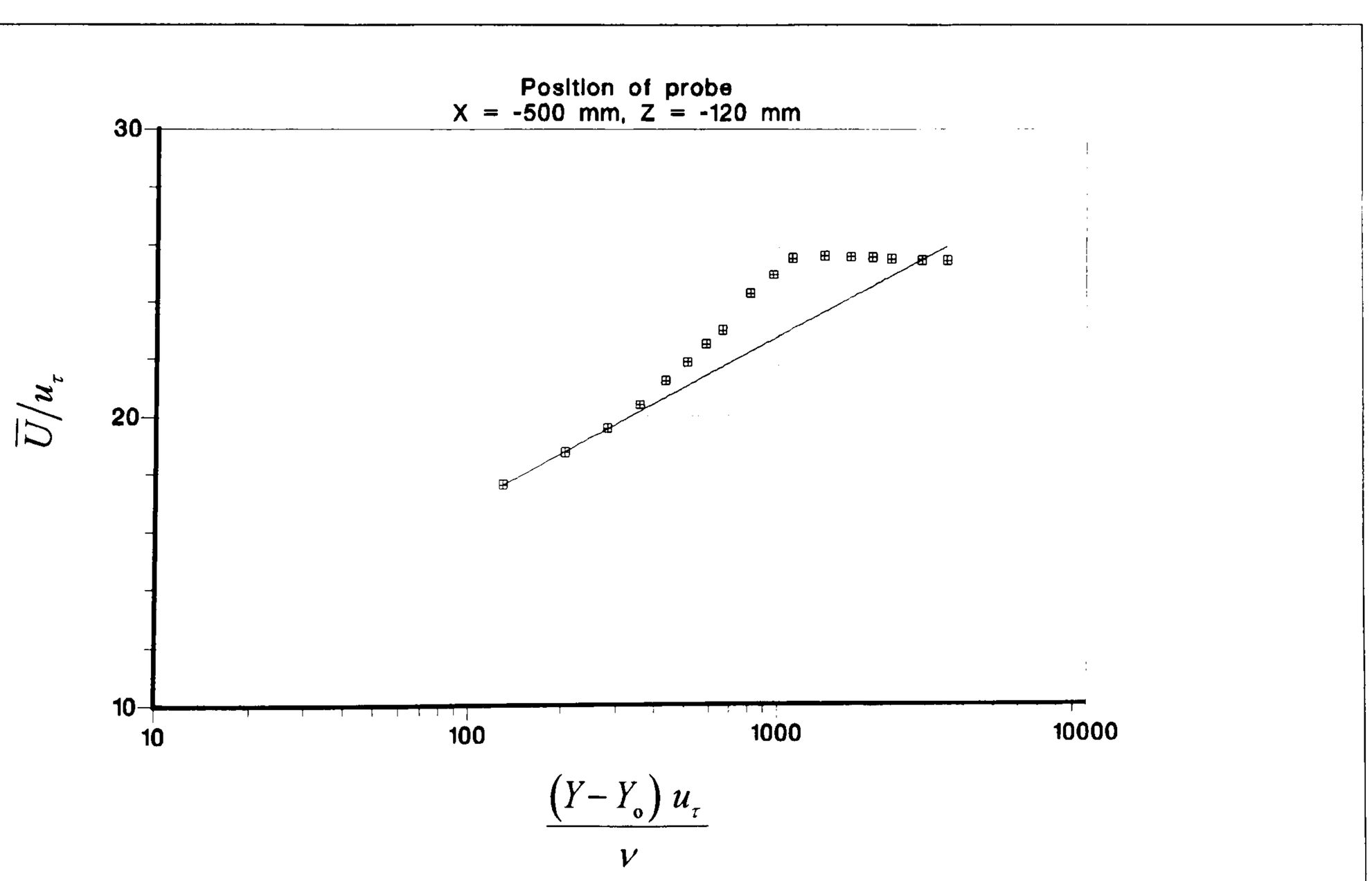

Figure 43 Semi-logarithmic plot of the velocity profile at $(X,Z)/\text{mm} = (-500,-120)$, compared with the log-law: $\frac{\overline{U}}{u_\tau} = 5.75 \log\left(\frac{u_\tau (Y - Y_o)}{\nu}\right) + 5.5$.

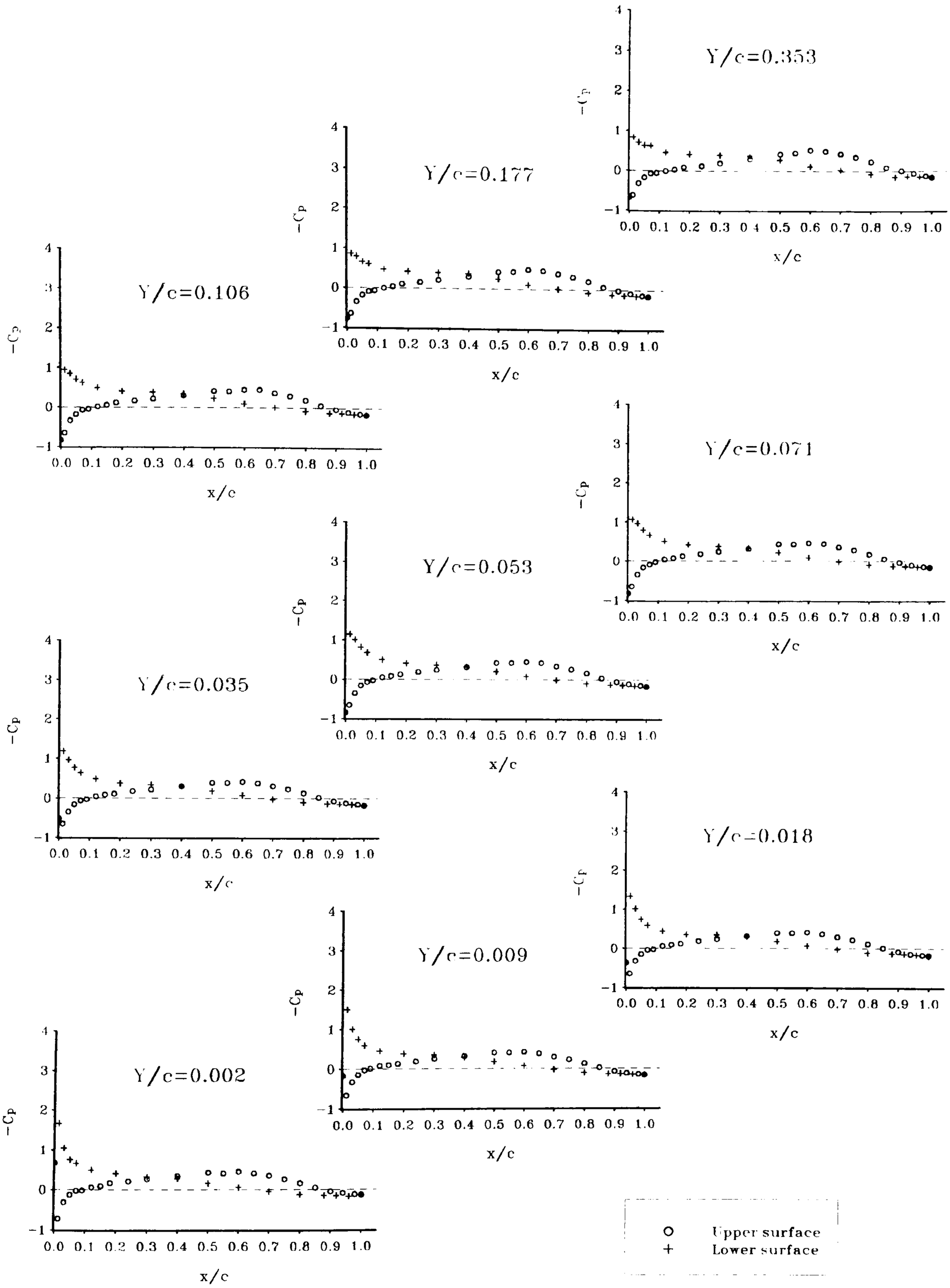

Figure 44(a) Pressure distributions on the wing, at various non-dimensional spanwise distances Y/*c* from the junction, at $\alpha = -3°$.

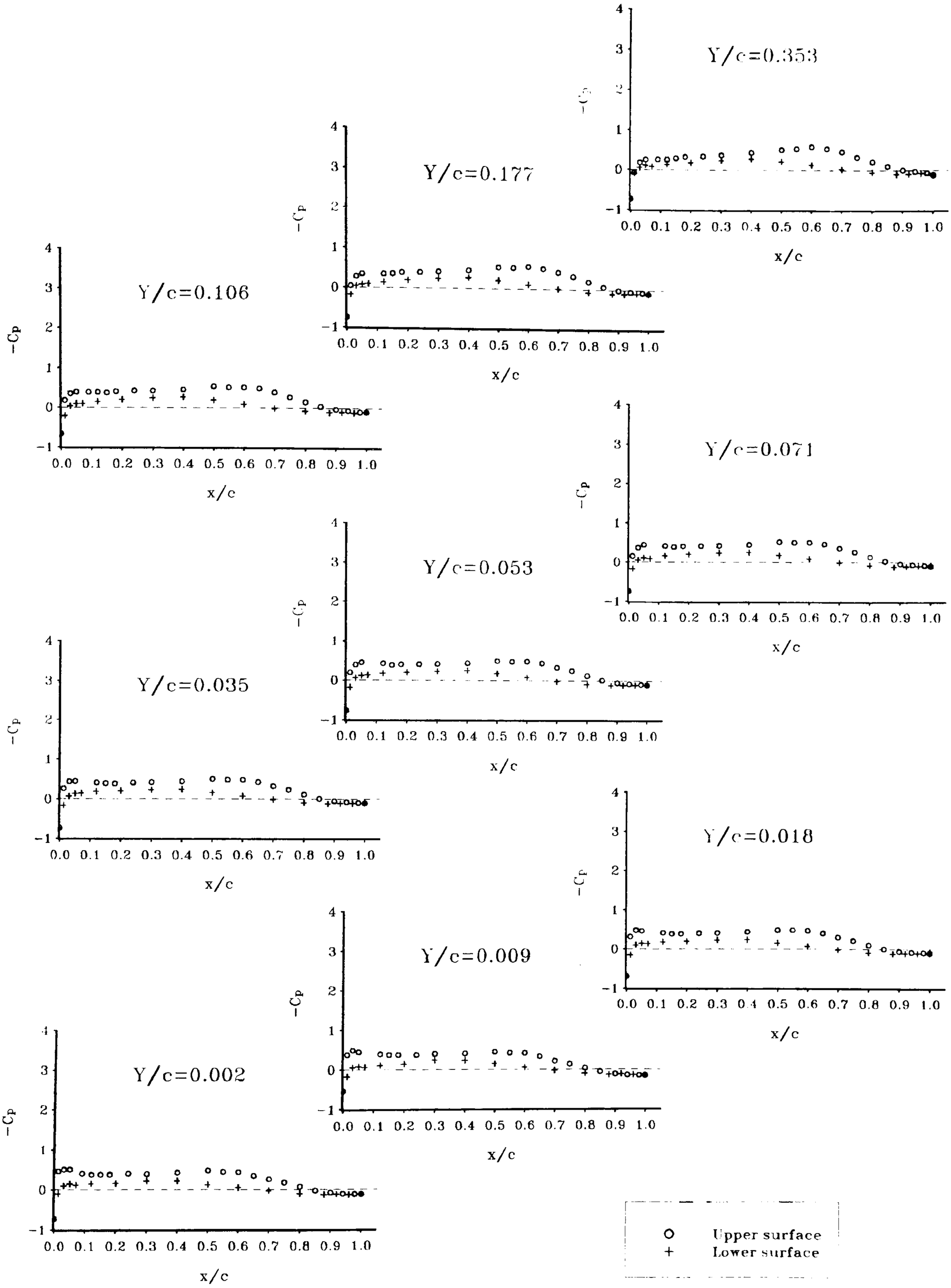

Figure 44(b) Pressure distributions on the wing, at various non-dimensional spanwise distances Y/c from the junction, at $\alpha = 0°$.

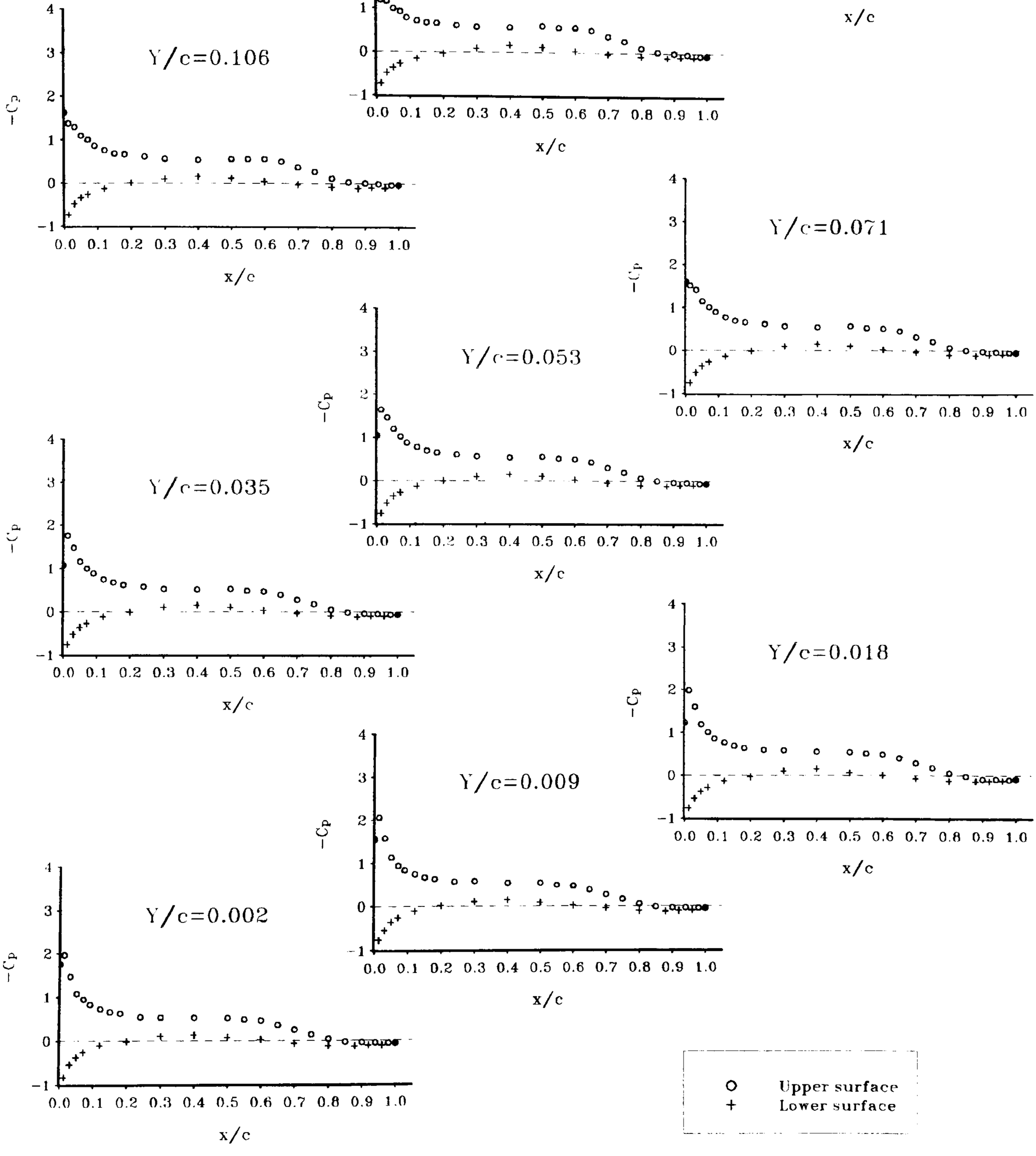

Figure 44(c) Pressure distributions on the wing, at various non-dimensional spanwise distances Y/c from the junction, at $\alpha = +3°$.

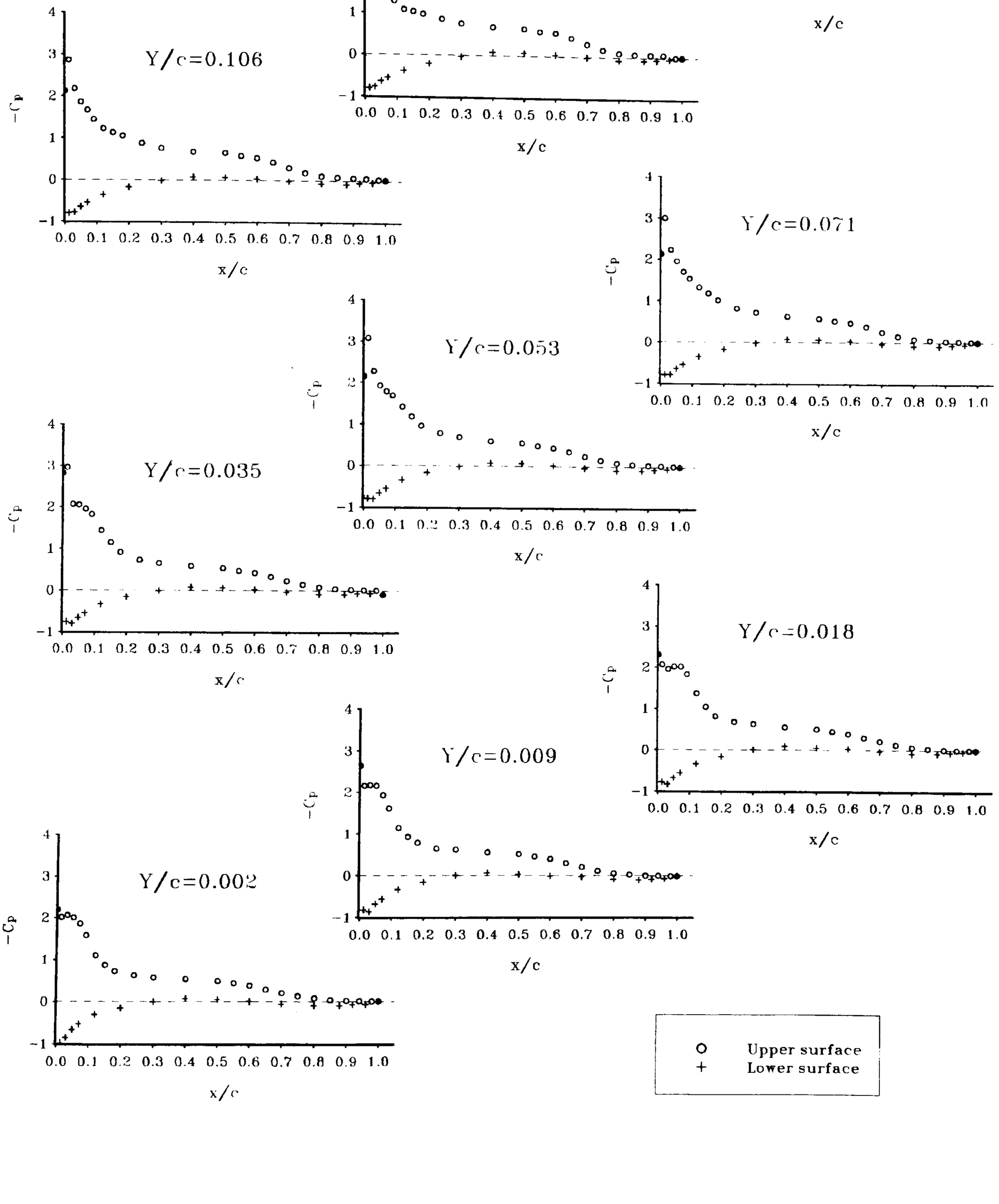

Figure 44(d) Pressure distributions on the wing, at various non-dimensional spanwise distances Y/c from the junction, at $\alpha = +6°$.

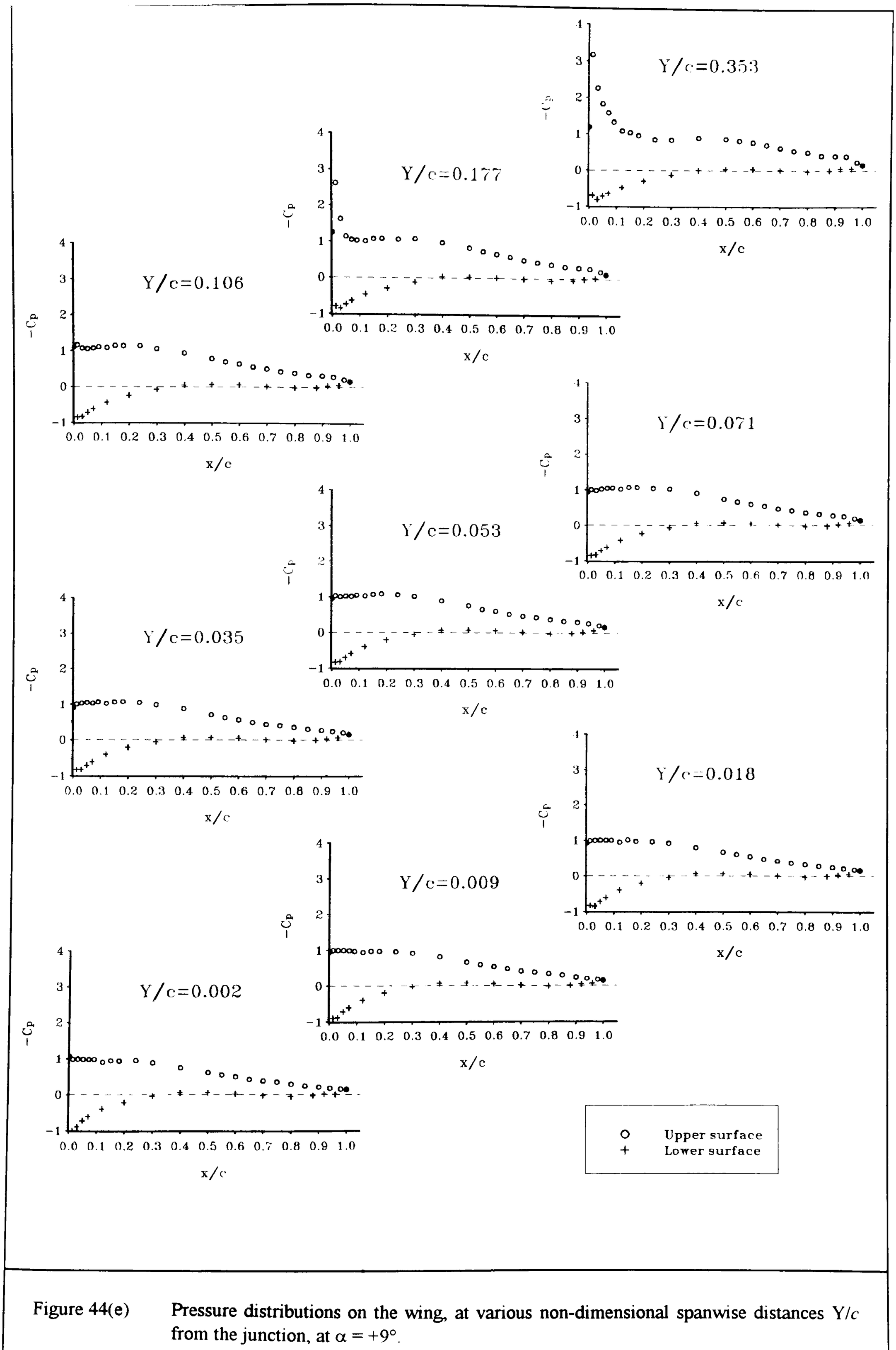

Figure 44(e) Pressure distributions on the wing, at various non-dimensional spanwise distances Y/*c* from the junction, at $\alpha = +9°$.

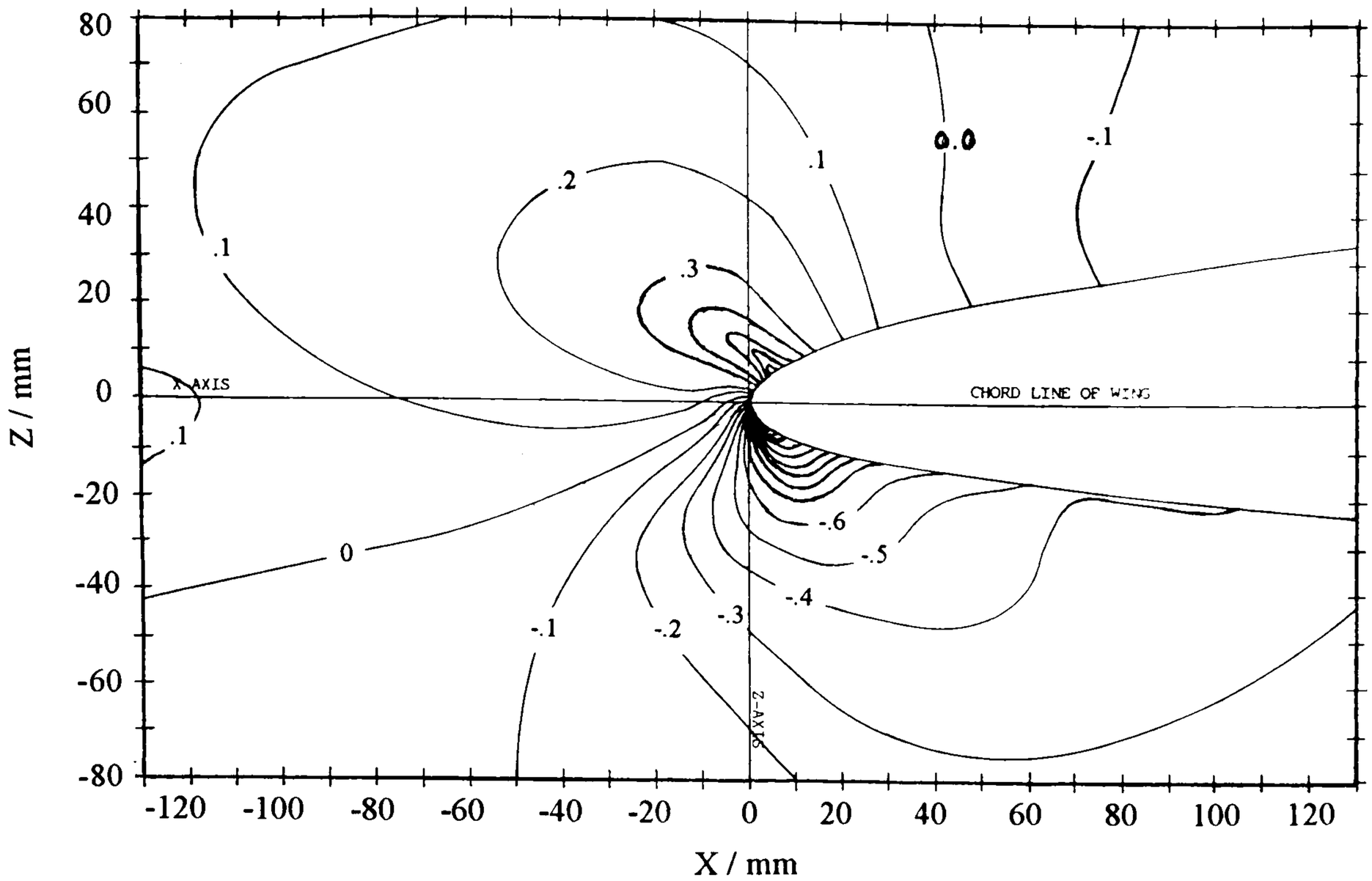

Figure 45(a) Surface Cp contours on the plate, around the leading edge of the junction, at $\alpha = -3°$.

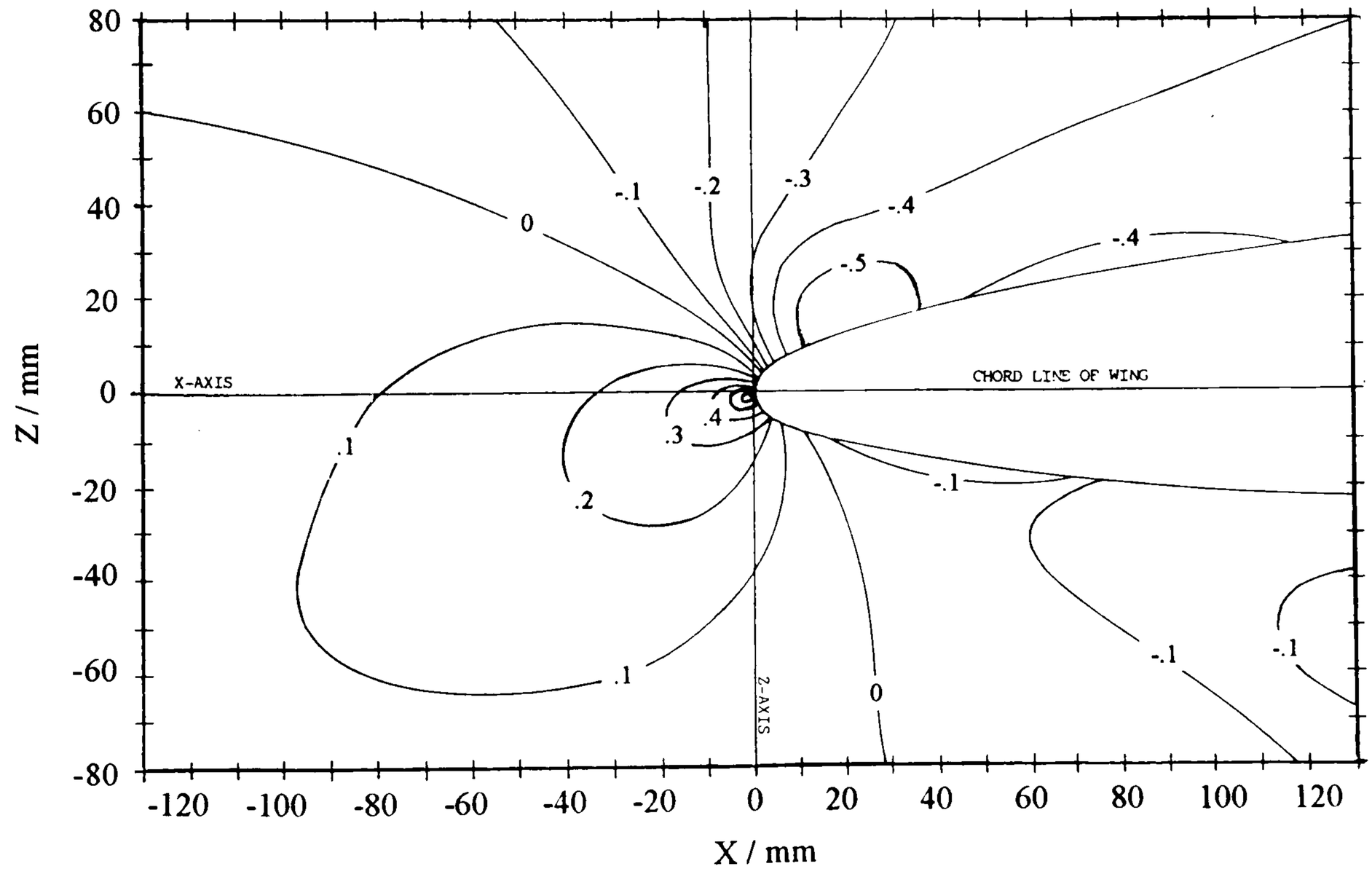

Figure 45(b) Surface Cp contours on the plate, around the leading edge of the junction, at $\alpha = 0°$.

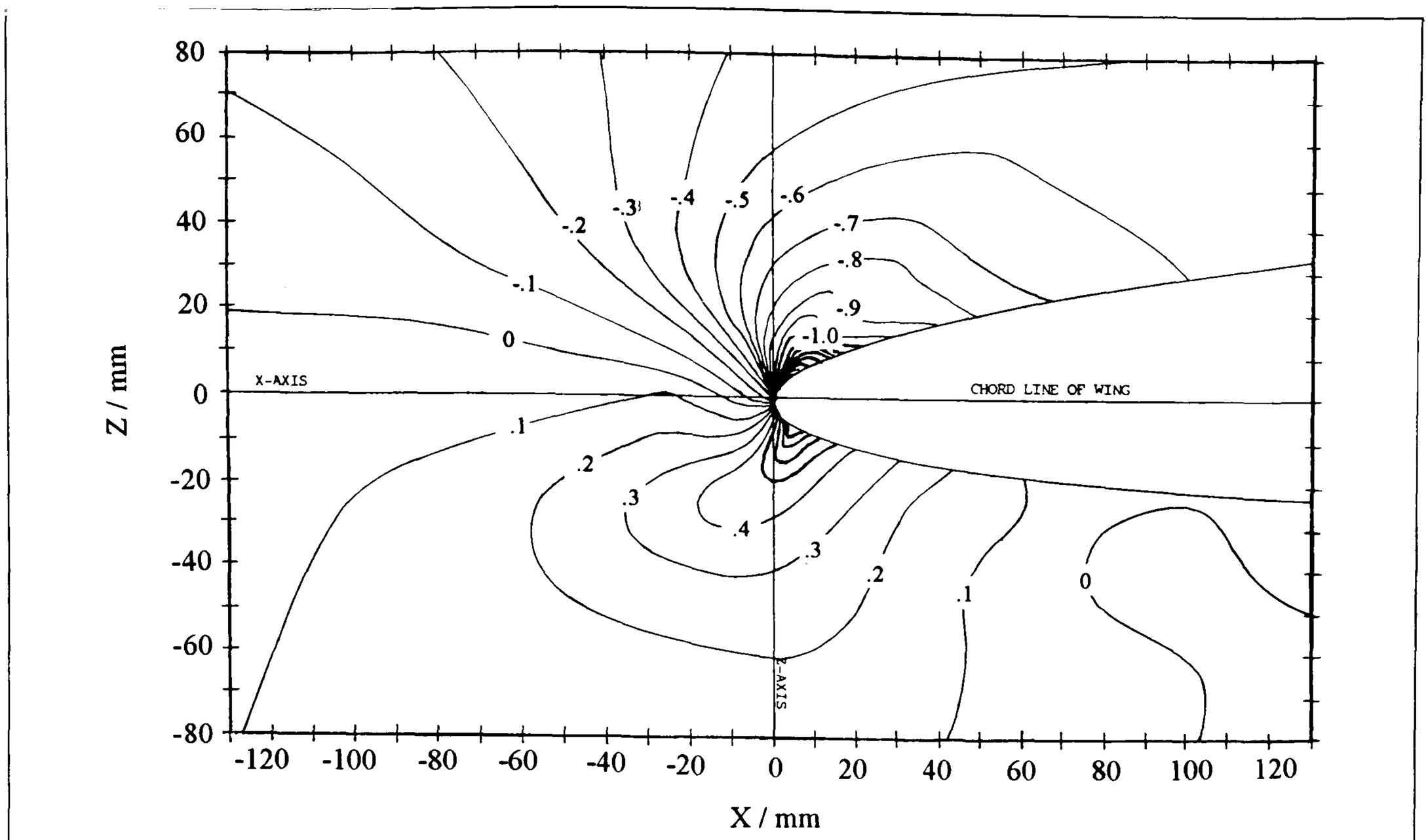

Figure 45(c) Surface Cp contours on the plate, around the leading edge of the junction, at $\alpha = +3°$.

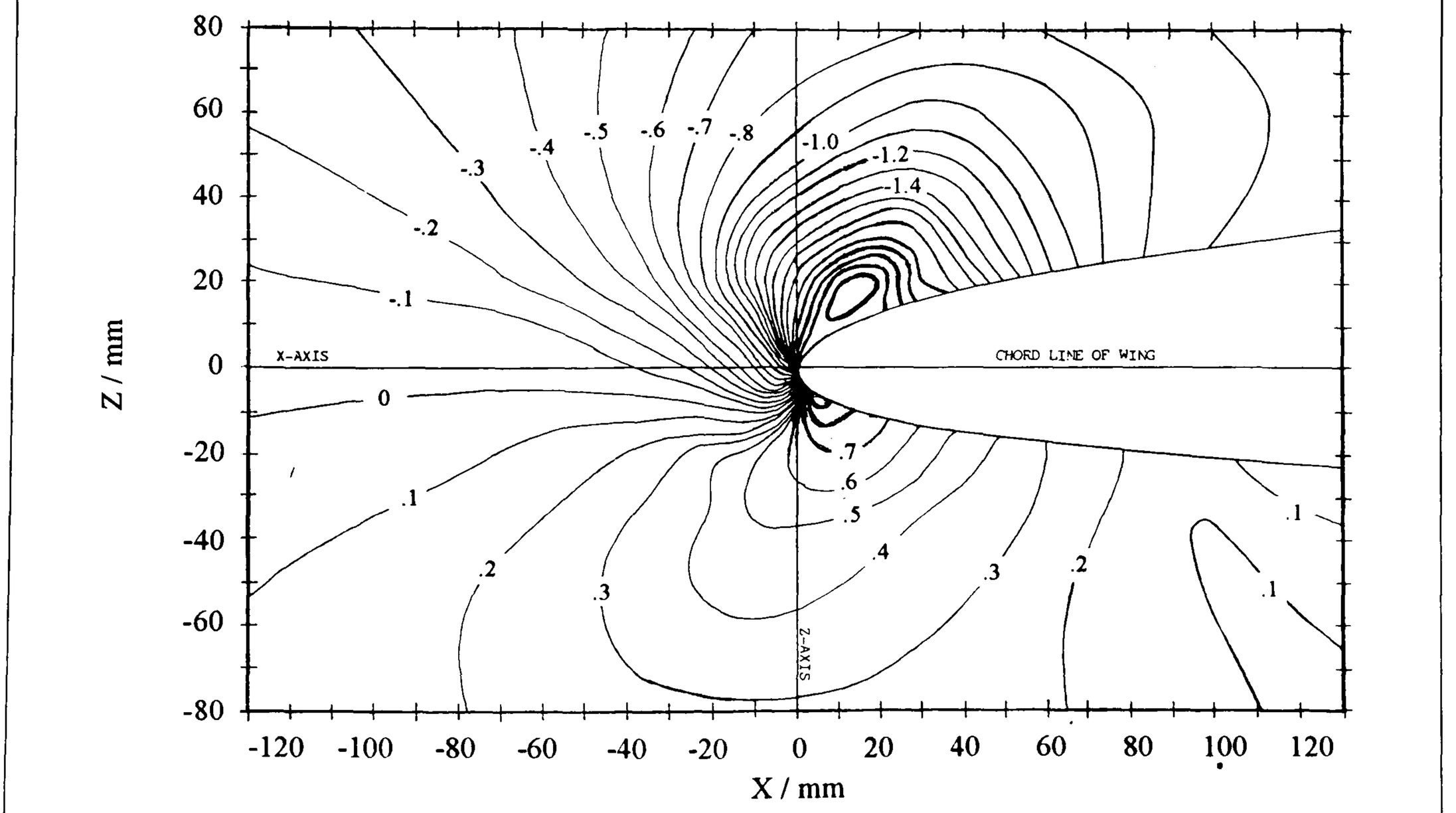

Figure 45(d) Surface Cp contours on the plate, around the leading edge of the junction, at $\alpha = +6^{c}$.

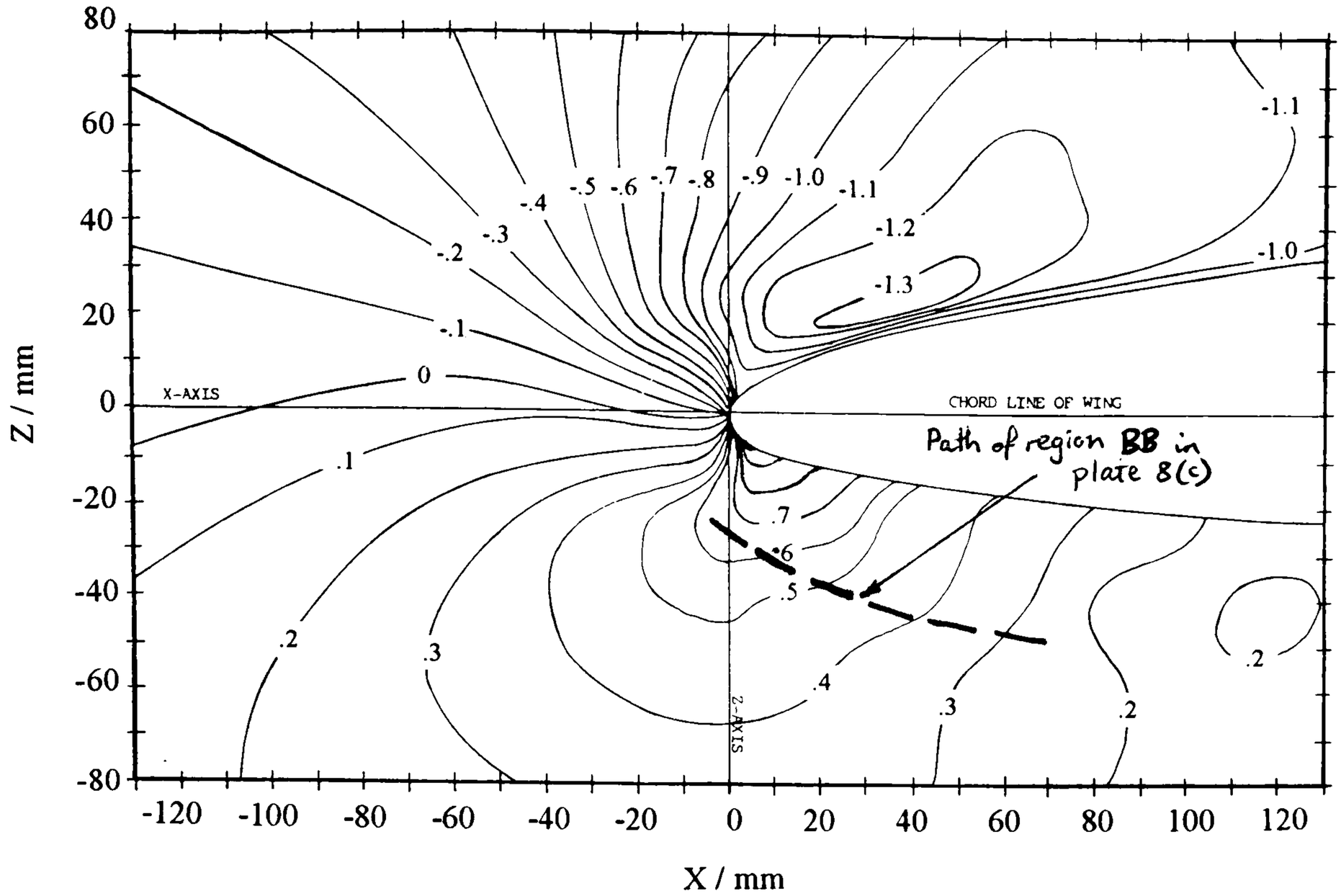

Figure 45(e) Surface Cp contours on the plate, around the leading edge of the junction, at $\alpha = +9°$.

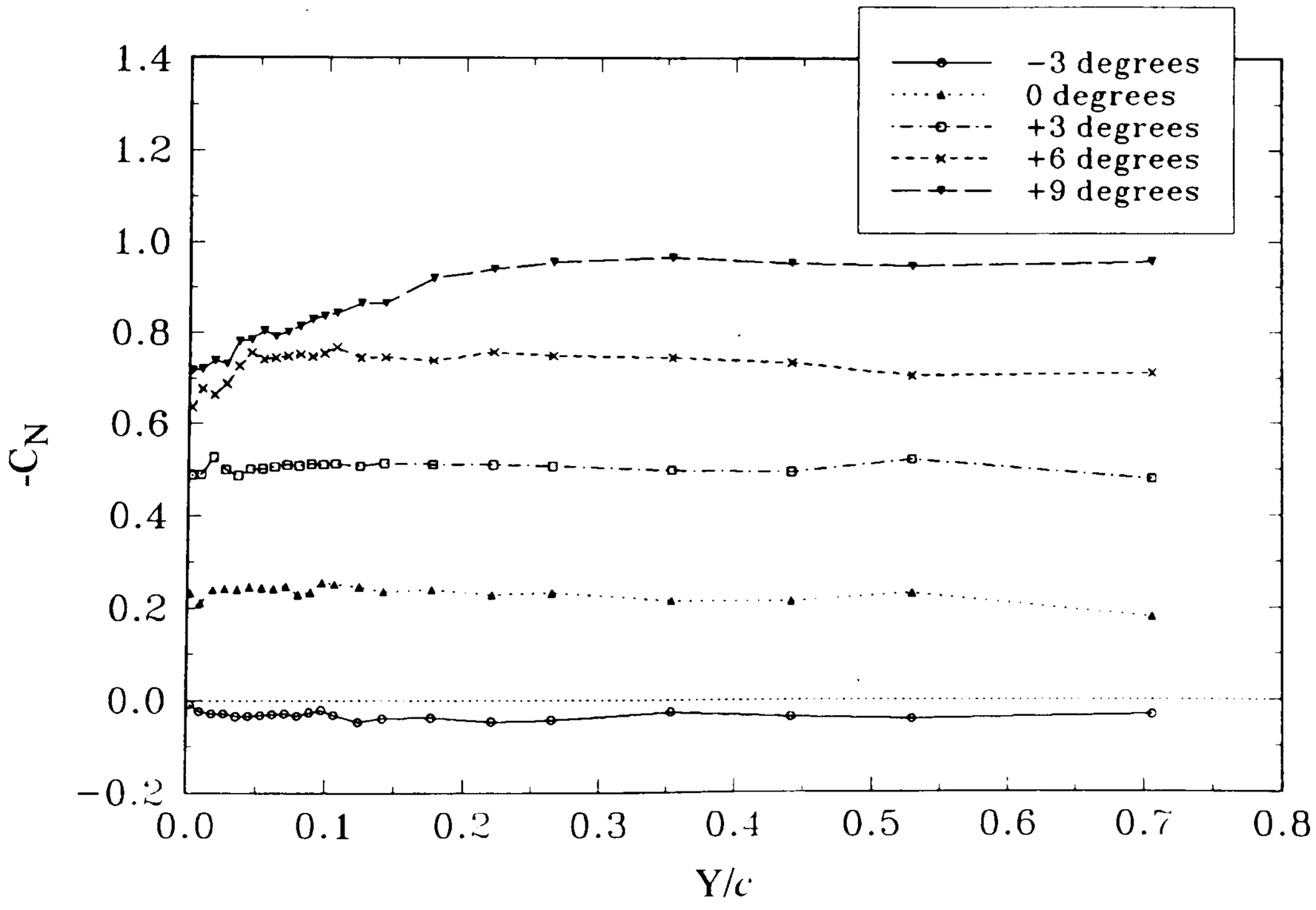

Figure 46 Spanwise distribution of normal-force coefficient at $\alpha = -3°$, 0°, +3°, +6° & +9°.

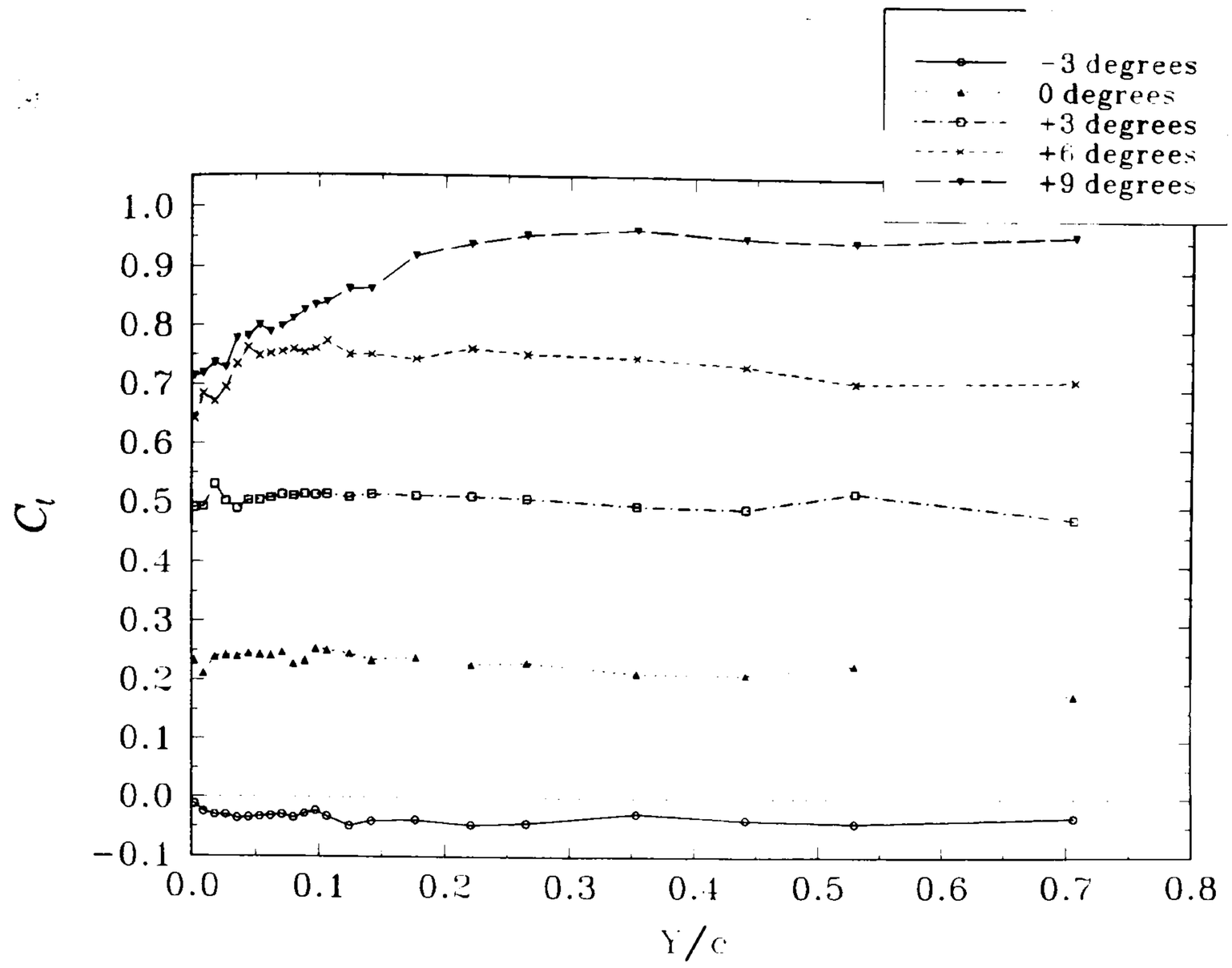

Figure 47 Spanwise distribution of lift-force coefficient at α = -3°, 0°, +3°, +6° & +9°.

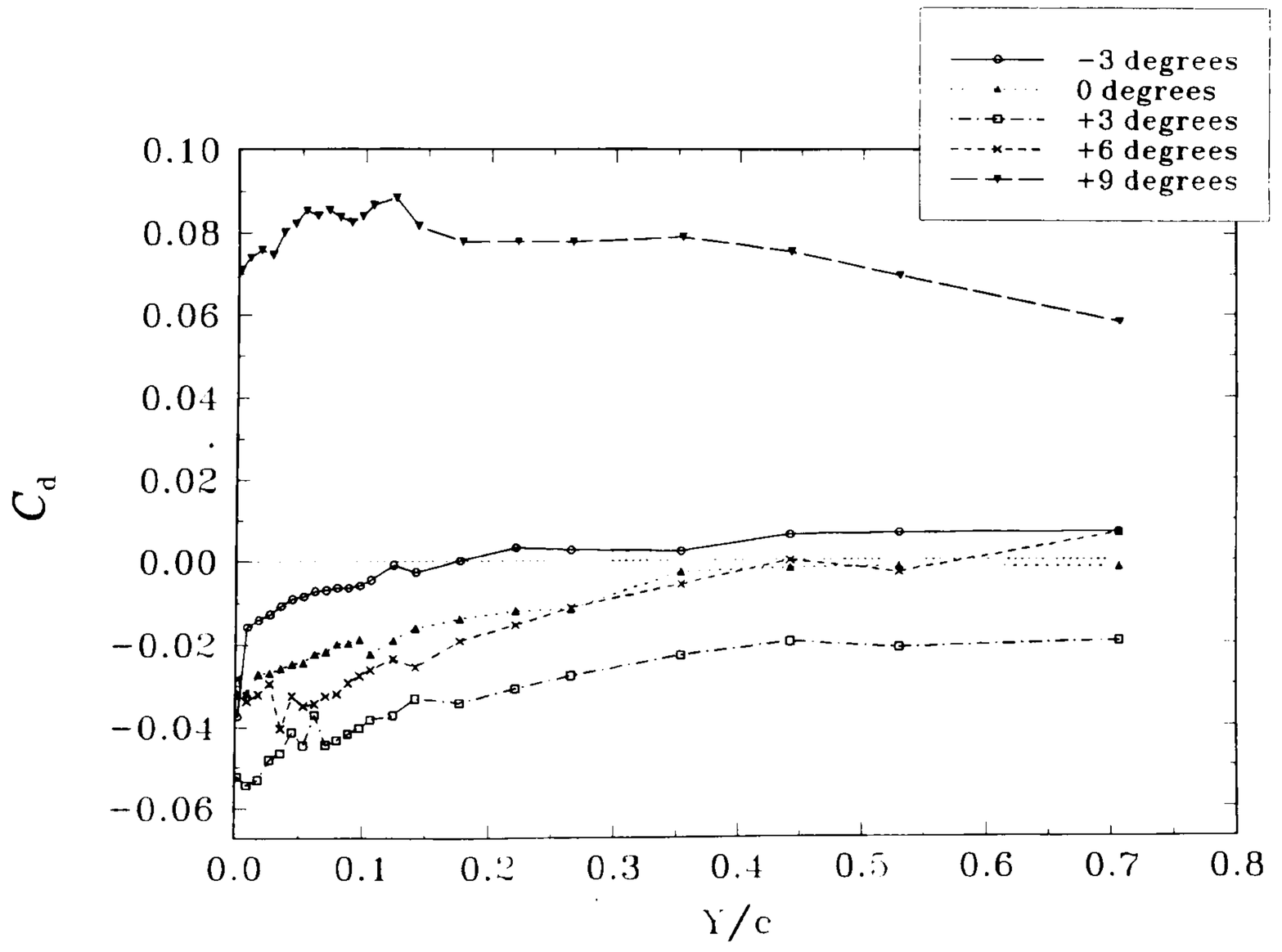

Figure 48 Spanwise distribution of pressure-drag force coefficient at α = -3°, 0°, +3°, +6° & +9°.

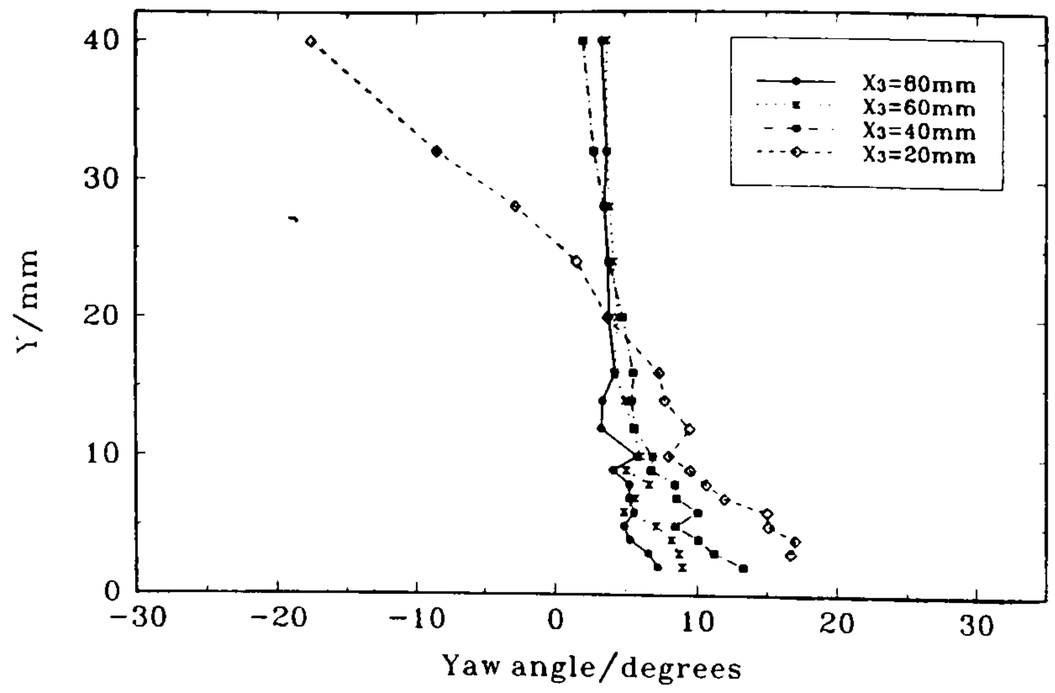

(a) Plane *A*

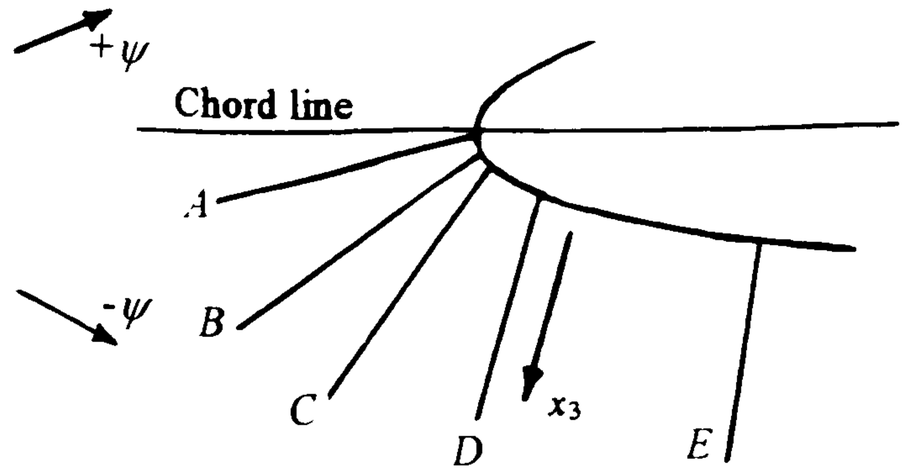

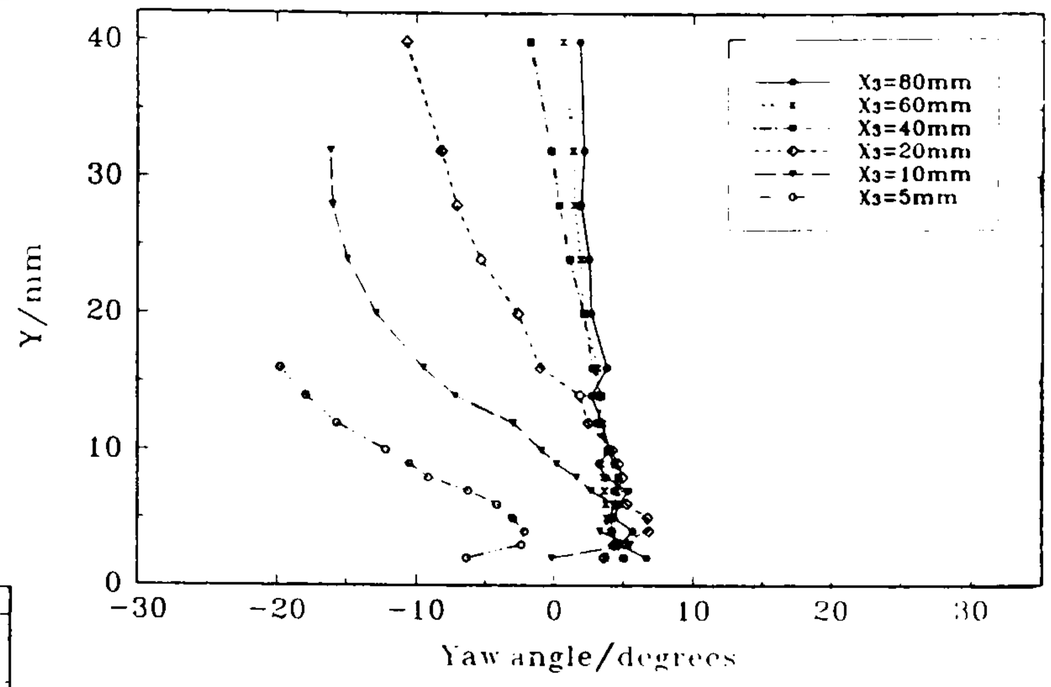

(b) Plane *B*

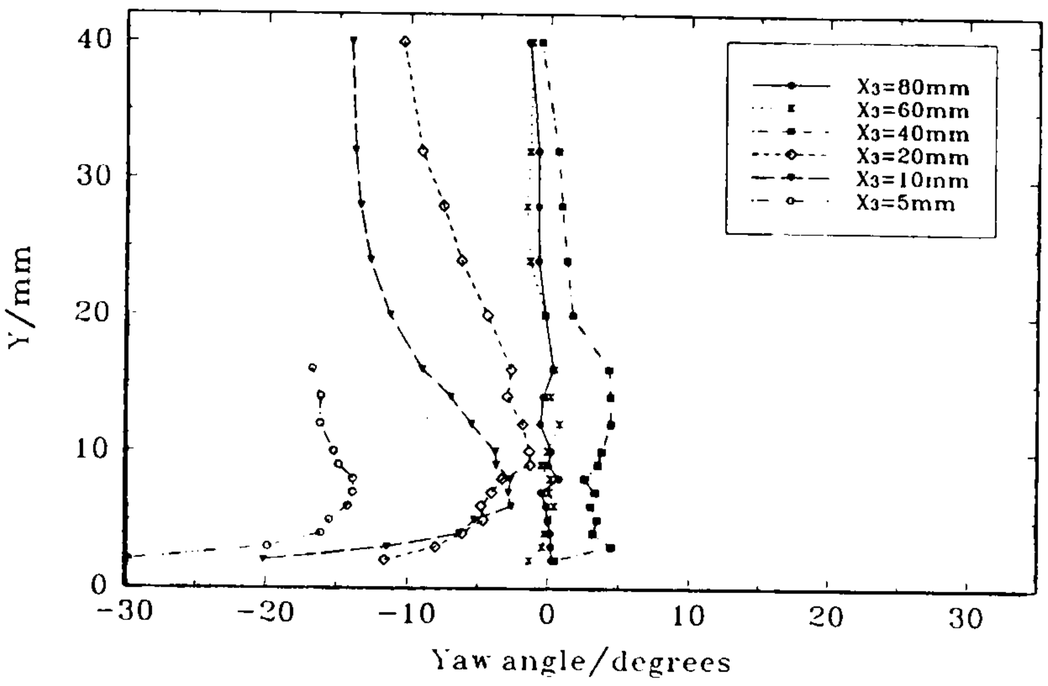

(c) Plane *C*

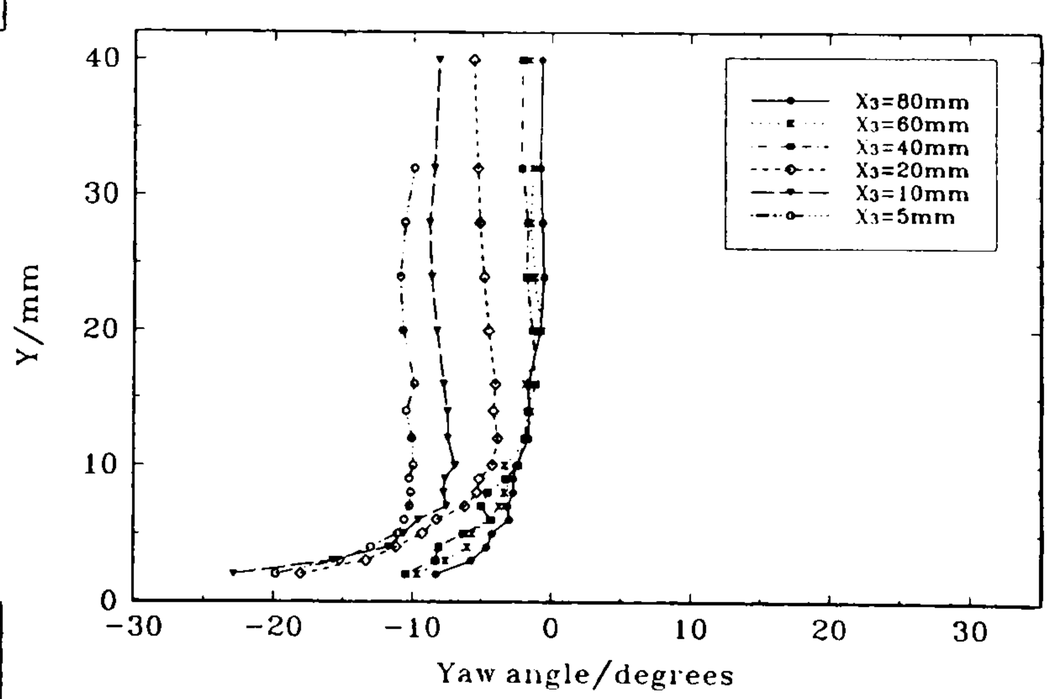

(d) Plane *D*

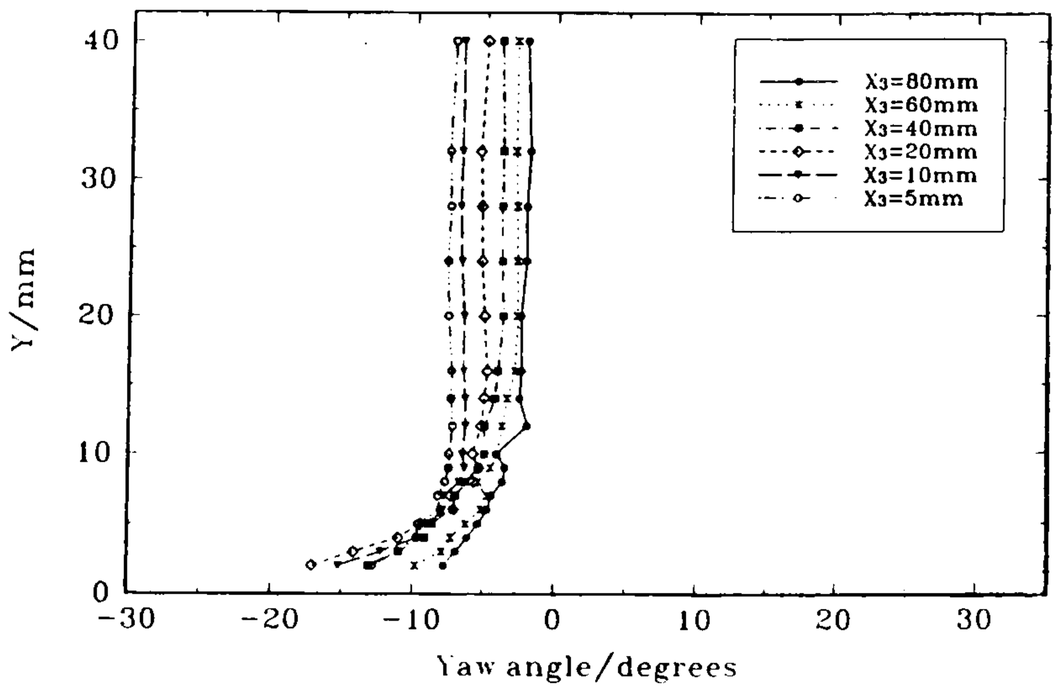

(e) Plane *E*

Figure 49 Profiles of flow yaw angle through the plate boundary layer, in the leading-edge region at $\alpha = 0°$, in planes normal to the tangent to the local wing profile around the leading edge (coordinate system (Y, β_s, x_3)) shown in figures 37 & 40).

(continued...

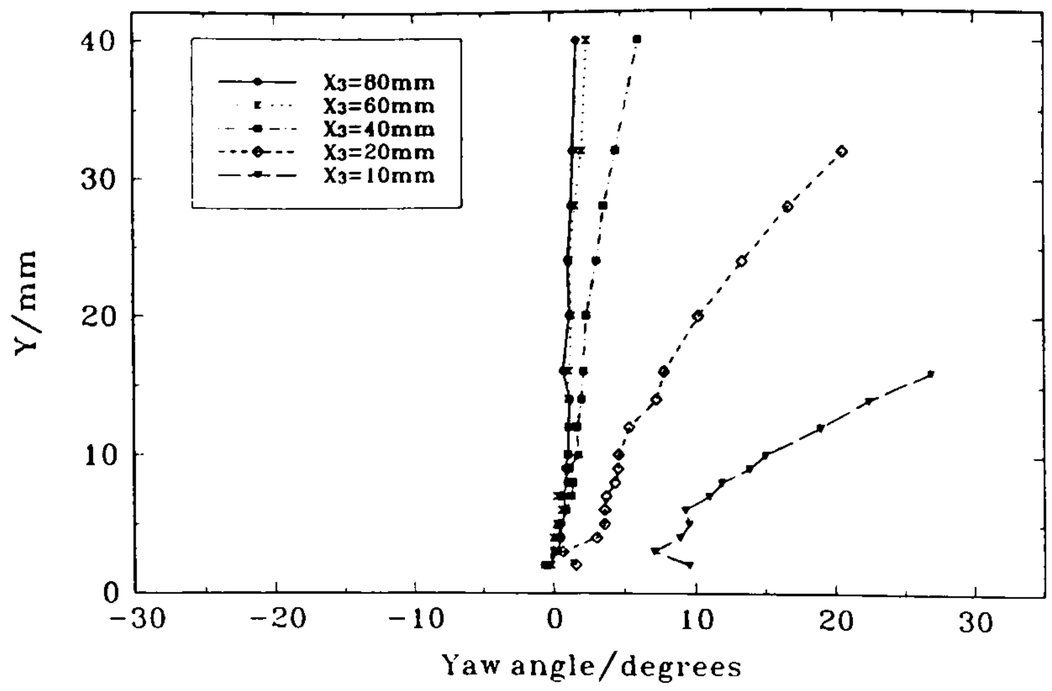

(f) Plane *F*

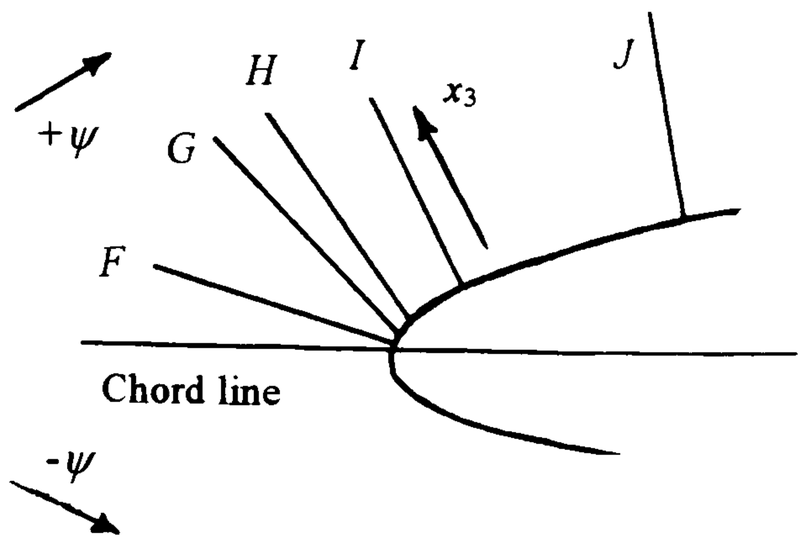

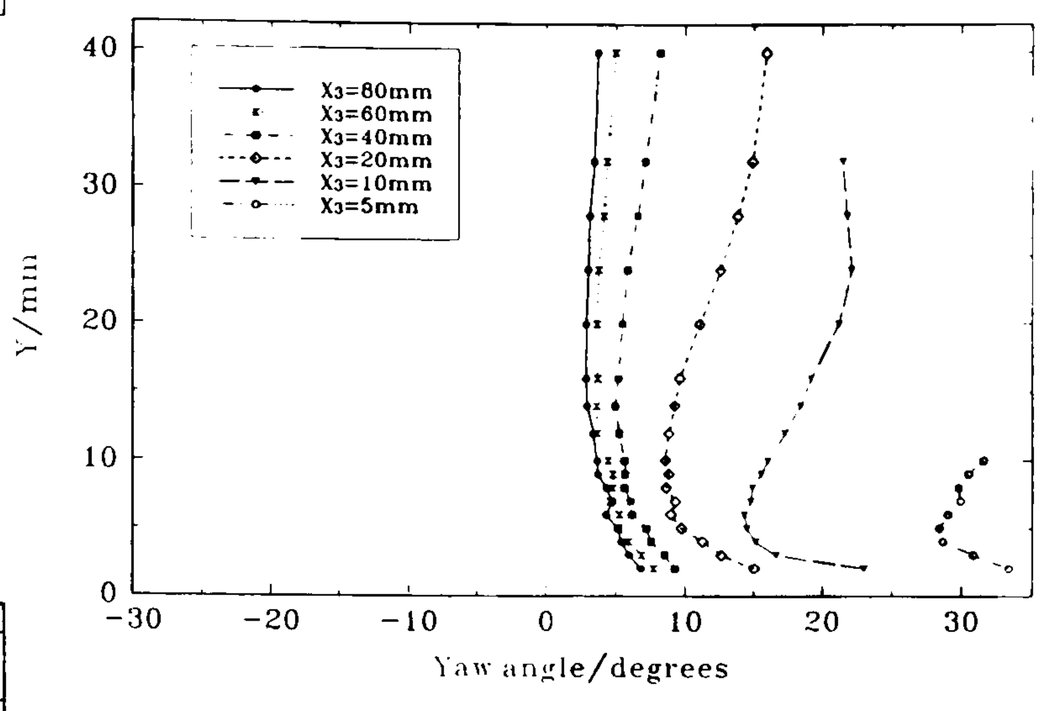

(g) Plane *G*

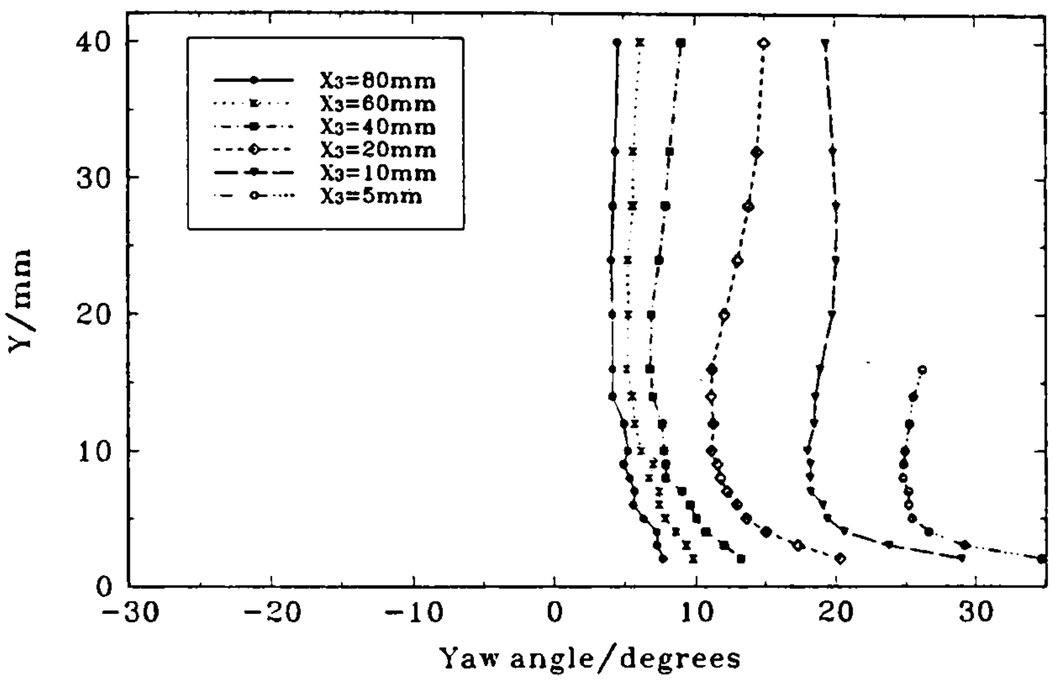

(h) Plane *H*

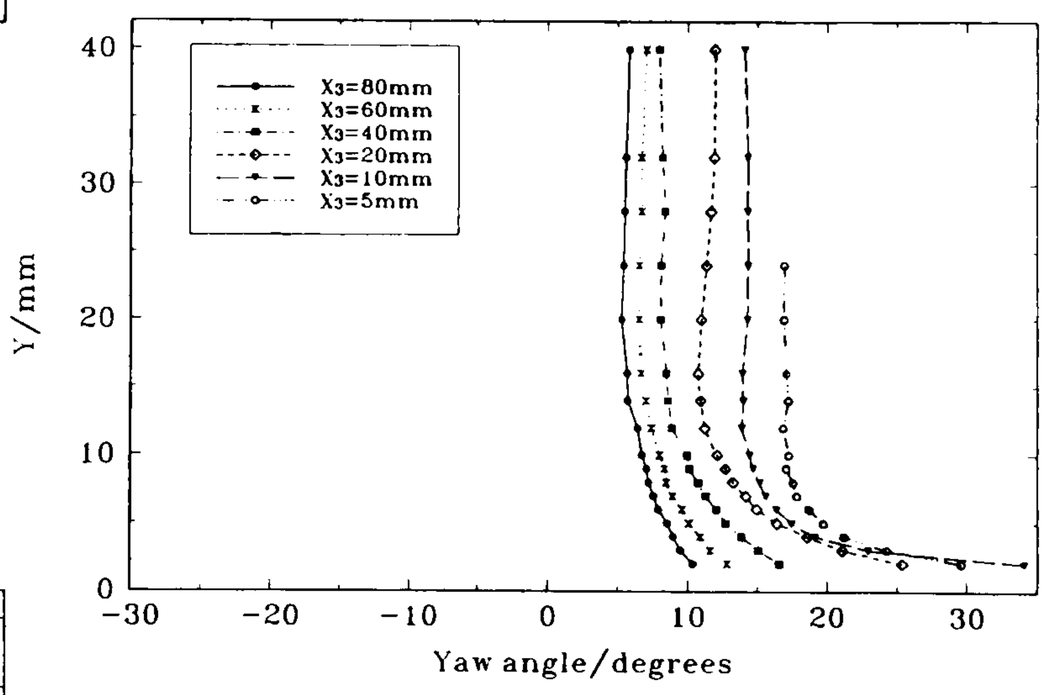

(i) Plane *I*

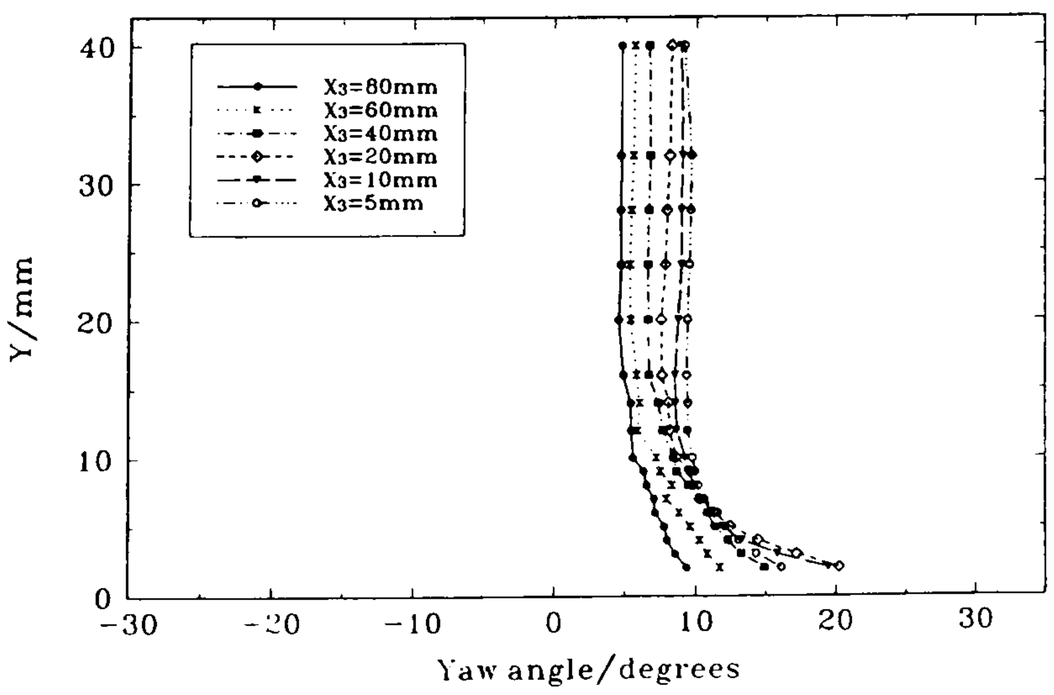

(j) Plane *J*

Figure 49 Profiles of flow yaw angle through the plate boundary layer, in the leading-edge region at $\alpha = 0°$, in planes normal to the tangent to the local wing profile around the leading edge (coordinate system (Y, β_s, x_3 Y) shown in figures 37 & 40).

...concluded)

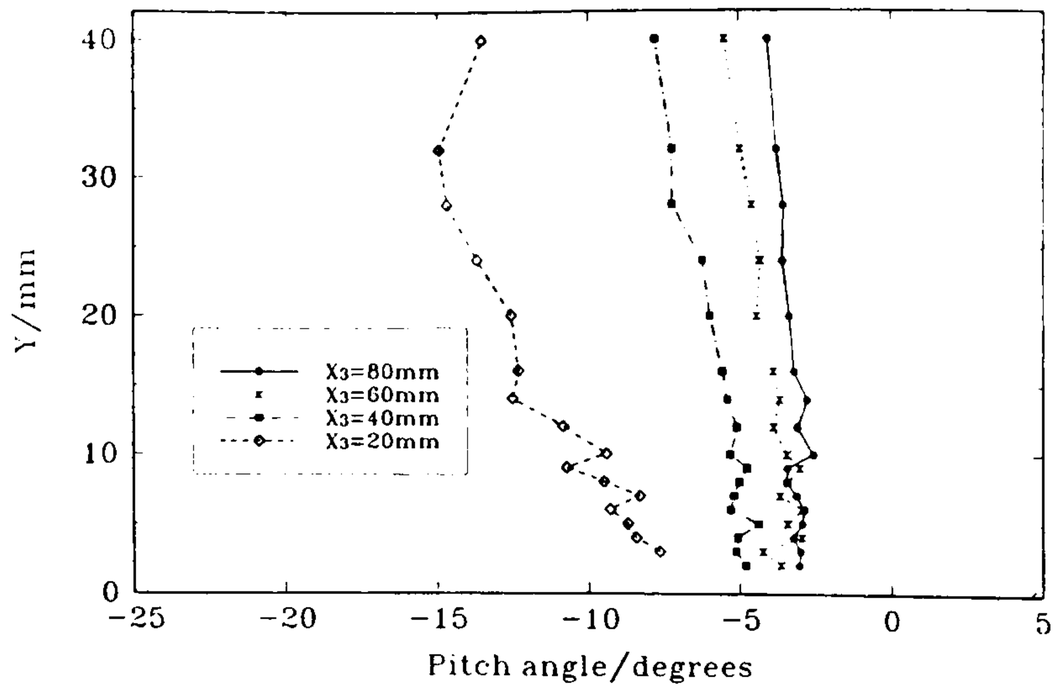

(a) Plane *A*

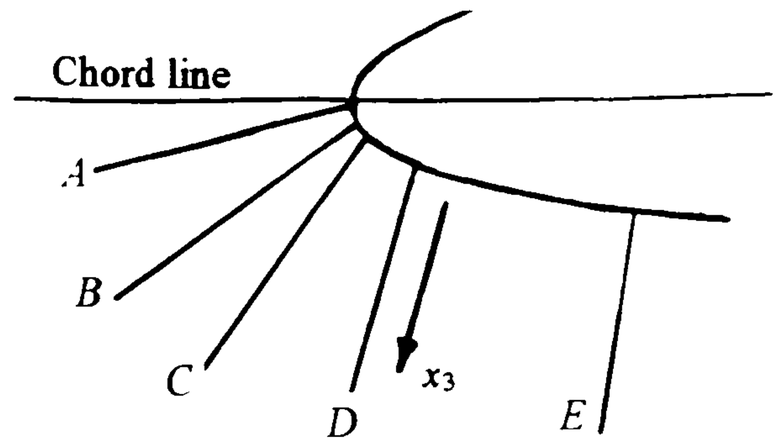

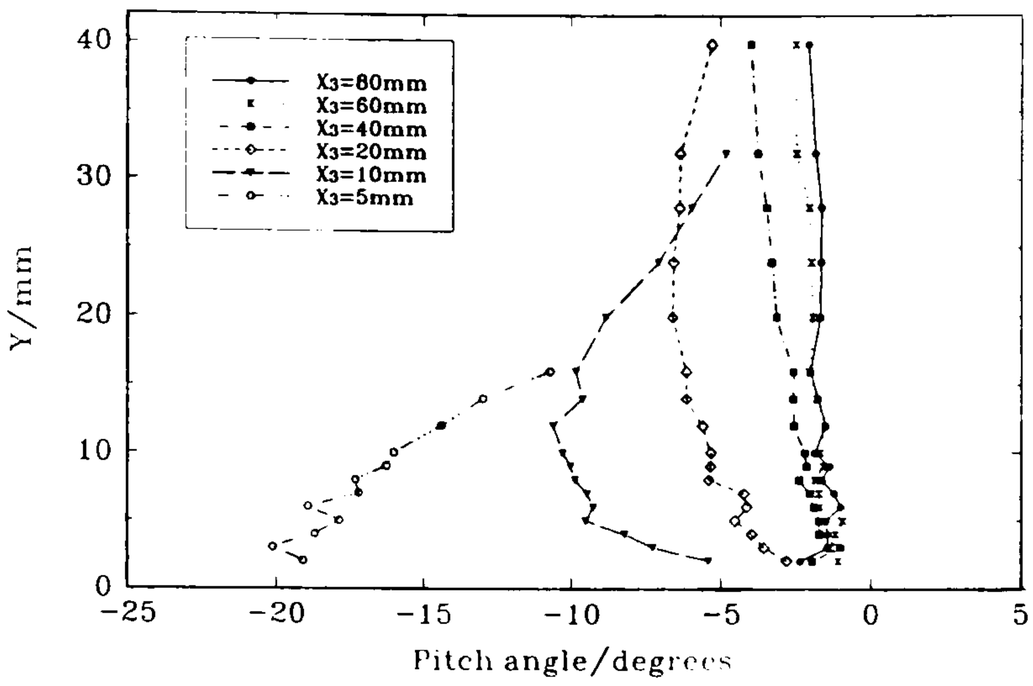

(b) Plane *B*

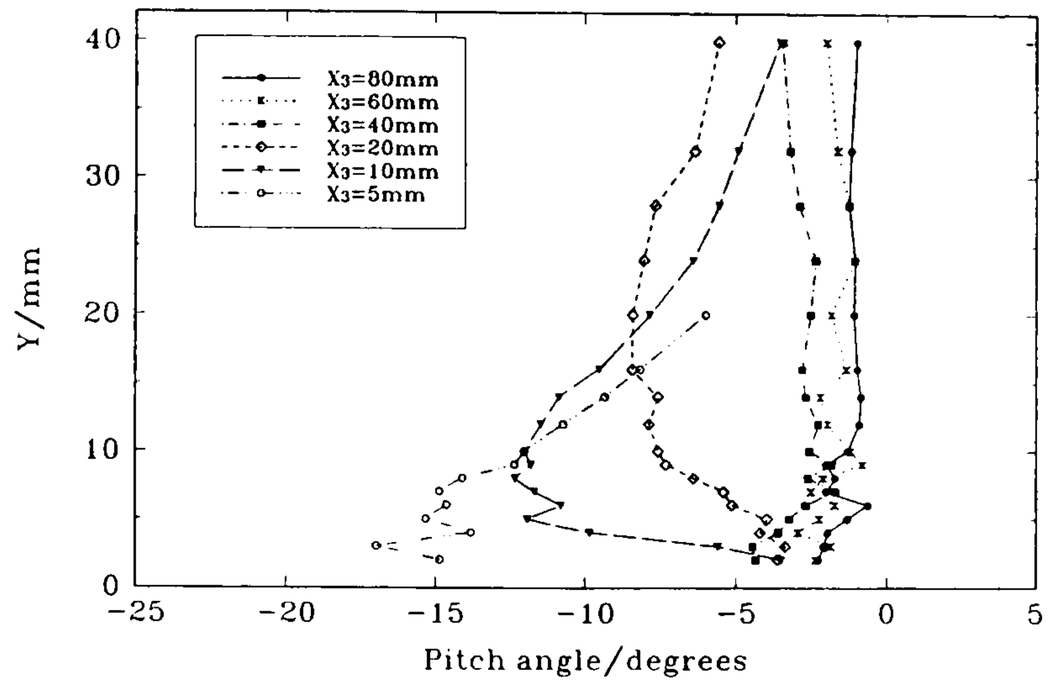

(c) Plane *C*

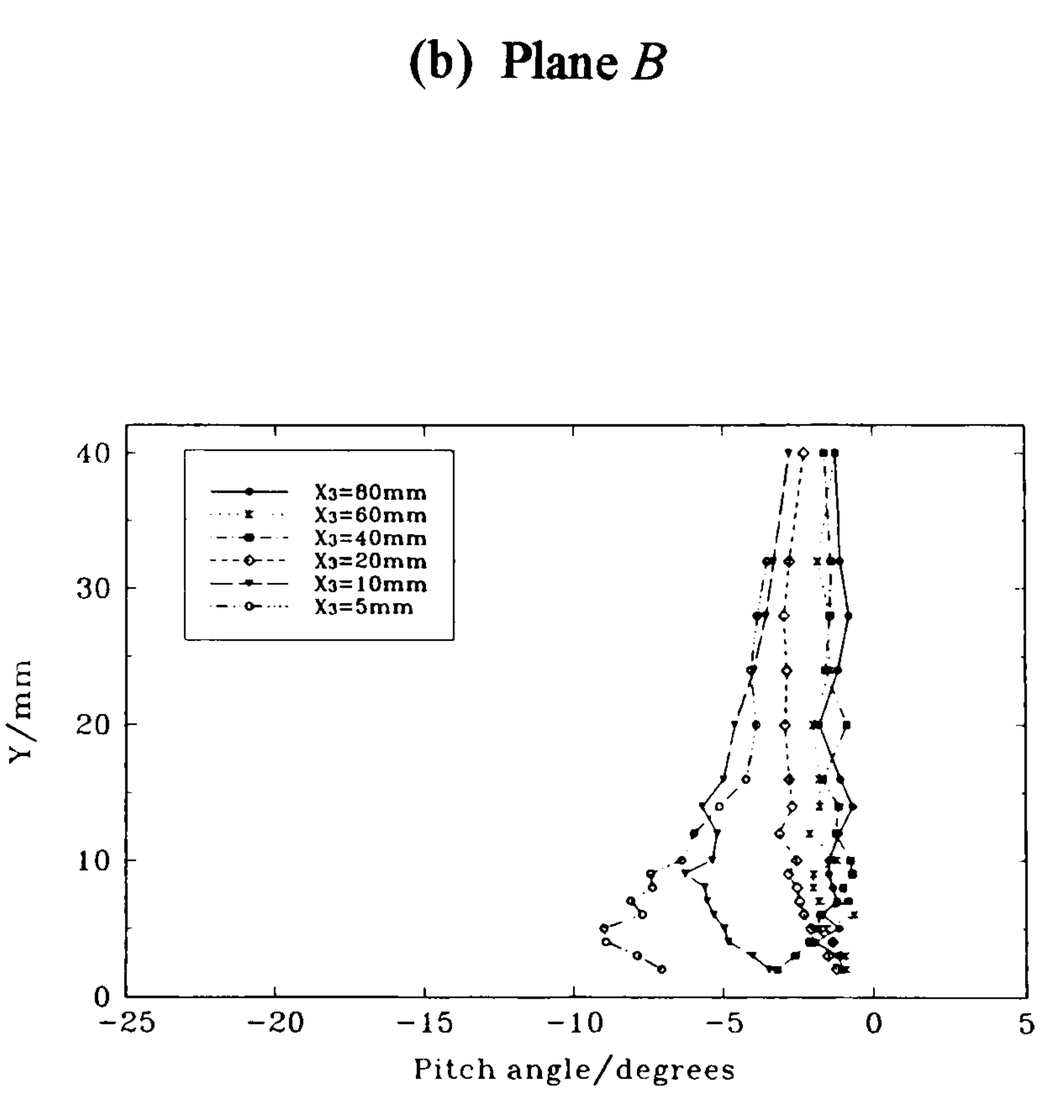

(d) Plane *D*

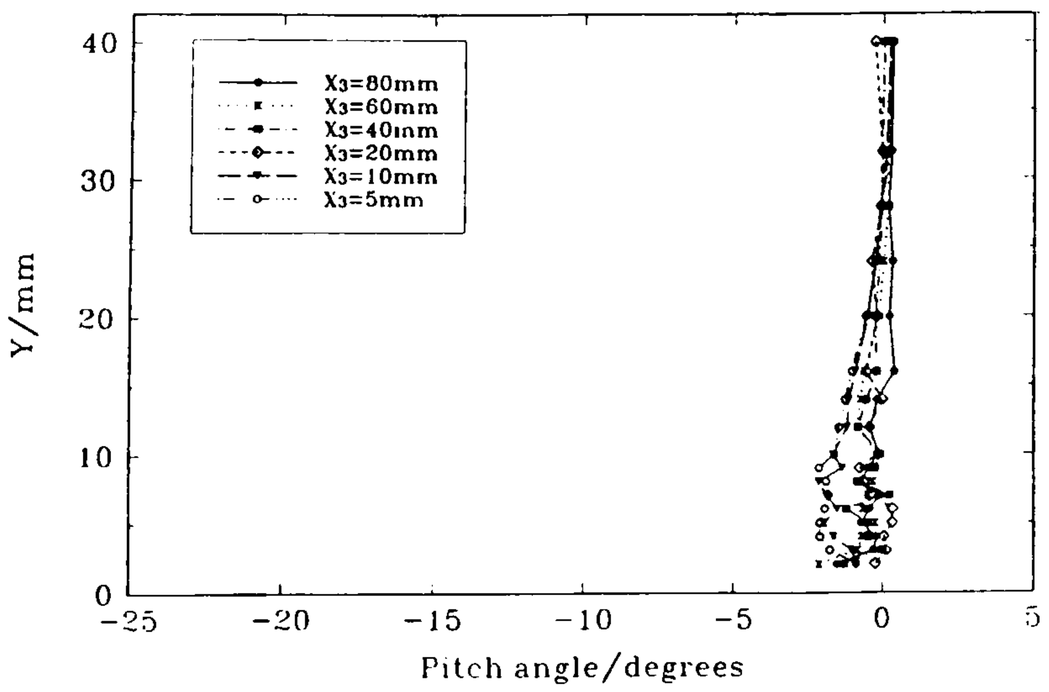

(e) Plane *E*

Figure 50 Profiles of flow pitch angle through the plate boundary layer, in the leading-edge region at $\alpha = 0°$, in planes normal to the tangent to the local wing profile around the leading edge.

(continued...

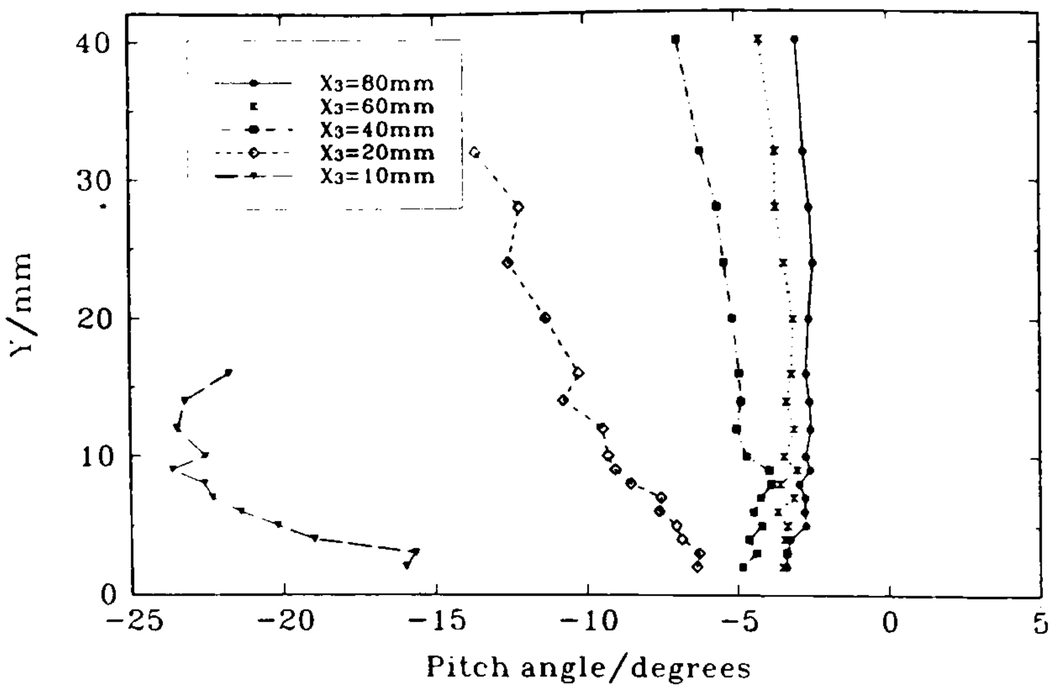

(f) Plane *F*

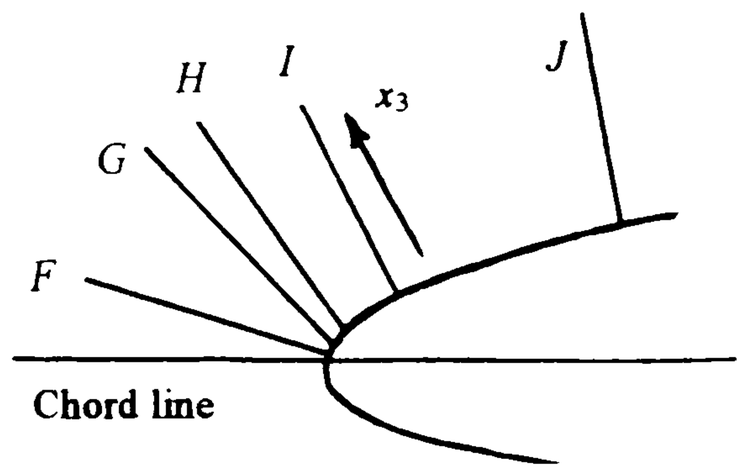

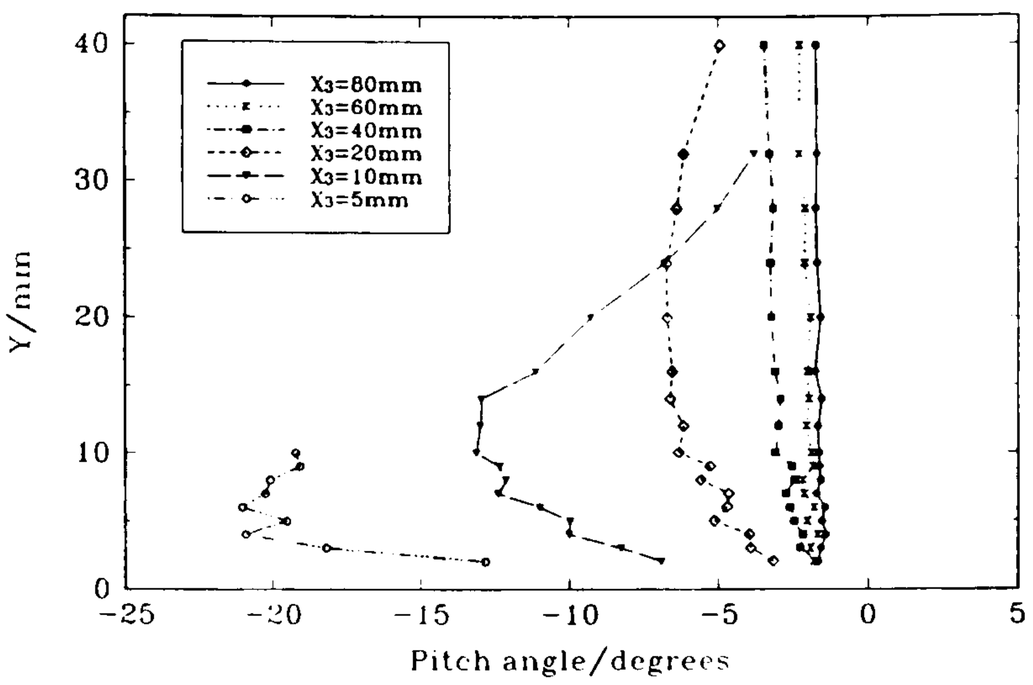

(g) Plane *G*

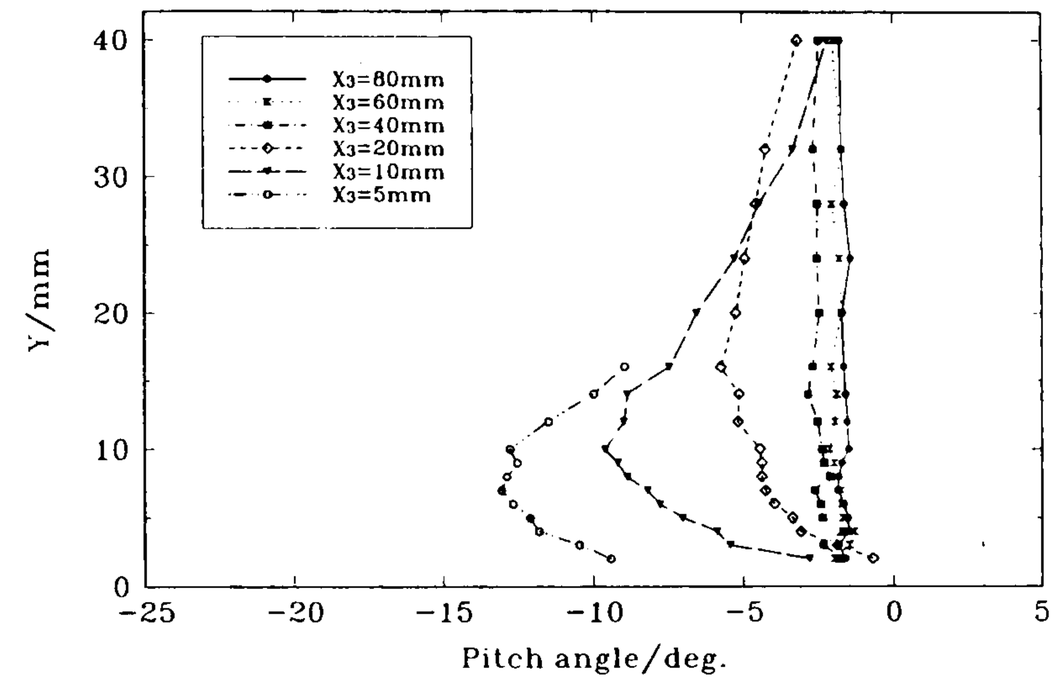

(h) Plane *H*

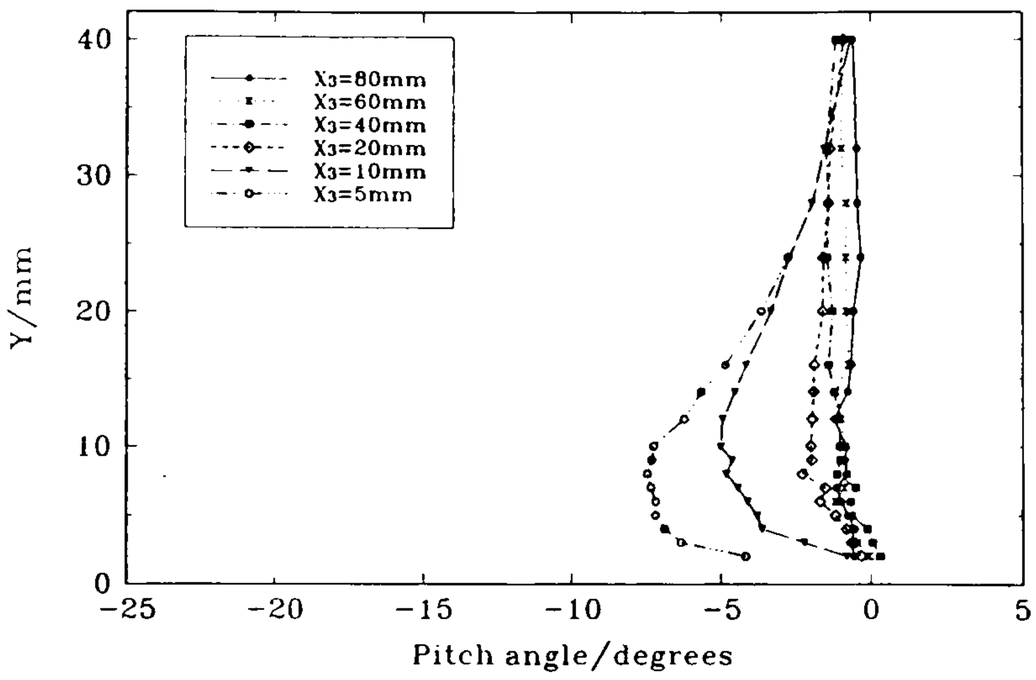

(i) Plane *I*

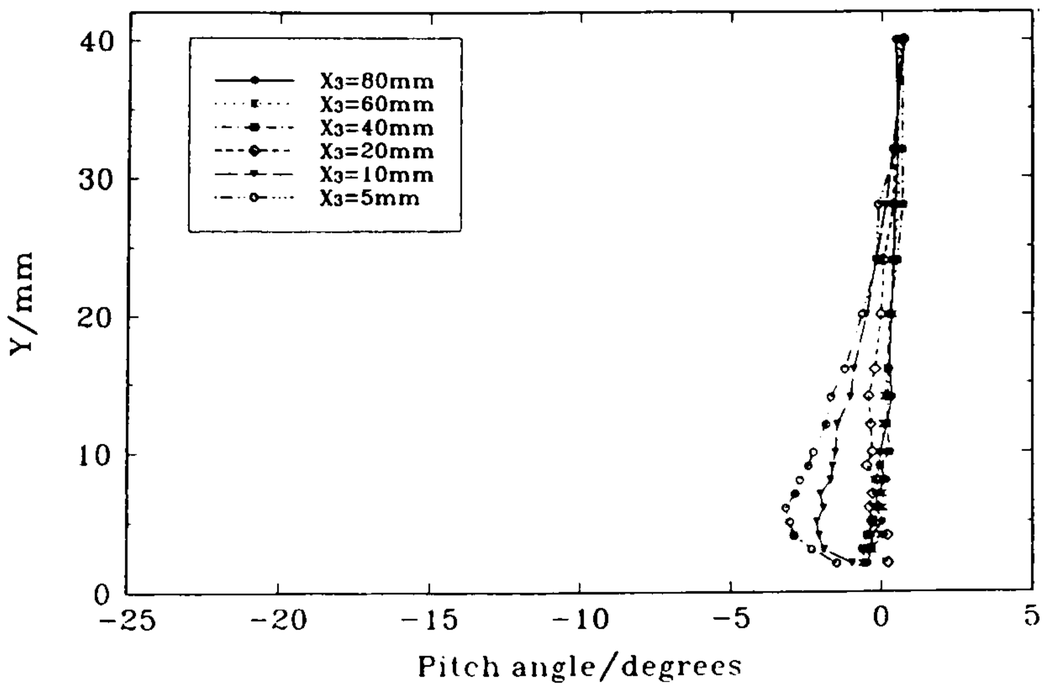

(j) Plane *J*

Figure 50 Profiles of flow pitch angle through the plate boundary layer, in the leading-edge region at $\alpha = 0°$, in planes normal to the tangent to the local wing profile around the leading edge.

...concluded)

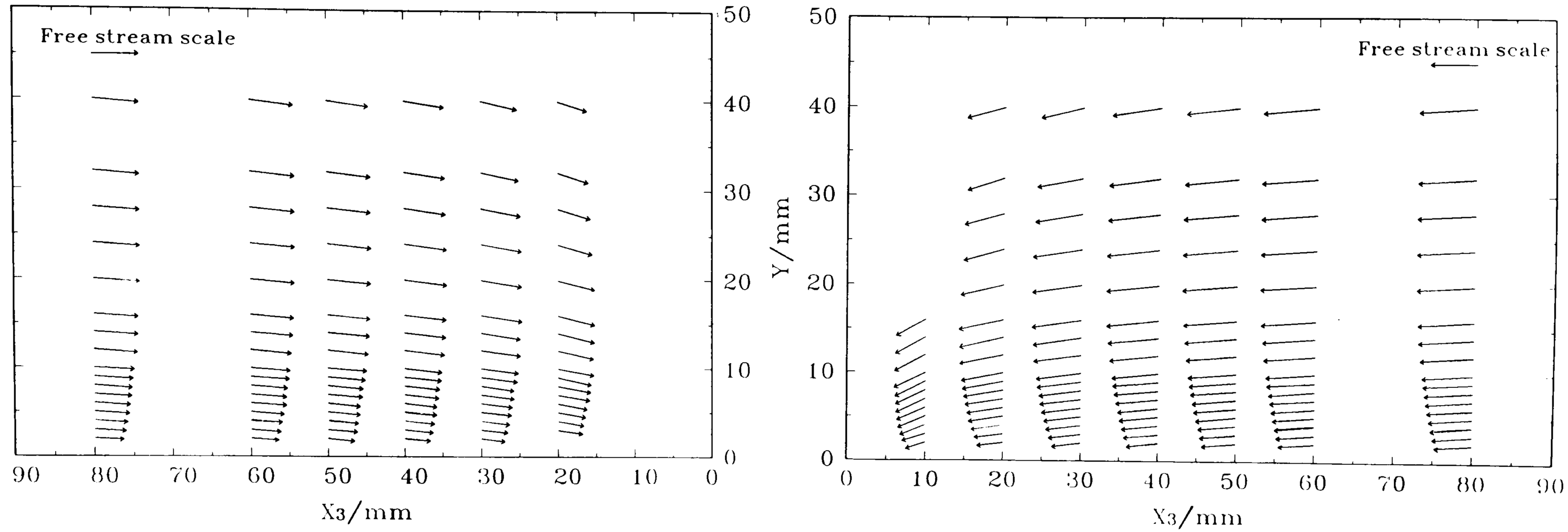

(a) Plane *A*

(b) Plane *F*

Figure 51 Cross-flow velocity vectors in the junction at $\alpha = 0°$, in planes normal to the tangents to the wing profile on both sides of the junction at $X = 0.5$ mm:
(a) Plane A — $\beta_S = -13.6°$ & (b) Plane F — $\beta_S = 15.9°$.

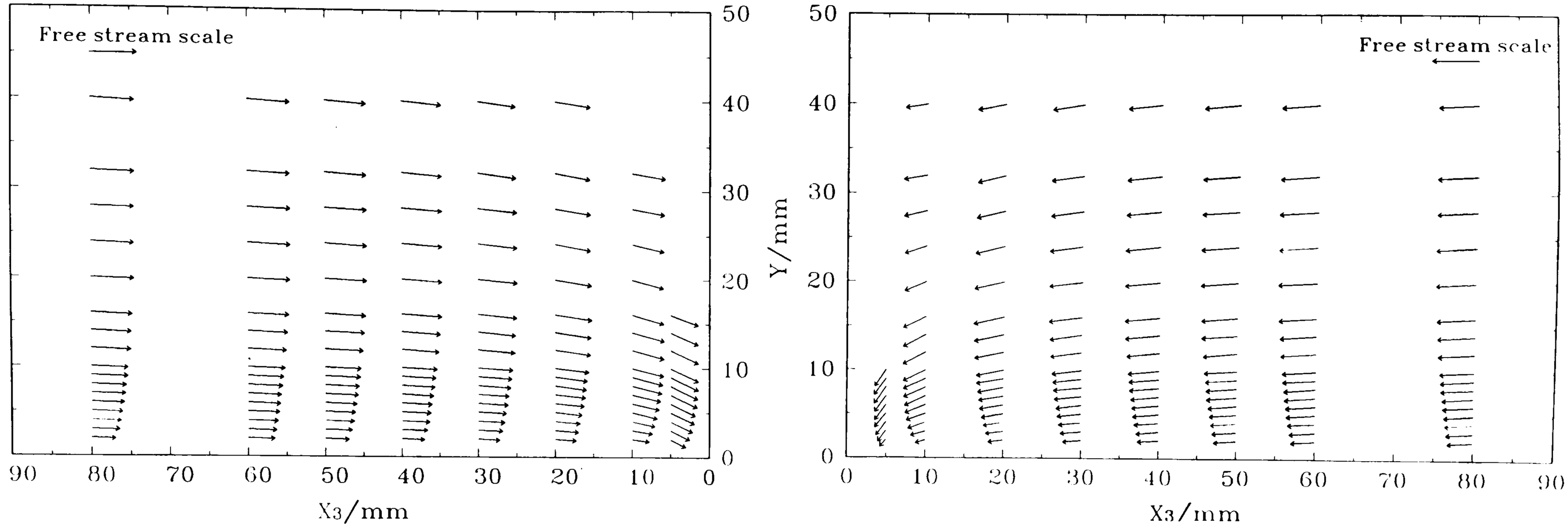

(a) Plane *B*

(b) Plane *G*

Figure 52 Cross-flow velocity vectors in the junction at $\alpha = 0°$, in planes normal to the tangents to the wing profile on both sides of the junction at $X = 1$ mm:
(a) Plane B — $\beta_s = -35.8°$ & (b) Plane G — $\beta_s = 44.2°$.

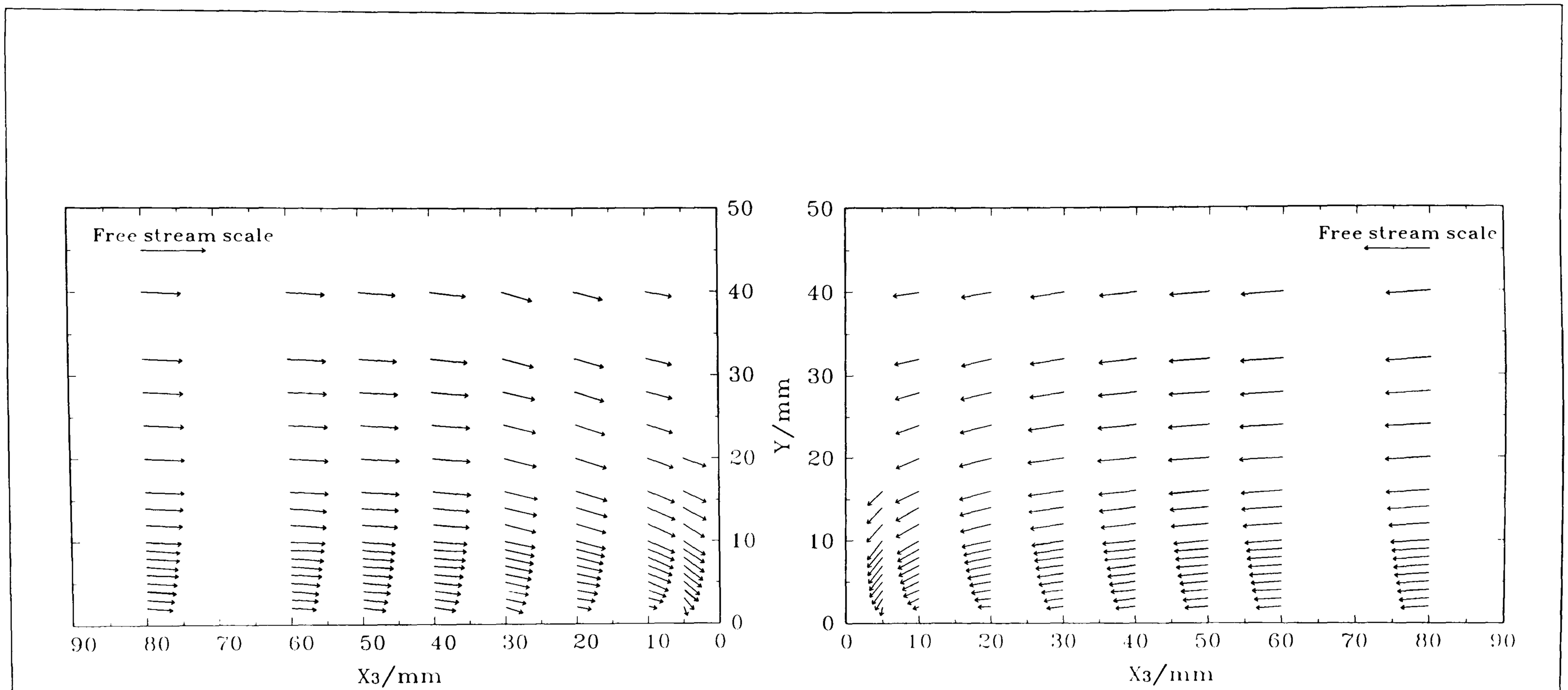

(a) Plane *C*

(b) Plane *H*

Figure 53 Cross-flow velocity vectors in the junction at $\alpha = 0°$, in planes normal to the tangents to the wing profile on both sides of the junction at $X = 2.5$ mm:
(a) Plane C — $\beta_s = -54°$ & (b) Plane H — $\beta_s = 53.4°$.

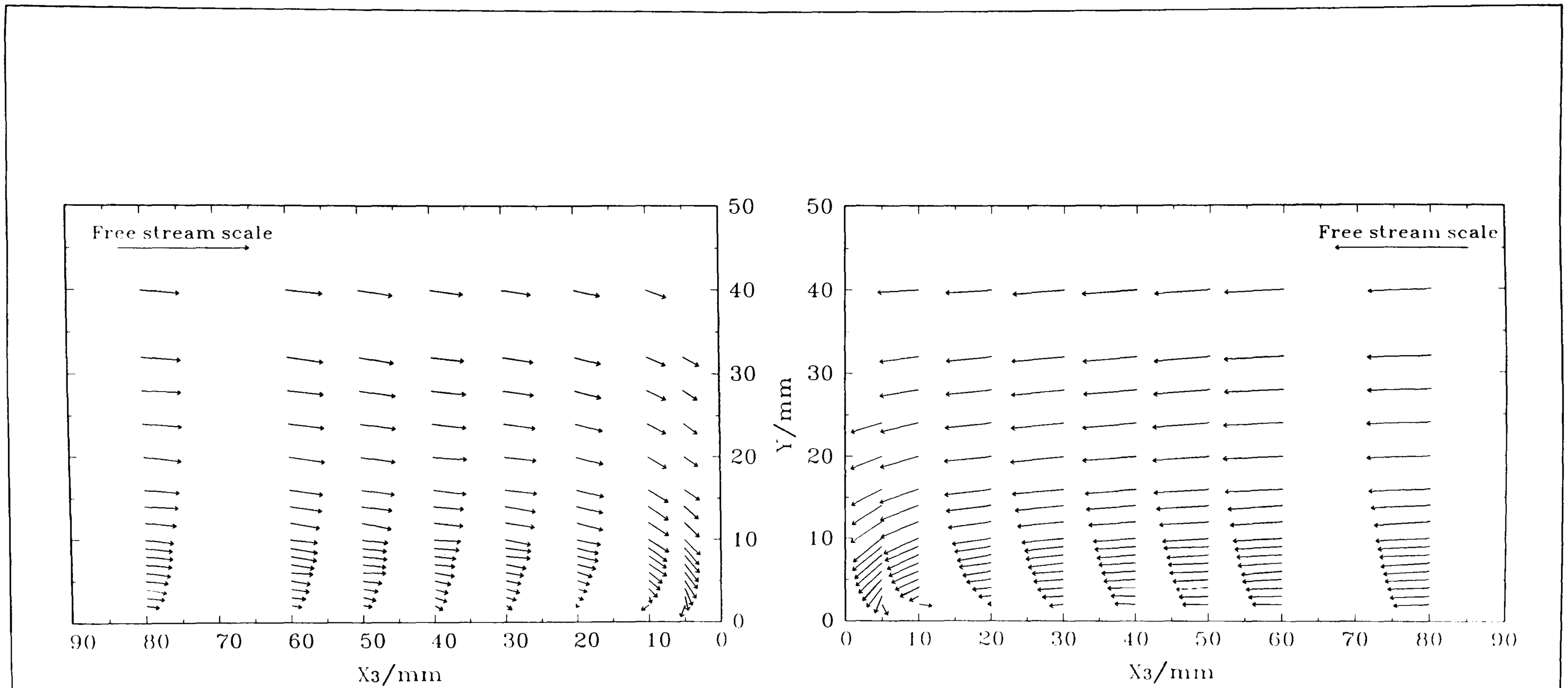

(a) Plane *D*

(b) Plane *I*

Figure 54 Cross-flow velocity vectors in the junction at $\alpha = 0°$, in planes normal to the tangents to the wing profile on both sides of the junction at $X = 10$ mm:
(a) Plane D — $\beta_s = -72.8°$ & (b) Plane I — $\beta_s = 62.8°$.

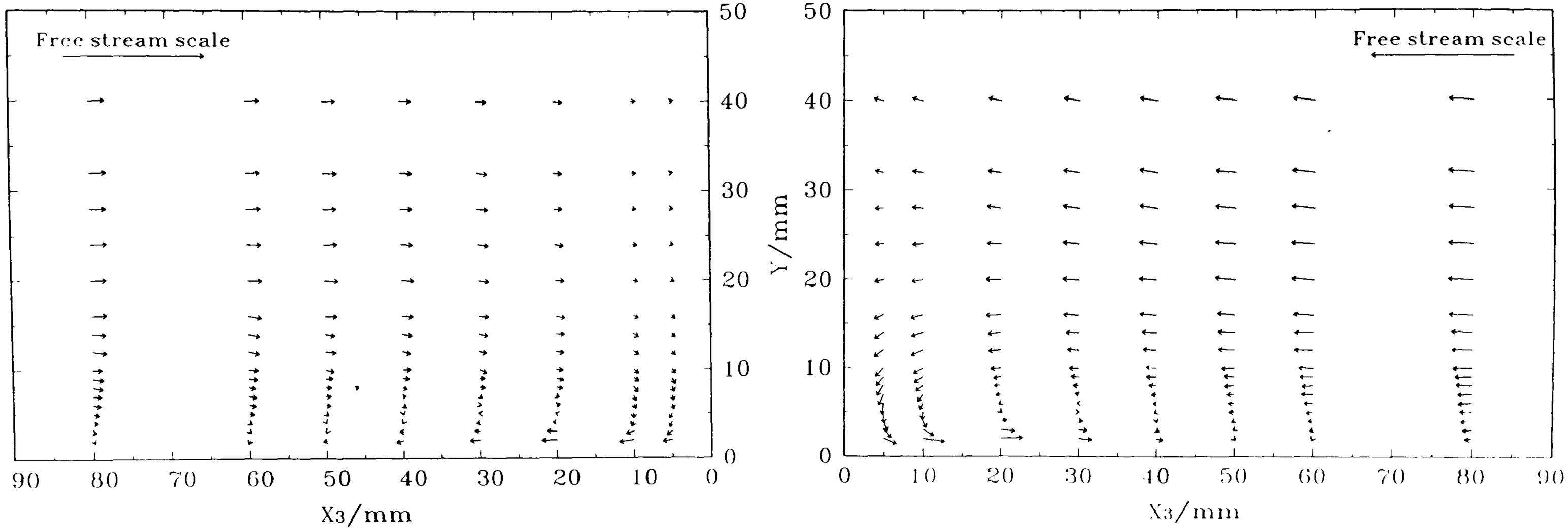

(a) Plane *E*

(b) Plane *J*

Figure 55 Cross-flow velocity vectors in the junction at $\alpha = 0°$, in planes normal to the tangents to the wing profile on both sides of the junction at $X = 40$ mm:
(a) Plane E — $\beta_S = -81.3°$ & (b) Plane J — $\beta_S = 77.9°$.

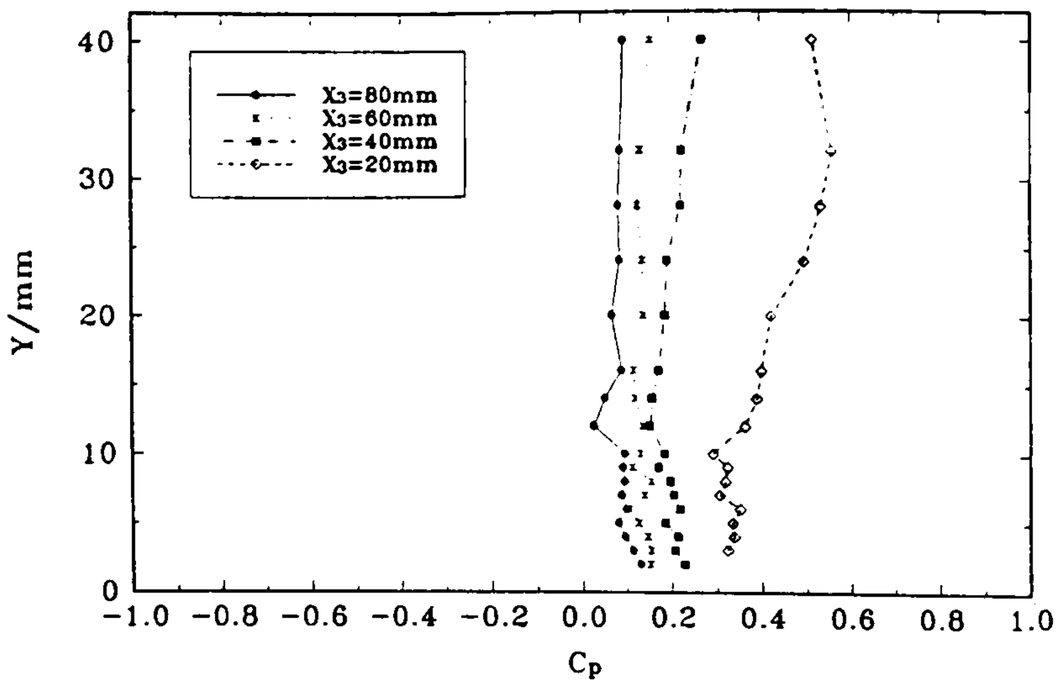

(a) Plane *A*

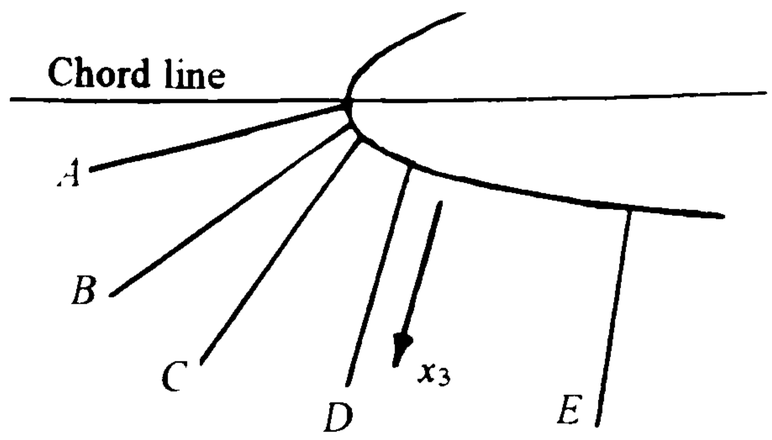

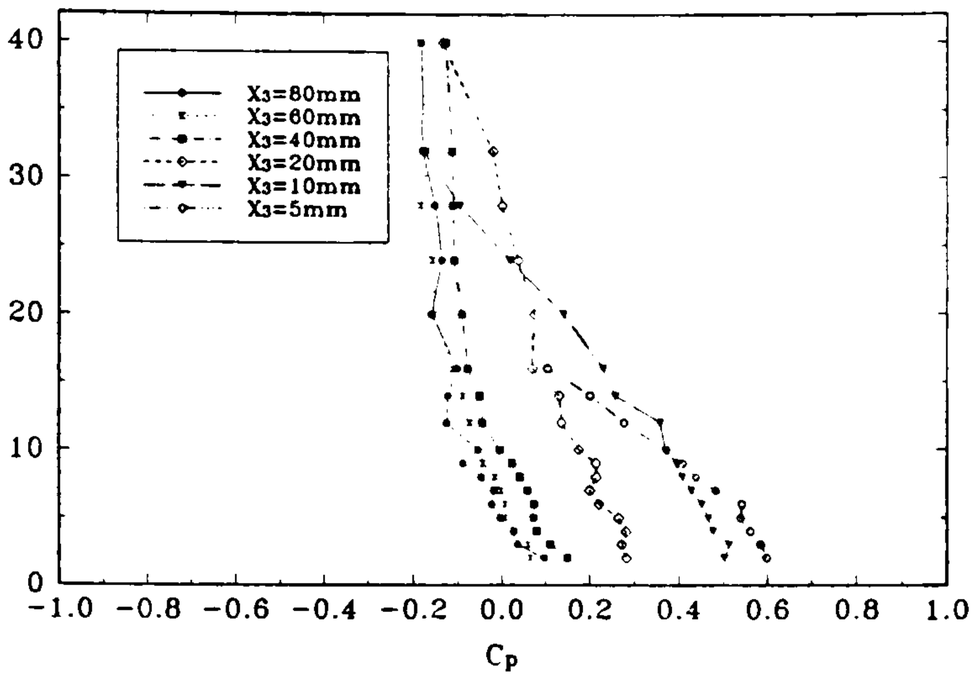

(b) Plane *B*

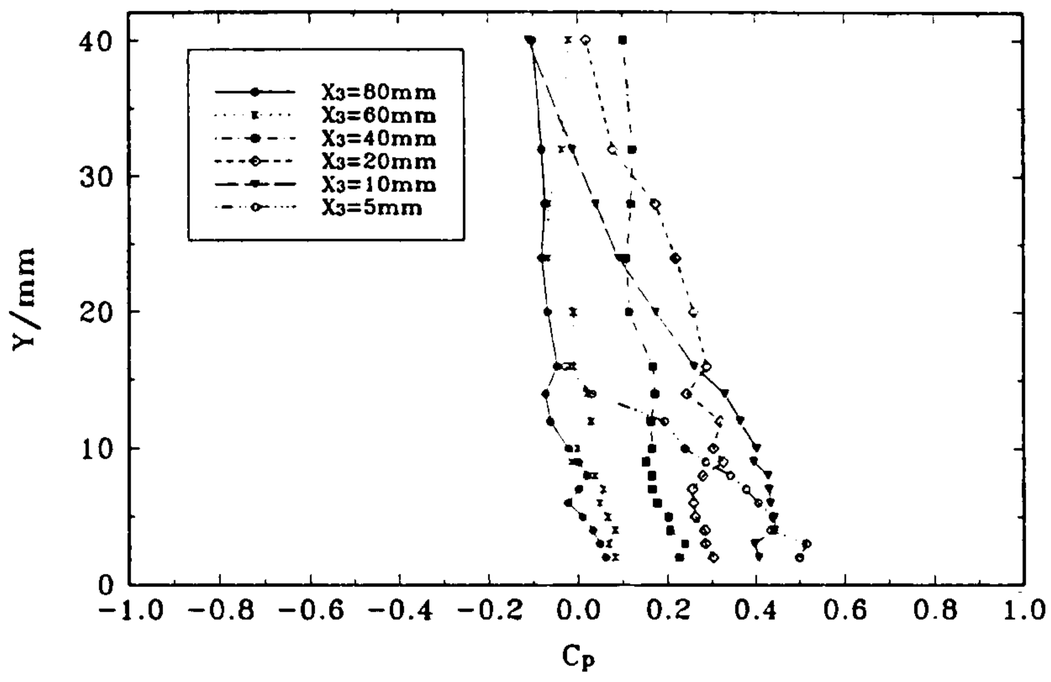

(c) Plane *C*

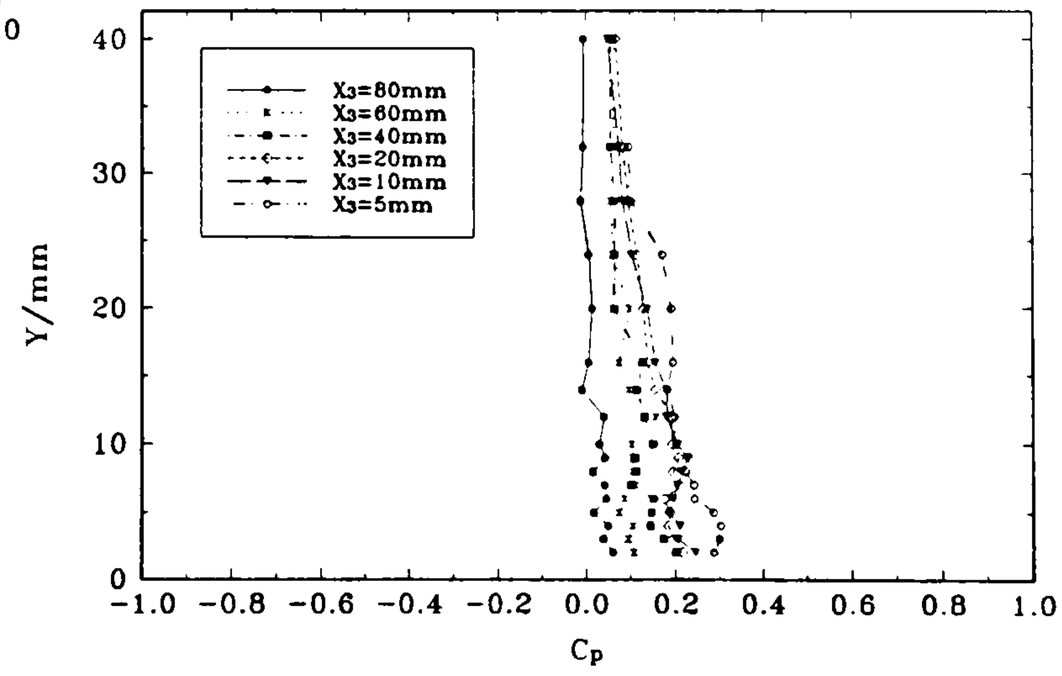

(d) Plane *D*

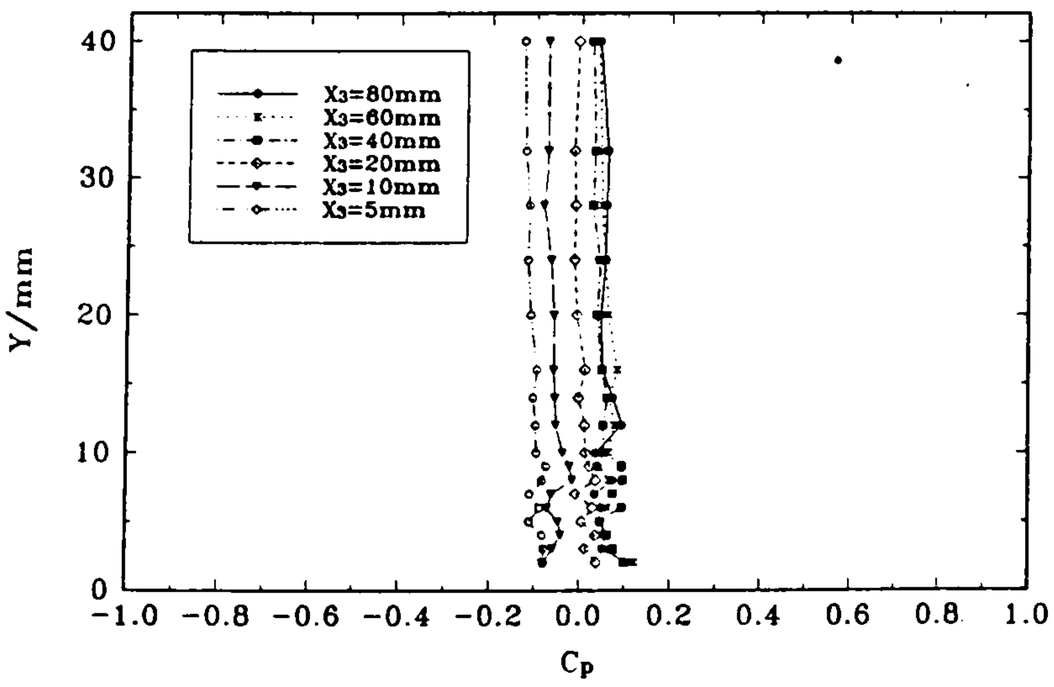

(e) Plane *E*

Figure 56 Profiles of static pressure coefficient through the plate boundary layer, in the leading-edge region at $\alpha = 0°$, in planes normal to the tangent to the local wing profile around the leading edge.

(continued...

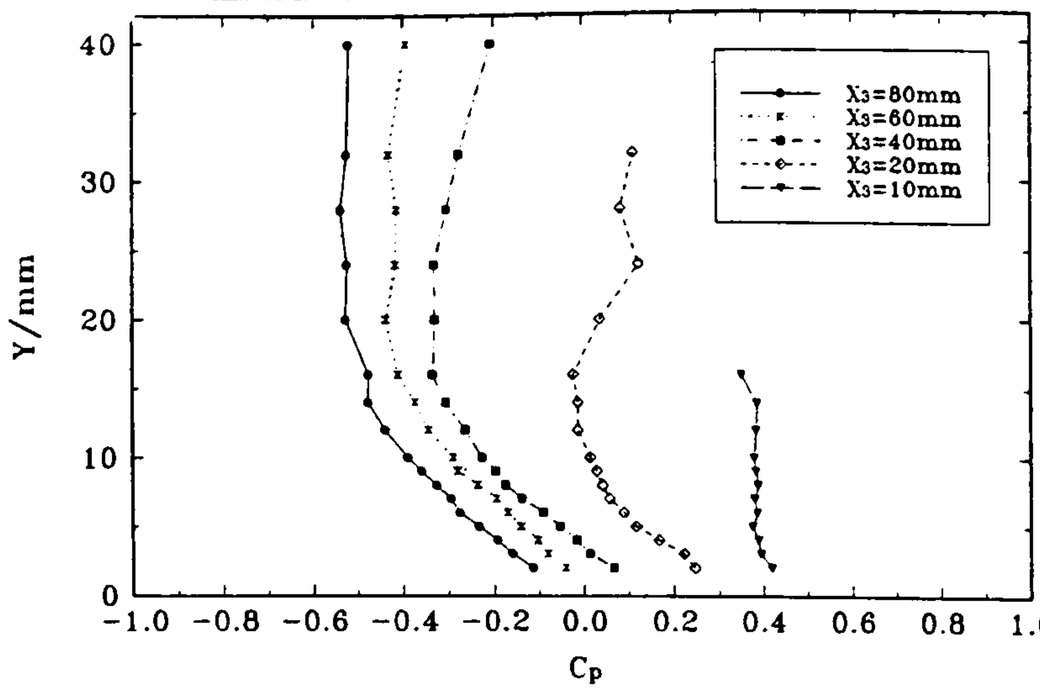

(f) Plane *F*

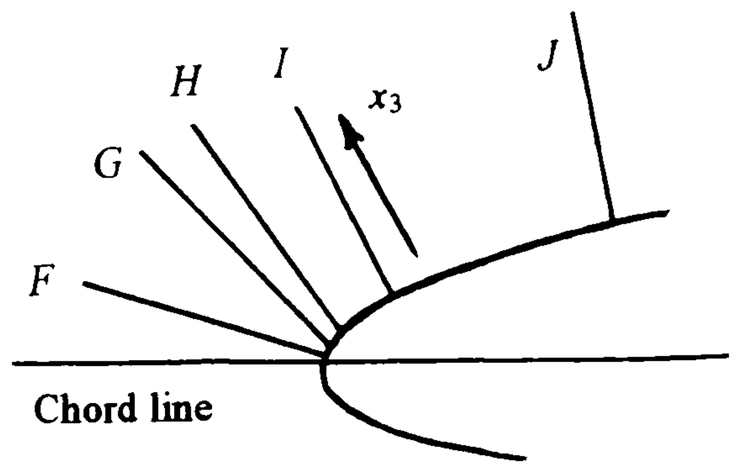

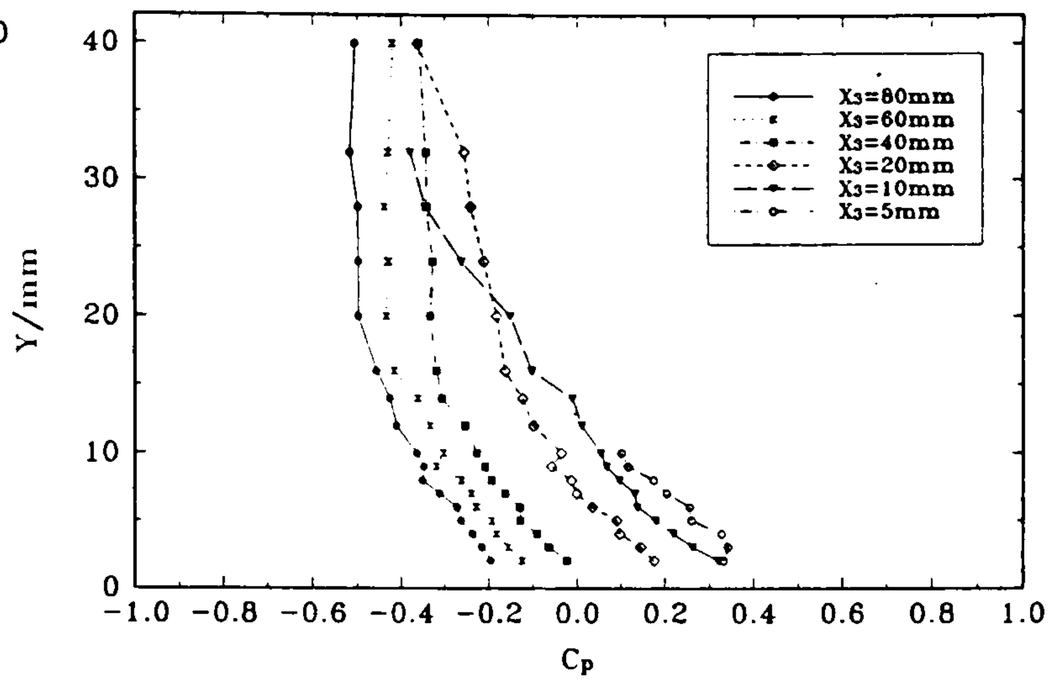

(g) Plane *G*

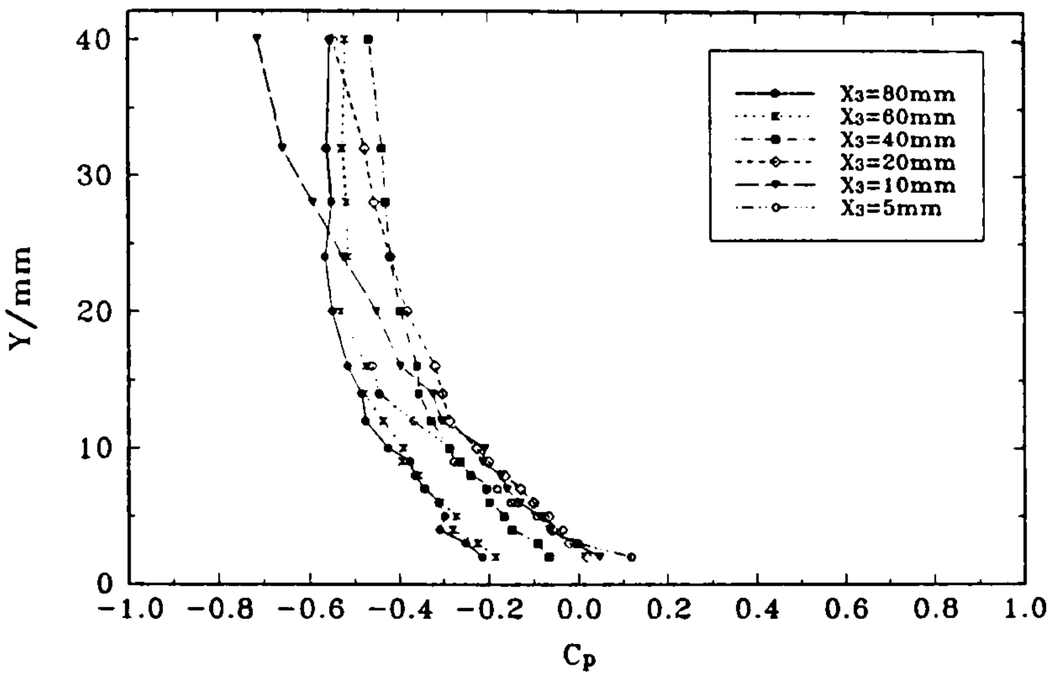

(h) Plane *H*

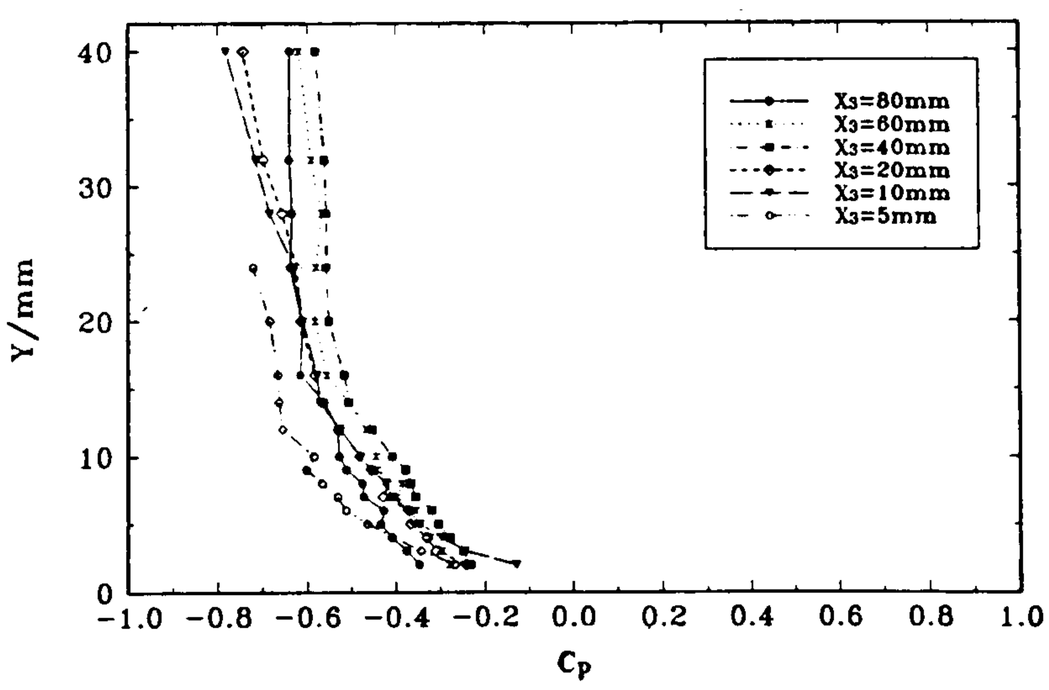

(i) Plane *I*

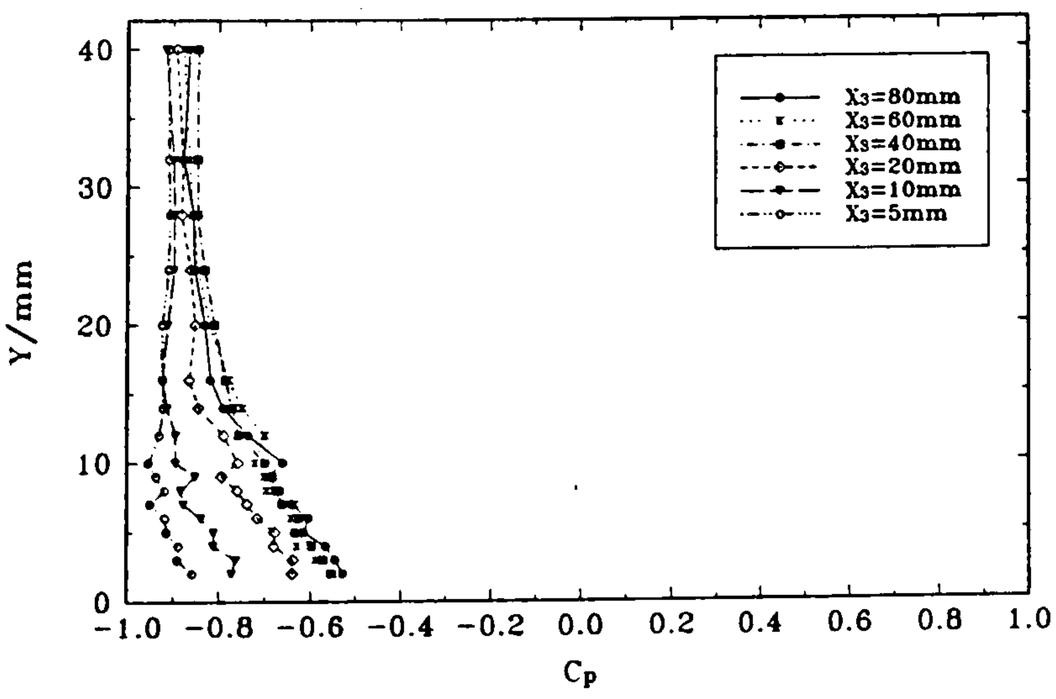

(j) Plane *J*

Figure 56 Profiles of static pressure coefficient through the plate boundary layer, in the leading-edge region at $\alpha = 0°$, in planes normal to the tangent to the local wing profile around the leading edge.

...concluded)

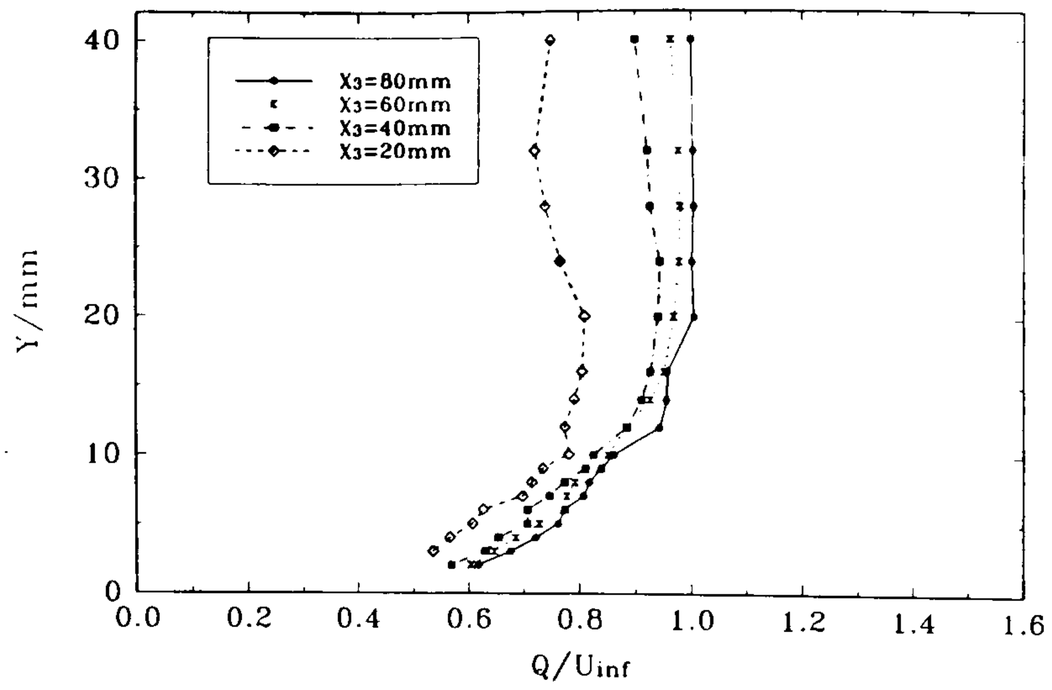

(a) Plane *A*

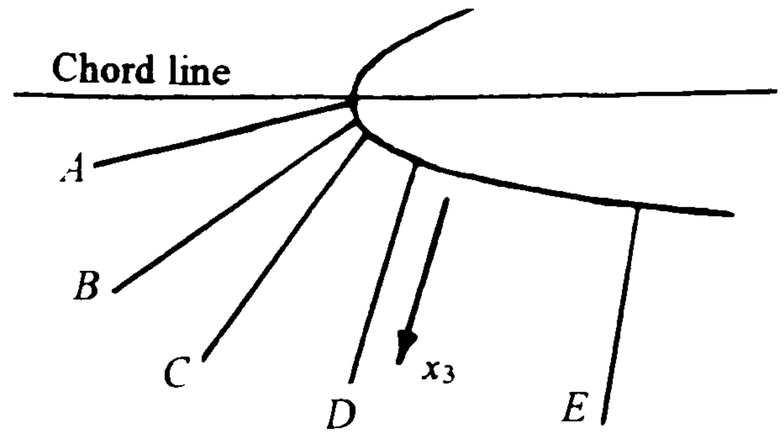

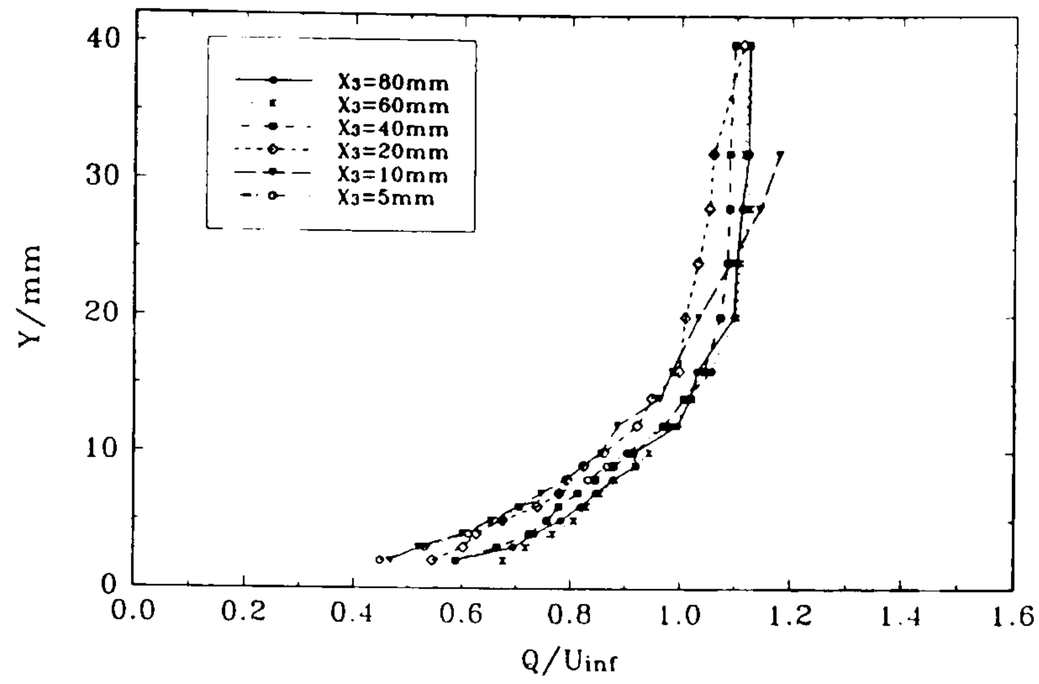

(b) Plane *B*

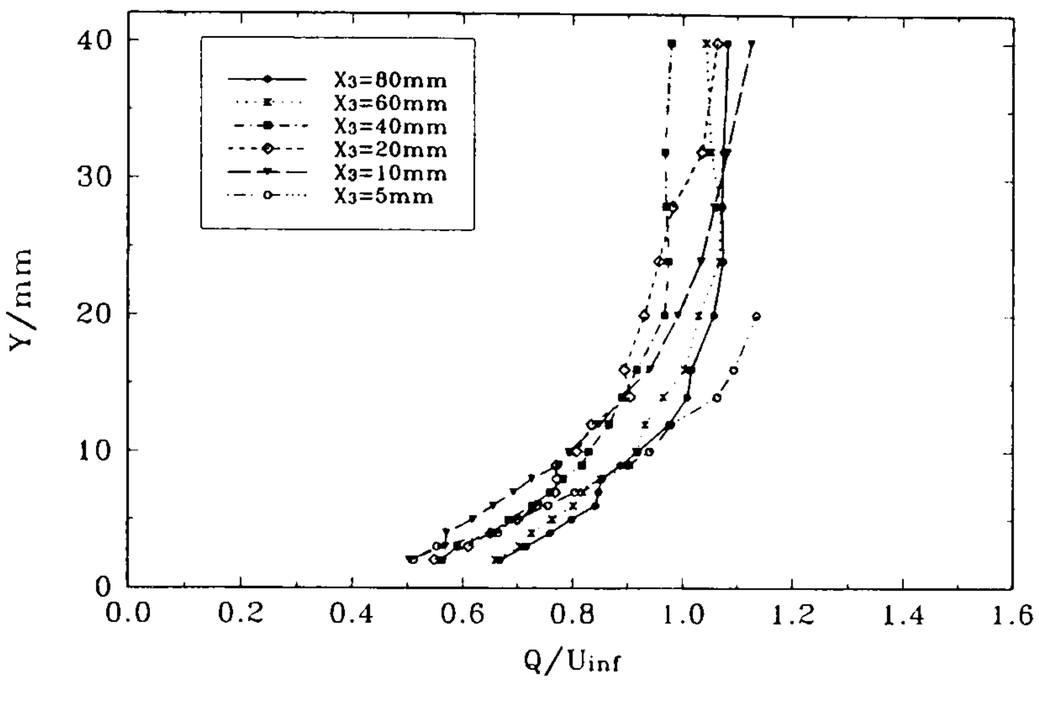

(c) Plane *C*

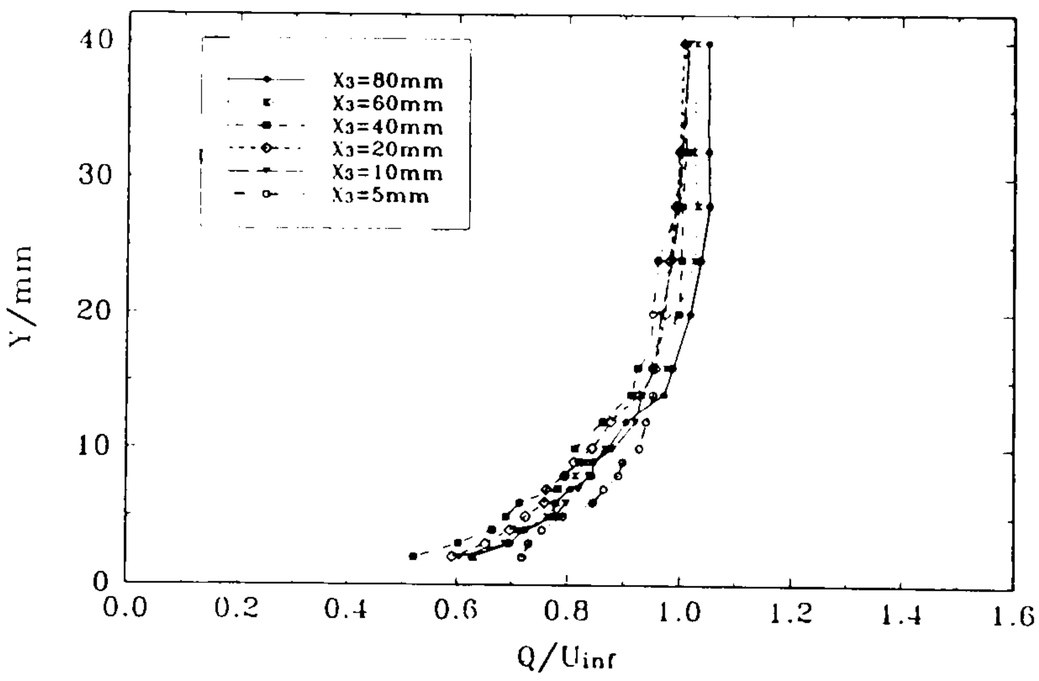

(d) Plane *D*

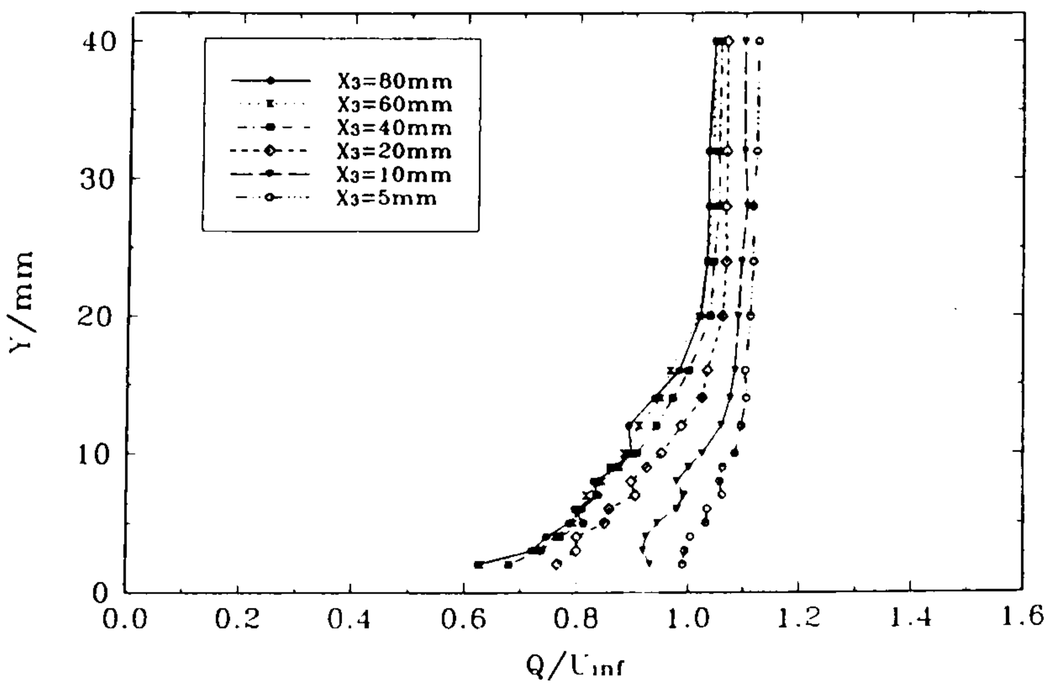

(e) Plane *E*

Figure 57 Profiles of velocity vector $Q\,U_\infty$ through the plate boundary layer, in the leading-edge region at $\alpha = 0°$, in planes normal to the tangent to the local wing profile around the leading edge.

(continued...

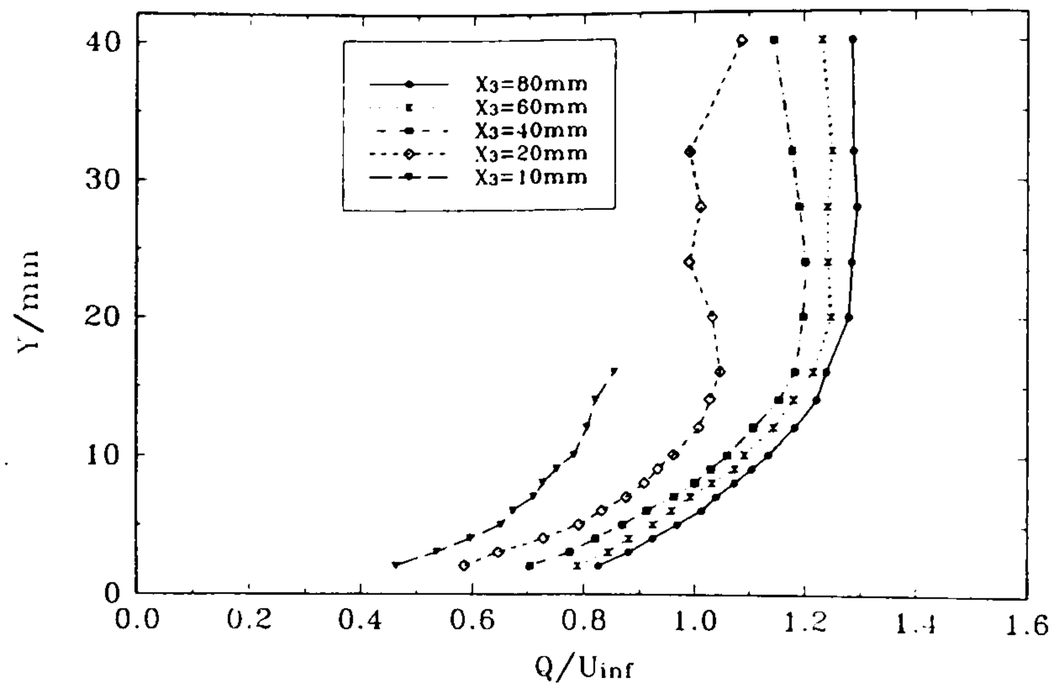

(f) Plane *F*

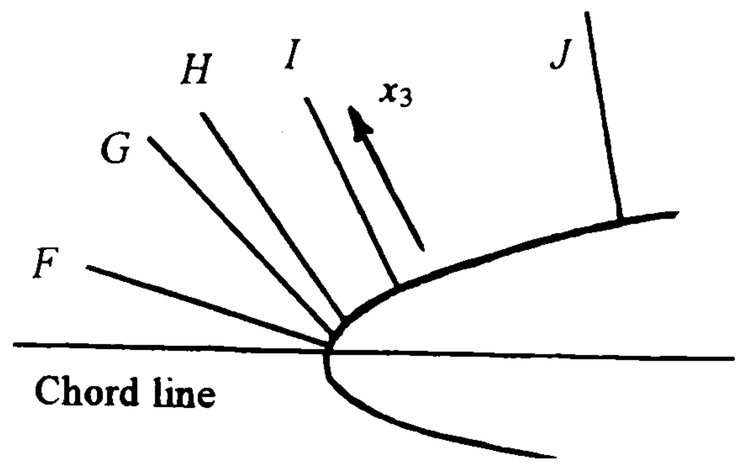

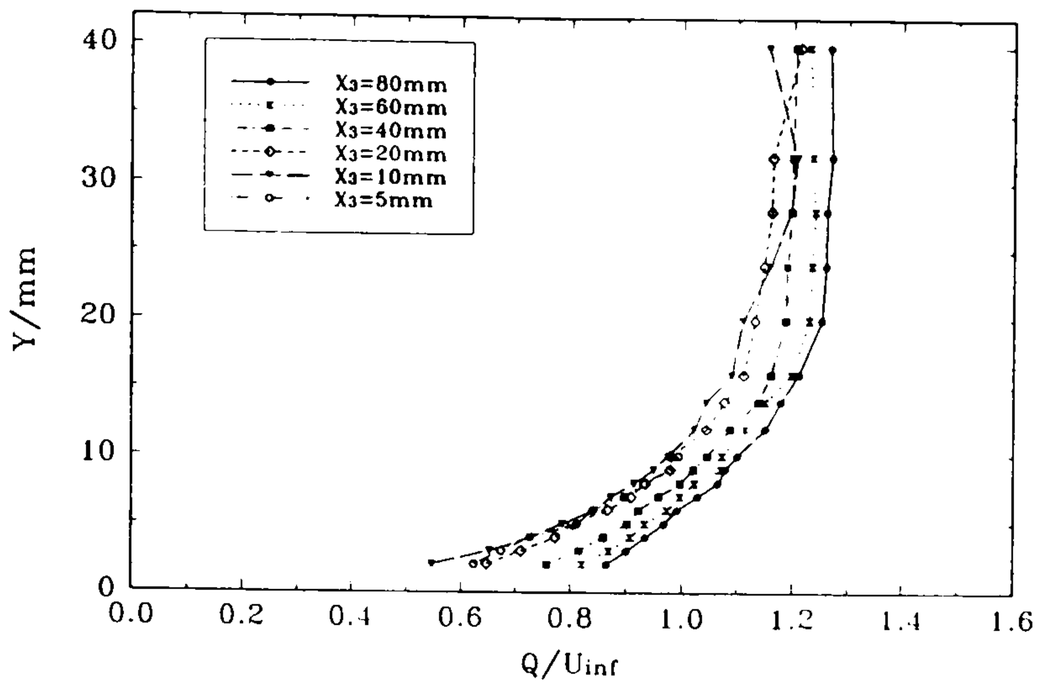

(g) Plane *G*

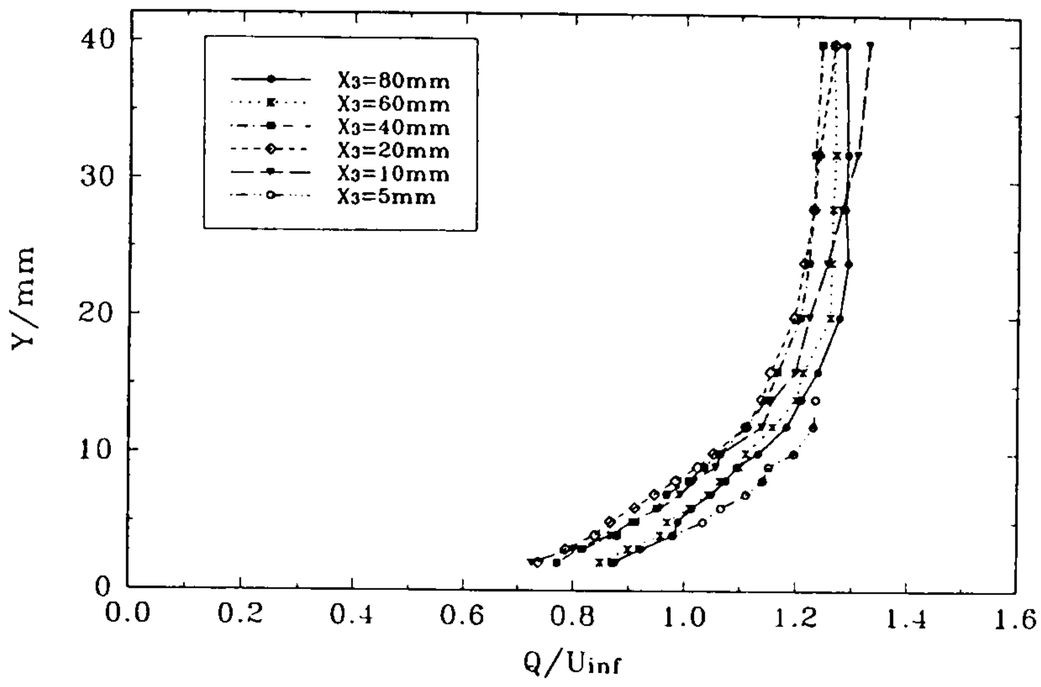

(h) Plane *H*

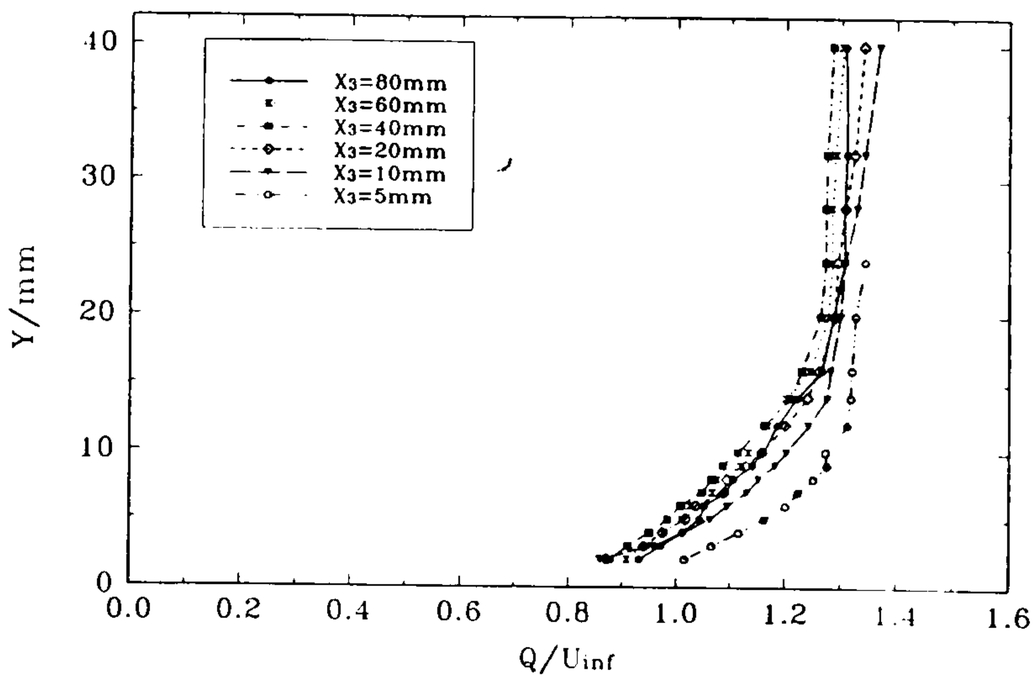

(i) Plane *I*

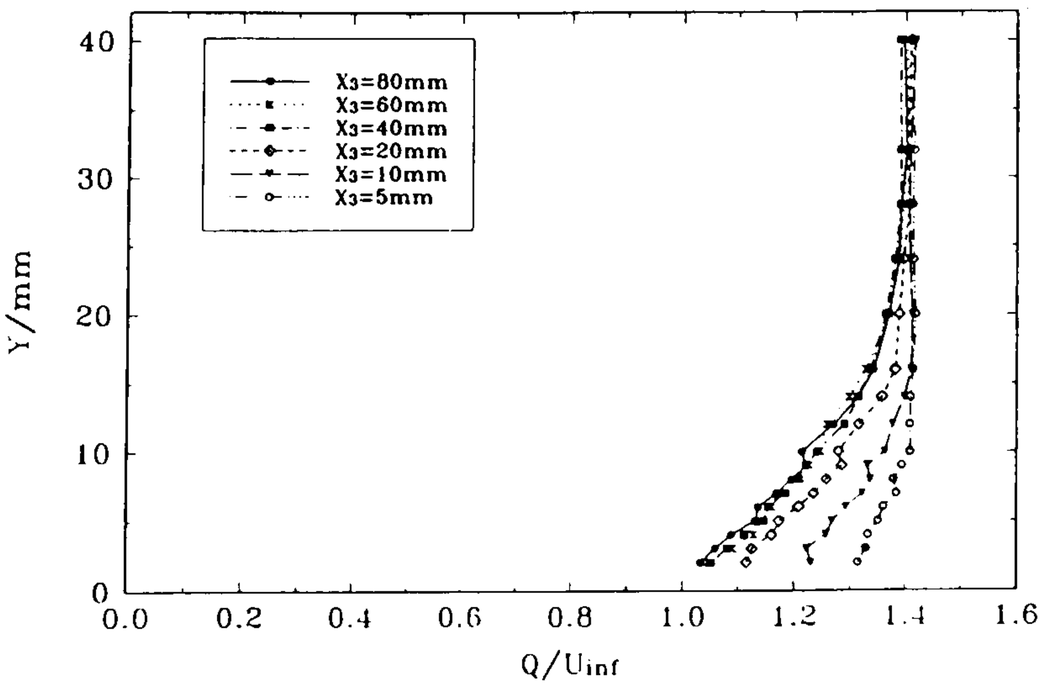

(j) Plane *J*

Figure 57 Profiles of velocity vector Q/U_∞ through the plate boundary layer, in the leading-edge region at $\alpha = 0°$, in planes normal to the tangent to the local wing profile around the leading edge.

...concluded)

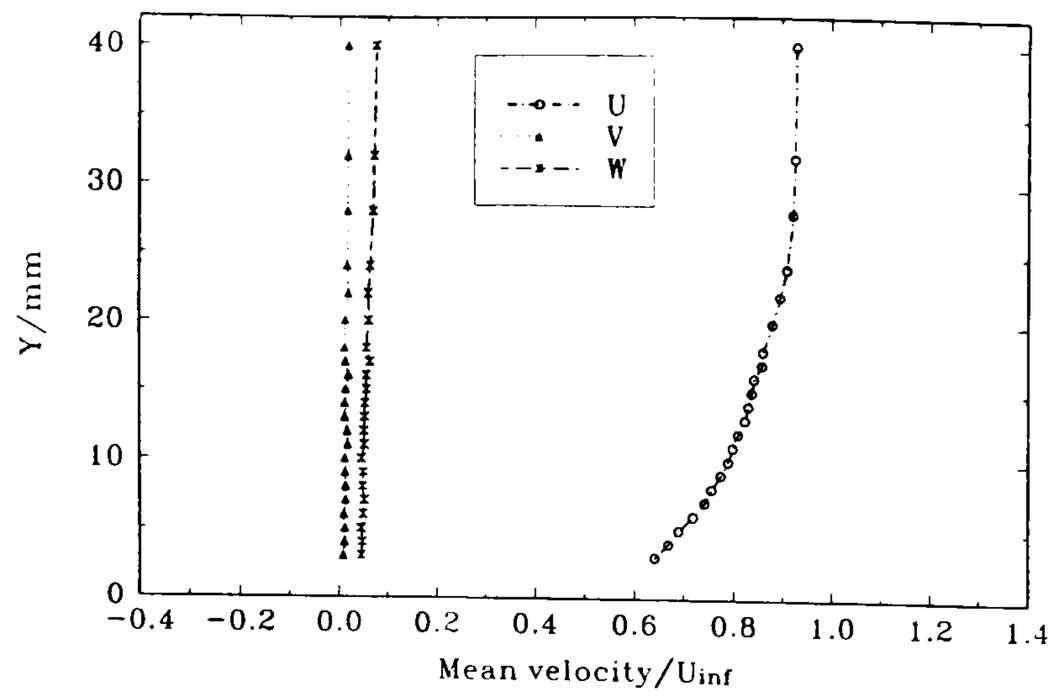

(a) $x_3 = 60$ mm

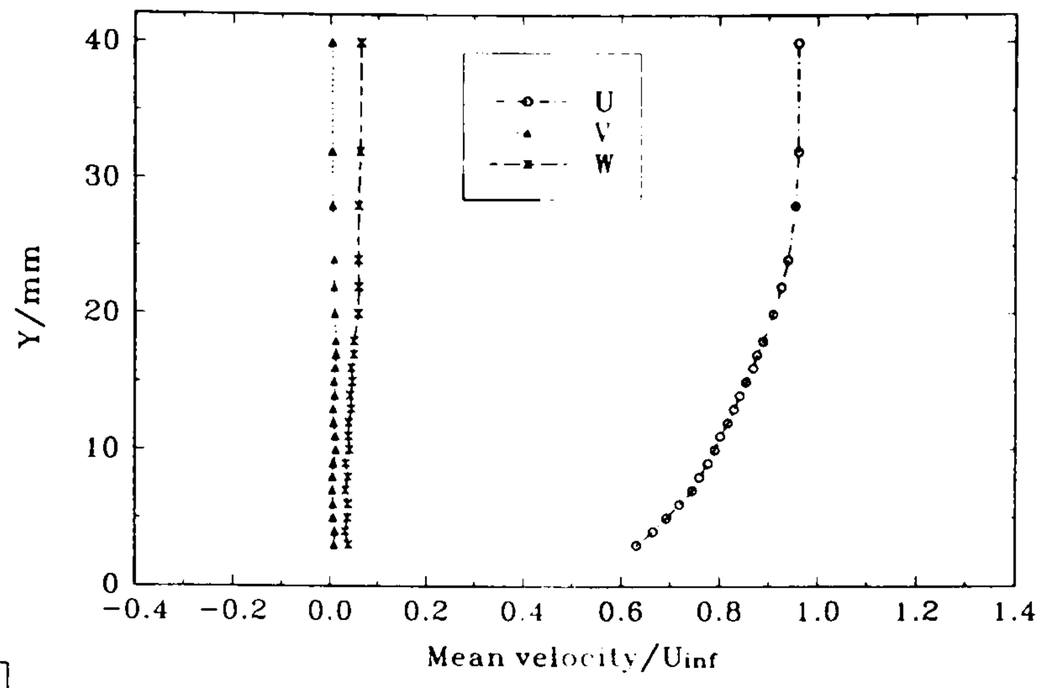

(b) $x_3 = 40$ mm

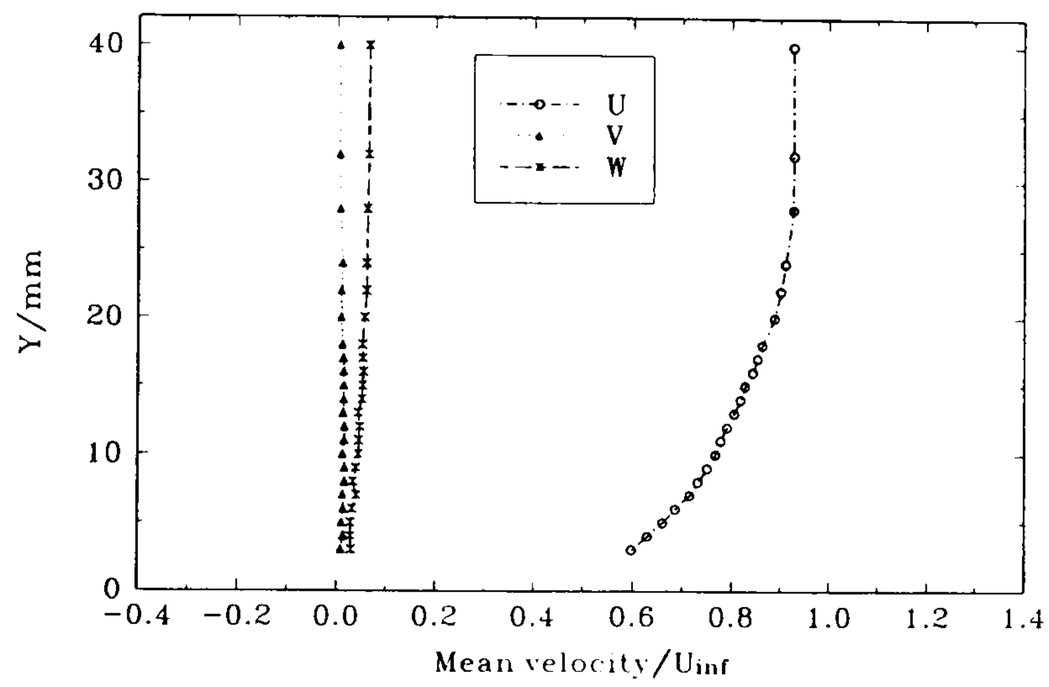

(c) $x_3 = 30$ mm

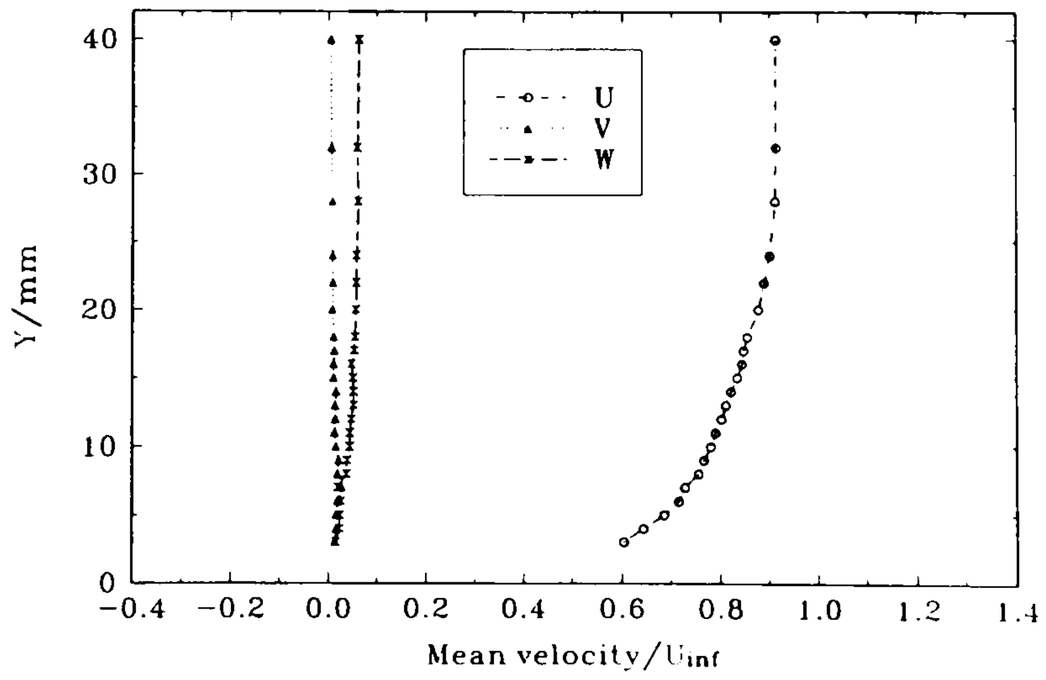

(d) $x_3 = 25$ mm

Figure 58 Profiles of $(\overline{U}, \overline{V}, \overline{W})/U_\infty$ through the plate boundary layer in Plane K, normal to the tangent to the wing lower-surface profile at $X = 300$ mm, at various distances from the junction. Wing incidence $\alpha = 0°$.

(continued...

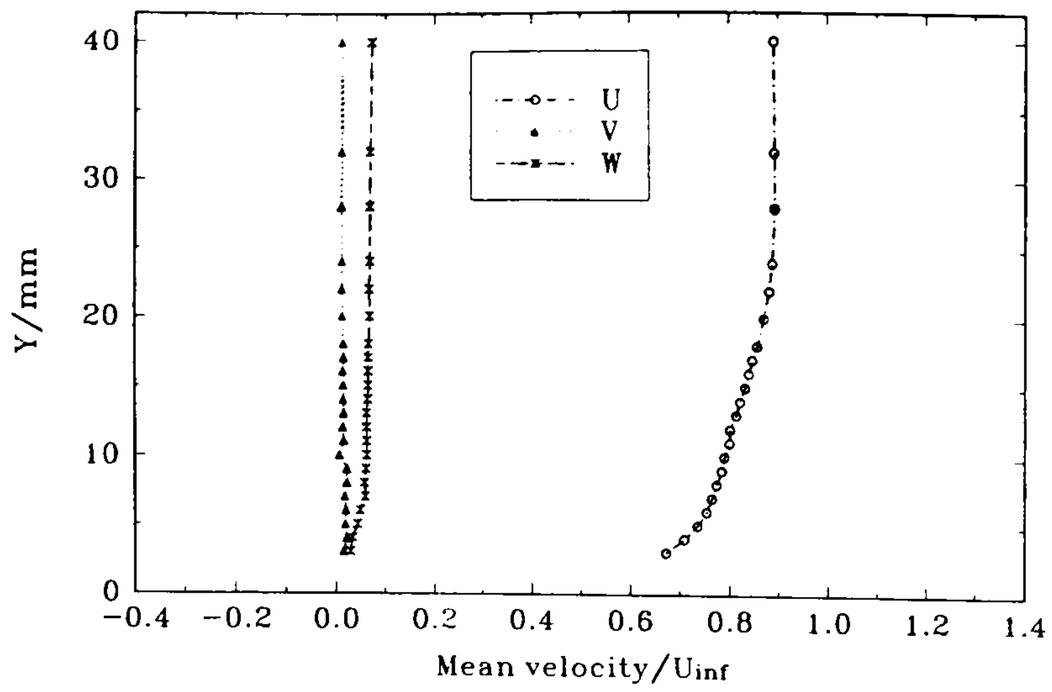

(e) $x_3 = 20$ mm

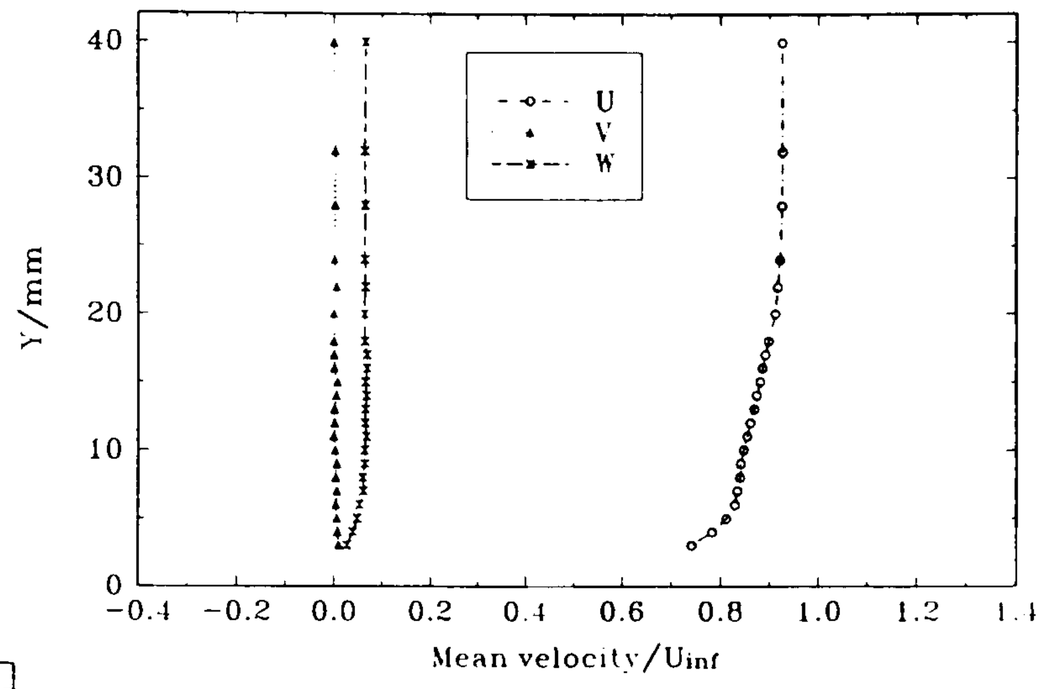

(f) $x_3 = 15$ mm

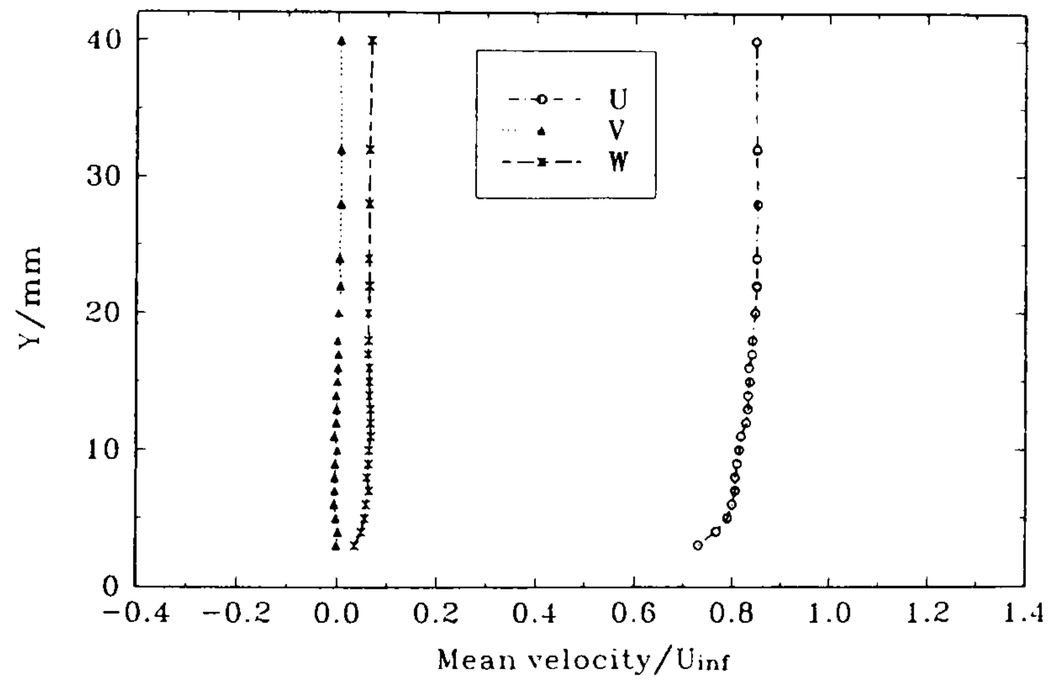

(g) $x_3 = 10$ mm

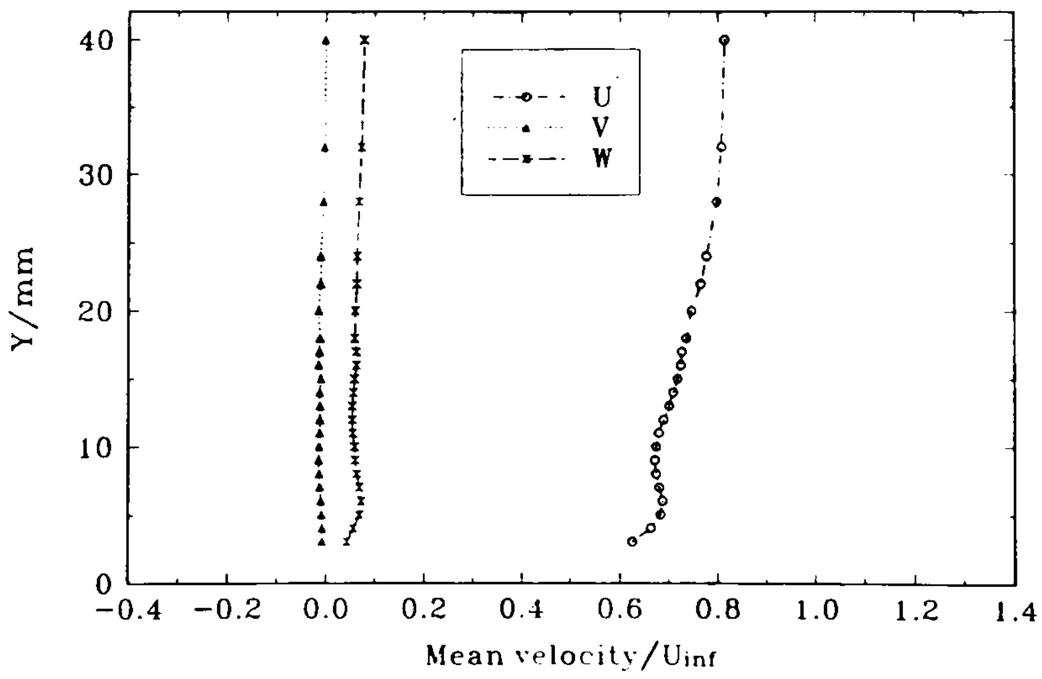

(h) $x_3 = 5$ mm

Figure 58 Profiles of $(\overline{U}, \overline{V}, \overline{W})/U_\infty$ through the plate boundary layer in Plane K, normal to the tangent to the wing lower-surface profile at $X = 300$ mm, at various distances from the junction. Wing incidence $\alpha = 0°$.

...concluded)

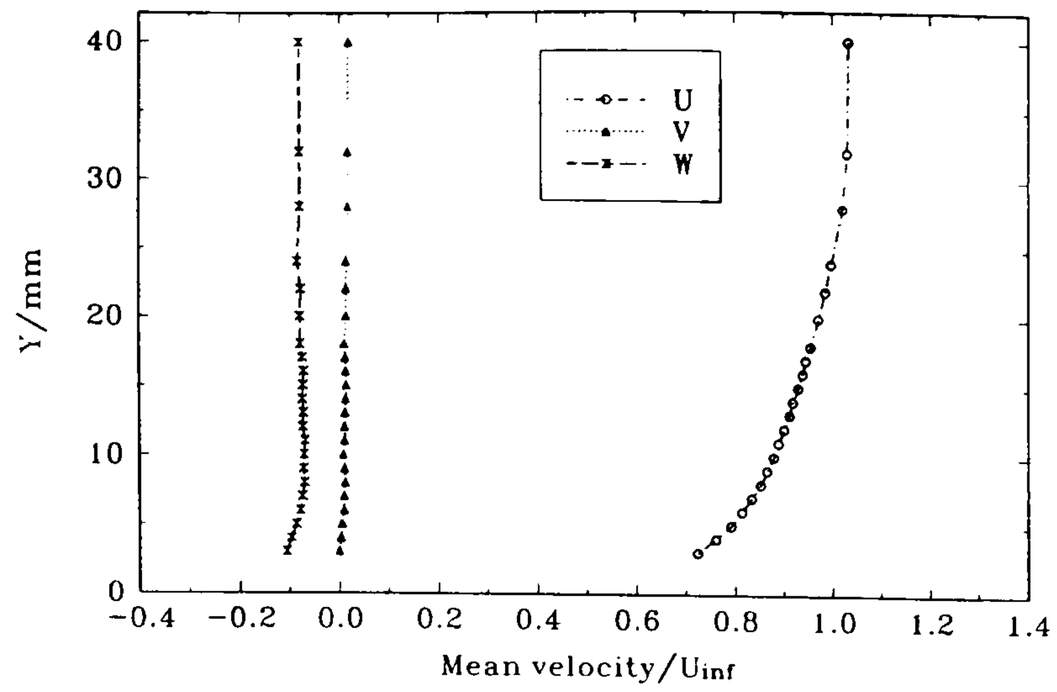

(a) $x_3 = 60$ mm

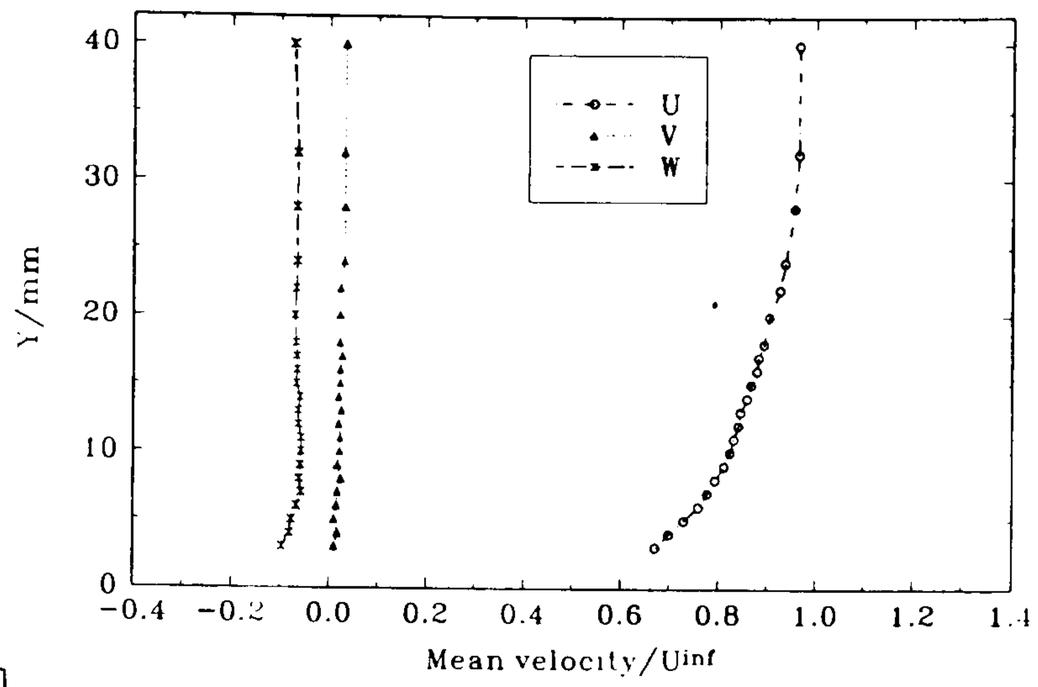

(b) $x_3 = 40$ mm

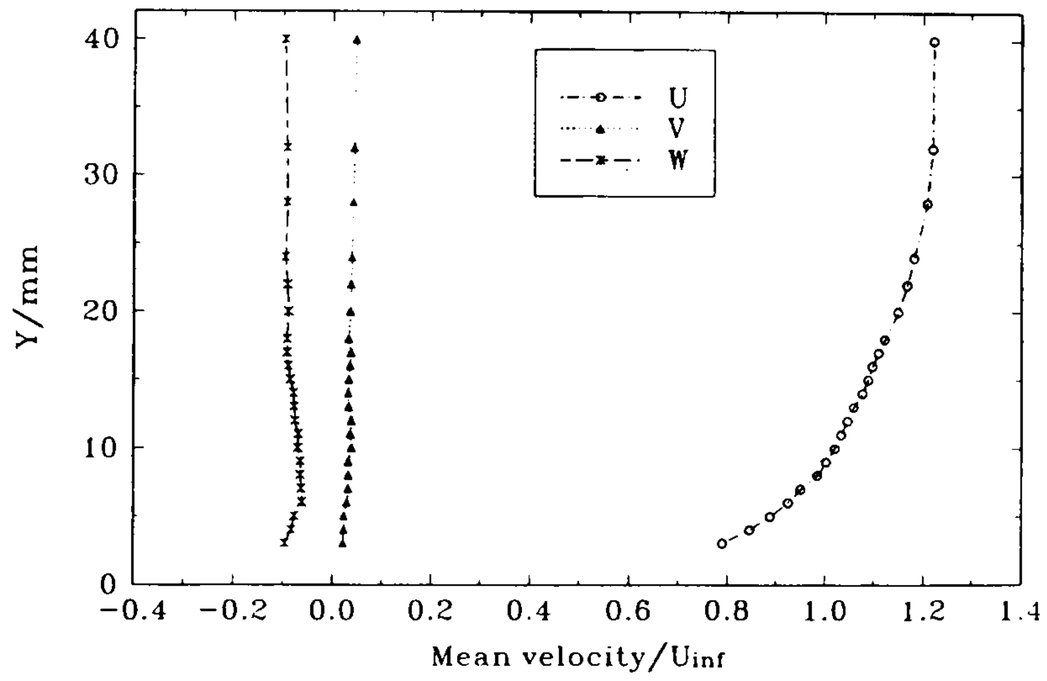

(c) $x_3 = 30$ mm

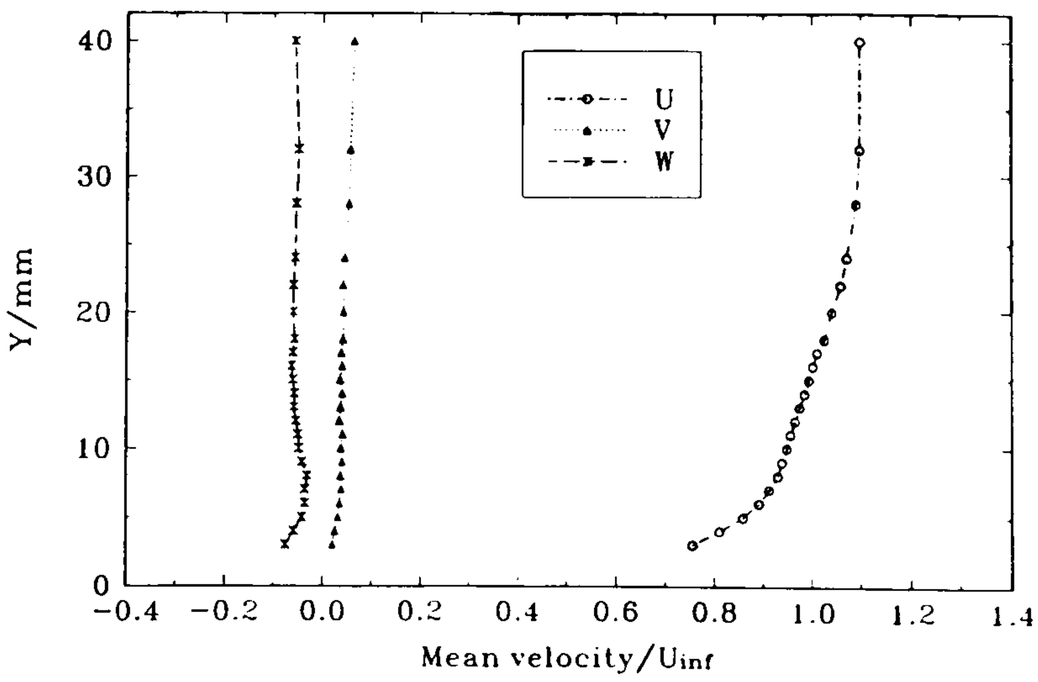

(d) $x_3 = 25$ mm

Figure 59 Profiles of $(\overline{U}, \overline{V}, \overline{W})/U_\infty$ through the plate boundary layer in Plane L, normal to the tangent to the wing upper-surface profile at $X = 300$ mm, at various distances from the junction. Wing incidence $\alpha = 0°$.

(continued...

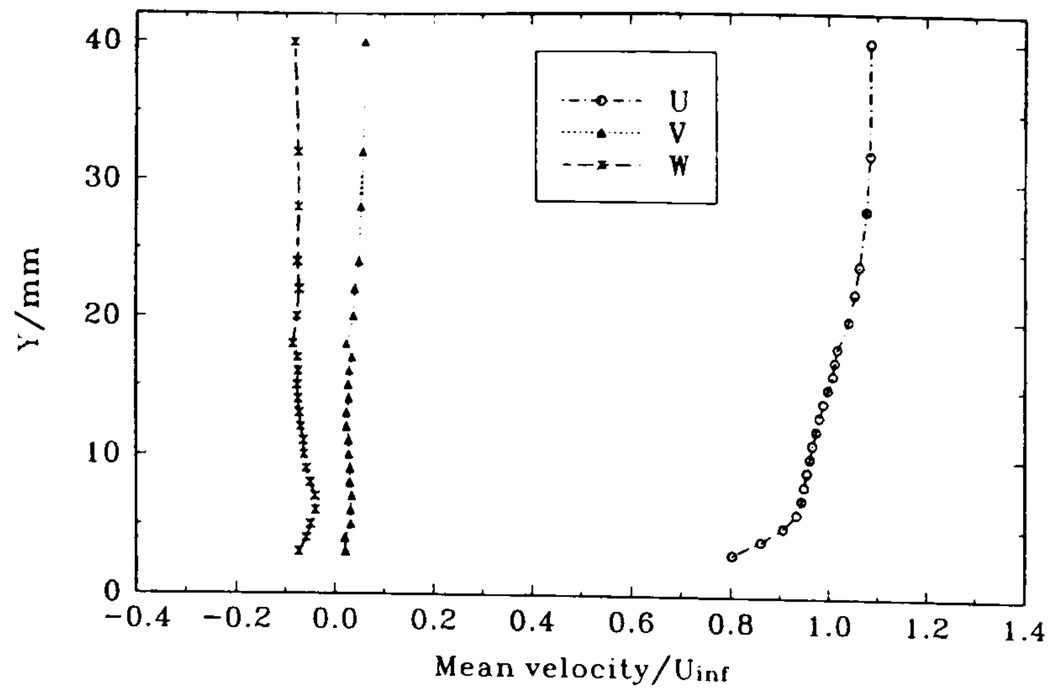

(e) $x_3 = 20$ mm

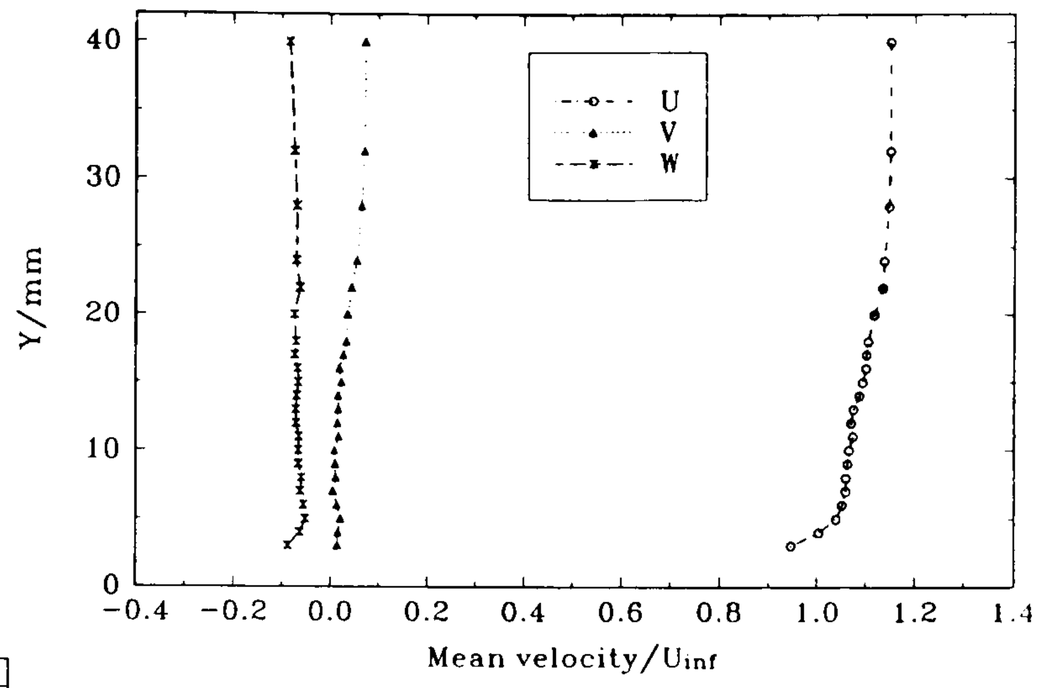

(f) $x_3 = 15$ mm

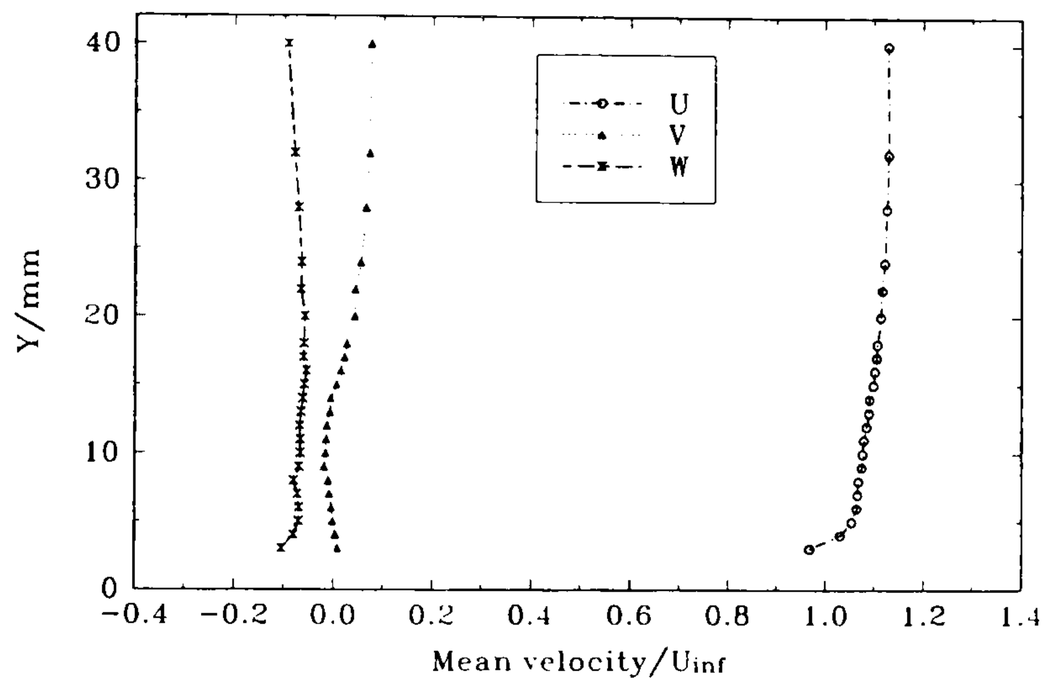

(g) $x_3 = 10$ mm

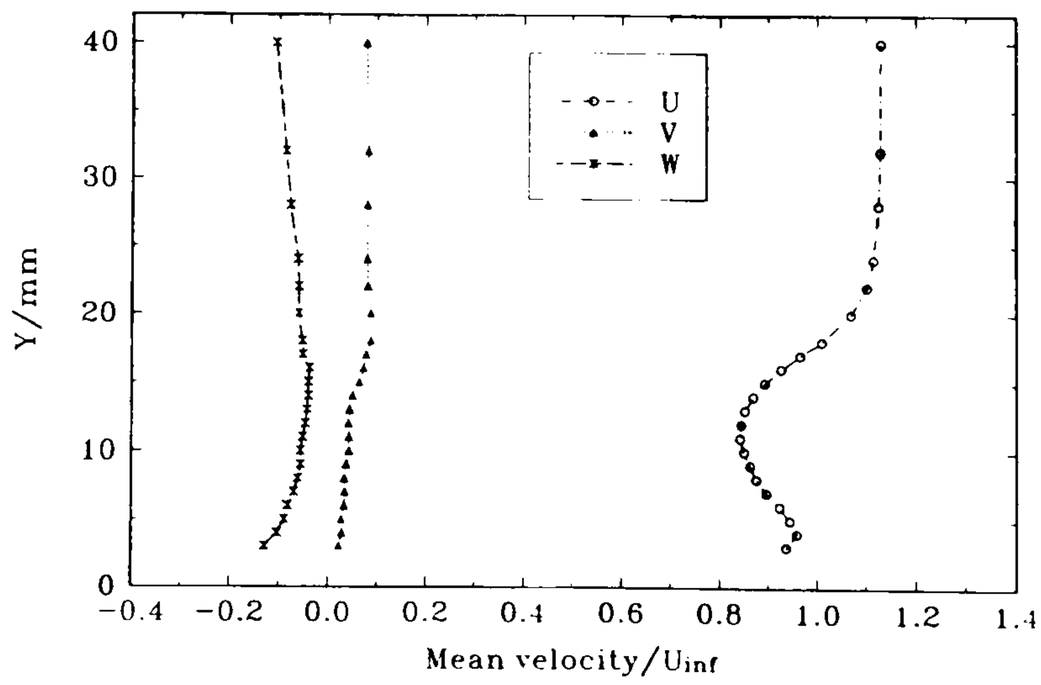

(h) $x_3 = 5$ mm

Figure 59 Profiles of $(\overline{U}, \overline{V}, \overline{W}) / U_\infty$ through the plate boundary layer in Plane L, normal to the tangent to the wing upper-surface profile at $X = 300$ mm, at various distances from the junction. Wing incidence $\alpha = 0°$.

...concluded)

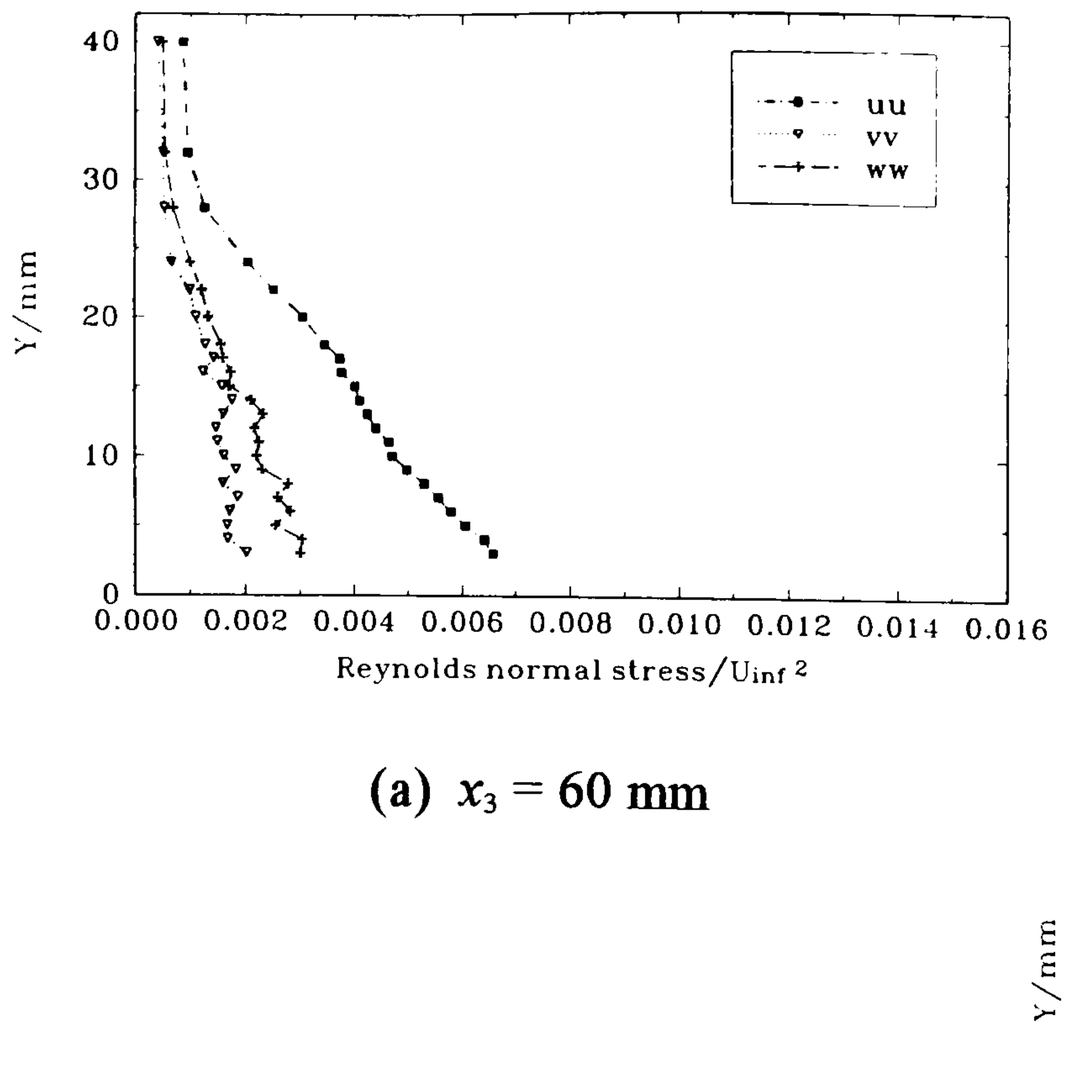

(a) $x_3 = 60$ mm

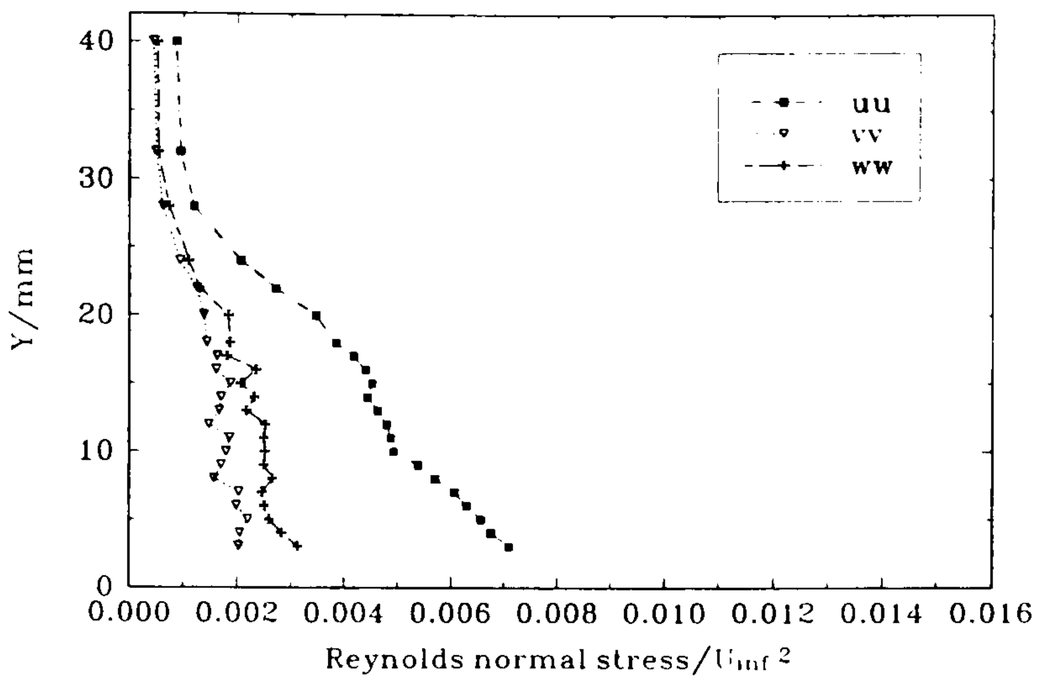

(b) $x_3 = 40$ mm

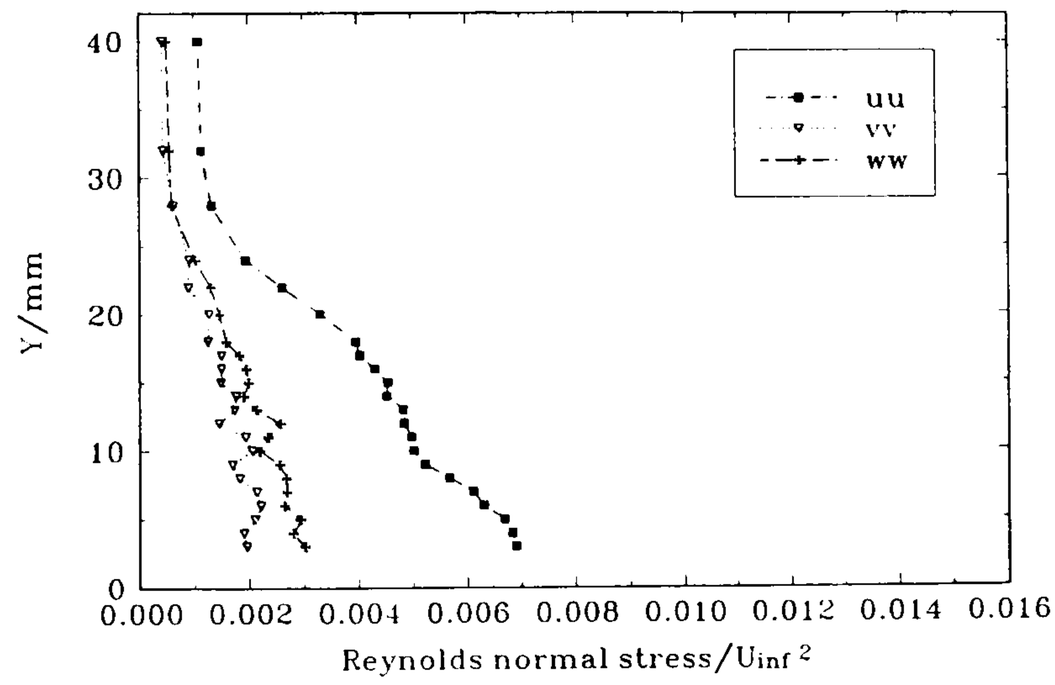

(c) $x_3 = 30$ mm

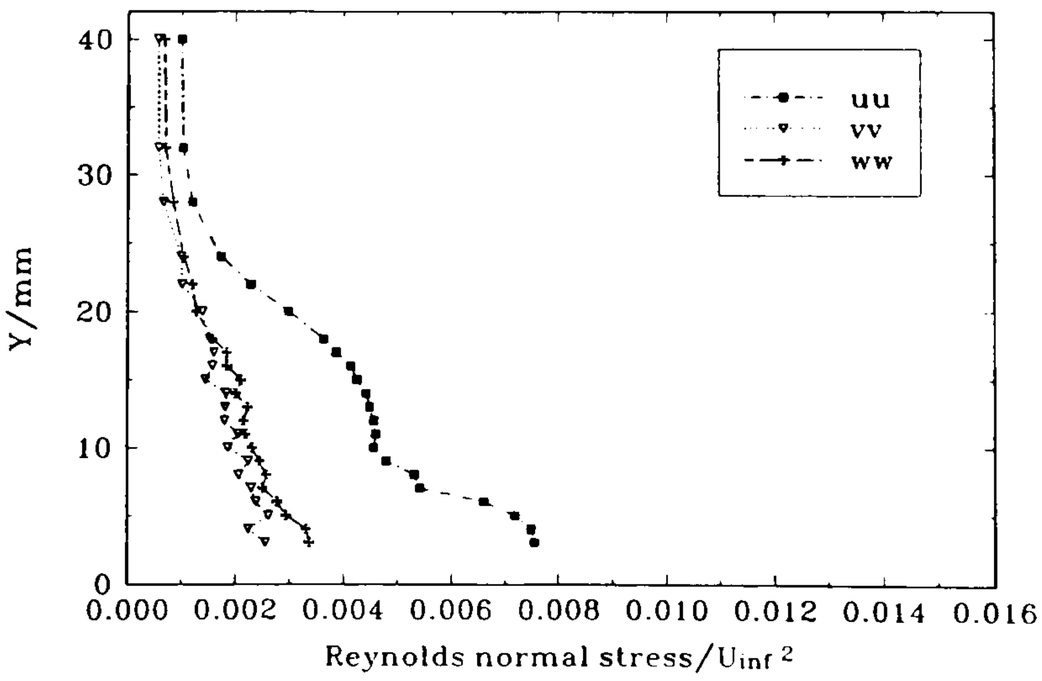

(d) $x_3 = 25$ mm

Figure 60 Profiles of $(\overline{u^2}, \overline{v^2}, \overline{w^2})/U_\infty^2$ through the plate boundary layer in plane X, normal to the tangent to the wing lower-surface profile at $X = 300$ mm, at various distances from the junction. Wing incidence = 0°.

(continued...

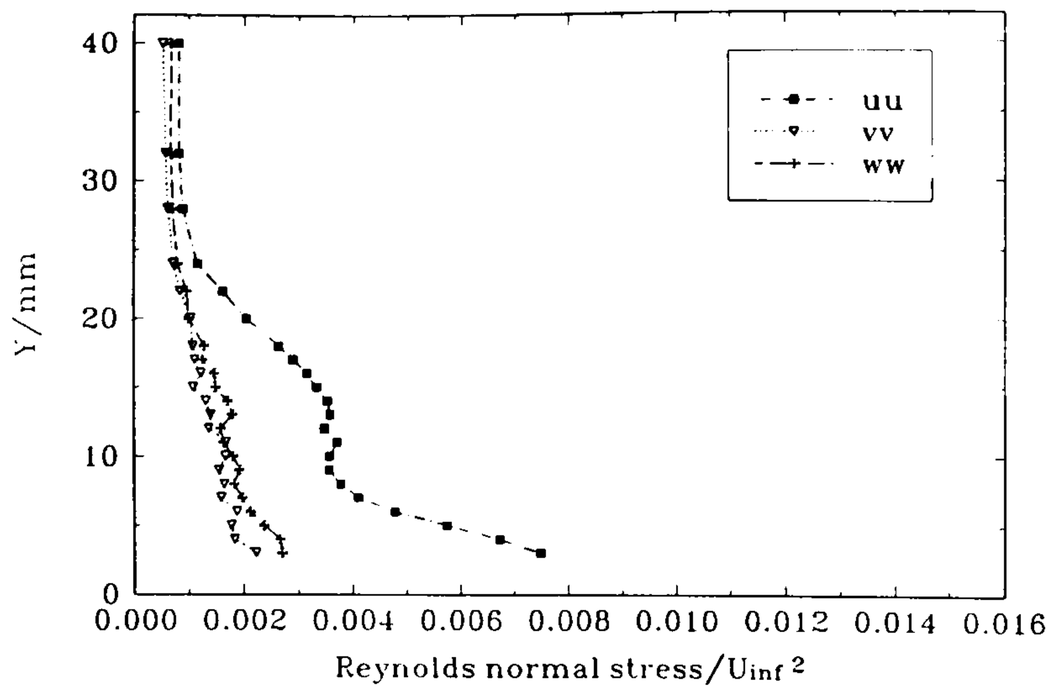

(e) $x_3 = 20$ mm

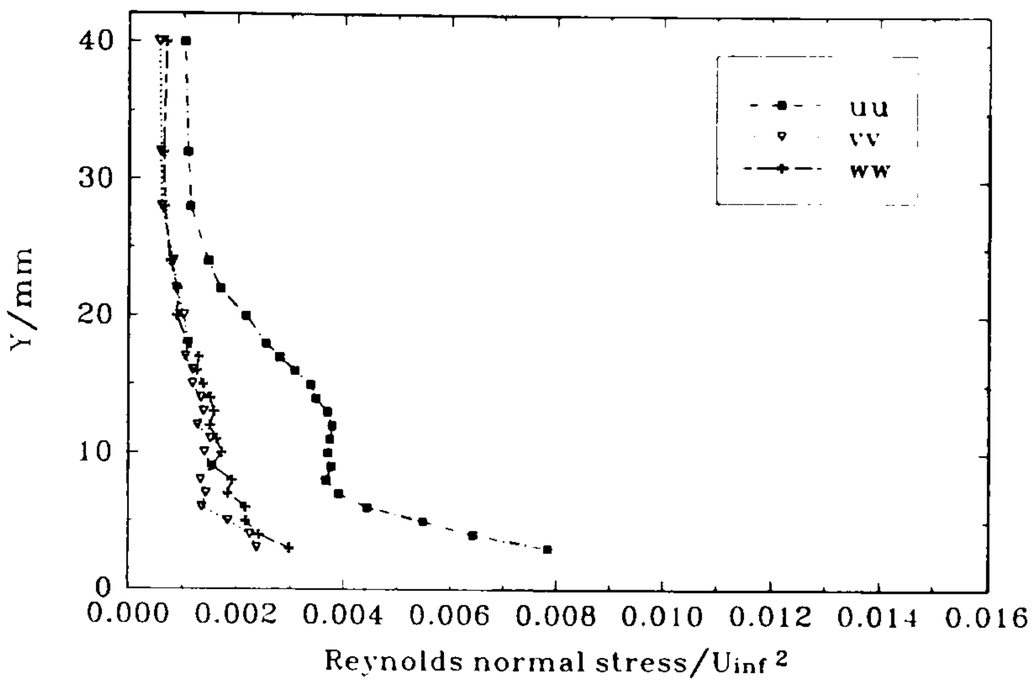

(f) $x_3 = 15$ mm

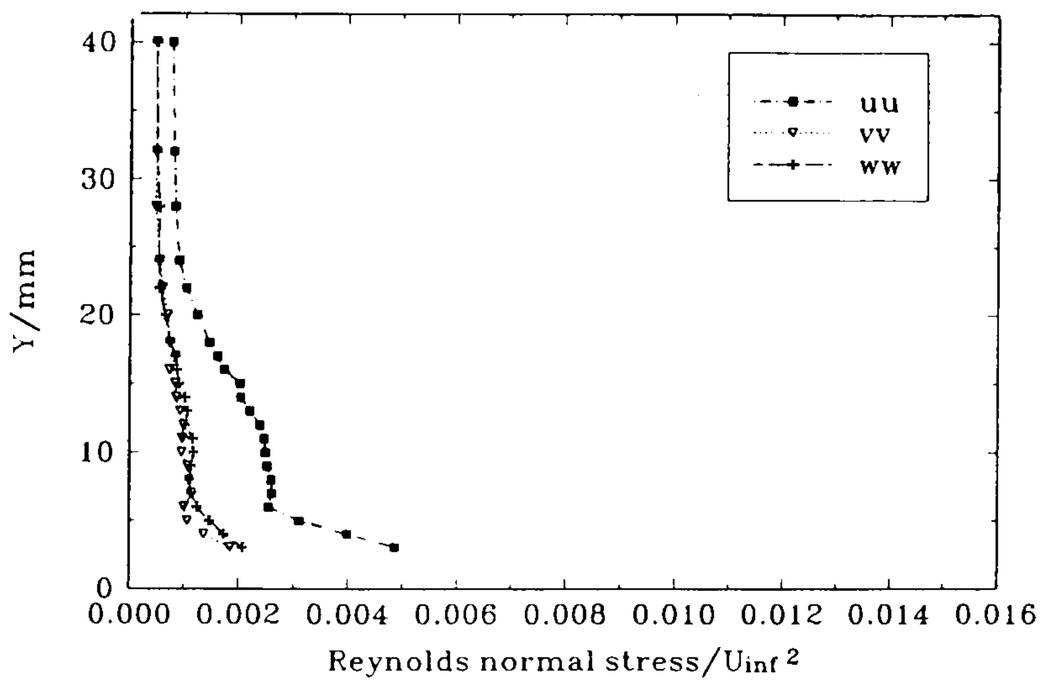

(g) $x_3 = 10$ mm

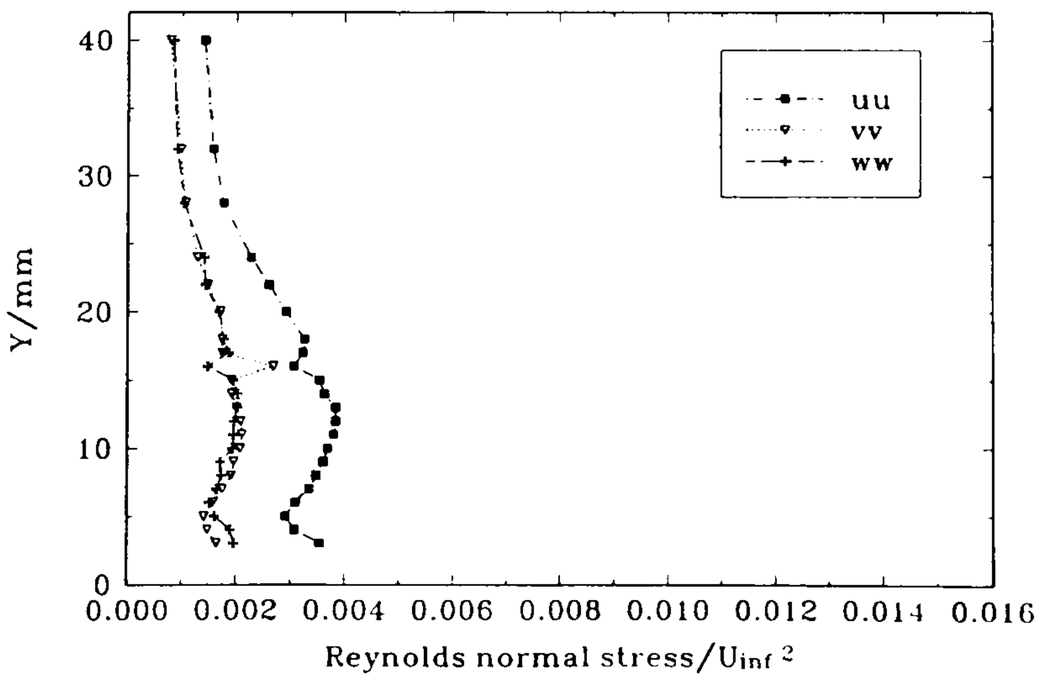

(h) $x_3 = 5$ mm

Figure 60 Profiles of $(\overline{u^2}, \overline{v^2}, \overline{w^2})/U_\infty^2$ through the plate boundary layer in plane K, normal to the tangent to the wing lower-surface profile at $X = 300$ mm, at various distances from the junction. Wing incidence = 0°.

...concluded)

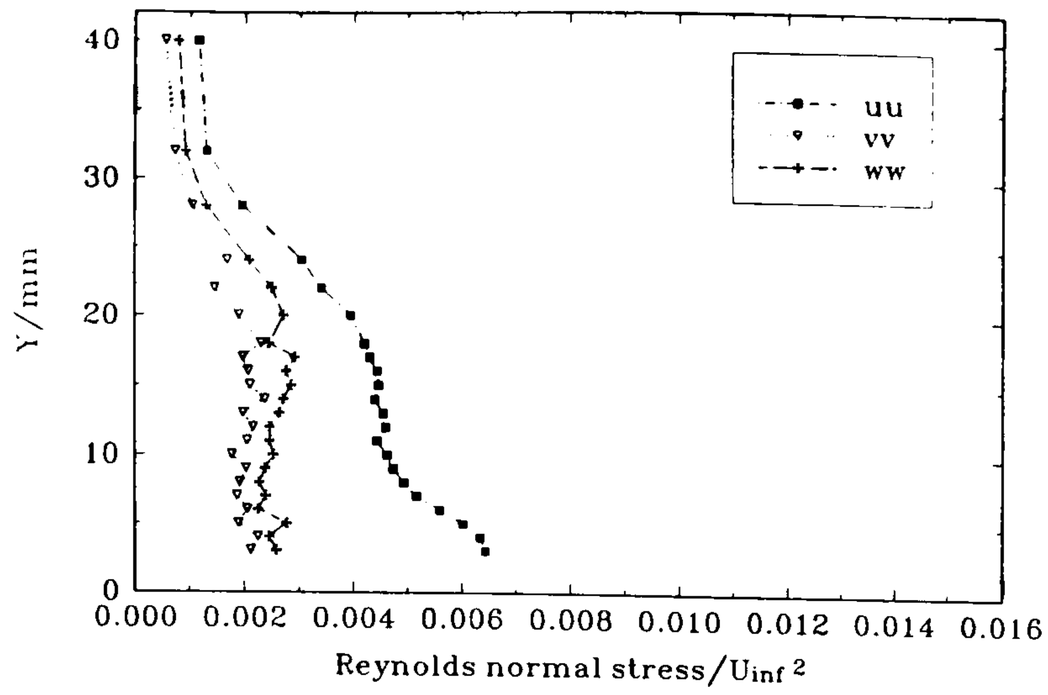

(a) $x_3 = 60$ mm

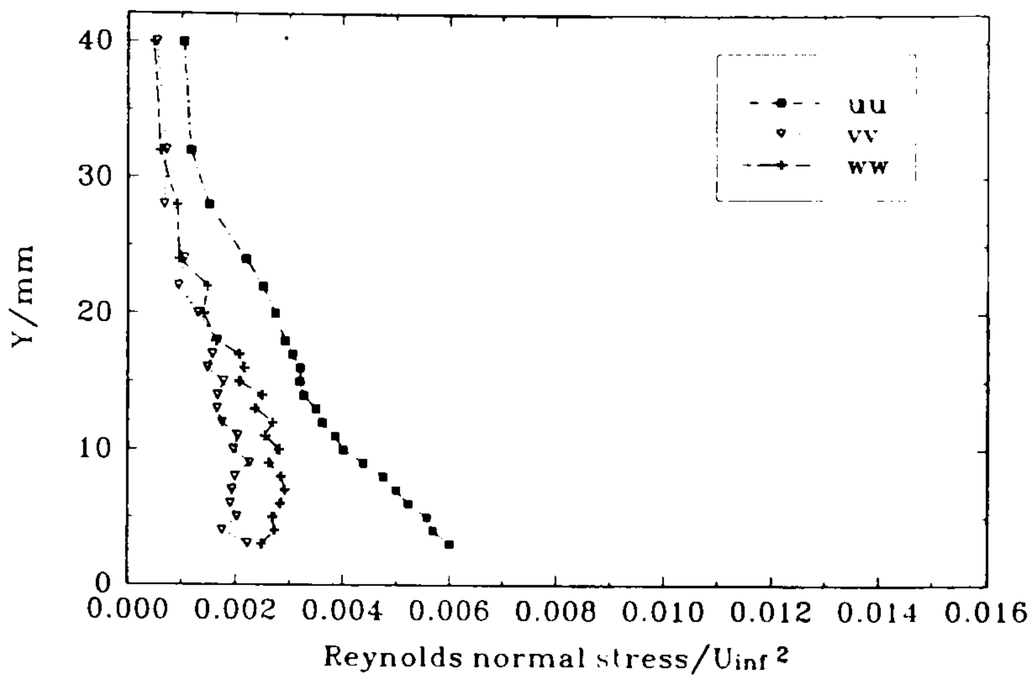

(b) $x_3 = 40$ mm

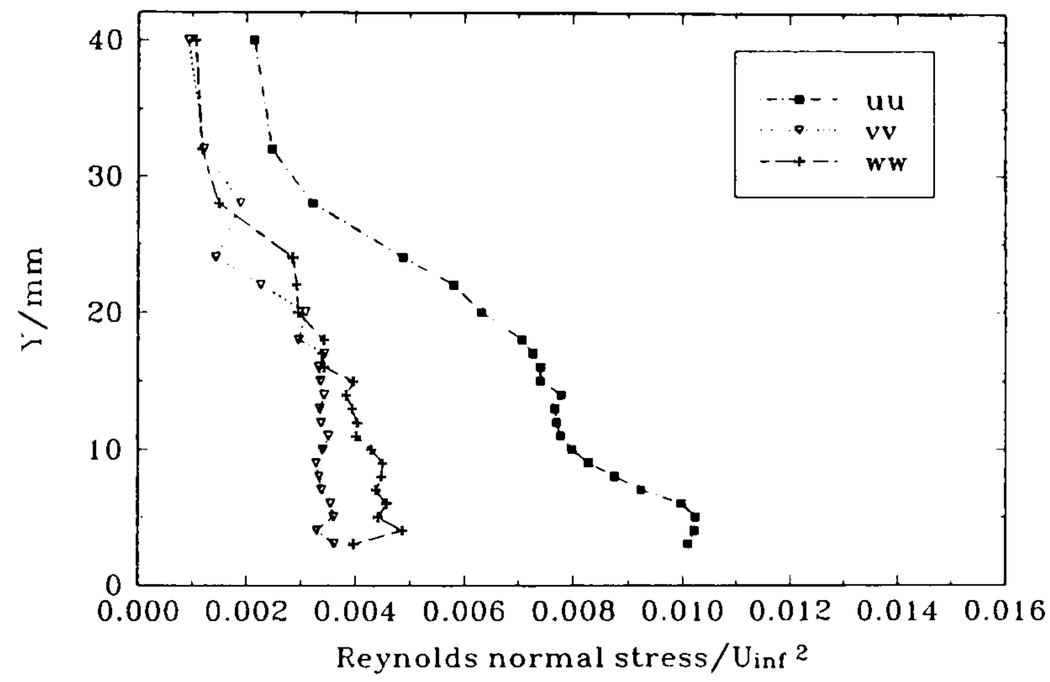

(c) $x_3 = 30$ mm

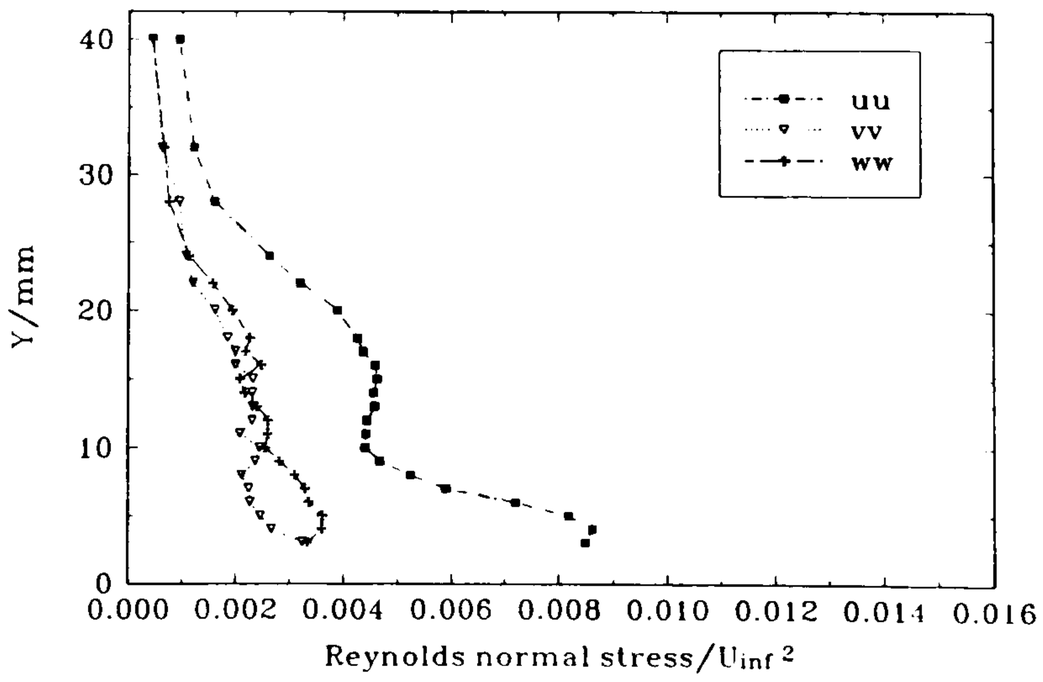

(d) $x_3 = 25$ mm

Figure 61 Profiles of $(\overline{u^2}, \overline{v^2}, \overline{w^2})/U_\infty^2$ through the plate boundary layer in plane L, normal to the tangent to the wing upper-surface profile at $X = 300$ mm, at various distances from the junction. Wing incidence = 0°.

(continued...

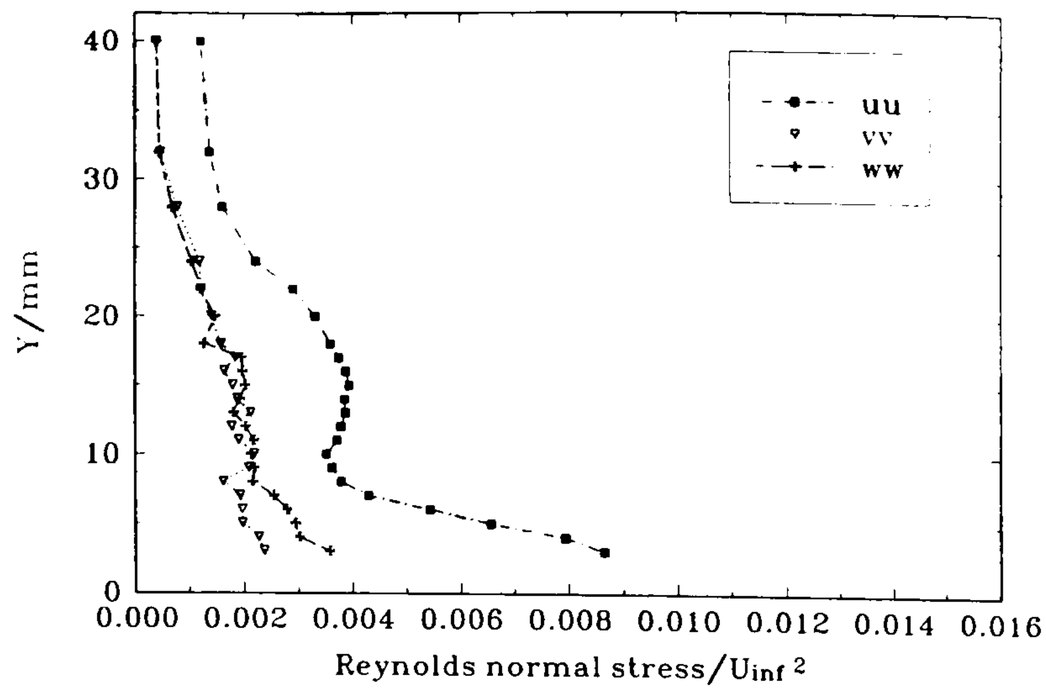

(e) $x_3 = 20$ mm

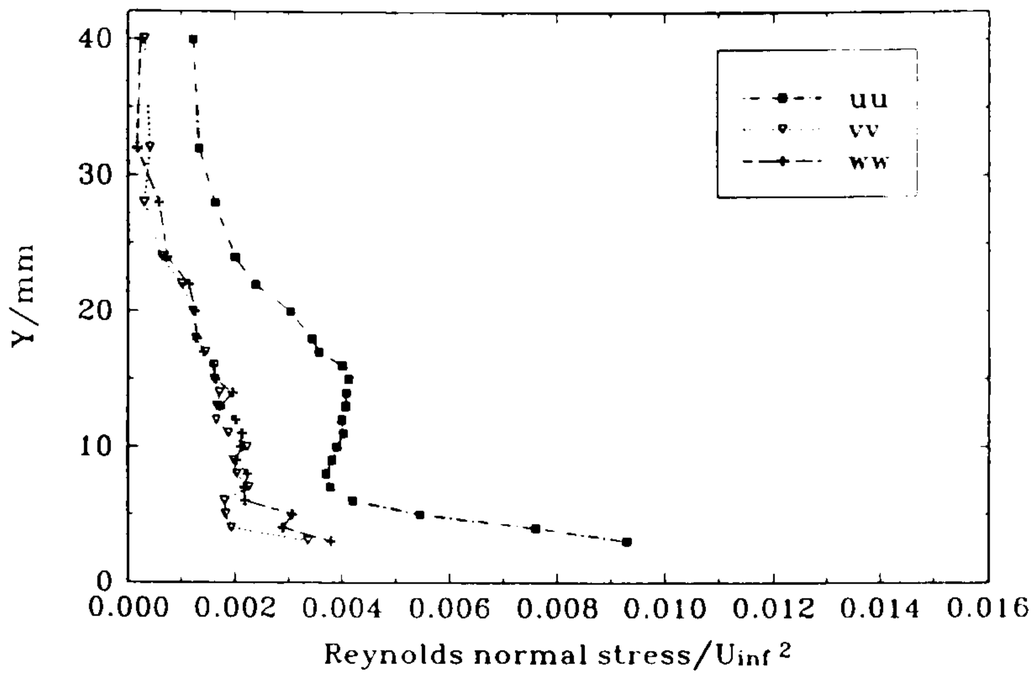

(f) $x_3 = 15$ mm

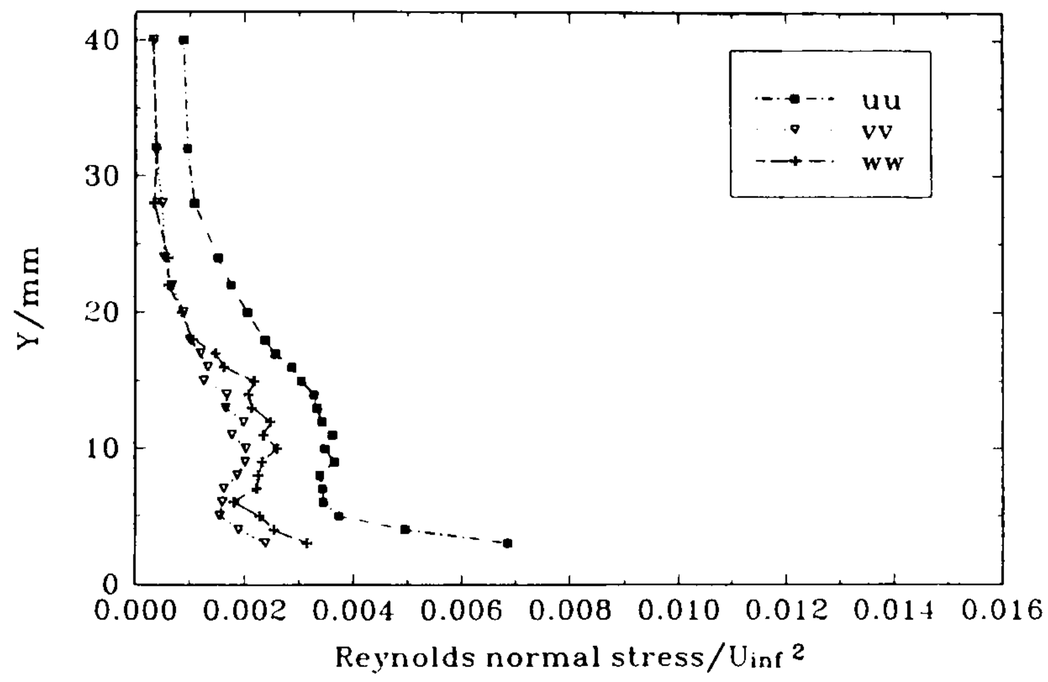

(g) $x_3 = 10$ mm

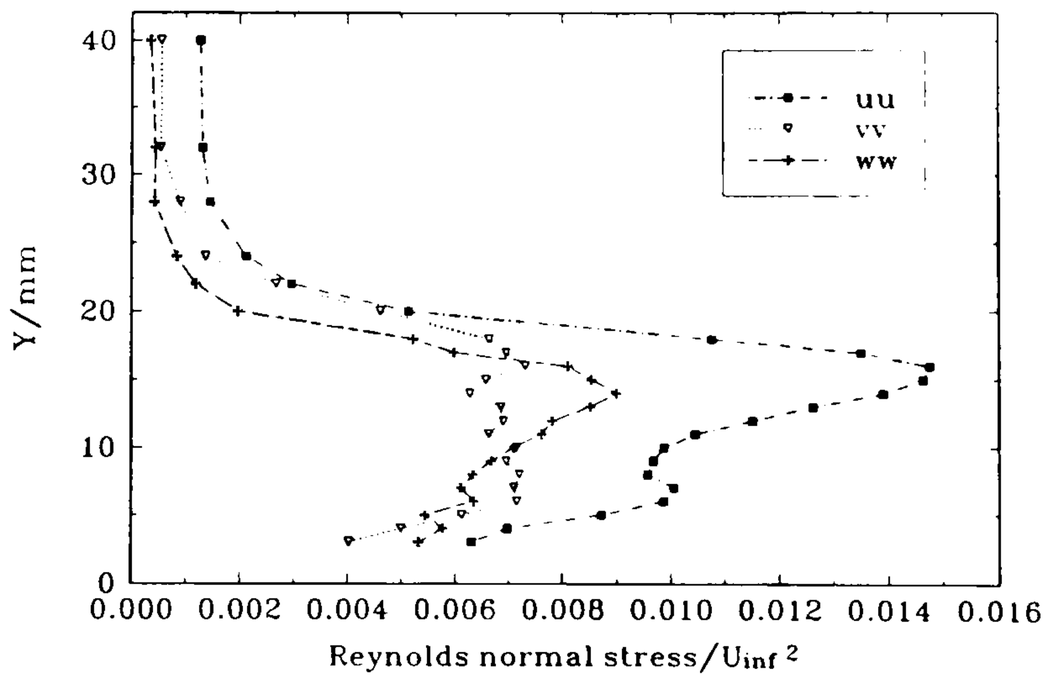

(h) $x_3 = 5$ mm

Figure 61 Profiles of $(\overline{u^2}, \overline{v^2}, \overline{w^2})/U_\infty^2$ through the plate boundary layer in plane L, normal to the tangent to the wing upper-surface profile at $X = 300$ mm, at various distances from the junction. Wing incidence = 0°.

...concluded)

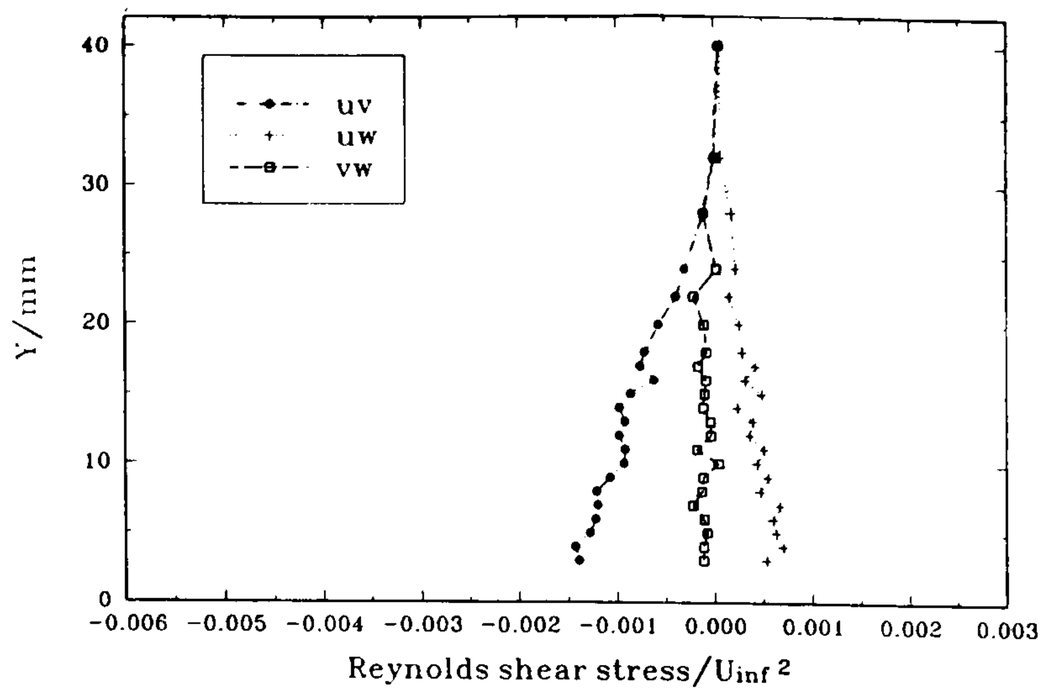

(a) $x_3 = 60$ mm

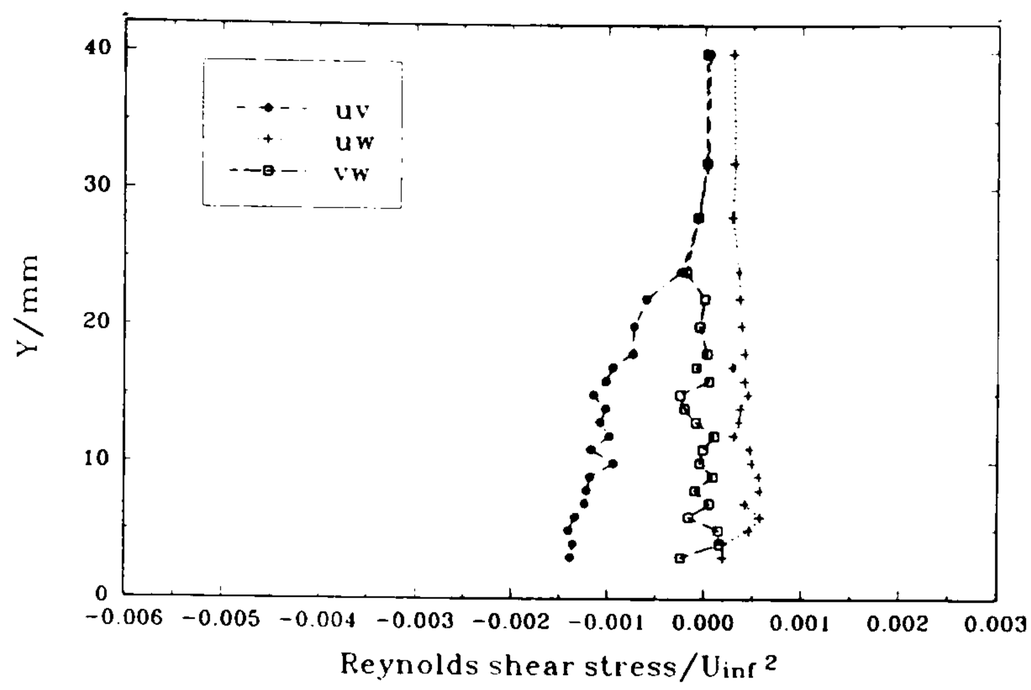

(b) $x_3 = 40$ mm

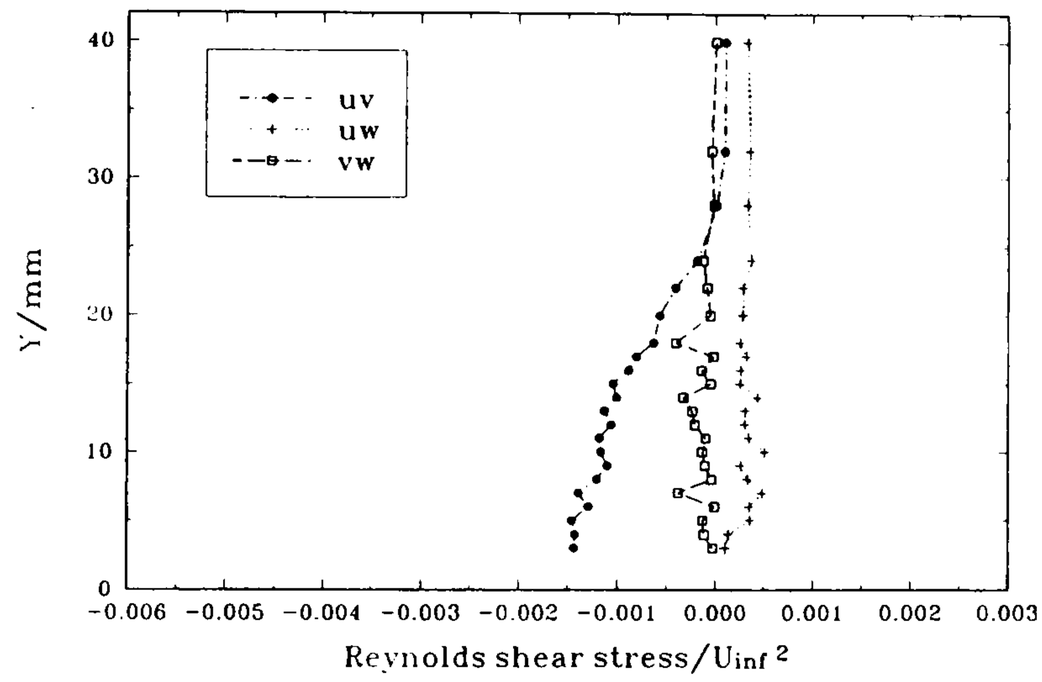

(c) $x_3 = 30$ mm

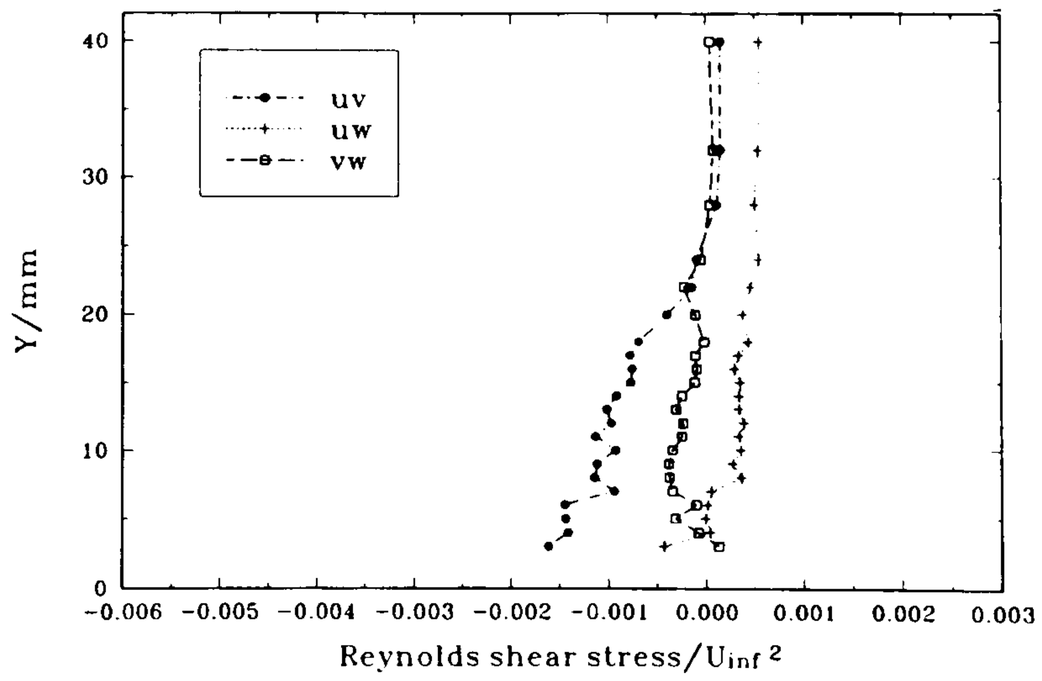

(d) $x_3 = 25$ mm

Figure 62 Profiles of $(\overline{uv}, \overline{uw}, \overline{vw})/U_\infty^2$ through the plate boundary layer in plane K, normal to the tangent to the wing lower-surface profile at $X = 300$ mm, at various distances from the junction. Wing incidence = 0°.

(continued...

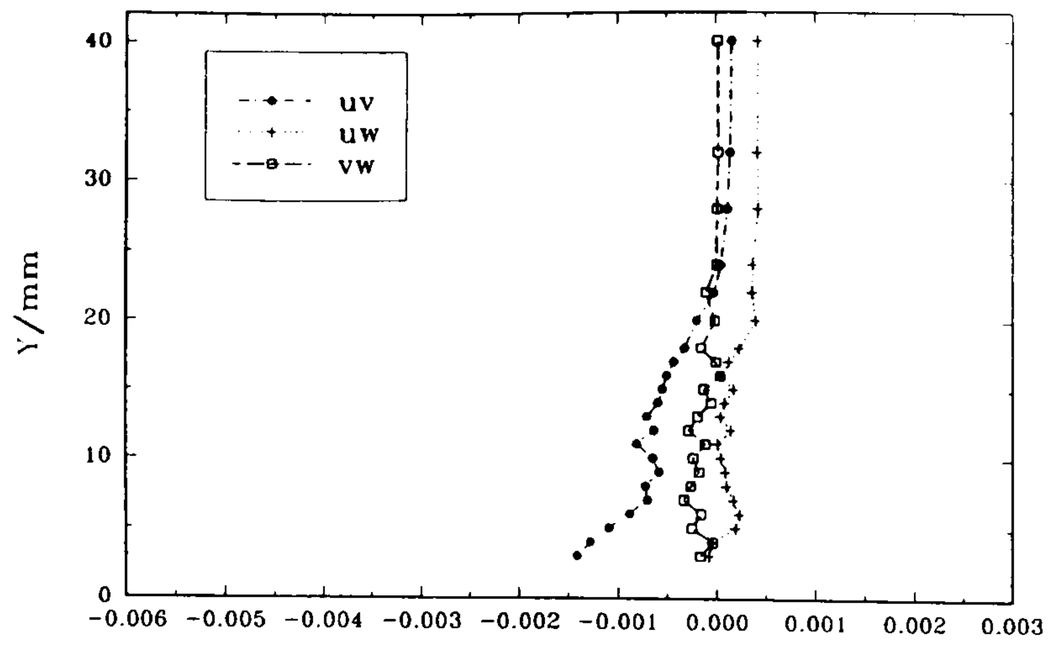

(e) $x_3 = 20$ mm

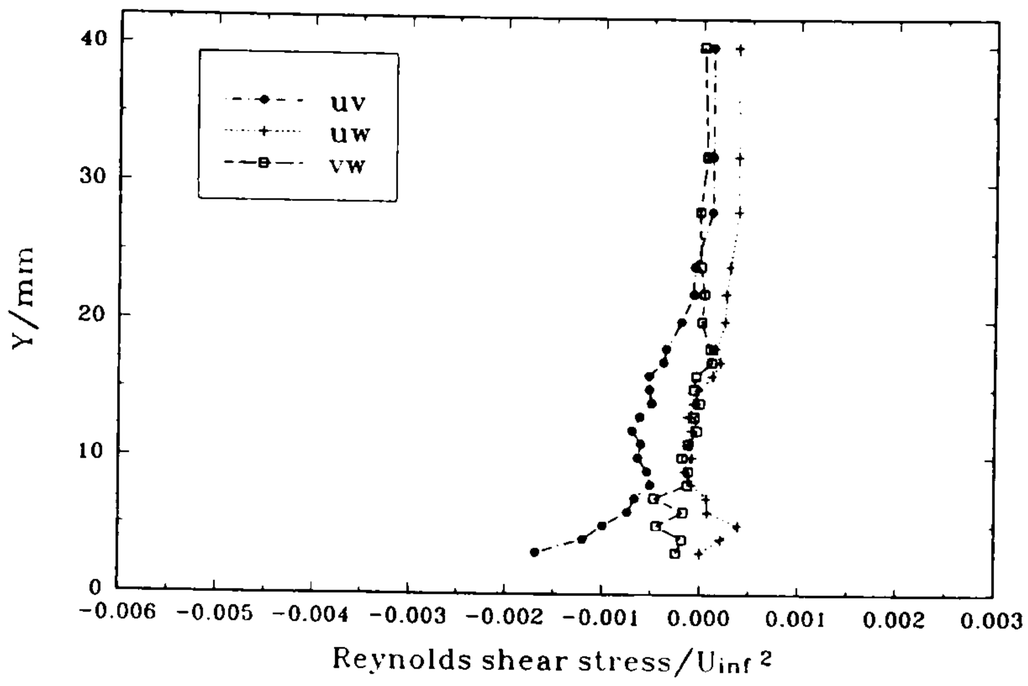

(f) $x_3 = 15$ mm

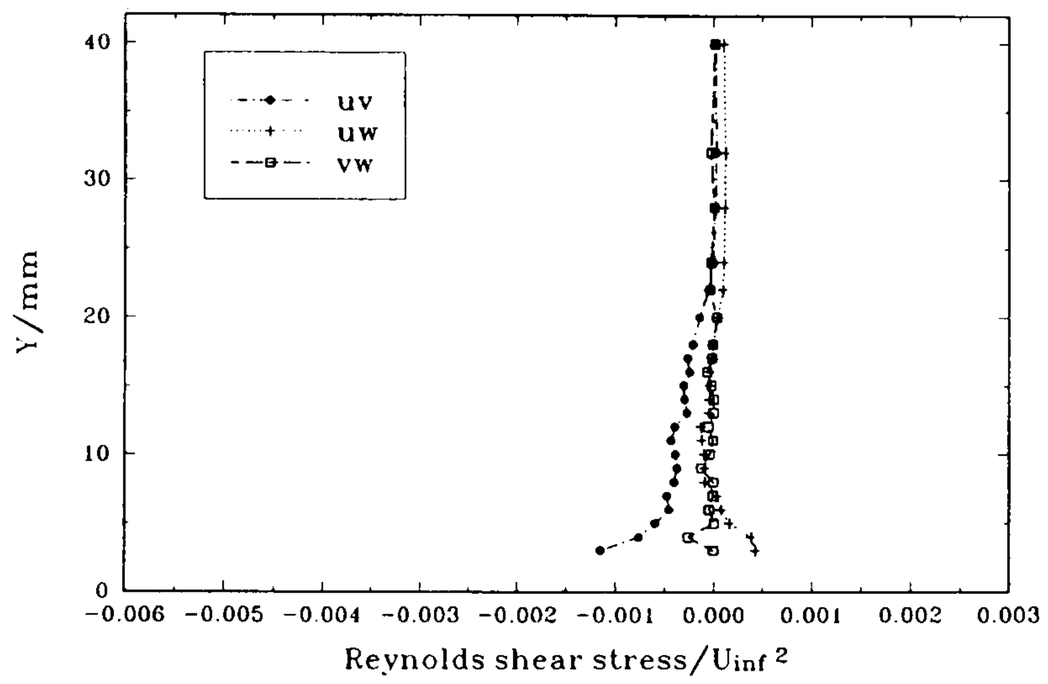

(g) $x_3 = 10$ mm

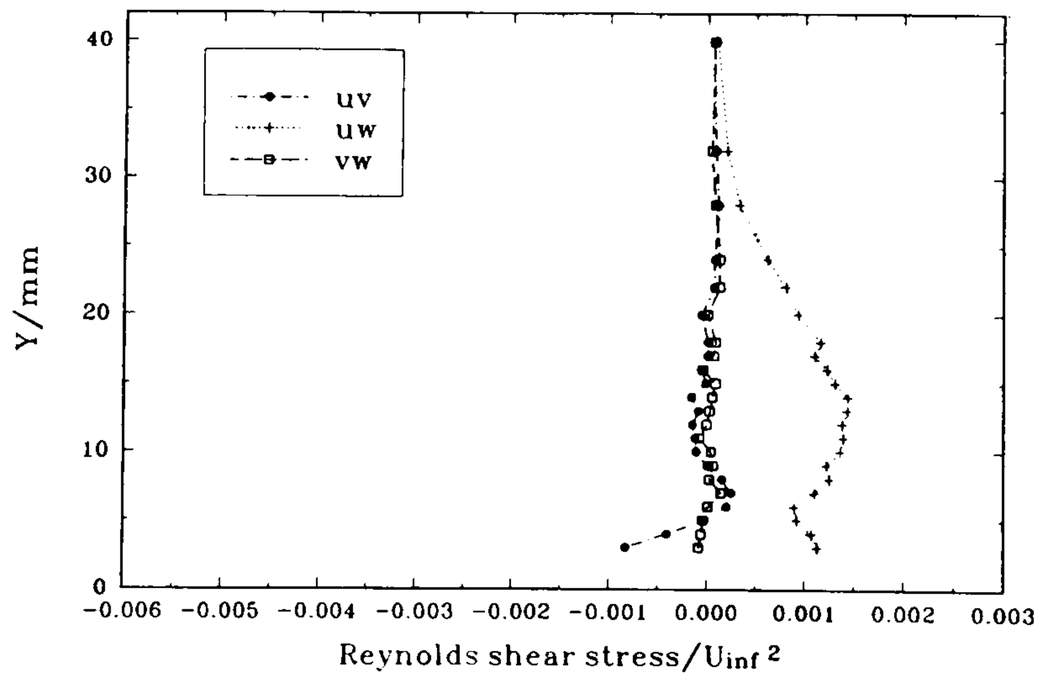

(h) $x_3 = 5$ mm

Figure 62 Profiles of $(\overline{uv}, \overline{uw}, \overline{vw})/U_\infty^2$ through the plate boundary layer in plane K, normal to the tangent to the wing lower-surface profile at $X = 300$ mm, at various distances from the junction. Wing incidence = 0°.

...concluded)

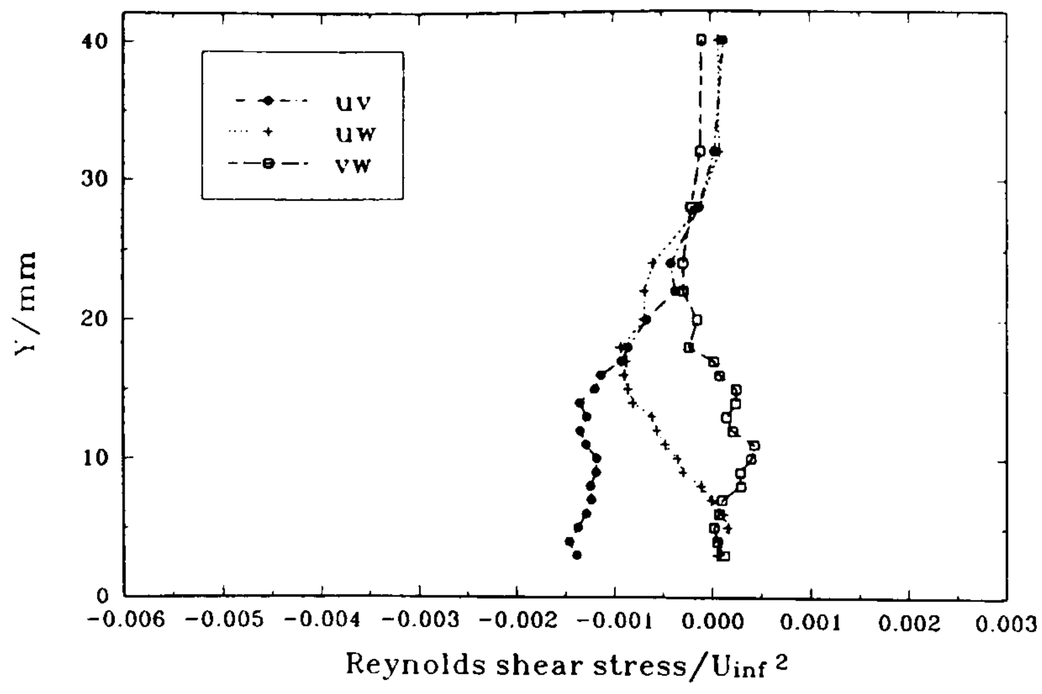

(a) $x_3 = 60$ mm

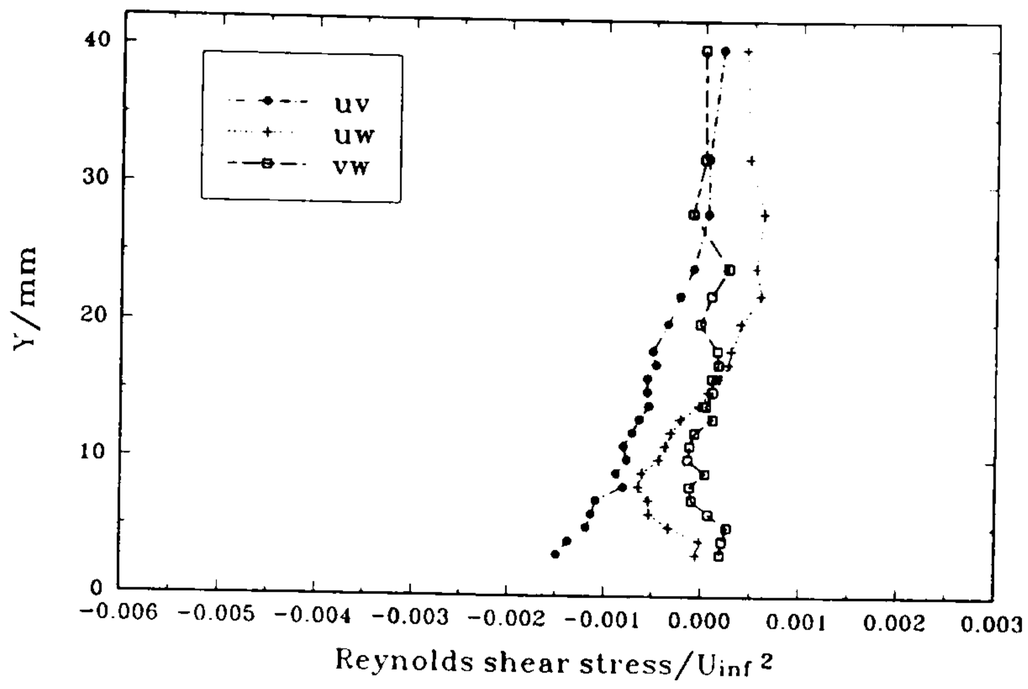

(b) $x_3 = 40$ mm

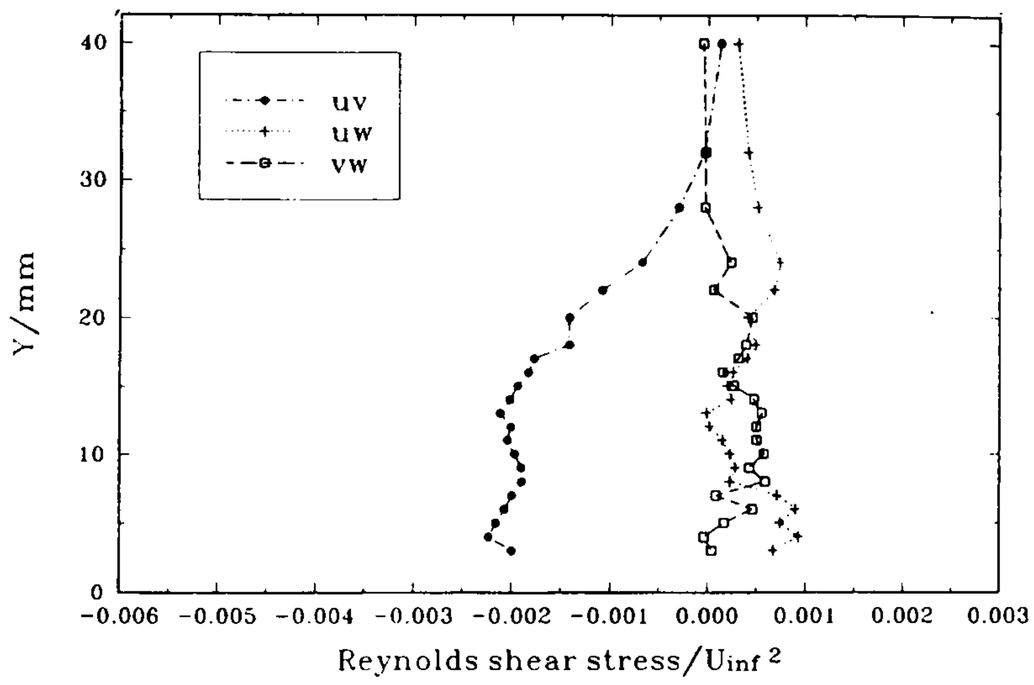

(c) $x_3 = 30$ mm

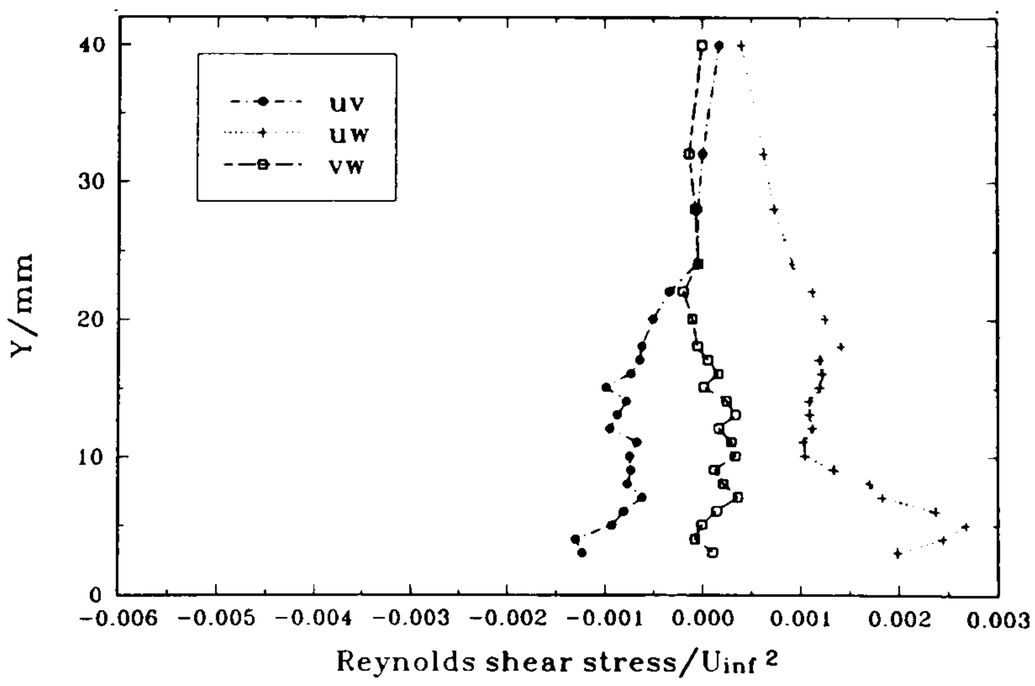

(d) $x_3 = 25$ mm

Figure 63 Profiles of $(\overline{uv}, \overline{uw}, \overline{vw})/U_\infty^2$ through the plate boundary layer in plane L, normal to the tangent to the wing upper-surface profile at $X = 300$ mm, at various distances from the junction. Wing incidence = 0°.

(continued...

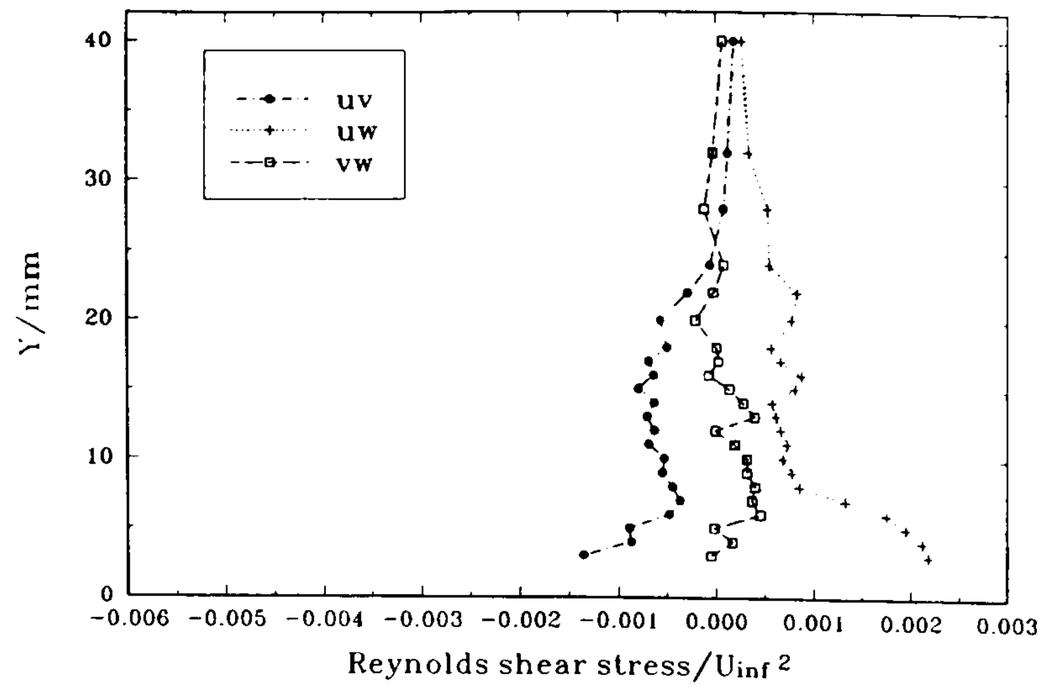

(e) $x_3 = 20$ mm

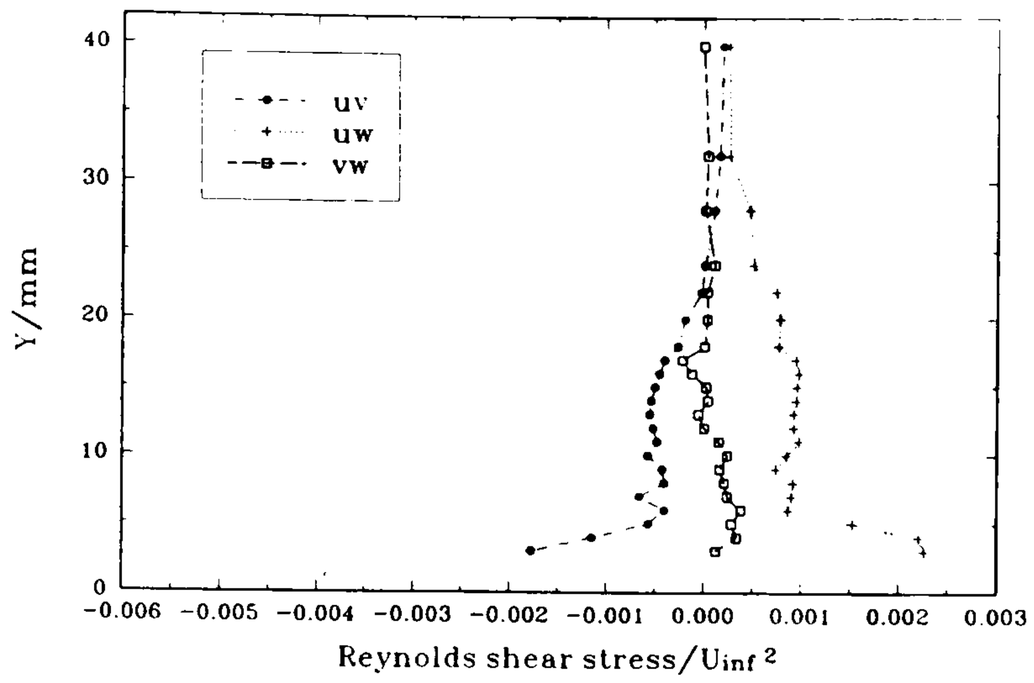

(f) $x_3 = 15$ mm

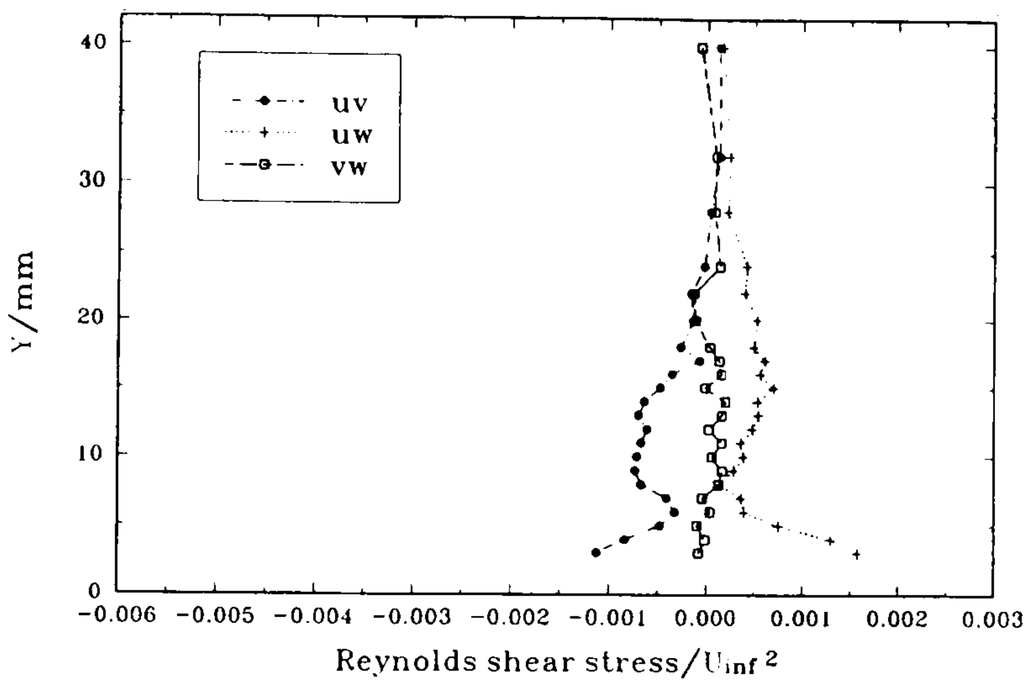

(g) $x_3 = 10$ mm

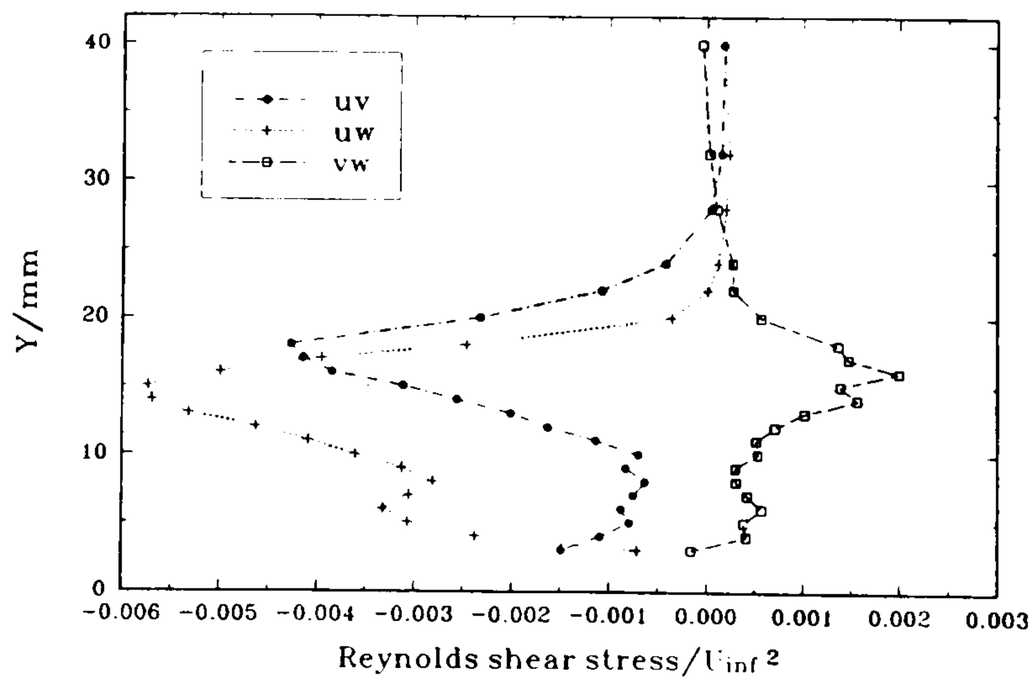

(h) $x_3 = 5$ mm

Figure 63 Profiles of $(\overline{uv}, \overline{uw}, \overline{vw})/U_\infty^2$ through the plate boundary layer in plane L, normal to the tangent to the wing upper-surface profile at $X = 300$ mm, at various distances from the junction. Wing incidence = 0°.

...concluded)

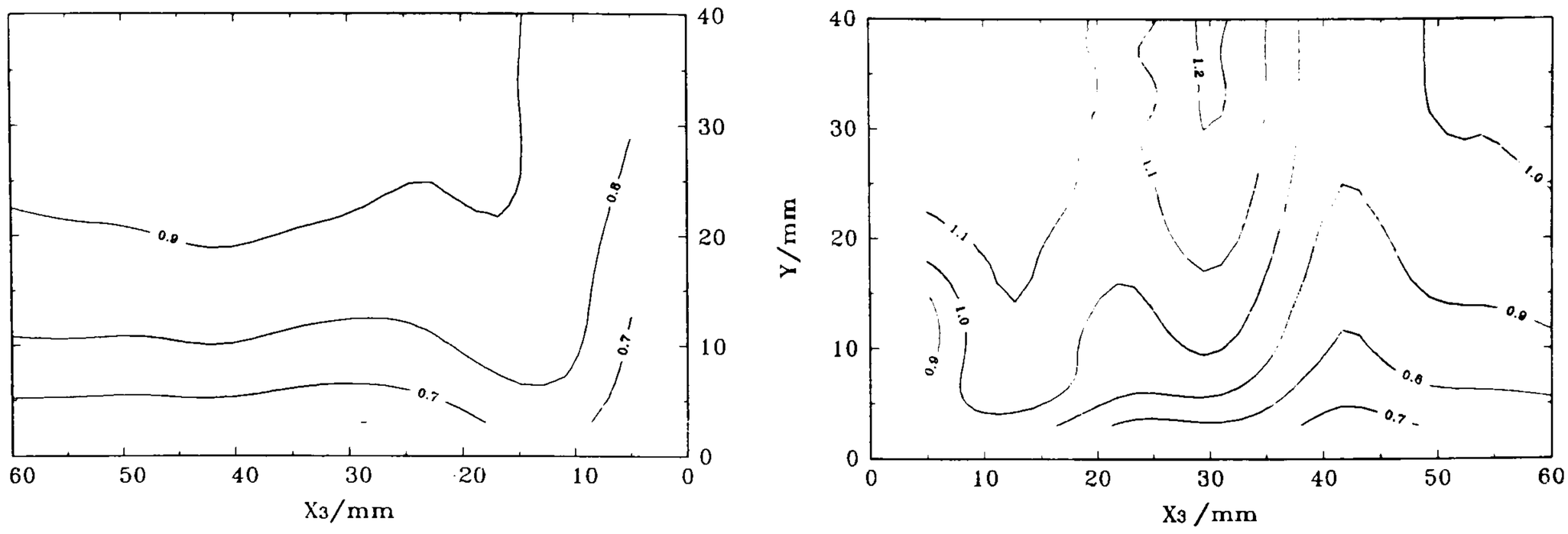

(a) Plane *K* (b) Plane *L*

Figure 64 Contours of $\overline{U} / U_\infty$ in the junction at $\alpha = 0°$ (viewed from downstream), in the planes normal to the tangent to the wing profile on both sides of the junction at $Y = 300$ mm: (a) Plane K — $\beta_S = -96.1°$ & (b) Plane L — $\beta_S = 92.4°$.

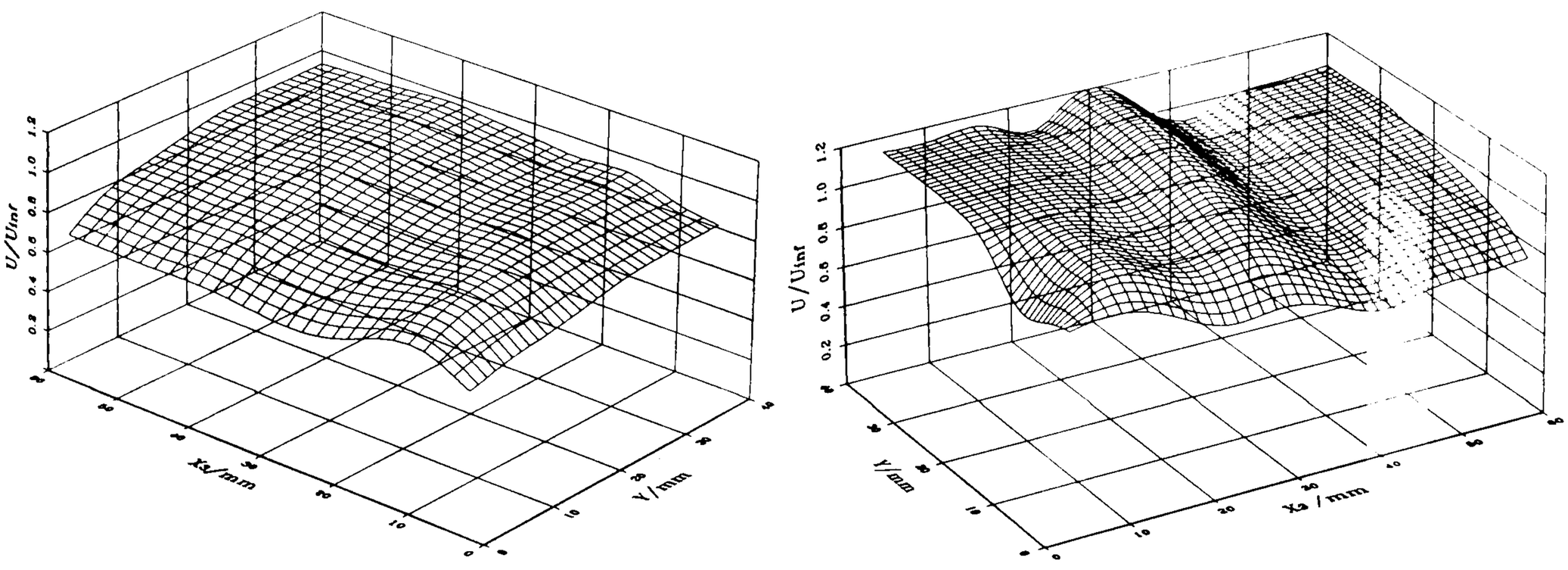

(a) Plane *K* (b) Plane *L*

Figure 65 Surface maps of $\overline{U} / U_\infty$ in the junction at $\alpha = 0°$, in the planes normal to the tangent to the wing profile on both sides of the junction at $Y = 300$ mm: (a) Plane K — $\beta_S = -96.1°$ & (b) Plane L — $\beta_S = 92.4°$.

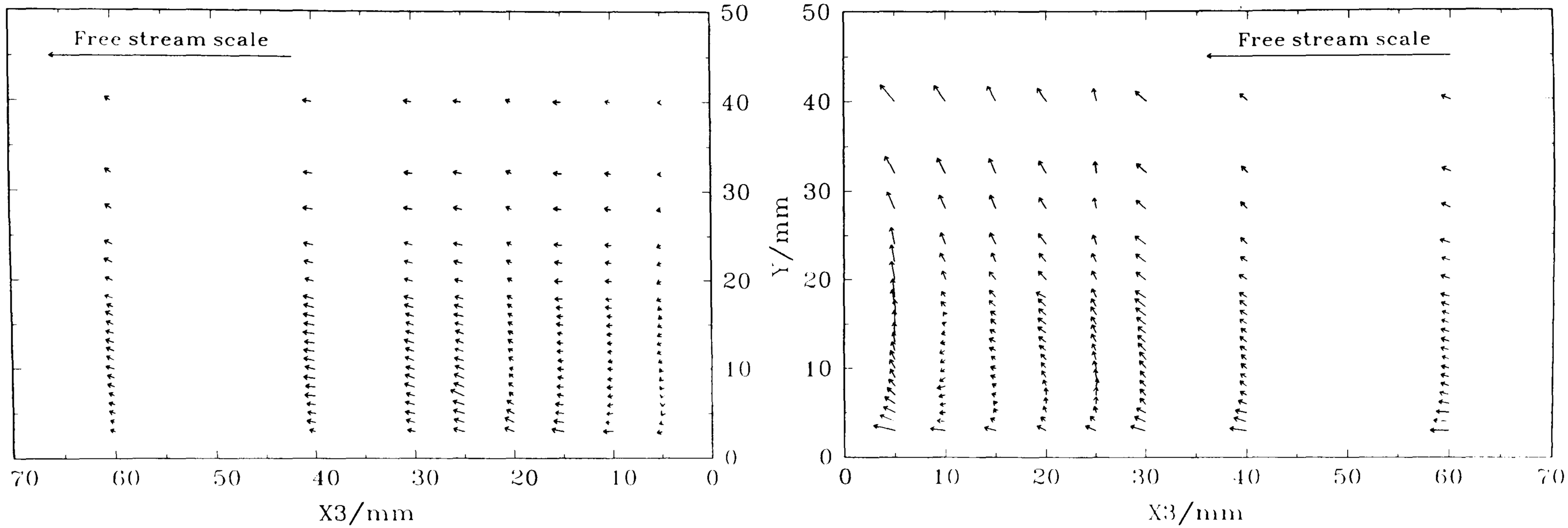

(a) Plane *K*

(b) Plane *L*

Figure 66 Cross-flow velocity vectors in the junction at $\alpha = 0°$ (viewed from downstream), in the planes normal to the tangent to the wing profile on both sides of the junction at $X = 300$ mm:

(a) Plane K — $\beta_S = -96.1°$ & (b) Plane L — $\beta_S = 92.4°$.

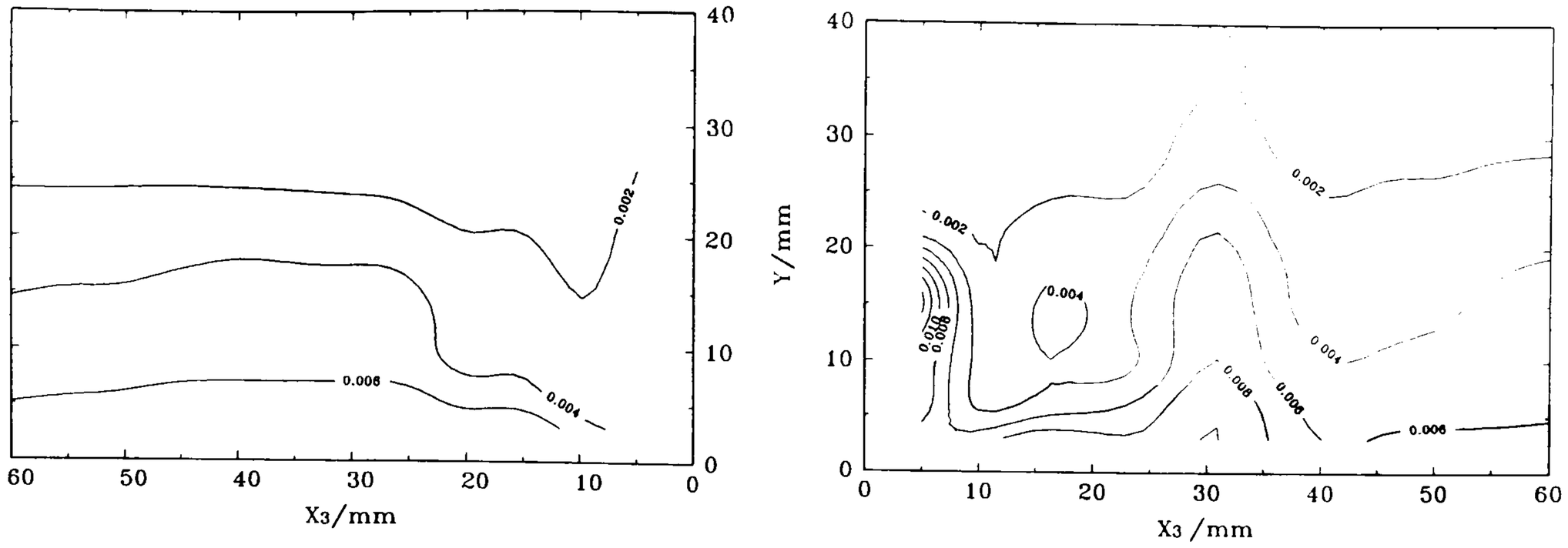

Figure 67 Contours of $(\overline{u^2}, \overline{v^2}, \overline{w^2})/U_\infty^2$ in the junction at $\alpha = 0°$ (viewed from downstream), in planes normal to the tangent to the wing profile on both sides of the junction at $X = 300$ mm: (a) $\overline{u^2}/U_\infty^2$, (b) $\overline{v^2}/U_\infty^2$ & (c) $\overline{w^2}/U_\infty^2$.

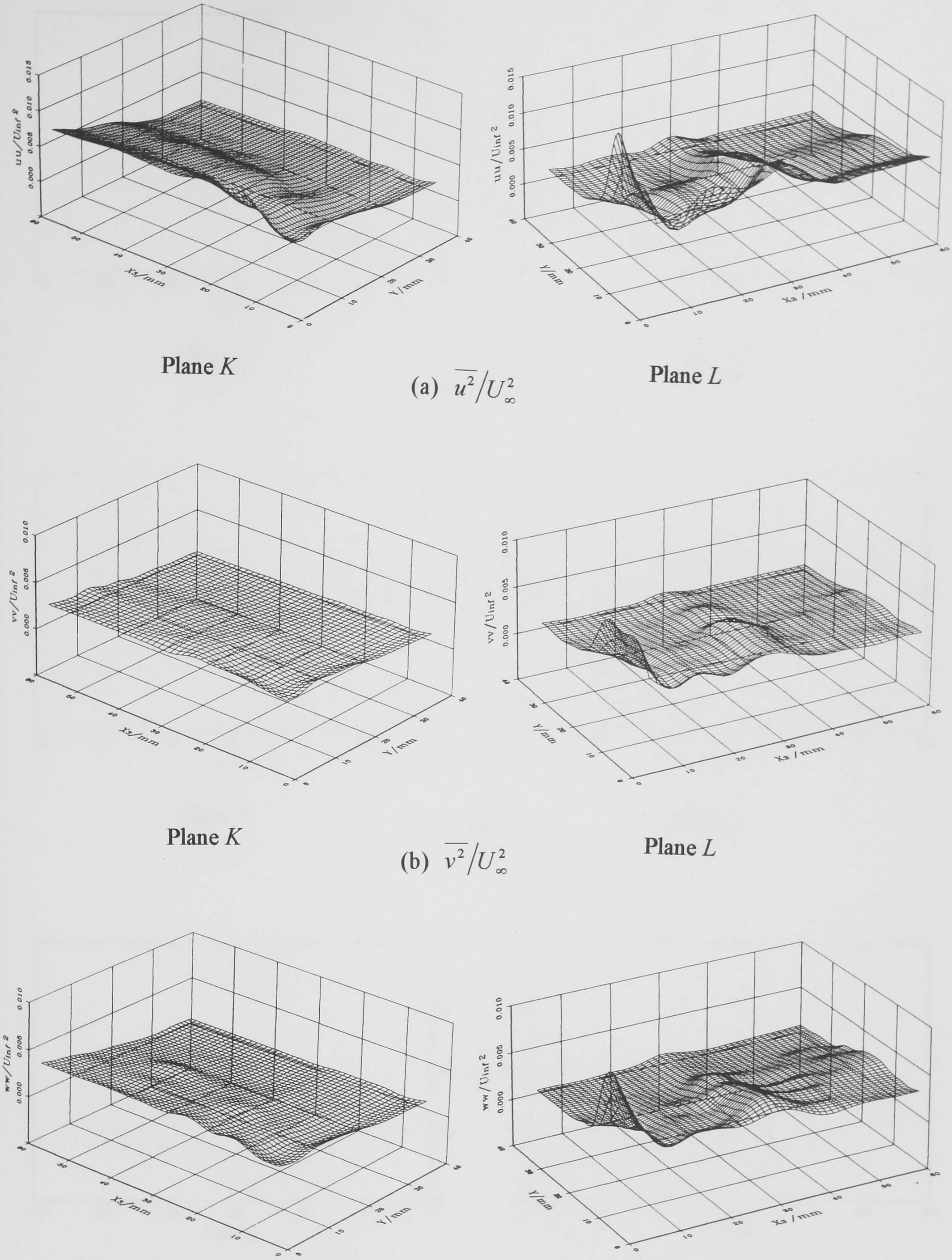

Plane K — (a) $\overline{u^2}/U_\infty^2$ — Plane L

Plane K — (b) $\overline{v^2}/U_\infty^2$ — Plane L

Plane K — (c) $\overline{w^2}/U_\infty^2$ — Plane L

Figure 68 Surface maps of $(\overline{u^2},\overline{v^2},\overline{w^2})/U_\infty^2$ in the junction at $\alpha = 0°$, in planes normal to the tangent to the wing profile on both sides of the junction at $X = 300$ mm:
(a) $\overline{u^2}/U_\infty^2$, (b) $\overline{v^2}/U_\infty^2$ & (c) $\overline{w^2}/U_\infty^2$.

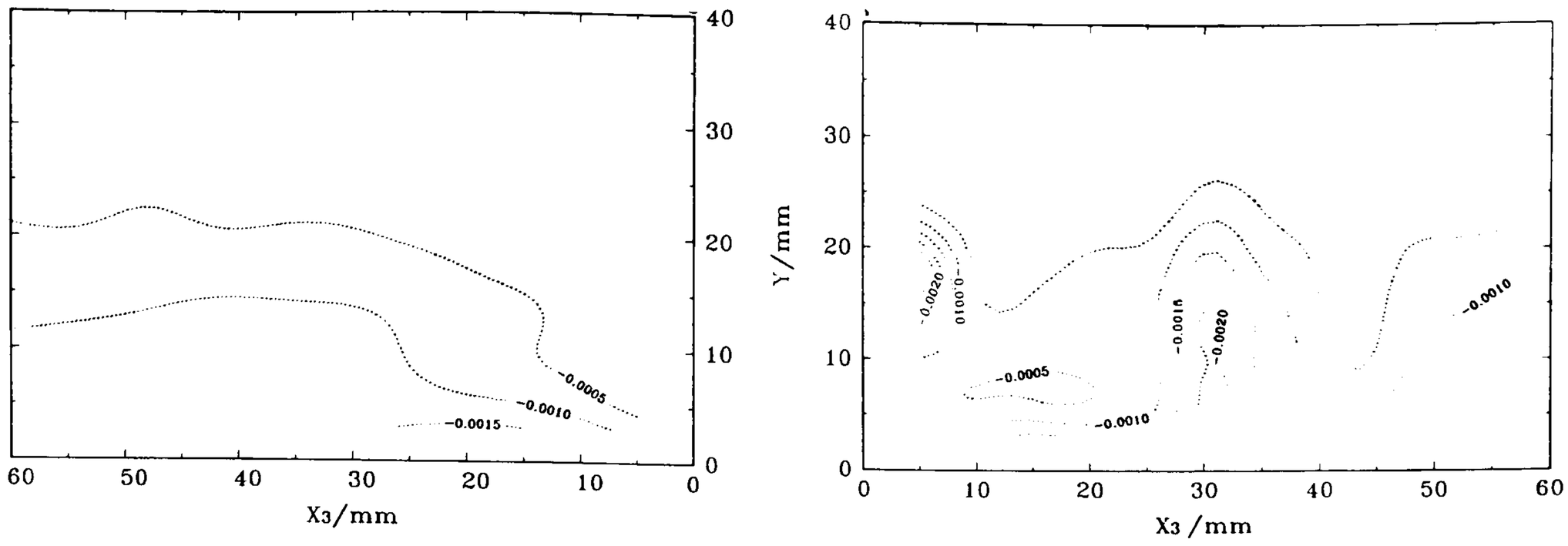

Figure 69 Contours of $(\overline{uv}, \overline{uw}, \overline{vw})/U_\infty^2$ in the junction at $\alpha = 0°$ (viewed from downstream), in planes normal to the tangent to the wing profile on both sides of the junction at $X = 300$ mm: (a) $\overline{uv}/U_\infty^2$, (b) $\overline{uw}/U_\infty^2$ & (c) $\overline{vw}/U_\infty^2$.

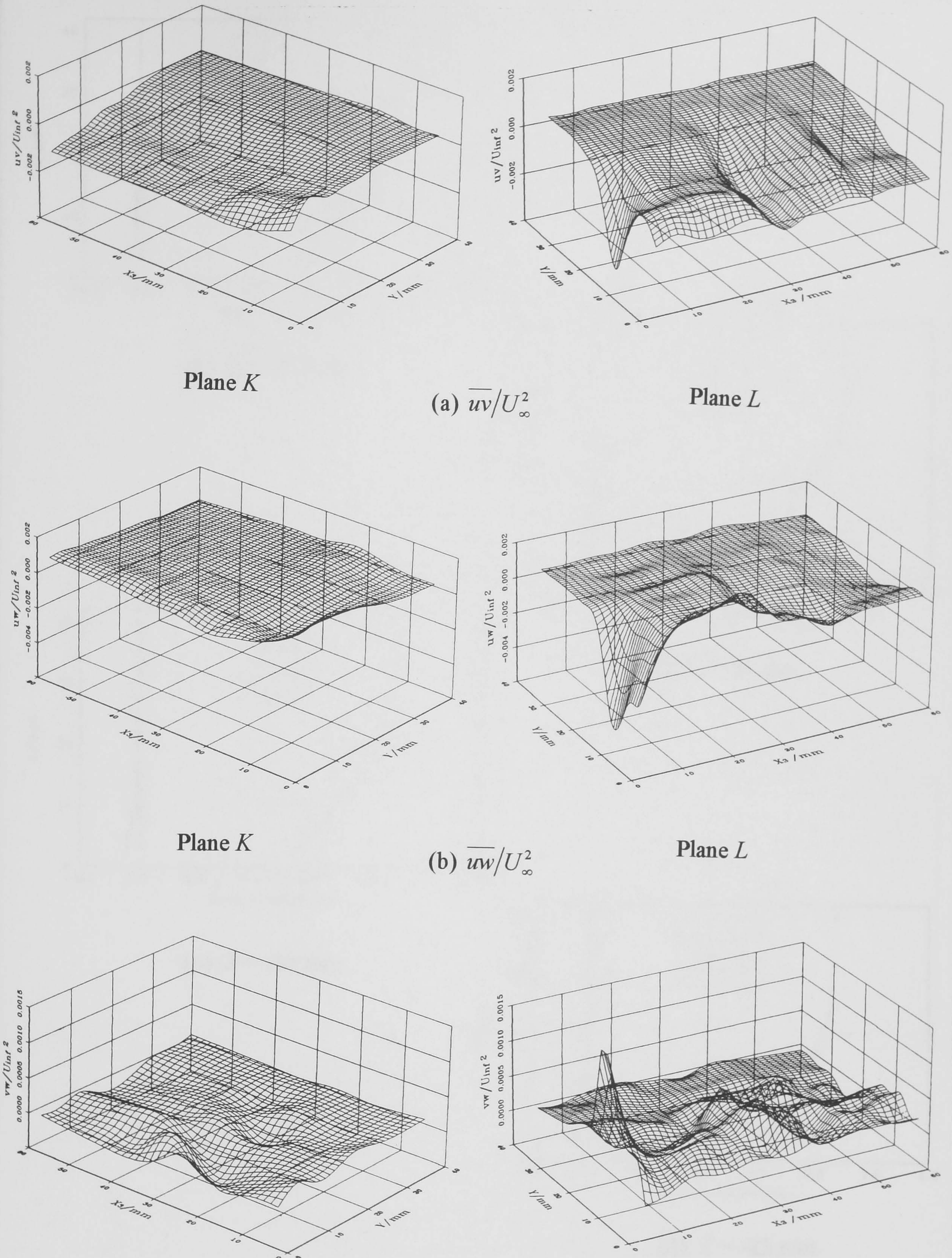

Figure 70 Surface maps of $(\overline{uv},\overline{uw},\overline{vw})/U_\infty^2$ in the junction at $\alpha = 0°$, in planes normal to the tangent to the wing profile on both sides of the junction at $X = 300$ mm:
(a) $\overline{uv}/U_\infty^2$, (b) $\overline{uw}/U_\infty^2$ & (c) $\overline{vw}/U_\infty^2$.

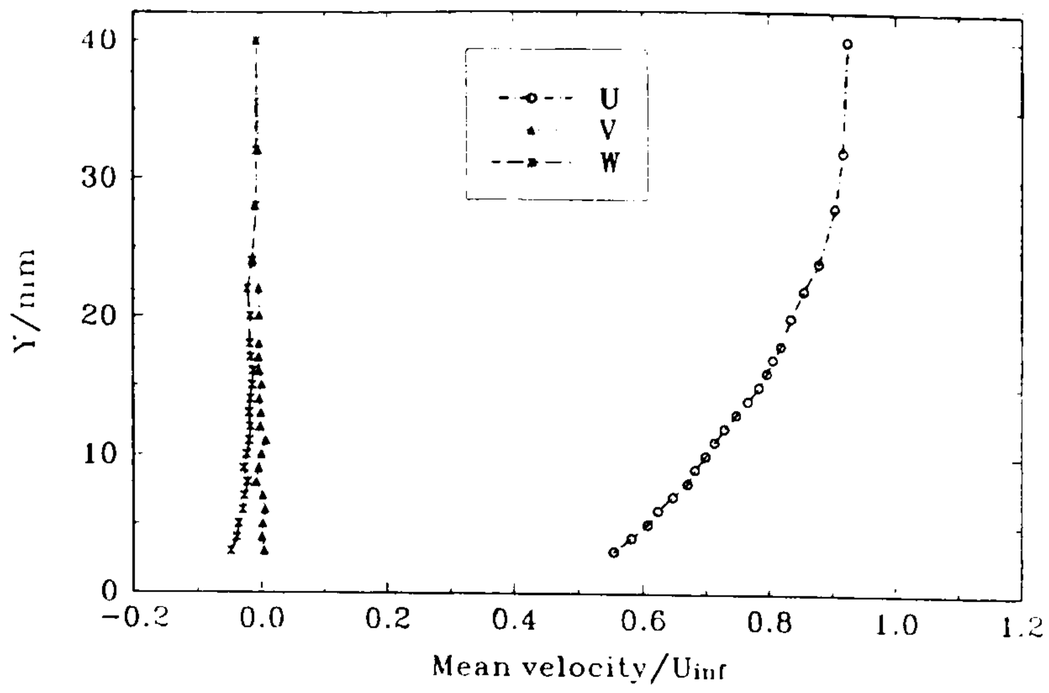

(a) Z = -60 mm

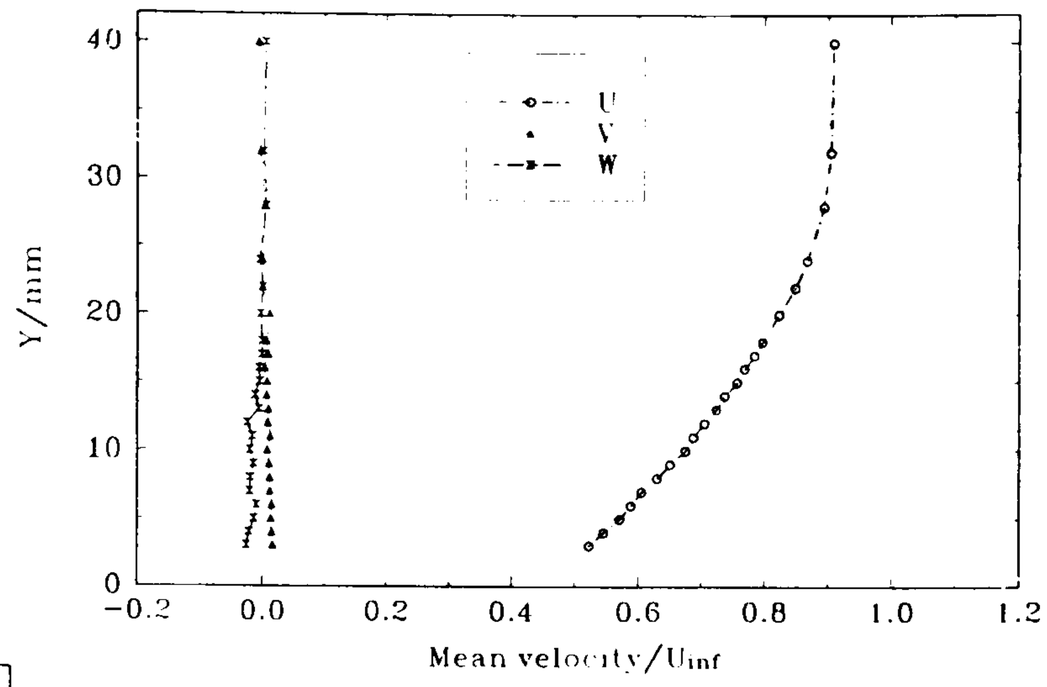

(b) Z = -40 mm

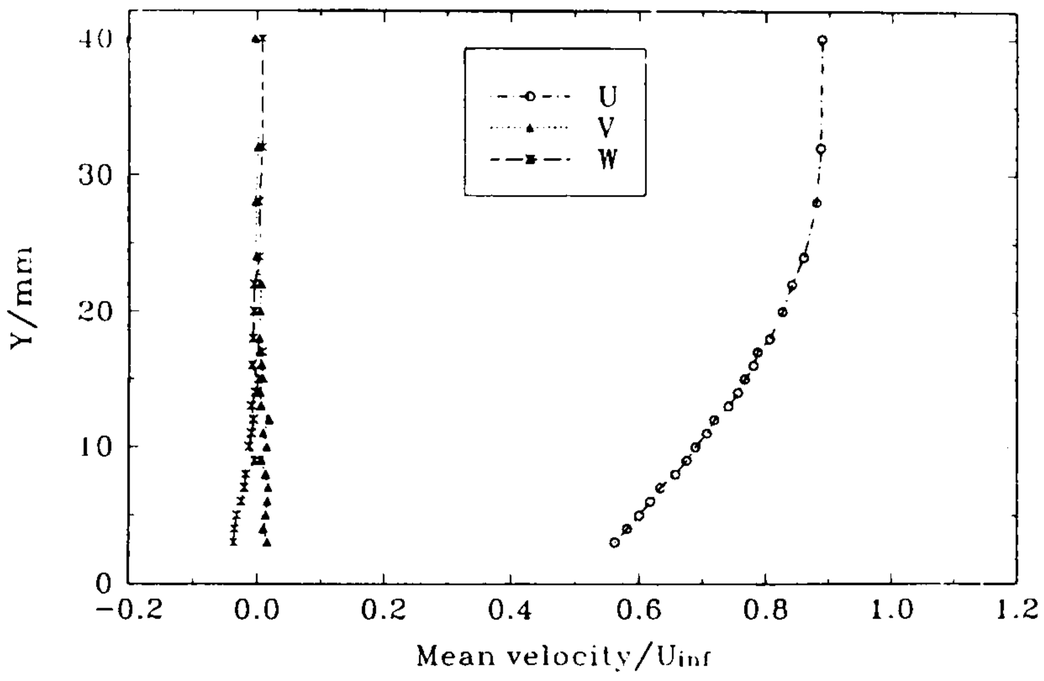

(c) Z = -30 mm

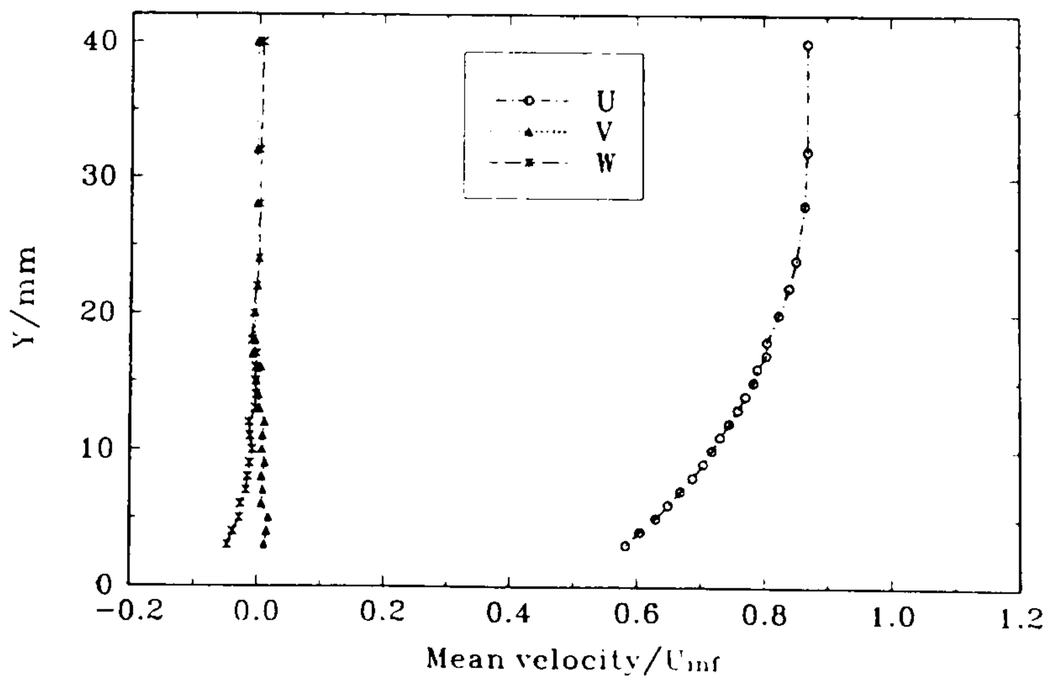

(d) Z = -25 mm

Figure 71 Profiles of $(\overline{U}, \overline{V}, \overline{W})/U_\infty$ through the plate boundary layer at $\alpha = 0°$ in plane TE (X = 500 mm), at various distances normal to the chord line in the -Z direction.

(continued...

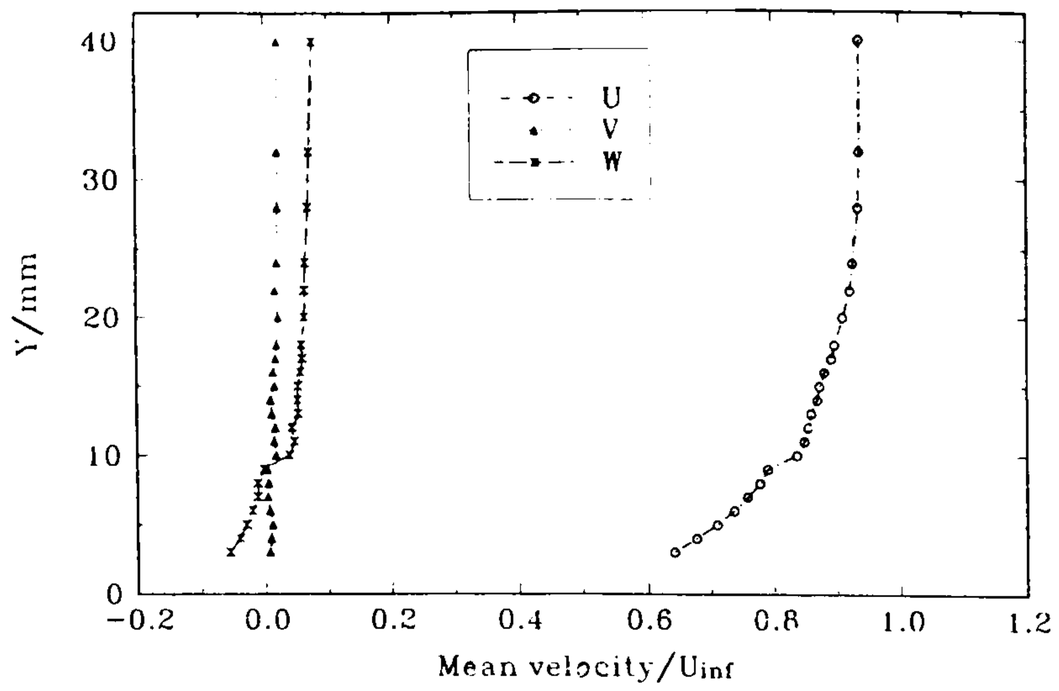

(e) Z = -20 mm

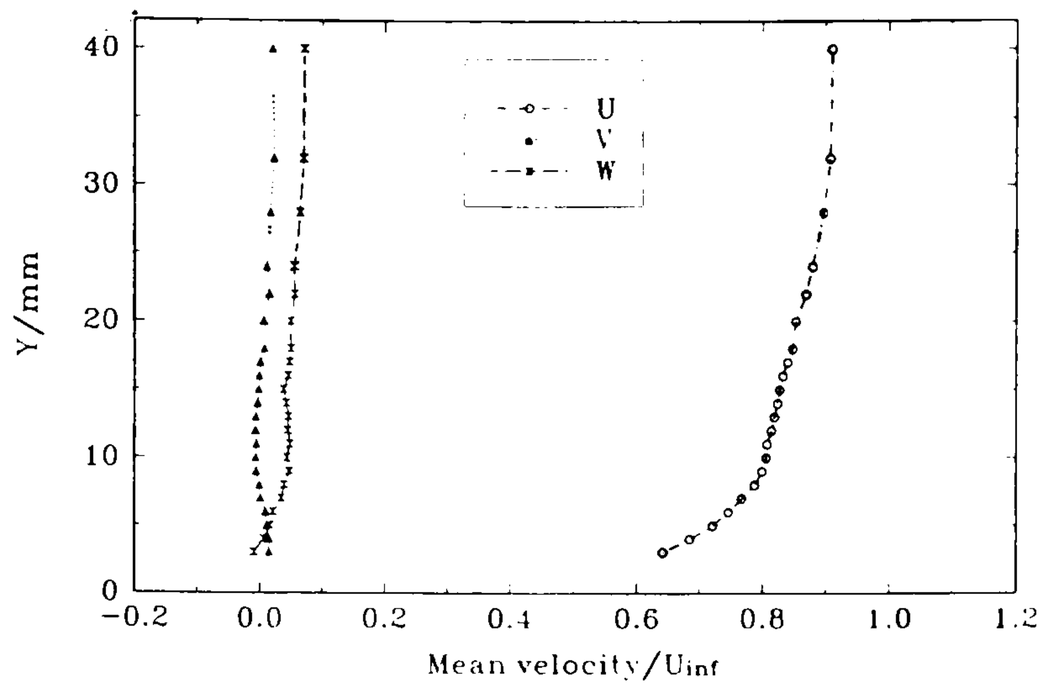

(f) Z = -15 mm

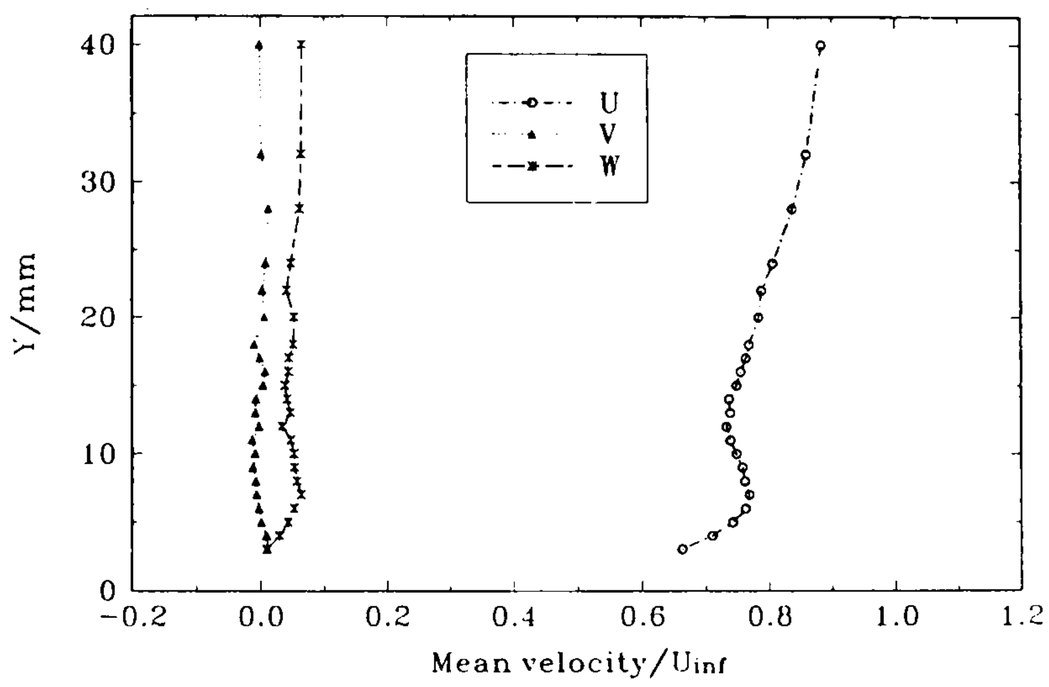

(g) Z = -10 mm

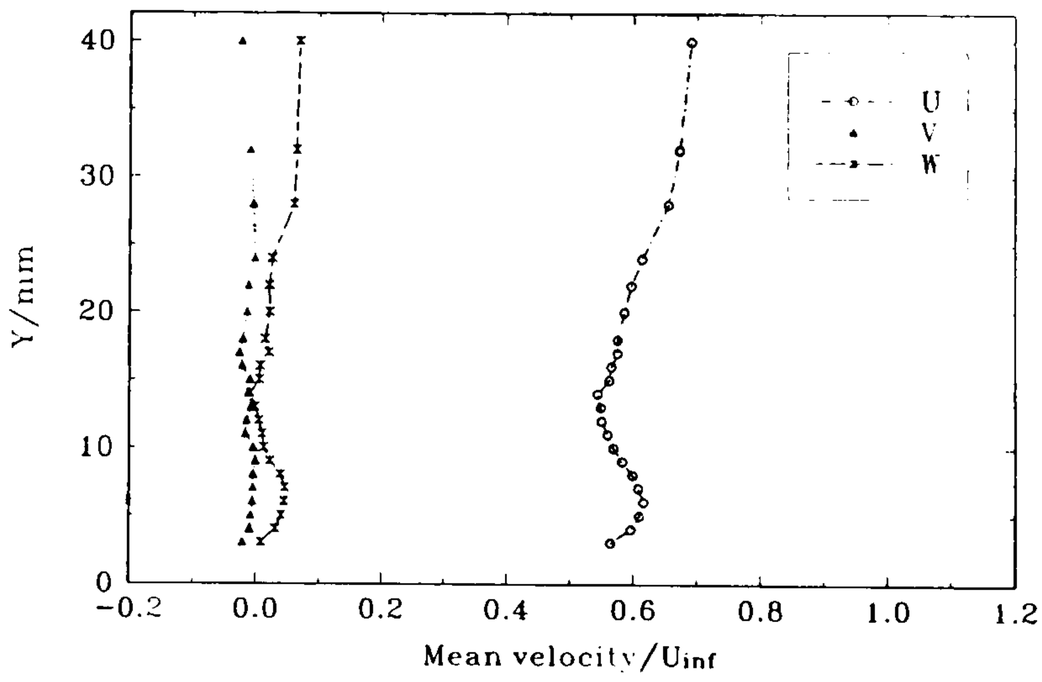

(h) Z = -5 mm

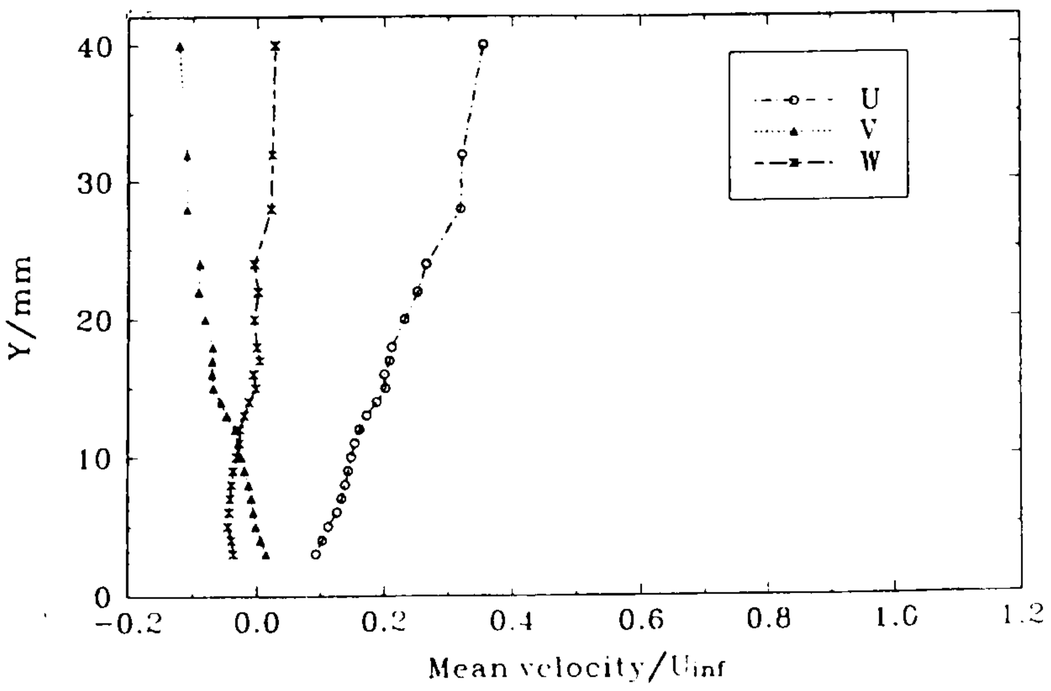

(i) Z = -0 mm

Figure 71 Profiles of $(\overline{U}, \overline{V}, \overline{W})/U_\infty$ through the plate boundary layer at α = 0°, in plane TE (X = 500 mm), at various distances normal to the chord line in the -Z direction.

...concluded)

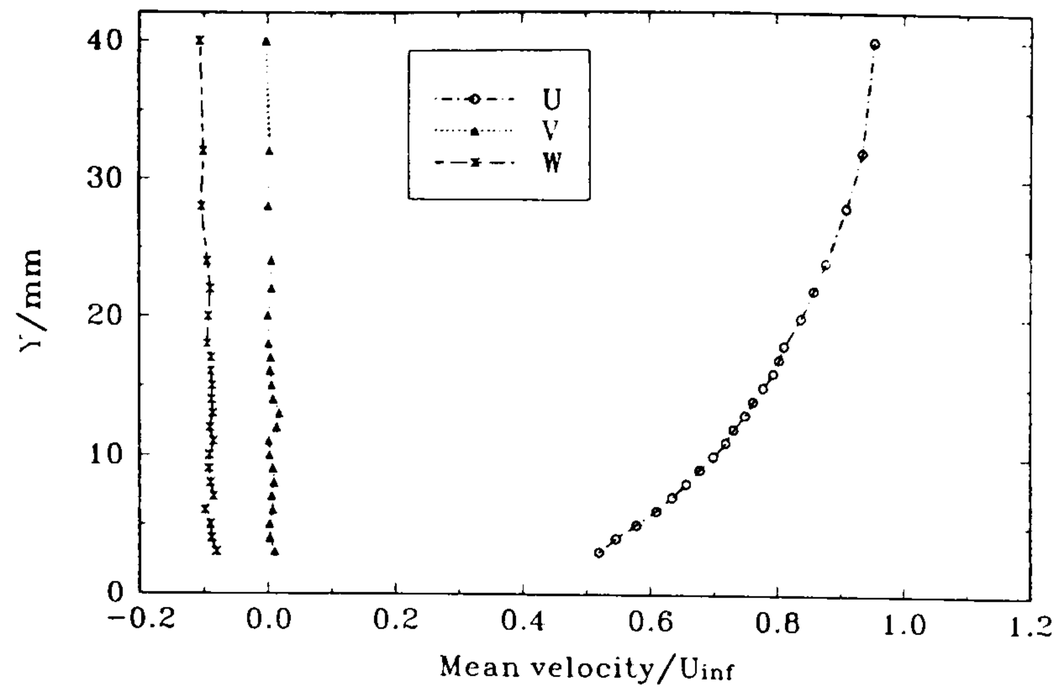

(a) $Z = +60$ mm

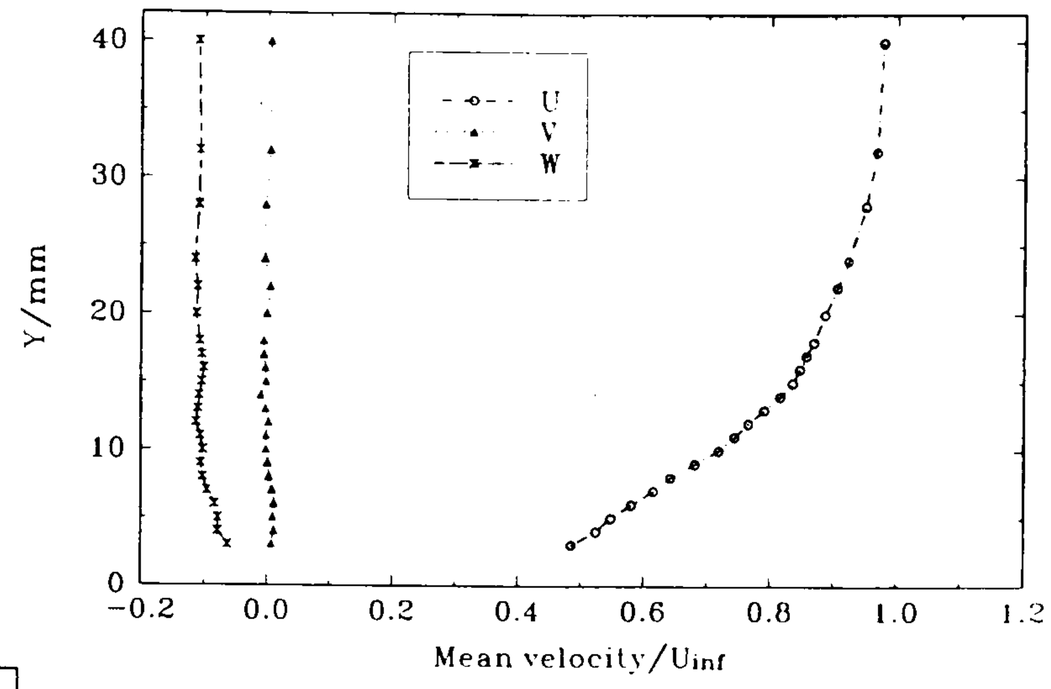

(b) $Z = +40$ mm

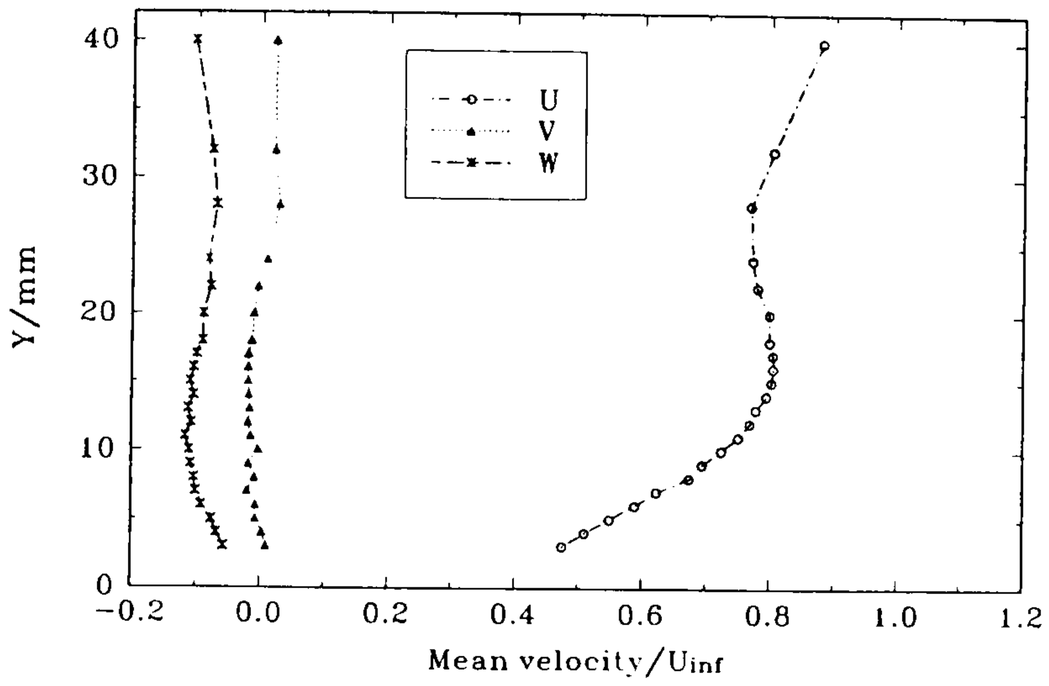

(c) $Z = +30$ mm

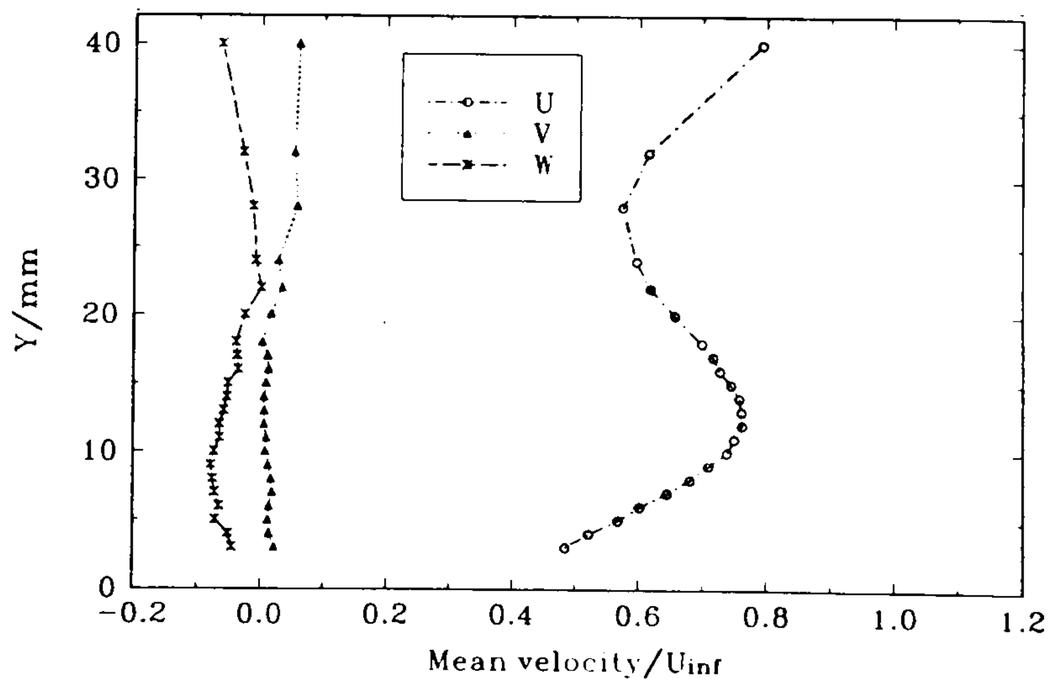

(d) $Z = +25$ mm

Figure 72 Profiles of $(\overline{U}, \overline{V}, \overline{W}) / U_\infty$ through the plate boundary layer at $\alpha = 0°$, in plane TE ($X = 500$ mm), at various distances normal to the chord line in the $+Z$ direction.

(continued...

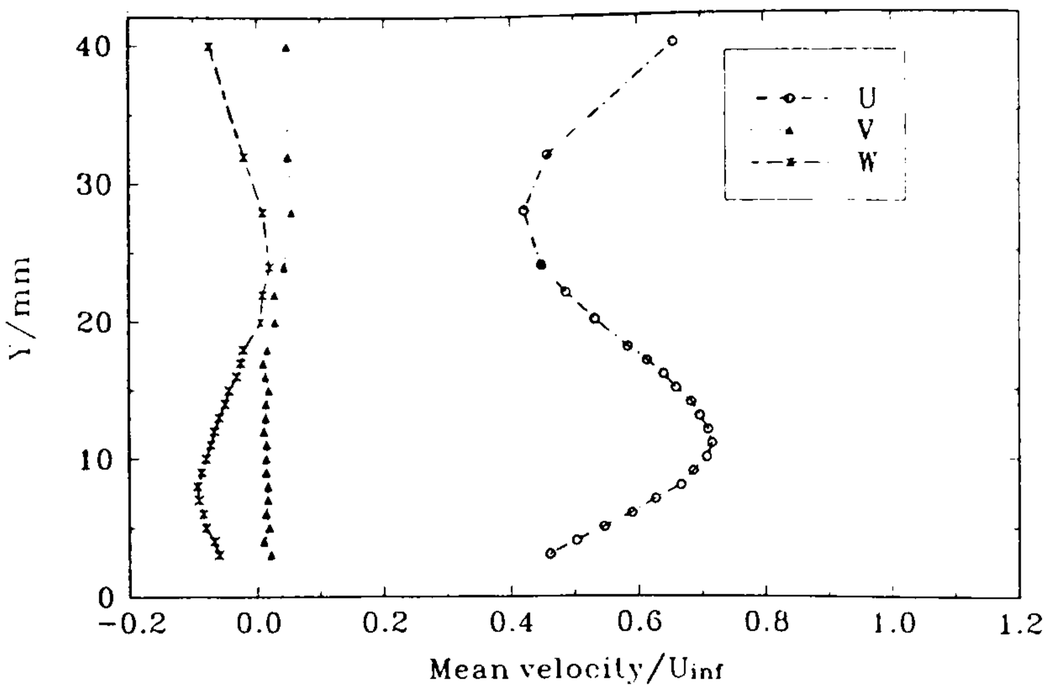

(e) $Z = +20$ mm

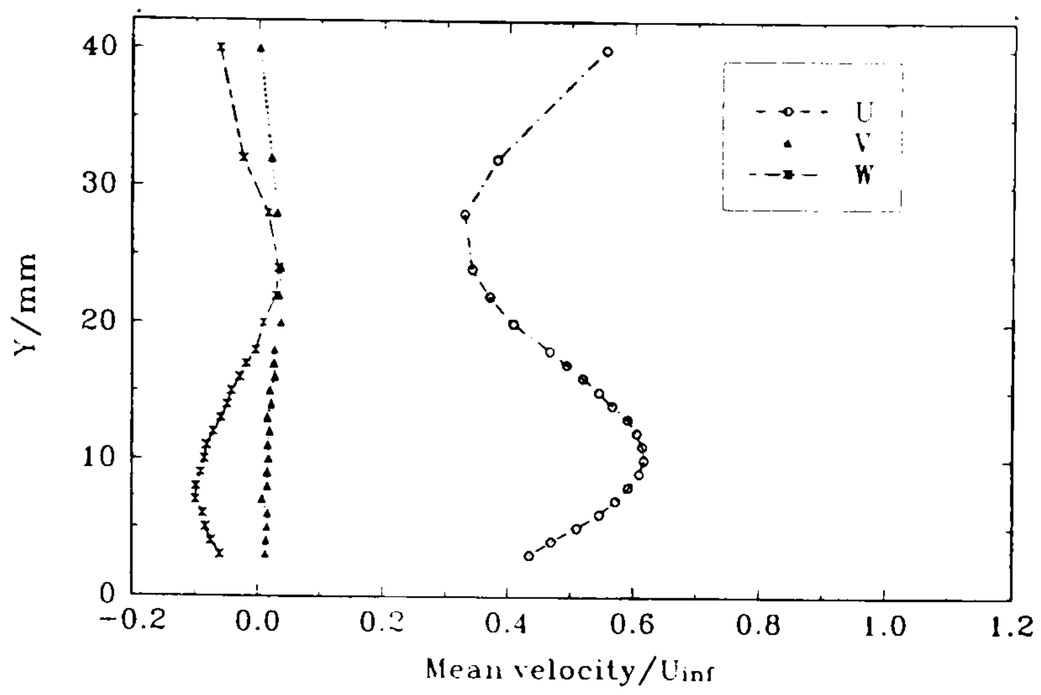

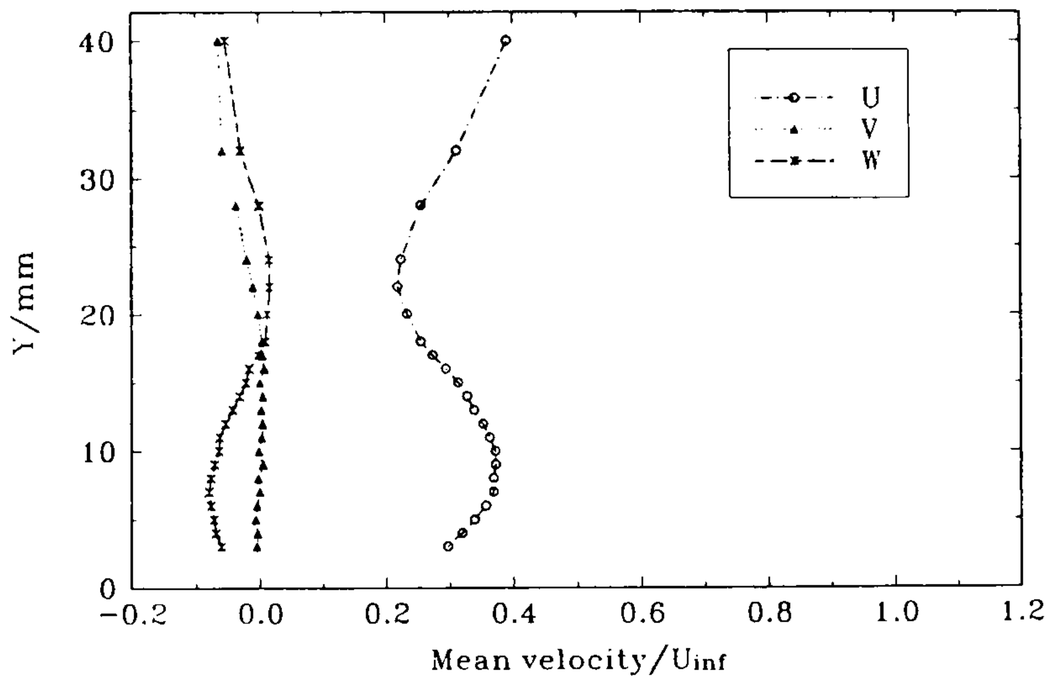

(f) $Z = +15$ mm

(g) $Z = +10$ mm

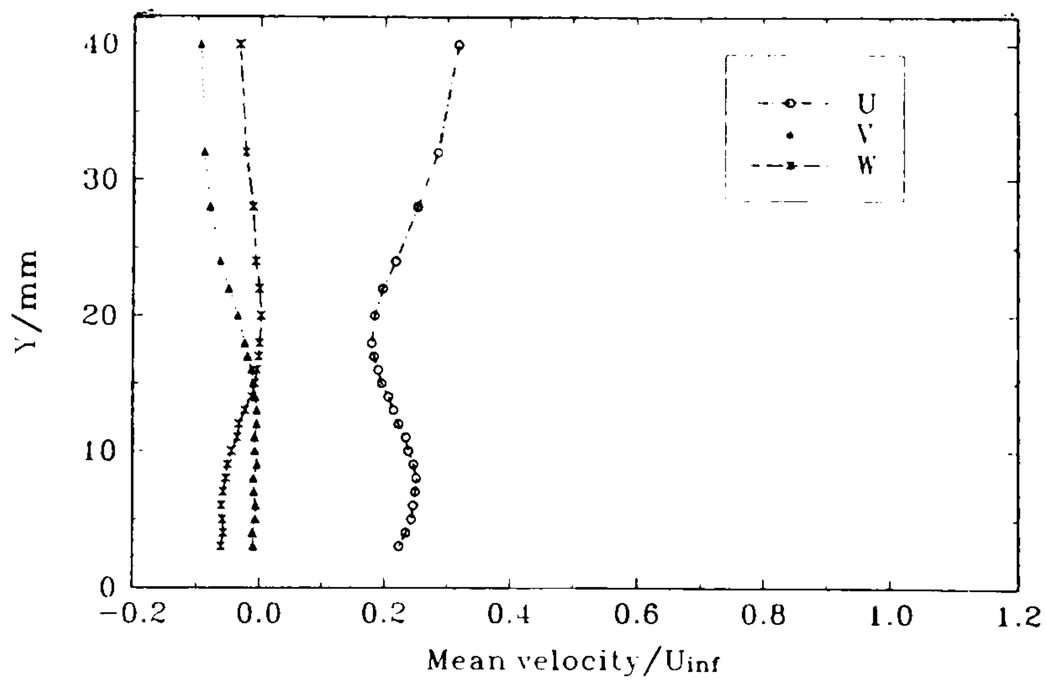

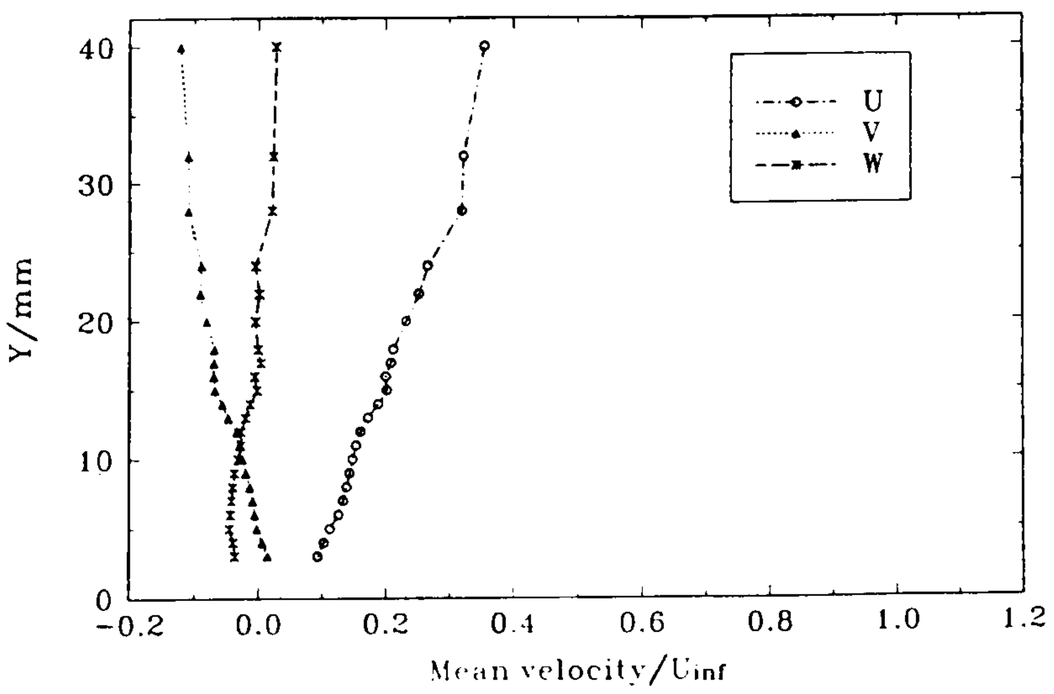

(h) $Z = +5$ mm

(i) $Z = +0$ mm

Figure 72 Profiles of $(\overline{U}, \overline{V}, \overline{W})/U_\infty$ through the plate boundary layer at $\alpha = 0°$, in plane TE ($Y = 500$ mm), at various distances normal to the chord line in the $+Z$ direction.

...concluded)

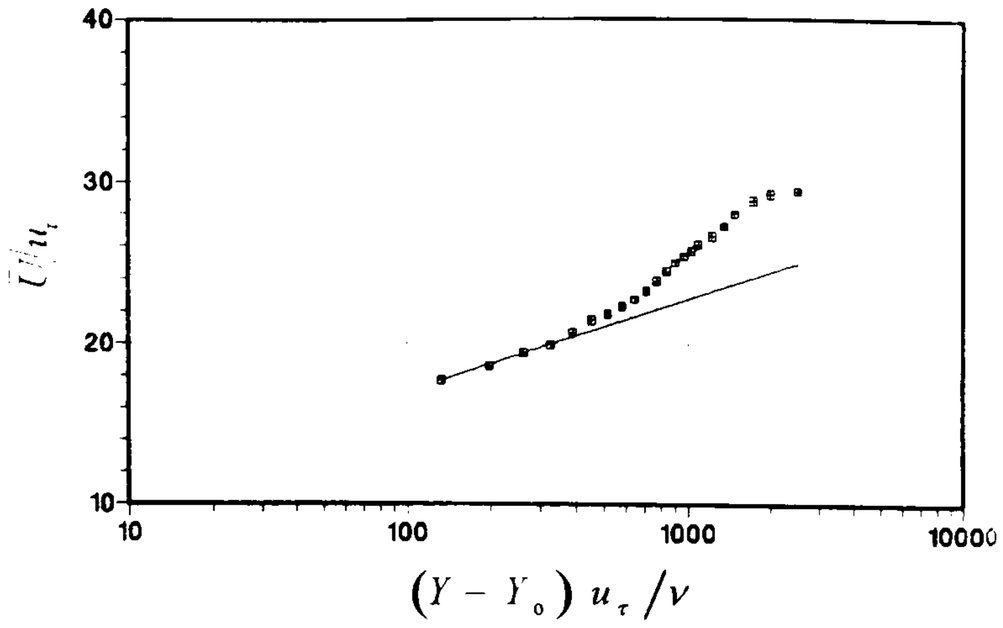

(a) Z = -60 mm

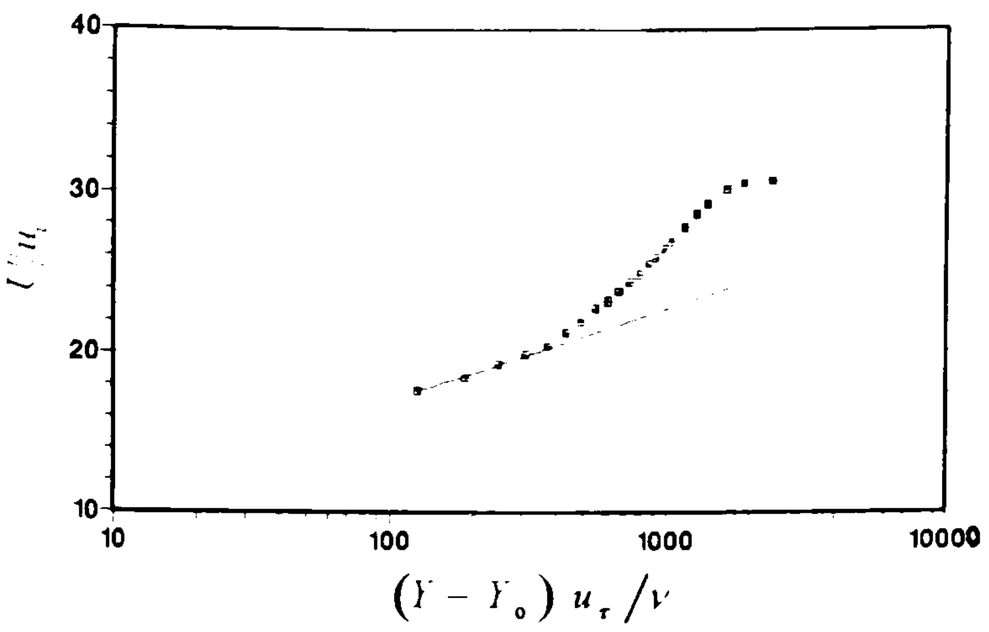

(b) Z = -40 mm

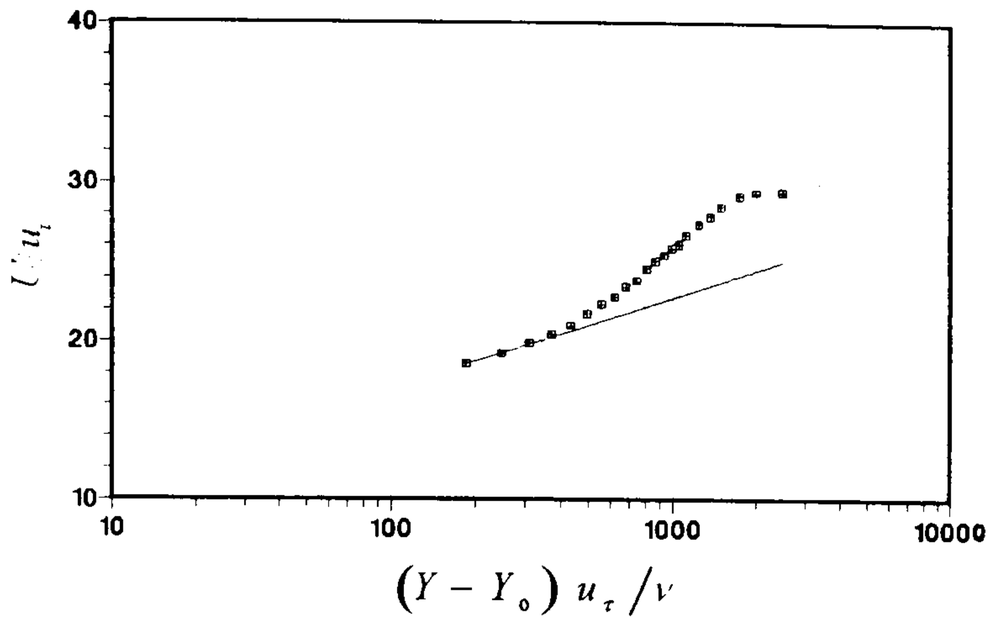

(c) Z = -30 mm

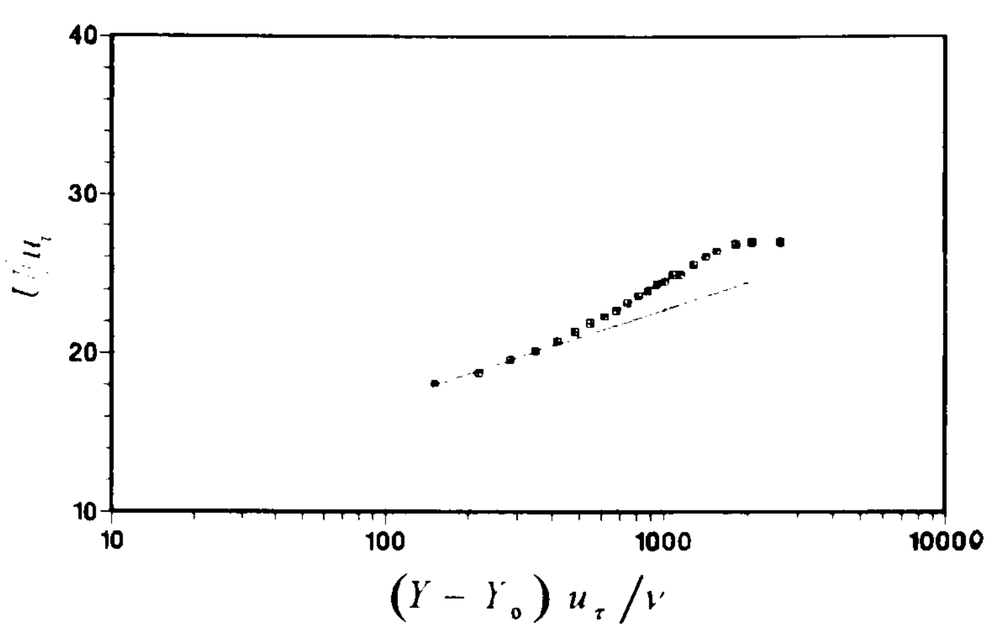

(d) Z = -25 mm

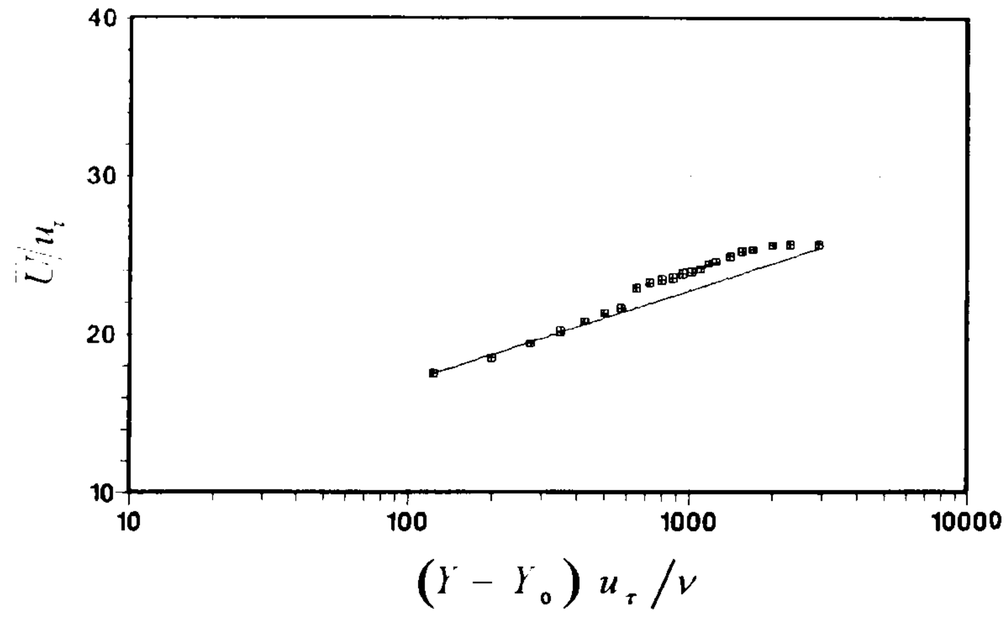

(e) Z = -20 mm

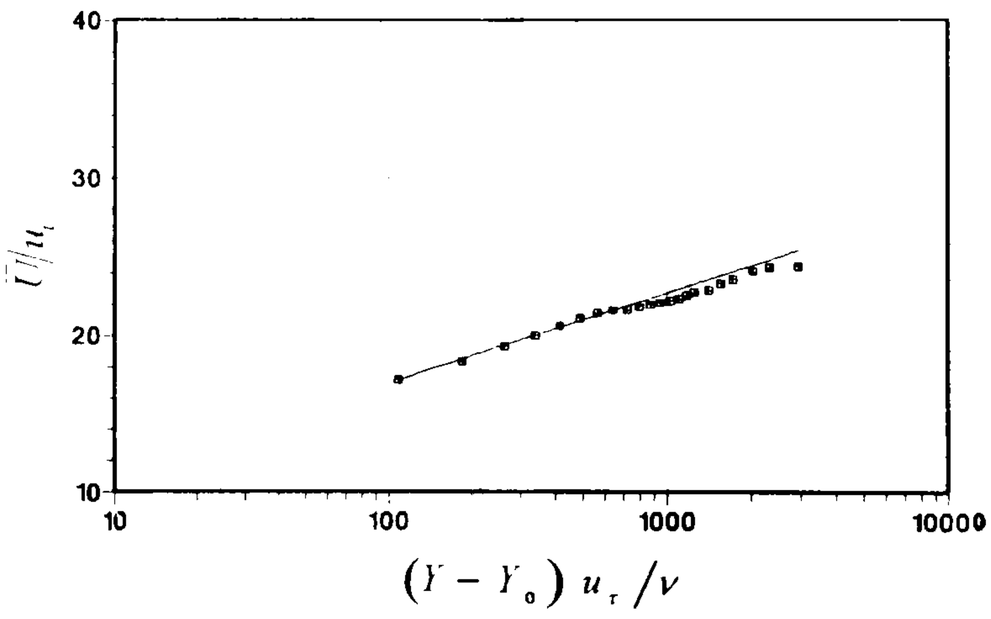

(f) Z = -15 mm

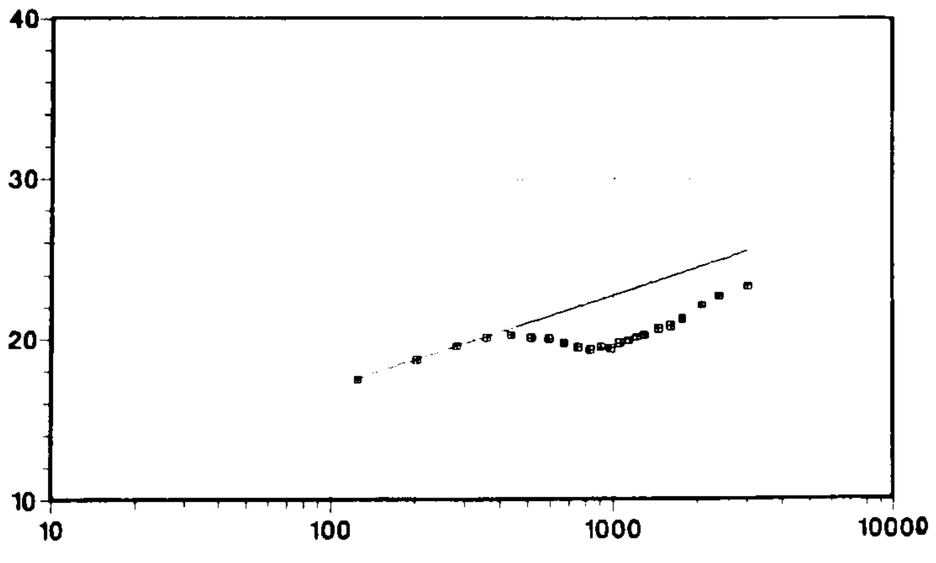

(g) Z = -10 mm

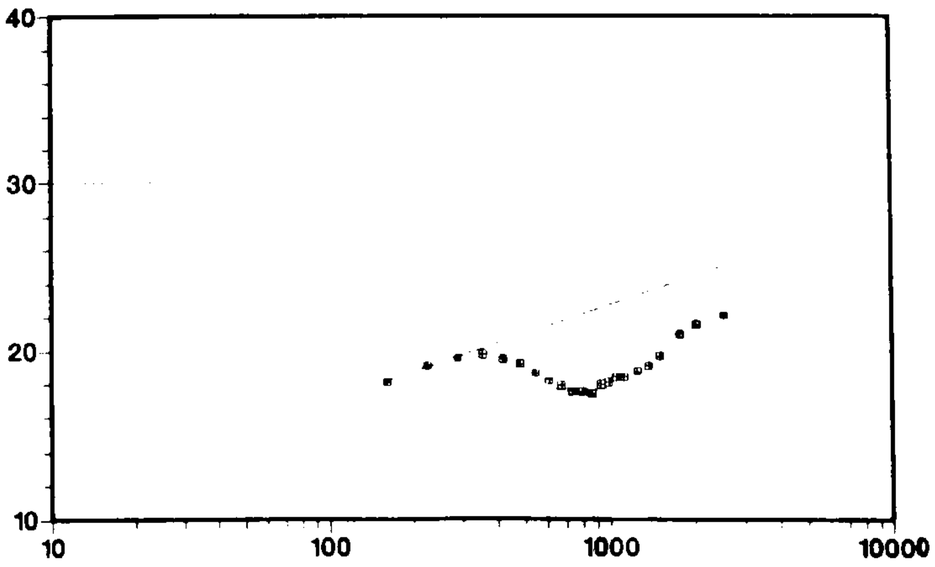

(h) Z = -5 mm

Figure 73 Semi-logarithmic plots of the measured $\overline{U}$ -velocity profiles, compared with the log-law:

$$\frac{\overline{U}}{u_\tau} = 5.75 \log\left(\frac{u_\tau (Y - Y_0)}{\nu}\right) + 5.5,$$

at stations in plane TE (X = 500 mm), in the -Z direction.

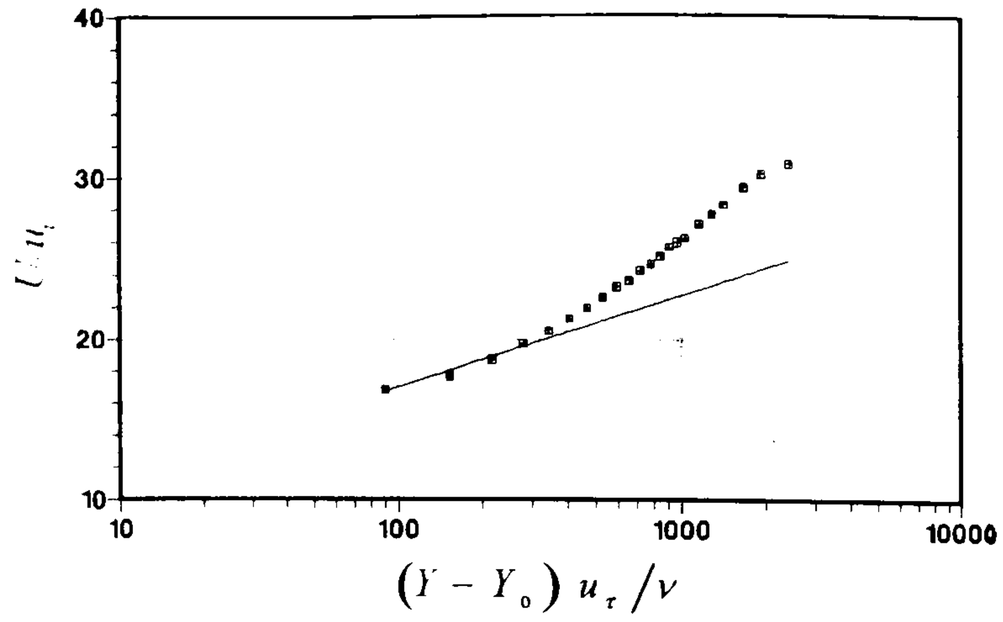

(a) $Z = 60$ mm

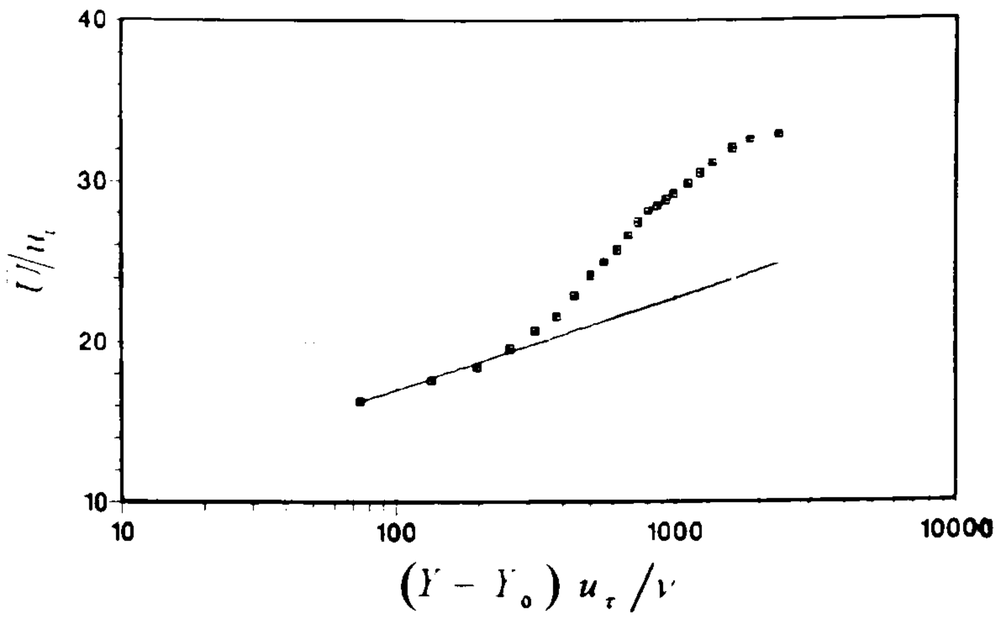

(b) $Z = 40$ mm

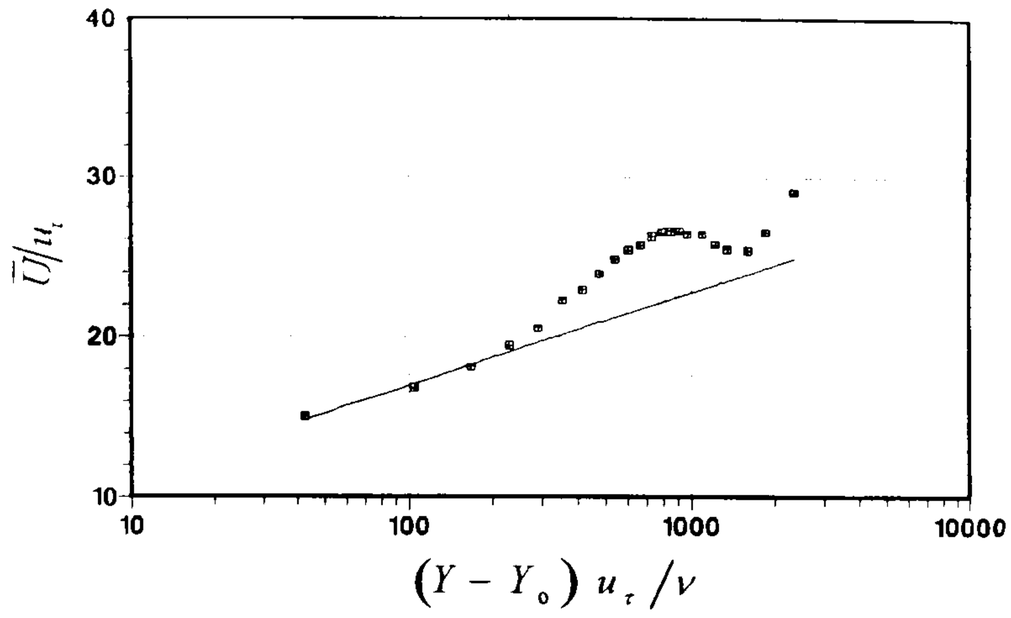

(c) $Z = 30$ mm

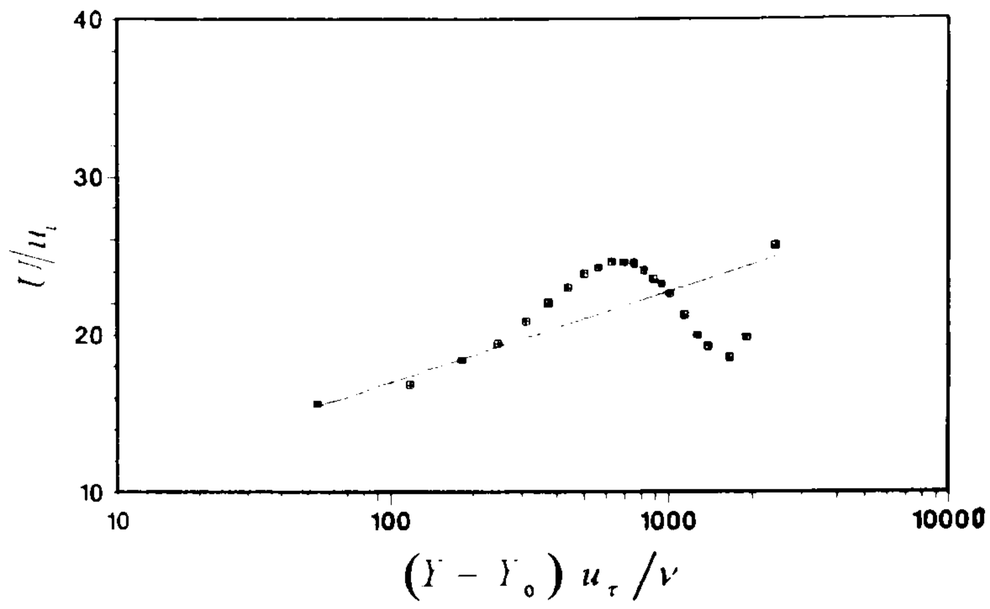

(d) $Z = 25$ mm

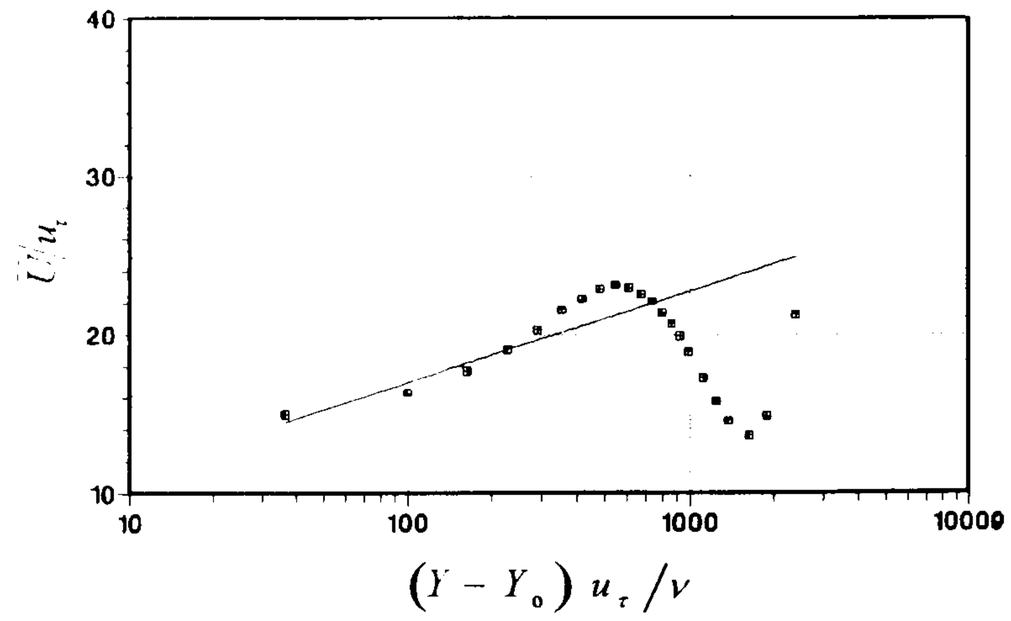

(e) $Z = 20$ mm

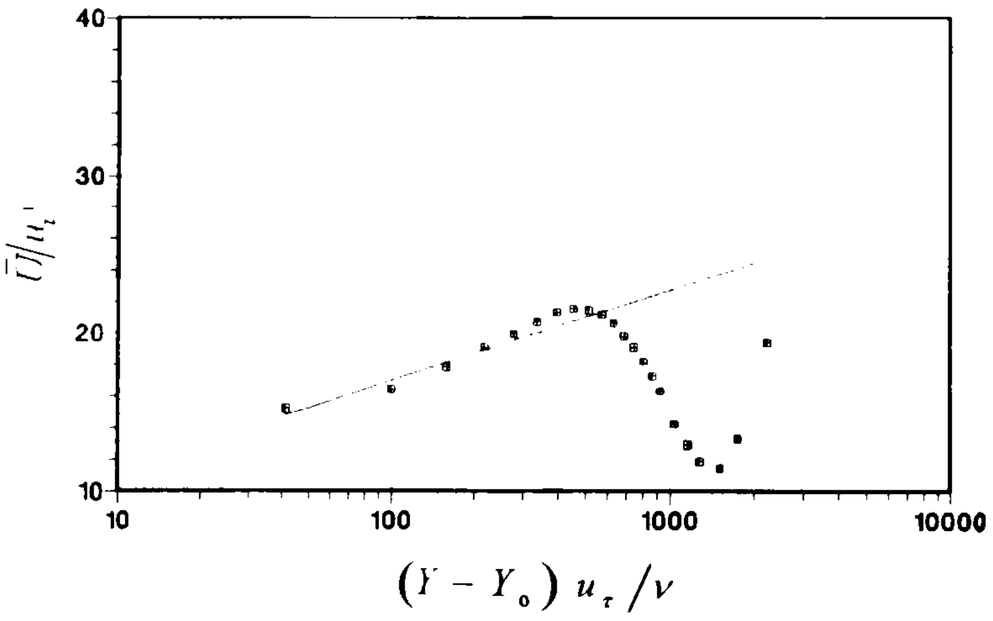

(f) $Z = 15$ mm

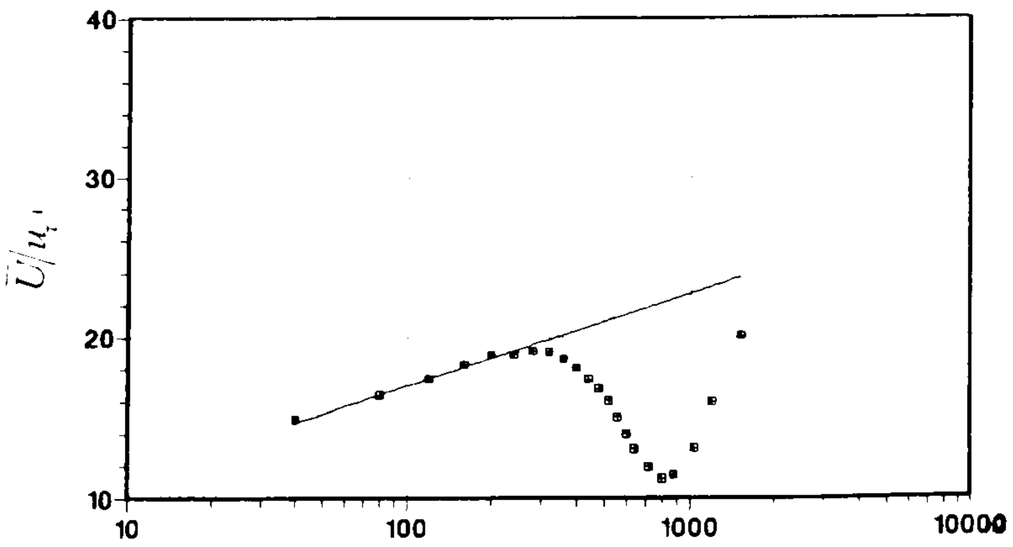

(g) $Z = 10$ mm

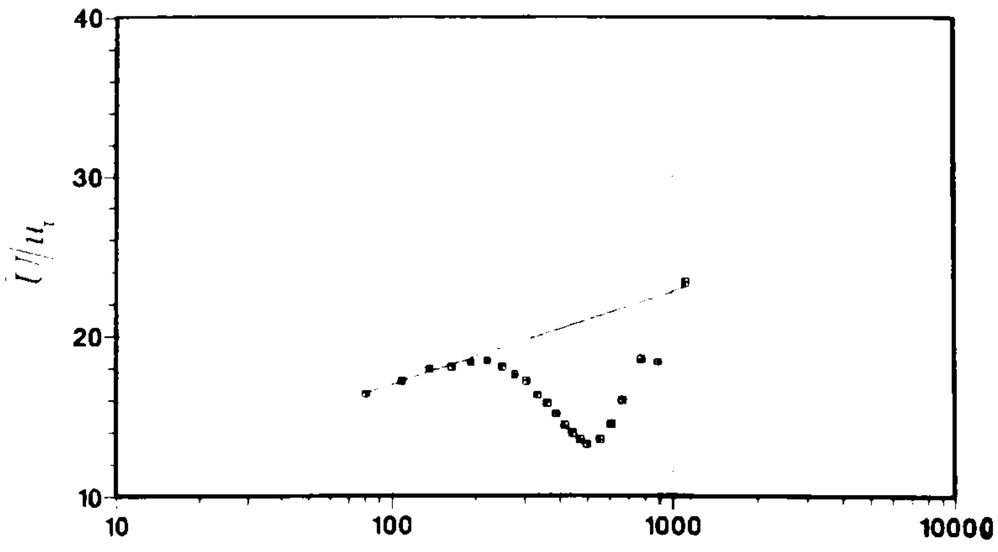

(h) $Z = 5$ mm

Figure 74 Semi-logarithmic plots of the measured $\overline{U}$ -velocity profiles, compared with the log-law:

$$\frac{\overline{U}}{u_\tau} = 5.75 \log\left(\frac{u_\tau (Y - Y_0)}{\nu}\right) + 5.5,$$

at stations in plane TE ($X = 500$ mm), in the $+Z$ direction.

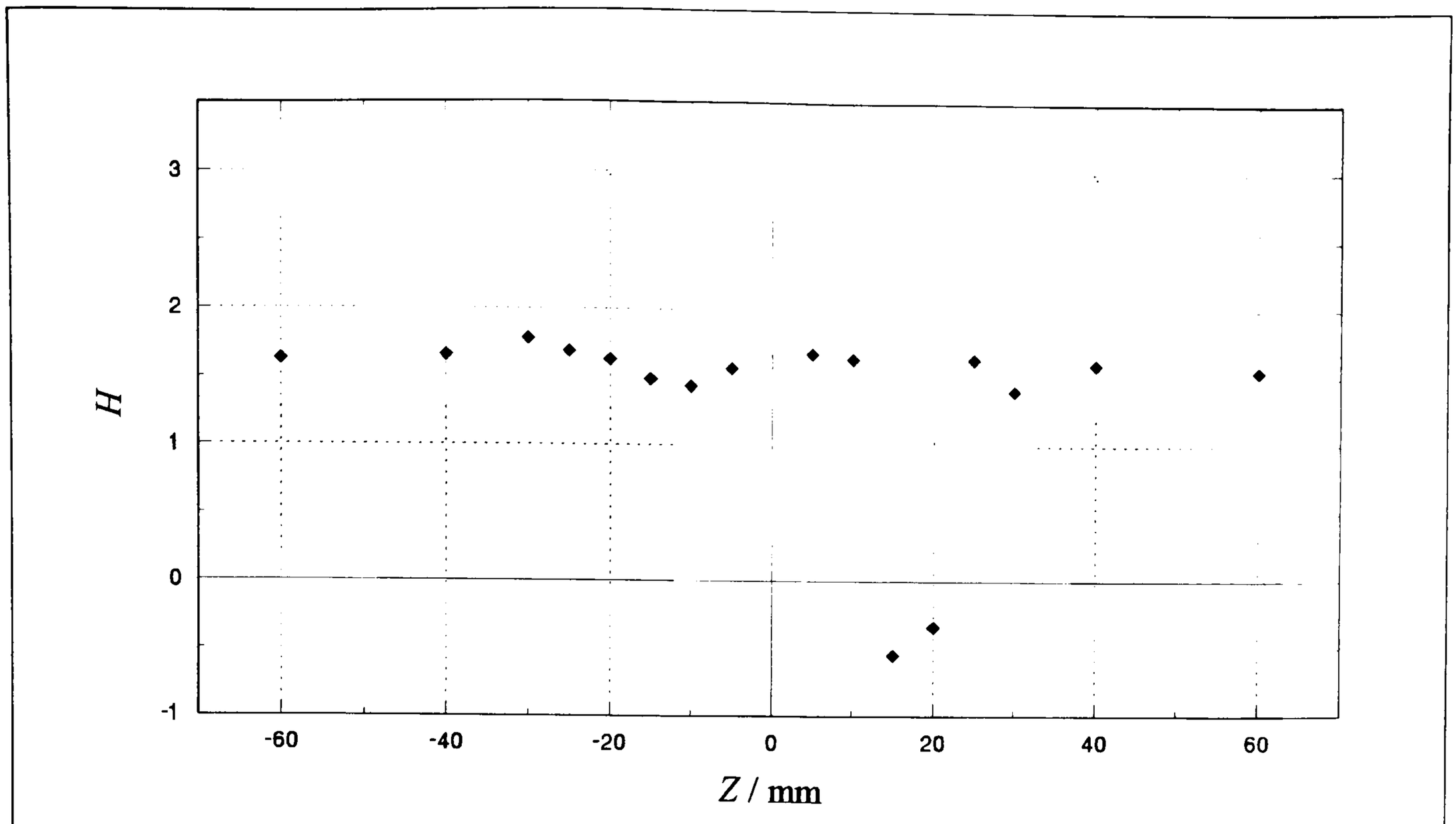

Figure 75 Distribution of boundary-layer shape parameter H , in plane *TE* ($Y = 500$ mm).

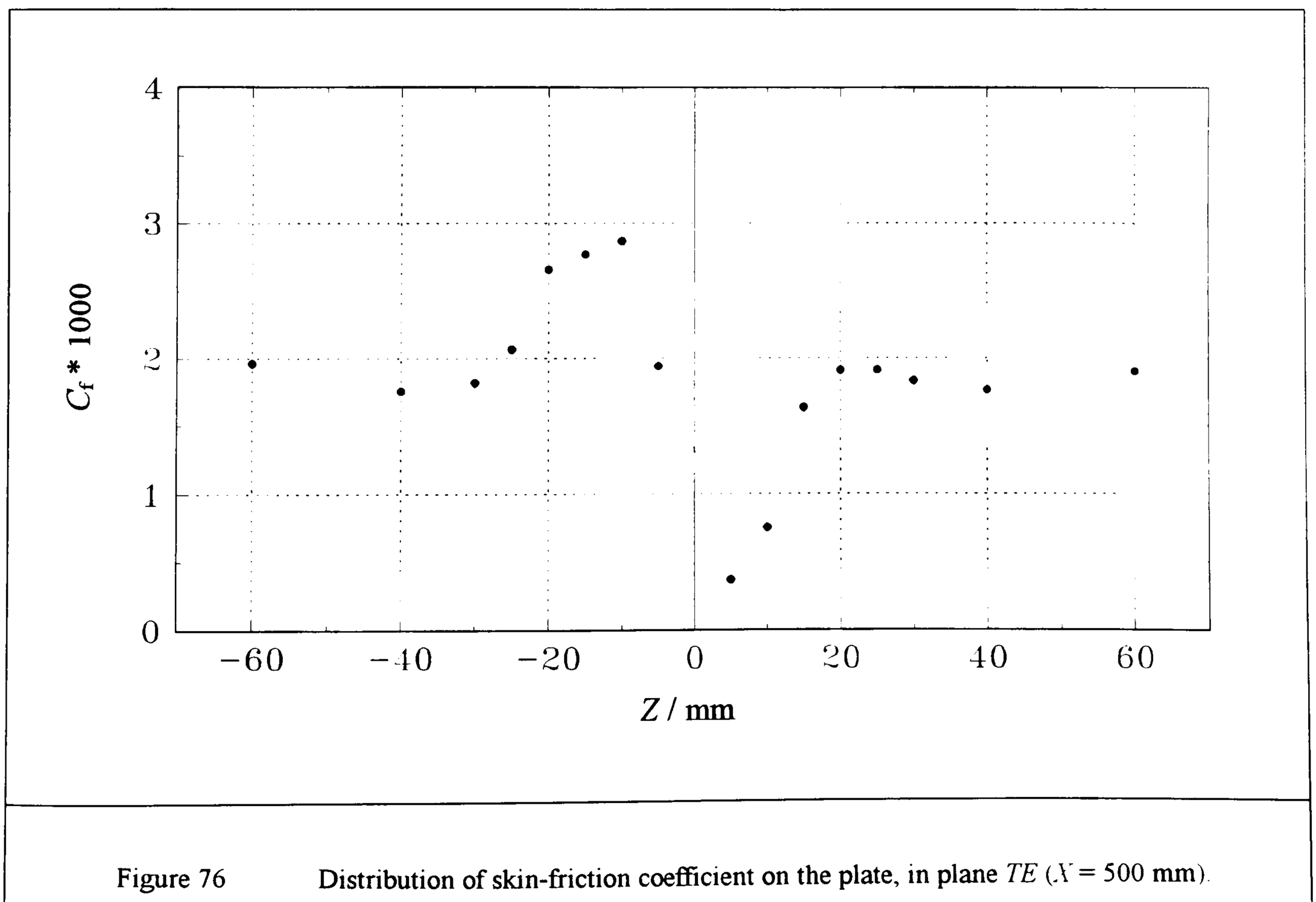

Figure 76 Distribution of skin-friction coefficient on the plate, in plane *TE* ($Y = 500$ mm).

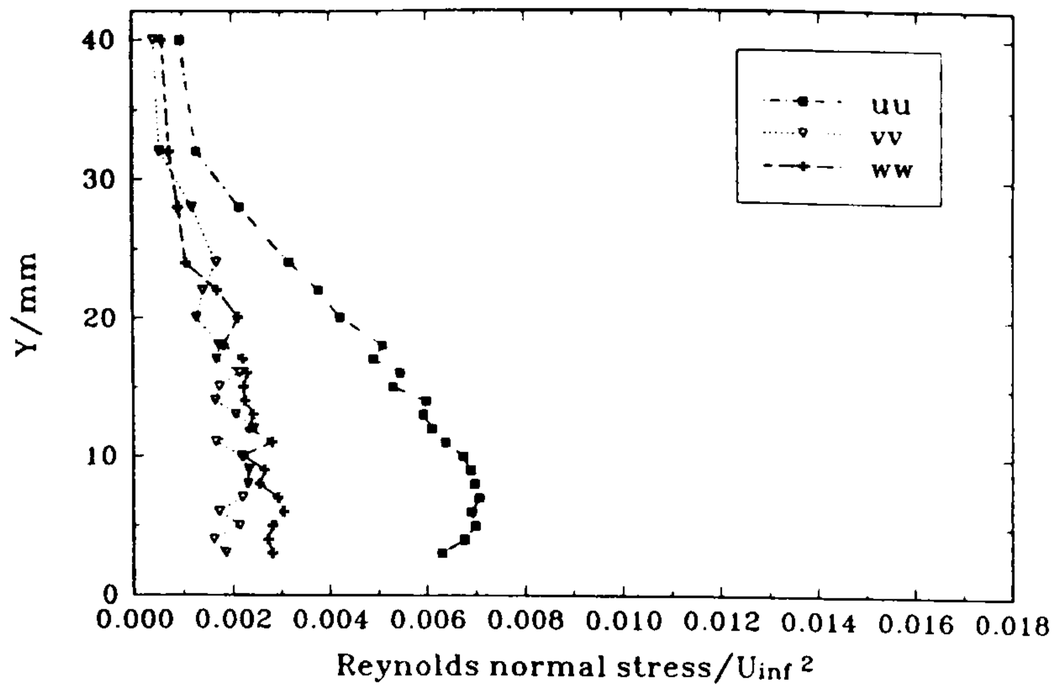

(a) Z = -60 mm

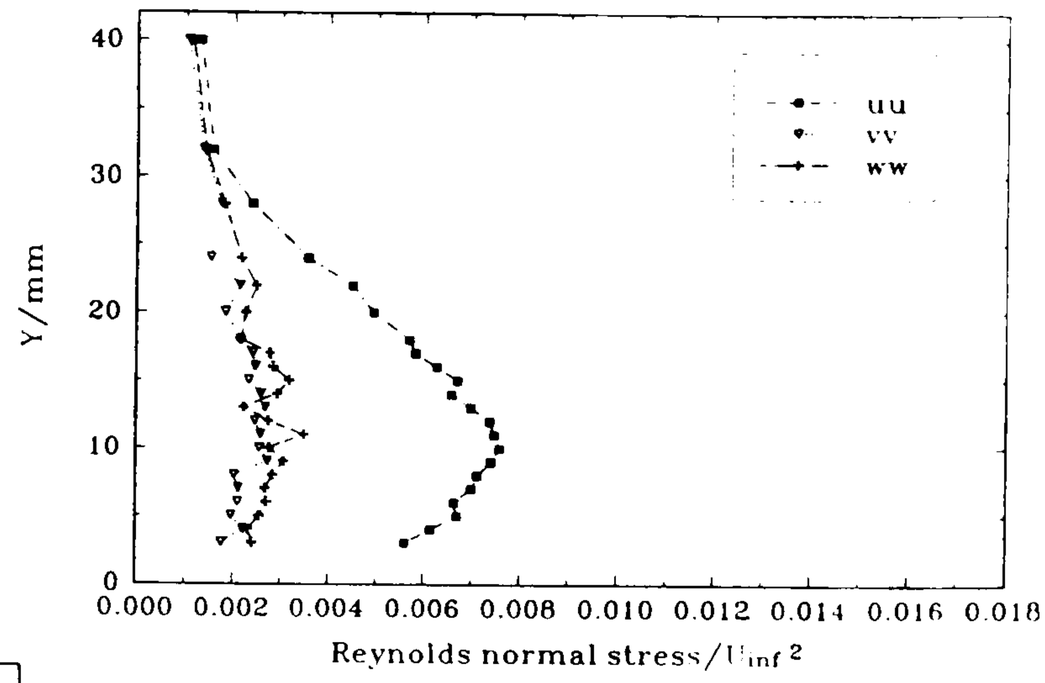

(b) Z = -40 mm

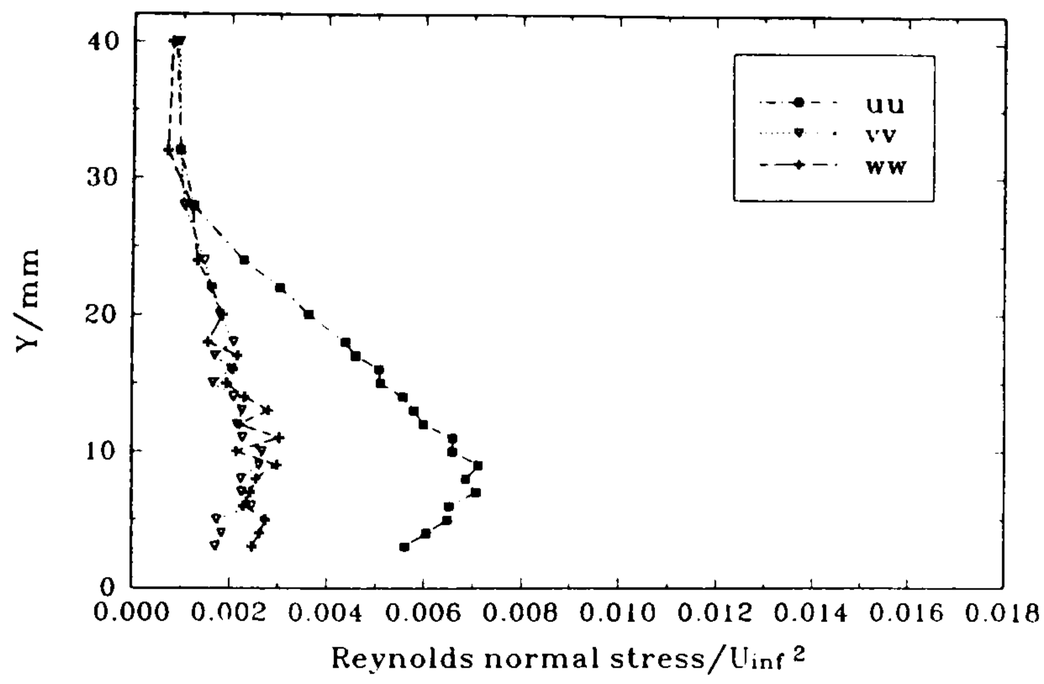

(c) Z = -30 mm

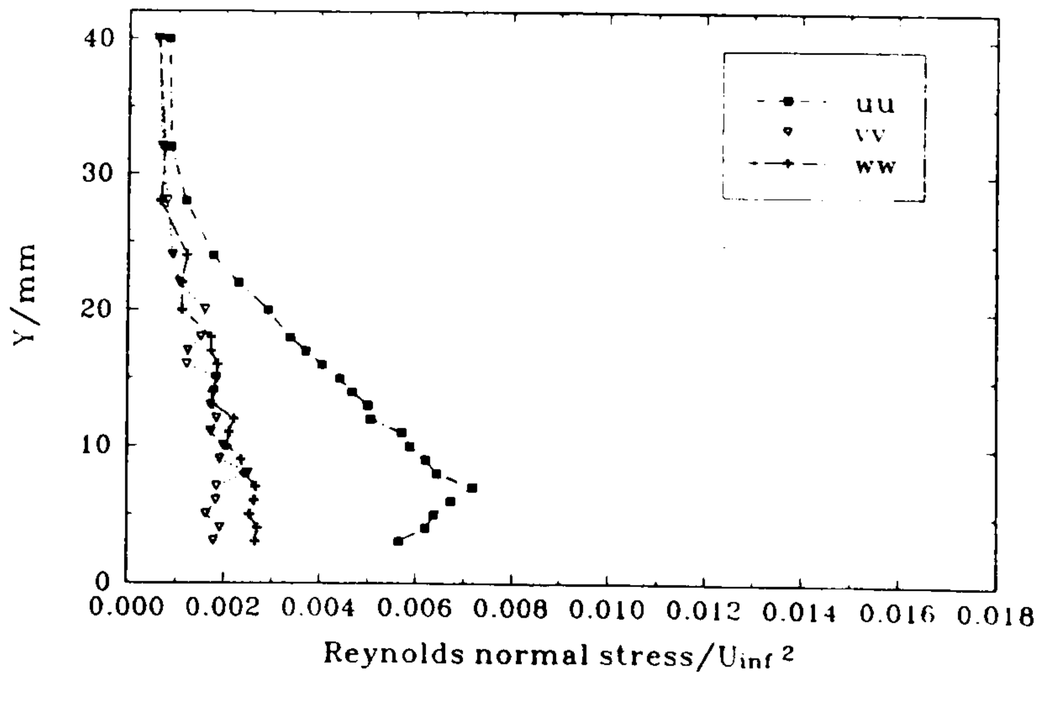

(d) Z = -25 mm

Figure 77 Profiles of $(\overline{u^2}, \overline{v^2}, \overline{w^2})/U_\infty^2$ through the plate boundary layer at $\alpha = 0°$, in plane TE (Y = 500 mm), at various distances normal to the chord line in the -Z direction.

(continued...

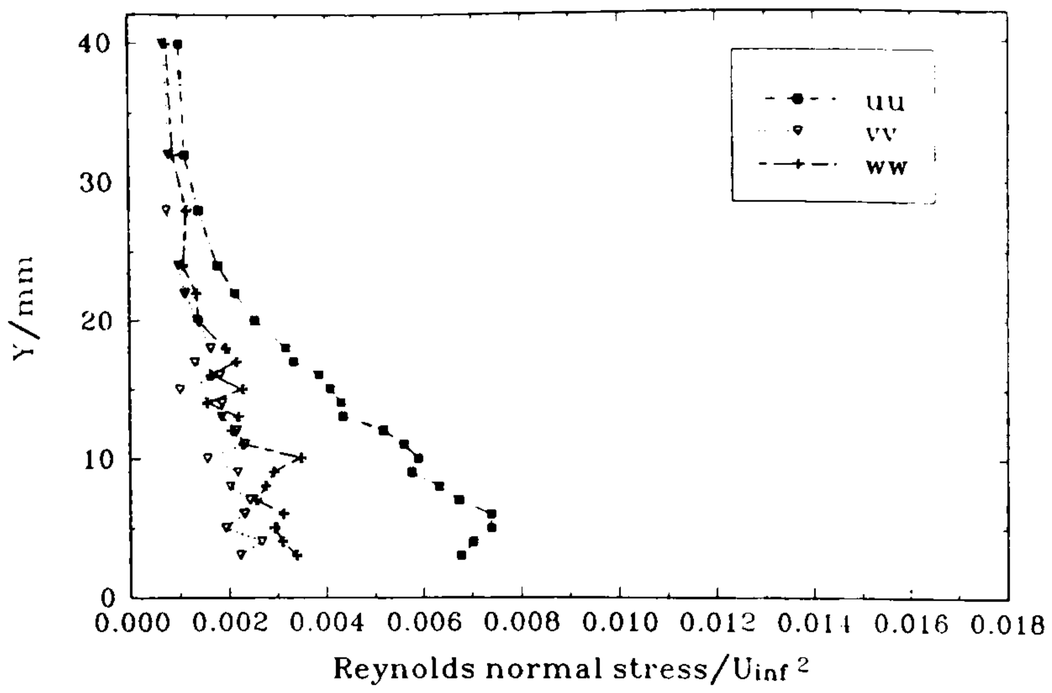

(e) Z = -20 mm

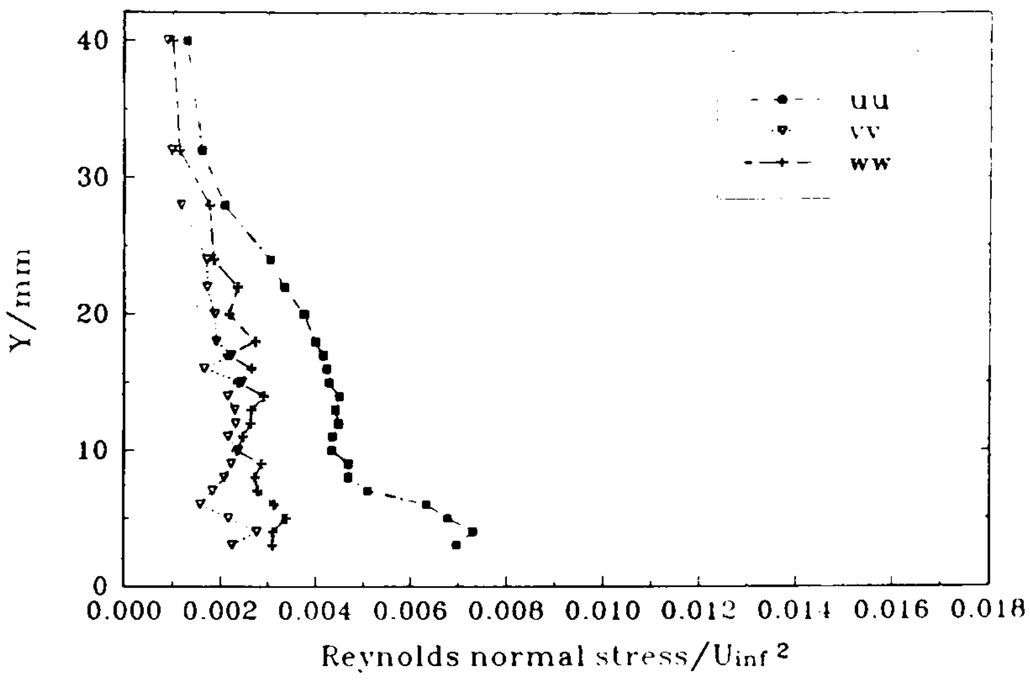

(f) Z = -15 mm

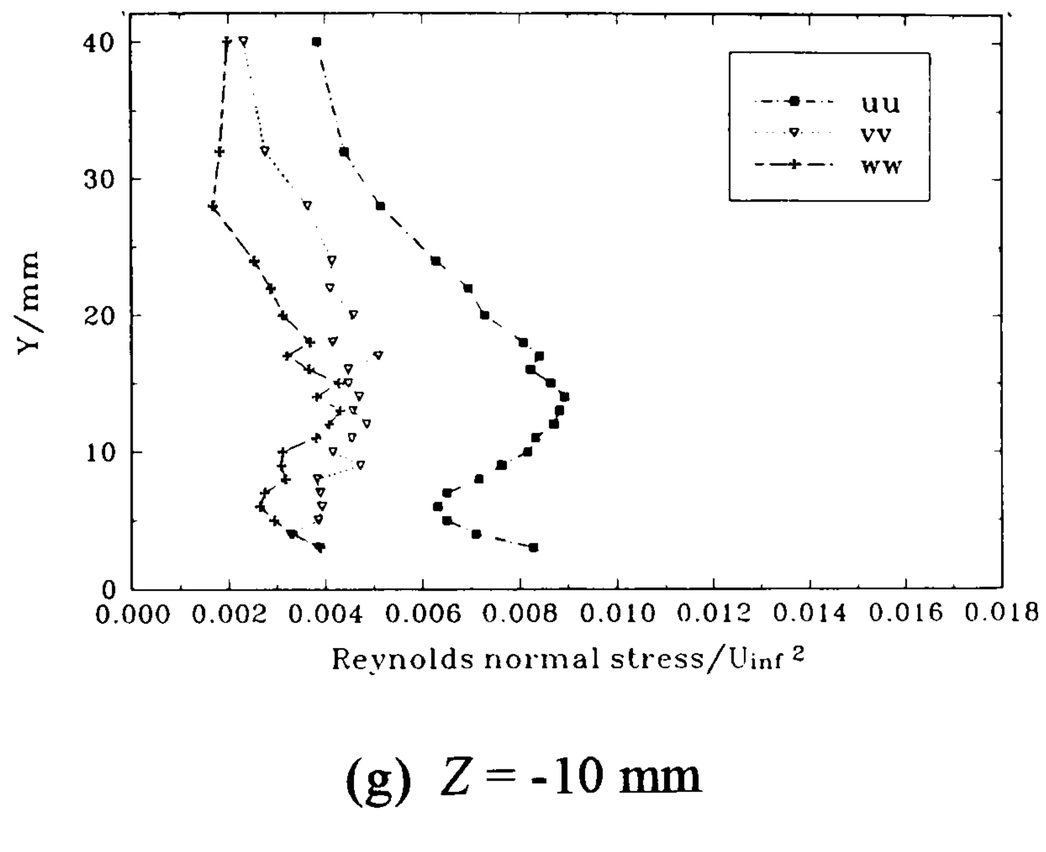

(g) Z = -10 mm

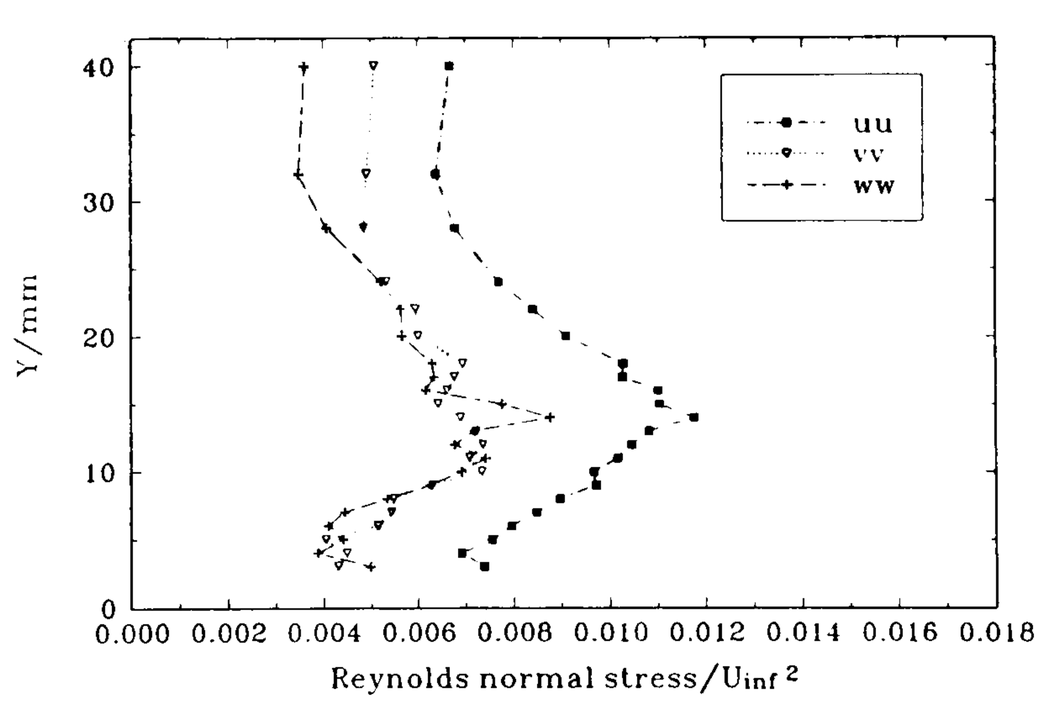

(h) Z = -5 mm

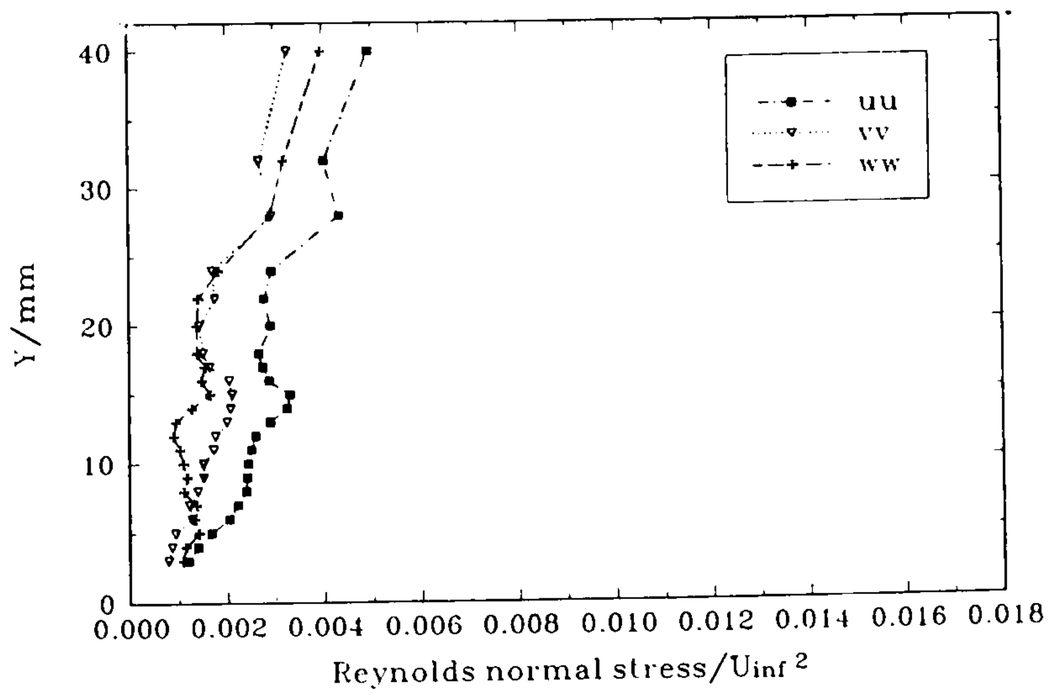

(i) Z = -0 mm

Figure 77 Profiles of $(\overline{u^2}, \overline{v^2}, \overline{w^2})/U_\infty^2$ through the plate boundary layer at α = 0°, in plane TE (Y = 500 mm), at various distances normal to the chord line in the -Z direction.

...concluded)

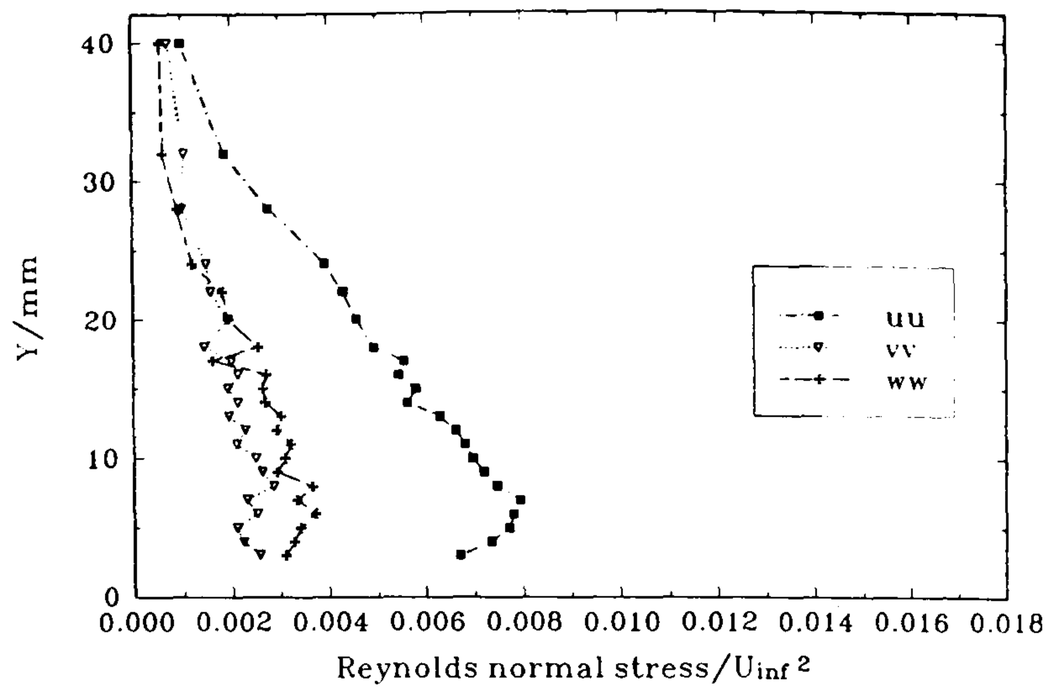

(a) $Z = +60$ mm

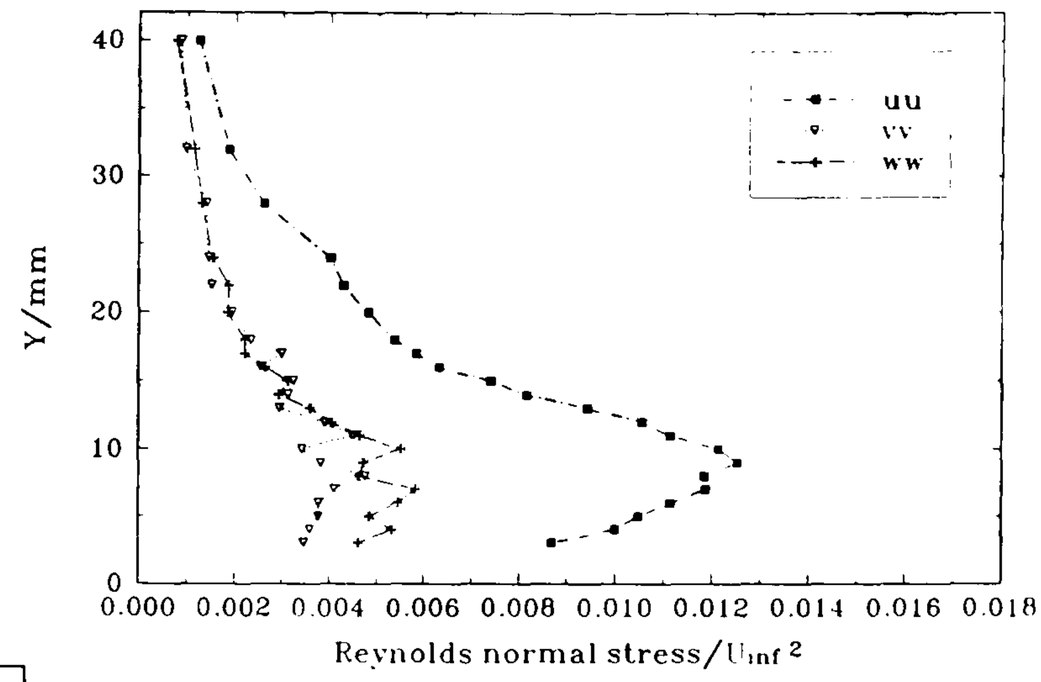

(b) $Z = +40$ mm

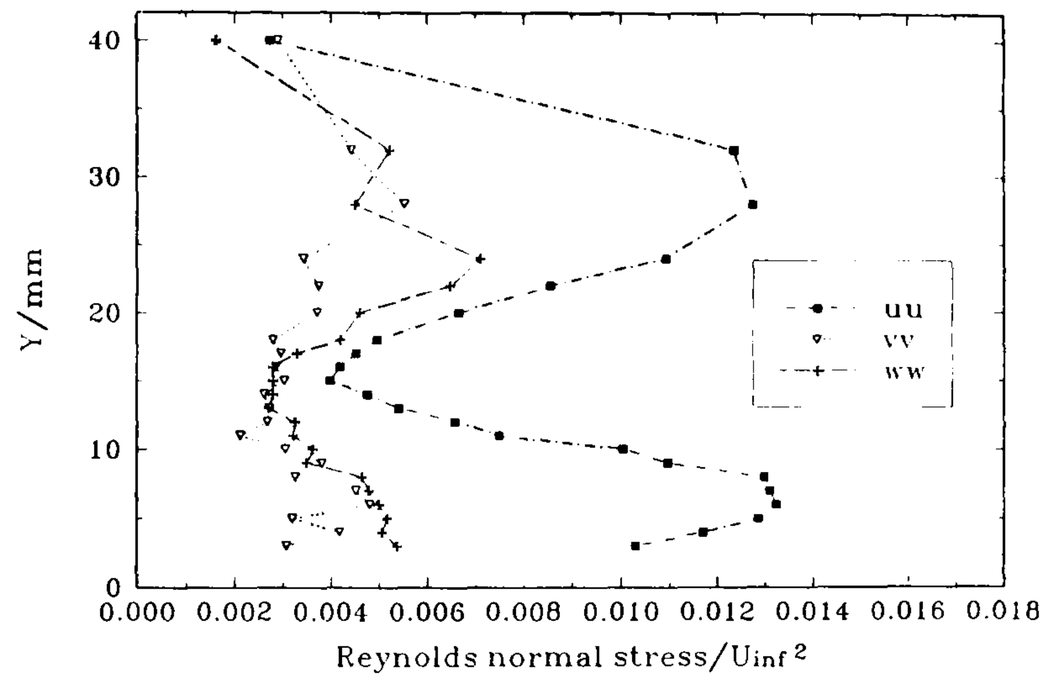

(c) $Z = +30$ mm

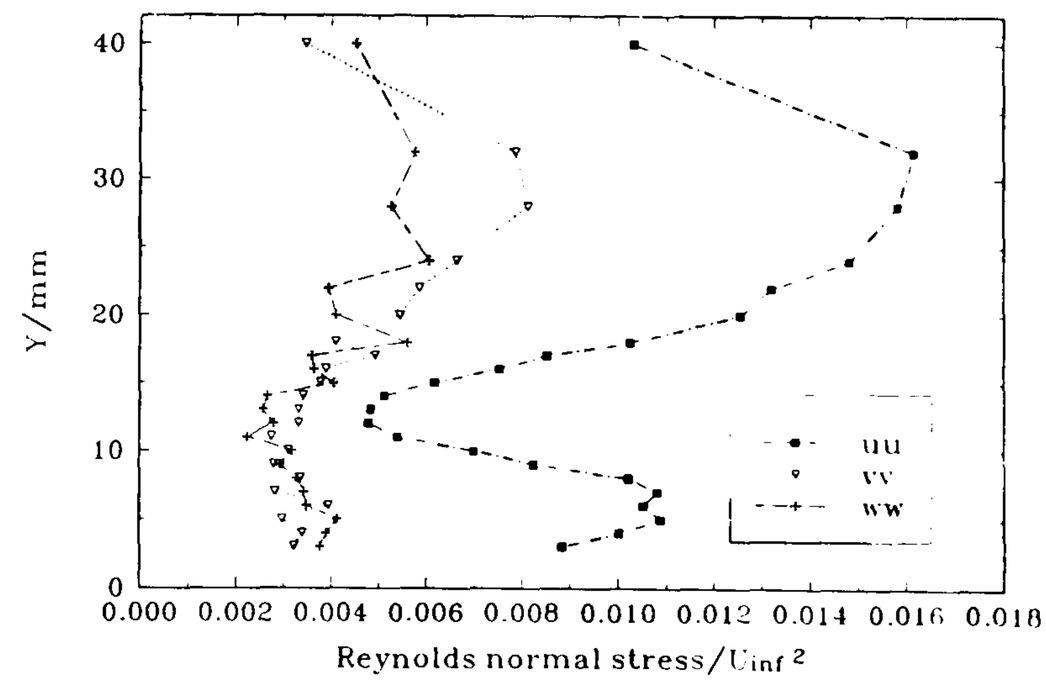

(d) $Z = +25$ mm

Figure 78 Profiles of $(\overline{u^2}, \overline{v^2}, \overline{w^2})/U_\infty^2$ through the plate boundary layer at $\alpha = 0°$, in plane TE ($Y = 500$ mm), at various distances normal to the chord line in the $+Z$ direction.

(continued...

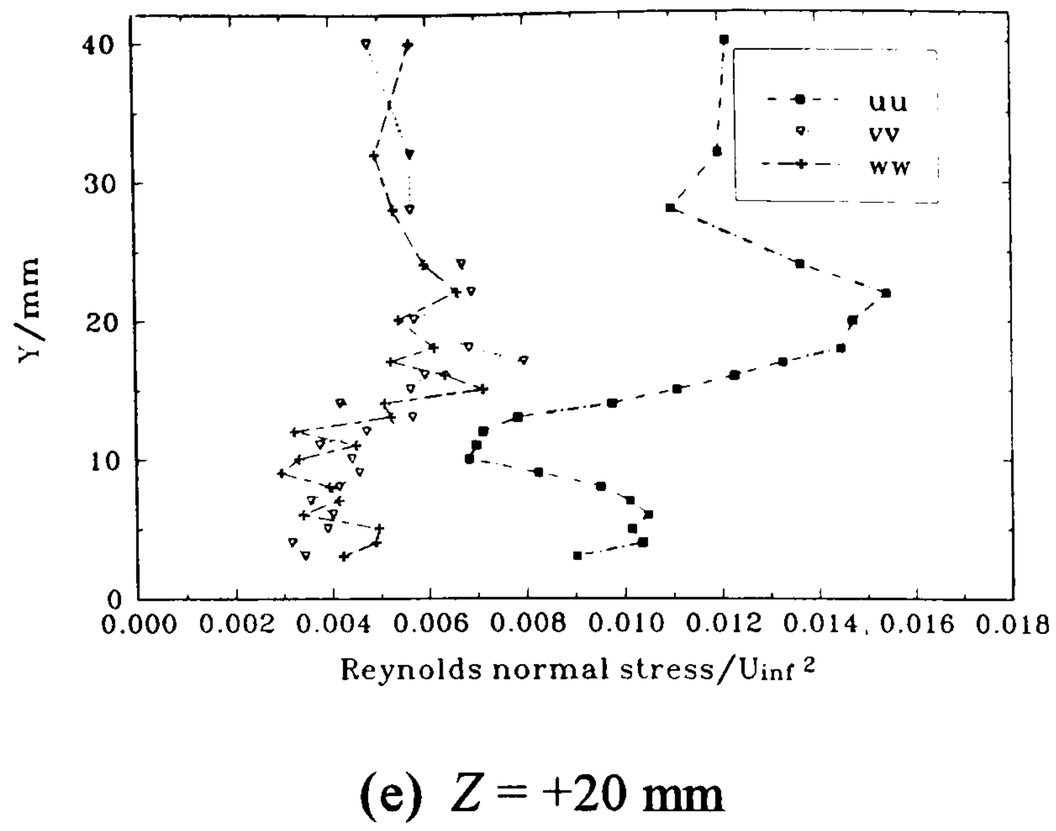

(e) $Z = +20$ mm

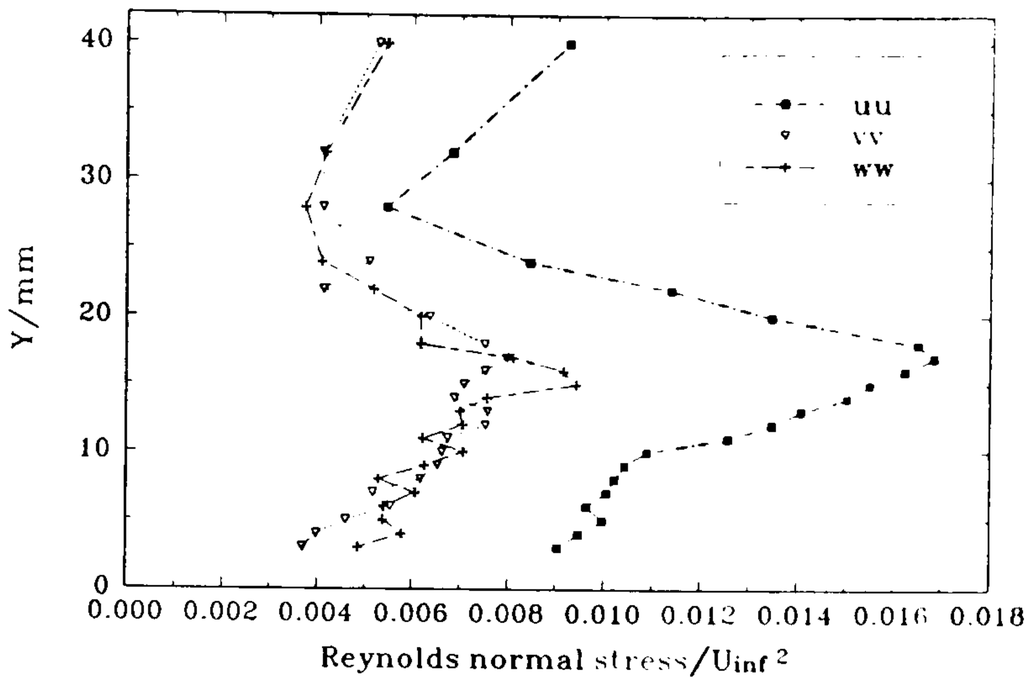

(f) $Z = +15$ mm

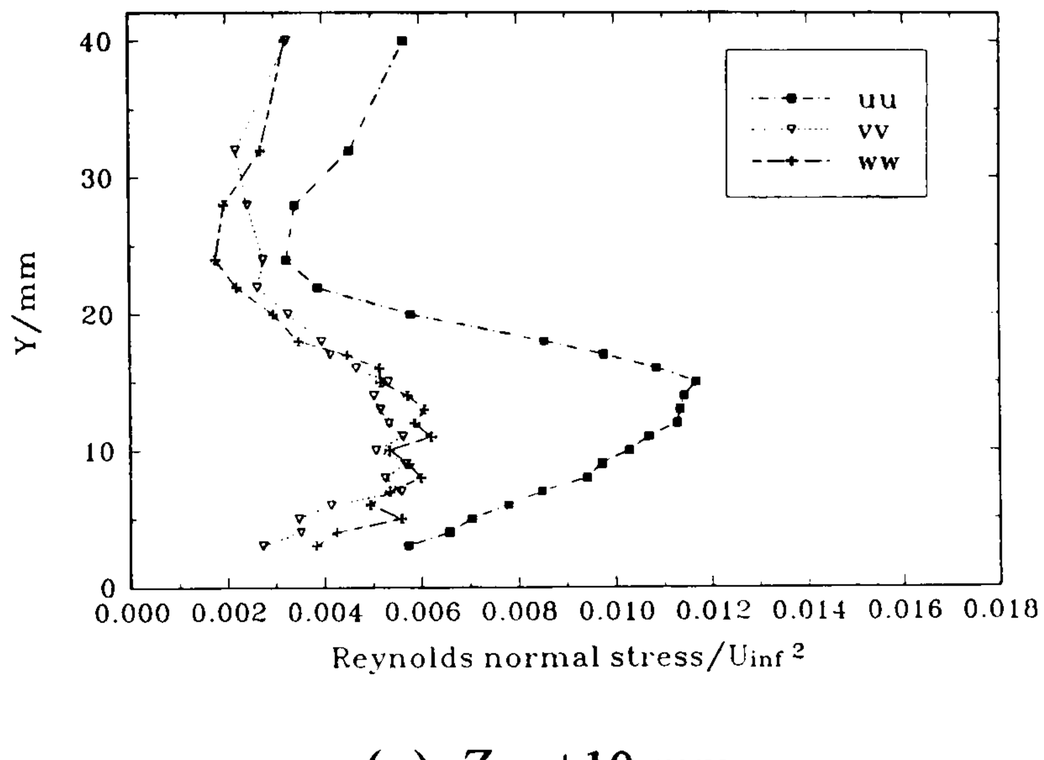

(g) $Z = +10$ mm

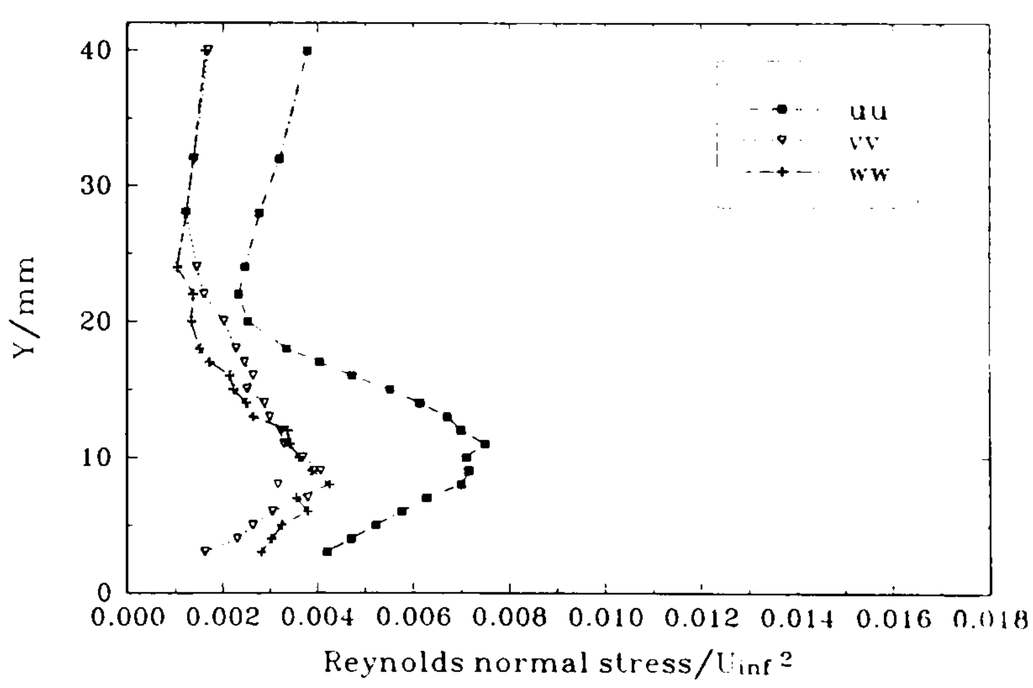

(h) $Z = +5$ mm

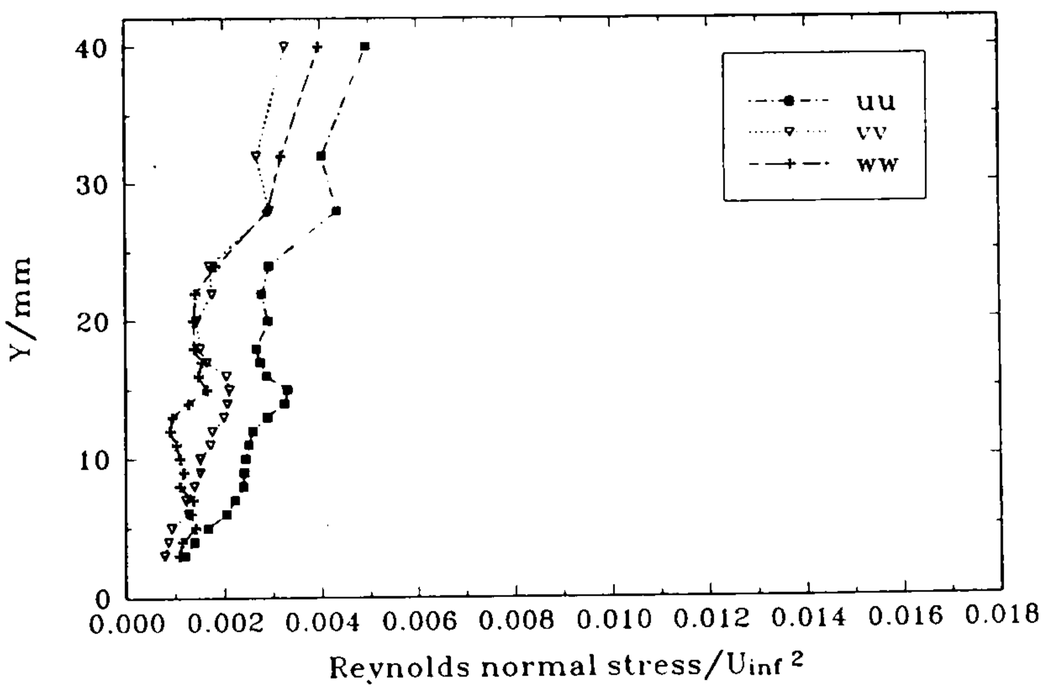

(i) $Z = +0$ mm

Figure 78 Profiles of $(\overline{u^2}, \overline{v^2}, \overline{w^2})/U_\infty^2$ through the plate boundary layer at $\alpha = 0°$, in plane TE ($Y = 500$ mm), at various distances normal to the chord line in the $+Z$ direction.

...concluded)

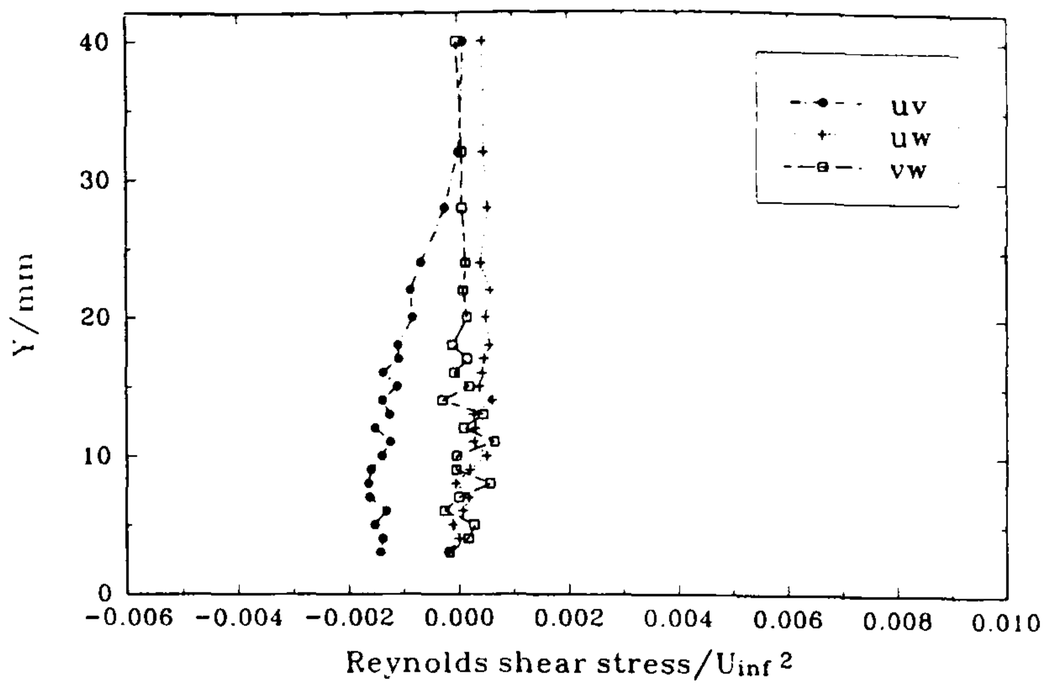

(a) Z = -60 mm

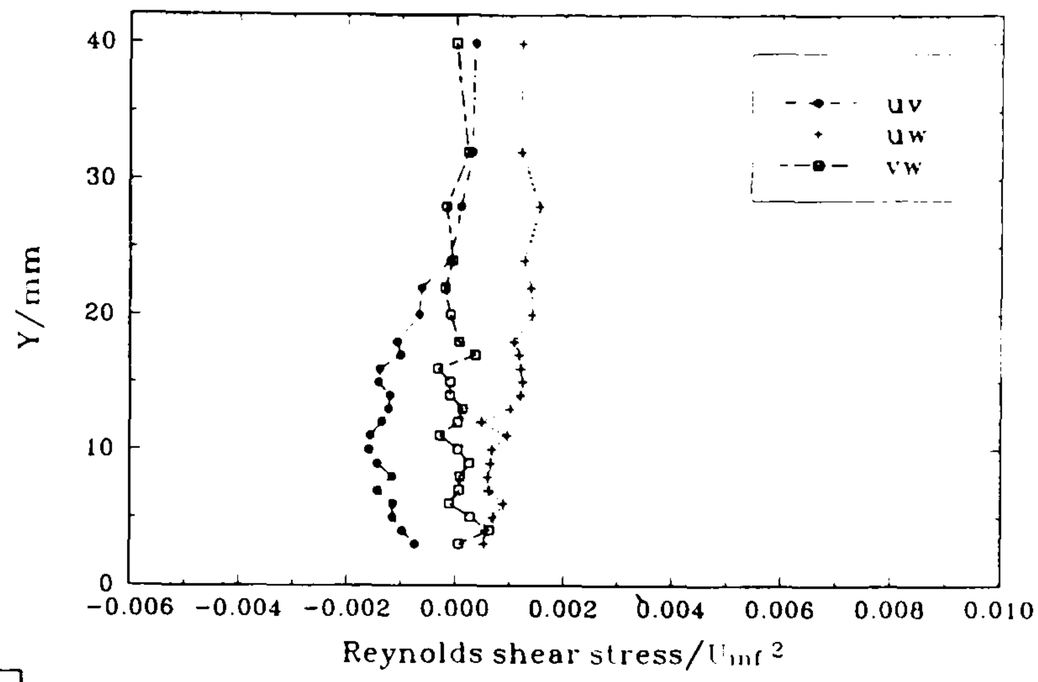

(b) Z = -40 mm

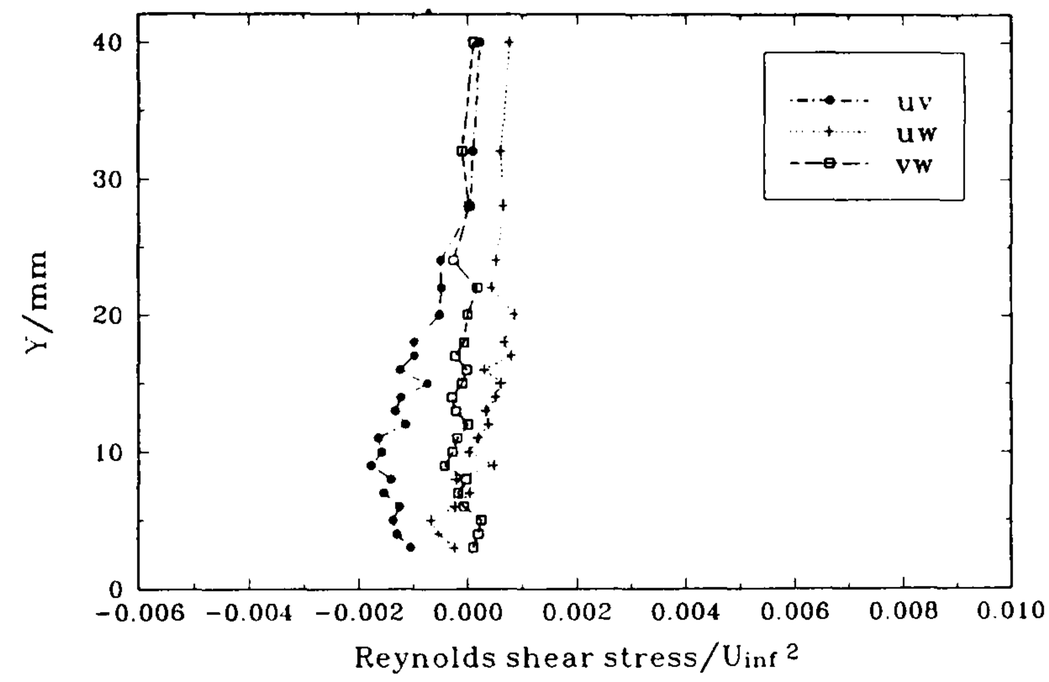

(c) Z = -30 mm

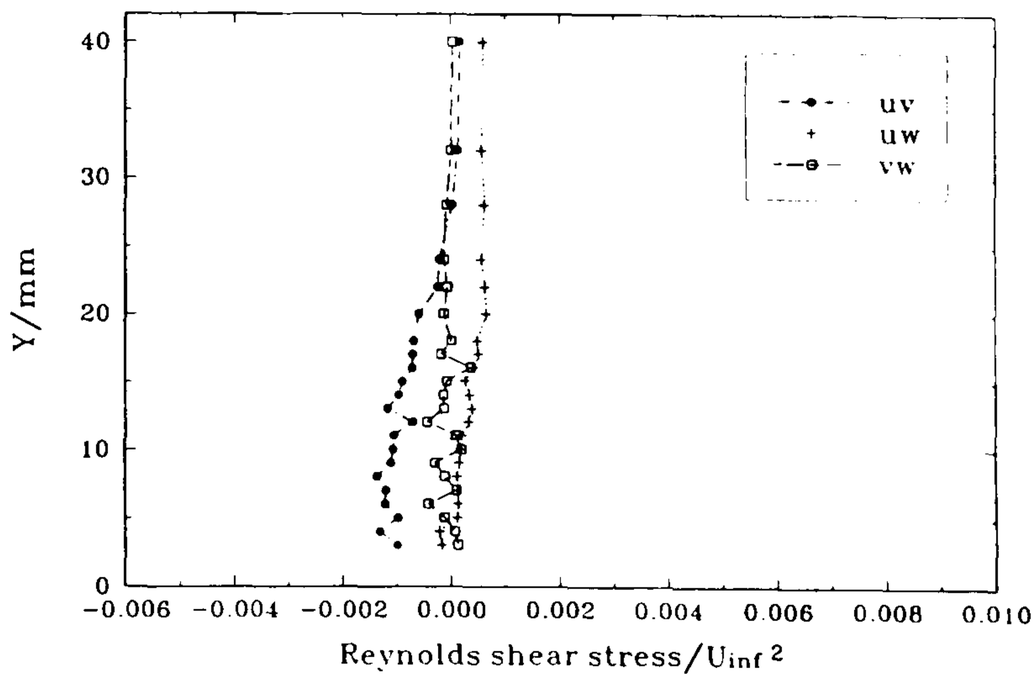

(d) Z = -25 mm

Figure 79 Profiles of $(\overline{uv}, \overline{uw}, \overline{vw})/U_\infty^2$ through the plate boundary layer at α = 0°, in plane TE (Y = 500 mm), at various distances normal to the chord line in the -Z direction.

(continued...

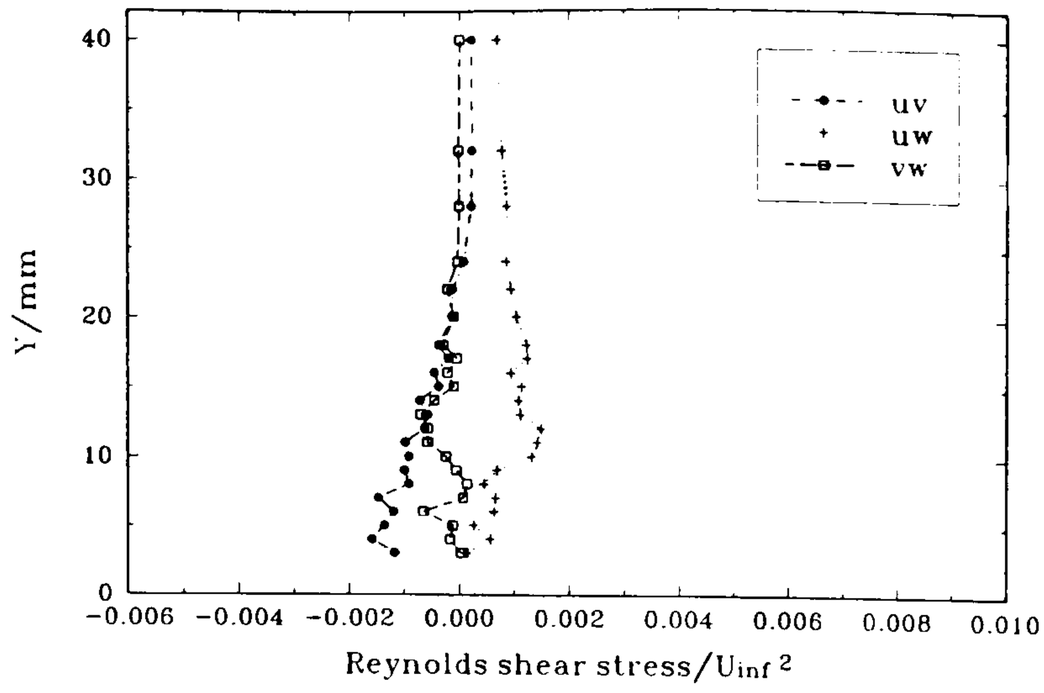

(e) Z = -20 mm

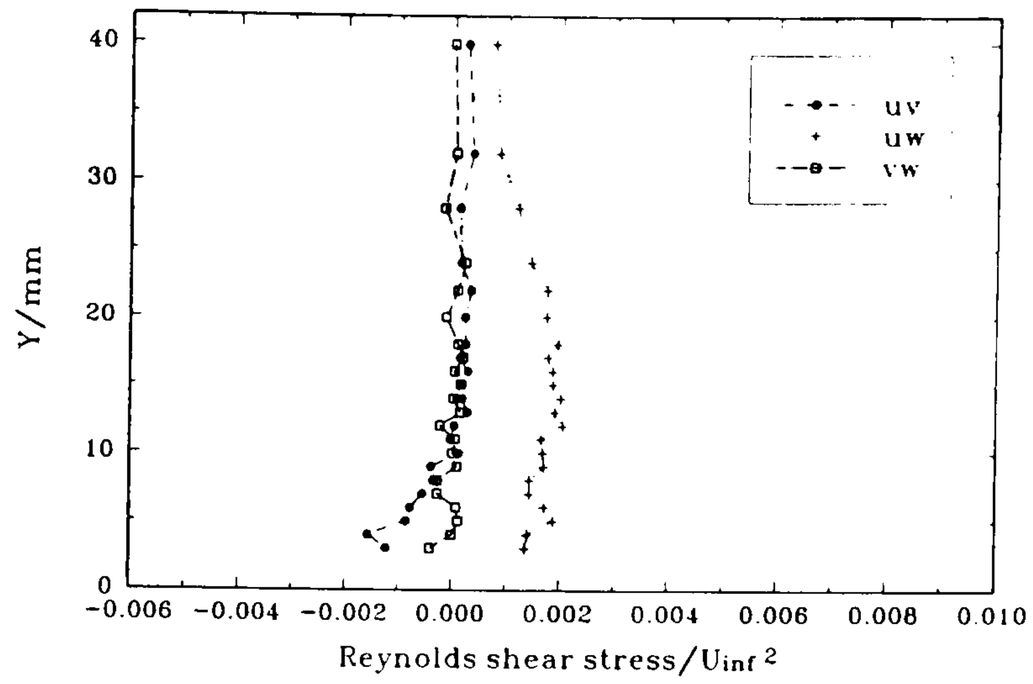

(f) Z = -15 mm

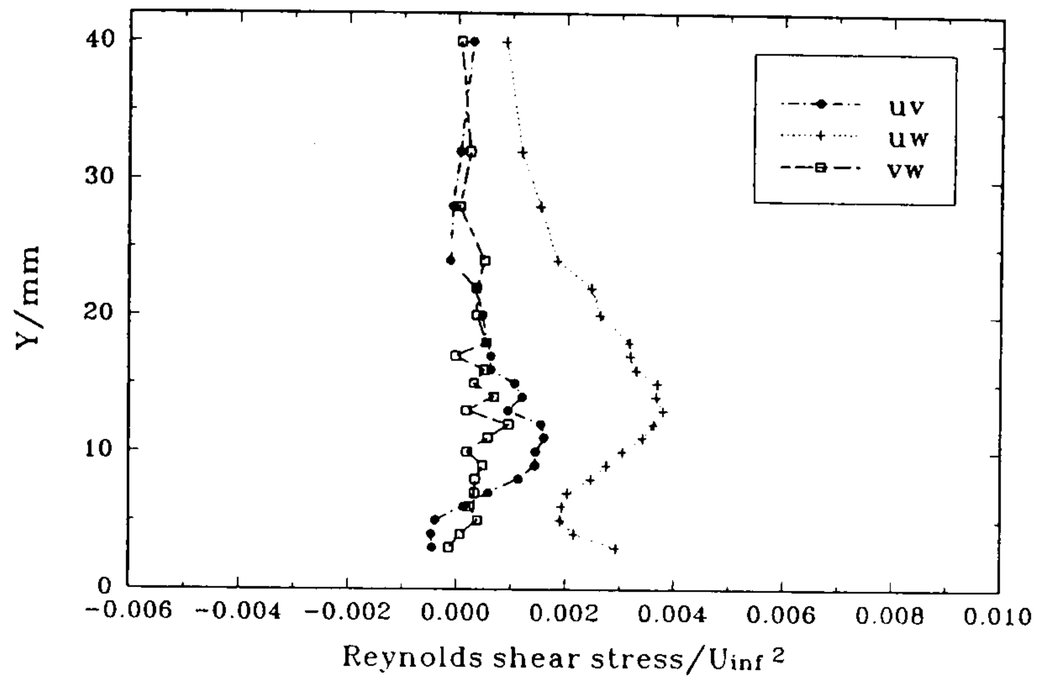

(g) Z = -10 mm

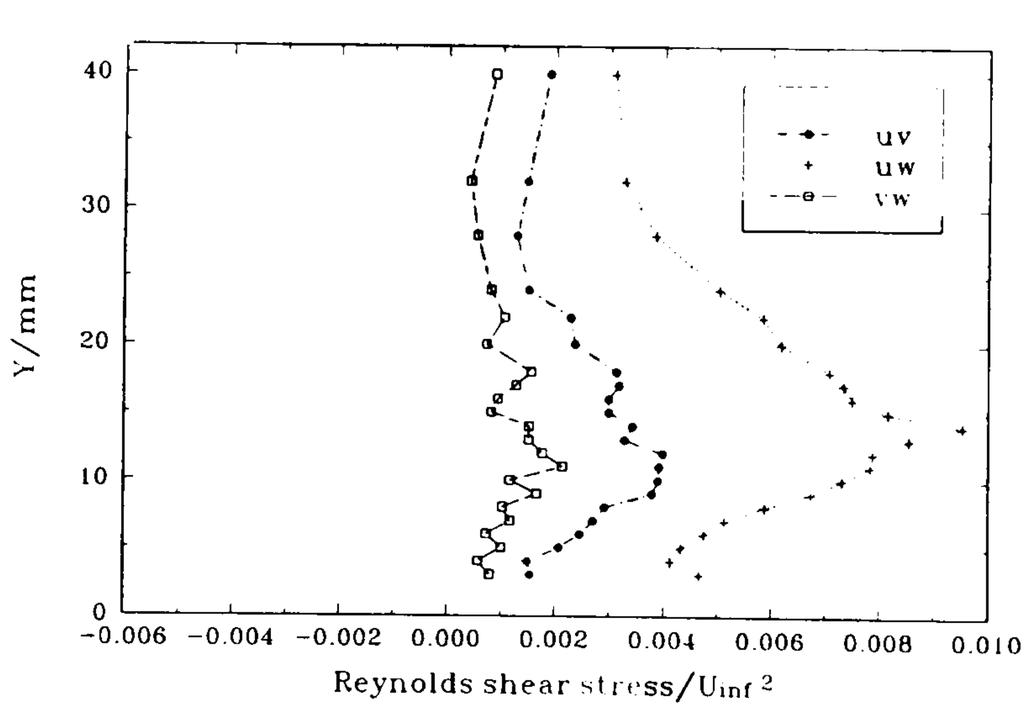

(h) Z = -5 mm

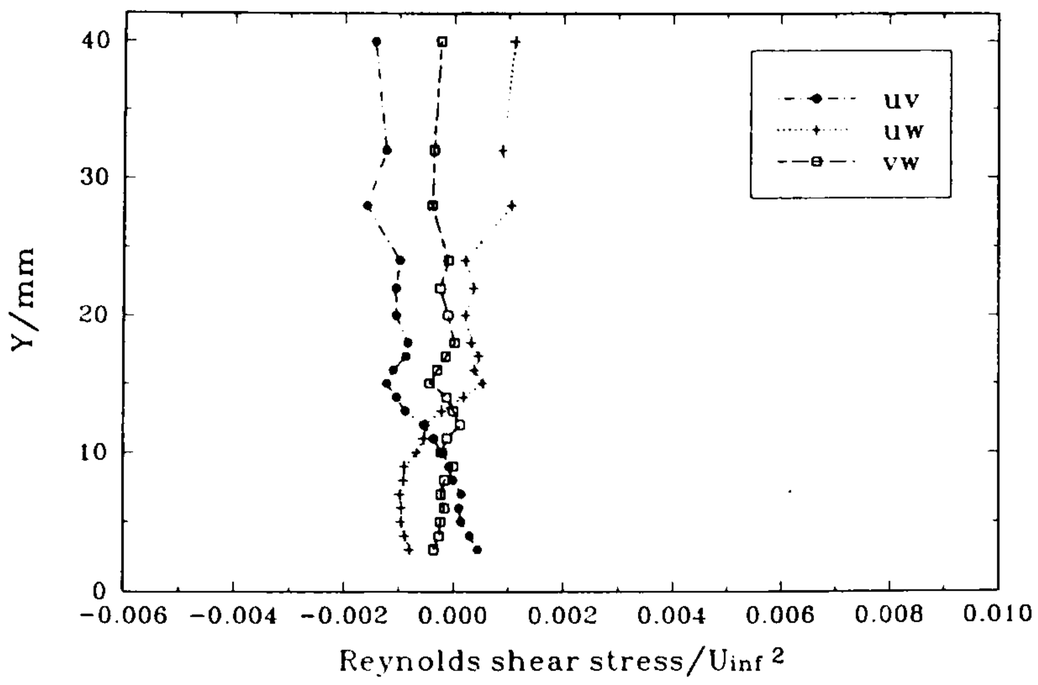

(i) Z = -0 mm

Figure 79 Profiles of $(\overline{uv},\overline{uw},\overline{vw})/U_\infty^2$ through the plate boundary layer at α = 0°, in plane TE (X = 500 mm), at various distances normal to the chord line in the -Z direction.

...concluded)

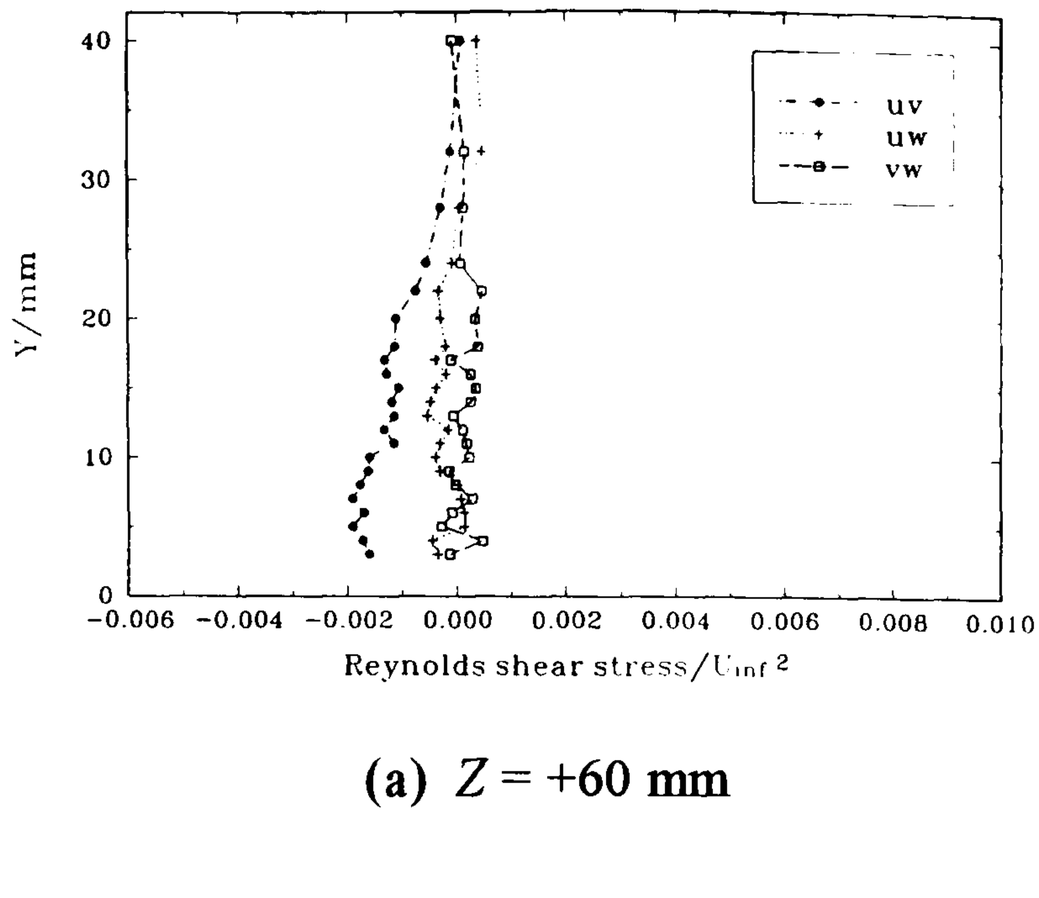

(a) $Z = +60$ mm

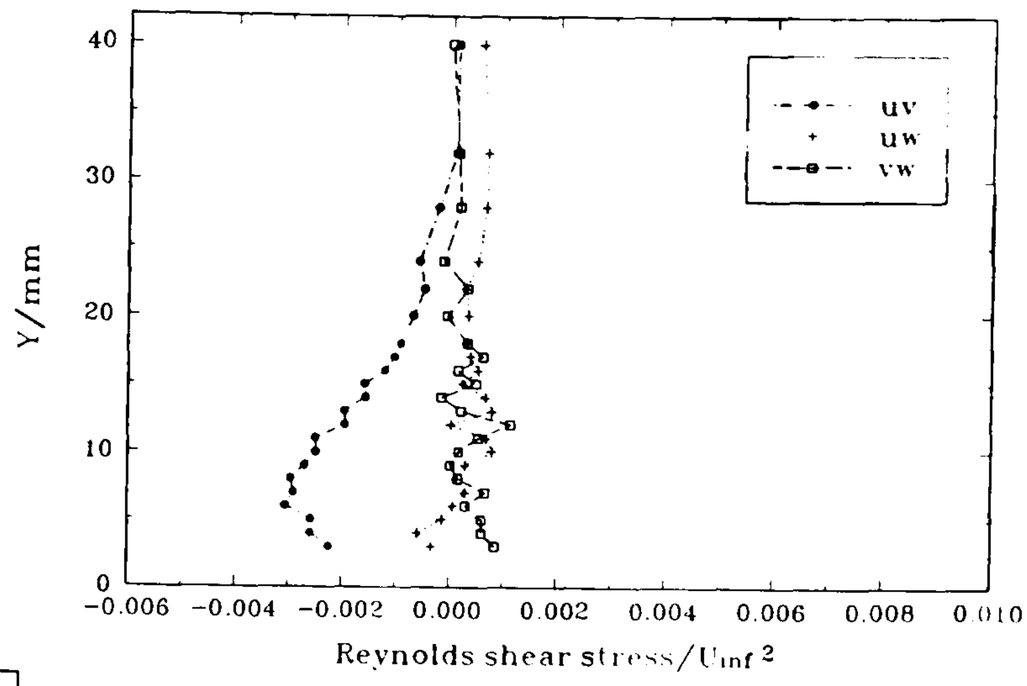

(b) $Z = +40$ mm

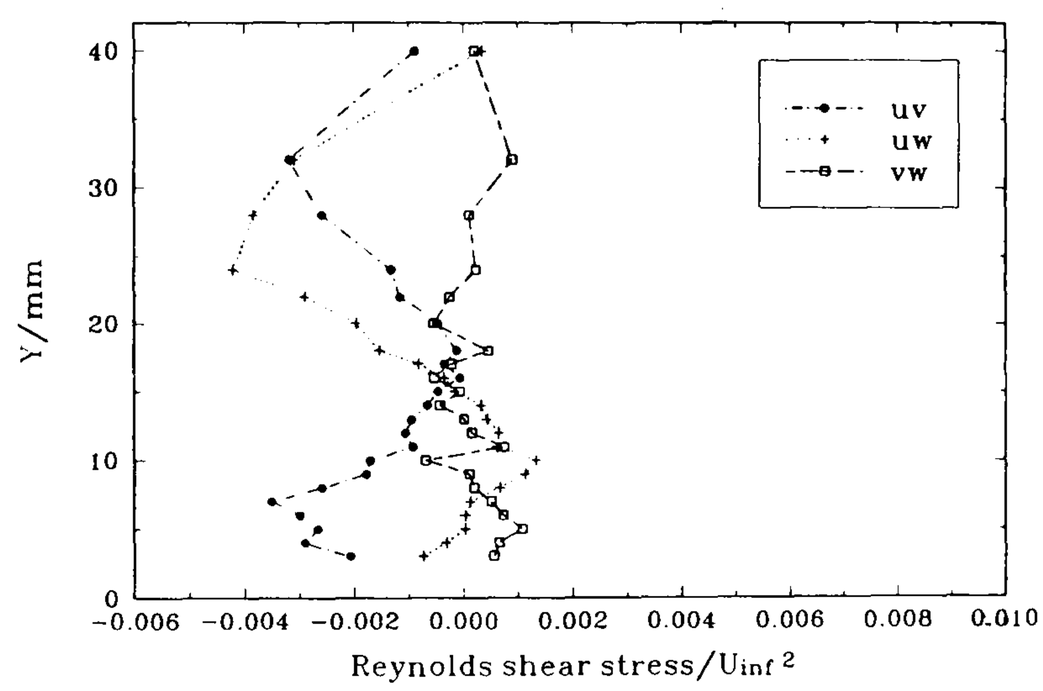

(c) $Z = +30$ mm

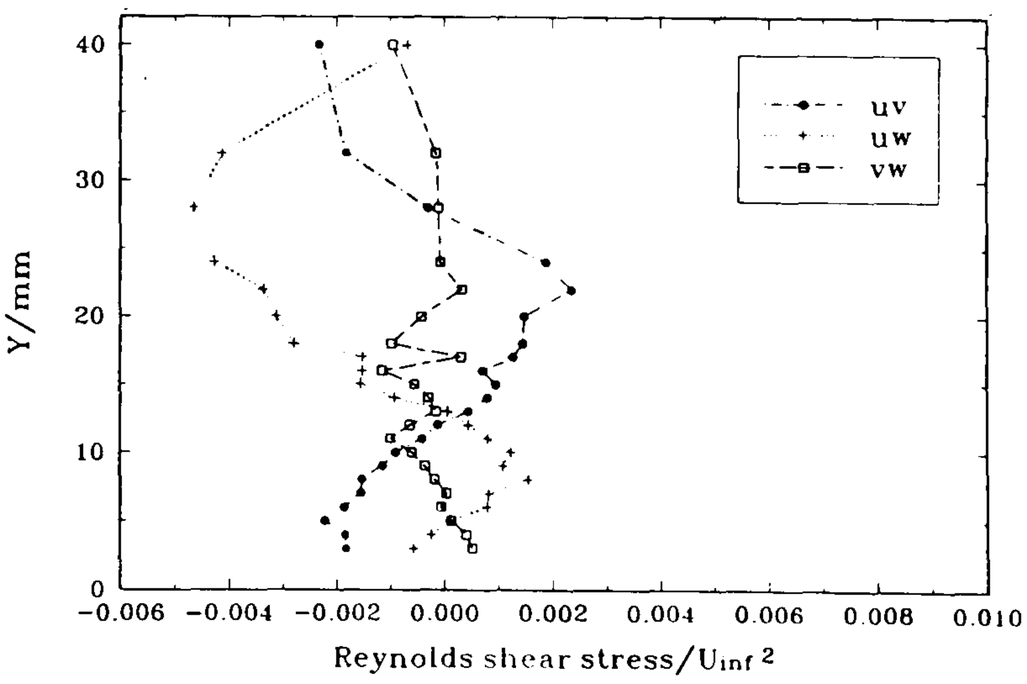

(d) $Z = +25$ mm

Figure 80 Profiles of $(\overline{uv}, \overline{uw}, \overline{vw})/U_\infty^2$ through the plate boundary layer at $\alpha = 0°$, in plane TE ($Y = 500$ mm), at various distances normal to the chord line in the $+Z$ direction.

(continued...

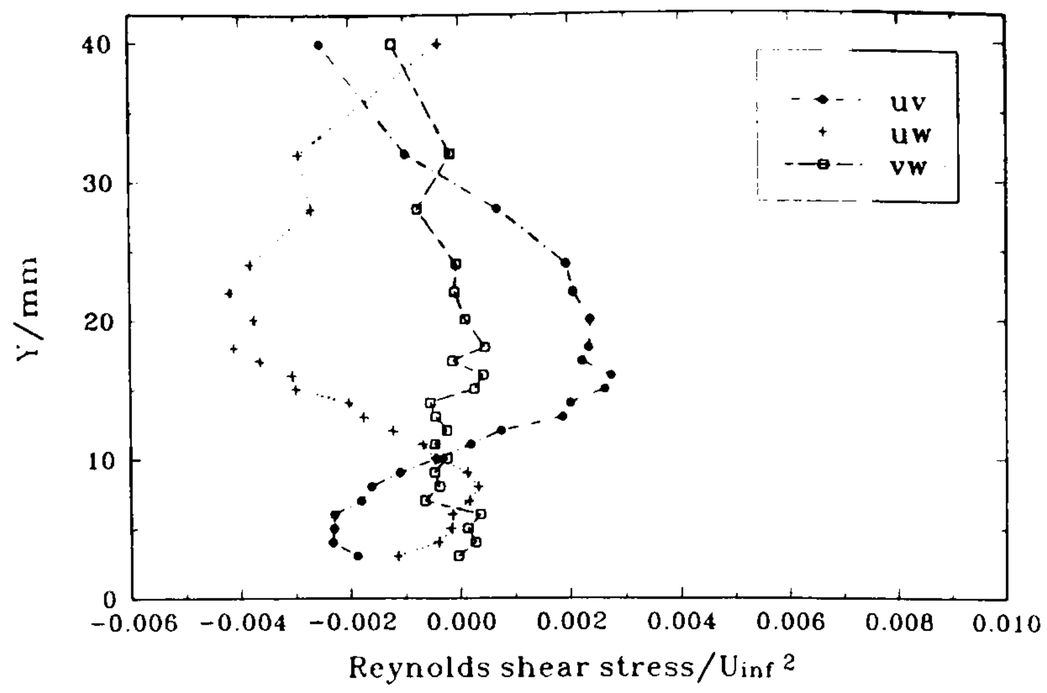

(e) $Z = +20$ mm

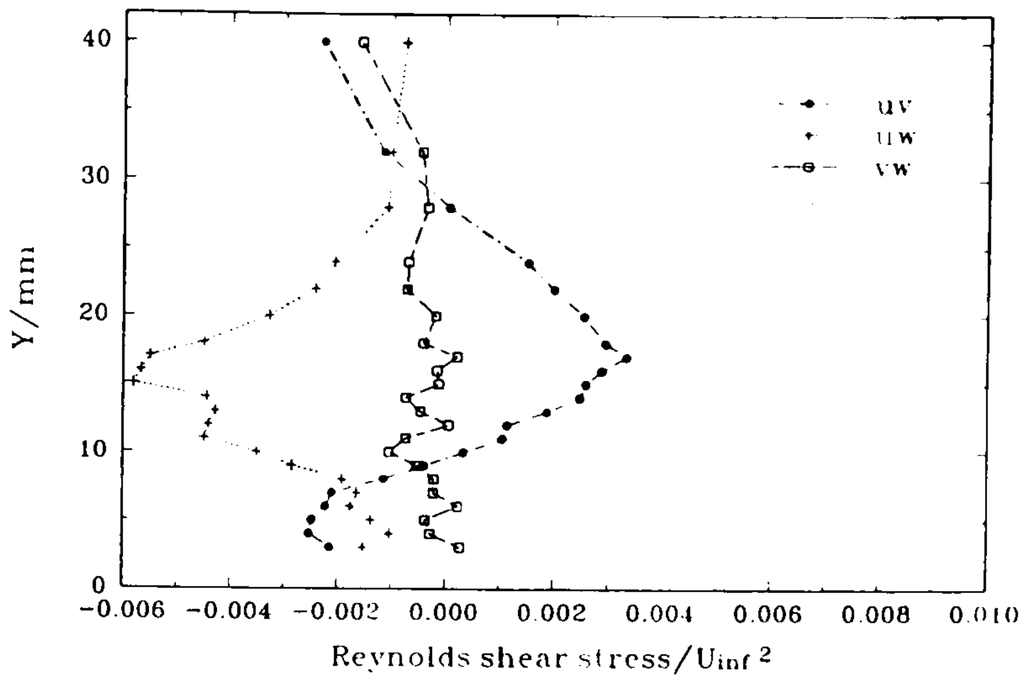

(f) $Z = +15$ mm

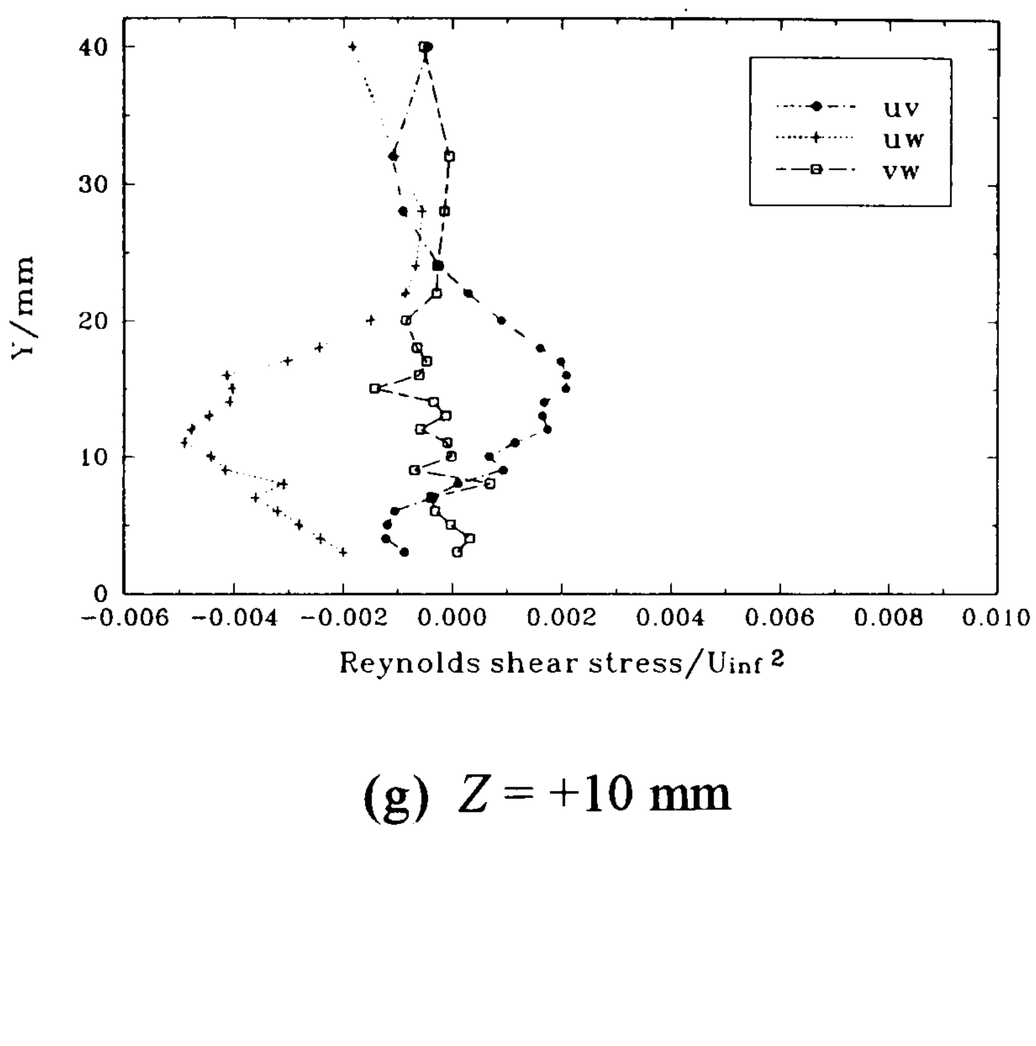

(g) $Z = +10$ mm

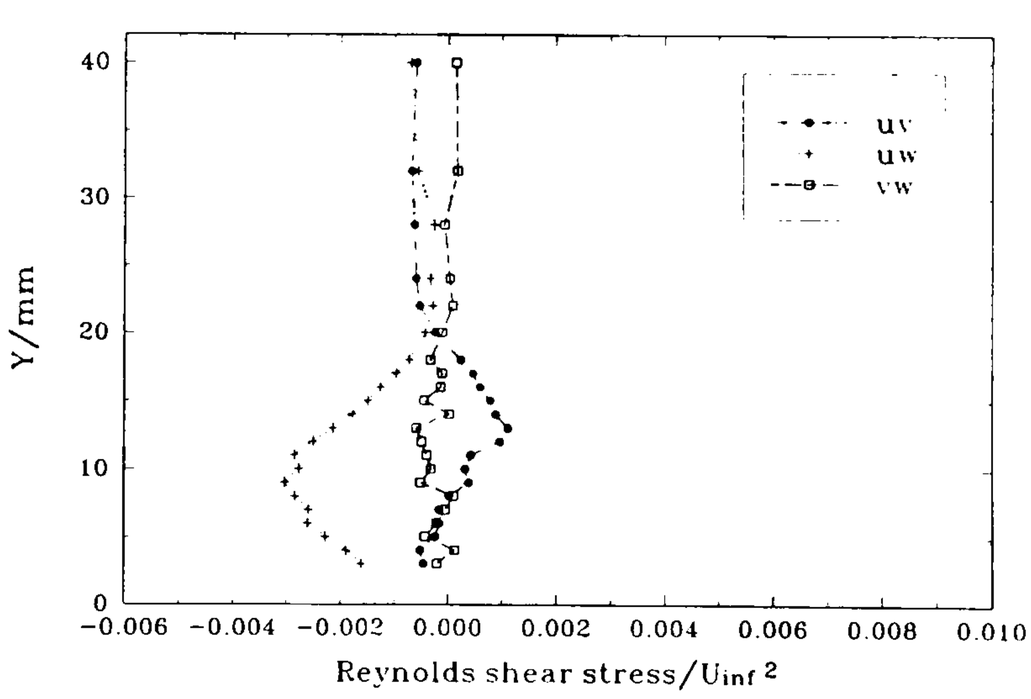

(h) $Z = +5$ mm

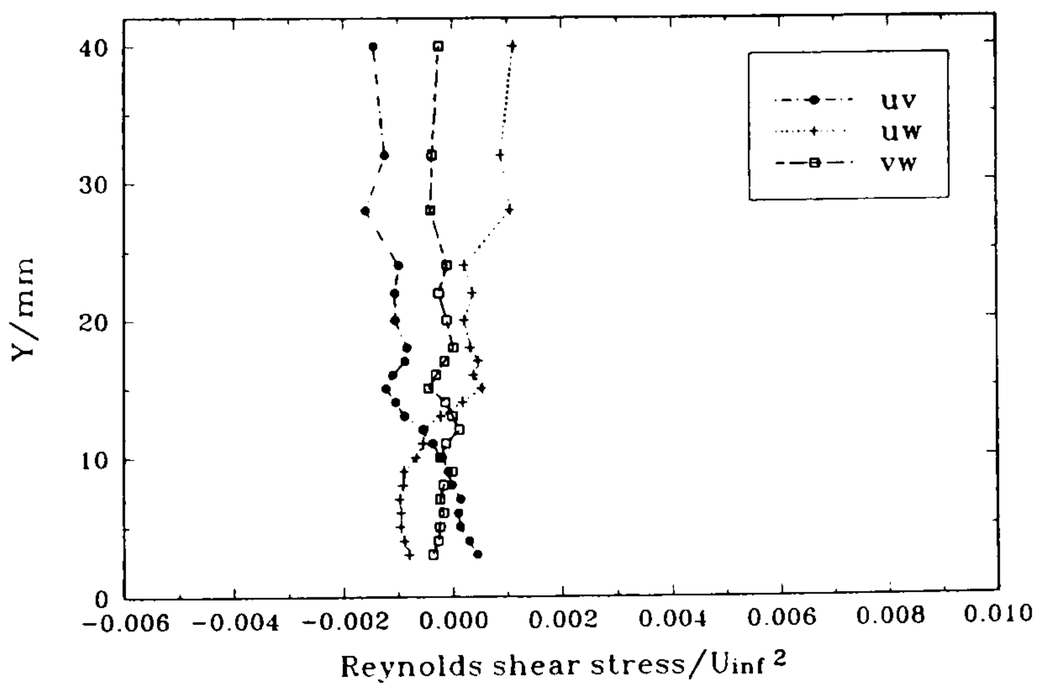

(i) $Z = +0$ mm

Figure 80 Profiles of $(\overline{uv}, \overline{uw}, \overline{vw})/U_\infty^2$ through the plate boundary layer at $\alpha = 0°$, in plane TE ($Y = 500$ mm), at various distances normal to the chord line in the $+Z$ direction.

...concluded)

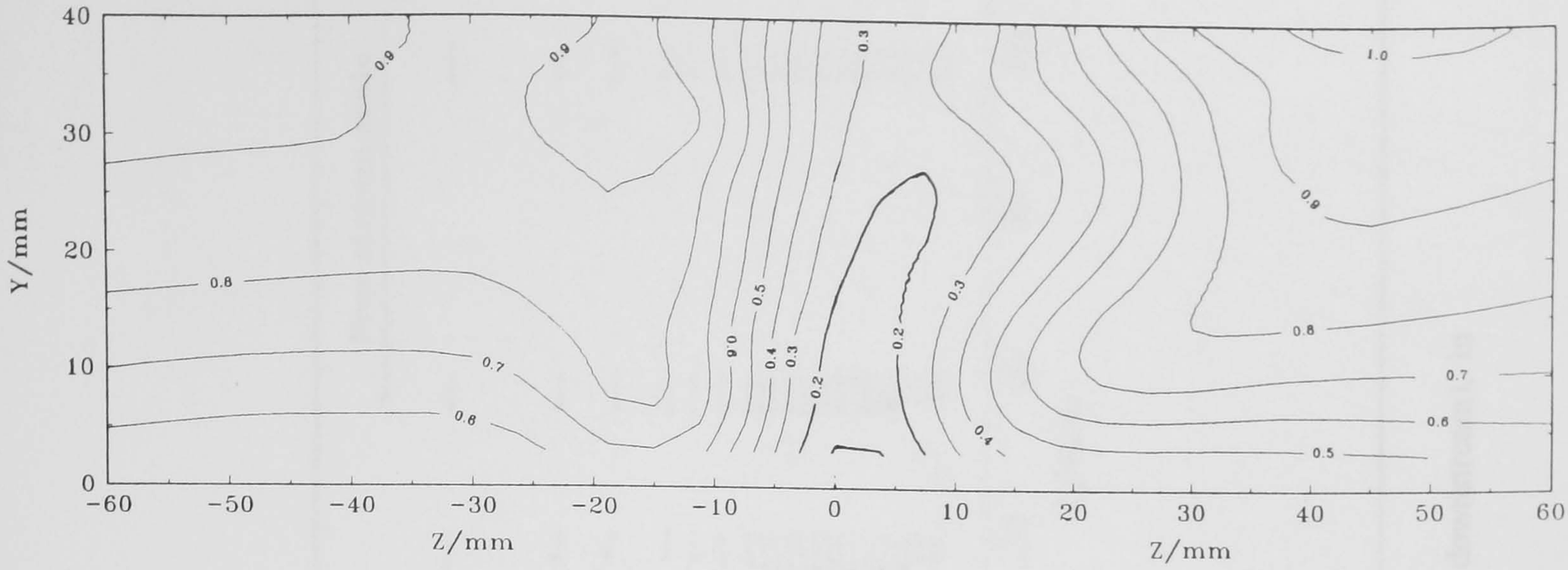

Figure 81 Contours of $\overline{U} / U_\infty$ in the junction at $\alpha = 0°$ (viewed from downstream), in plane TE ($X = 500$ mm).

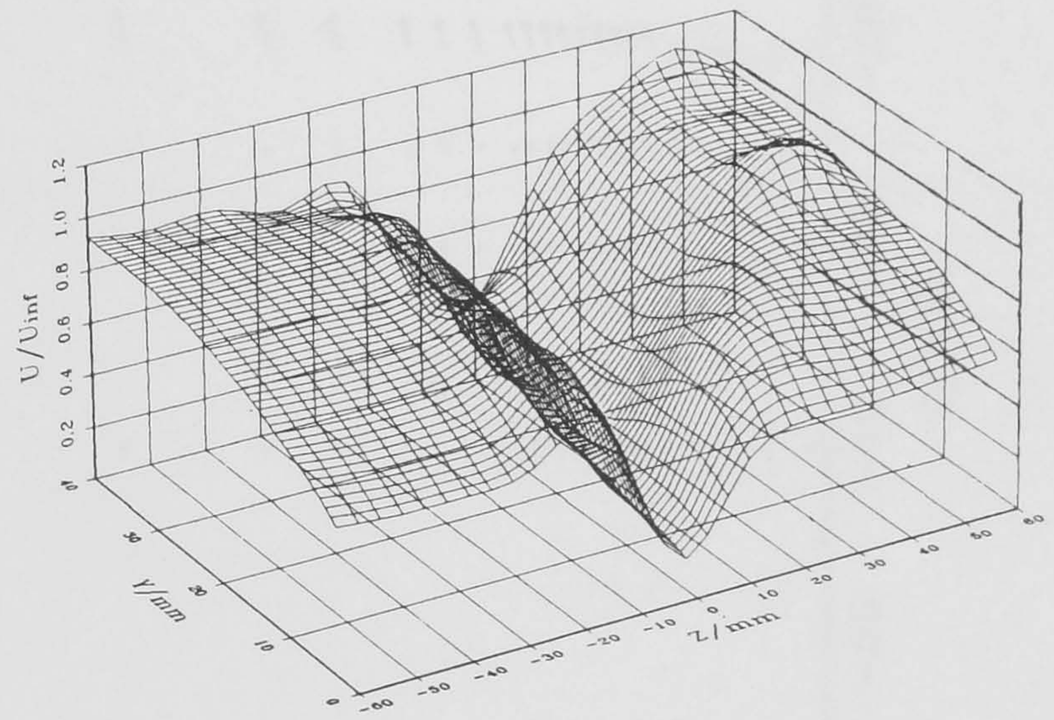

Figure 82 Surface map of $\overline{U} / U_\infty$ in the junction at $\alpha = 0°$, in plane TE ($X = 500$ mm).

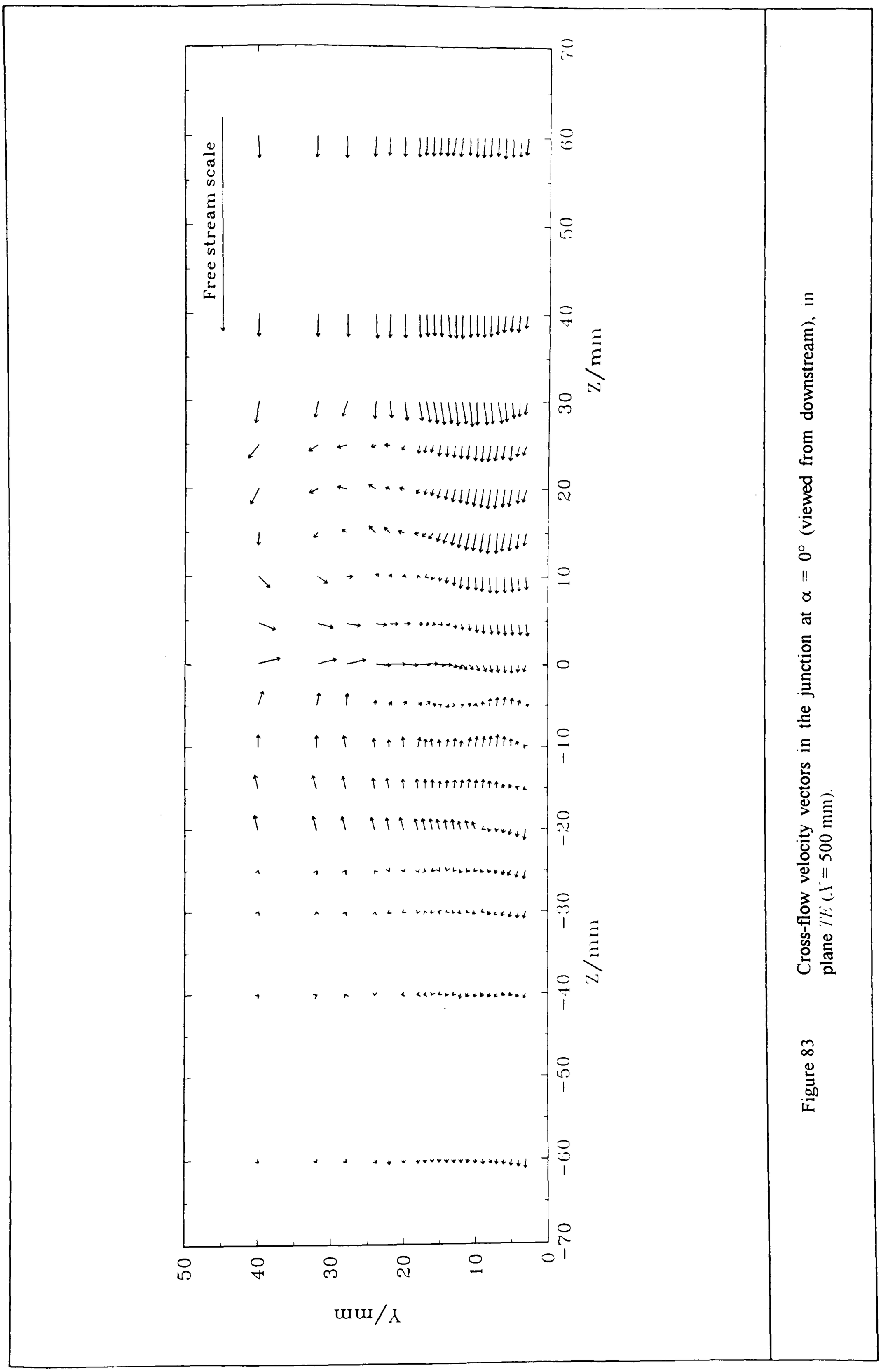

Figure 83 Cross-flow velocity vectors in the junction at $\alpha = 0°$ (viewed from downstream), in plane YE ($X = 500$ mm).

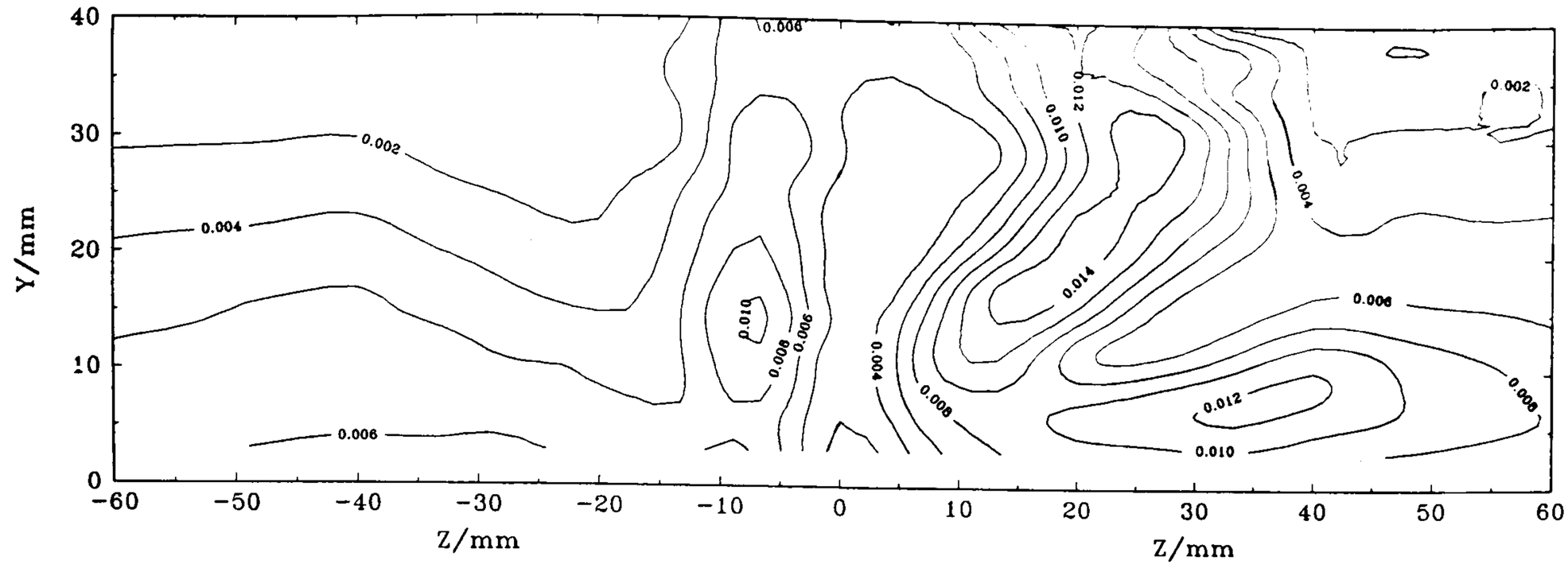

(a) $\overline{u^2}/U_\infty^2$

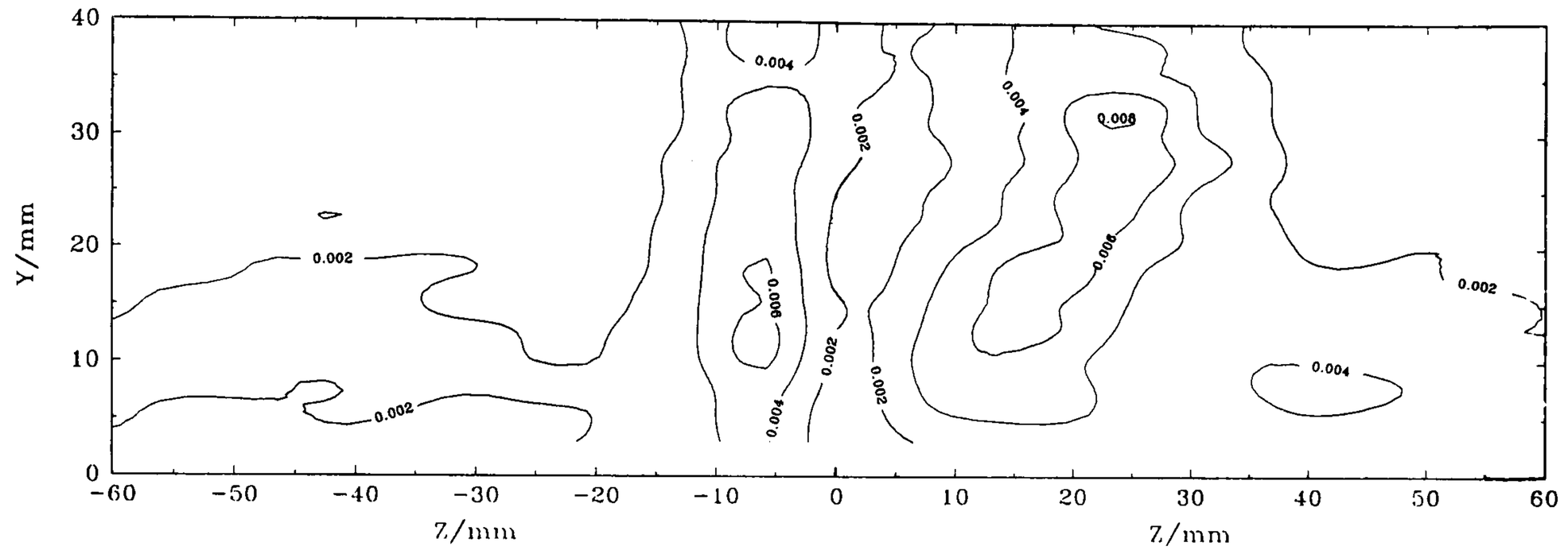

(b) $\overline{v^2}/U_\infty^2$

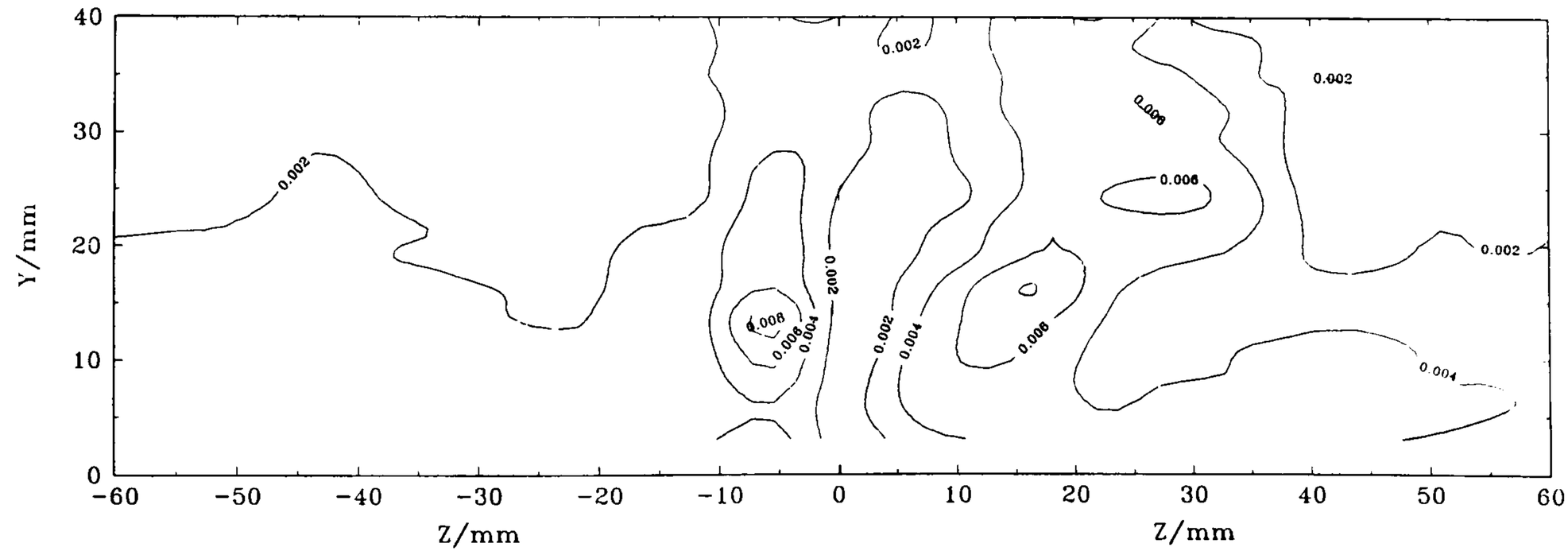

(c) $\overline{w^2}/U_\infty^2$

Figure 84 Contours of $(\overline{u^2}, \overline{v^2}, \overline{w^2})/U_\infty^2$ in the junction at $\alpha = 0°$ (viewed from downstream), in plane *TE* ($X = 500$ mm):
(a) $\overline{u^2}/U_\infty^2$, (b) $\overline{v^2}/U_\infty^2$ & (c) $\overline{w^2}/U_\infty^2$.

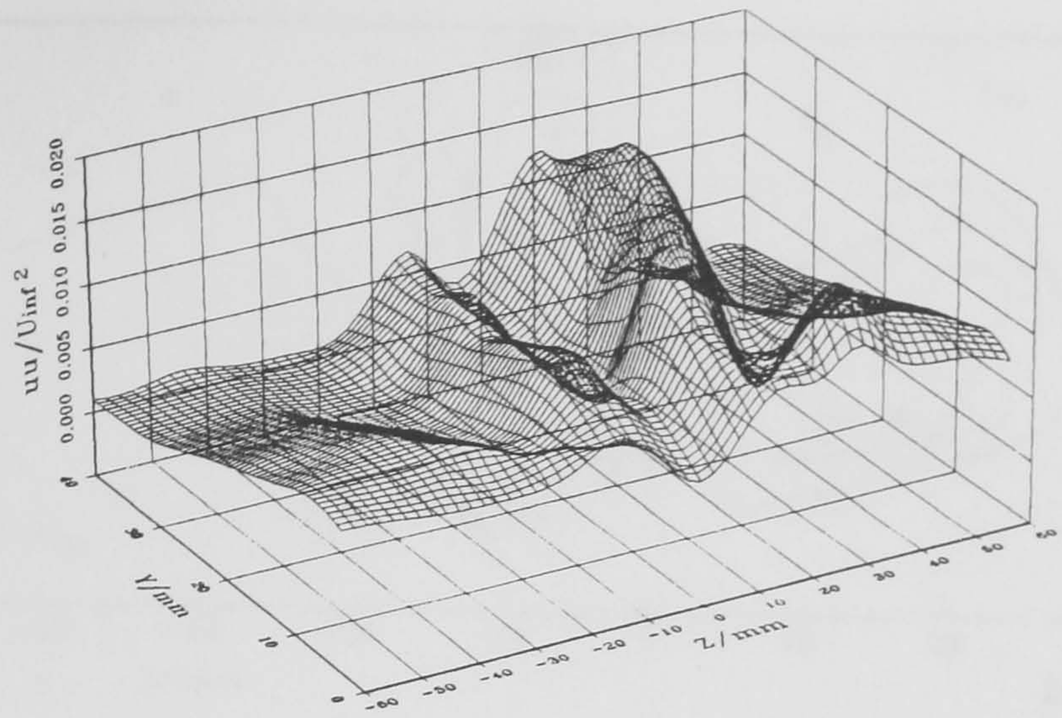

(a) $\overline{u^2}/U_\infty^2$

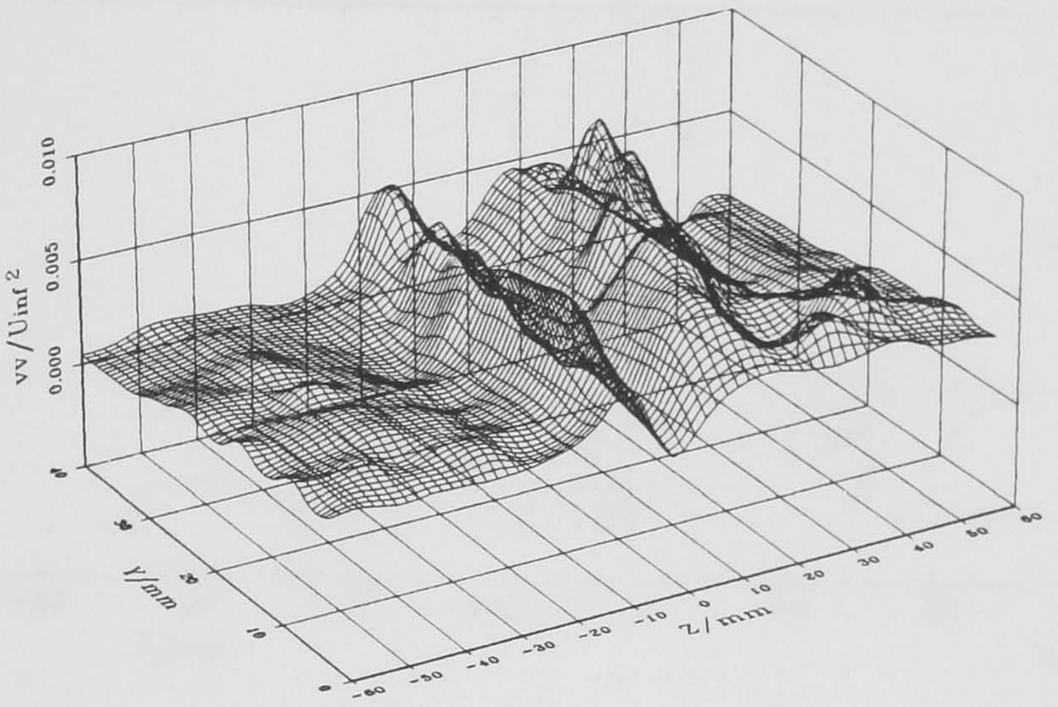

(b) $\overline{v^2}/U_\infty^2$

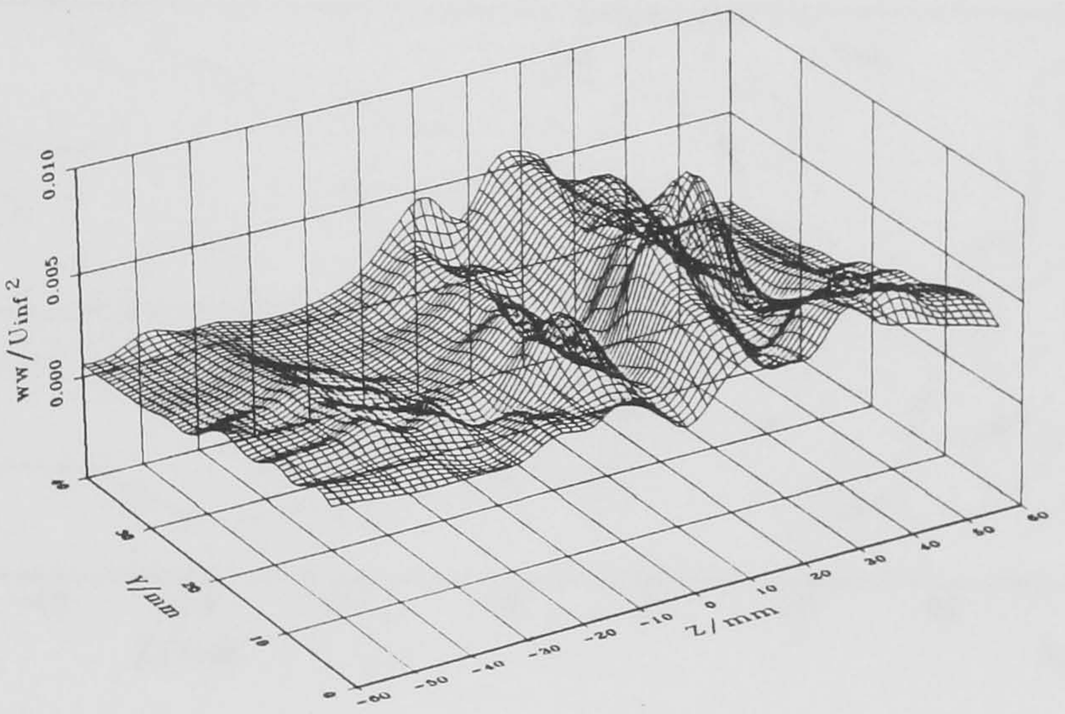

(c) $\overline{w^2}/U_\infty^2$

Figure 85 Surface maps of $(\overline{u^2}, \overline{v^2}, \overline{w^2})/U_\infty^2$ in the junction at $\alpha = 0°$, in plane TE ($X = 500$ mm): (a) $\overline{u^2}/U_\infty^2$, (b) $\overline{v^2}/U_\infty^2$ & (c) $\overline{w^2}/U_\infty^2$.

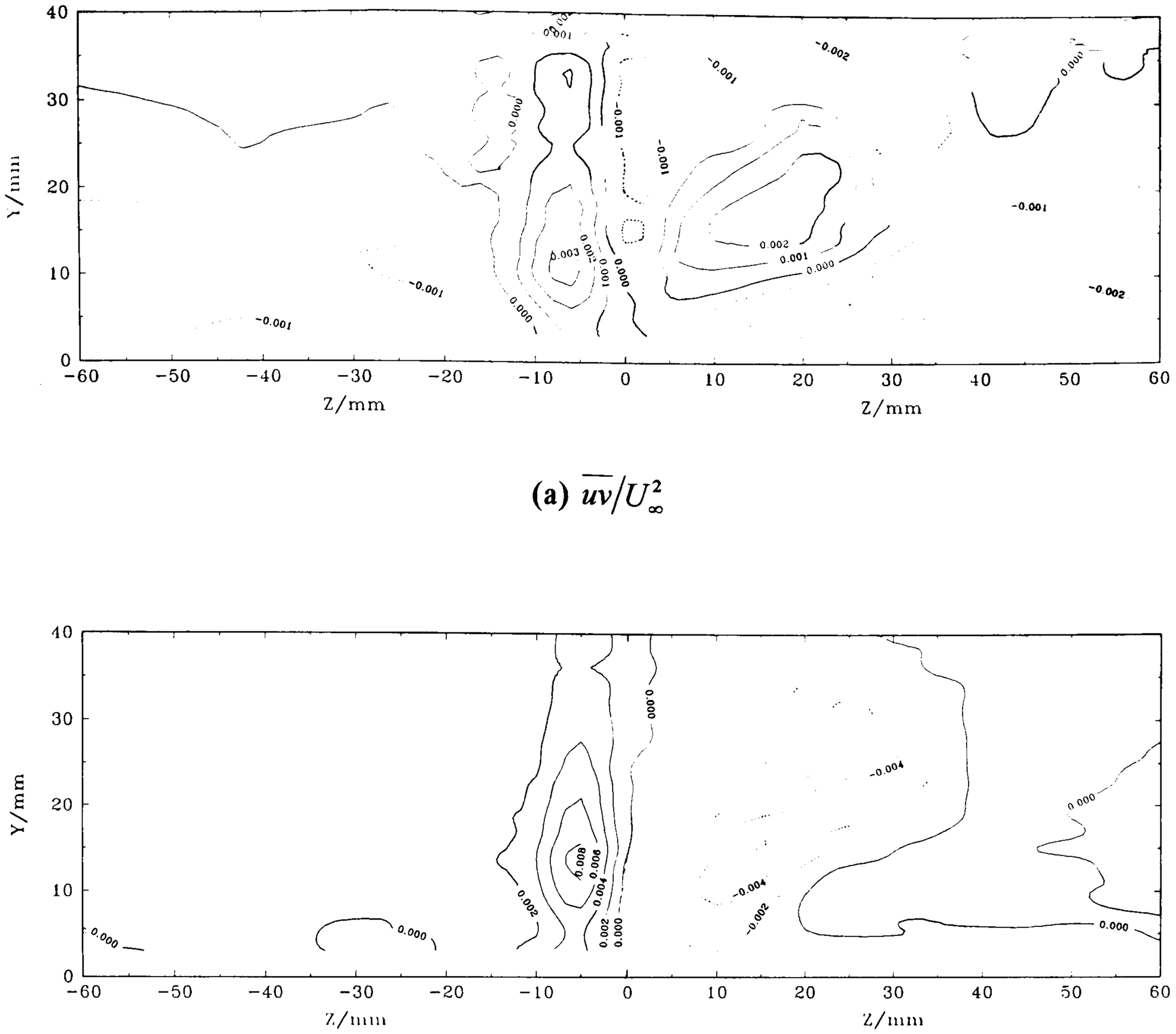

(a) $\overline{uv}/U_\infty^2$

(b) $\overline{uw}/U_\infty^2$

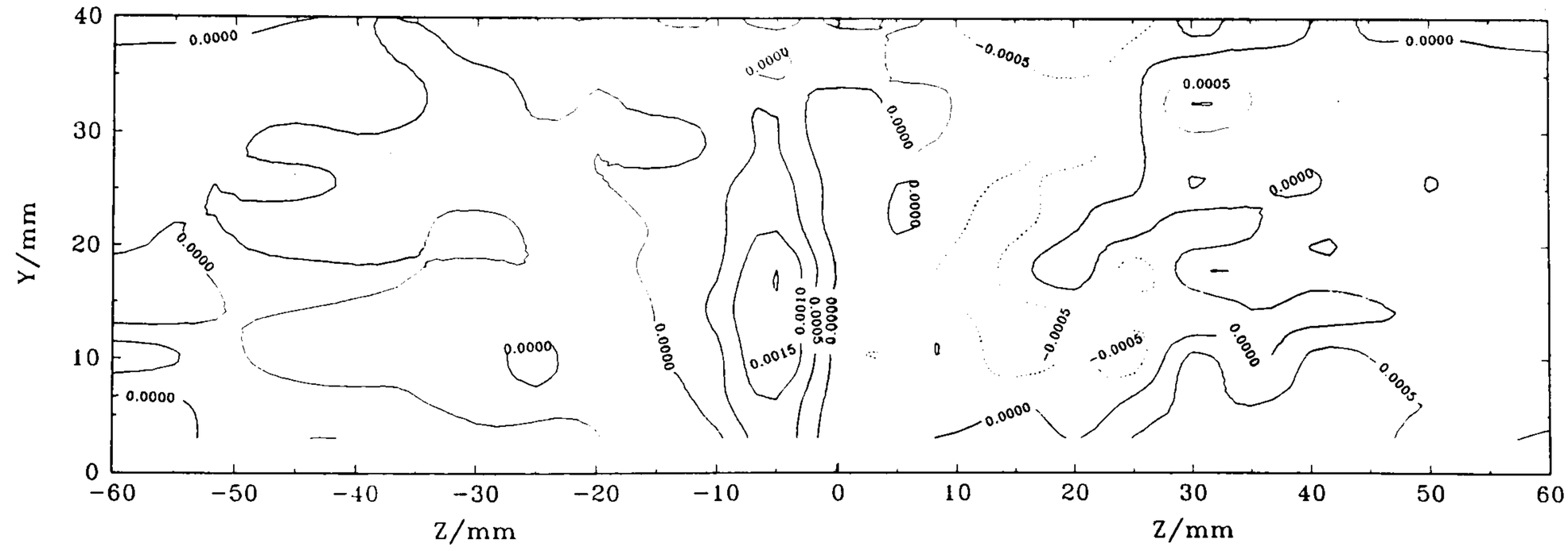

(c) $\overline{vw}/U_\infty^2$

Figure 86 Contours of $(\overline{uv},\overline{uw},\overline{vw})/U_\infty^2$ in the junction at $\alpha = 0°$ (viewed from downstream), in plane *TE* ($X = 500$ mm):
(a) $\overline{uv}/U_\infty^2$, (b) $\overline{uw}/U_\infty^2$ & (c) $\overline{vw}/U_\infty^2$.

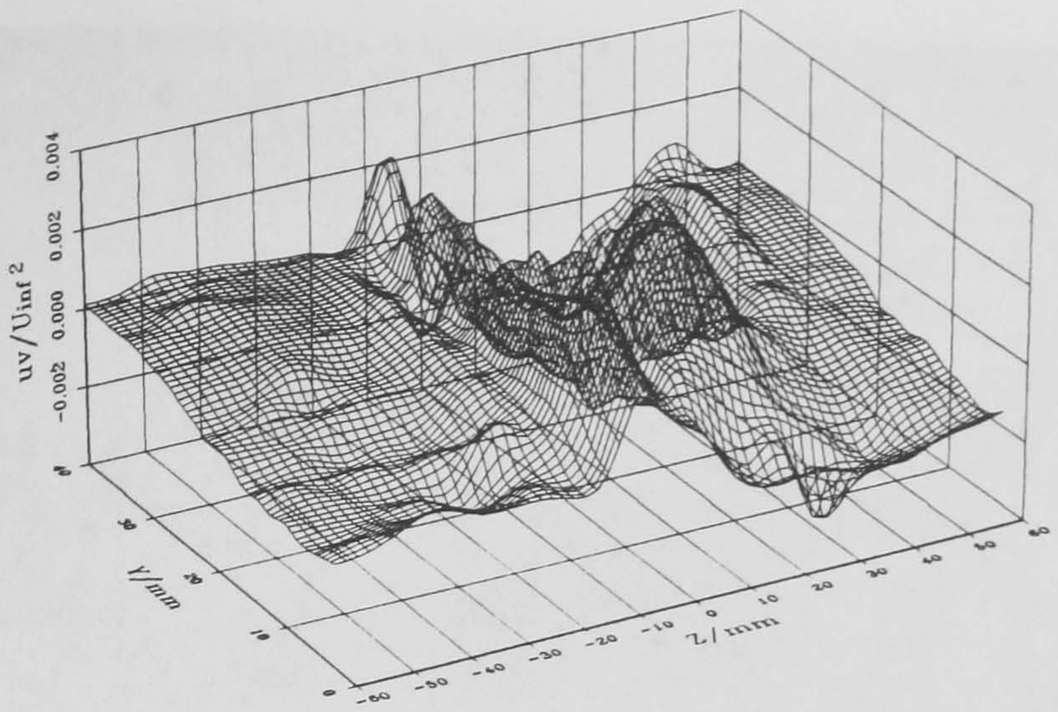

(a) $\overline{uv}/U_\infty^2$

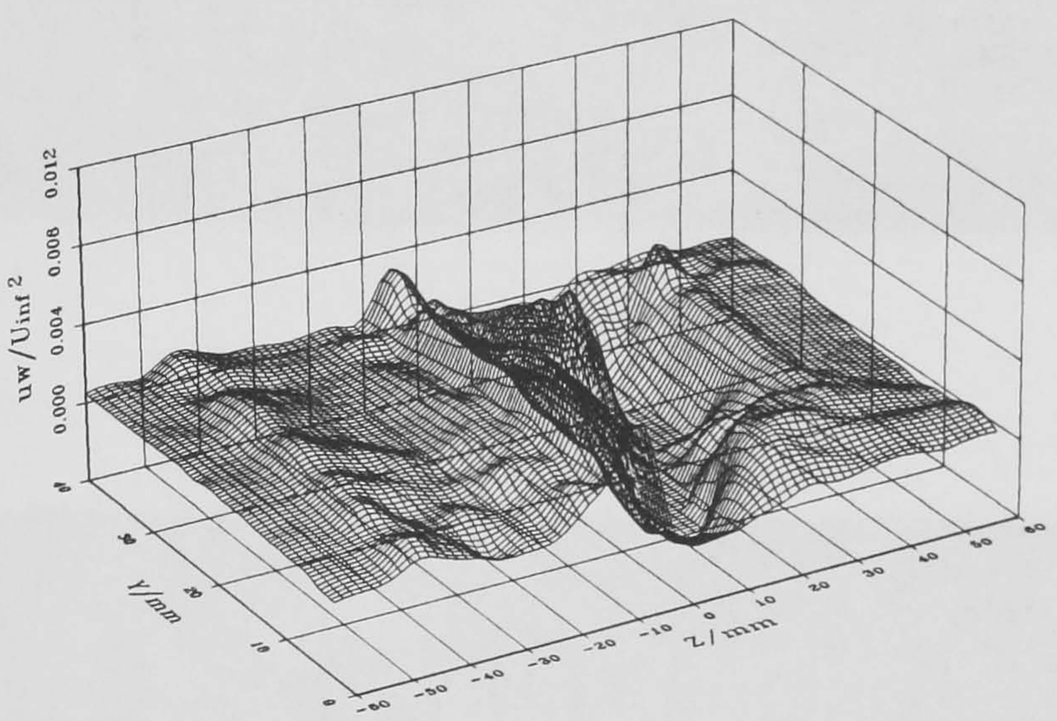

(b) $\overline{uw}/U_\infty^2$

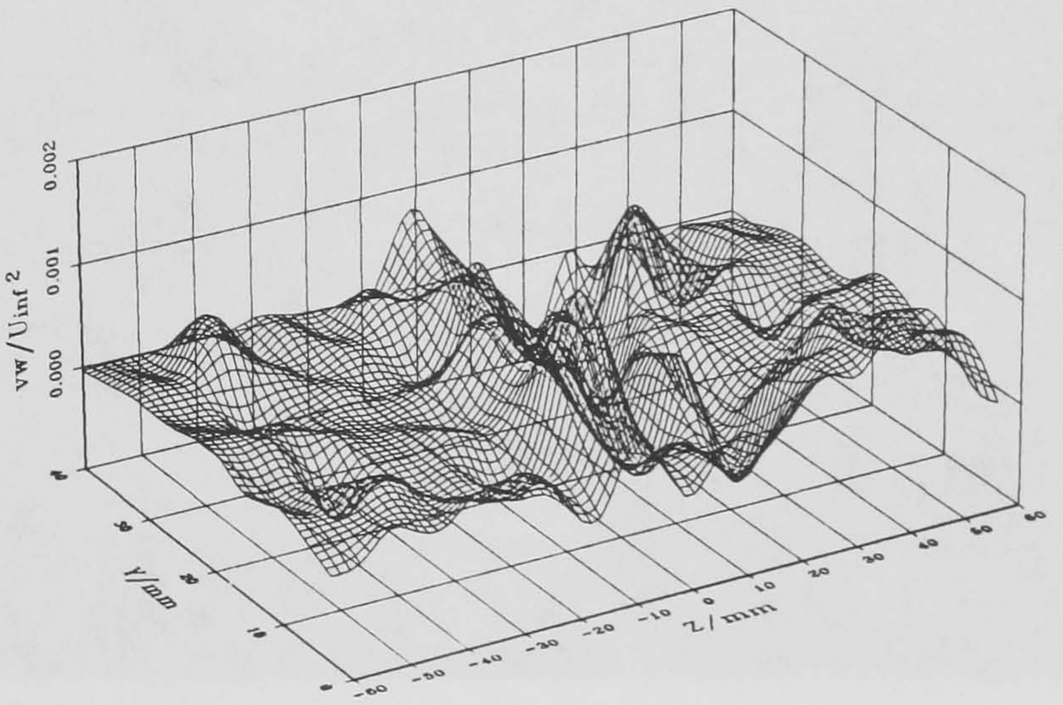

(c) $\overline{vw}/U_\infty^2$

Figure 87 Surface maps of $(\overline{uv}, \overline{uw}, \overline{vw})/U_\infty^2$ in the junction at $\alpha = 0$ in plane *TE* ($X = 500$ mm): (a) $\overline{uv}/U_\infty^2$, (b) $\overline{uw}/U_\infty^2$ & (c) $\overline{vw}/U_\infty^2$.

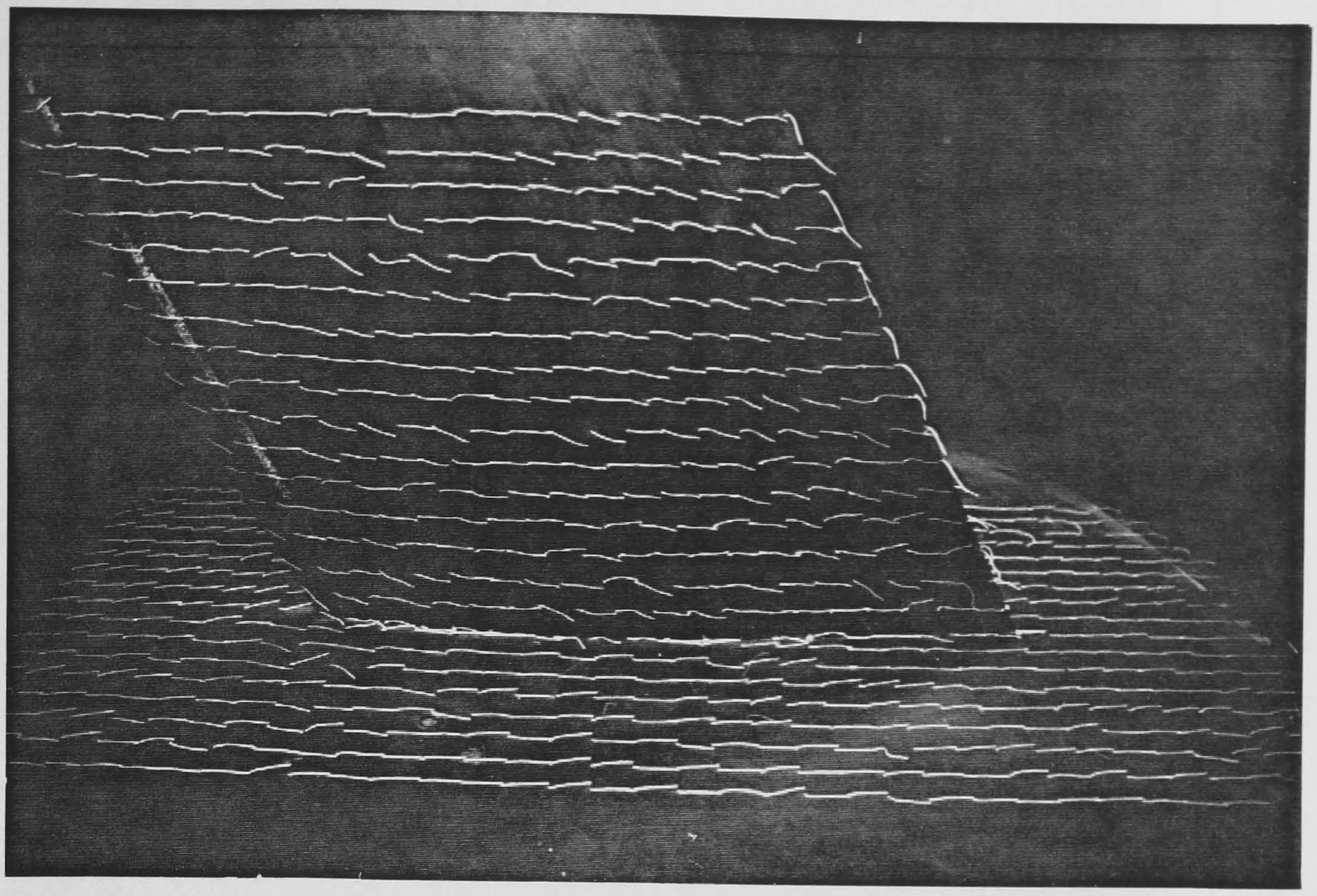

(a)

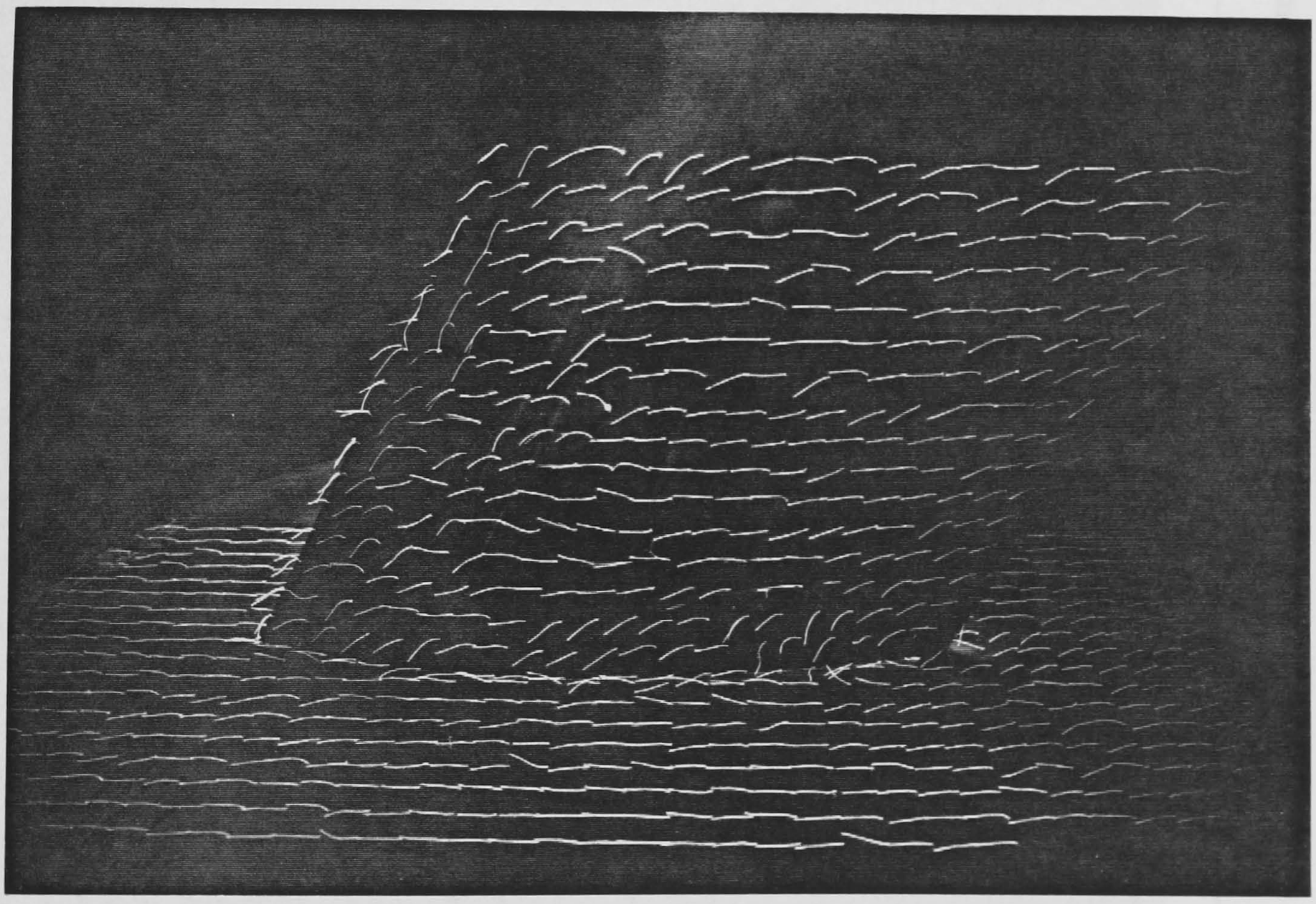

(b)

Plate 1 Orientation of cotton tufts at zero wind speed, on:
(a) wing lower surface and -Z side of the plate &
(b) wing upper surface and +Z side of the plate.

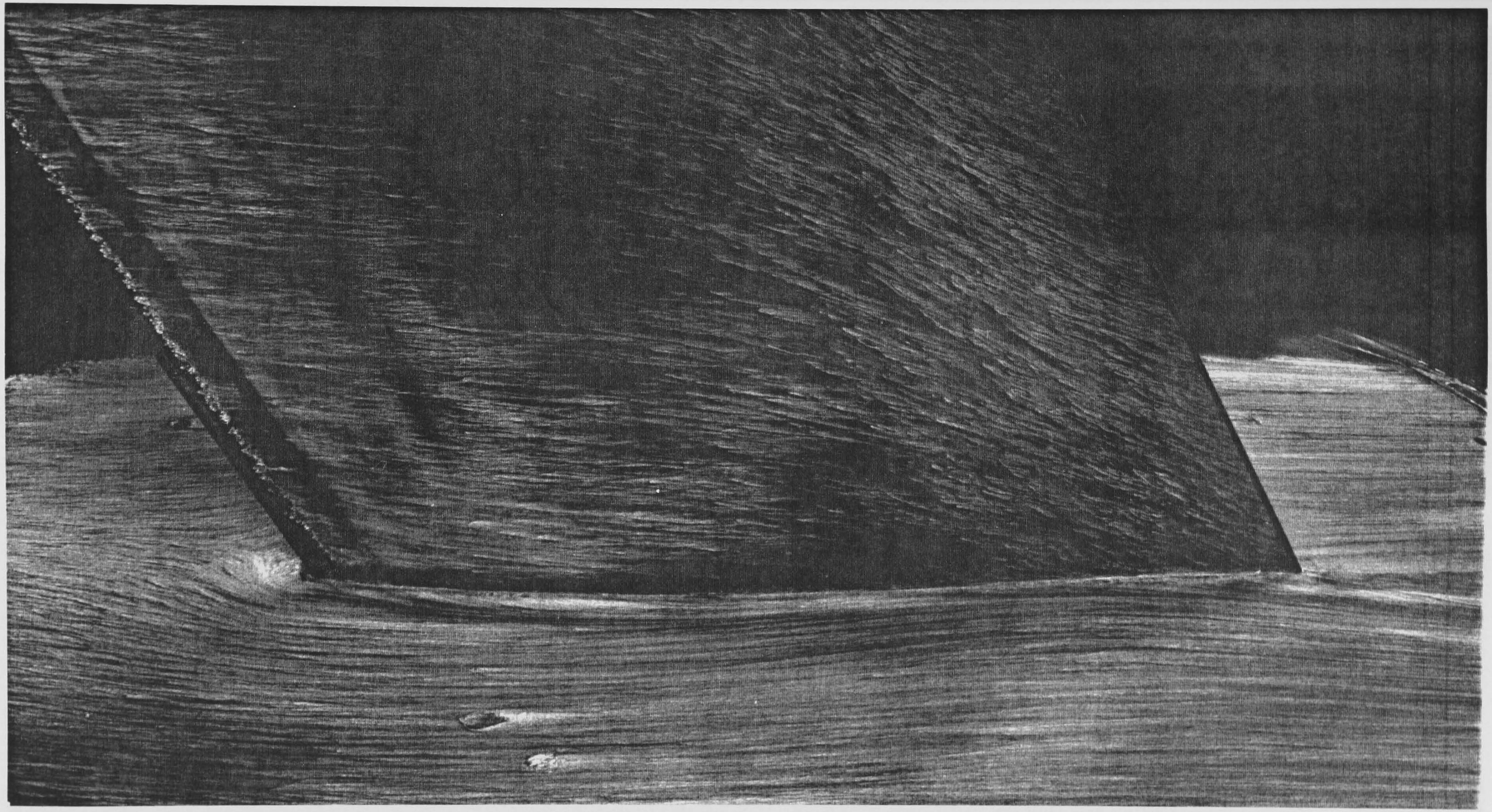

Plate 2(a) Surface oil-flow patterns on the plate and lower surface of the wing at $\alpha = -3°$, free stream from left to right.

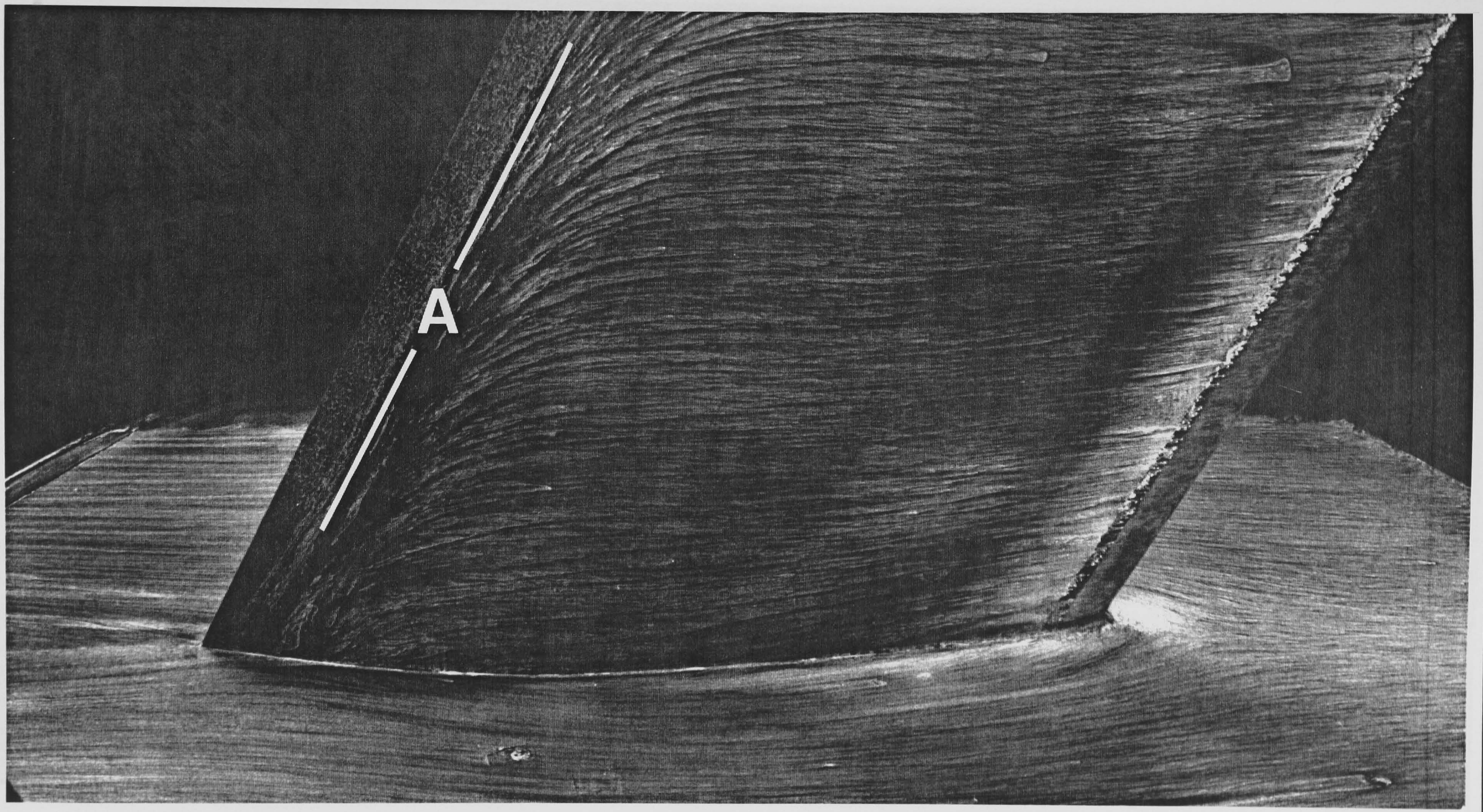

Plate 2(b) Surface oil-flow patterns on the plate and upper surface of the wing at $\alpha = -3°$, free stream from right to left.

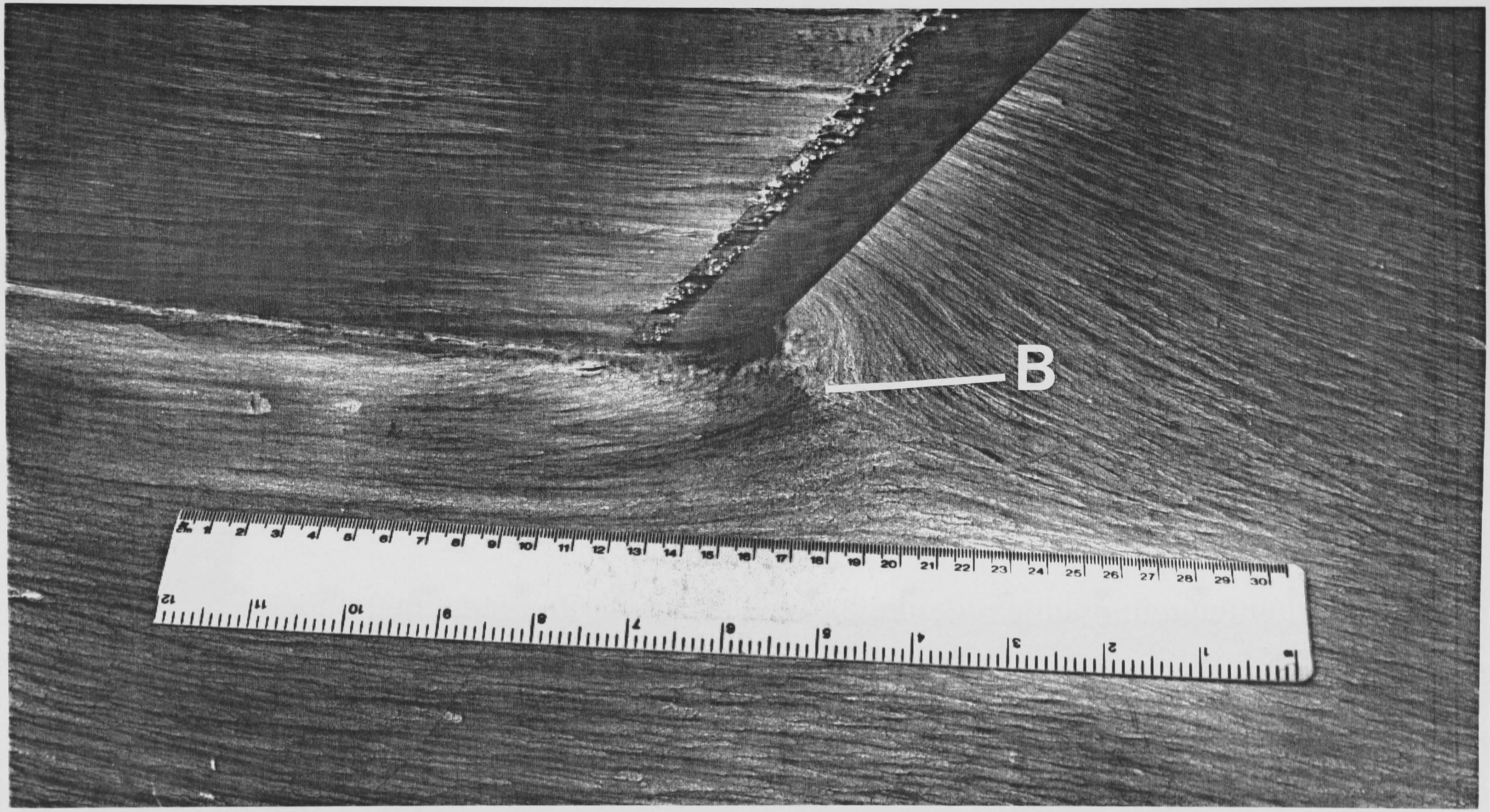

Plate 2(c) Surface oil-flow patterns around the leading edge of the junction at $\alpha = -3°$, viewed from the +Z side of the junction, free stream from right to left.

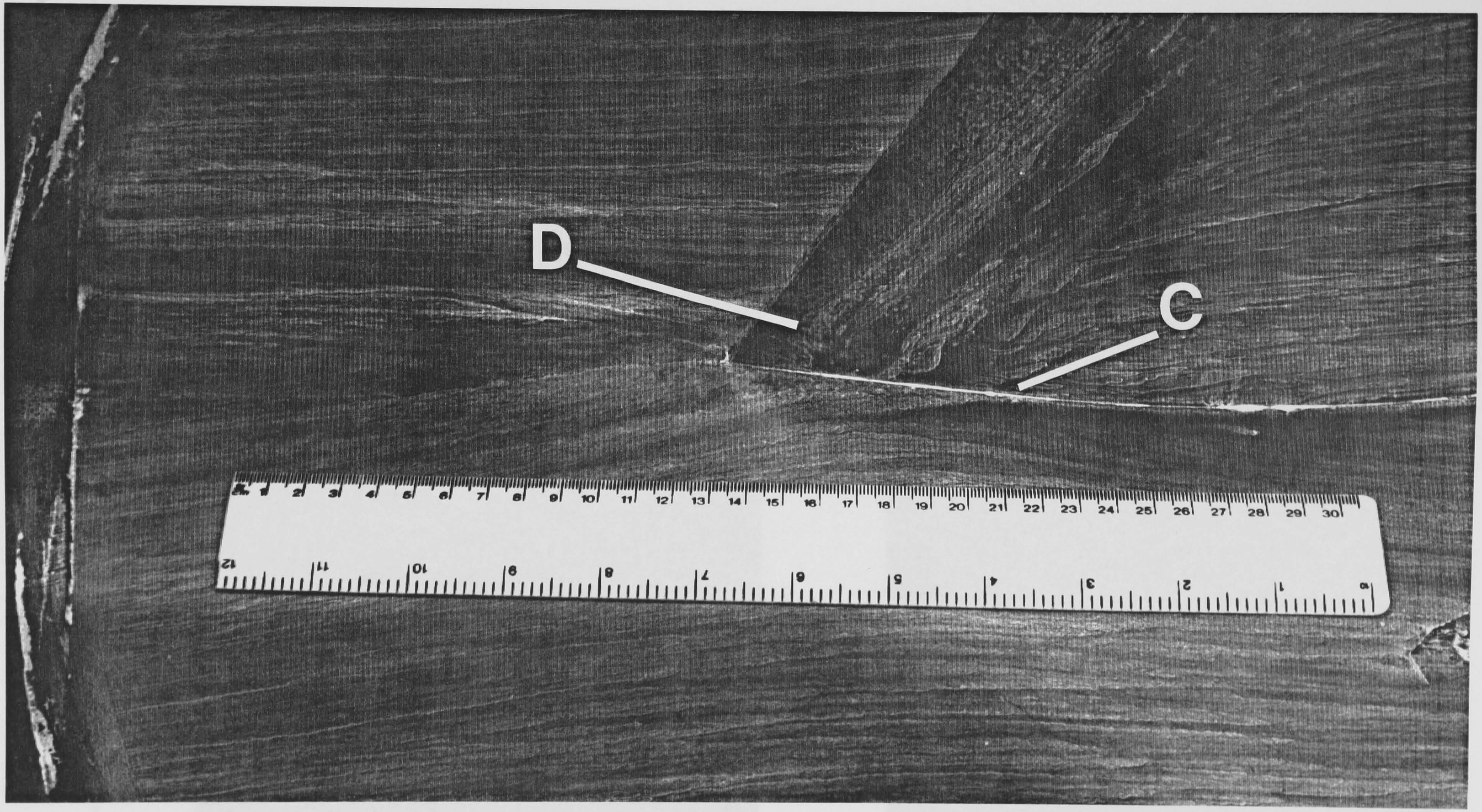

Plate 2(d) Surface oil-flow patterns in the trailing edge region at $\alpha = -3°$, viewed from the +Z side of the junction, free stream from right to left.

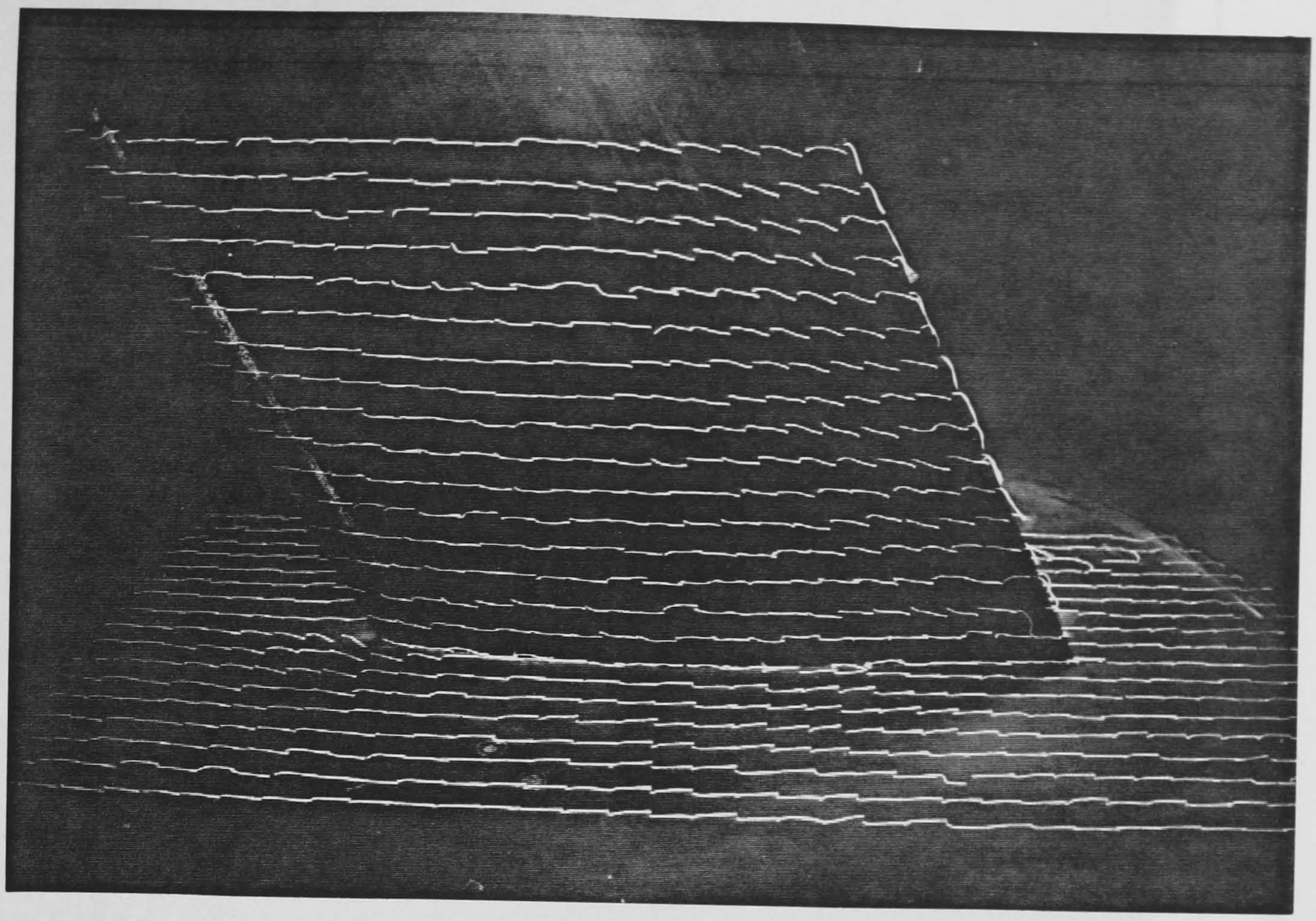

(i)

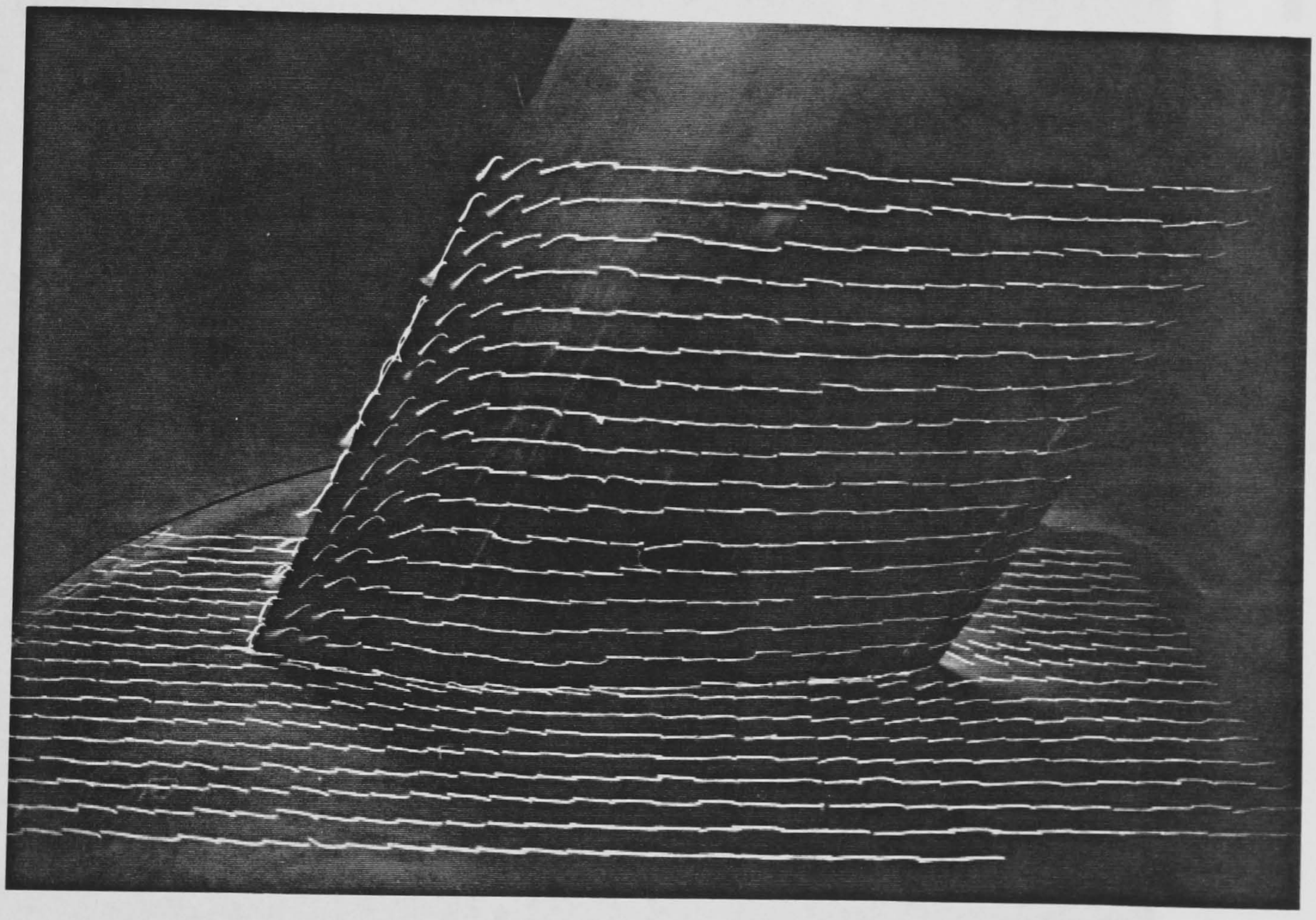

(ii)

Plate 2(e) Tuft behaviour at $\alpha = -3°$ on:
(i) wing lower surface and $-Z$ side of the plate &
(ii) wing upper surface and $+Z$ side of the plate.

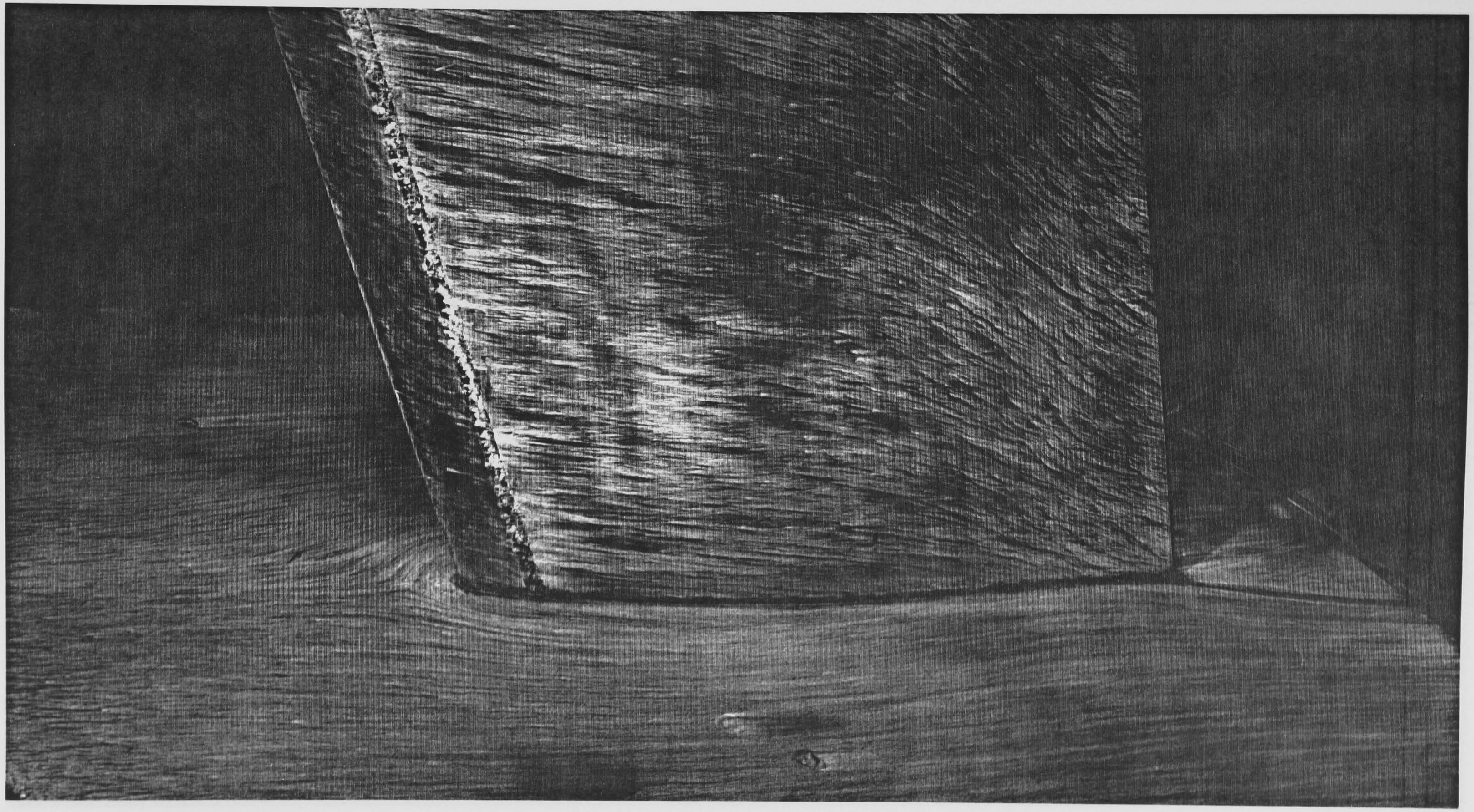

Plate 3(a) Surface oil-flow patterns on the plate and lower surface of the wing at $\alpha = 0°$, free stream from left to right.

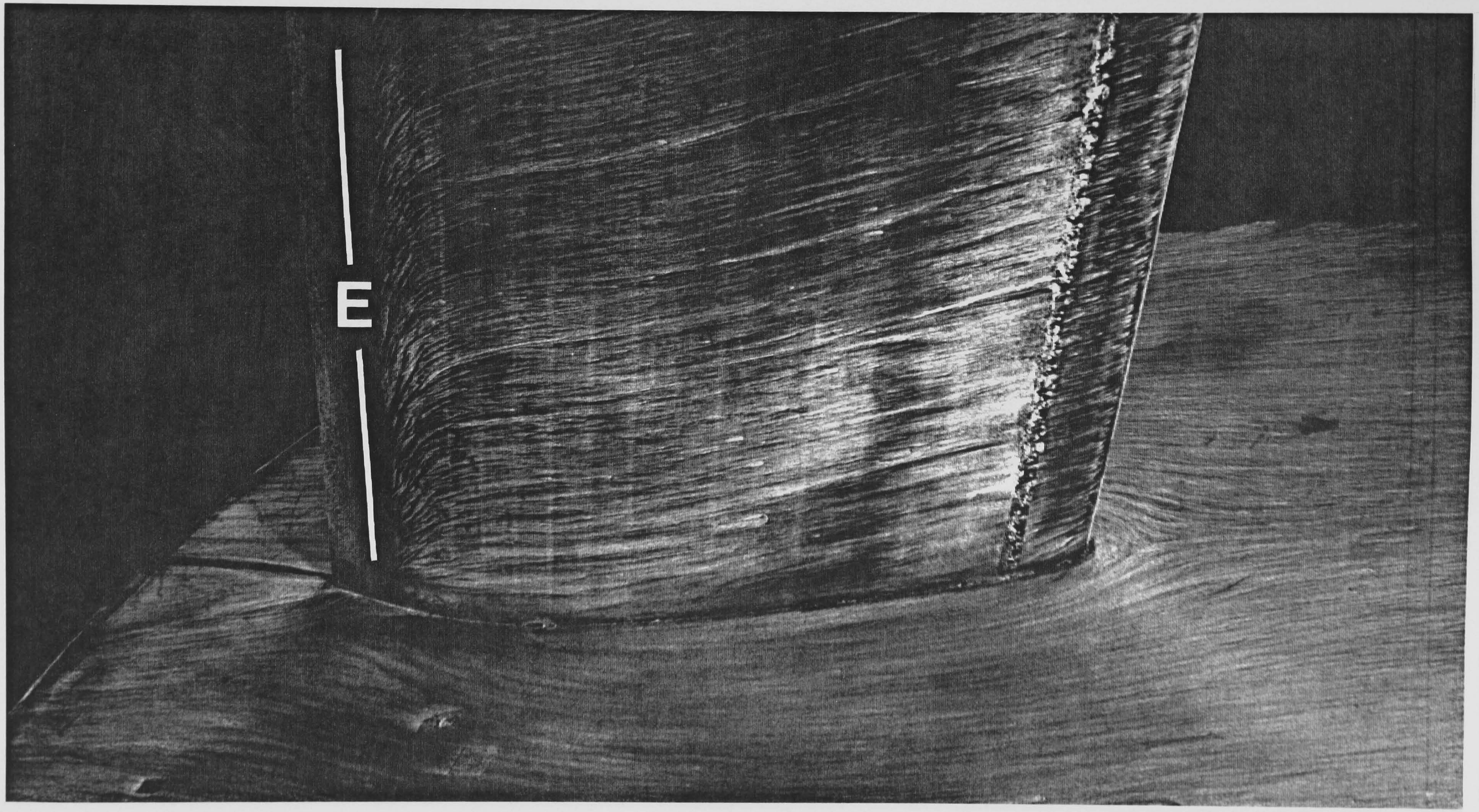

Plate 3(b) Surface oil-flow patterns on the plate and upper surface of the wing at $\alpha = 0°$, free stream from right to left.

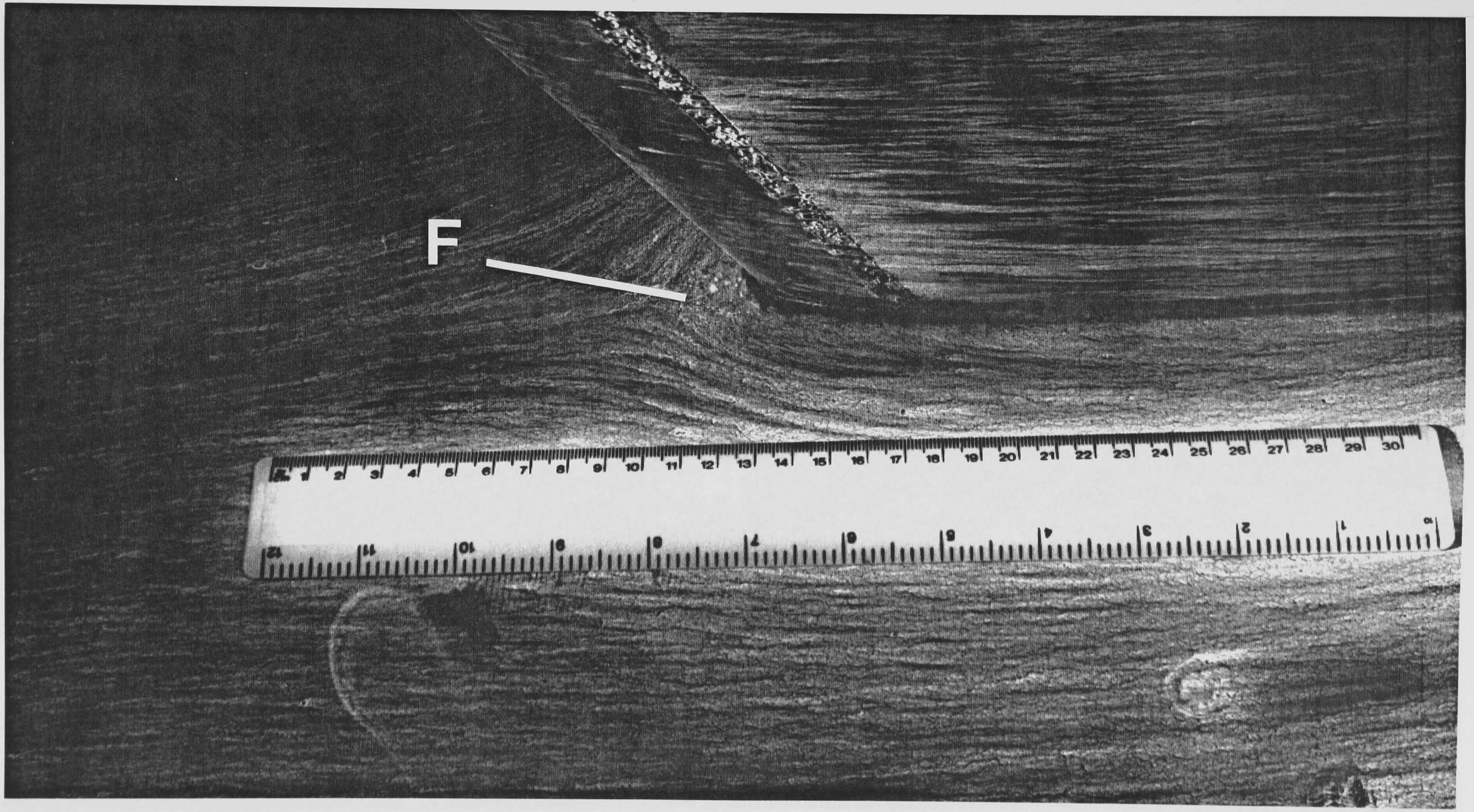

Plate 3(c) Surface oil-flow patterns around the leading edge of the junction at $\alpha = 0°$, viewed from the -Z side of the junction, free stream from left to right.

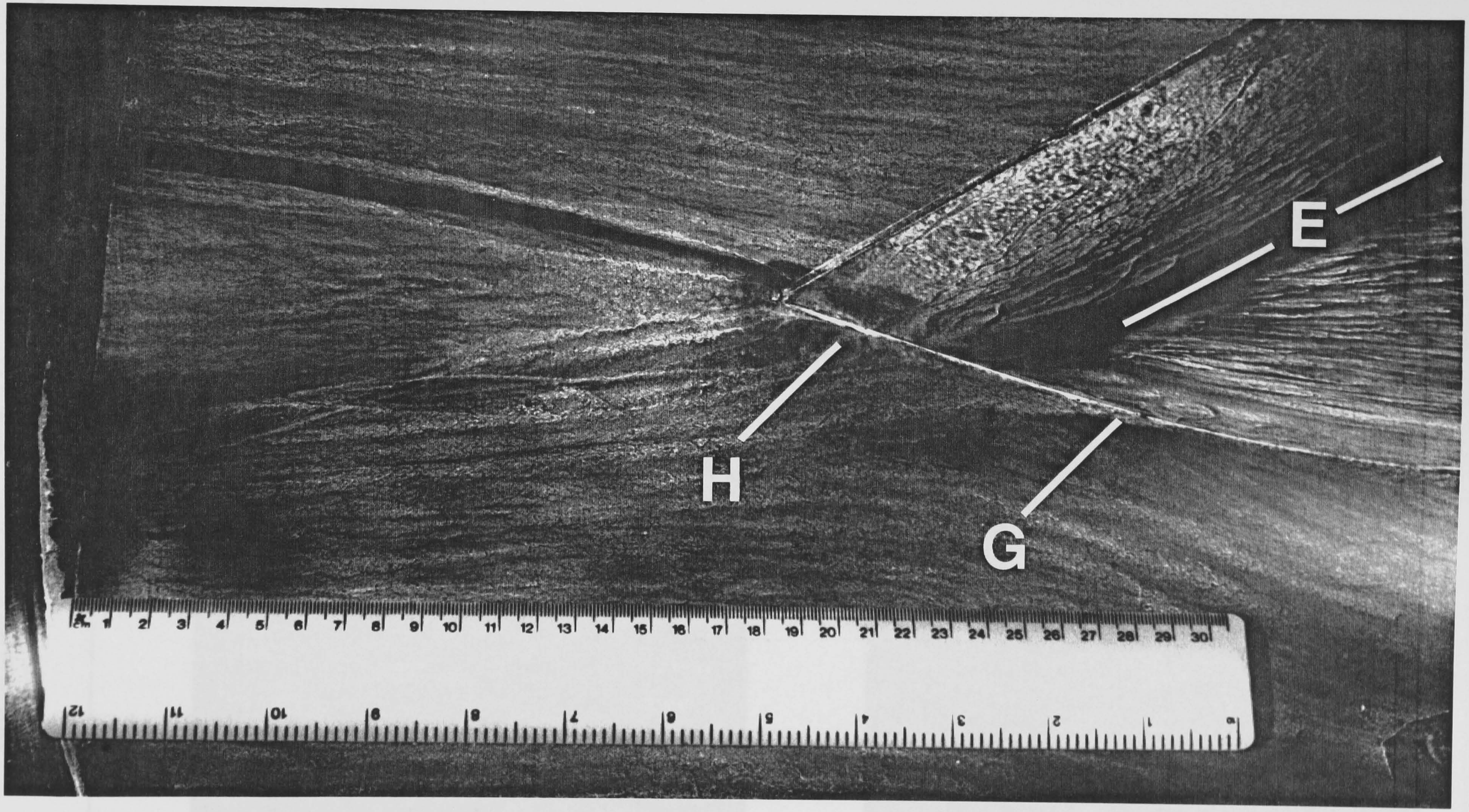

Plate 3(d) Surface oil-flow patterns in the trailing edge region at $\alpha = 0°$, viewed from the +Z side of the junction, free stream from right to left.

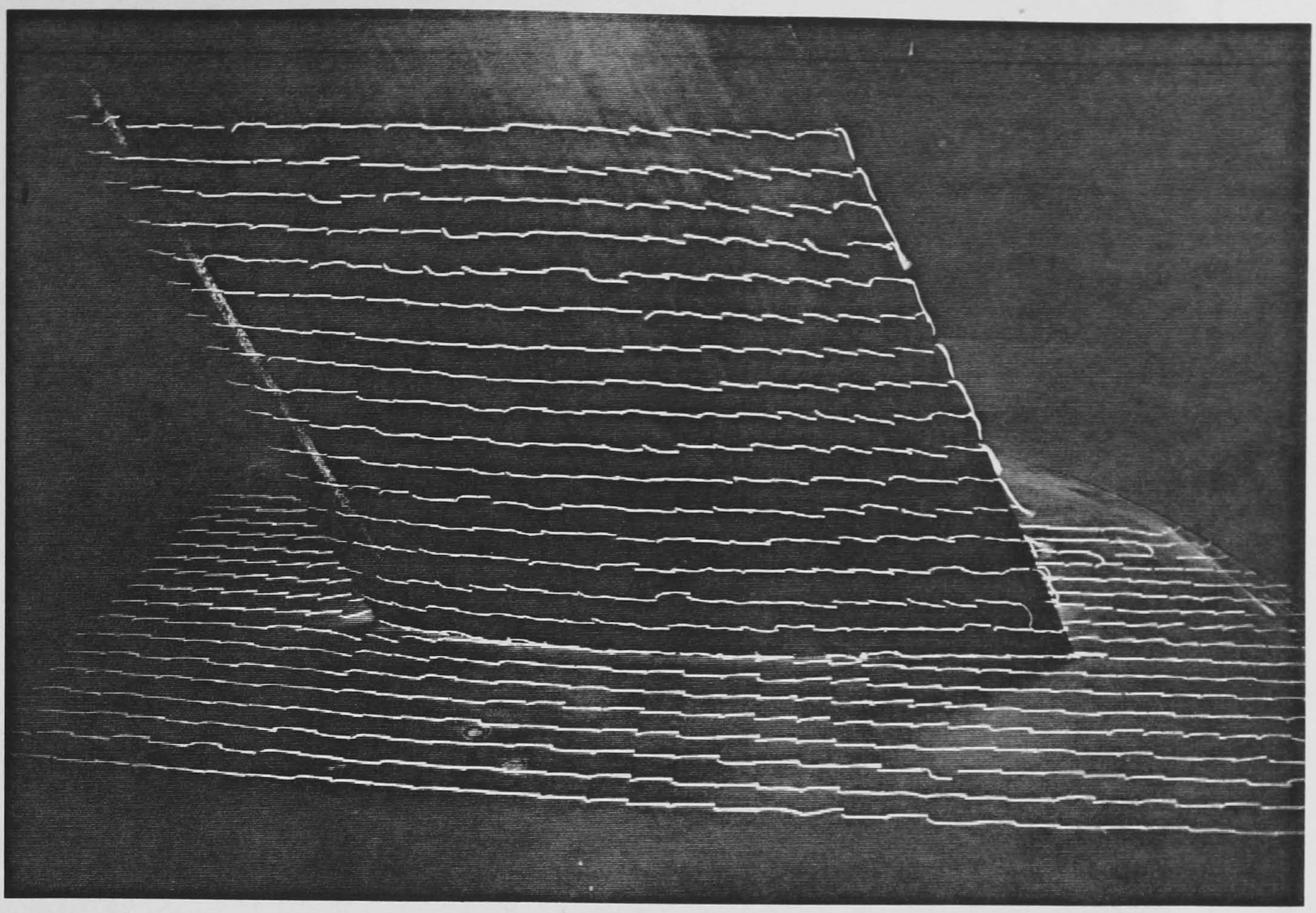

(i)

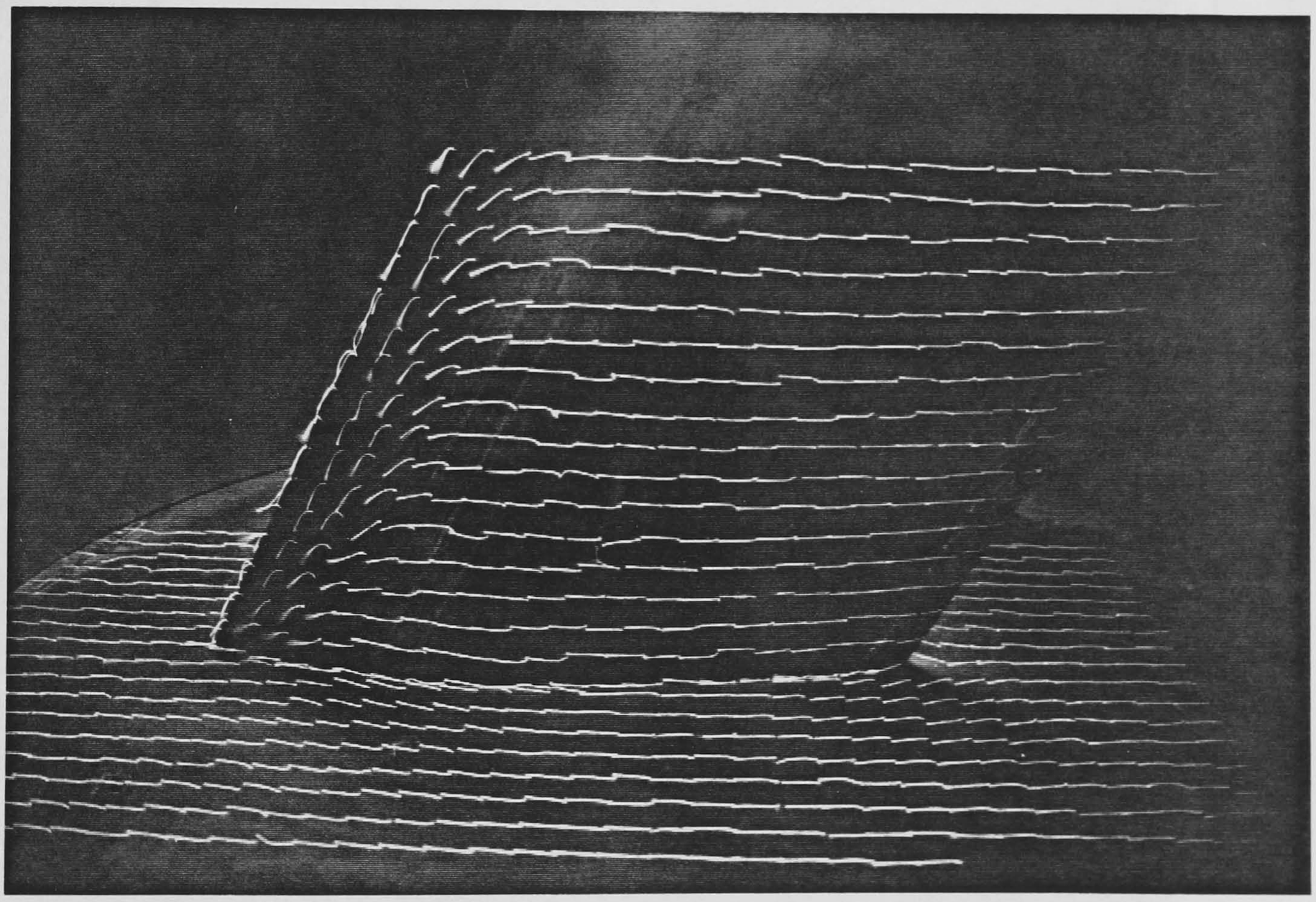

(ii)

Plate 3(e) Tuft behaviour at $\alpha = 0°$ on:
(i) wing lower surface and -Z side of the plate &
(ii) wing upper surface and +Z side of the plate.

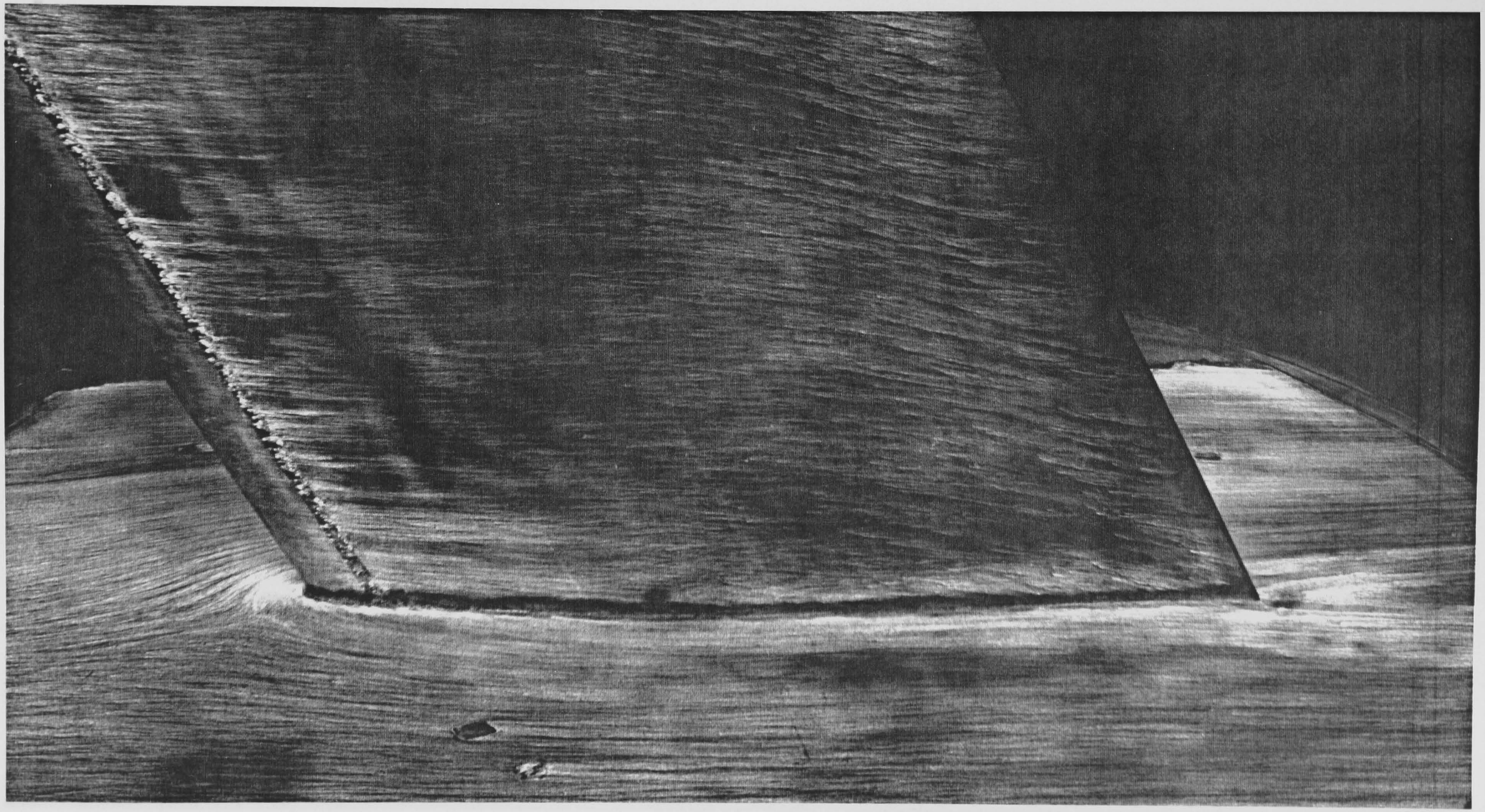

Plate 4(a) Surface oil-flow patterns on the plate and lower surface of the wing at $\alpha = +3°$, free stream from left to right.

Plate 4(b) Surface oil-flow patterns on the plate and upper surface of the wing at $\alpha = +3°$, free stream from right to left.

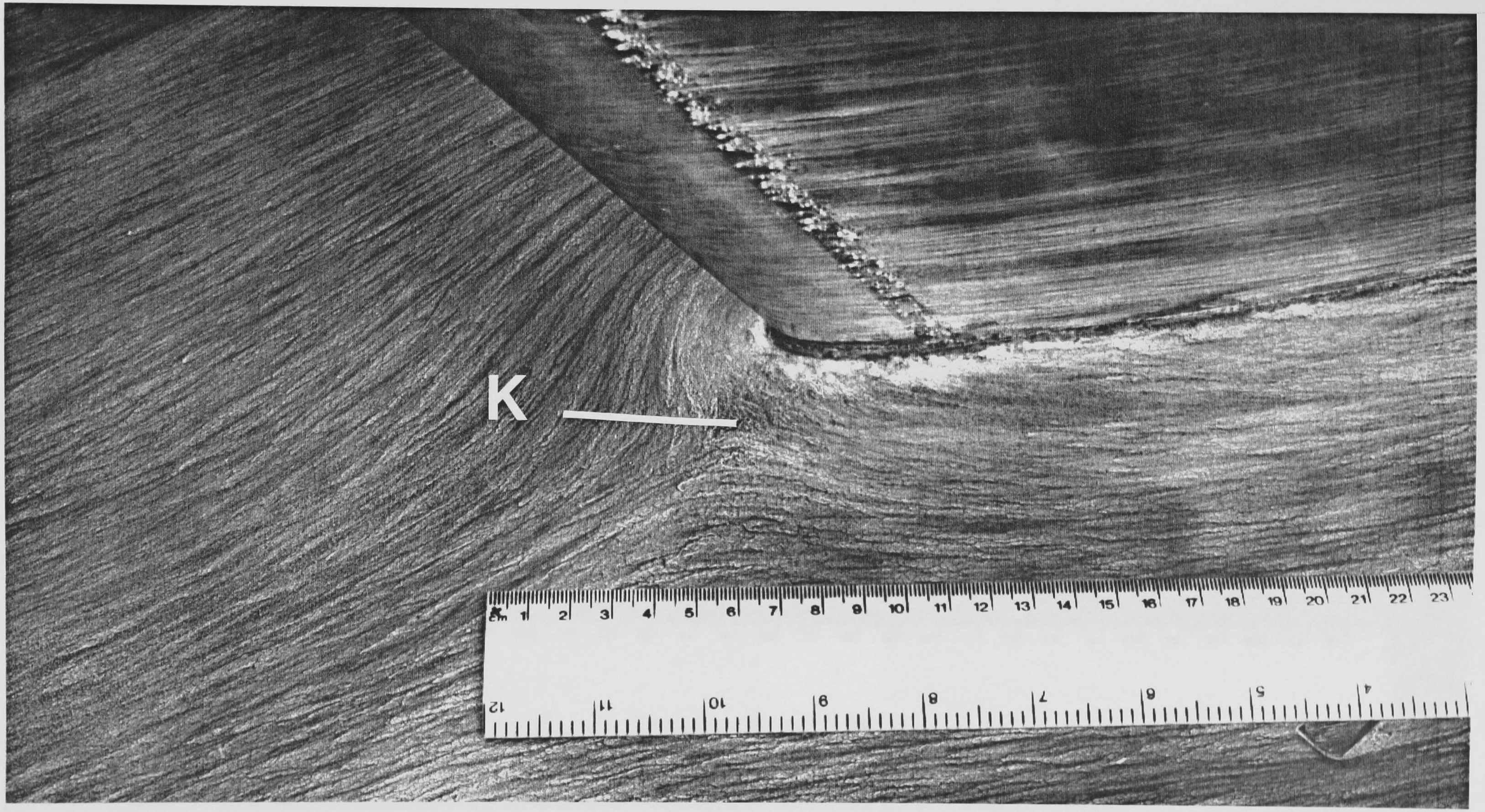

Plate 4(c) Surface oil-flow patterns around the leading edge of the junction at $\alpha = +3°$, viewed from the -Z side of the junction, free stream from left to right.

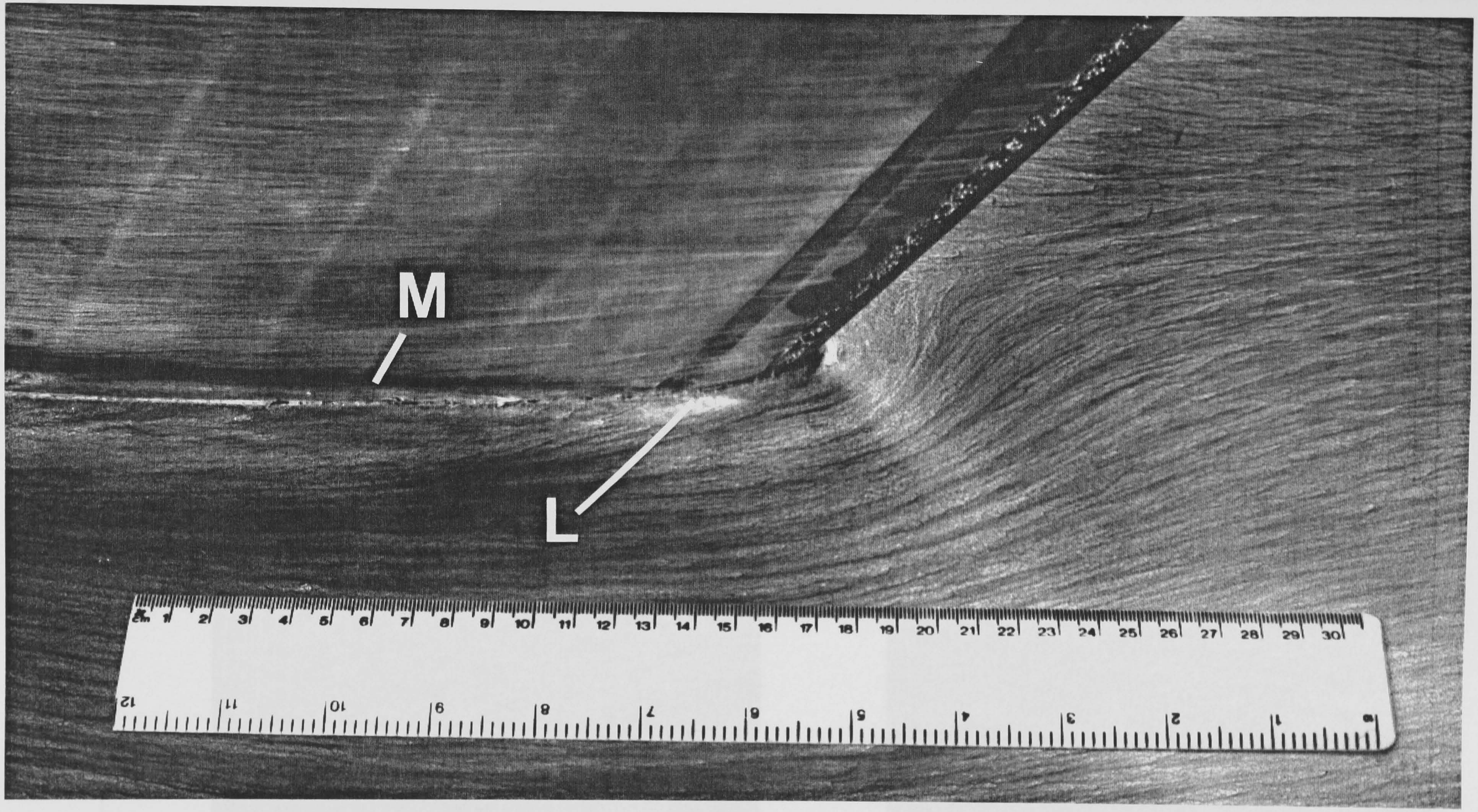

Plate 4(d) Surface oil-flow patterns around the leading edge of the junction at $\alpha = +3°$, viewed from the +Z side of the junction, free stream from right to left.

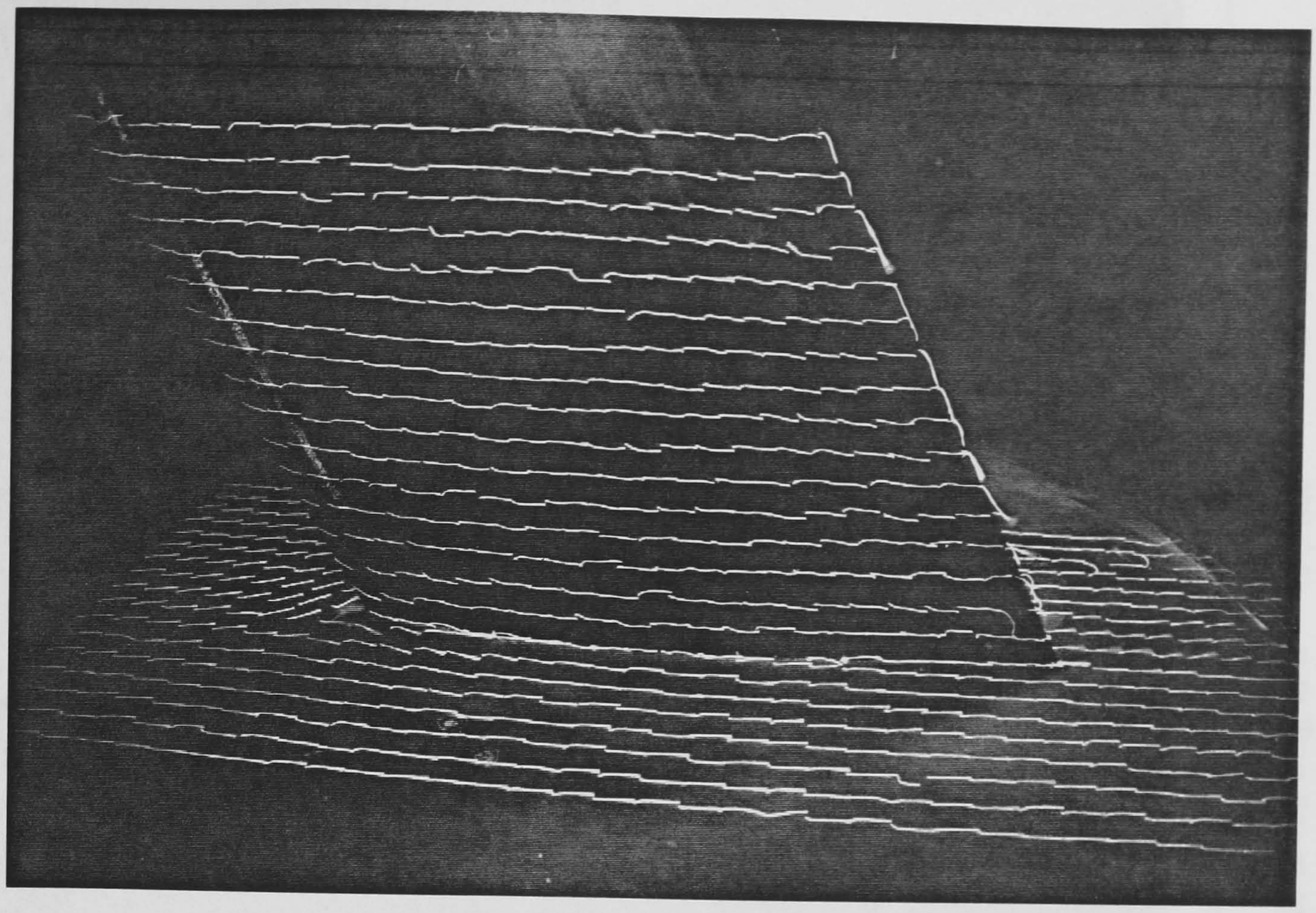

(i)

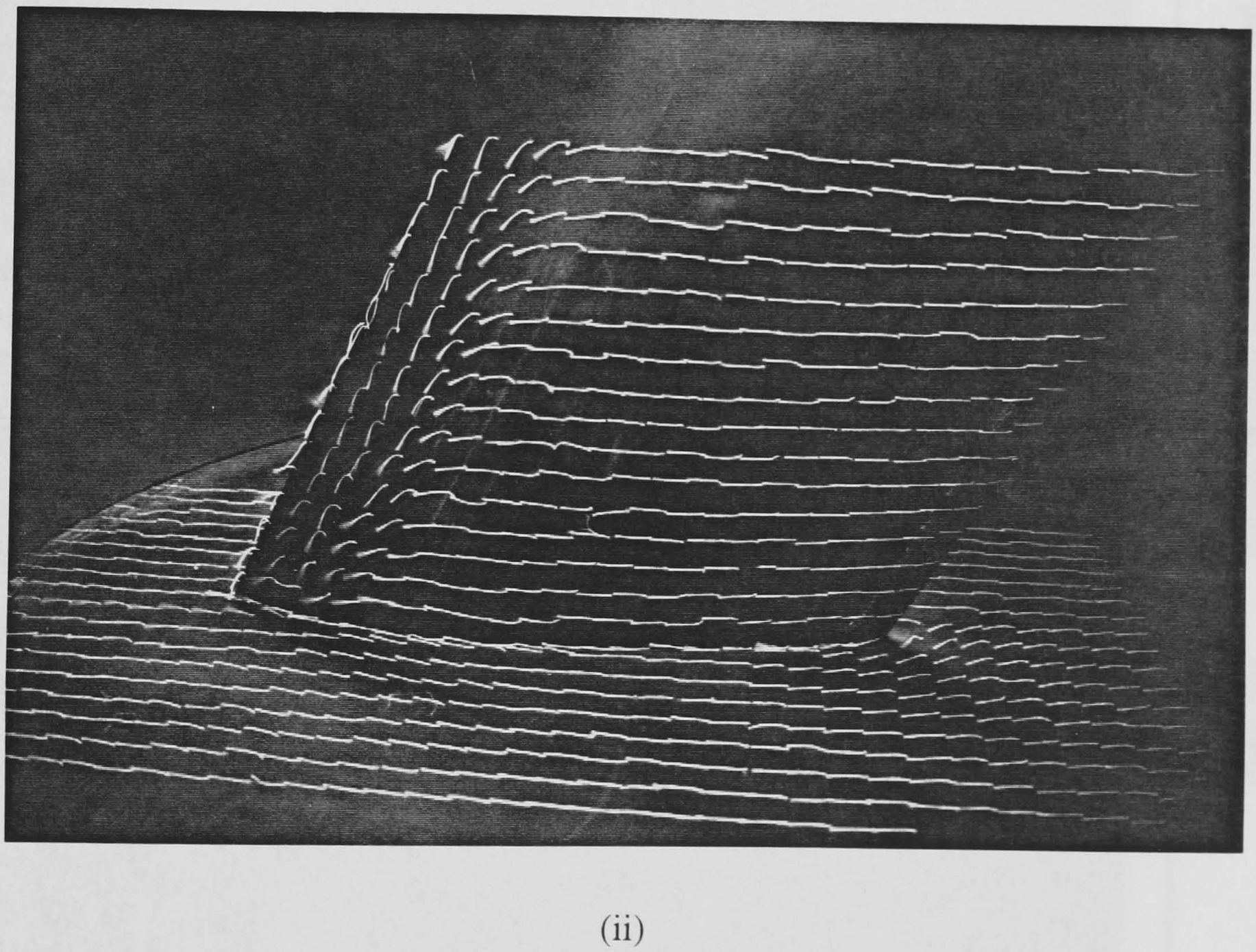

(ii)

Plate 4(e) Tuft behaviour at $\alpha = +3°$ on:
(i) wing lower surface and $-Z$ side of the plate &
(ii) wing upper surface and $+Z$ side of the plate.

Plate 5(a) Surface oil-flow patterns on the plate and lower surface of the wing at $\alpha = +6°$, free stream from left to right.

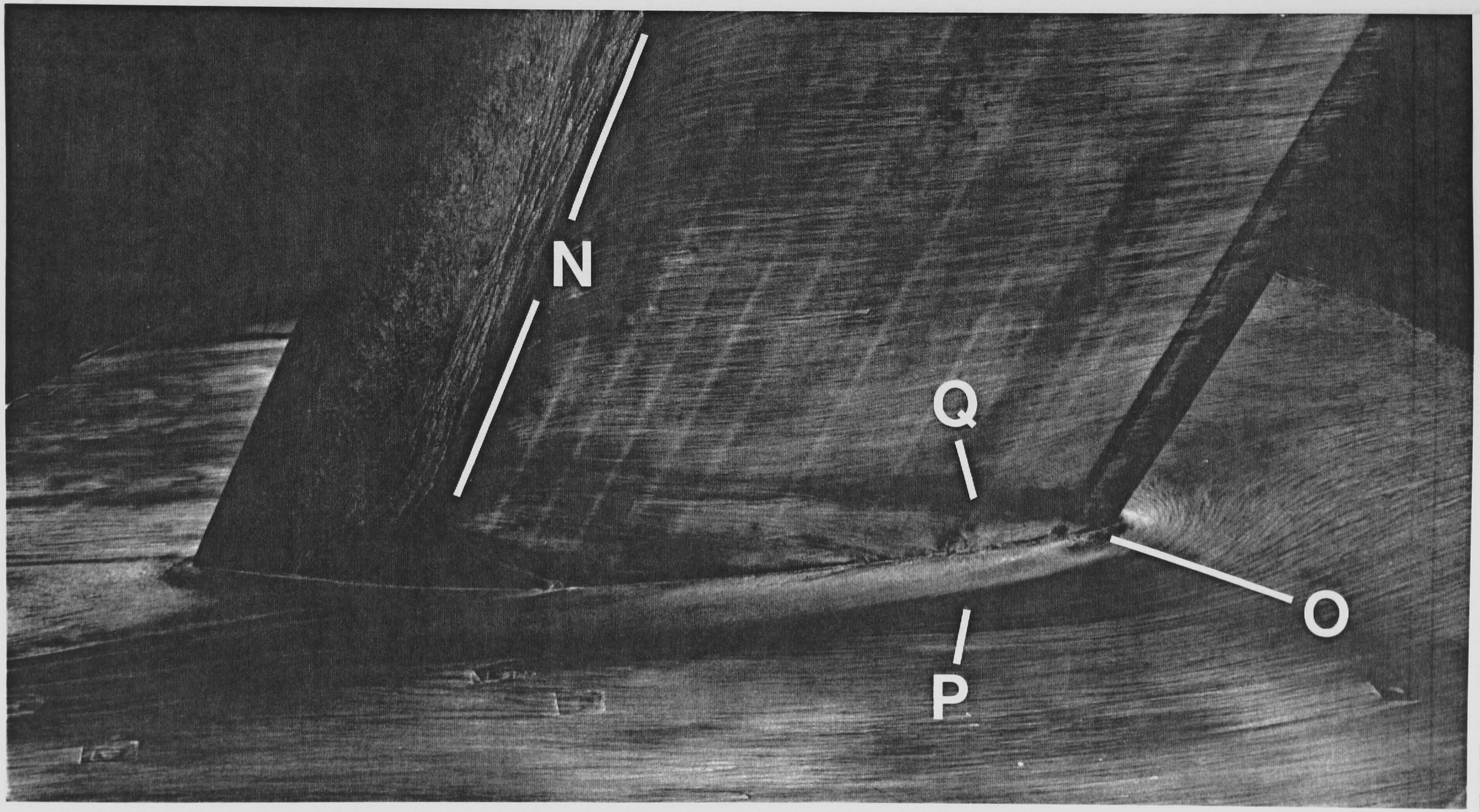

Plate 5(b) Surface oil-flow patterns on the plate and upper surface of the wing at $\alpha = +6°$, free stream from right to left.

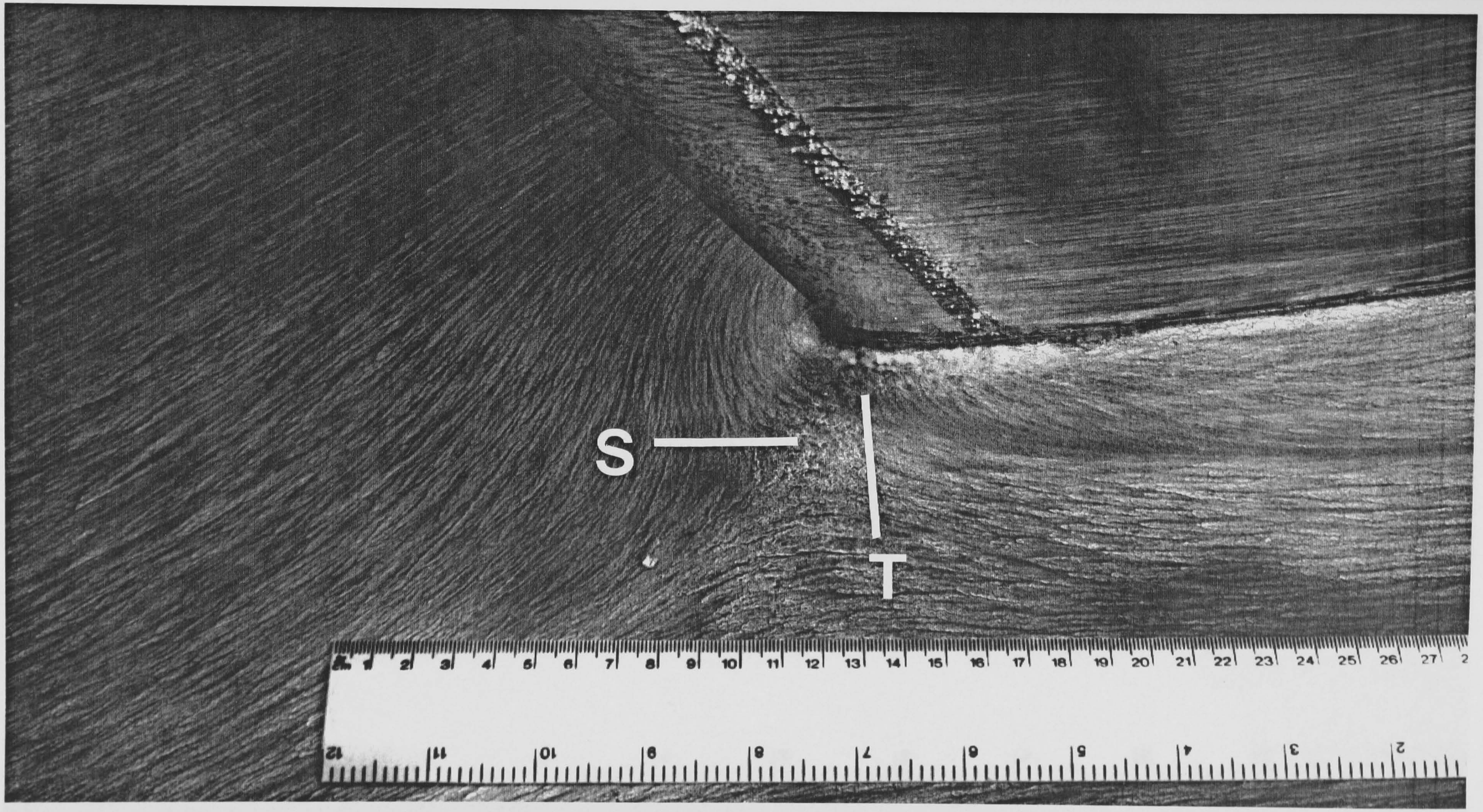

Plate 5(c) Surface oil-flow patterns around the leading edge of the junction at $\alpha = +6°$, viewed from the Z side of the junction, free stream from left to right.

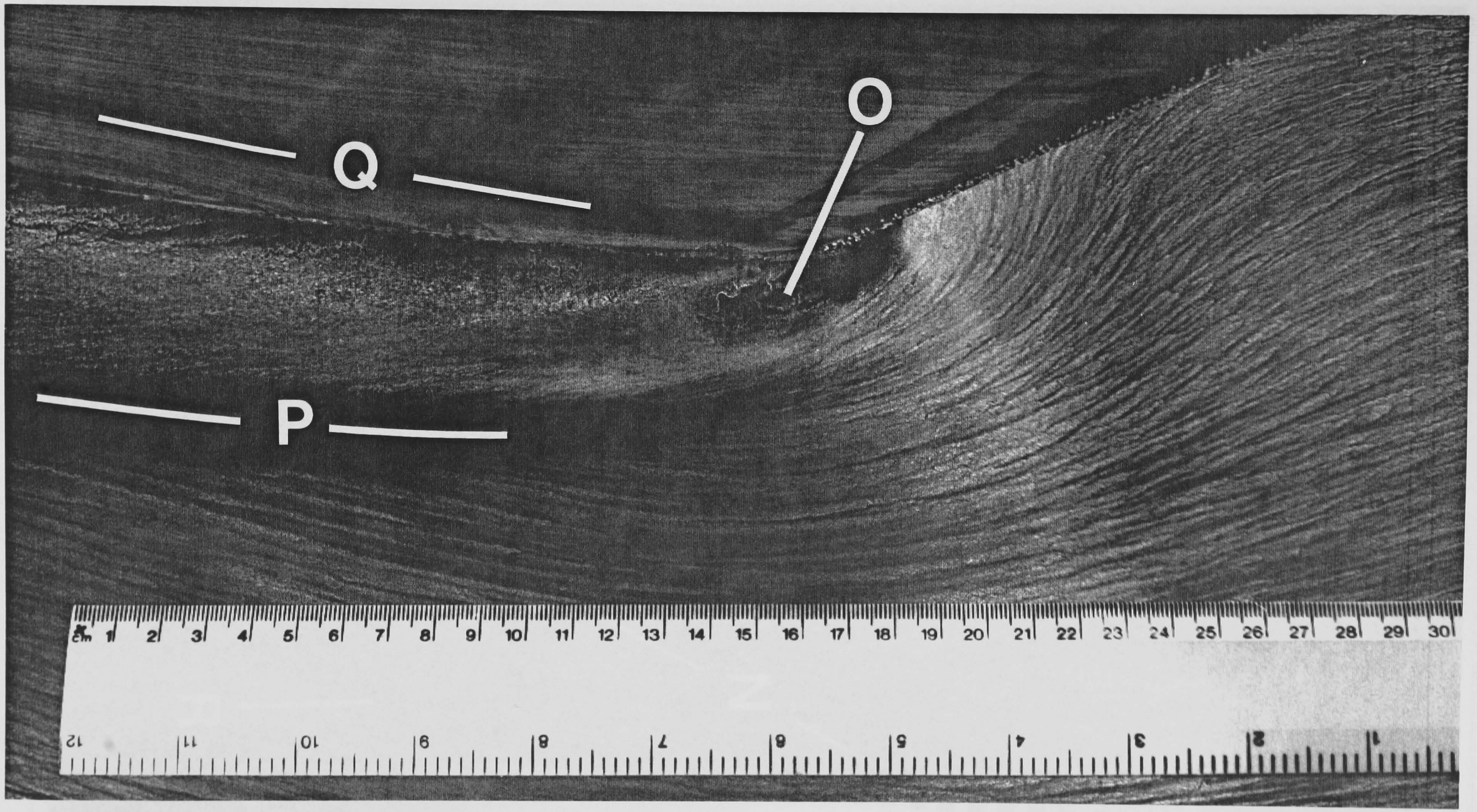

Plate 5(d) Surface oil-flow patterns around the leading edge of the junction at $\alpha = +6°$, viewed from the +Z side of the junction, free stream from right to left.

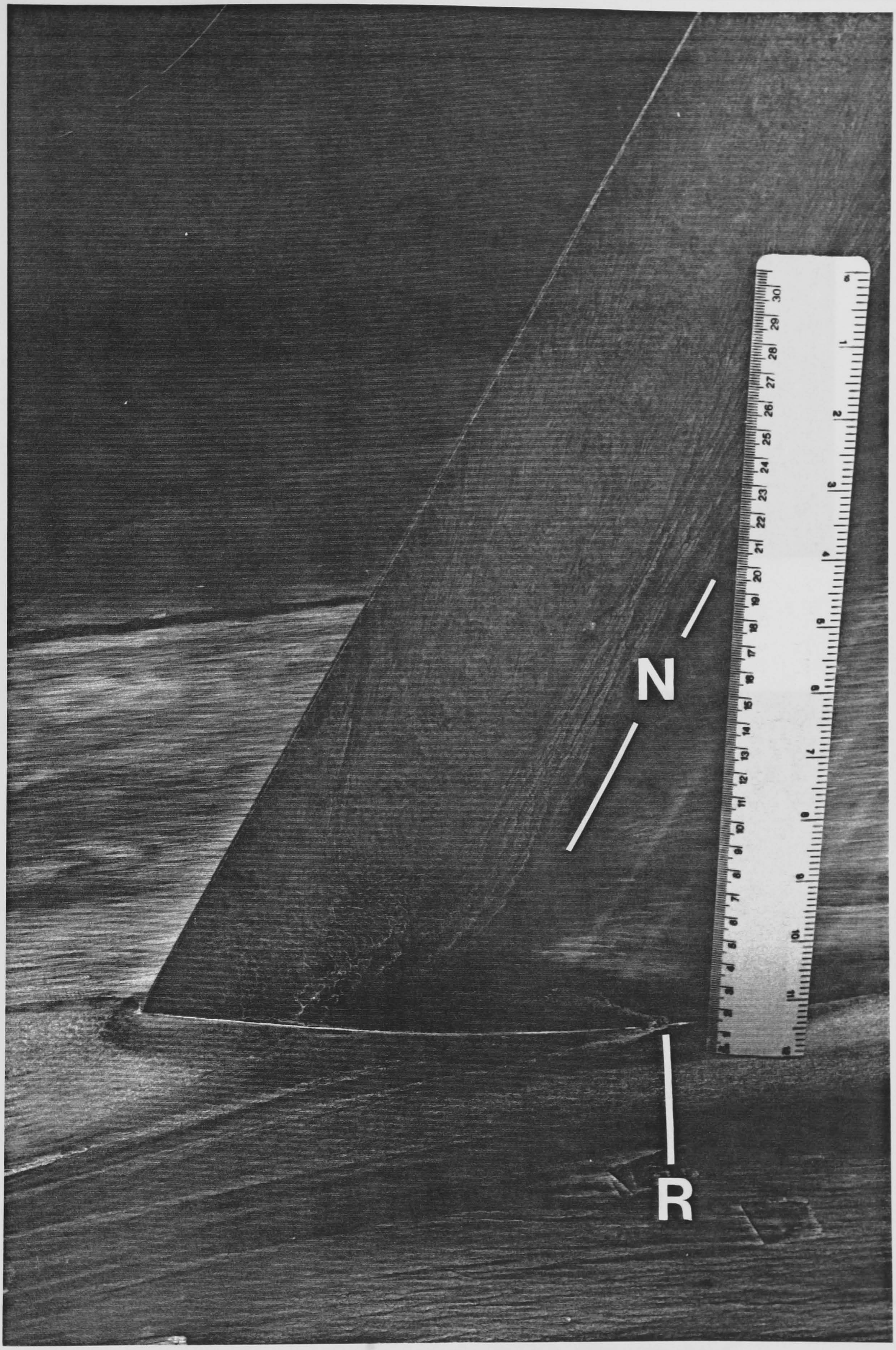

Plate 5(e) Surface oil-flow patterns in the trailing-edge region of the junction, at $\alpha = +6°$, viewed from the +Z side of the junction, free stream from right to left.

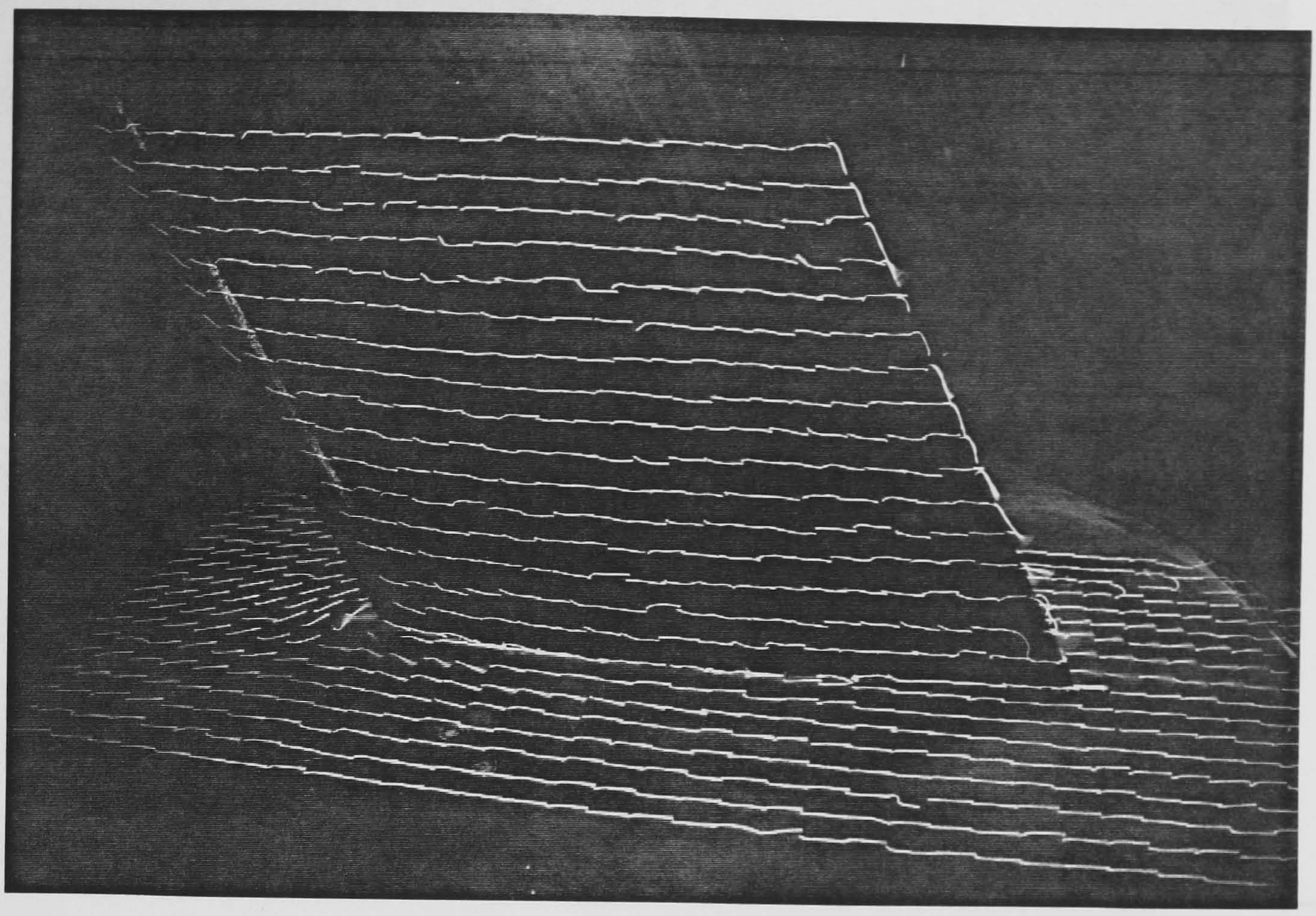

(i)

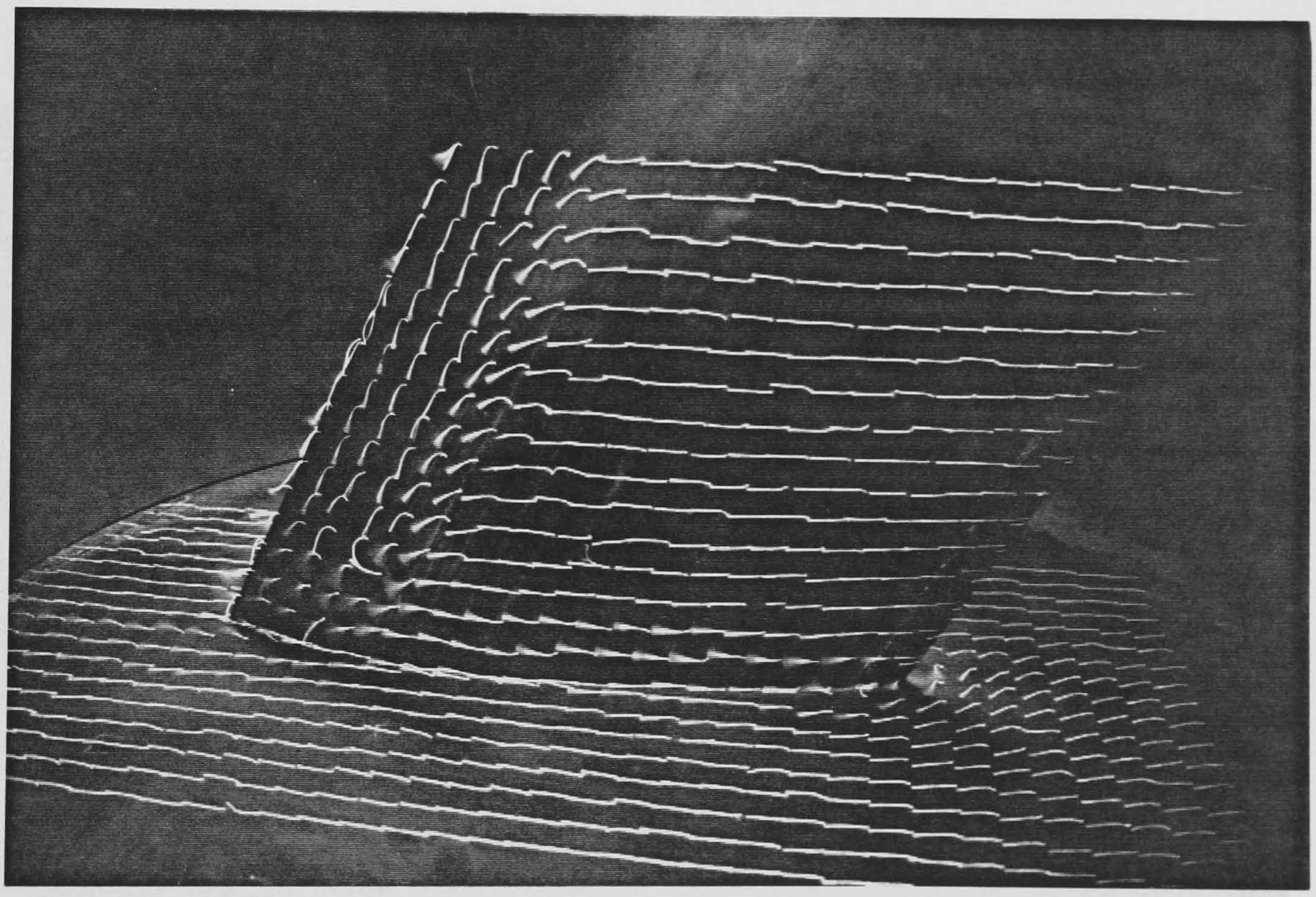

(ii)

Plate 5(f) Tuft behaviour at $\alpha = +6°$ on:
(i) wing lower surface and $-Z$ side of the plate &
(ii) wing upper surface and $+Z$ side of the plate.

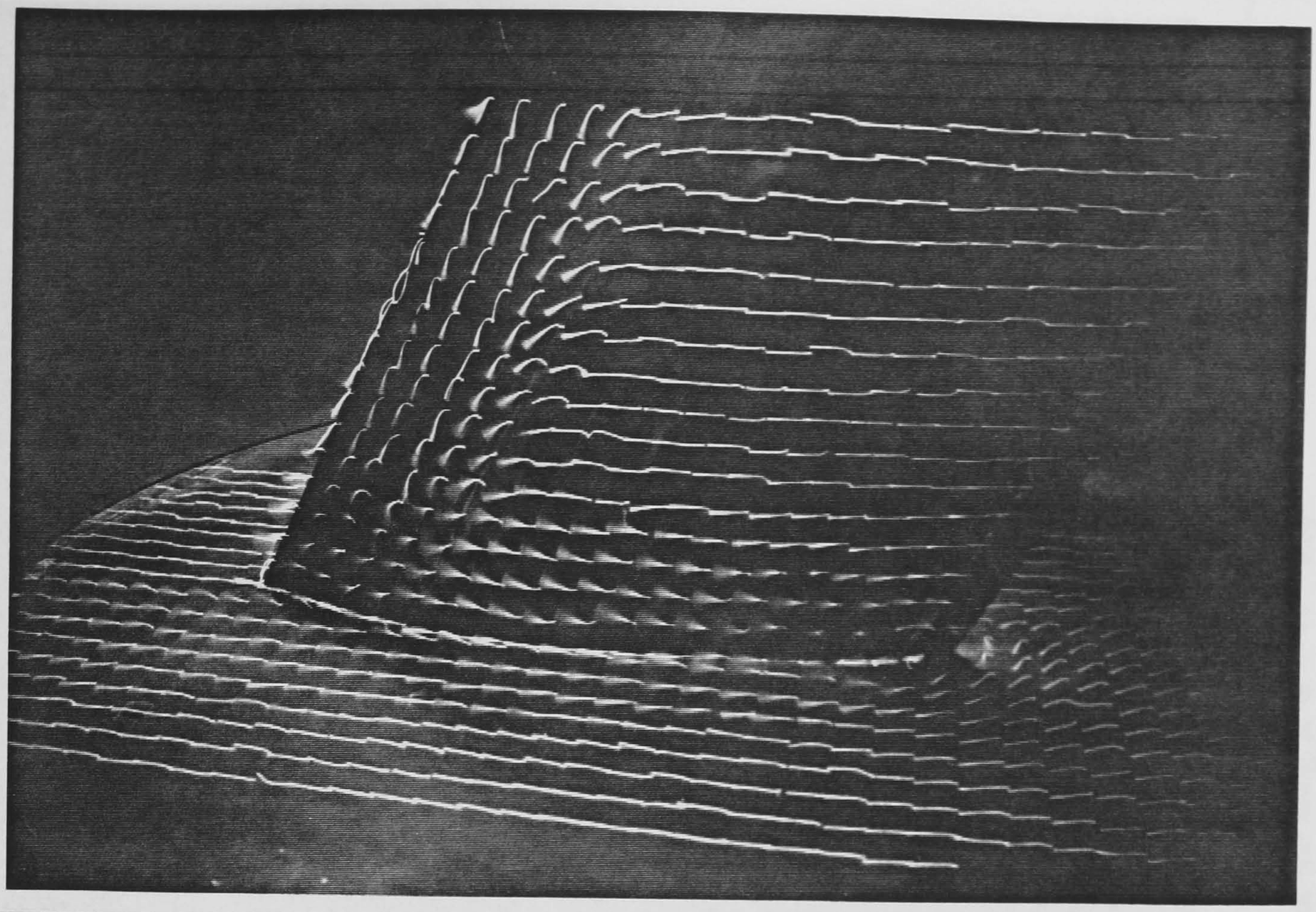

Plate 6 Tuft behaviour on the upper surface of the wing and +Z side of the plate at $\alpha = +7°$.

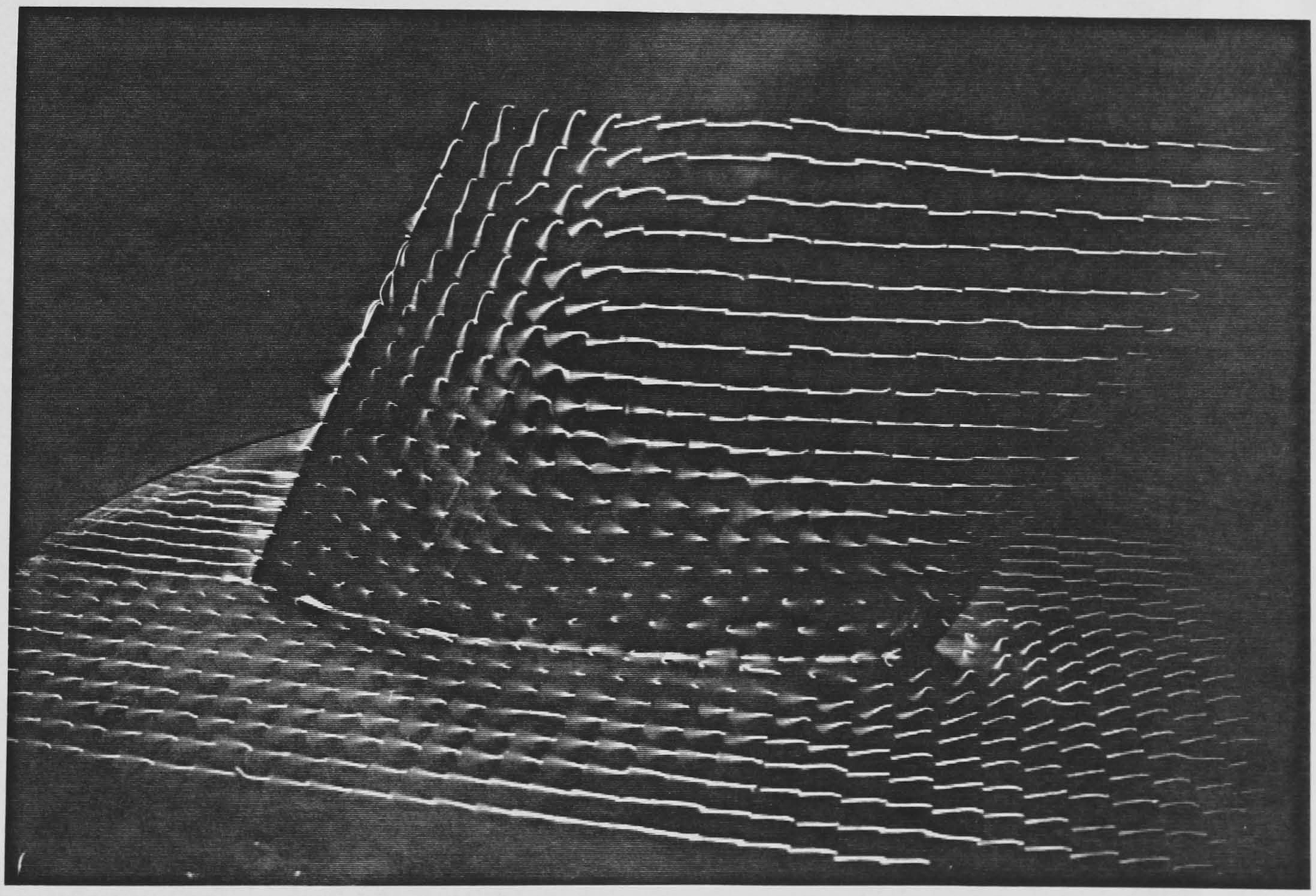

Plate 7 Tuft behaviour on the upper surface of the wing and +Z side of the plate at $\alpha = +8°$.

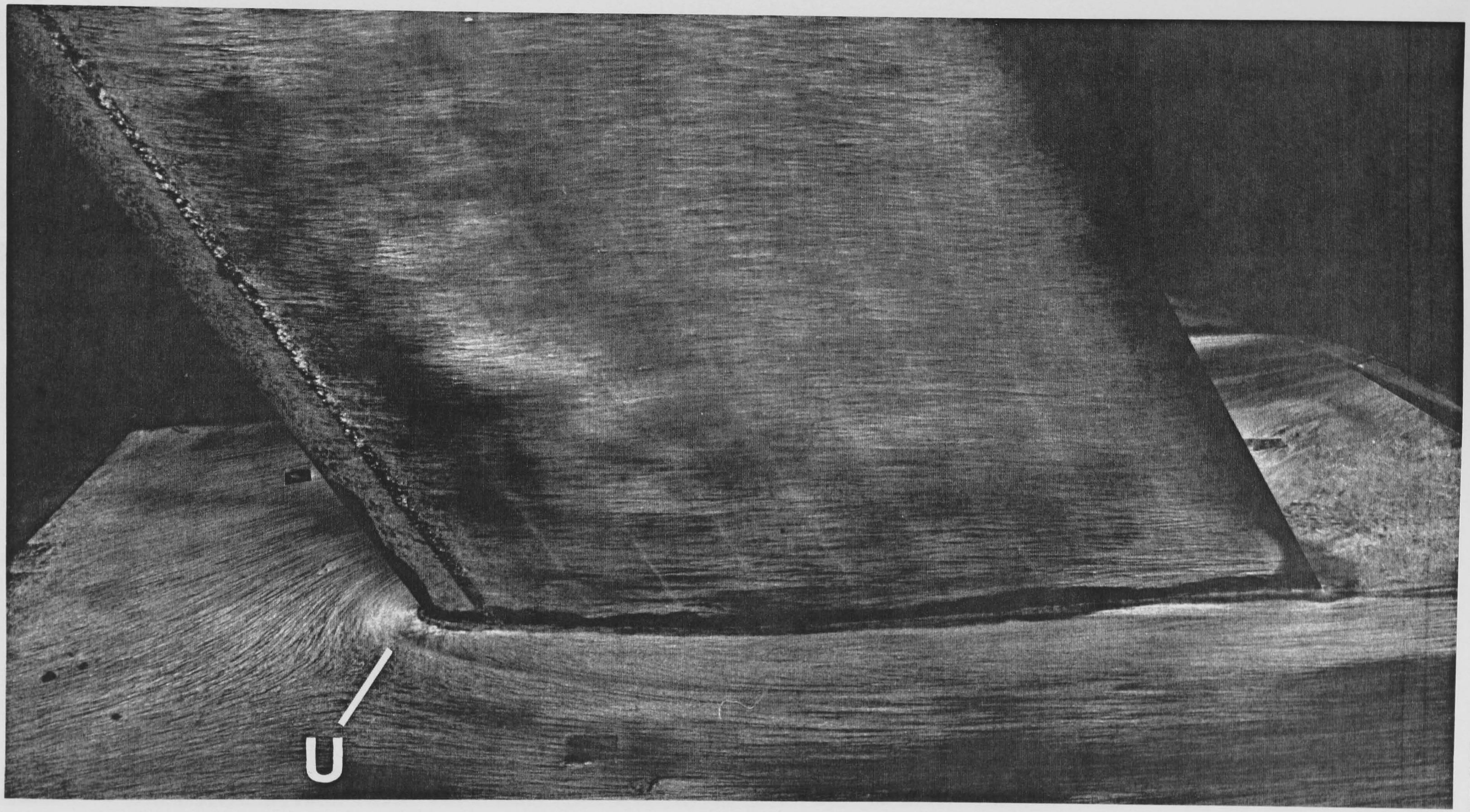

Plate 8(a) Surface oil-flow patterns on the plate and lower surface of the wing at $\alpha = +9°$, free stream from left to right.

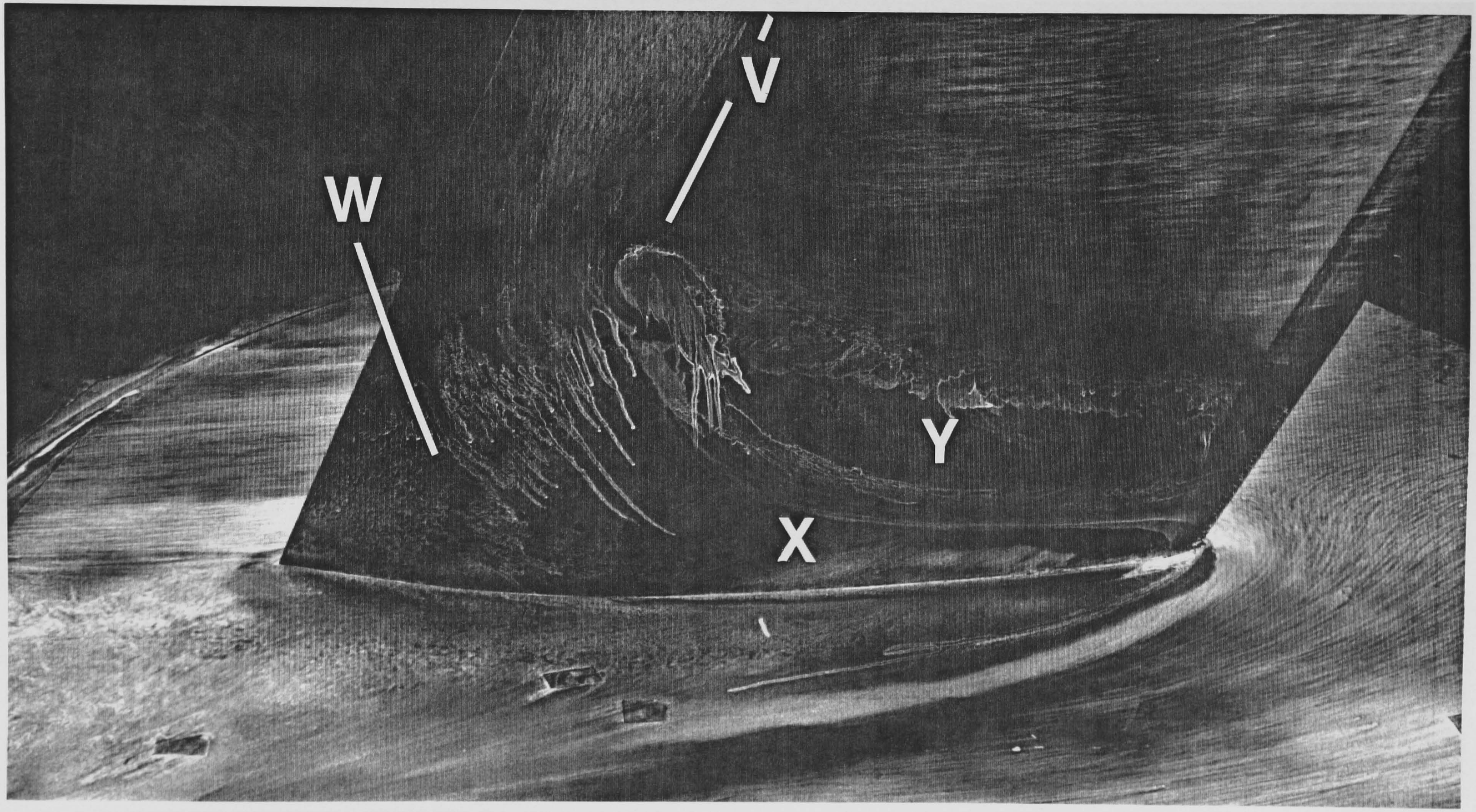

Plate 8(b) Surface oil-flow patterns on the plate and upper surface of the wing at $\alpha = +9°$, free stream from right to left.

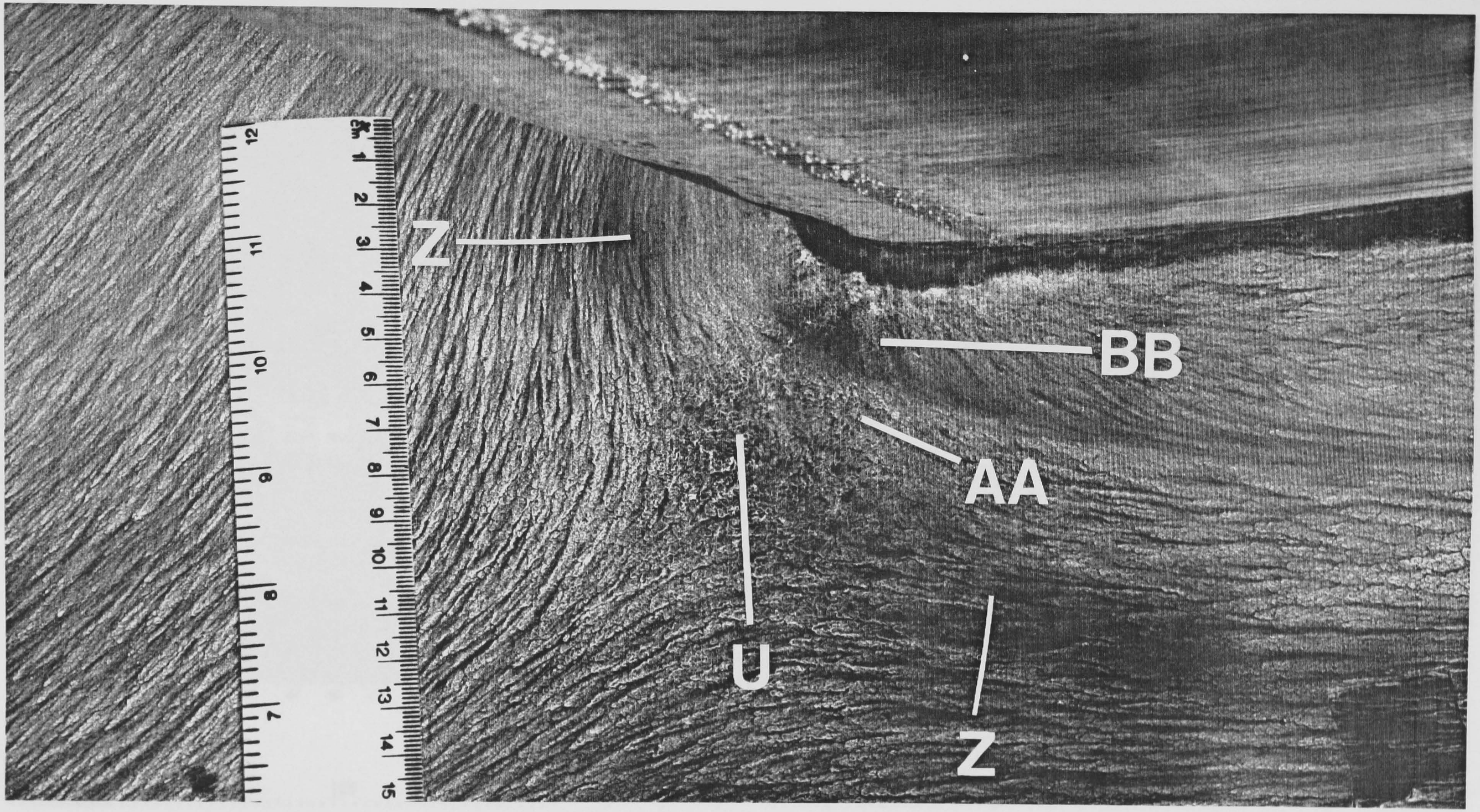

Plate 8(c) Surface oil-flow patterns around the leading edge of the junction at $\alpha = +9°$, viewed from the -Z side of the junction, free stream from left to right.

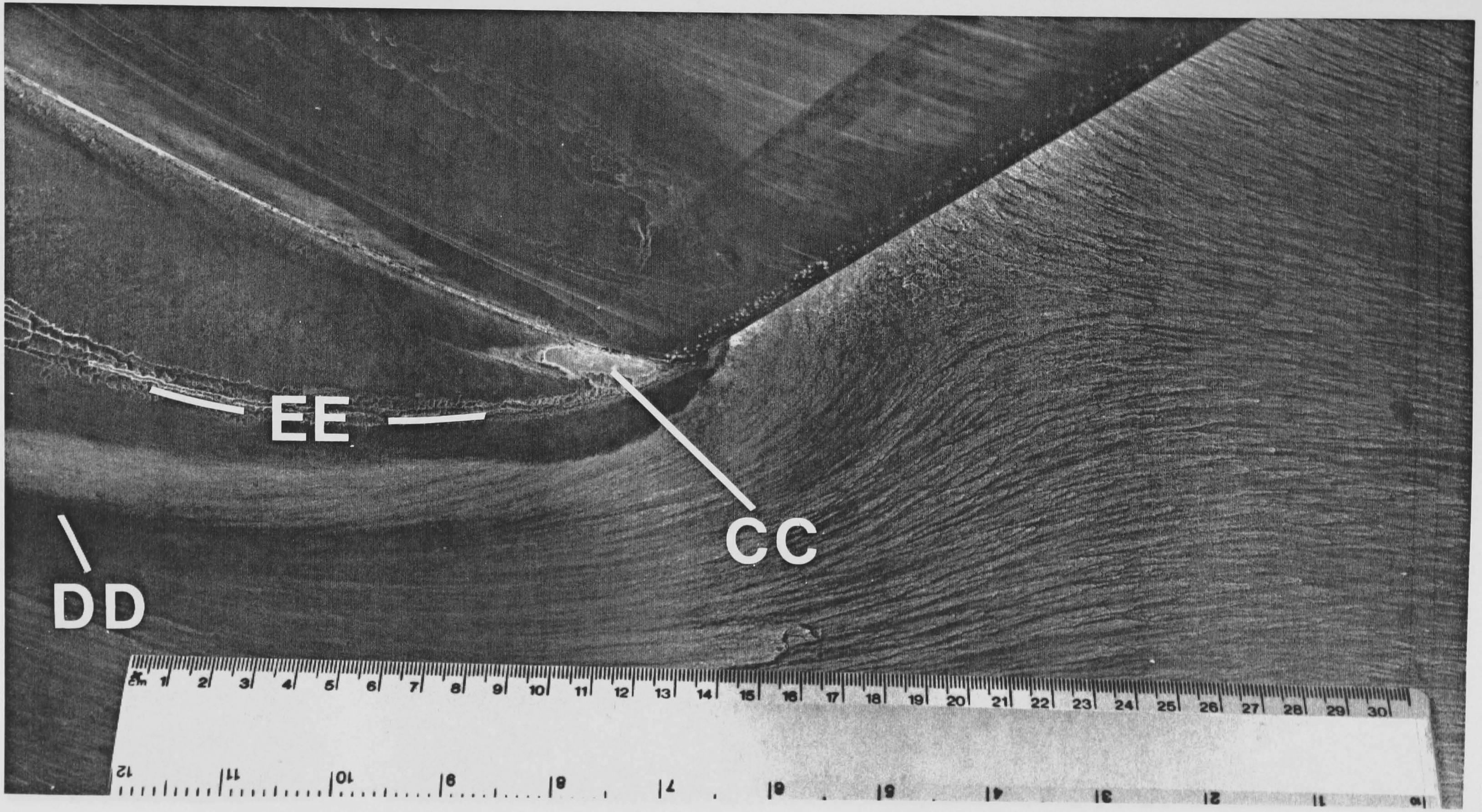

Plate 8(d) Surface oil-flow patterns around the leading edge of the junction at $\alpha = +9°$, viewed from the +Z side of the junction, free stream from right to left.

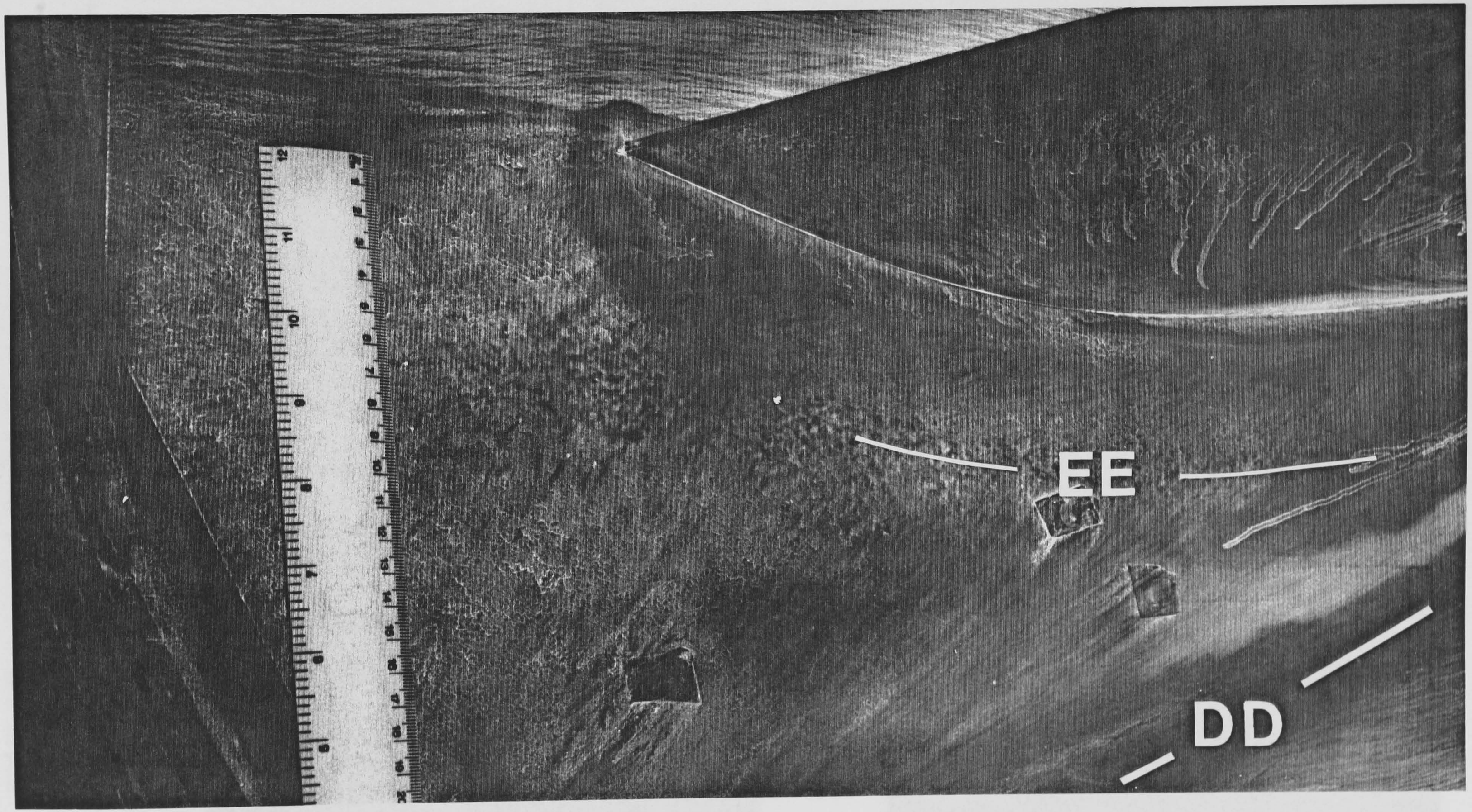

Plate 8(e) Surface oil-flow patterns on the plate in the trailing-edge region, at $\alpha = +9°$, viewed from the +Z side of the junction, free stream from right to left.

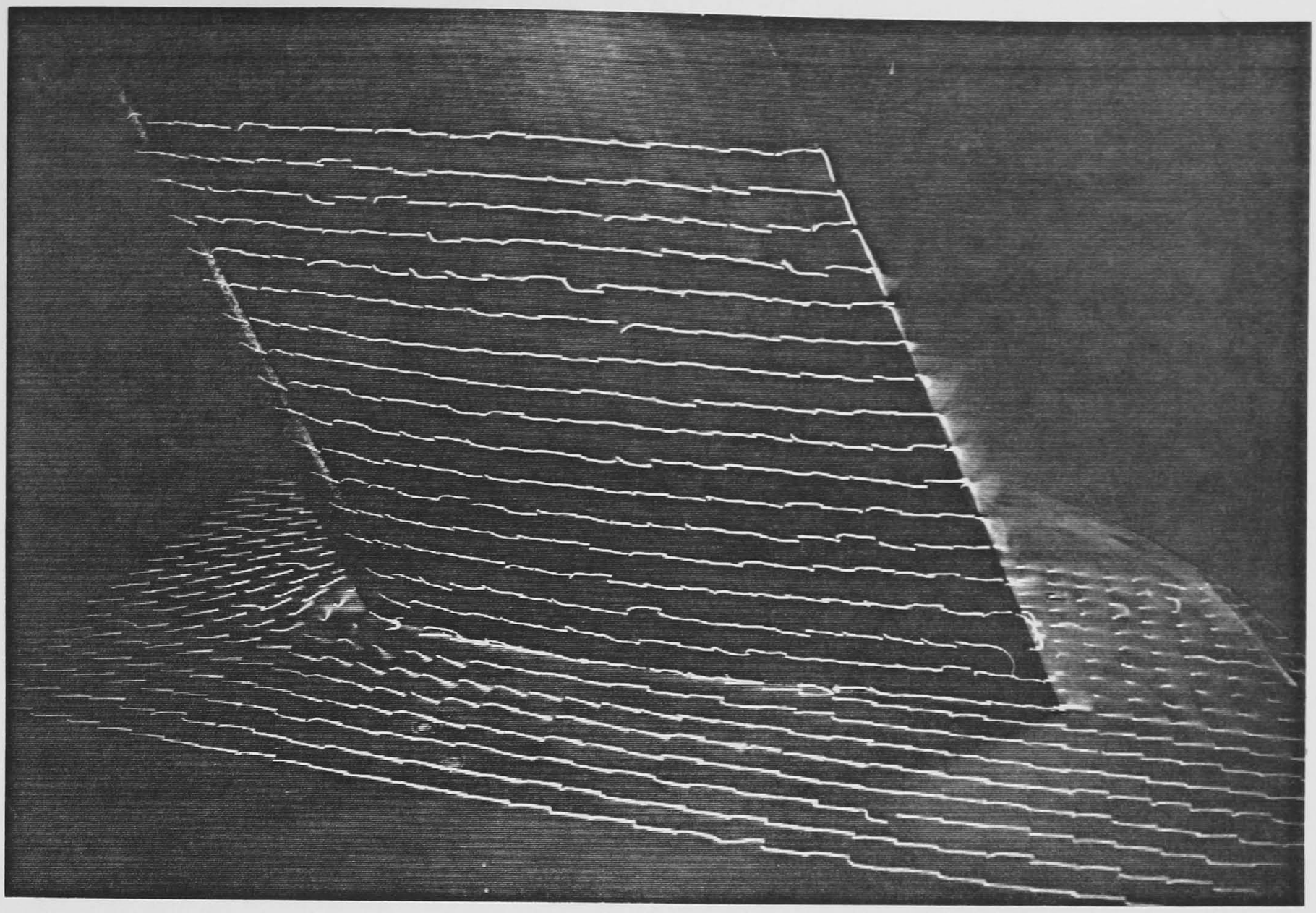

(i)

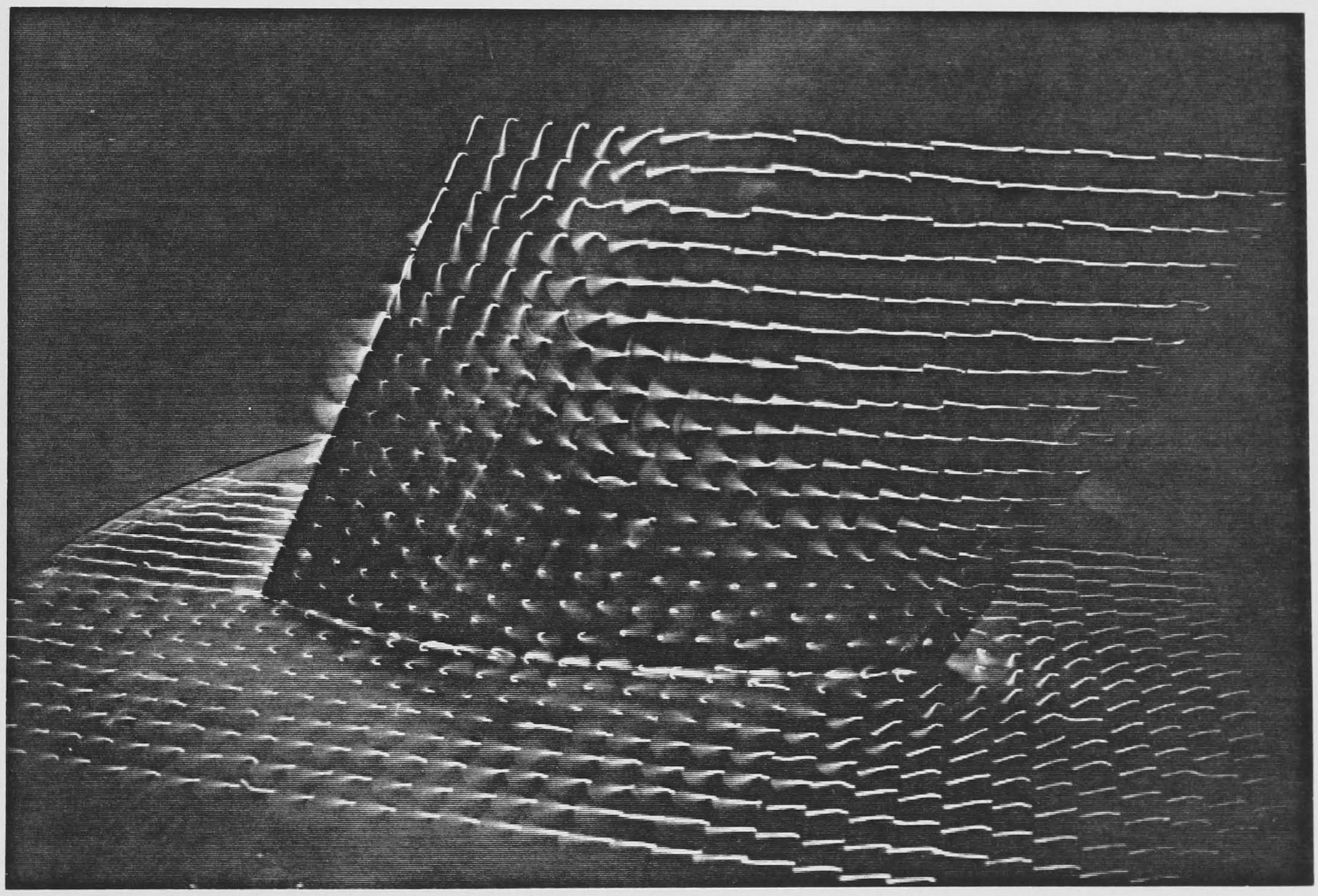

(ii)

Plate 8(f) Tuft behaviour at $\alpha = +9°$ on:
(i) wing lower surface and $-Z$ side of the plate &
(ii) wing upper surface and $+Z$ side of the plate.